

# **Intrazeolite Chemistry**



# Intrazeolite Chemistry

**Galen D. Stucky, EDITOR**

*E. I. du Pont de Nemours and Company*

**Francis G. Dwyer, EDITOR**

*Mobil Research and Development  
Corporation*

Based on a symposium sponsored  
by the Division of Inorganic Chemistry  
at the 184th Meeting  
of the American Chemical Society,  
Kansas City, Missouri,  
September 12–17, 1982  
and a symposium sponsored  
by the Division of Petroleum Chemistry  
at the 183rd Meeting  
of the American Chemical Society,  
Las Vegas, Nevada,  
March 28–April 2, 1982

A C S   S Y M P O S I U M   S E R I E S **218**

**AMERICAN CHEMICAL SOCIETY**  
**WASHINGTON, D.C.      1983**



**Library of Congress Cataloging in Publication Data**

Intrazeolite chemistry.

(ACS symposium series, ISSN 0097-6156; 218)

Includes bibliographies and index.

1. Zeolites—Congresses.

I. Stucky, Galen D., 1936- . II. Dwyer, Francis G., 1931- . III. American Chemical Society. Division of Inorganic Chemistry. IV. American Chemical Society. Division of Petroleum Chemistry. V. Series.

TP159.M6I57 1983 666.86 83-3818  
ISBN 0-8412-0774-7

Copyright © 1983

American Chemical Society

All Rights Reserved. The appearance of the code at the bottom of the first page of each article in this volume indicates the copyright owner's consent that reprographic copies of the article may be made for personal or internal use or for the personal or internal use of specific clients. This consent is given on the condition, however, that the copier pay the stated per copy fee through the Copyright Clearance Center, Inc. for copying beyond that permitted by Sections 107 or 108 of the U.S. Copyright Law. This consent does not extend to copying or transmission by any means—graphic or electronic—for any other purpose, such as for general distribution, for advertising or promotional purposes, for creating new collective work, for resale, or for information storage and retrieval systems. The copying fee for each chapter is indicated in the code at the bottom of the first page of the chapter.

The citation of trade names and/or names of manufacturers in this publication is not to be construed as an endorsement or as approval by ACS of the commercial products or services referenced herein; nor should the mere reference herein to any drawing, specification, chemical process, or other data be regarded as a license or as a conveyance of any right or permission, to the holder, reader, or any other person or corporation, to manufacture, reproduce, use, or sell any patented invention or copyrighted work that may in any way be related thereto.

PRINTED IN THE UNITED STATES OF AMERICA

**American Chemical  
Society Library**

1155 16th St. N. W.

In Intrazeolite Chemistry: Stucky, G., et al.;

ACS Symposium Series, American Chemical Society, Washington, DC, 1983.

# ACS Symposium Series

**M. Joan Comstock, *Series Editor***

## *Advisory Board*

David L. Allara

Robert Baker

Donald D. Dollberg

Brian M. Harney

W. Jeffrey Howe

Herbert D. Kaesz

Marvin Margoshes

Donald E. Moreland

Robert Ory

Geoffrey D. Parfitt

Theodore Provder

Charles N. Satterfield

Dennis Schuetzle

Davis L. Temple, Jr.

Charles S. Tuesday

C. Grant Willson

## FOREWORD

The ACS SYMPOSIUM SERIES was founded in 1974 to provide a medium for publishing symposia quickly in book form. The format of the Series parallels that of the continuing ADVANCES IN CHEMISTRY SERIES except that in order to save time the papers are not typeset but are reproduced as they are submitted by the authors in camera-ready form. Papers are reviewed under the supervision of the Editors with the assistance of the Series Advisory Board and are selected to maintain the integrity of the symposia; however, verbatim reproductions of previously published papers are not accepted. Both reviews and reports of research are acceptable since symposia may embrace both types of presentation.

## PREFACE

**Z**EOLITE AND INTRAZEOLITE CHEMISTRY are the subjects of two symposia dealing with a dynamic and rapidly growing field in which a broad range of new chemistry, from solid state to organic, is being explored. Zeolites introduce both unusual activity and selectivity into heterogeneous adsorption and catalytic processes and are the inorganic analogues of enzymes in living systems.

The 27 papers in this volume present a cross section of synthesis, characterization, and chemical studies by academic and industrial researchers. Although zeolite research activity has been predominantly industrially based, increasing effort and results are now emanating in academic laboratories. The synergism and mutual stimulation of these efforts can be expected to increase the quality and quantity of current and future research involving microporous crystalline molecular sieves.

The search for solid state materials that have all or a large portion of their framework atoms available as adsorption sites is leading to new classes of substances that require a redefinition of the word "zeolite." The etymology of zeolite begins with Greek words "zein" and "lithos," which have been condensed to the Swedish "zeolit" or "boiling stone." J. V. Smith in the *American Mineral Society Spec. Paper* (1963) expanded this description to "an aluminosilicate framework structure enclosing cavities occupied by large ions and water molecules, both of which have considerable freedom of movement, permitting ion exchange and reversible dehydration" with formula  $M_{x/n}[(AlO_2)_x(SiO_2)_y]mH_2O$ . Cartraud, Cointot, and Renaud (*J. Chem. Soc.*, 1981) discuss the zeolitic properties of the hexacyanoferrate(II),  $K_2Zn_3[Fe(CN)_6]_2 \cdot XH_2O$ , so that in fact these materials need not contain aluminum, silicon, or oxygen and may be transition metal based. In this book a new class of microporous crystalline inorganic molecular sieves that contain no silicon is described. The scope of future "zeolite" symposia will undoubtedly include an increasing number of materials that have framework structures made up of atomic elements from a large portion of the periodic table.

The synthesis of zeolites has long been regarded as an art with procedures and reactants reminiscent of those described by Chaucer for the synthesis of the philosopher's stone.

Unslekked lyme, chalk, and gayre of an ey,  
Poudres dyvers and asshes, dong, and cley . . .

The importance of recognizing and dealing with zeolite synthesis as a kinetic process that involves the isolation of metastable phases is pointed out in this book in a variety of ways. An examination of the extensive scientific and patent literature on zeolite synthesis rapidly convinces one that a lack of understanding of this point has been a major bottleneck in the characterization of zeolite chemical and physical properties. The zeolite properties are defined not only by synthesis parameters, but also by treatment following synthesis; for example, most synthesis treatment of zeolites with fluorine can be used to modify hydrophobicity drastically and increase catalytic activity for *n*-butane cracking.

The second section of the book is concerned with characterization. The development and use of powerful, new analytical techniques, such as high-resolution solid state nuclear magnetic resonance, electron microscopy and microanalysis, and powder neutron diffraction structural analysis have made it possible to define the phase inhomogeneity, lattice defects, and framework disorder that one would expect from metastable phases. Zeolite A is the simplest zeolite that has been structurally characterized with a Si/Al ratio of 1, the minimum value necessary to satisfy Pauling, Loewenstein, and Dempsey and Olsen's rules. The first structural analysis of zeolite A was reported by Reed and Breck (*J. Amer. Chem. Soc.*, 1956). Differentiation of Si and Al sites is difficult by x-ray analysis and this difficulty, plus the flexibility inherent in the zeolite framework, which is displayed on dehydration or supported ion migration, results in a structural problem that was not resolved for over 25 years by numerous investigators. The symposia upon which this book is based were the first in which a mutually satisfactory solution to the structure of zeolite A was reported. The resolution of the structure of zeolite A has pointed out the usefulness of high-resolution solid state NMR and of powder neutron diffraction. These studies provide the groundwork for deciphering more complicated zeolite structures and their framework order and/or disorder.

Supported non-framework elements, as well as substituted or doped framework atoms, have been important for zeolite catalyst regeneration. By incorporating metal atoms into a microporous crystalline framework, a local transition state selectivity can be built into the active site of a catalytic process that is not readily attainable in homogeneous catalysis. The use of zeolites for carrying out catalysis with supported transition metal atoms as active sites is just beginning. The local environment of transition metal elements as a function of reaction parameters is being defined by in situ Mössbauer spectroscopy, electron spin echo measurements, EXAFS, and other novel spectroscopic techniques. This research is described in the second part of this text.

Diffusion, absorption, and mass transport properties, of course, also define microporous molecular sieve selectivity. No other physical proper-



ties are more important to understand and to define for the characterization of zeolites. This area of research is summarized in a manuscript by Douglas Ruthven. It is worth noting the suggestion of one reviewer that the presentation and topic deserves to be expanded into a text on its own. The ability of zeolites to differentiate between nearly identical molecules such as O<sub>2</sub> and N<sub>2</sub> is examined by D. T. Hayhurst and M. D. Sefcik.

The catalytic activity of zeolites in alkane to olefin reactions, photochemical conversion reactions, Fischer–Tropsch hydrogenation, isocyanation, carbonylation, and related chemistry make up the last theme. An important focus of this is to explore the utility of zeolites as selective heterogeneous catalysts for reactions that involve Group VIII metals. The mechanistic nature of some of this chemistry is presented, along with the characterization of supported organometallic transition metal complexes.

One of the most exciting aspects of zeolite chemistry is our increasing understanding of the functionality of framework structure, chemisorption, and mass transport as related to chemical behavior. The research in this area has resulted in numerous advances during the past 2 years, many of which are presented in this text. It is expected that the applications and interest in crystalline molecular sieves will continue to expand rapidly.

GALEN D. STUCKY  
E. I. du Pont de Nemours and Company  
December 16, 1982

# Factors Influencing the Synthesis of Zeolites A, X, and Y

JOHN A. KOSTINKO

J. M. Huber Corporation, Chemicals Division, Havre de Grace, MD 21078

The synthesis of zeolite A, mixtures of A and X, and zeolite X using batch compositions not previously reported are described. The synthesis regions defined by triangular coordinates demonstrate that any of these materials may be made in the same area. The results are described in terms of the time required to initiate crystallization at a given reaction temperature. Control of the factors which can influence the crystallization time are discussed in terms of "time table selectors" and "species selectors". Once a metastable species has preferentially crystallized, it can transform to a more stable phase. For example, when synthesis conditions are chosen to produce zeolite A, the rate of hydroxysodalite formation is dependent on five variables. These variables and their effect on the conversion of zeolite A to hydroxysodalite are described mathematically.

Review of the literature and existing patents indicates that the state of the art restricts the formation of a given zeolite to a specific batch composition range (1-9). Convention also implies that the use of triangular coordinate graphics to depict mole percent  $\text{Na}_2\text{O}$ ,  $\text{SiO}_2$  and  $\text{Al}_2\text{O}_3$  in the batch indicates which species of zeolite will form. Figure 1 represents a composite of patented batch compositions for the synthesis of zeolites A, X and Y. It should be noted that batch composition ranges shown for the different zeolites never overlap. Although this concept has been used in the past, it does not reliably predict results. This is demonstrated by the experimental data plotted on Figure 2 which shows the composition ranges which can be used to prepare zeolite A (A-B-C-D), X (A-E-F-G) and mixtures of A and X in the same batch (H-I-J-K). These ranges not only overlap, they also extend into areas previously designated for preparing zeolite Y. The data on

0097-6156/83/0218-0003\$06.00/0  
© 1983 American Chemical Society

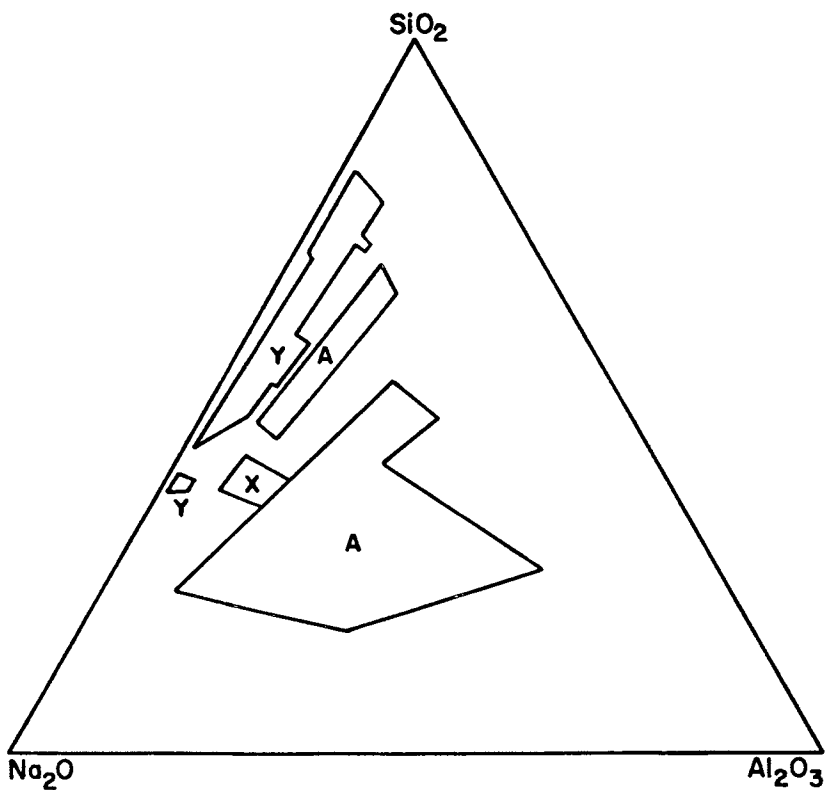


Figure 1. Patented batch compositions for the synthesis of zeolites A, X, and Y. Coordinates expressed as mole percent.

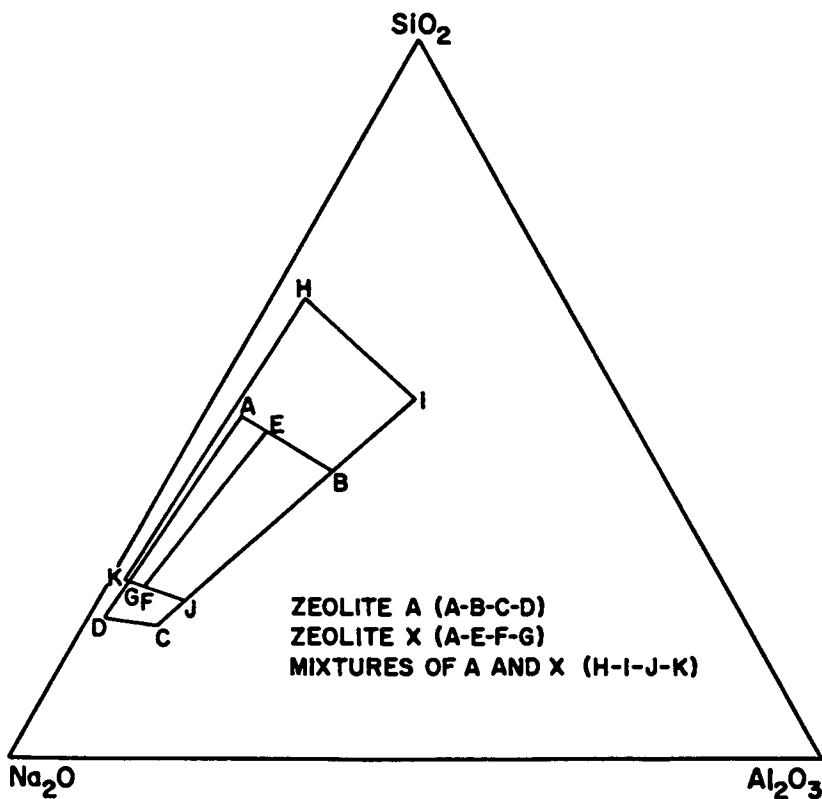


Figure 2. Experimental batch compositions for the synthesis of zeolite A, mixtures of A and X, and zeolite X. Coordinates expressed as mole percent.

Table I demonstrates that the conventional explanation for the overlap of ranges in terms of batch oxide molar ratios is inadequate and merely suggests recipes for preparing a given zeolite.

### Experimental

The reactants used for preparing the zeolite batches were granular sodium aluminate ( $\text{Na}_2\text{O}-\text{Al}_2\text{O}_3-3\text{H}_2\text{O}$ -Fisher Scientific), sodium silicate solution ( $\text{Na}_2\text{O}-2.48\text{SiO}_2-19.94 \text{H}_2\text{O}$ ) and 50% sodium hydroxide solution (mercury cell type, Diamond-Shamrock).

The dry sodium aluminate was first dissolved in 1.7 times its weight of water and then all 50% caustic requirements were added. The sodium silicate solution was diluted with any water requirement not used to dissolve the dry sodium aluminate. Both solutions were heated to the desired reaction temperature, and then the hot sodium aluminate solution was quickly added to the hot sodium silicate solution (less than 30 seconds) with agitation. The mixture was then agitated until the resulting gel broke down to a homogenous, creamy slurry.

The slurry was divided into 300 gram portions, sealed in polymethylpentene containers, and placed in an oven. All reactions were conducted under static conditions and temperatures were maintained plus or minus 1 degree centigrade. Samples were removed from the oven at desired time intervals, then filtered and washed repeatedly with hot deionized water and oven dried at 100 degrees centigrade.

Time required to initiate crystallization was determined by analyzing the products using standard X-ray diffraction techniques.

### Results and Discussion

A better understanding of the reason for the overlap of ranges can be achieved if one thinks of the oxide molar ratios in terms of crystallization accelerators and decelerators. When one examines Figures 3 and 4, it becomes clear that the molar ratios  $\text{H}_2\text{O}/\text{Na}_2\text{O}$ ,  $\text{Na}_2\text{O}/\text{SiO}_2$  and  $\text{SiO}_2/\text{Al}_2\text{O}_3$  are interacting in a manner which relates the type of zeolite formed to the reaction time necessary for the initiation of crystallization at a given temperature. When this time is short, mixtures of zeolite A and hydroxysodalite are formed, but when the time is longer, zeolite A is formed. When the time is still longer, zeolite X is formed. When the time is between that necessary for the formation of zeolite A and that necessary for the formation of zeolite X, then a combination of zeolite A and X is formed. Table II summarizes the relationship between crystallization time and species within the range of synthesis conditions which were studied.

By combining published results with the present work, it would appear that within the range of synthesis conditions tested there is a continuum between the species hydroxysodalite, zeolite A, zeolite X, and zeolite Y. This concept is depicted on Figure 5,

TABLE I  
Effect of Batch Composition on Zeolite Synthesis at 100°C

| <u>H<sub>2</sub>O/Na<sub>2</sub>O</u> | <u>Na<sub>2</sub>O/SiO<sub>2</sub></u> | <u>SiO<sub>2</sub>/Al<sub>2</sub>O<sub>3</sub></u> | <u>Time Required<br/>To Initiate<br/>Crystallization,<br/>Hours</u> | <u>Zeolite<br/>Formed</u> |
|---------------------------------------|--|--|---|---------------------------|
| 15                                    | 1.6                                    | 1.5  | 0.5   | HS                        |
| 15                                    | 1.6                                    | 2.0  | 0.5   | A                         |
| 15                                    | 1.6                                    | 2.5  | 0.5   | A + HS                    |
| 15                                    | 1.6                                    | 3.0  | 0.5   | A + HS                    |
| 15                                    | 2.4                                    | 1.5  | 0.5   | A + HS                    |
| 15                                    | 2.4                                    | 2.0  | 0.5   | A + HS                    |
| 15                                    | 2.4                                    | 2.5  | 0.5   | HS                        |
| 15                                    | 2.4                                    | 3.0  | 1.0   | HS                        |
| 20                                    | 1.6                                    | 2.0  | 0.5   | A                         |
| 20                                    | 1.6                                    | 2.5  | 1.0   | A                         |
| 20                                    | 1.6                                    | 3.0  | 1.0   | A                         |
| 20                                    | 1.6                                    | 7.3  | 2.0   | A                         |
| 20                                    | 2.4                                    | 1.5  | 0.5   | A + HS                    |
| 20                                    | 2.4                                    | 2.0  | 0.5   | A + HS                    |
| 20                                    | 2.4                                    | 2.5  | 0.5   | A                         |
| 20                                    | 2.4                                    | 3.0  | 0.5   | A                         |
| 25                                    | 1.6                                    | 1.5  | 1.0   | A                         |
| 25                                    | 1.6                                    | 2.0  | 1.0   | A                         |
| 25                                    | 1.6                                    | 2.5  | 1.5   | A                         |
| 25                                    | 1.6                                    | 3.0  | 2.0   | A                         |
| 25                                    | 2.4                                    | 1.5  | 1.0   | A                         |
| 25                                    | 2.4                                    | 2.0  | 1.0   | A                         |
| 25                                    | 2.4                                    | 2.5  | 1.0   | A                         |
| 25                                    | 2.4                                    | 3.0  | 1.0   | A                         |
| 30                                    | 1.2                                    | 2.5  | 3.0   | A + X                     |
| 30                                    | 1.2                                    | 3.3  | 6.0   | X                         |
| 30                                    | 1.2                                    | 5.3  | 8.0   | X                         |
| 30                                    | 1.2                                    | 7.3  | 8.0   | X                         |
| 30                                    | 1.6                                    | 2.5  | 2.0   | A + X                     |
| 30                                    | 1.6                                    | 5.3  | 3.0   | A + X                     |
| 30                                    | 1.6                                    | 6.3  | 3.0   | A + X                     |
| 30                                    | 1.6                                    | 7.3  | 5.0   | A + X                     |

TABLE II  
Relationship Between Time Required for Crystallization  
and the Type of Zeolite Formed

| <u>Time Required To<br/>Initiate Crystallization,<br/>Hours at 100°C</u> | <u>Zeolite Species Formed</u> |
|--|-------------------------------|
| 0.5  | A + HS                        |
| 0.5 - 3.0  | A                             |
| 2.0 - 3.0  | A + X                         |
| 3.0 - 12.0   | X                             |
| greater than 12.0  | Y                             |

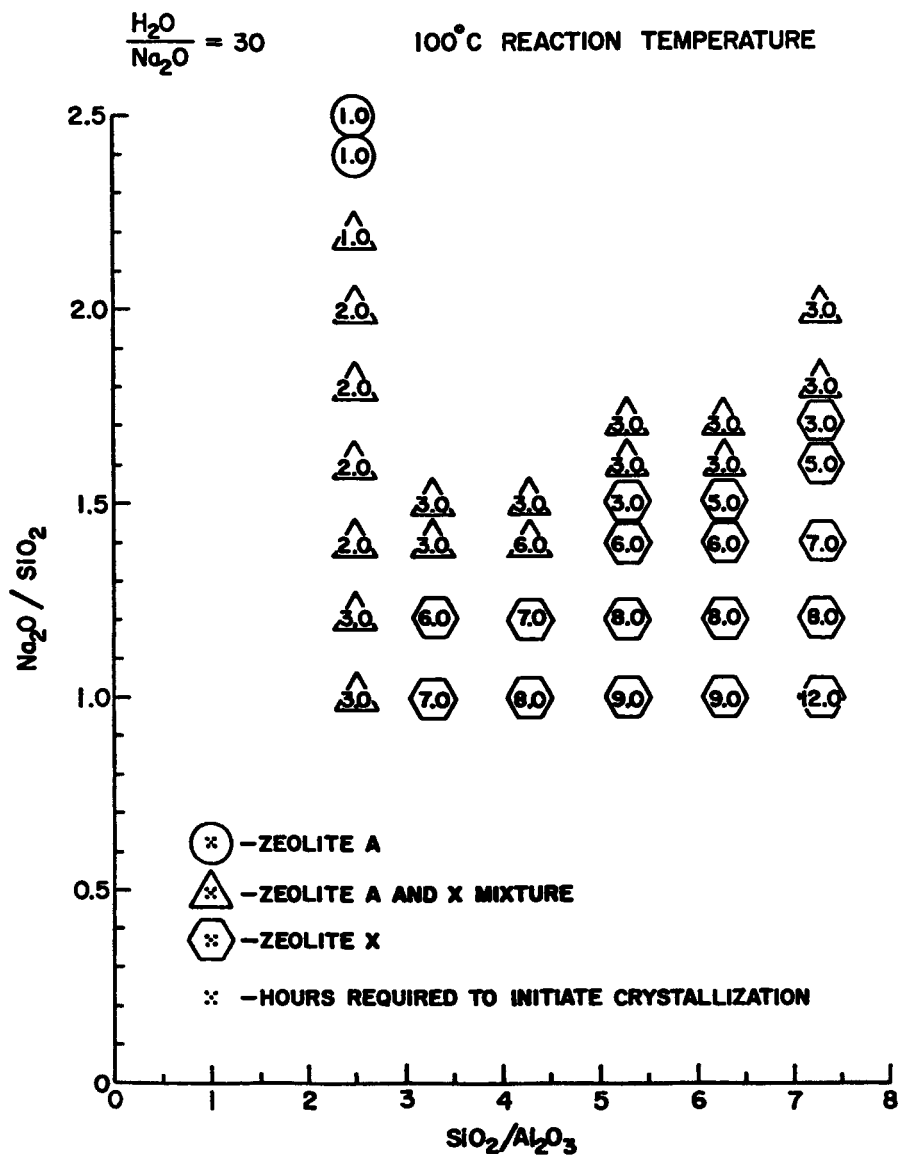


Figure 3. Effect of batch composition on the synthesis of zeolites A and X.

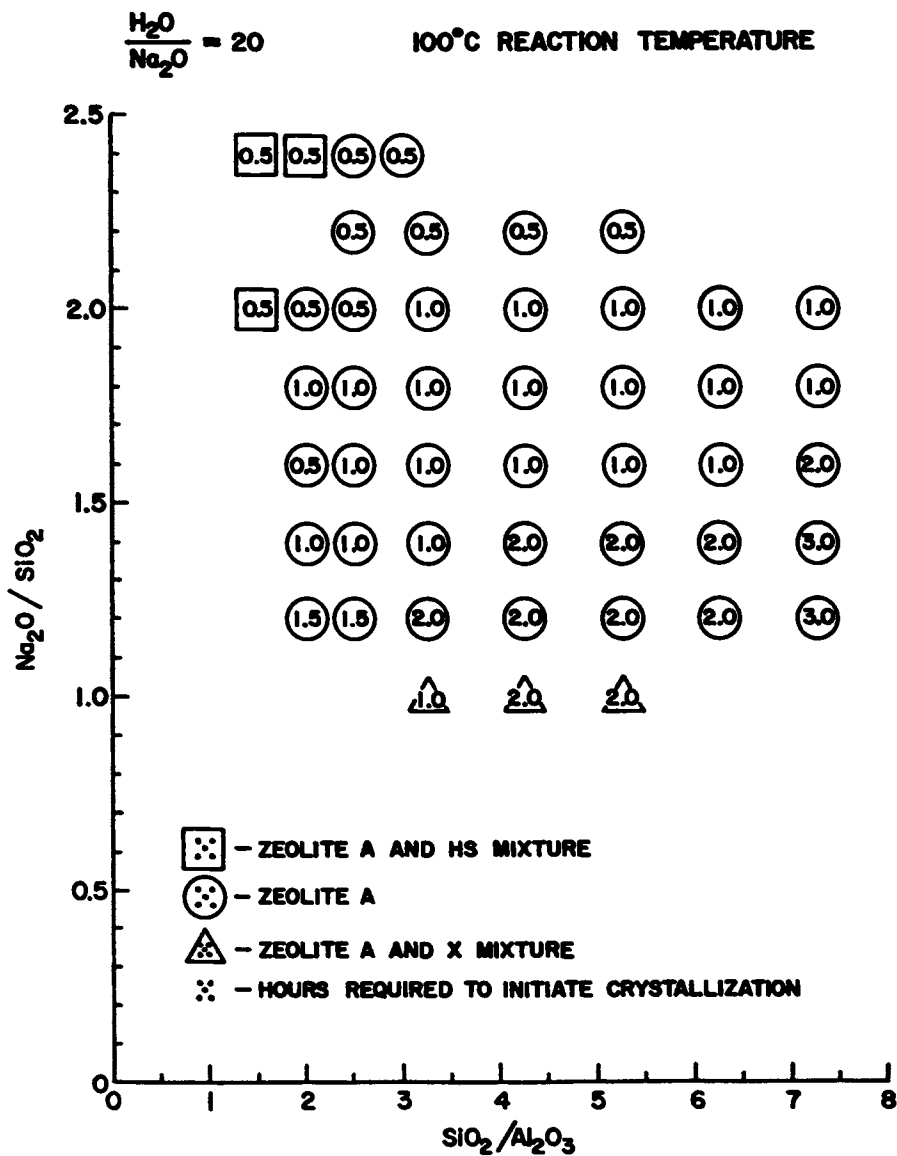


Figure 4. Effect of batch composition on the synthesis of zeolites A and X.



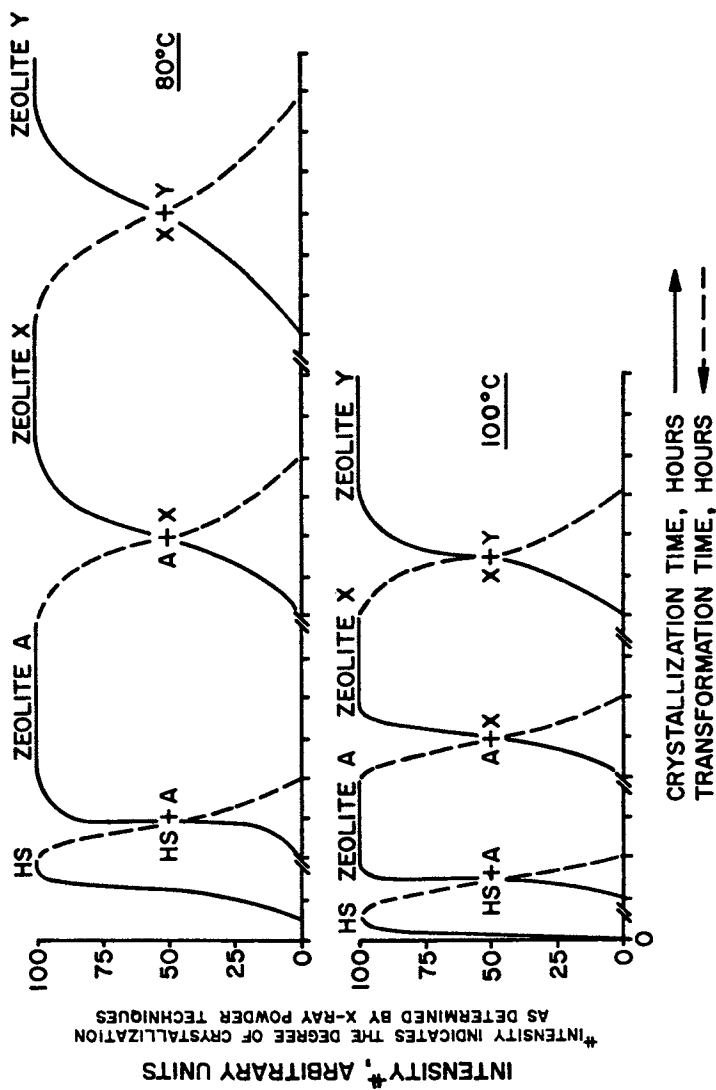


Figure 5. Crystallization of zeolites HS, A, X, and Y as a function of time.

where the dashed lines are suggested by the test results and the solid lines represent the previously established relative crystallization times for these zeolites (3, 4, 9, 10, 11). The existence of a continuum between these species is supported by the following:

1. The relative position of the species formed with respect to time required for crystallization has previously been established.
2. Mixtures of zeolite A and X have been prepared in the same batch.
3. Zeolite A remaining in its mother liquor and reacted for extended periods of time will convert into hydroxysodalite (12).
4. Overextended crystallization periods usually result in a decrease in the SiO<sub>2</sub> content of zeolite Y (9).
5. Figures 6, 7 and 8 demonstrate how the species detected can change with time. Both the conversion of zeolite A to hydroxysodalite and the conversion of zeolite X to zeolite A can be easily seen in this three hour time sequence.

The reaction time necessary for crystallization at a given reaction temperature can be controlled in a variety of ways, but the major way of controlling reaction time is by adjusting the water to sodium oxide molar ratio of the reaction mixture. The reaction time necessary to form these zeolites is directly proportional to the water to sodium oxide molar ratio used. For example, when the synthesis conditions indicate that the water to sodium oxide molar ratio for making zeolite A is between 15:1 and 20:1; for making a combination of zeolite X and zeolite A it should be between 25:1 and 35:1. Therefore, to synthesize zeolite A in a reaction mixture having a sodium oxide to silica molar ratio and a silica to alumina molar ratio where normally zeolite X would be formed, one would decrease the water to sodium oxide ratio.

This relationship between the water to sodium oxide molar ratio and the type of zeolite formed was not previously known. For example, U.S. patents issued to Milton (1, 7), show a water to sodium oxide molar ratio of from 35 to 200 for the production of zeolite A and a water to sodium oxide molar ratio of from 35 to 60 for the production of zeolite X. If anything, this would imply that the reaction mixture for preparing zeolite A should have a higher water to sodium oxide molar ratio than the reaction mixture for preparing zeolite X. In U.S. patent 3,119,659, the water to sodium oxide molar ratio for the production of zeolite A is from 30 to 60. None of the above examples show that the water to sodium oxide molar ratio should be higher for making zeolite X than for making zeolite A.

Another way of controlling the reaction time necessary for crystallization at a given temperature is by adjusting the sodium oxide to silica molar ratio of the reaction mixture. The reaction time necessary to form these zeolites is inversely proportional to the sodium oxide to silica molar ratio used. The effect of sodium oxide to silica molar ratio is less pronounced than that of water to sodium oxide molar ratio.

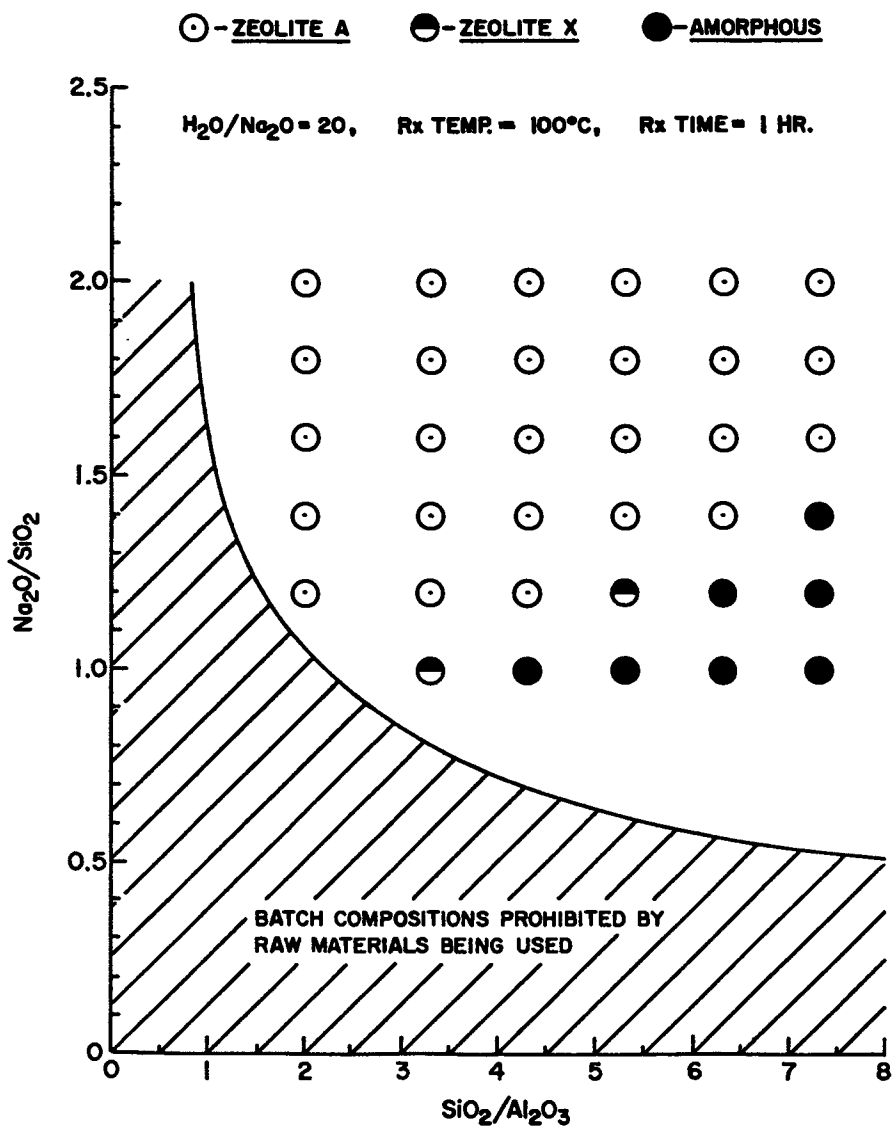


Figure 6. Effect of reaction time on zeolite phase transformation. Keys to symbols indicate species detected after 1 hour.

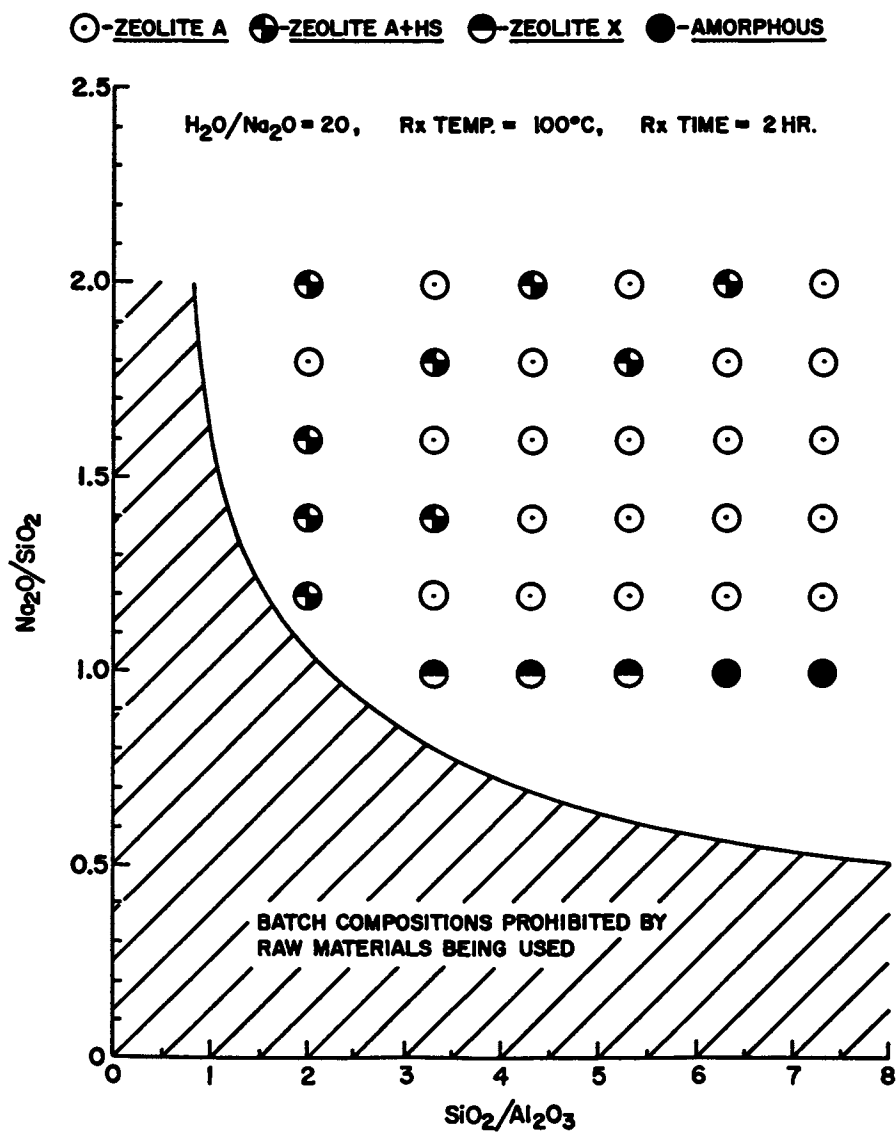


Figure 7. Effect of reaction time on zeolite phase transformation. Keys to symbols indicate species detected after 2 hours.

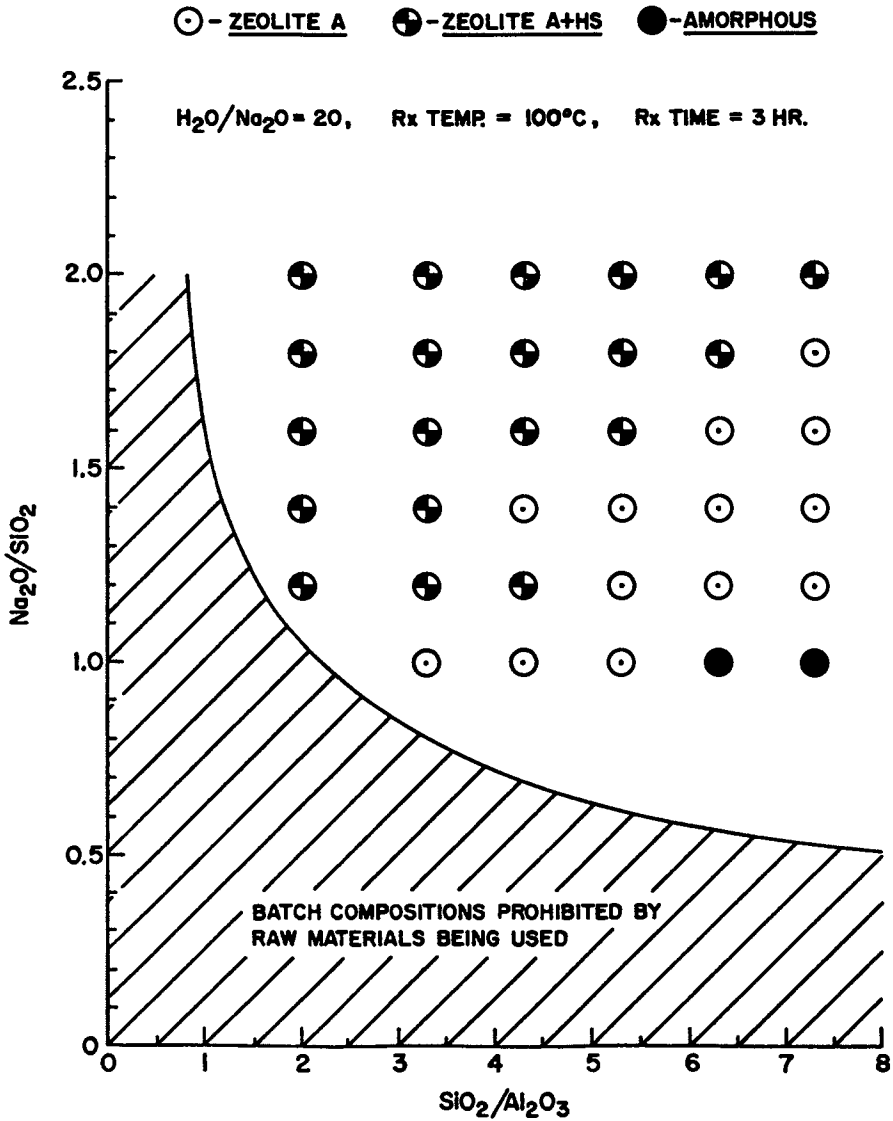


Figure 8. Effect of reaction time on zeolite phase transformation. Keys to symbols indicate species detected after 3 hours.

Adjusting the silica to alumina molar ratio of the reaction mixture also affects the reaction time necessary for crystallization at a given reaction temperature, but this effect is less than the effect of sodium oxide to silica molar ratio, which in turn is much less than the effect of water to sodium oxide molar ratio. The reaction time necessary to form these zeolites is directly proportional to the silica to alumina molar ratio.

Four additional factors can also contribute to a limited shift in the time required for crystallization. These are the rate at which the sodium aluminate solution is added to the sodium silicate solution (13), anion activation (14, 15, 16), the source of  $\text{SiO}_2$  (17), and the reaction temperature (10). It has been found that the effect of these variables is most pronounced when synthesizing higher  $\text{SiO}_2/\text{Al}_2\text{O}_3$  ratio zeolites, such as X and Y. Their effect on the synthesis of zeolite A is considerably less and sometimes negligible.

These seven factors which determine the time required for crystallization can be divided into timetable selectors and species selectors. Rate of addition, anion activation, source of  $\text{SiO}_2$  and reaction temperature can all be considered "timetable selectors". In effect, they establish a timetable which specifies a minimum reaction time for each of the species HS, A, X and Y (Figure 5). The batch composition factors  $\text{H}_2\text{O}/\text{Na}_2\text{O}$ ,  $\text{Na}_2\text{O}/\text{SiO}_2$  and  $\text{SiO}_2/\text{Al}_2\text{O}_3$  play a different role and can be considered as "species selectors". Once the timetable has been established, these factors govern which species will crystallize from the batch. Their control over the minimum time required for crystallization allows one to slide up and down the timetable and selectively produce HS, mixtures of A and HS, A, mixtures of A and X, X, etc. They are used to adjust the time required to initiate crystallization so that it will match a particular zeolite in the pre-established timetable. Although timetable selectors can only change reaction time, species selectors can change both the species formed and reaction time. When preparing these zeolites, this dual effect must be considered. Any variation from the desired batch composition can present problems if the test is designed to react for a fixed period of time. Variations which slow down the reaction could produce a zeolite which has poor properties simply because it has not completely crystallized. If one has variations which speed up the reaction, one could produce a mixture of zeolite phases.

Thus, the reaction time necessary for crystallization at a given temperature can be increased by increasing the water to sodium oxide ratio; decreasing the sodium oxide to silica molar ratio; increasing the silica to alumina molar ratio; adding the sodium aluminate to the sodium silicate at a slow rate of addition; using raw materials which contain no "activating" anions; using an inactive source of  $\text{SiO}_2$ ; and reacting the batch at a low temperature. The type of zeolite formed depends on the total effect of the water to sodium oxide molar ratio and all of the additional factors mentioned above.

If one assumes that these different crystal species are merely metastable intermediates in the continuum HS-A-X-Y, the SiO<sub>2</sub> content of the precipitated amorphous precursor would specify the starting position in the continuum. The reaction environment would then dictate which species, with SiO<sub>2</sub>/Al<sub>2</sub>O<sub>3</sub> ratio  $\leq$  to that of the precursor, will crystallize. Whenever the temperature is sufficient, the free energy relationship between these zeolites will permit any of them to form.

The metastable form which preferentially crystallizes could then transform to a more stable phase (i.e. zeolite Y  $\rightarrow$  zeolite X or zeolite A  $\rightarrow$  hydroxysodalite). Nucleation and growth rates would then become the limiting factors in determining how long this would take. For example, when synthesis conditions are chosen to produce zeolite A, the rate of hydroxysodalite formation is dependent on five variables. These variables and their effect on the conversion of zeolite A to hydroxysodalite are as follows:

Batch H<sub>2</sub>O/Na<sub>2</sub>O - Lower values accelerate the reaction  
Higher values dampen the reaction

Batch Na<sub>2</sub>O/SiO<sub>2</sub> - Higher values accelerate the reaction  
Lower values dampen the reaction

Batch SiO<sub>2</sub>/Al<sub>2</sub>O<sub>3</sub> - Lower values accelerate the reaction  
Higher values dampen the reaction

Reaction Temperature - Higher values accelerate the reaction  
Lower values dampen the reaction

Reaction Time - Longer times produce more hydroxysodalite  
Shorter times produce less hydroxysodalite

Rate of addition, source of SiO<sub>2</sub> and low levels of anion activators had little influence within the synthesis conditions tested.

Starting with any given set of zeolite A synthesis conditions, one may control the amount of hydroxysodalite formed by properly manipulating these variables. It should be noted that more than one factor can vary at the same time. If their variation produces compensating effects, i.e. lower Na<sub>2</sub>O/SiO<sub>2</sub> ratio and lower H<sub>2</sub>O/Na<sub>2</sub>O ratio, it is possible that they will cancel each other out and produce no detectable change in the results.

Examples of how these variables affect the conversion of zeolite A to hydroxysodalite are shown on Table III. Regression analysis of data relating these five variables to the amount of hydroxysodalite found in zeolite A batches gives the following equation:

$$\% \text{ HS} = e^{(x^2)}$$

where  $e = 2.7183$  and  $x = A(\text{H}_2\text{O}/\text{Na}_2\text{O}) + B(\text{SiO}_2/\text{Al}_2\text{O}_3) + C(\text{Temp}/10) - D(\text{Temp}/10)^2 + E(\text{Temp}/10)^3 - F(\text{Time})^2 + G(\text{Time})^3 - H(\text{H}_2\text{O}/\text{SiO}_2) - I(\text{H}_2\text{O}/\text{Na}_2\text{O} \times \text{SiO}_2/\text{Al}_2\text{O}_3) - J(\text{H}_2\text{O}/\text{Na}_2\text{O} \times \text{Temp}/10) + K(\text{H}_2\text{O}/\text{Na}_2\text{O} \times \text{Time}) + L(\text{Na}_2\text{O}/\text{Al}_2\text{O}_3) + M(\text{Na}_2\text{O}/\text{SiO}_2 \times \text{Temp}/10) - N(\text{SiO}_2/\text{Al}_2\text{O}_3 \times \text{Temp}/10) + O(\text{Temp}/10 \times \text{Time}) + P(\text{H}_2\text{O}/\text{Na}_2\text{O} + \text{Na}_2\text{O}/\text{SiO}_2) - Q$

Continued on page 18.

TABLE IIIControl of Hydroxysodalite Formation

| $\frac{\text{H}_2\text{O}}{\text{Na}_2\text{O}}$                                | $\frac{\text{Na}_2\text{O}}{\text{SiO}_2}$ | $\frac{\text{SiO}_2}{\text{Al}_2\text{O}_3}$ | Rx Temp,<br>°C | Rx Time,<br>Hours | XRD,<br>% HS |
|---|--|--|----------------|-------------------|--------------|
| 15  | 1.6  | 2.0  | 100            | 0.5               | 0            |
|   |  |  |                | 1.0               | 10           |
|   |  |  |                | 1.5               | 27           |
| 25  | 1.6  | 2.0  | 100            | 0.5               | 0            |
|   |  |  |                | 1.0               | 0            |
|   |  |  |                | 1.5               | 0            |
| Effect of $\text{H}_2\text{O}/\text{Na}_2\text{O}$ on hydroxysodalite formation |  |  |                |                   |              |
| 20  | 2.4  | 2.0  | 100            | 0.5               | 4            |
|   |  |  |                | 1.0               | 9            |
|   |  |  |                | 1.5               | 15           |
| 20  | 1.6  | 2.0  | 100            | 0.5               | 0            |
|   |  |  |                | 1.0               | 2            |
|   |  |  |                | 1.5               | 2            |
| Effect of $\text{Na}_2\text{O}/\text{SiO}_2$ on hydroxysodalite formation       |  |  |                |                   |              |
| 20  | 2.0  | 2.0  | 100            | 0.5               | 3            |
|   |  |  |                | 1.0               | 5            |
|   |  |  |                | 1.5               | 8            |
| 20  | 2.0  | 3.0  | 100            | 0.5               | 0            |
|   |  |  |                | 1.0               | 0            |
|   |  |  |                | 1.5               | 4            |
| Effect of $\text{SiO}_2/\text{Al}_2\text{O}_3$ on hydroxysodalite formation     |  |  |                |                   |              |
| 20  | 2.4  | 2.0  | 100            | 0.5               | 4            |
|   |  |  |                | 1.0               | 9            |
|   |  |  |                | 1.5               | 15           |
| 20  | 2.4  | 2.0  | 80             | 0.5               | 0            |
|   |  |  |                | 1.0               | 0            |
|   |  |  |                | 1.5               | 0            |
| Effect of temperature on hydroxysodalite formation                              |  |  |                |                   |              |

The effect of time on hydroxysodalite formation can be seen in all of the examples shown above.



Temp = degrees Centigrade; Time = hours;  $H_2O$ ,  $Na_2O$ ,  $SiO_2$ ,  $Al_2O_3$  = moles

|             |            |            |
|-------------|------------|------------|
| A = 0.2671  | G = 0.0020 | M = 0.0861 |
| B = 0.7907  | H = 0.0279 | N = 0.0284 |
| C = 70.0131 | I = 0.0312 | O = 0.0353 |
| D = 7.9198  | J = 0.0294 | P = 0.0202 |
| E = 0.2997  | K = 0.0040 | Q = 207.25 |
| F = 0.0432  | L = 0.0372 |            |

Multiple Correlation Coefficient = .994  
Standard Error of the Estimate =  $\pm 2.6\%$

Given a set of synthesis conditions and sufficient reaction time to produce hydroxysodalite, pure zeolite A can be obtained by decreasing the reaction time until the % HS approaches 0. If the reaction time is fixed, any of the other variables can be varied and achieve the same result. An example of how reaction time affects the conversion of zeolite A to hydroxysodalite, when all other variables are held constant, appears on Figure 9.

In summary, the particular zeolite species or mixture of species which crystallizes can be controlled and is predictable within the synthesis conditions studied. This control can be achieved by applying the concept of a continuum between the species HS-A-X-Y, utilizing the timetable selectors to establish a fixed frame of reference, and using the species selectors to selectively produce a desired zeolite. Once the desired species has crystallized, it is then possible to regulate and predict its conversion to the species which precedes it in the continuum.

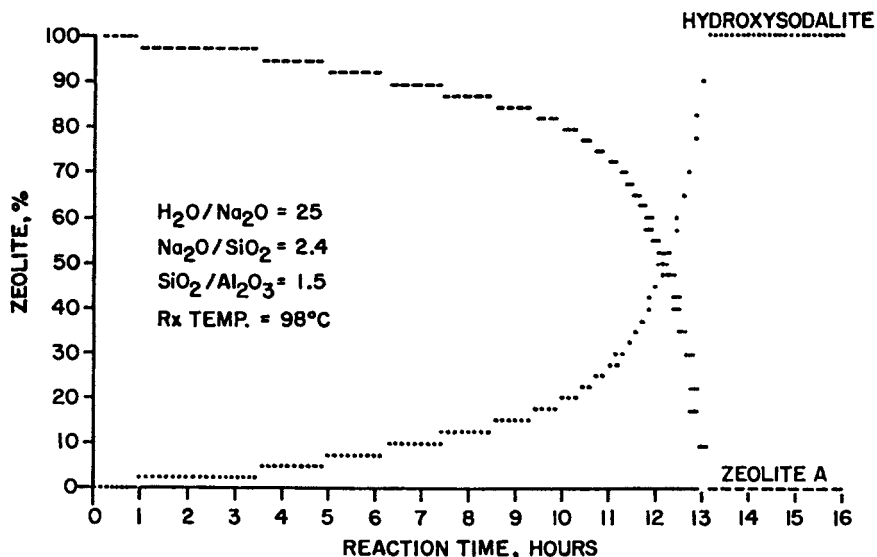


Figure 9. Effect of time on the conversion of zeolite A to hydroxysodalite. Values are calculated using % HS equation.

Literature Cited

1. Milton, R. M.; U.S. Patent 2,882,243.
2. Barrer, R. M., Bromley, Bultitude, F. W., Harwell, and Didcot; U.S. Patent 2,982,612.
3. Weber, H.; U.S. Patent 3,058,805.
4. Howell, P. A.; U.S. Patent 3,101,251.
5. Taggart, L. L., Eden, and Ribaud, G. L.; U.S. Patent 3,119,659.
6. Williams, L. E., Mays, R. K., and Wagner, J. E.; U.S. Patent 4,041,135.
7. Milton, R. M.; U.S. Patent 2,882,244.
8. Gottstine, J. G., and Westerland, E. H.; U.S. Patent 2,979,381.
9. Breck, D. W.; U.S. Patent 3,130,007.
10. Breck, D. W.; Flanigen, E. M. "Molecular Sieves"; Society of Chemical Industry: London, 1968; p. 47.
11. Breck, D. W.; Eversole, W. G.; Milton, R. M.; Reed, T. B.; Thomas, T. L. *J. Am. Chem. Soc.* 1956, 78, 5963.
12. Breck, D. W., "Zeolite Molecular Sieves"; J. Wiley and Sons: New York, 1974; p. 277.
13. Kerr, G. T. *J. Phys. Chem.* 1968, 72, 1385.
14. Robson, H. E.; Riley, K. L.; Maness, D. D. "Molecular Sieves II"; Katzer, J. R., Ed.; American Chemical Society: Washington, DC, 1977; p. 233.
15. Lowe, B. M.; MacGlip, N. A.; Whittam, T. V. "Proc. Fifth Int. Conf. Zeolites"; Rees, L. V., Ed.; Heyden and Sons Ltd.: London, 1980; p. 85.
16. Kostinko, J. A.; U.S. Patent 4,264,562.
17. Coombs, D. S.; Ellis, A. J.; Fyfe, W. F.; Taylor, A. M. *Geochem. Cosmochim. Acta* 1959, 17, 53.

RECEIVED November 4, 1982

# Synthesis and Characterization of a New Zeolite of the Offretite Type

MARIO L. OCCELLI and ANTHONY J. PERROTTA  
Gulf Research & Development Company, Pittsburgh, PA 15230

An offretite-type zeolite has been synthesized in the tetramethyl ammonium-rubidium-alumina-silica-water system by the formation of a hydrogel of composition:  $\text{Al}_2\text{O}_3:13.0\text{SiO}_2:2.0\text{Rb}_2\text{O}:9.0[(\text{CH}_3)_4\text{N}]_2\text{O}:380\text{H}_2\text{O}$ . Crystallization of the gel at temperatures ranging from 95° to 150°C gives crystals characterized by a BET surface area of 380-420 m<sup>2</sup>/g and pore volume of 0.22-0.24 cc/g. The typical crystals composition (on a dry basis) is  $\text{Al}_2\text{O}_3:8.7\text{SiO}_2:0.9\text{Rb}_2\text{O}:0.085[(\text{CH}_3)_4\text{N}]_2\text{O}$ . Crystal properties have been investigated by X-ray powder diffraction, sorption, SEM, infrared, and thermal analysis techniques. (Rb,TMA) offretite appear to crystallize as irregular, rod-like particles having a high thermal stability. The oxidative decomposition of TMA cations occur in two steps at 300°C and 430°C causing the appearance of new bands in the OH stretching region. Rb-Offretite sorbs 1.17 mmole/g n-butane and 1.01 mmole/g isobutane at 26°C. Their isosteric heat of sorption are nearly independent of coverage and amount of 9.2 and 12.3 Kcal/mole, respectively.

Offretite is a hexagonal zeolite first discovered by Professor Gonnard(1) in 1890 in amygdaloidal basalt at Mount Semouse near Montbreson, France. Offretite has been synthesized by Rubin,(2) and Aiello and Barrer(3) from aluminosilicate hydrogels in a TMA (tetramethylammonium)-KOH-NaOH mixed base system. Aiello and Barrer noted that this zeolite can be grown from gels in the presence of KOH-TMAOH but not in the presence of NaOH-TMAOH. Sand(4) has shown that offretite can be synthesized without TMA-OH from NaOH-KOH solutions. The synthesis of offre-

0097-6156/83/0218-0021\$06.00/0  
© 1983 American Chemical Society

tite crystals always included the presence of potassium ions until fairly recently when Barrer and Sieber(5) were able to crystallize this zeolite from a LiOH-CsOH-TMAOH containing hydrogel. It is the purpose of this paper to describe the Perrotta(6) synthesis of a new zeolite of the offretite type crystallized from a potassium free, aluminosilicate hydrogel in the presence of Rb-TMA ions.

### Experimental

Rubidium-TMA-offretite was crystallized from a  $\text{Al}_2\text{O}_3\text{-SiO}_2\text{-Rb}_2\text{O-TMAOH H}_2\text{O}$  gel prepared from high purity grade reactants. Aqueous rubidium chloride, aluminum nitrate, and TMA hydroxide solutions were mixed in a polypropylene beaker and then slowly added to silica sol (LUDOX-AS, 30 wt%  $\text{SiO}_2$ ) under vigorous stirring. The resulting hydrogel was allowed to cold age at room temperature for a few hours and then heated at  $\sim 95^\circ\text{C}$  in a sealed polypropylene bottle. The crystals were separated from the mother liquor by centrifugation and subsequently washed with distilled water. The crystals were dried in air at  $100^\circ\text{C}$ . (H,Rb) offretite was obtained by ion exchanging the calcined, TMA-free, Rb-offretite with a 0.5 M  $\text{NH}_4\text{NO}_3$  solution at  $80^\circ\text{C}$  for 4 hr. Decomposition of the ammonium ions was obtained by heating in air at  $550^\circ\text{C}$  overnight.

A Perkin-Elmer TGS-2 thermogravimetric system(7) was used to measure sorption of normal and isobutane. A schematic diagram of this apparatus is shown in Figure 1. The microbalance, equipped with temperature control and weight monitor units, is connected to a vacuum system which consists of an oil diffusion pump backed up by a mechanical pump. Included in the vacuum system are a Texas Instrument Precision quartz spiral pressure gauge, a Veeco ionization-type vacuum gauge and a Varian VacIon pump. The catalyst sample was suspended in a sample pan surrounded by a platinum resistance heater. This heater was controlled by a temperature program controller. The weight change of the catalyst during an experiment was monitored by a balance control unit and recorded by a Hewlett-Packard 7100B recorder. The sensitivity of the microbalance was  $\pm 0.2 \mu\text{g}$ .

DSC and TGA measurements were carried out using a DuPont 1090 thermal analyzer using high purity nitrogen or oxygen as purge gases and heating rates of  $10^\circ\text{C}/\text{min}$ . The thermal stability of the crystals was investigated by observing crystallinity changes in samples heated in the temperature range of  $540\text{-}980^\circ\text{C}$  for a period of 4 hr. All powder diffraction measurements were obtained on a Picker X-ray diffractometer at a scan rate of  $1^\circ/\text{min}$  using monochromatic  $\text{Cu-K}_\alpha$  radiation. Scanning electron micrographs (SEM) were taken with a JEOL (Japanese Electron Optic Laboratory) JSM-35 instrument. Infrared measurements were performed on a NICOLET 7000 FTIR spectrometer. Samples were pressed at 1500 atm into thin, self supporting wafers approximately 1 in. in diameter. The wafers were then mounted in an optical cell. The IR cell

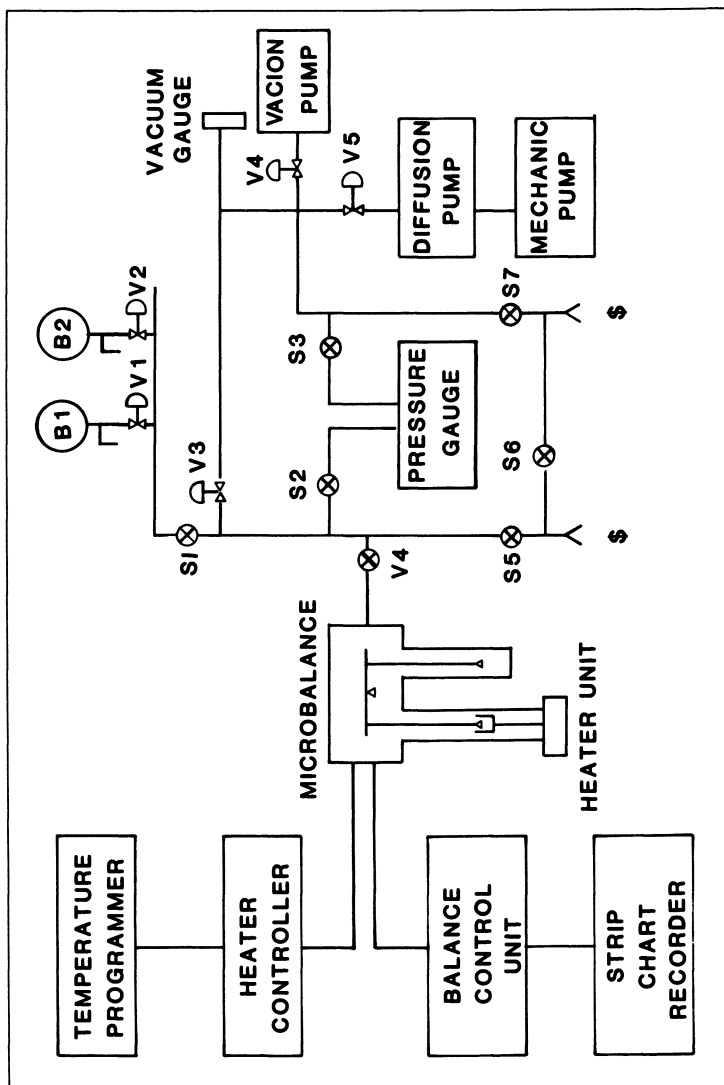


Figure 1.  
Thermogravimetric system

allowed the thermal treatment in vacuo of the samples up to 400°C and direct loading of pyridine vapors. Pyridine was sorbed at 25°C on wafers that had been heat treated at 400°C for 1 hr. Degassing of the pyridine loaded samples was conducted at different temperatures and their IR spectra recorded.

### Results and Discussion

Synthesis The investigation of the  $\text{Al}_2\text{O}_3:\text{SiO}_2:\text{Rb}_2\text{O}:([\text{CH}_3]_4\text{N})_2\text{O}:\text{H}_2\text{O}$  system has shown the existence of three different crystalline phases. Representative synthesis data is shown in Table I. All phases were formed below 120°C and obtained in a 5-30 day crystallization period. At low TMAOH and silica concentration ( $\text{SiO}_2/\text{Al}_2\text{O}_3 = \text{TMAOH}/\text{Al}_2\text{O}_3 = 5.0-6.0$ ), the phase  $\text{RbAlSiO}_4 \cdot 1.3\text{H}_2\text{O}$  crystallizes from the hydrogel. By increasing both the silica and the TMA ion levels, a new zeolite of the offretite type appears. The x-ray diffractogram for this phase is shown in Figure 2. A further increase in the silica, rubidium, and TMAOH content at constant alumina concentration results in the crystallization of a new sodalite-type phase. The X-ray data of this new sodalite species, with the computed cell constant, are given in Table II. The cell dimension of 8.94 Å is slightly larger than the cell dimension of hydroxysodalite which is 8.86 Å. (8)

Quality (Rb,TMA) offretite crystals are best obtained from hydrogels of composition:  $\text{Al}_2\text{O}_3:12.0\text{SiO}_2:2.0\text{Rb}_2\text{O}:9.0([\text{CH}_3]_4\text{N})_2\text{O}:360\text{H}_2\text{O}$ . Crystals are characterized by a BET surface area of 360-420 m<sup>2</sup>/g and a nitrogen pore volume of 0.20-0.24 cc/g. The scanning electron micrographs in Figure 3, show that (Rb,TMA) offretite crystallizes as rod-like particles, irregular in shape, frequently containing very small amounts of an unidentifiable phase. As in zeolite A(9) and Y,(10) the crystallization reaction is autocatalytic in nature. In fact a small addition of seed crystals yields a significant decrease in crystallization time. As expected, faster crystallization times can also be induced by increasing crystallization temperature, (see Table I). Typical composition of the crystallization product is:  $\text{Al}_2\text{O}_3:8.6\text{SiO}_2:0.95\text{Rb}_2\text{O}:0.071([\text{CH}_3]_4\text{N})_2\text{O}$ . The high  $\text{SiO}_2/\text{Al}_2\text{O}_3$  ratio observed ( $8.0 < \text{SiO}_2/\text{Al}_2\text{O}_3 \lesssim 9.1$ ) may be responsible for the excellent thermal stability exhibited by these crystals. After calcination in air at 870°C for 4 hr they retained ~80% of their original crystallinity (see Figure 4). A similarly prepared sample of (Na,K,TMA) offretite retained only a 34% crystallinity when treated in a similar manner. Aiello and Barrer(3) have shown that during (Na,K,TMA) offretite crystallization, an increase in the K/(K+Na) ratio results in an increase in the silica level of the crystals. A larger cation like rubidium may indirectly promote the higher  $\text{SiO}_2$  content exhibited by this Rb-zeolite of the offretite type because it encourages the less bulky  $\text{Si}^{4+}$  to isomorphously substitute for the  $\text{Rb}^+-\text{AlO}_2^-$  combination in the offretite lattice.

Table I  
THE  $\text{Al}_2\text{O}_3$ - $\text{SiO}_2$ - $\text{Rb}_2\text{O}$ - $([\text{CH}_3]_4\text{N})_2\text{O}$ - $\text{H}_2\text{O}$  SYSTEM

| <u>Gel Composition</u>        |   | <u>T(°C)</u> | <u>t Days</u> | <u>Phases Present</u>                           |
|-------------------------------|---|--------------|---------------|---|
| $\text{Al}_2\text{O}_3$ :5.0  | $\text{SiO}_2$ :2.0 $\text{Rb}_2\text{O}$ :5.5( $[\text{CH}_3]_4\text{N}$ ) $_2\text{O}$ :250 $\text{H}_2\text{O}$  | 90           | 5             | $\text{RbAlSiO}_4 \cdot 1.3 \text{H}_2\text{O}$ |
| $\text{Al}_2\text{O}_3$ :5.0  | $\text{SiO}_2$ :2.0 $\text{Rb}_2\text{O}$ :5.5( $[\text{CH}_3]_4\text{N}$ ) $_2\text{O}$ :260 $\text{H}_2\text{O}$  | 90           | 6             | $\text{RbAlSiO}_4 \cdot 1.3 \text{H}_2\text{O}$ |
| $\text{Al}_2\text{O}_3$ :12.0 | $\text{SiO}_2$ :2.0 $\text{Rb}_2\text{O}$ :8.5( $[\text{CH}_3]_4\text{N}$ ) $_2\text{O}$ :360 $\text{H}_2\text{O}$  | 90           | 8             | Offretite Type                                  |
| $\text{Al}_2\text{O}_3$ :13.0 | $\text{SiO}_2$ :2.0 $\text{Rb}_2\text{O}$ :9.0( $[\text{CH}_3]_4\text{N}$ ) $_2\text{O}$ :360 $\text{H}_2\text{O}$  | 90           | 17            | Offretite Type                                  |
| $\text{Al}_2\text{O}_3$ :13.0 | $\text{SiO}_2$ :2.0 $\text{Rb}_2\text{O}$ :9.0( $[\text{CH}_3]_4\text{N}$ ) $_2\text{O}$ :360 $\text{H}_2\text{O}$  | 90           | 11*           | Offretite Type                                  |
| $\text{Al}_2\text{O}_3$ :13.0 | $\text{SiO}_2$ :2.0 $\text{Rb}_2\text{O}$ :9.0( $[\text{CH}_3]_4\text{N}$ ) $_2\text{O}$ :360 $\text{H}_2\text{O}$  | 120          | 4             | Offretite Type                                  |
| $\text{Al}_2\text{O}_3$ :14.0 | $\text{SiO}_2$ :2.0 $\text{Rb}_2\text{O}$ :9.0( $[\text{CH}_3]_4\text{N}$ ) $_2\text{O}$ :380 $\text{H}_2\text{O}$  | 90           | 25            | Offretite+ Sodalite                             |
| $\text{Al}_2\text{O}_3$ :16.5 | $\text{SiO}_2$ :4.0 $\text{Rb}_2\text{O}$ :11.0( $[\text{CH}_3]_4\text{N}$ ) $_2\text{O}$ :510 $\text{H}_2\text{O}$ | 95           | 27            | Sodalite+ Offretite                             |

\* Seeded (1 g Rb-offretite crystals per 870 g of gel, dry basis).

Table II  
X-RAY DATA FOR TMA-Rb SODALITE

| <u>d (Å)</u><br><u>Observed</u> | <u>d (Å)</u><br><u>Calculated</u> | <u>hkl</u> |
|---------------------------------|-----------------------------------|------------|
| 6.33                            | 6.32                              | 110        |
| 4.46                            | 4.47                              | 200        |
| 3.66                            | 3.65                              | 211        |
| 3.15                            | 3.16                              | 220        |
| 2.82                            | 2.83                              | 310        |
| 2.58                            | 2.58                              | 222        |
| 2.23                            | 2.235                             | 400        |
| 2.10                            | 2.108                             | 330        |
| 1.90                            | 1.898                             | 332        |
| 1.75                            | 1.753                             | 501        |
| 1.63                            | 1.631                             | 521        |
| 1.58                            | 1.580                             | 440        |
| 1.54                            | 1.533                             | 530        |
| 1.49                            | 1.490                             | 442        |
| 1.45                            | 1.451                             | 532        |

$$d_0 = 8.94 \text{ \AA}$$

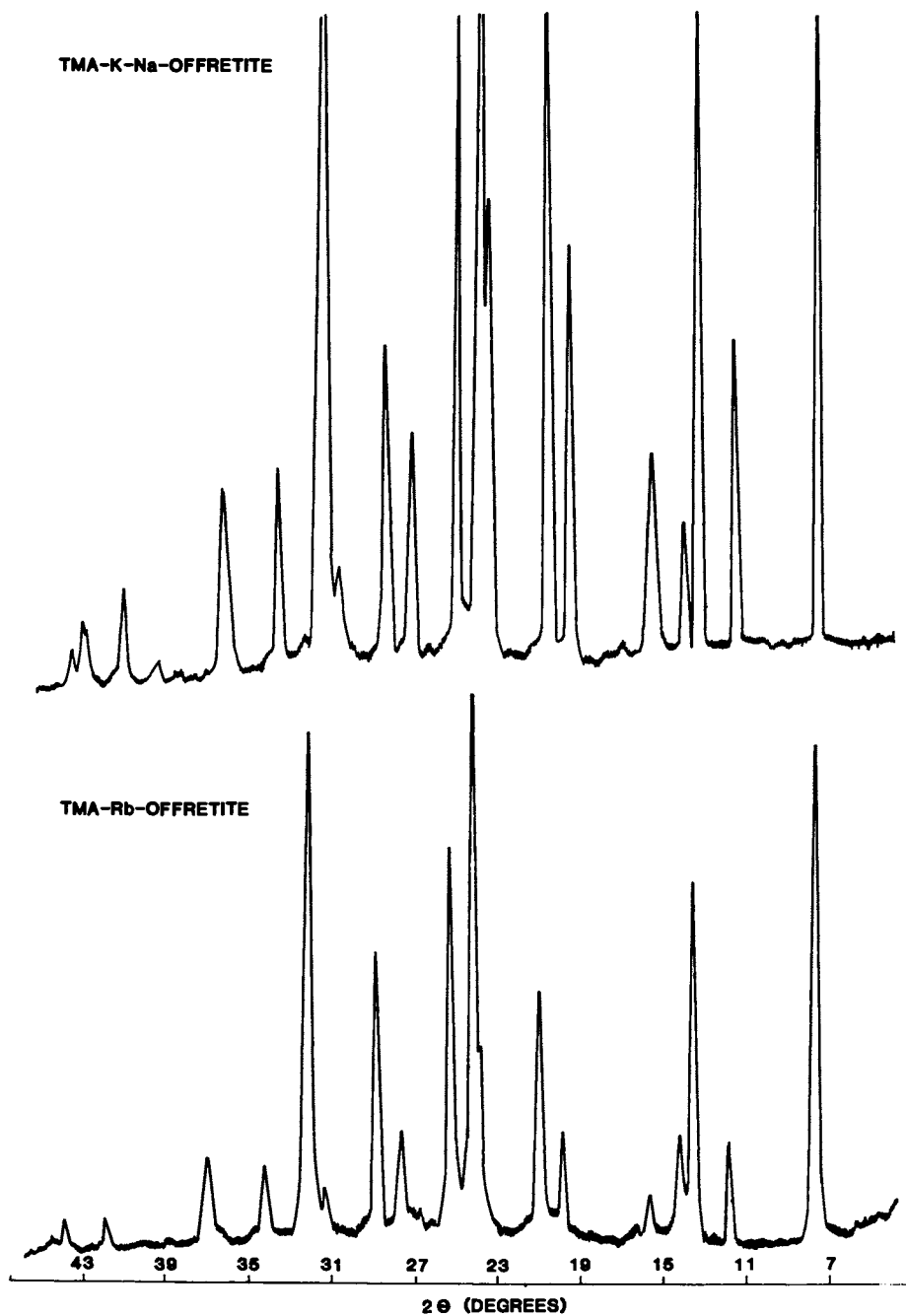
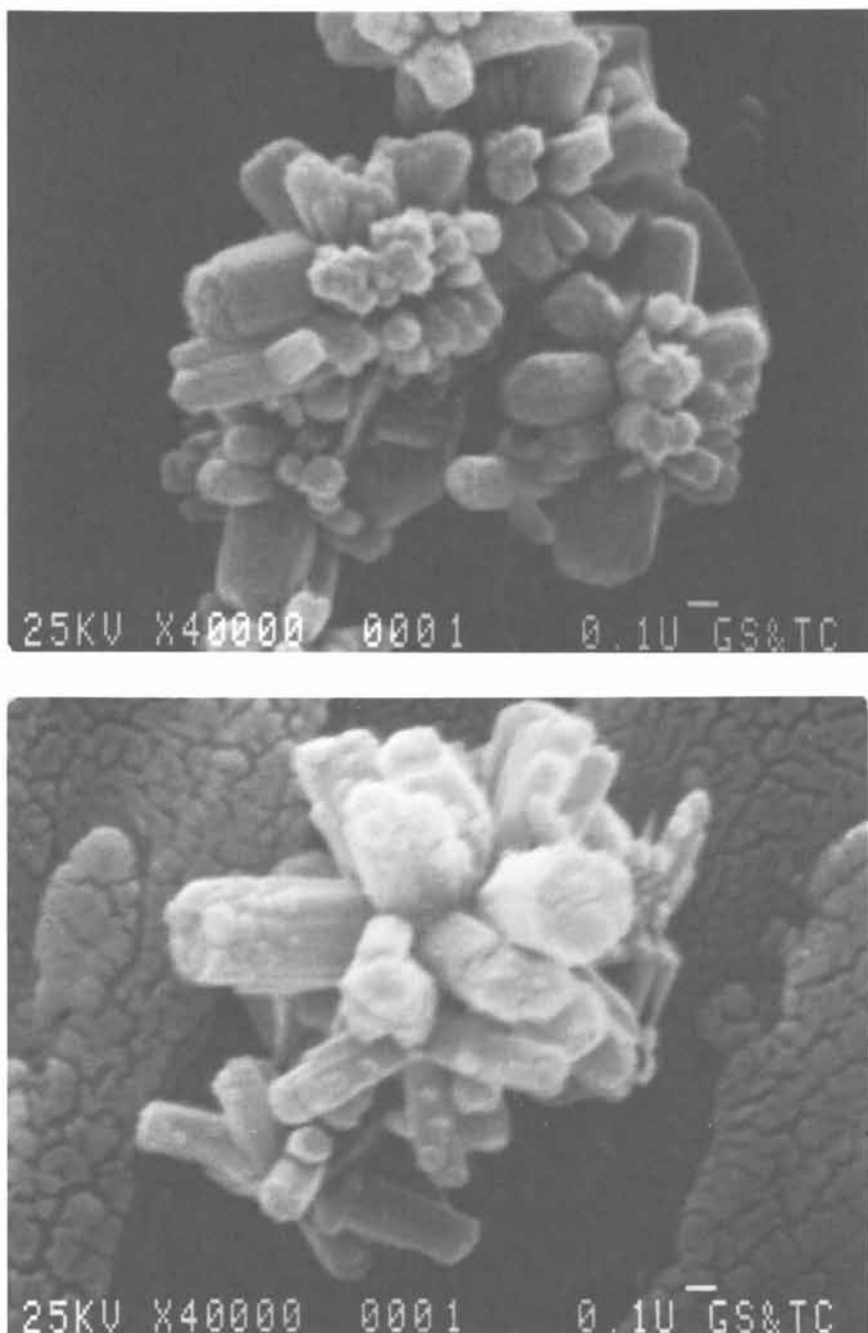


Figure 2.  
X-Ray diffractograms for (Rb, TMA) offretite and (Na, K, TMA) offretite.





**Figure 3.**  
Scanning electron micrographs for (Rb,TMA) offretite

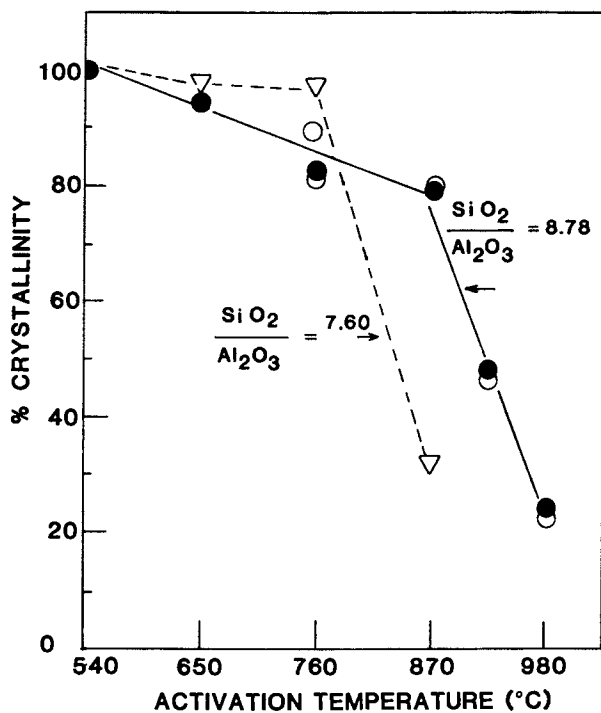


Figure 4. The thermal stability of (Rb, TMA) (solid line) and (Na, K, TMA) (broken line) offretite crystals. The crystallinity of the samples dried at 250 °C/4 hrs was arbitrarily taken as 100%.

Thermal Analysis The DTA profile for (Rb,TMA) offretite in Figure 5 shows the existence of three well defined peaks representing dehydration and decompositions of TMA cations. The endothermal dehydration is essentially completed at 220°C. The oxidative decomposition of TMA ions occurs in two steps at 330 and 435°C respectively. The exchangeable TMA ions in the large, main channels are probably decomposed at the lower temperature and the nonexchangeable TMA ions, entrapped in the gmelinite cages, decompose at the higher temperature.(11) The thermogravimetric curve in Figure 6 correlates well with the DTA profile in Figure 5 and shows that sorbed and zeolitic water contribute a 13.0 wt% loss. The weight loss between 220 and 500°C is due to the breakdown of intracrystalline TMA ions. The remaining weight change (1.2 wt%) represents the dehydroxylation of the OH-groups generated during the thermal decomposition of the TMA ions. The total weight loss was 3.64 mg. When heating was conducted in oxygen, an additional 2.1 wt% was lost due to the oxidation of otherwise residual carbon deposits.

Sorption Measurements Sorption isotherms for normal and isobutane were obtained on a sample of Rb-offretite which had been calcined in air at 550°C overnight. The curves in Figures 7 and 8, together with the Clausius-Clapeyron equation, were used to measure isosteric heats of sorption. At a coverage of ~0.4 mmoles/g,  $\Delta H = 7.47$  Kcal/mole for n-butane. By increasing the sorbate loading to 0.79 mmoles/g the heat of sorption increased slightly (to 8.5 kcal/mole) indicating the lack of preferential sorption centers in Rb-offretite crystals. For isobutane the  $\Delta H$  was 10.2 kcal/mole.

At 26°C ( $P/P_0 \approx 0.4$ ) the equilibrium loading for n-butane is 1.17 mmoles/g. This loading does not differ greatly from the isobutane equilibrium capacity (1.01 mmoles/g) suggesting that these Rb-offretite crystals are probably free from salt occlusion and/or stacking faults.

Infrared Analysis As described by Wu et al.(11) TMA decomposition in offretite crystals can be followed by observing the decrease in intensity with temperature of the TMA ion bands and by the concomitant appearance of new bands in the OH stretching region (see Figures 9 and 10). The IR spectra of (Rb,TMA) offretite at different temperatures is shown in Figure 9. The band at 3741  $\text{cm}^{-1}$  is due to terminal Si-OH groups. The appearance of a new band at 3615  $\text{cm}^{-1}$  is due to OH groups generated during TMA decomposition at 400°C. The protic nature of these hydroxyls was confirmed by their interaction with pyridine (see Figure 11). In the pyridine loaded sample, the band at 3615  $\text{cm}^{-1}$  disappears while new adsorption bands due to chemisorbed pyridine are generated in the 1400-1650  $\text{cm}^{-1}$  region (see Figure 12). Upon heating in vacuo at 400°C for 1 hr, these new bands disappear and the band at 3615  $\text{cm}^{-1}$  is restored (see Figures 11 and 12). The spectra given in Figure 9 includes the spectra of a (Rb-TMA) offretite sample

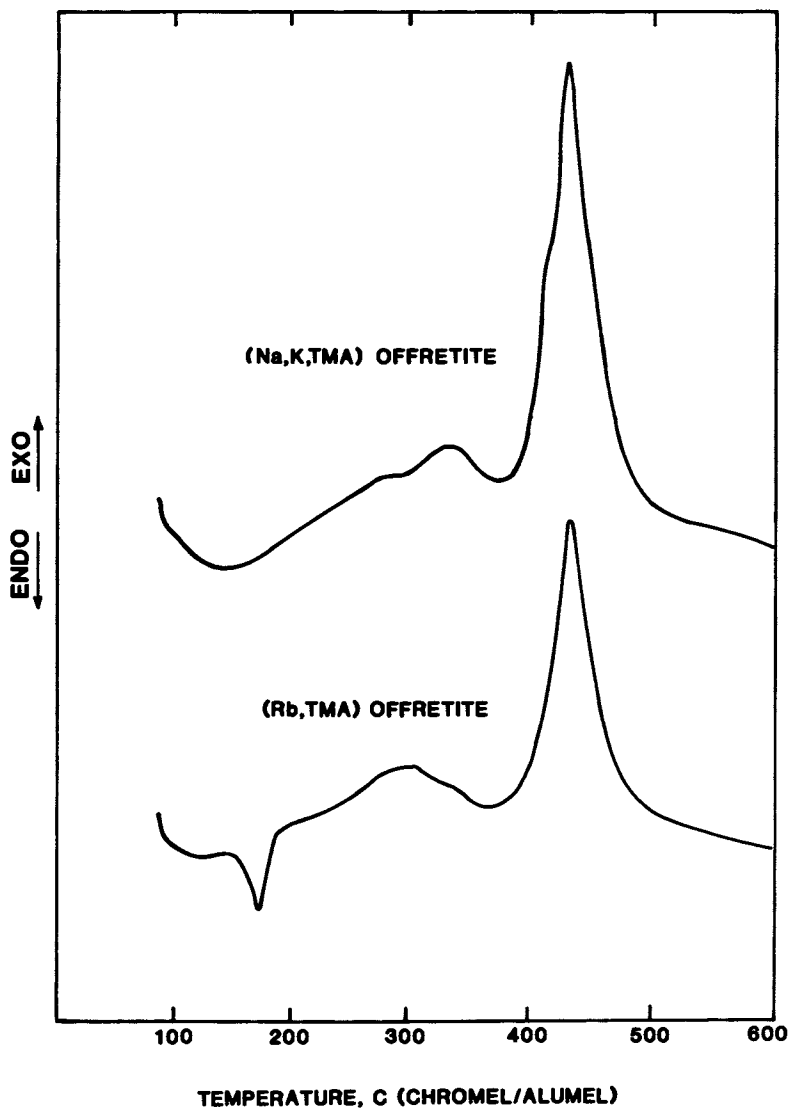


Figure 5.  
DTA profile for (Rb,TMA) offretite and (Na,K,TMA) offretite in oxygen. Sample weight: 9.8 mg. Heating rate: 10 °C/min. Oxygen flow rate: 55 CC/min.

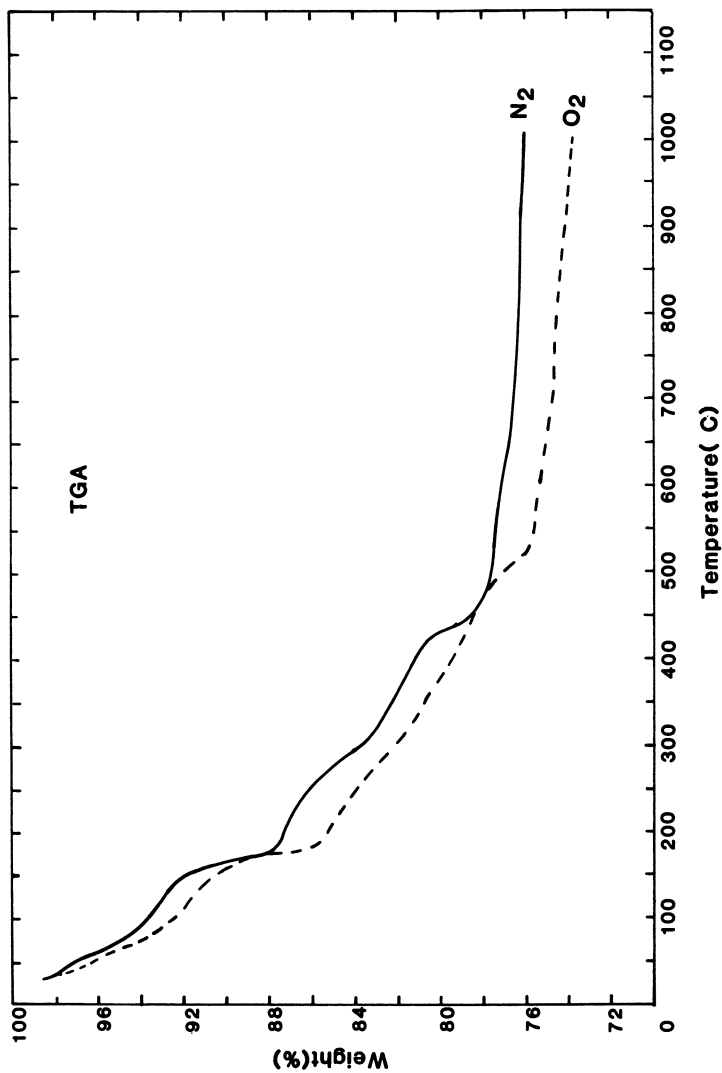


Figure 6.  
Thermograms of (Rb,TMA) offretite crystals in oxygen and nitrogen.  
Sample weight: 15.15 mg. Heating rate 10 °C/min. Gas flow rate:  
180 CC/min.

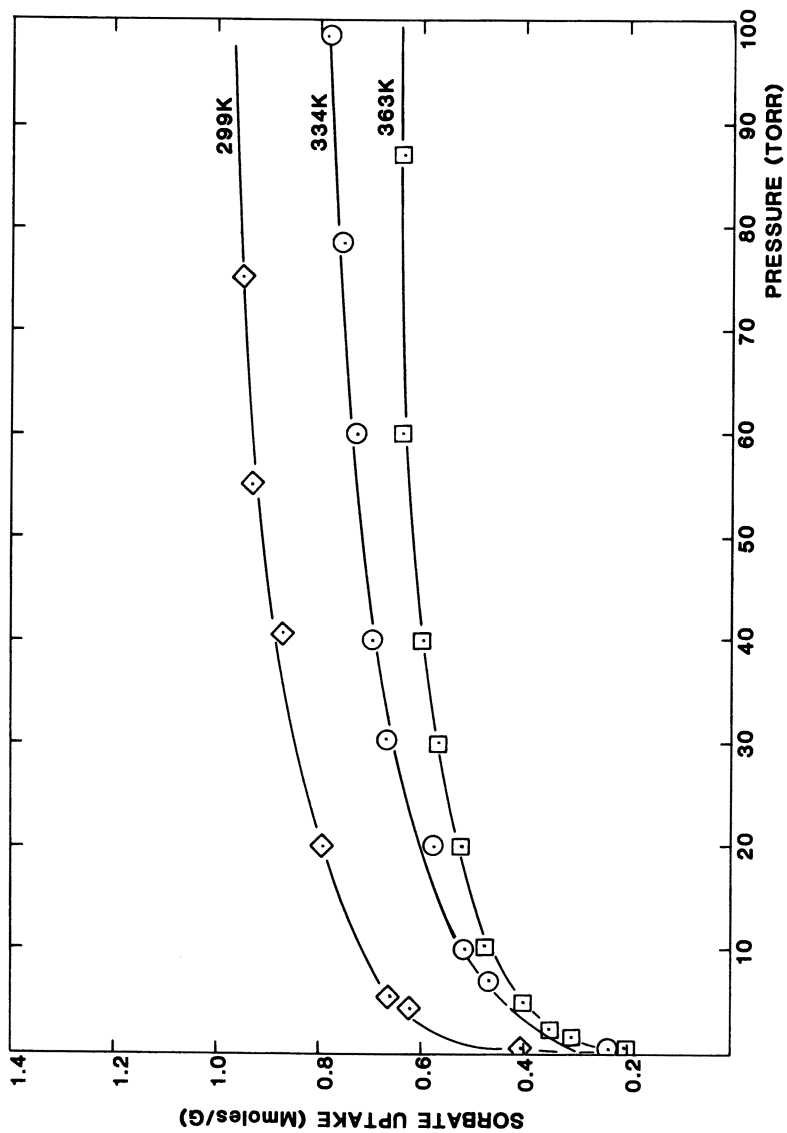


Figure 7.  
Normal butane sorption isotherms on Rb offretite.

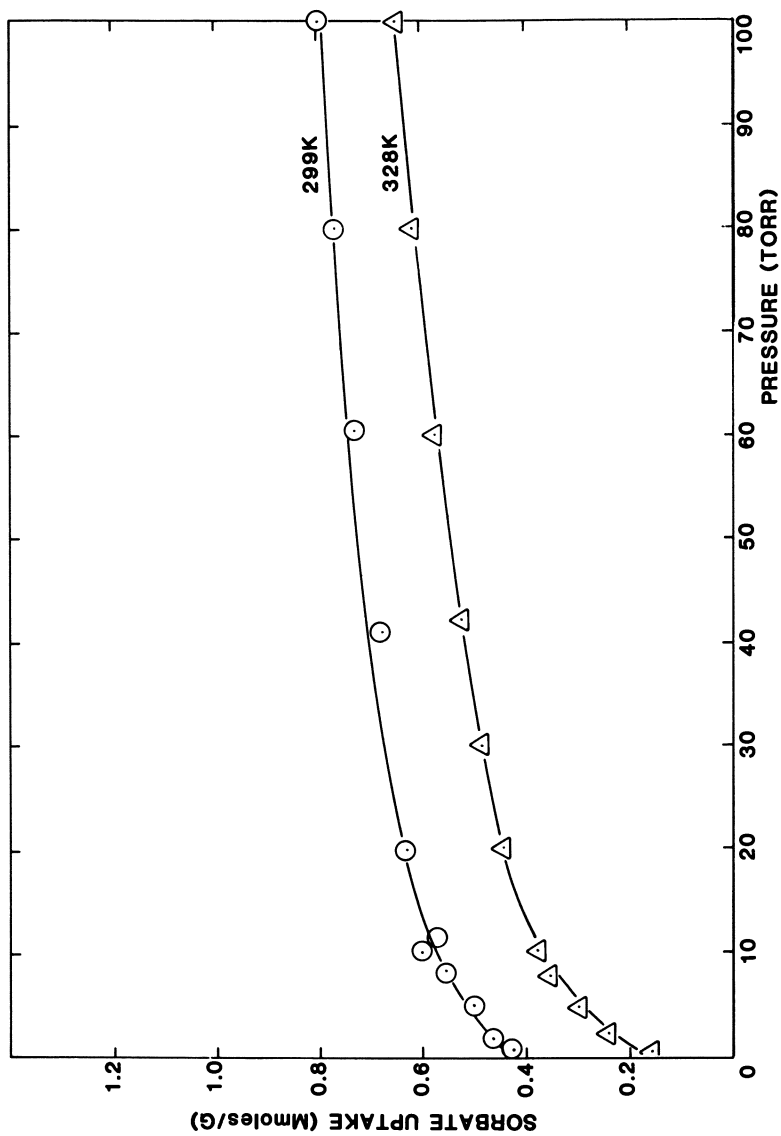


Figure 8.  
Isobutane sorption isotherms on Rb offretite.

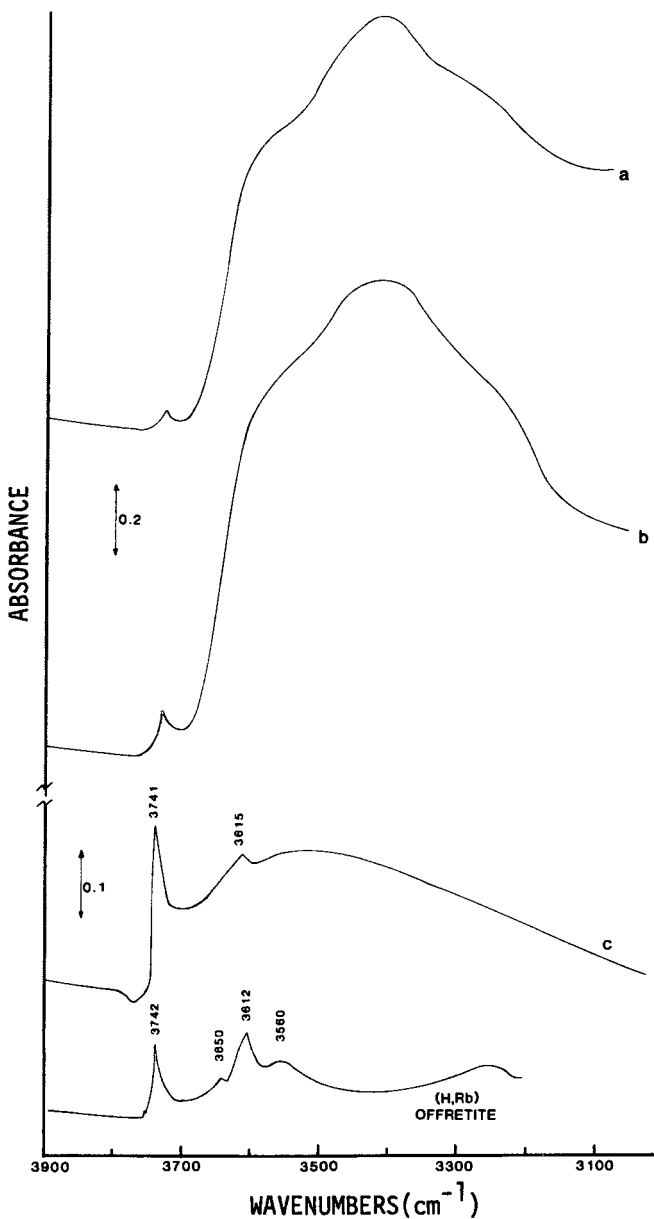


Figure 9.

Infrared absorption bands in the OH-Stretching region for (Rb,TMA) offretite heated in vacuo at 100(a), 200(b), and 400 °C(c). The spectra of (H,Rb) offretite is shown for comparison purposes



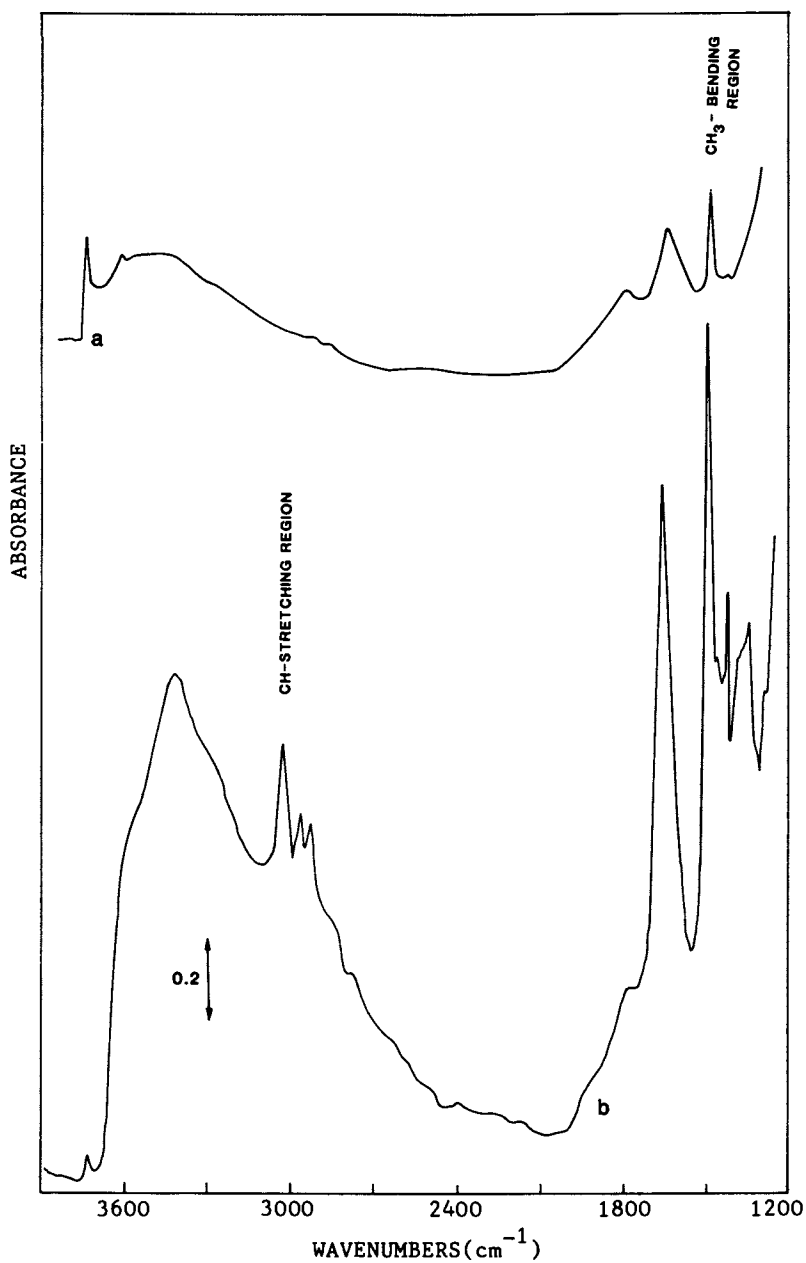


Figure 10. Infrared absorption bands in the 3900 to 1200  $\text{cm}^{-1}$  region for (Rb, TMA) offretite heated in vacuo at 100(a) and 400°C(b).

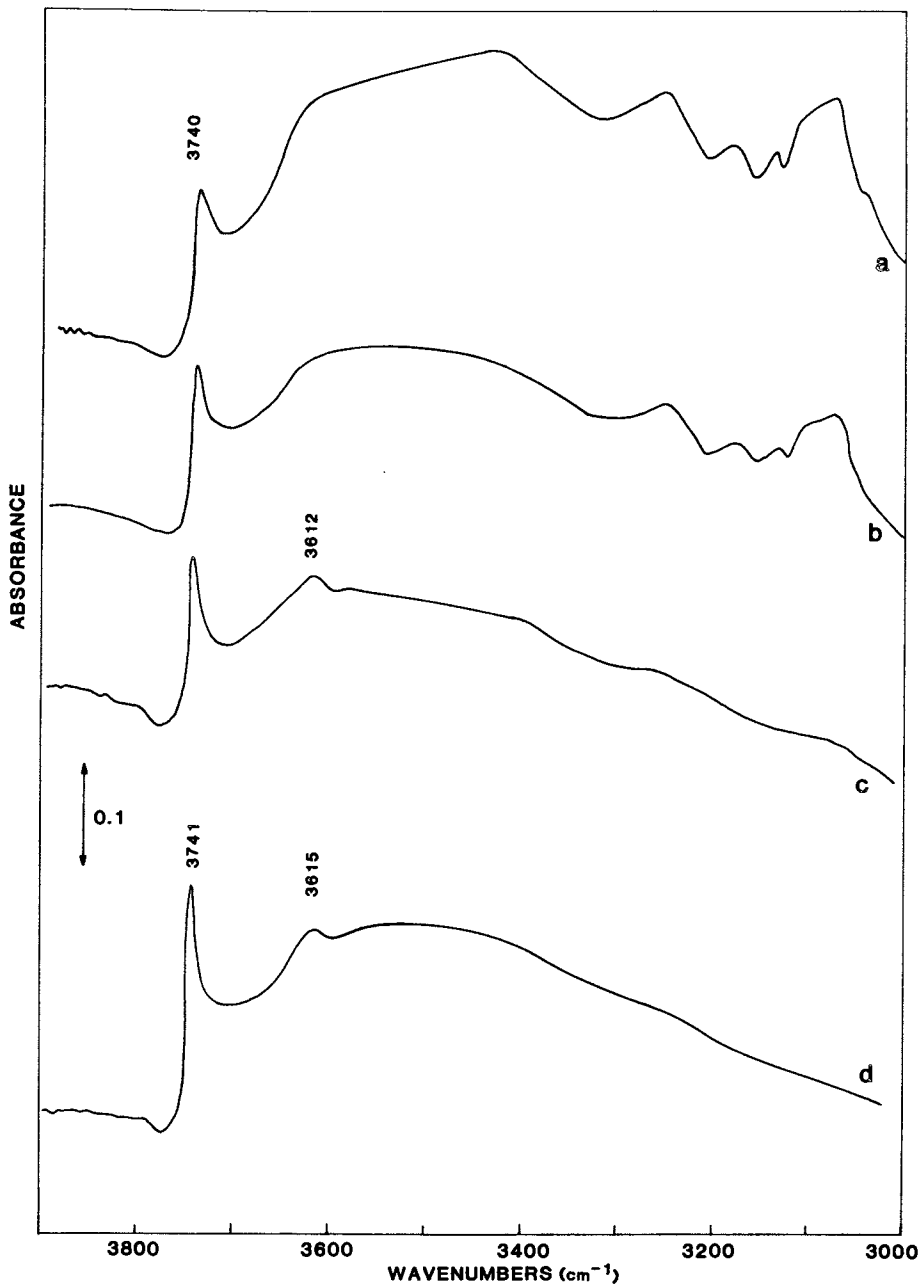


Figure 11.

Infrared spectra of Rb-offretite before and after room temperature sorption of pyridine. Outgassing temperatures: (a) 100, (b) 200, (c) 400 °C. Curve (d) refers to the Rb-offretite crystals used

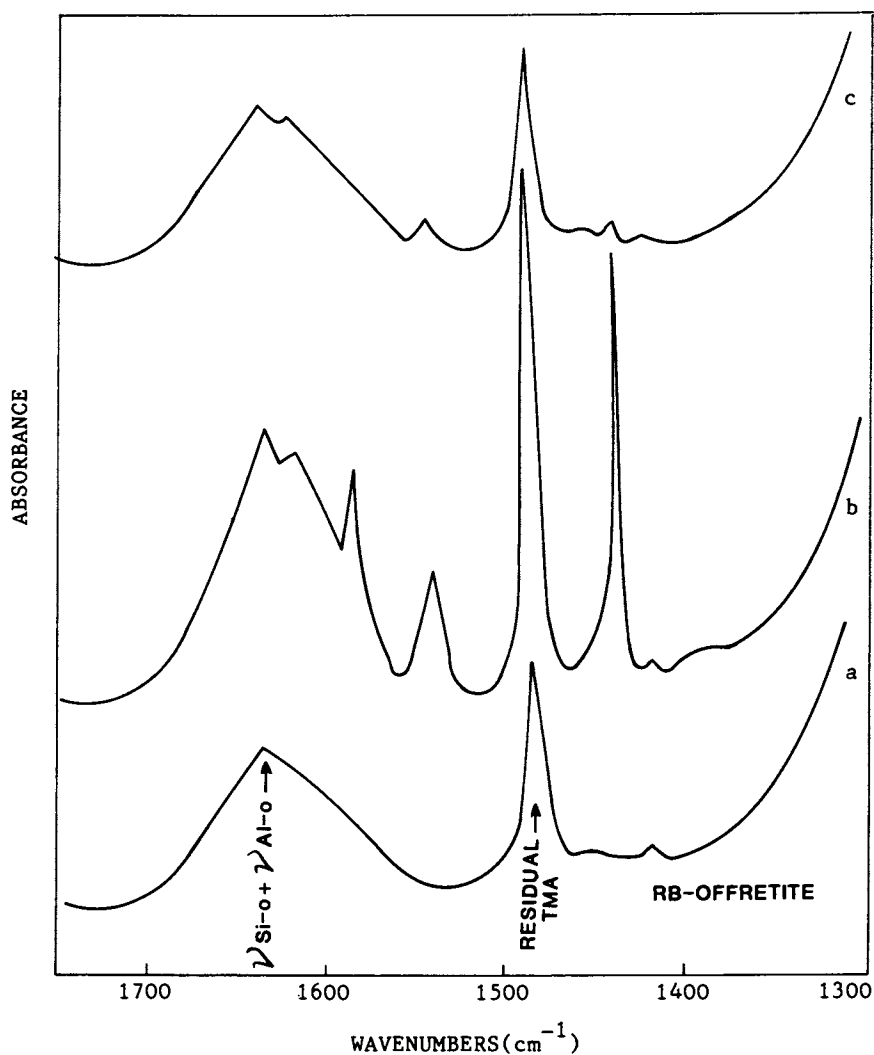


Figure 12.

Variation of IR band intensity of chemisorbed pyridine. Outgassing temperatures: (b) 100 °C (c) 400 °C. Curve (a) refers to the calcined Rb-offretite crystals used.

which has been calcined at 550°C overnight,  $\text{NH}_4^+$  exchanged, oven dried, and then heated in air at 500°C for 4 hr. This spectra shows that by replacing Rb ions with protons, new bands at 3650 and 3560  $\text{cm}^{-1}$  appear while the Si-OH band remains fairly constant at 3741  $\text{cm}^{-1}$ . The acidic strength of these bands is evident by their strong interaction with pyridine which is mostly retained even after desorbing in vacuo at 400°C for 1 hr (see Figure 13).

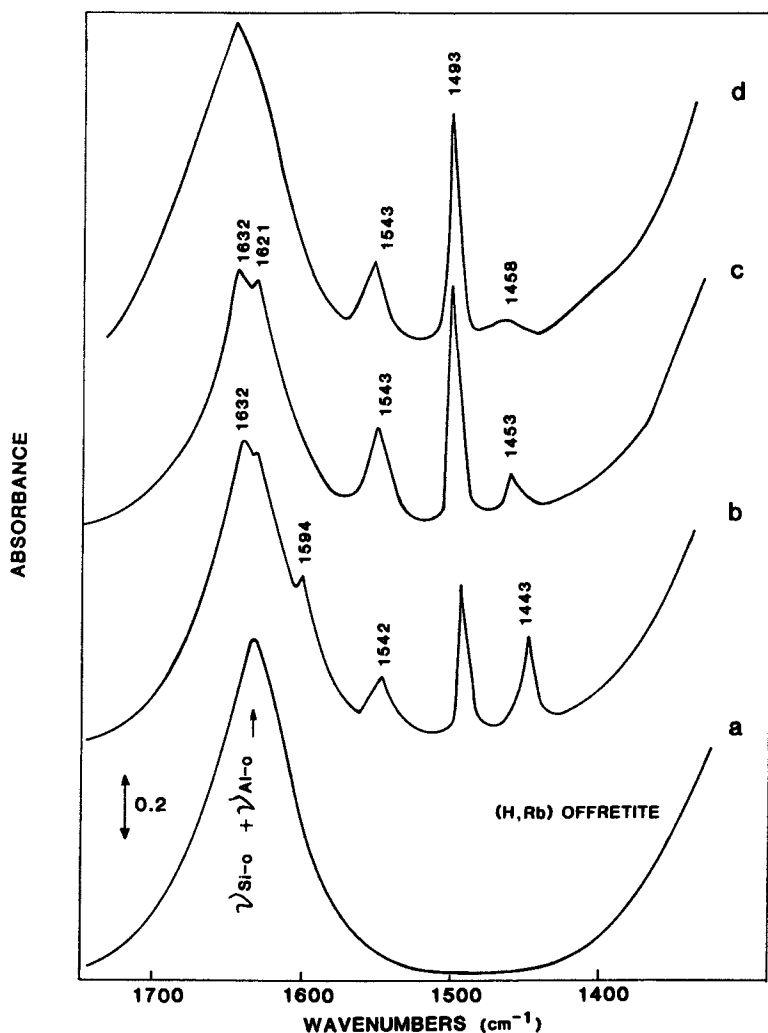


Figure 13.

Infrared spectra of (H,Rb) offretite before and after room temperature sorption of pyridine. Outgassing temperatures: (b) 25, (c) 100, and (d) 400 °C. Curve (a) refers to the (HRb) offretite crystals used

The spectra in Figure 9 is somewhat different from the spectra of offretite crystals synthesized in the NaOH-KOH-TMAOH mixed base system. Wu et al.(11), in addition to our observed band at  $3615\text{ cm}^{-1}$ , reported the appearance of acidic bands at  $3690$  and  $3550\text{ cm}^{-1}$ . In contrast, Mirodatos et al.(12) reported the appearance of only one, weakly acidic band at  $3660\text{ cm}^{-1}$ . The TMA content and the concentrations of different charge compensating cations may be responsible for these differences.

### Conclusions

The investigation of the alumina-silica-rubidium-TMA system has shown the existence of three different crystalline phases. From an hydrogel of composition  $\text{Al}_2\text{O}_3:13.0\text{SiO}_2:2.0\text{Rb}_2\text{O}:9.0[(\text{CH}_3)_4\text{N}]_2\text{O}:360\text{H}_2\text{O}$  a new zeolite of the offretite type crystallizes as irregular, rod-like crystals characterized by a BET surface area of  $380\text{--}420\text{ cm}^2/\text{g}$ , a pore volume of  $0.20\text{--}0.24\text{ cc/g}$ , and good thermal stability to  $\sim 870^\circ\text{C}$ . The oxidative decomposition of TMA ions generates acidic OH groups which vibrate at  $3615\text{ cm}^{-1}$ . The exchange of rubidium with ammonium ions produce new hydroxyls which vibrate at  $3650$  and  $3560\text{ cm}^{-1}$ . Rb-offretite sorbs almost equimolar amounts of normal and isobutane suggesting that these crystals are probably free of salt occlusion and/or stacking faults.

### Acknowledgments

We thank Professor J. Hightower for allowing the use of his thermogravimetric system; Dr. F. S. S. Hwu for many helpful suggestions during the sorption measurements; and Dr. J. Lester for assistance with IR data generation. Thanks are also due to Drs. H. E. Swift and J. V. Kennedy for critically reviewing this manuscript.

### Literature Cited

1. Gonnard, F. C. *R. Acad. Sci.*, 1890, 111, 1002.
2. Rubin, M. K., German Patent No. P1806154.6, 1968.
3. Aiello, R.; R. M. Barrer *J. Chem. Soc. (A)*, 1970, 1470.
4. Sand, L. B., U.S. Patent No. 4,093,699 1978.
5. Barrer, R. M.; Sieber, M. *J. Chem. Soc. Dalton*, 1977, 1020.
6. Perrotta, A. J., U.S. Patent Pending.
7. Hwu, S. S. F., Ph.D Thesis, Rice University, Houston, Texas 1981.
8. Breck, D. W. *Zeolite Molecular Sieves*, J. Wiley & Sons 1974.
9. Kerr, G. T. *J. Phys. Chem.*, 1966, 70, 1047.
10. McDaniel, C. V.; Mather, P. K., U.S. Patent No. 3,808,326 1974.
11. Wu, E. L.; White, T. E., Jr.; Venuto, P. B., *J. Catalysis* 1971 21, 384.
12. Mirodatos, C.; Abou-Kais, A.; Vadrine, J. C.; Barthomeuf, D. *J. Chim. Phys.*, 1978, 57.

RECEIVED November 16, 1982

## Zeolite Modification—Direct Fluorination

BRENT M. LOK, F. P. GORTSEMA, CELESTE A. MESSINA, H. RASTELLI,  
and T. P. J. IZOD

Union Carbide Corporation, Tarrytown Technical Center, Tarrytown, NY 10591

Dilute fluorine gas (0-20%) can be used to treat zeolites at near-ambient temperature and pressure. Most of the resulting materials retain very high crystallinity even after 600°C postcalcination for two hours. Both framework infrared spectra and X-ray powder diffraction patterns clearly show structural dealumination and stabilization. The hydrophobic nature of the fluorine-treated and 600°C-calcined material is shown by a low water adsorption capacity and selective adsorption of n-butanol from a 1 vol.% n-butanol-water solution. Fluorination also changes the catalytic activity of the zeolite as measured by an n-butane cracking method.

Over the past thirty years, zeolite science has grown into a major branch of chemistry. A large number of new zeolite materials have been made by both direct hydrothermal synthesis and by post-synthesis modification. This has led to a large number of new applications in such diverse fields as catalysis, adsorption and ion exchange. In synthesis alone, over one hundred new zeolites have been produced. These are divided into two major classes: ones with low silicon to aluminum ratios ( $\text{Si/Al} < 10$ ) and ones with high silicon to aluminum ratios ( $\text{Si/Al} > 10$ ). The low silicon to aluminum ratio zeolites have hydrophilic surfaces, a large number of exchangeable cations and acid sites with moderate to high strength. On the other hand, the high silicon to aluminum ratio zeolites have an organophilic surface, a relatively small number of exchangeable cations and a relatively small number of acid sites with high strength.

Many low silicon to aluminum ratio zeolites can be structurally modified to have a high silicon to aluminum ratio and, thus, in many respects, behave like a high silicon to aluminum ratio

0097-6156/83/0218-0041\$06.00/0  
© 1983 American Chemical Society

zeolite. The known methods of synthesis of these materials include mineral or weak organic acid extraction of acid-stable zeolites such as clinoptilolite (1) and mordenite (2-7), hydrothermal treatment (8-9) and reaction with organic complexing agents (EDTA) (10) or acetylacetone (11) or chromic salts (12). Very recently, zeolites have also been modified by chlorine (13) and chlorine-related compounds at high temperature (14, 15). The known modification methods can be further classified as either liquid or vapor phase treatments. The acid washing, organic complexing agent extraction and chromic salt treatments fall into the first class while the steaming and the chlorine and related compounds reactions belong to the second class.

Fundamentally, all the modification methods follow the same principle, that is, to remove structural aluminum. After the removal, a structural defect site is usually created. A widely accepted hypothesis is that this structural defect site is a hydroxyl nest (1). It has been further hypothesized that under the proper conditions, a silica molecule would be inserted into the vacant site and, thus, anneal the structural defect (16). The source of the silica can be either the treating reagent (14) or the zeolite sample itself through rearrangement of silica from another part of the framework or from a silica impurity within the sample. (Note that in the chromic salt case, chromia rather than silica is claimed to be inserted in the structure.) Because of the dealumination and the silica insertion, the treated samples are usually found to have a higher framework silicon to aluminum ratio and a higher thermal stability than the untreated materials. Furthermore, hydrophobic surface properties usually result from substantial dealumination (7).

We believe the use of a direct gaseous phase fluorination process for modifying the surface and structure of zeolites to be a new process (18). The literature does contain references to the use of hydrogen fluoride (20, 22, 23), boron trifluoride (21, 24), aluminum monofluoride (sic) (19) and silica difluoride (sic) (19) to treat the surface of a zeolite to obtain higher catalytic activity. However, the use of fluorine gas to modify both surface and structure has not been reported before. The purpose of this paper is to report results of fluorination of zeolites and to describe the process involved in such a treatment. Detailed results on fluorine-treated zeolites and their unusual properties, both adsorptive and catalytic, will be discussed in forthcoming papers.

## Experimental

### Treatment Conditions

Table I lists the zeolite samples used in this study along with their chemical composition and source of manufacture. Either ammonium ion-exchanged or acid-washed zeolites were employed to

avoid the formation of cation fluorides in the pore system. Both precalcined and uncalcined samples were used. The results indicate that the properties of treated products are similar regardless of their calcination state.

Table I  
CHEMICAL COMPOSITION AND SOURCE OF VARIOUS MATERIALS TESTED

| Zeolite                                   | Chemical Compositions (wt %)   |                  |                       |                                   | Mole Ratio |      |                                  | Source   |
|---|--------------------------------|------------------|-----------------------|-----------------------------------|------------|------|----------------------------------|----------|
|   | (On dry basis with no binder)  |                  |                       |                                   | Si/Al      | M/Al | NH <sub>4</sub> <sup>+</sup> /Al |          |
|   | Al <sub>2</sub> O <sub>3</sub> | SiO <sub>2</sub> | Na <sub>2</sub> O     | (NH <sub>4</sub> ) <sub>2</sub> O |            |      |                                  |          |
| LZ-105 <sup>a</sup>                       | 4.28                           | 90.2             | 2.86                  | -                                 | 17.9       | 1.10 | -                                | This lab |
| LZ-105 <sup>b</sup>                       | 3.73                           | 95.0             | 0.03                  | -                                 | 21.6       | 0.01 | -                                | This lab |
| H-zeolon                                  | 10.9                           | 89.3             | 0.17                  | -                                 | 7.0        | 0.03 | -                                | Norton   |
| Erionite <sup>c</sup>                     | 18.6                           | 77.2             | 2.00                  | 3.1                               | 3.53       | 0.12 | 0.32                             | This lab |
|   |                                |                  | (Na+K) <sub>2</sub> O |                                   |            |      |                                  |          |
| Erionite <sup>d</sup>                     | 18.8                           | 78.8             | 0.98                  | 2.2                               | 3.53       | 0.06 | 0.23                             | This lab |
| NH <sub>4</sub> ,<br>TMA-Ω                | 17.1                           | 72.0             | 0.04                  | 7.9                               | 3.58       | -    | 0.91                             | This lab |
| NH <sub>4</sub> , K-L                     | 19.5                           | 68.8             | 3.6                   | 8.1                               | 3.0        | 0.20 | 0.81                             | This lab |
|   |                                |                  | (K <sub>2</sub> O)    |                                   |            |      |                                  |          |
| NH <sub>4</sub> <sup>y</sup> <sup>c</sup> | 20.6                           | 74.8             | 0.14                  | 4.3                               | 3.09       | 0.01 | 0.41                             | This lab |

a. 20 wt % alumina bonded.

b. Acid washed and 20 wt % alumina bonded.

c. Mild steaming followed by NH<sub>4</sub><sup>+</sup> exchange with hot NH<sub>4</sub>Cl solution.

d. Mild steaming and NH<sub>4</sub>Cl exchange repeated.

The powder sample, in 5 to 20 gram quantities, was placed in a Teflon container. Then, to remove the bulk water, the sample was evacuated at 60°C in a stainless steel reactor chamber (volume - 50 dm<sup>3</sup>) equipped with a thermocouple, a pressure gauge, three gas inlets and a vacuum outlet. The three gas inlets were used to introduce fluorine, nitrogen and oxygen. The desired amount of fluorine gas (0-20 volume %) was introduced after the reactor chamber had first been filled with a predetermined amount of nitrogen and oxygen. The total gas pressure in the reactor was always slightly lower than one atmosphere pressure for safety reasons. The concentration of a particular gas was measured in pressure percent by means of a pressure gauge and then converted to volume percent by assuming the ideal gas law. The sample was kept in the reactor chamber in contact with fluorine for a specified period and then the reactor chamber was evacuated and, subsequently, flushed with nitrogen gas. During the treatment process, the reactor was maintained at ambient or 60°C. However, the actual sample temperature, as measured by a thermocouple in contact with the powder sample, was found to be much higher than the reactor temperature due to the exothermic nature of the fluorination reaction. To desorb fluorine and related gases,



samples were either post-activated at 150°C under vacuum or flushed with dry nitrogen for ten minutes. The treated samples were optionally postcalcined at 600°C for 2 hours and stored in zipper-seal plastic bags and kept in a desiccator.

Table II lists the treatment conditions.

Table II  
FLUORINE TREATMENT CONDITIONS

| Sample # | Zeolite                          | Treatment Conditions |                   |                   |              |        | F <sub>2</sub> Content <sup>e</sup><br>(wt %) |
|----------|----------------------------------|----------------------|-------------------|-------------------|--------------|--------|---|
|          |                                  | F %<br>2<br>Vol %    | O %<br>2<br>Vol % | Duration<br>(min) | Temp<br>(°C) | Type   |   |
| 1        | LZ-105 <sup>a</sup>              | 10                   | 2                 | 10                | 60           | Severe | N.A.  |
| 2        | LZ-105 <sup>b</sup>              | 5                    | 5                 | 15                | 60           | Severe | 2.4 <sup>f</sup>                              |
| 3        | H-zeolon                         | 10                   | 2                 | 10                | 60           | Severe | 3.5 <sup>f</sup>                              |
| 4        | H-zeolon                         | 5                    | 0 <sup>g</sup>    | 30                | 25           | Severe | 10.0  |
| 5        | H-zeolon                         | 1                    | 0 <sup>g</sup>    | 45                | 25           | Mild   | N.A.  |
| 6        | Erionite <sup>c</sup>            | 5                    | 5                 | 5                 | 60           | Severe | 4.6   |
| 7        | Erionite <sup>d</sup>            | 5                    | 5                 | 5                 | 60           | Severe | N.A.  |
| 8        | NH <sub>4</sub> , TMA-Ω          | 5                    | 5                 | 5                 | 60           | Severe | 4.4   |
| 9        | NH <sub>4</sub> , K-L            | 5                    | 5                 | 5                 | 60           | Severe | 4.8   |
| 10       | NH <sub>4</sub> , Y <sup>c</sup> | 2                    | 0 <sup>g</sup>    | 5                 | 60           | Mild   | N.A.  |
| 11       | NH <sub>4</sub> , Y <sup>c</sup> | 2                    | 0 <sup>g</sup>    | 15                | 25           | Mild   | 2.2   |
| 12       | NH <sub>4</sub> Y <sup>c</sup>   | 1                    | 0 <sup>g</sup>    | 15                | 25           | Mild   | N.A.  |

- a. 20 wt % alumina bonded.  
 b. Acid washed and 20 wt % alumina bonded.  
 c. Mild steaming followed by NH<sub>4</sub><sup>+</sup> exchange with hot NH<sub>4</sub>Cl solution.  
 d. Mild steaming and NH<sub>4</sub>Cl exchange repeated.  
 e. F<sub>2</sub> content analyzed after fluorination.  
 f. F<sub>2</sub> content analyzed after 600°C calcination and 2 1/2 hr. Soxhlet extraction subsequent to fluorination.  
 g. Samples treated in a flow-through reactor with premixed F<sub>2</sub>-N<sub>2</sub> mixture.  
 N.A. - Not analyzed.

### Characterization

For sample characterization, a Philips X-ray diffractometer employing CuK<sub>α</sub> radiation was used over a 2θ range of 4° to 56° at a scan rate of 2 degrees/min. I. R. spectra were obtained from 0.5 in. diameter KBr pellets (for framework spectra) and self-supported wafers (for hydroxyl region spectra). Two concentrations were usually employed in KBr pellets: 0.25 mg sample per 350 mg KBr and 1 mg sample per 350 mg KBr. Spectra were recorded with a Nicolet model 7199 FT-IR spectrometer. Gas phase adsorption studies on treated samples were carried out using a McBain-Baker gravimetric adsorption system with quartz springs. Samples were activated at 350°C, 1x10<sup>-4</sup> torr for about 16 hours before

the adsorption measurement. A binary liquid (1 vol % n-butanol in water) shake test (25) was conducted by mixing 0.5 g of the sample with 5 cm<sup>3</sup> or 0.25 g of the sample with 2.5 cm<sup>3</sup> of the n-butanol-H<sub>2</sub>O solution in a glass vial. The slurry was well shaken mechanically for one and a half to two hours. The mother liquor was analyzed by gas chromatography. A delta hexane loading test (26) was used as one of the measurements of surface hydrophobicity and organophilicity. Water was adsorbed onto the sample at near saturation pressure (~20 torr) and ambient temperature. Then, when the water adsorption reached equilibrium, 50 torr of n-hexane vapor was introduced. The additional amount adsorbed is termed the delta hexane loading.

Finally, the catalytic activity was measured by a 2 mole % n-butane cracking method described in detail on another paper (27).

### Results

To illustrate the dealumination and structure stabilization in treated zeolites, severely treated and postcalcined ones are chosen as examples. The degree of dealumination, nevertheless, can be controlled by varying the treatment conditions.

#### X-Ray Diffraction

For LZ-105 (28), there is very little observable change in the X-ray spectra before and after treatment. Full retention of crystallinity is evident. However, reduction in intensity for the peak at  $2\theta = 24.4^\circ$  is noted. Such an intensity change is also very prominent in the spectrum of fluoride silicalite, a silica polymorph synthesized in the presence of a fluoride salt (29).

For H-zeolon, erionite and NH<sub>4</sub>Y, there are noticeable changes in both peak intensity and peak positions, especially for those treated under severe conditions (Figures 1a, b, c). The substantial increase in peak intensities for low angle peaks observed in the X-ray spectra of fluorine treated H-zeolon, erionite and NH<sub>4</sub>Y is also found in the X-ray spectra of the hydrothermally treated samples (9). In addition to the intensity changes, all the X-ray peaks for the fluorine-treated samples are slightly shifted to higher  $2\theta$  values compared to the untreated materials. Shifts to higher  $2\theta$  values usually imply a decrease in unit cell size associated with dealumination and structure stabilization. Similar peak shifts have also been observed for high temperature-steamed samples (9).

For both NH<sub>4</sub>K-L and NH<sub>4</sub>TMA- $\Omega$ , the X-ray diffraction spectra (Figure 1d, e) indicate that both zeolites retain most of their crystallinity after fluorine treatment and 500°C calcination. Except for some minor changes in peak intensity for fluorine-treated NH<sub>4</sub>K-L, there is no evidence of peak intensity and position change as found for other treated zeolites. After 600°C calcination in air, a further loss of crystallinity is seen for fluorine-treated NH<sub>4</sub>K-L. However, NH<sub>4</sub>TMA- $\Omega$  loses virtually all crystallinity.

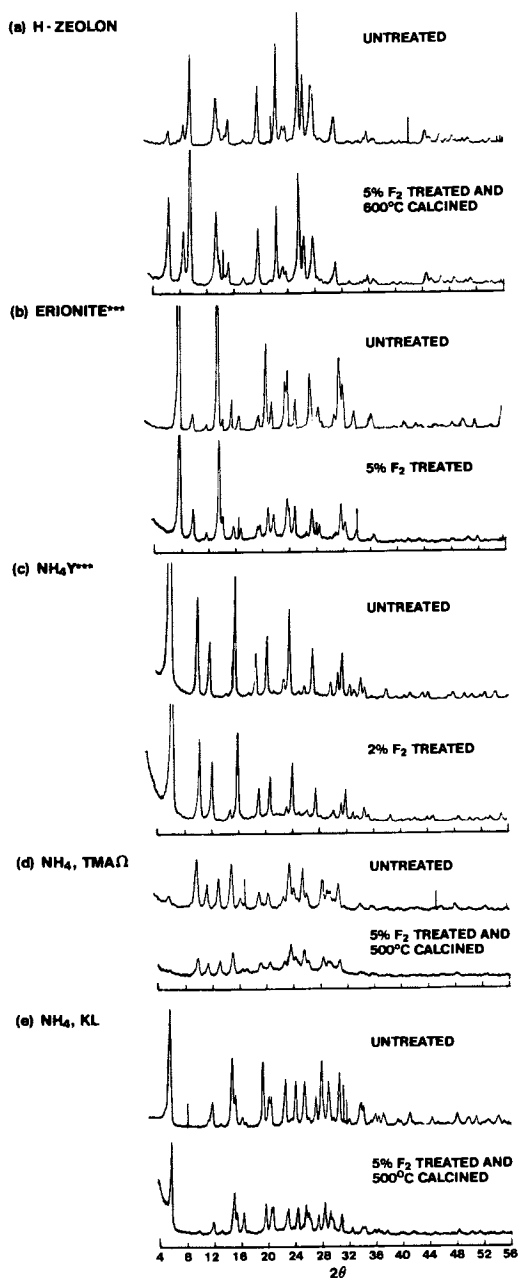


Figure 1.  
X-Ray diffraction spectra of fluorine-treated zeolites

### I. R. Spectra

#### Framework Region (400 $\text{cm}^{-1}$ - 1600 $\text{cm}^{-1}$ )

It is well known in the literature (30) that a shift of certain I. R. bands to higher wave numbers is evidence of dealumination. Since LZ-105 has a relatively high Si/Al ratio (Si/Al = 21.6), the shifts of band positions are small. In addition to the band position shifts in fluorine-treated LZ-105, sharpening of peaks at 628 and 587  $\text{cm}^{-1}$  occurs, indicative of structure stabilization. For all the 600°C-calcined fluorine-treated H-zeolon and  $\text{NH}_4\text{Y}$  zeolites, band position shifts and band sharpening are prominent in the I. R. framework spectra as shown in Figures 2a and 2b, respectively. These samples show as much as 20  $\text{cm}^{-1}$  up-shift in the 1078, 799 and 637  $\text{cm}^{-1}$  bands for H-zeolon and 1059  $\text{cm}^{-1}$  band for  $\text{NH}_4\text{Y}$  zeolite. The splitting of the band at 579  $\text{cm}^{-1}$  and the shifting and splitting of the band at 637  $\text{cm}^{-1}$  into two bands at 594 and 571  $\text{cm}^{-1}$  and 669 and 658  $\text{cm}^{-1}$  and the appearance of multiple bands in the region of 800  $\text{cm}^{-1}$  to 700  $\text{cm}^{-1}$  are observed for the fluorine-treated H-zeolon. A doublet near 1200  $\text{cm}^{-1}$  and shoulders at 795 and 485  $\text{cm}^{-1}$  appear in the fluorine-treated  $\text{NH}_4\text{Y}$  spectrum. These prominent changes strongly confirm that substantial dealumination and structure stabilization occur for H-zeolon and  $\text{NH}_4\text{Y}$  zeolite after fluorination and calcination.

The spectrum for the 600°C-calcined fluorine-treated erionite sample shows substantial shifts in band positions, but band sharpening is less obvious. The bands at 1082, 792, 578, 470 and 438  $\text{cm}^{-1}$  are shifted to 1098, 814, 585, 477 and 444  $\text{cm}^{-1}$ , respectively, after fluorine treatment and 600°C calcination. The large shifts observed are evidence of dealumination. The splitting of the 1082  $\text{cm}^{-1}$  band into a doublet located at 1098 and 1085  $\text{cm}^{-1}$  and some degree of band sharpening imply structure stabilization for fluorine treated erionite.

Finally, I. R. spectra for fluorine-treated and then 500°C-calcined  $\text{NH}_4\text{K-L}$  and  $\text{NH}_4\text{TMA-}\Omega$  (Figures 2c and 2d) show an up-shift of band positions, but loss of spectral resolution. Thus, the I. R. results indicate that the two zeolites undergo structural dealumination by fluorine treatment and subsequent calcination, but both show no evidence of structure stabilization.

#### OH Region (3100 $\text{cm}^{-1}$ - 3900 $\text{cm}^{-1}$ )

Before treatment, acid-washed LZ-105 shows two distinct bands in the OH region I. R. spectrum: one at 3745  $\text{cm}^{-1}$  and the other at 3615  $\text{cm}^{-1}$ . The former is attributable to OH groups on terminal zeolite surfaces or amorphous impurity material. The 3615  $\text{cm}^{-1}$  band is believed to be related to the Bronsted acid sites in LZ-105. After fluorination and 600°C calcination, both the 3615 and 3745  $\text{cm}^{-1}$  bands disappear.

American Chemical

Society Library

1155 16th St. N. W.

Washington, D. C. 20036

In Intrazeolite Chemistry, Stucky, G. V. Ed.

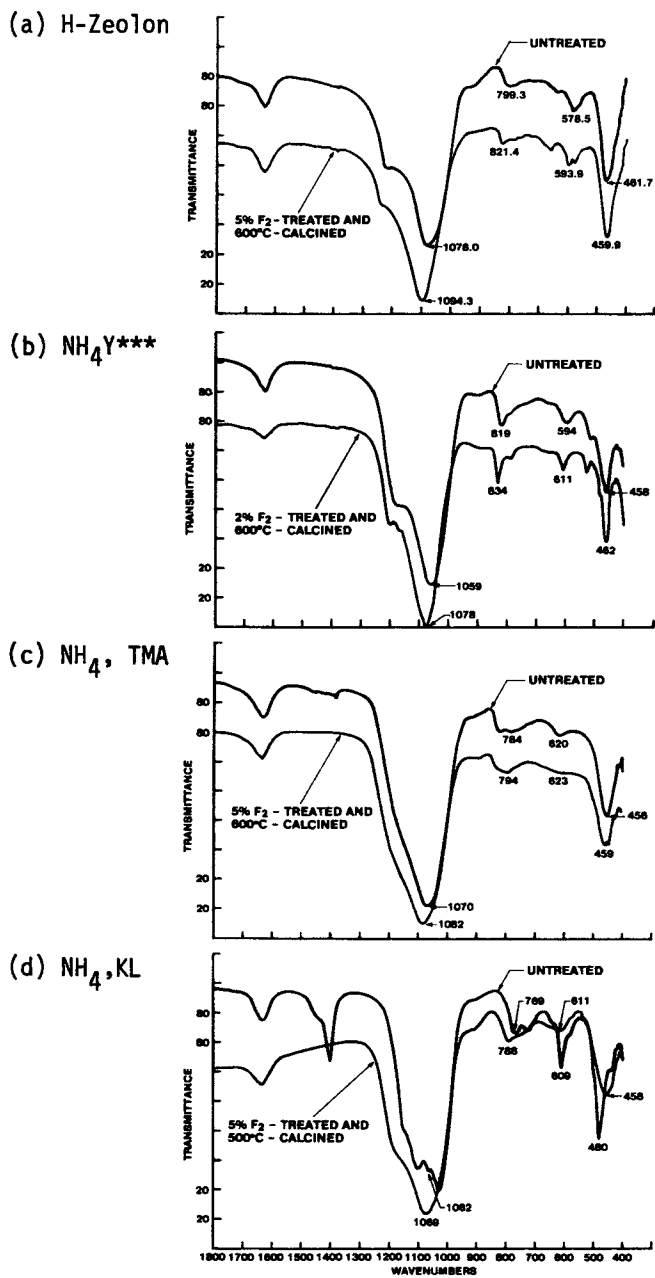


Figure 2.  
Framework infrared spectra of fluorine-treated zeolites

In the H-zeolon case, two different types of hydroxyl groups are found in the zeolite (Figure 3a). One band at  $3745\text{ cm}^{-1}$  splits after fluorination into two bands: one still at  $3745\text{ cm}^{-1}$  with much lower intensity and the other at  $3713\text{ cm}^{-1}$ . Then upon calcination at  $500^\circ\text{C}$ , the two peaks become one peak at  $3745\text{ cm}^{-1}$  with a substantially reduced intensity. The other hydroxyl group band at  $3624\text{ cm}^{-1}$  decreases in intensity after fluorination and then completely disappears after calcination at  $600^\circ\text{C}$ .

Similar observations of reduced intensity for the fluorine-treated sample and nearly complete elimination of bands for the treated and  $600^\circ\text{C}$ -calcined sample are found for erionite and  $\text{NH}_4\text{Y}$  (Figure 3b). Since fluorine-treated  $\text{NH}_4\text{K-L}$  and  $\text{NH}_4\text{TMA-}\Omega$  lose crystallinity upon  $600^\circ\text{C}$  calcination, the OH region spectra were taken after  $500^\circ\text{C}$  calcination. Both show substantial reduction in intensity for Bronsted acid OH groups (bands in the region of  $3630\text{--}3680\text{ cm}^{-1}$ ) and some reduction of intensity for the  $3745\text{ cm}^{-1}$  band.

#### McBain-Bakr Adsorption

#### Oxygen Adsorption at $-183^\circ\text{C}$

The adsorption of oxygen is used here as another measure of total crystallinity (Table III). LZ-105, H-zeolon, erionite,  $\text{NH}_4\text{TMA-}\Omega$ ,  $\text{NH}_4\text{K-L}$  and  $\text{NH}_4\text{Y}$  all show 10-20% loss in their total oxygen capacities. There are at least two explanations for such a reduction. First, the total pore volume is lowered because the total crystallinity after fluorination decreases slightly. Second, the fluorine treatment results in the entrapment of fluoride compounds such as  $\text{MF}$ ,  $\text{AlF}_3$ ,  $\text{AlF}_2(\text{OH})$ ,  $\text{AlF}(\text{OH})_2$ , etc. in the pore systems.

#### Water Adsorption at $25^\circ\text{C}$

The adsorption of water is used in this study as one of the measures of surface hydrophobicity. As the data in Table IV show, the fluorine-treated and subsequently calcined LZ-105, H-zeolon, erionite and  $\text{NH}_4\text{Y}$  all have low water capacity as compared to their untreated counterparts. The reduction in water capacity (>50 vol % at 4.6 torr) is appreciably greater than the reduction in oxygen capacity (<20 vol % at 100 torr). Such a large reduction in water capacity is explained by the surface hydrophobicity (loss of surface and structural OH groups) as a result of fluorination. The increase in delta hexane loading as shown in Table IV also indicates an increase in organophilic sites for the fluorine-treated zeolite. Note that the decrease in delta hexane loading for fluorine-treated erionite is anomalous, but is probably related to the change in pore and cage size by fluoride salts. (Note erionite is the only small pore zeolite treated.)

## (a) H-Zeolon

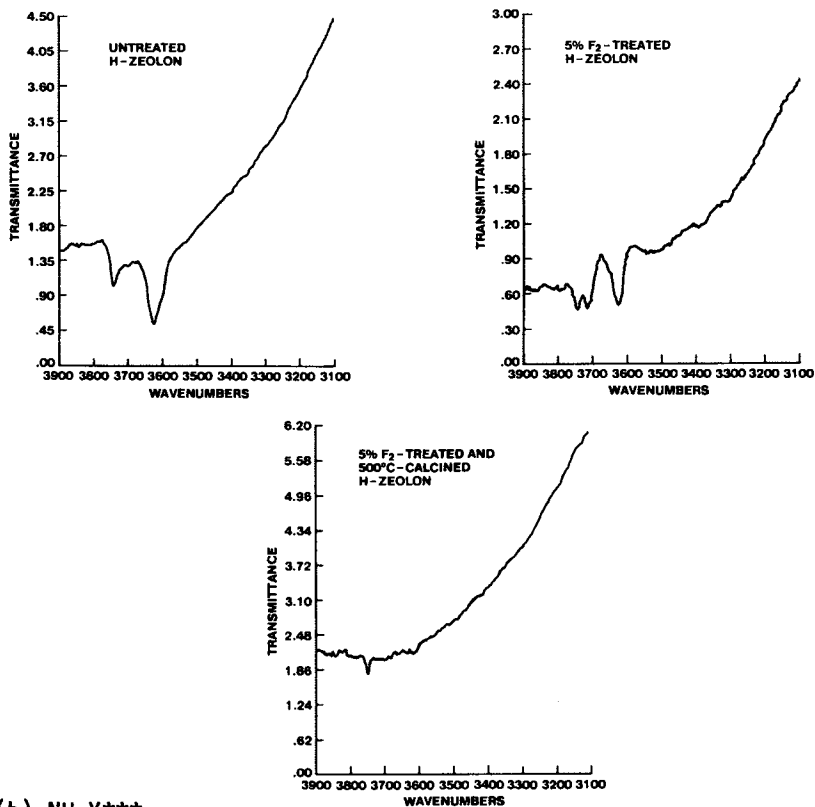
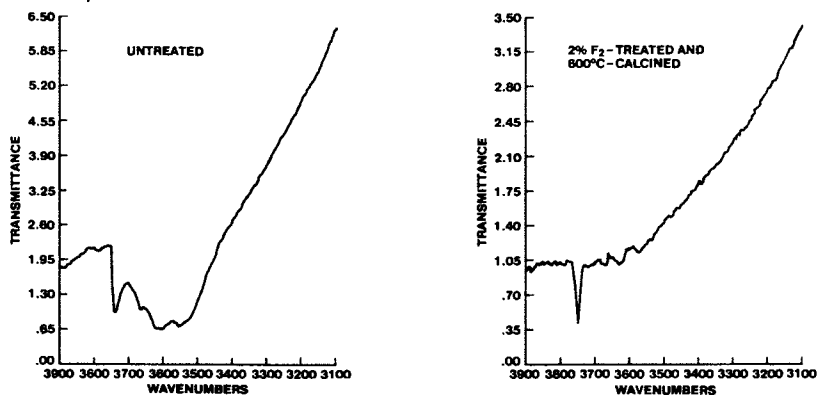
(b) NH<sub>4</sub>Y\*\*\*

Figure 3.  
Hydroxyl region infrared spectra of fluorine-treated zeolites

In contrast, the 500°C-calcined fluorine-treated  $\text{NH}_4\text{K-L}$  and  $\text{NH}_4\text{TMA-}\Omega$  show about the same capacity loss (~15 vol %) for water (at 4.6 torr) as for oxygen (at 100 torr). Therefore, these two zeolites apparently did not develop hydrophobicity after fluorination.

### 1 Vol % n-Butanol-Water Shake Test

A simple shake test with aqueous 1 vol % n-butanol solution has been developed to test the selective adsorption of organic molecules over water molecules by a hydrophobic and organophilic adsorbent (26). Table V gives the results for several fluorine-treated zeolites and their untreated counterparts. The data clearly indicate that fluorine treatment of LZ-105, H-zeolon and  $\text{NH}_4\text{Y}$  materials substantially increases their selectivity for n-butanol over water.

Table III  
OXYGEN ADSORPTION AT  $-183^\circ\text{C}$

| Sample # | Zeolite                          | Description | $X/m$ ( $\text{cm}^3/100\text{g}$ ) |                    |
|----------|----------------------------------|-------------|-------------------------------------|--------------------|
|          |                                  |             | 100 Torr<br>( $P/P_0=0.13$ )        | Near<br>Saturation |
| 1        | LZ-105 <sup>a</sup>              | Untreated   | 12.1                                | 12.6               |
|          | LZ-105 <sup>a</sup>              | Treated     | 9.3                                 | 9.3                |
| 3        | H-zeolon                         | Untreated   | 17.7                                | 19.0               |
|          | H-zeolon                         | Treated     | 15.9                                | 20.0               |
| 6        | Erionite <sup>b</sup>            | Untreated   | 18.3                                | 19.8               |
|          | Erionite <sup>b</sup>            | Treated     | 15.1                                | 17.3               |
| 8        | $\text{NH}_4\text{TMA-}\Omega$   | Untreated   | 13.1                                | 23.0               |
|          | $\text{NH}_4\text{TMA-}\Omega$   | Treated     | 10.5                                | 14.5               |
| 9        | $\text{NH}_4\text{K-L}$          | Untreated   | 15.3                                | 19.3               |
|          | $\text{NH}_4\text{K-L}$          | Treated     | 13.1                                | 18.3               |
| 10       | $\text{NH}_4\text{Y}^{\text{b}}$ | Untreated   | 21.3                                | 27.1               |
|          | $\text{NH}_4\text{Y}^{\text{b}}$ | Treated     | 17.2                                | 24.2               |

a. 20 wt % alumina bonded.

b. Mild steaming followed by  $\text{NH}_4^+$  exchange with hot  $\text{NH}_4\text{Cl}$  solution.



Table IV  
WATER LOADING AT 23°C

| Sample # | Zeolite                        | Description | $X/m(\text{cm}^3/100\text{g})$ |                    | $\Delta\text{Hexane}$ |
|----------|--------------------------------|-------------|--------------------------------|--------------------|-----------------------|
|          |                                |             | 4.6 Torr<br>(P/Po=0.22)        | Near<br>Saturation |                       |
| 1        | LZ-105 <sup>a</sup>            | Untreated   | 6.5                            | 10.9               | +2.0                  |
|          | LZ-105 <sup>a</sup>            | Treated     | 1.4                            | 3.4                | +6.0                  |
| 3        | H-zeolon                       | Untreated   | 16.0                           | 20.7               | -0.2                  |
|          | H-zeolon                       | Treated     | 3.5                            | 15.1               | +1.1                  |
| 6        | Erionite <sup>b</sup>          | Untreated   | 14.8                           | 20.4               | -0.12                 |
|          | Erionite <sup>b</sup>          | Treated     | 7.2                            | 18.6               | -0.45                 |
| 8        | NH <sub>4</sub> ,TMA-Ω         | Untreated   | 14.3                           | 28.4               | -                     |
|          | NH <sub>4</sub> ,TMA-Ω         | Treated     | 12.2                           | 28.4               | -                     |
| 9        | NH <sub>4</sub> ,K-L           | Untreated   | 17.4                           | 23.2               | -                     |
|          | NH <sub>4</sub> ,K-L           | Treated     | 14.2                           | 24.8               | -                     |
| 10       | NH <sub>4</sub> Y <sup>b</sup> | Untreated   | 23.2                           | 30.6               | 0.2                   |
|          | NH <sub>4</sub> Y <sup>b</sup> | Treated     | 8.4                            | 25.6               | 1.6                   |

a. 20 wt % alumina bonded.

b. Mild steaming followed by NH<sub>4</sub><sup>+</sup> exchange with hot NH<sub>4</sub>Cl solution.

#### n-Butane Cracking Test

The results for the n-butane cracking test expressed in terms of pseudo-first-order rate constants are tabulated in Table VI. Fluorinated water-washed and fluorinated calcined samples were also tested. Water washing promotes removal of entrapped soluble fluoride compounds. The calcination was carried out on LZ-105 and erionite samples treated under relatively severe conditions. As the data in Table VI show, the catalytic activity of the fluorinated zeolites can be either drastically increased or decreased depending on the treatment conditions and post-fluorination treatment. Varying the treatment conditions should allow the catalytic activity of a zeolite to be modified as desired.

Table V  
SHAKE TEST RESULTS

| Sample # | Zeolite   | Wt of Sample (g) | n-Butanol Concentration           |   | %n-Butanol Removal |   |
|----------|---|------------------|-----------------------------------|---|--------------------|---|
|          |   |                  | Solution added (cm <sup>3</sup> ) | Initial Solution (g/100 cm <sup>3</sup> ) |                    | Final Solution (g/100 cm <sup>3</sup> ) |
| 1        | Untreated LZ-105 <sup>a</sup>                       | 0.25             | 2.5                               | 0.81                                      | 0.17               | 79%                                     |
|          | Treated LZ-105 <sup>a</sup>                         | 0.25             | 2.5                               | 0.81                                      | 0.15               | 81%                                     |
| 3        | Untreated H-zeolon                                  | 0.25             | 2.5                               | 0.81                                      | 0.81               | 0                                       |
|          | Treated H-zeolon                                    | 0.25             | 2.5                               | 0.81                                      | 0.47               | 42%                                     |
| 7        | Untreated erionite <sup>b</sup>                     | 0.50             | 5.0                               | 0.81                                      | 0.91               | -12% <sup>c</sup>                       |
|          | Treated erionite <sup>b</sup>                       | 0.50             | 5.0                               | 0.81                                      | 1.00               | -23% <sup>c</sup>                       |
| 10       | Untreated NH <sub>4</sub> <sup>+</sup> <sup>b</sup> | 0.50             | 5.0                               | 0.81                                      | 0.75               | 7%                                      |
|          | Treated NH <sub>4</sub> <sup>+</sup> <sup>b</sup>   | 0.50             | 5.0                               | 0.81                                      | 0.51               | 37%                                     |

All samples were calcined at 600°C after fluorination, before shake test.

a. 20 wt % alumina-bonded.

b. Mild steaming followed by NH<sub>4</sub><sup>+</sup> exchange with hot NH<sub>4</sub>Cl solution.

c. Negative sign indicates selective water removal.

Table VI  
n-BUTANE CRACKING ACTIVITIES

| Sample # | Zeolite                        | n-Butane cracking activity (pseudo first order rate constant $K_A$ ) ( $\text{cm}^3/\text{g}\cdot\text{min}$ ) |                         |                     |                       |
|----------|--------------------------------|--|-------------------------|---------------------|-----------------------|
|          |                                | Untreated  | F <sub>2</sub> -treated | Washed <sup>d</sup> | Calcined <sup>e</sup> |
| 2        | LZ-105 <sup>a</sup>            | 26   | 21                      | 70                  | 0.9                   |
| 4        | H-zeolon                       | 135  | 7.8                     | -                   | -                     |
| 5        | H-zeolon                       | 135  | 247                     | -                   | -                     |
| 7        | Erionite <sup>c</sup>          | 22   | 12.5                    | 17.4                | 1.6                   |
| 8        | NH <sub>4</sub> ,TMA- $\Omega$ | 156  | 232                     | 191                 | -                     |
| 9        | NH <sub>4</sub> ,K-L           | 3.1  | 0.7                     | 1.4                 | -                     |
| 11       | NH <sub>4</sub> Y <sup>b</sup> | 36.8   | 45.3                    | -                   | -                     |
| 12       | NH <sub>4</sub> Y <sup>b</sup> | 36.8   | 55.9                    | -                   | -                     |

- a. Acid-washed and 20 wt % alumina-bonded.  
 b. Mild steaming followed by NH<sub>4</sub><sup>+</sup> exchange with hot NH<sub>4</sub>Cl solution.  
 c. Mild steaming and NH<sub>4</sub>Cl exchange repeated.  
 d. Water-washed after fluorination.  
 e. 600°C-calcined after fluorination.

n-Butane cracking test performed at 500°C, 2 mole % n-butane in He, 50 cm<sup>3</sup>/min flow rate, 10 min analysis and sample wt 0.5 - 5 grams.

#### LZ-105, H-Zeolon, Erionite and NH<sub>4</sub>Y

##### Dealumination and Structure Stabilization

The results obtained from X-ray diffraction and framework I. R. spectroscopy are very similar to high-temperature steaming results (9). The common features include changes in peak intensities and shifting in peak positions as seen by X-ray diffraction and band shifting and sharpening as seen by I. R. framework spectra. Both X-ray peak intensity changes (increase of low 2 $\theta$  peak intensity) and I. R. band shifts to higher wave numbers are evidence of dealumination. Likewise, both X-ray peak position shifts to higher 2 $\theta$  values and I. R. band sharpening are signs of structure stabilization.

##### Hydrophobicity

Substantial increase in hydrophobicity is found in fluorine-treated and subsequently 600°C-calcined samples. Such an increase in hydrophobicity is reflected directly in the water adsorption data, delta hexane loading and n-butanol shake test results. The OH region I. R. spectra for these treated materials also show substantial to total loss of hydroxyl groups. The treated erionite sample, however, fails to show either an increase in delta hexane

loading or selective removal of n-butanol. These results probably can be better explained by a decrease in pore size due to the formation of fluoride salts after fluorination rather than by a lack of surface hydrophobicity.

#### NH<sub>4</sub>, TMA-Ω and NH<sub>4</sub>,K-L

The results indicate that both NH<sub>4</sub>,TMA-Ω and NH<sub>4</sub>,K-L are dealuminated upon fluorination. Strong supporting evidence comes from framework I. R. data where the shifts in band position to higher wave numbers are as much as 20 cm<sup>-1</sup>. However, there is no evidence of structure stabilization. Also McBain water adsorption data give no indication of surface hydrophobicity. Therefore, it is likely that structure defects are formed in these two zeolites as a result of dealumination and cause low thermal stability.

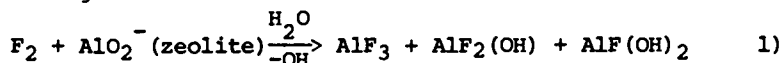
#### n-Butane Cracking Activities

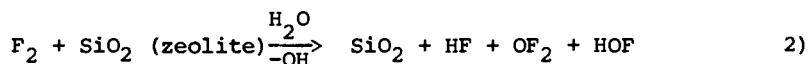
Careful study of the Table II treatment conditions and the Table VI n-butane cracking activity data leads to the following generalizations. A high n-butane cracking activity can be achieved by a "mild" fluorination process. On the other hand, a low n-butane cracking activity can be achieved by a "severe" fluorination process. However, the terms "mild" and "severe" should be defined according to the structure type. For example, the 1% fluorine and 45 minute-treated H-zeolon has a much higher n-butane cracking activity than the untreated one. On the other hand, the 5% fluorine and 30 minute-treated-H-zeolon lost most of its activity. Therefore, for H-zeolon, the latter treatment conditions are termed "severe". However, the "mild" conditions for H-zeolon are no longer "mild" for a less stable structure type, i.e., Y zeolite. Finally, a drastic loss in catalytic activity can be achieved by "severe" treatment followed by high-temperature calcination. The increase in catalytic activity after fluorination can be explained by the increase in silicon to aluminum ratio, by the formation of defect sites, by the formation of Lewis acid sites such as AlF<sub>3</sub>, AlF<sub>2</sub>(OH) and AlF(OH)<sub>2</sub> compounds and by the effect of fluoride as a promoter. However, it is not likely that the increase in catalytic activity is due to promotion by an adsorbed gaseous phase or by water-soluble fluorides, since the n-butane cracking test is run after one hour calcination in helium at 500°C and since the water washed fluorine-treated samples generally show an increase in activity.

#### Possible Reactions

The following simplified reactions are proposed:

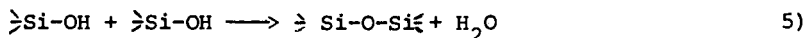
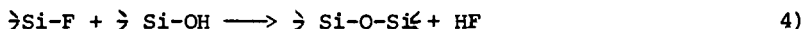
1. During treatment:





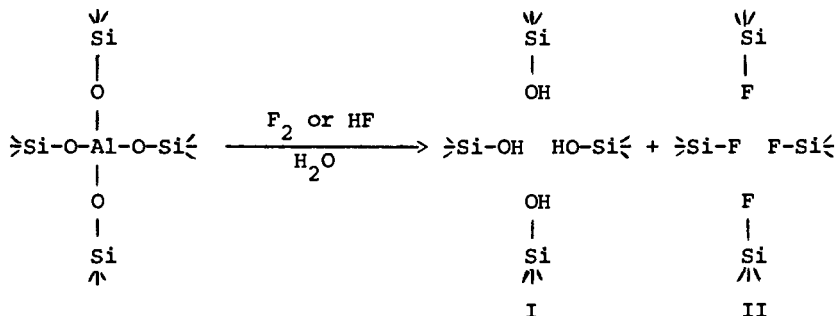
2. During 600°C post-treatment calcination:

Structure and surface reaction -

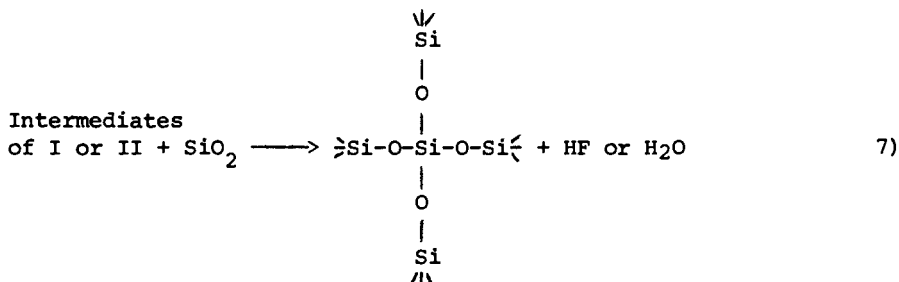


Reactions 1 and 3 could also occur at high temperature if fluorine exists.

3. Dealumination and structural stabilization:



+ Intermediates +  $AlF_3$  +  $AlF_2(OH)$  +  $AlF(OH)_2$  of I and II 6)



Reaction 7, which involves silica insertion, probably occurs at elevated temperatures since structure stabilization is observed mainly after high-temperature calcination.

### Conclusion

In this paper, data have been presented to show that zeolites can be modified by direct fluorination at ambient conditions with

a dilute fluorine-in-air stream. The rate of reaction and resultant properties, including dealumination, structural stabilization, surface hydrophobicity and catalytic activity, are dependent on the zeolite framework topology and composition, the treatment conditions and the post-treatment conditions. Under "severe" treatment conditions, some of the zeolites show a high degree of dealumination, which with subsequent structure stabilization, leads to surface hydrophobicity and reduction in catalytic activity. Under "mild" treatment conditions, the catalytic activity of a zeolite can be almost doubled. It is our belief that the fluorination process adds flexibility in the choice of materials, hydrophilic to hydrophobic, catalytically inactive to very active, to be used in adsorption and catalysis and introduces another dimension into zeolite modification chemistry.

#### Acknowledgment

The authors would like to thank Union Carbide Corporation for permission to publish this article. We are also grateful to E. M. Flanigen, R. L. Patton and G. W. Skeels for many helpful discussions, to C. L. Angell for the I. R. spectra and to P. F. Stone for her help in treating samples.

#### Literature Cited

1. Barrer, R. M. and Makki, M. B. Can. J. Chem. 1964, 42, 1481.
2. Belenykaja, I. M., Dubinin, M. M. and Krishtofori, I. I. Izv. Akad. Nauk SSSR 1967, Ser. Khim., 2164.
3. Dubinin, M. M., Fedorova, G. M., Plavnik, D. M., Piguzova, L. I. and Prokofeva, E.N. Izv. Akad. Nauk SSSR 1968, Ser. Khim., 2429.
4. Eberly, P. E., Jr. and Kimberlin, C. N., Jr. Ind. Eng. Chem., Prod. Res. Dev. 1970, 9, 335.
5. Kranich, W. L., Ma, Y. H., Sand, L. B., Weiss, A. H. and Zwiebel, I. Adv. Chem. Ser. 1970, No. 101, 502.
6. Chang, H. D., Ph.D. Thesis 1970, Worcester Polytechnic Institute.
7. (a) Chen, N. Y. and Smith, F.A. Inorg. Chem. 1976, 15, 295; (b) Chen, N. Y. J. Phys. Chem. 1976, 80, 60.
8. McDaniel, C. V. and Maher, P. K. "Molecular Sieves" 1968, Society of Chemical Industry, London, p. 186.
9. Patton, R. L., unpublished data.
10. (a) Kerr, G. T. J. Phys. Chem. 1968, 72, 2594; (b) Kerr, G. T. J. Phys. Chem. 1968, 73, 2780.
11. (a) Beaumont, R. and Barthomeuf, D. J. Catal. 1972, 26, 218; (b) Beaumont, R. and Barthomeuf, D. J. Catal. 1972, 27, 45.
12. Garwood, W. E., Lucki, S. J., Chen, N. Y. and Bailor, J. C., Jr. Inorg. Chem. 1978, 17, 610.
13. French Patent 2,303,764 assigned to BASF (1976).

14. Beyer, H. K. and Belenykaja, I. "Catalysis by Zeolites", 1980, Elsevier Scientific Publishing Co., Amsterdam, p. 203.
15. Fejes, P., Kiricsi, I., Hannus, I., Kiss, A. and Schobel, G. React. Kinet. Catal. Lett. 1980, 14, 481.
16. (a) Peri, J. B., Proc. 5th Int'l. Cong. on Catalysis, Miami Beach, 1972, p. 329; (b) Breck, D. W. "Zeolite Molecular Sieves" John Wiley and Sons, New York, 1974, p. 517.
17. Chen, N. Y. J. Phys. Chem. 1976, 80, 60.
18. Lok, B. M. and Izod, T. P. J. "Molecular Sieve Modification I - Direct Fluorination" 1982, Zeolites, 2, 66.
19. Fishel, N. A., U. S. Patent 3,413,370 (1968).
20. Shell Int'l. Research Maatschappij, N. V., Netherlands Appl. 6,616,241 (1968).
21. Hervert, G. L., U. S. Patent 3,467,728 (1969).
22. Voorhies, A., Jr., U. S. Patent 3,630,965 (1971).
23. Takase, S., Shioiri, T. and Ushio, M., German Offen. 2,219,736 (1972).
24. Sobel, J. E., U. S. Patent 3,763,261 (1973).
25. Flanigen, E. M. and Cannan, T. R., private communication.
26. Flanigen, E. M. and Cannan, T. R., private communication.
27. Rastelli, H., Jr., Lok, B. M., Duisman, J. A., Earls, D. E. and Mullhaupt, J. T., "Characterization of Zeolite Acidity I. The Cracking of 2 Mole % n-Butane Over a Fixed Zeolite Bed", presented at the 7th Canadian Symp. on Catalysis, 1980, Edmonton, Canada and the Canadian J. of Chem. Eng. 1982, 60, 44.
28. Grose, R. W. and Flanigen, E. M., U. S. Patent 4,257,885 (1981).
29. Flanigen, E. M. and Patton, R. L., U. S. Patent 4,073,865 (1978).
30. See for example Flanigen, E. M., "Zeolite Chemistry and Catalysis", 1976, ACS Monograph 171, p. 80 and references therein.

RECEIVED November 29, 1982

# Inorganic Cation Exchange Properties of Zeolite ZSM-5

P. CHU and F. G. DWYER

Mobil Research and Development Corporation, Paulsboro, NJ 08066

The discovery of the zeolite ZSM-5 has led to the development of catalysts for a wide variety of process applications in petroleum refining, petrochemical manufacture and synthetic fuels. In order to further elucidate the structural characteristics and the basic chemical nature of this most interesting material the ion exchange characteristics have been studied for a wide spectrum of cations using a variety of morphological and compositional forms of the zeolite. The results of this study have shown the ion selectivities to be considerably different from those of the conventional synthetic zeolites A, X and Y. Up to the limit of cation size capable of penetration of the ZSM-5 pore opening, the selectivity for inorganic cations was primarily dependent upon base ion size rather than charge. These cation selectivities are explained in terms of electrostatic forces and pore dimensions of the zeolite and are related to the shape selective catalytic and adsorptive properties of catalysts made from ZSM-5.

The unique nature of ZSM-5 as a catalyst and as a zeolite has been well documented (1-3), as shown by the wide spectrum of chemistry it can catalyze as well as the wide range of morphologies and composition in which it can be synthesized. In addition, ZSM-5 exhibits ion exchange properties that, in some cases, are very different from other zeolites. Results from the study of these ion exchange characteristics have been used effectively in developing optimal methods for conversion of ZSM-5 into catalytic forms and in supplying information concerning the zeolite structure not discernible by other techniques that could lead to more active, selective and stable catalysts.

0097-6156/83/0218-0059\$06.00/0  
© 1983 American Chemical Society



The structure of ZSM-5 has been determined by Kokotailo et al. (4). Its framework contains a novel configuration of linked  $\text{SiO}_2$  and  $\text{Al}_2\text{O}_3$  tetrahedra as groups of five-membered rings. The skeletal diagrams of the (010) and (100) faces of a ZSM-5 unit cell are shown in Figures 1a and 1b revealing the two channel structures. The elliptical 10-membered ring apertures, shown in Figure 1a, are the entrances to the straight channels which run parallel to [010]. The nearly circular 10 membered ring apertures, shown in Figure 1b, are the entrances to the sinusoidal channels which run parallel to [100].

ZSM-5, in the as synthesized form, is not readily susceptible to ion exchange due to the hindrance from bulky quaternary cations and occluded organic materials which are believed to be located in the channel system. Incoming and outgoing ions all have to pass through the channels and apertures to complete the ion exchange process. Therefore, in order to obtain intrinsic ion exchange information, these bulky organics must be removed and replaced by smaller cations such as  $\text{Na}^+$  or  $\text{NH}_4^+$ . The method of removal of the organics used in this study was by thermal treatment although chemical treatment is also an effective mode of removal.

Although ZSM-5 has been synthesized with  $\text{SiO}_2/\text{Al}_2\text{O}_3$  of almost unbounded limits, in this study we investigated materials with  $\text{SiO}_2/\text{Al}_2\text{O}_3$  of 40 to 200. It should also be noted that even at the lowest  $\text{SiO}_2/\text{Al}_2\text{O}_3$ , the cation exchange capacity of ZSM-5 is only 0.75 meq/g as compared to 4 to 7 meq/g for zeolites A, X and Y and 3 to 5 meq/g for most cation exchange resins. The extremely high  $\text{SiO}_2/\text{Al}_2\text{O}_3$  ZSM-5 materials are less desirable for use in ion exchange studies due to practical difficulty in obtaining accurate elemental analysis at such low levels.

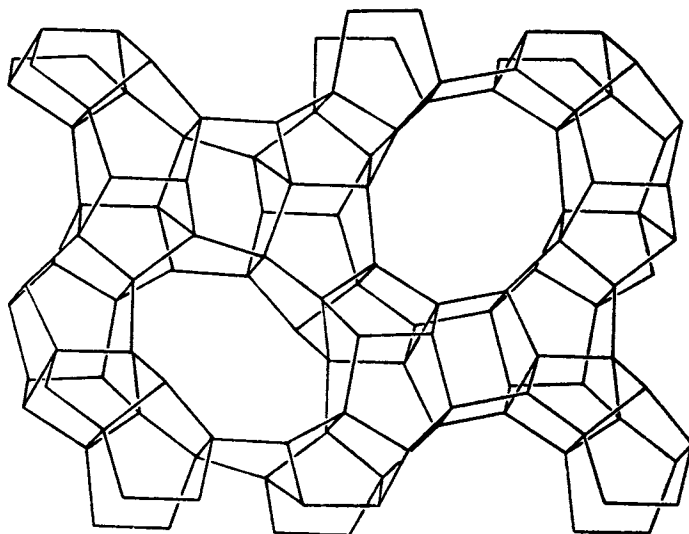
## Experimental

### ZSM-5 Zeolite Synthesis

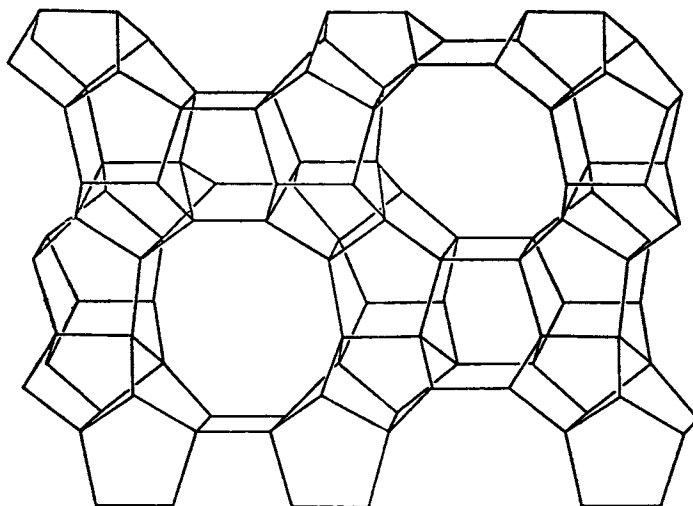
All the ZSM-5 zeolites were synthesized by reacting an aluminosilicate gel containing Na and tetrapropylammonium cations. The detailed procedure is described elsewhere (3). The samples of varying  $\text{SiO}_2/\text{Al}_2\text{O}_3$  ratio were obtained by adjusting the silica to alumina ratio in the starting reaction mixture. All zeolite samples were highly crystalline ZSM-5 as determined by x-ray diffraction. Chemical compositions of the ZSM-5 samples were determined by conventional chemical analysis and are shown in Table I. Some typical morphologies of ZSM-5 crystals are presented in Figure 2.

### Pure Ionic Forms of ZSM-5

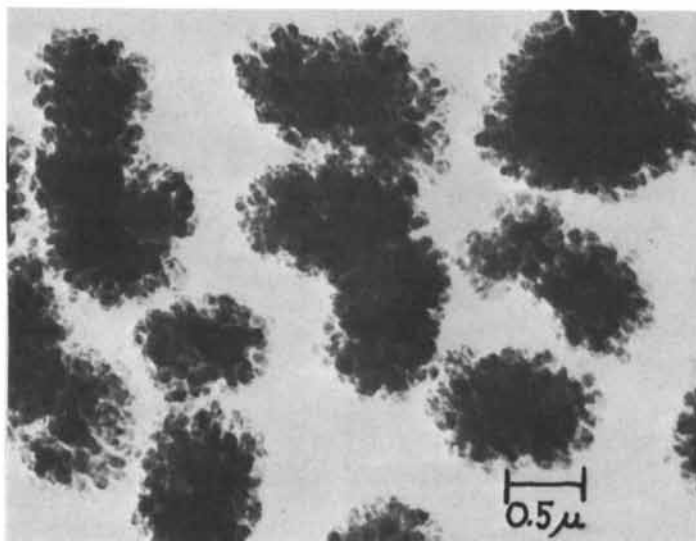
The "as synthesized" ZSM-5 contains tetrapropylammonium and sodium ions in its pores and structure. The total cation to Al site ratio is generally greater than one indicating salt occlu-



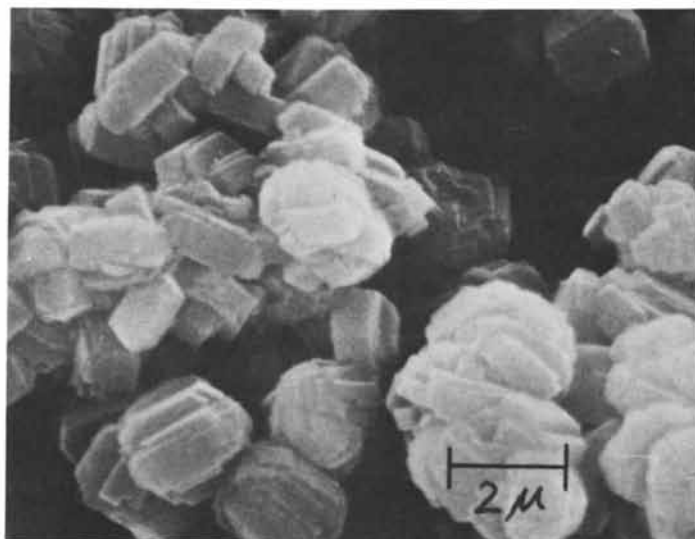
**Figure 1a**  
**Skeletal Diagram of the (010) - Face of the**  
**ZSM-5 Unit Cell to Show the Elliptical Apertures**  
**of the Straight Channels**



**Figure 1b**  
**Skeletal Diagram of the (100) - Face of the**  
**ZSM-5 Unit Cell to Show the Nearly Circular**  
**Apertures of the Sinusoidal Channels**



TEM of  $0.02\mu$  Crystal



SEM of  $2\mu$  Crystal

**Figure 2**  
**Micrograph of  $0.02\mu$  and  $2\mu$  ZSM-5 Crystals**

sions, primarily organic salts. Occluded organic salts as well as TPA cations, which are larger than the pore opening of ZSM-5, impedes ionic movement during the ion exchange process, therefore, prior to any ion exchange experiments, the bulky TPA ions and occluded material were removed and a pure cationic form was used as the base form for ion exchange. The pure ammonium or sodium form can be prepared by a 500°C calcination of "as synthesized" ZSM-5 in an ammonia atmosphere followed by repeated ammonium or sodium ion exchange. The exchanged products have excellent crystallinity and a cation to Al ratio of about one. The composition of the various sodium ZSM-5 samples used in this work is presented in Table I.

TABLE I  
Composition of Pure Ionic Forms of ZSM-5

| SiO <sub>2</sub> /Al <sub>2</sub> O <sub>3</sub> | 40    | 70    | 70    | 70    | 206   | 140   | 140             |
|--|-------|-------|-------|-------|-------|-------|-----------------|
| Cation Form                                      | Na    | Na    | Na    | Na    | Na    | Na    | NH <sub>4</sub> |
| Composition<br>(mole ratio)                      |       |       |       |       |       |       |                 |
| Al <sub>2</sub> O <sub>3</sub>                   | 1.0   | 1.0   | 1.0   | 1.0   | 1.0   | 1.0   | 1.0             |
| SiO <sub>2</sub>                                 | 40.4  | 75.4  | 71.0  | 77.5  | 206   | 142   | 142             |
| Na <sub>2</sub> O                                | 0.901 | 0.945 | 0.991 | 0.925 | 1.053 | 0.983 | 0.01            |
| N <sub>2</sub> O                                 | 0.048 | 0.056 | 0.067 | 0.075 | 0.092 | 0.040 | 1.08            |
| (Na+N)/Al  | 0.95  | 1.00  | 1.06  | 1.00  | 1.08  | 1.02  | 1.09            |
| Crystallinity, %                                 | 95    | 90    | 100   | 95    | 105   | 100   | 90              |

### Ion Exchange

The data for the ion exchange isotherms were obtained from batch experiments conducted in a constant temperature agitated system utilizing tightly sealed polypropylene bottles. Conventional chemical analyses were used to obtain the cation distribution data in both zeolite and exchange solution phases. Most of the exchanges were carried out at ambient temperature for 24-72 hours. Preliminary tests had shown that equilibrium was essentially reached within a few hours.

## Results and Discussion

### Ion Exchange Isotherms

Equilibrium exchange of some typical monovalent and polyvalent cations were studied mainly at 25°C, with a few cases at 75°C, to show the effect of temperature on the equilibrium. All the results are presented in the form of ion exchange isotherms, Figures 3 to 11. In these figures, the ordinate,  $Z_x$ , is the equivalent fraction of the ingoing ion X in the zeolite phase and the abscissa,  $S_x$ , is that of the exchange solution phase. The equivalent

fractions  $Z_x$ ,  $S_x$  can be defined more explicitly as follows:

$$Z_x = \frac{\text{equivalents of X in zeolite}}{\text{gram-atoms of Al in zeolite}}$$

$$S_x = \frac{\text{normality of X in solution}}{\text{total normality of cations in solution}}$$

This type of graphical presentation points out not only the ease of ion exchange but any sieving action of the zeolite caused by the size of exchanging ions.

Since  $\text{NH}_4\text{ZSM-5}$  is the precursor of acid ZSM-5 catalysts, the  $\text{NH}_4^+ - \text{Na}^+$  exchange of ZSM-5 has been extensively studied to determine the best conditions for effective  $\text{Na}^+$  removal. When the exchange was performed on an "as synthesized" ZSM-5 sample in which the organic cation, TPA, and occluded organic salts remain in the crystal structure, only two-thirds of the original sodium was removed as shown in Figure 3. On the other hand, all sodium ions were removed with ease from a pure sodium form of ZSM-5 in which the TPA ions have been thermally decomposed and replaced with sodium ions. The TPA ion and the occluded organic salts apparently provided sufficient steric hindrance to prevent the movement of the ingoing  $\text{NH}_4^+$  ions and/or the remaining outgoing  $\text{Na}^+$  ions.

Three pure NaZSM-5 samples with  $\text{SiO}_2/\text{Al}_2\text{O}_3$  ratios of 40, 70 and 140, respectively, were used in the  $\text{NH}_4^+ - \text{Na}^+$  exchange studies. The isotherm (Figure 4) shows that  $\text{NH}_4^+$  selectivity is equal in all three cases. In his study of the ion exchange of Linde X and Linde Y zeolites, Sherry reported (5) different selectivity for these two zeolites which are isostructural but differing in their  $\text{SiO}_2/\text{Al}_2\text{O}_3$  ratios, 2.46 and 5.33, respectively. He has also found selectivity reversals in the  $\text{K}^+ - \text{Na}^+$ ,  $\text{Rb}^+ - \text{Na}^+$  and  $\text{Cs}^+ - \text{Na}^+$  isotherms of X but not in Y zeolite. He attributed these changes in selectivity to the different distribution of exchange sites among three different crystallographic locations in zeolites X and Y. The lack of selectivity change in ZSM-5 samples could be an indication of homogeneity in functional sites and/or that they are equally accessible to the  $\text{NH}_4^+$  ions studied.

Increasing the exchange temperature has a negative effect on the selectivity of  $\text{NH}_4^+$  for NaZSM-5 as shown in Figure 5. This fact has simplified the manufacturing procedure for ZSM-5 containing catalysts eliminating the need for heating the exchange solutions. This negative temperature effect is quite surprising. It has been common practice to increase the extent of  $\text{NH}_4^+$  exchange in faujasite by raising the temperature of the exchange solution. The negative temperature effect has been reported once previously by Vansant and et al. (6).

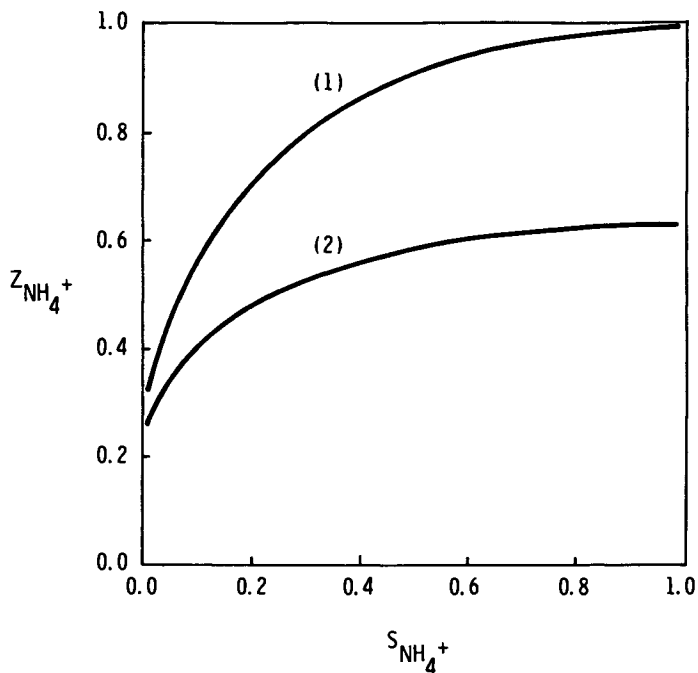


Figure 3  
The  $\text{NH}_4^+$ - $\text{Na}^+$  Exchange Isotherms of ZSM-5 at 25°C

- (1) Pure Na Form, Organics Removed
- (2) As Synthesized

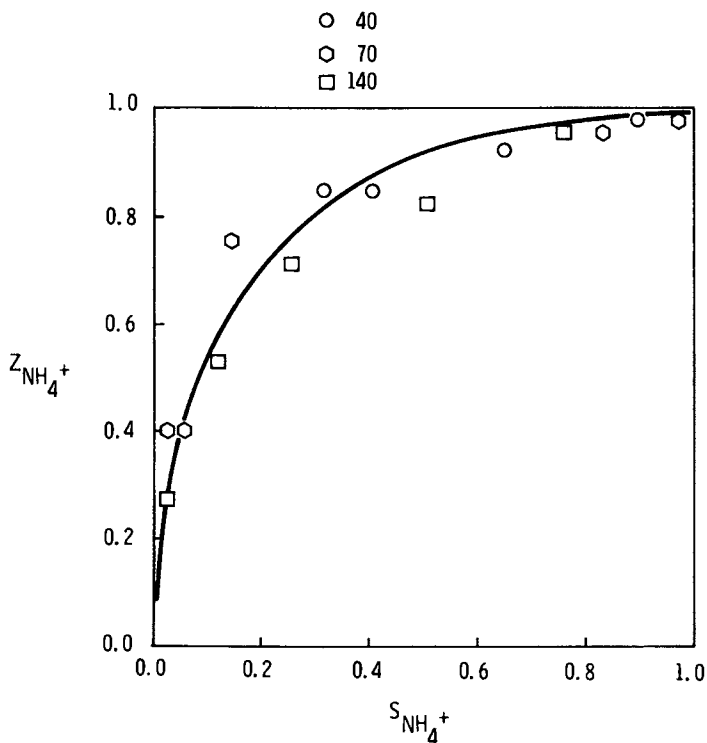
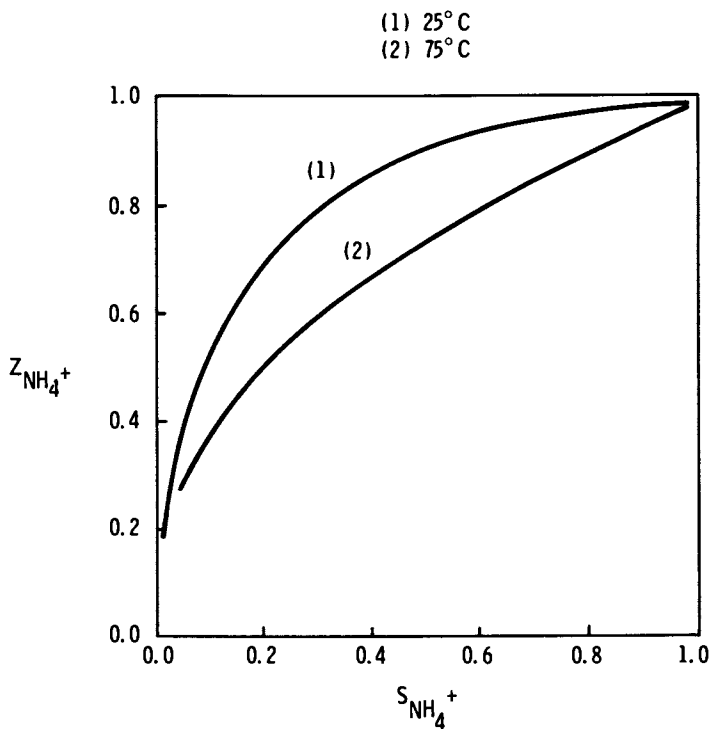


Figure 4  
The  $\text{NH}_4^+ - \text{Na}^+$  Exchange Isotherm of ZSM-5 of  
Varying  $\text{SiO}_2/\text{Al}_2\text{O}_3$  Ratios at  $25^\circ\text{C}$



**Figure 5**  
The Dependence of ZSM-5 Selectivity on the Temperature of Equilibration of  $\text{NH}_4^+$ - $\text{Na}^+$  Exchange

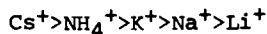


Most highly siliceous zeolites are stable toward acidic solutions. Mordenite has been treated with dilute to moderately acidic solutions to convert it into the hydronium ( $\text{H}_3\text{O}^+$ ) form without damaging the zeolite structure (7). We found that NaZSM-5 can also be efficiently exchanged into the hydronium form with acid or hydronium ion exchange resins (8). The  $\text{H}_3\text{O}^+$ - $\text{Na}^+$  exchange isotherm is shown in Figure 6. The hydronium ion is highly preferred over  $\text{Na}^+$  by ZSM-5. In addition, the  $\text{H}_3\text{O}^+$ - $\text{Na}^+$  exchange has been found to be reversible by sodium back exchange of hydronium ZSM-5 without any sign of hysteresis in the back exchange isotherm.

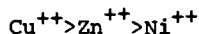
$\text{Cs}^+$  is one of the largest inorganic cations and has been used to measure the sieving action of zeolites or multiple pore openings. The  $\text{Cs}^+$ - $\text{NH}_4^+$  isotherm, as shown in Figure 7, did not indicate the presence of any inaccessible sites. Therefore, it is concluded that all the cations in ZSM-5 are located in channels and cavities with openings at least  $3.4\text{\AA}$ , the bare ionic diameter of the cesium ion. The selectivity of  $\text{NH}_4^+$ ZSM-5 for  $\text{Cs}^+$  is high and complete replacement of  $\text{NH}_4^+$  is readily achieved.

Another interesting aspect of the  $\text{Cs}^+$ - $\text{NH}_4^+$  exchange isotherm (Figure 7) is that two samples of ZSM-5 of different crystal sizes ( $0.02\mu$  and  $2\mu$ , respectively) were used. There is no significant difference in selectivity indicating that the experimental equilibration time is sufficient to eliminate any kinetic effects in the ion exchange and that  $\text{Cs}^+$  does not inhibit ion movement even in very large crystals.

The  $\text{K}^+$ - $\text{NH}_4^+$  and  $\text{Li}^+$ - $\text{NH}_4^+$  isotherms have also been determined as shown in Figure 8. Both  $\text{K}^+$  and  $\text{Li}^+$  as well as  $\text{Na}^+$  are less preferred than  $\text{NH}_4^+$  in ZSM-5. The overall selectivity ranking of these alkali metals and  $\text{NH}_4^+$  is:



The divalent cations studied in more detail were Cu, Zn and Ni. Their isotherms are shown in Figure 9, 10 and 11. All sodium ions were replaced by these divalent ions and their selectivity sequence was:



### Selectivity Correlation

The ion exchange properties of zeolite ZSM-5 are of interest for several reasons. The high  $\text{SiO}_2/\text{Al}_2\text{O}_3$  ratio of this material means low ion exchange capacity and the ion selectivity patterns of this unique, siliceous zeolite should be quite different from those of low  $\text{SiO}_2/\text{Al}_2\text{O}_3$  zeolites such as Linde A and synthetic

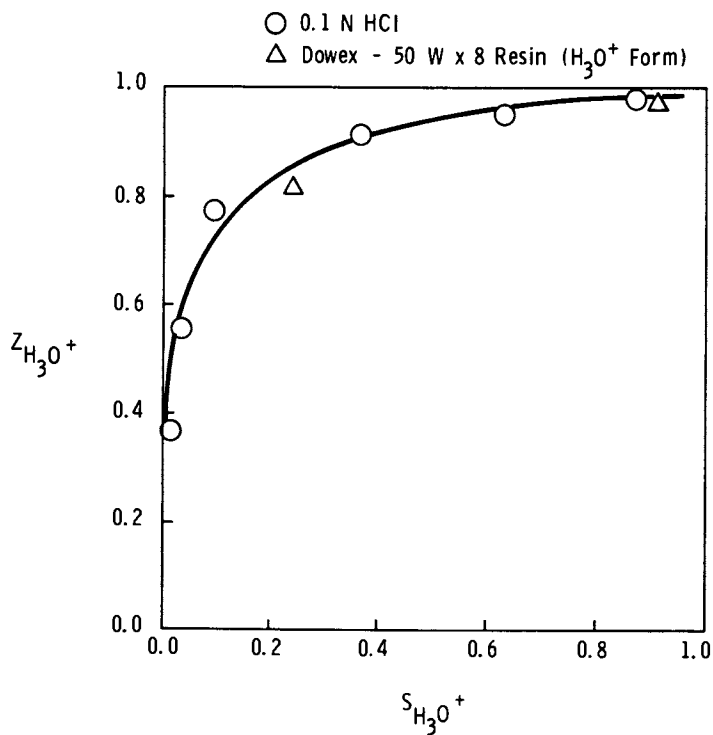
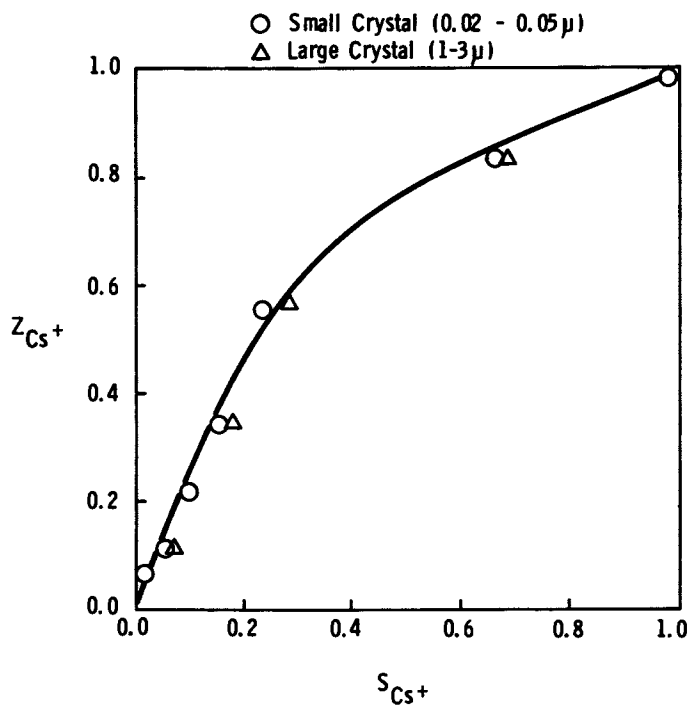


Figure 6  
Hydronium ( $\text{H}_3\text{O}^+$ ) Ion Exchange Isotherm of  
NaZSM-5 at 25°C



**Figure 7**  
**Effect of Crystal Size on the  $Cs^+ - NH_4^+$  Ion Exchange Isotherm of ZSM-5 at 25°C**

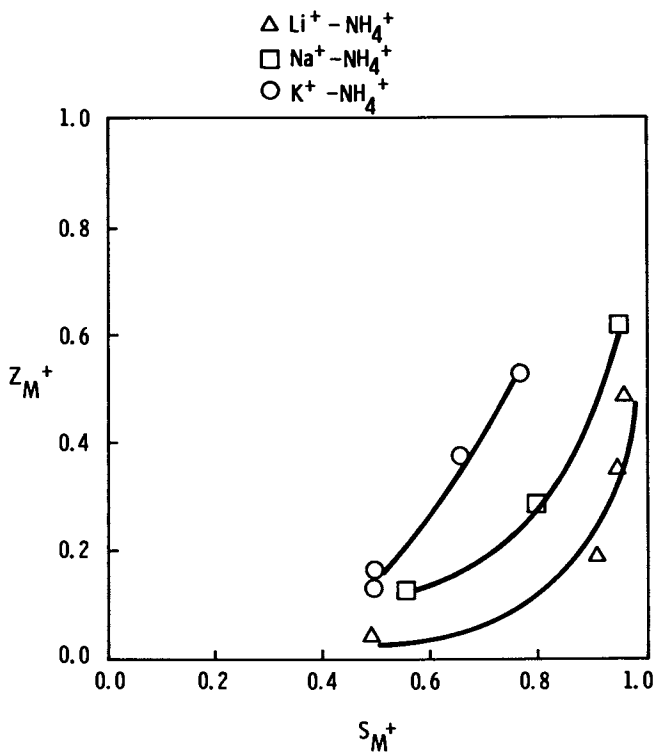


Figure 8  
Ion Exchange Isotherms of Some Alkali Metal  
Ions with  $\text{NH}_4\text{ZSM-5}$  at  $25^\circ\text{C}$

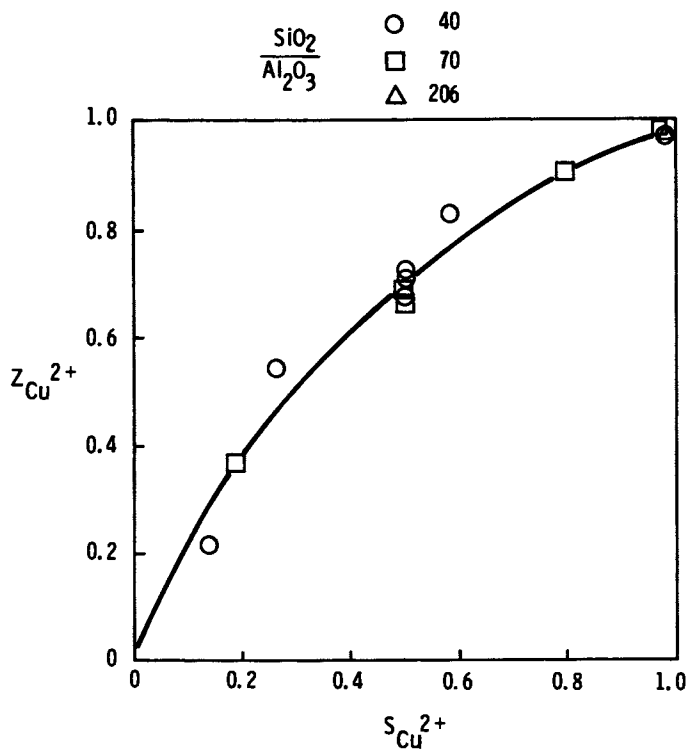


Figure 9  
 $\text{Cu}^{2+}\text{-Na}^+$  Exchange Isotherm of ZSM-5 at 25°C

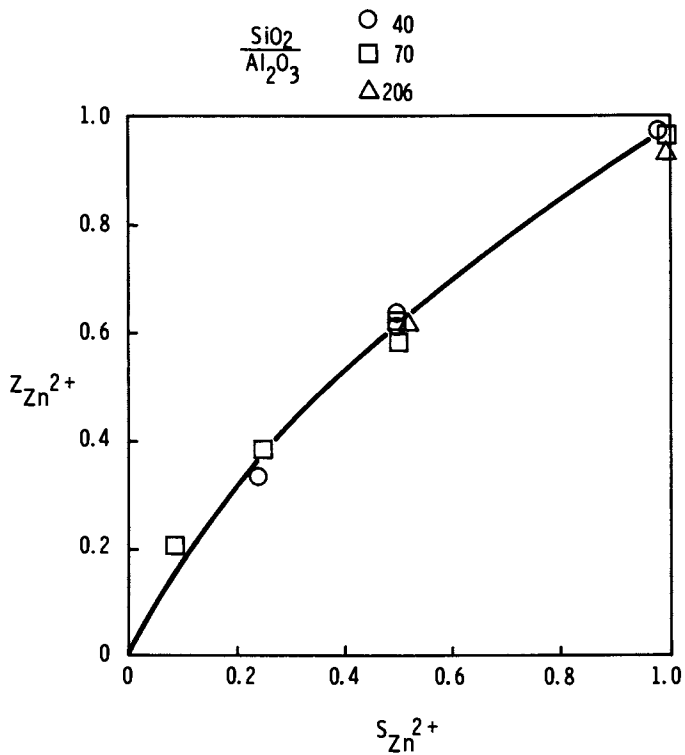


Figure 10  
 $\text{Zn}^{2+}\text{-Na}^+$  Exchange Isotherm of ZSM-5 at 25°C

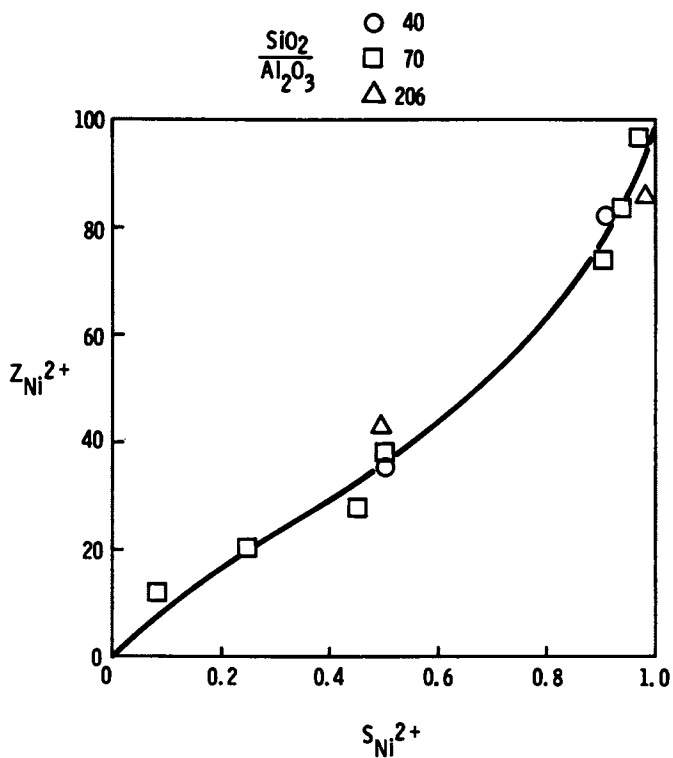


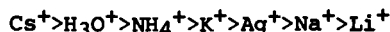
Figure 11  
 $Ni^{2+}$ - $Na^+$  Exchange Isotherm at 25°C

faujasites. Relative ion exchange selectivity of ZSM-5 zeolite for various cations has been obtained and expressed as the separation factor,  $\alpha$ , which is defined as:

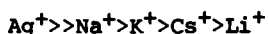
$$\alpha = \frac{Z_A S_B}{Z_B S_A}$$

Where  $\alpha^A_B$  is the separation factor of ion A over ion B and  $Z_A$ ,  $Z_B$ ,  $S_A$  and  $S_B$  are ionic fractions of A and B in the zeolite and solution phase, respectively. The  $\alpha^X_{Na}$  of ZSM-5 for a variety of cations obtained with an equi-molar equilibrating solution ( $S_X = S_{Na} = 0.5$ ) at 25°C, are listed together with the hydrated and unhydrated radii of the respective ions in Table II. The majority of the  $\alpha^X_{Na}$  values in Table II were extracted from the isotherms reported earlier. Several more of such ions as  $Ag^+$ ,  $Ba^{++}$ ,  $Ca^{++}$ ,  $Mg^{++}$ ,  $Al^{3+}$  and  $La^{3+}$  were obtained in a separate study to give a more complete spectrum of ions (9).

Within the monovalent ion series, the selectivity is directly proportional to the bare ionic radius, i.e., the larger the bare ionic radius the higher the selectivity. The selectivity sequence,



is similar to that of Linde Y (9) and mordenite and also polystyrene based resin with fixed sulfonate groups (10), but it is quite different from that of Linde X (7) which is,



The selectivity pattern of zeolites X and Y can be explained using Eisenman's model of electrostatic energy interaction (11) as pointed out by Sherry (12) and is applicable to ZSM-5 as well. In ZSM-5, as in any other zeolite, the functional group of fixed negative charge is the  $AlO_4$ -tetrahedra. As a first approximation, the electrostatic energy of the ion site interaction for a specific  $SiO_2/Al_2O_3$  ratio can be calculated using internal energies derived from the Coulomb's law for widely spaced sites thusly:

$$F_{el} = \frac{332}{\gamma^+ + \gamma^-} \quad (1)$$

where

- $F_{el}$  = Electrostatic energy in K cal. per mole
- $\gamma^+$  = Radius of the cation in Angstroms
- $\gamma^-$  = Radius of the anion in Angstroms



TABLE II  
Separation Factor ( $\alpha_{Na}^X$ ) of ZSM-5 at 25°C

| Ions (x)          | $\alpha_{Na}^X$<br>( $S_x = S_{Na} = 0.5$ ) | Ionic <sup>a</sup><br>Radii (Å) | Hydrated <sup>b</sup><br>Radii (Å) |
|-------------------|---|---------------------------------|------------------------------------|
| <b>Monovalent</b> |   |                                 |                                    |
| Cs                | 20  | 1.69                            | 3.29                               |
| H <sub>3</sub> O  | 18  | 1.5                             | (2.82) <sup>c</sup>                |
| NH <sub>4</sub>   | 13  | 1.48                            | 3.31                               |
| K                 | 5.2   | 1.33                            | 3.31                               |
| Ag                | 3.3   | 1.26                            | 3.41                               |
| Na                | 1.0   | 0.95                            | 3.58                               |
| Li                | 0.6   | 0.60                            | 3.82                               |
| <b>Divalent</b>   |   |                                 |                                    |
| Ba                | 0.24  | 1.35                            | 4.1                                |
| Ca                | 0.07  | 0.99                            | 4.2                                |
| Mg                | 0.11  | 0.65                            | 4.4                                |
| Cu                | 2.33  | 0.72                            | 4.2                                |
| Zn                | 1.63  | 0.74                            | 4.3                                |
| Ni                | 0.59  | 0.70                            | 4.04                               |
| <b>Trivalent</b>  |   |                                 |                                    |
| Al                | Low   | 0.50                            | 4.75                               |
| La                | 0.22  | 1.15                            | 4.52                               |

**Zeolite:** Precalcined at 1000°F for three hours in N<sub>2</sub>.

**Solution:** 0.1N mixed salt solution of chlorides. In case of Ag<sup>+</sup>, nitrates was used instead.

a. Electrolyte Solutions, Robinson and Stokes (1959), p. 461.

b. E. R. Nightingale, Jr., J. Phys. Chem., 63, 1381 (1959).

c. From molecular diameter of water.

Therefore, an open and more siliceous zeolite, such as ZSM-5, will provide a very weak anionic field strength. The weakest field pattern is the one in which selectivity increases with increasing ionic radius of the monovalent ions considered. If the hydration energy of the cation is considered, then the least hydrophilic ions are the most preferred ones in the weak field. Cs ion is one of the largest and least hydrated inorganic cations and has been found to be highly preferred by ZSM-5. Polyvalent cations, in ZSM-5, have much lower selectivities than most monovalent ions. The trend is the higher the valence of the cation, the lower its selectivity in ZSM-5. This trend is interesting because it is just the opposite of that of many organic cation exchange resins (10) and zeolites of lower  $\text{SiO}_2/\text{Al}_2\text{O}_3$  ratio, i.e., faujasite, zeolite A and etc. The low selectivity of polyvalent ions in ZSM-5 could be attributed to either of two major factors. The first is that the large hydration energy of polyvalent ions becomes the predominate term in a weak electrostatic matrix such as ZSM-5. The other is that the low density of the  $\text{AlO}_4$ -tetrahedral sites offer spatial limitations in accommodating ions of higher valency. Even for a ZSM-5 with 40  $\text{SiO}_2/\text{Al}_2\text{O}_3$ , the  $\text{AlO}_4$ -tetrahedron is only one out of the twenty tetrahedra in the structure. The interaction between  $\text{AlO}_4$ -sites is weak indeed providing that the  $\text{AlO}_4^-$  sites are randomly distributed throughout the structure. It is also difficult to describe the coordination of a polyvalent cation to such widely spaced negative sites.

### Conclusion

This study has brought out some unique ion exchange characteristics of the zeolite ZSM-5. Since the catalytic characteristics and the unexpected chemistry ZSM-5 promotes are well known, these ion exchange characteristics should not be totally unexpected. It is through studies such as this as well as catalytic studies that our knowledge of this unique zeolite will increase toward a fuller understanding of the overall chemistry of ZSM-5.

### Literature Cited

1. Meisel, S. L., McCullough, J. P., Lechthaler, C. H. and Weisz, P. B. Chem. Tech., 1976, 86.
2. Chang, C. D. and Silvestri, A. J. J. Catal., 1977, 47, 249.
3. Argauer, R. J. and Landolt, G. R., U. S. Patent 3,702,886.
4. Kokotailo, G. T., Lawton, S. L., Olson, D. H. and Meier, W. M. Nature (London), 1978, 272, Issue 5652, pp. 437-8.

5. Sherry, H. S. J. Phys. Chem., 1966, 70, 1158.
6. Vansant, E. F. and Uytterhoeven Advances in Chemistry Series 101, pp. 426-435.
7. Barrer, R. M. and Klinowski, J. J. Chem. Soc. Farad. Trans. I, 1975, 71, 690.
8. Chu, P. and Dwyer, F. G., 7th North Amer. Meeting of the Catalysis Soc., 1981.
9. Chu, P. unpublished results.
10. Helfferich, F. Ion Exchange, McGraw Hill Book Company, 1962, Chapter 5.
11. Eisenman, G. Biophysical J., 1962, 2, 259.
12. Sherry, H. S. Ion Exchange, Marinsky, J. A., Ed., Marcel Dekker, Inc., New York, 1969, Chapter 3, p. 120.

RECEIVED November 29, 1982

# Aluminophosphate Molecular Sieves: A New Class of Microporous Crystalline Inorganic Solids

STEPHEN T. WILSON, BRENT M. LOK, CELESTE A. MESSINA,  
THOMAS R. CANNAN, and EDITH M. FLANIGEN

Union Carbide Corporation, Tarrytown Technical Center, Tarrytown, NY 10591

A novel class of crystalline, microporous aluminophosphate phases has been discovered. It represents the first class of molecular sieves with framework oxide compositions free of silica. The new class of materials encompasses some fourteen reported three-dimensional microporous framework structures, and six two-dimensional layer-type structures. The three-dimensional structures include structural analogues of the zeolites sodalite and erionite-offretite. The novel phases can be synthesized hydrothermally in the presence of organic amines and quaternary ammonium templates. The template is entrapped or clathrated within the crystallizing aluminophosphate network. After thermal decomposition of the template the three-dimensional molecular sieves have the general composition of  $\text{Al}_2\text{O}_3 \cdot 1.0 \pm 0.2 \text{ P}_2\text{O}_5$ . The various structures exhibit intracrystalline adsorption pore volumes from 0.04 to 0.35  $\text{cm}^3/\text{g}$ , and pore sizes from 0.3 to 0.8 nm. The aluminophosphate frameworks are hydrophilic.

The aluminophosphate molecular sieves represent a new class of microporous inorganic solids with the potential to be as useful and as scientifically challenging as the aluminosilicate zeolites. These molecular sieves are the latest chapter in the history of framework oxide molecular sieves, a history which began with the discovery of the naturally occurring mineral zeolites. These mineral zeolites stimulated the very successful research that led to the preparation of synthetic zeolites. As this research progressed, ever more silica-rich frameworks were synthesized, culminating in the essential Al-free microporous silica polymorphs, such as silicalite. These latter materials preserve the molecular sieving property of the zeolite but lose the ion-exchange capabilities as Al is removed from the framework.

0097-6156/83/0218-0079\$08.00/0  
© 1983 American Chemical Society

## Background

Silicon and aluminum, of course, are not unique in their ability to form tetrahedrally coordinated oxide networks. The element phosphorus, at the right of silicon in the periodic table, frequently assumes tetrahedral coordination with oxygen. With phosphorus in the +5 oxidation state as phosphate, aluminum phosphate possesses many structural similarities to silica: 1)  $\text{AlPO}_4$  is isoelectronic with  $\text{Si}_2\text{O}_4$ . 2) The average of the ionic radii of  $\text{Al}^{3+}$  (0.39Å) and  $\text{P}^{5+}$  (0.17Å) is 0.28Å, very close to the ionic radius of  $\text{Si}^{4+}$  (0.26Å) (1). 3)  $\text{AlPO}_4$  and  $\text{SiO}_2$  form isomorphous dense phases with  $\text{Al}^{3+}$  alternating with  $\text{P}^{5+}$  in a tetrahedral oxide network. There are dense phases of  $\text{AlPO}_4$  corresponding to seven structural forms of  $\text{SiO}_2$ :  $\alpha$ - and  $\beta$ -quartz;  $\alpha$ -,  $\beta$ -, and  $\gamma$ -tridymite; and  $\alpha$ - and  $\beta$ -cristobalite (2).

These structural analogies between  $\text{AlPO}_4$  and  $\text{SiO}_2$  served as one stimulus for examining aluminophosphates as a potential source of microporous frameworks. A second stimulus was the extensive aluminophosphate synthesis literature, and, in particular, the ease of hydrothermal synthesis. Several metastable hydrated networks have been synthesized. For example, two forms of  $\text{AlPO}_4 \cdot 2\text{H}_2\text{O}$  are known, metavariscite and variscite. These have structures composed of alternating Al and P, with Al exhibiting octahedral coordination and P, tetrahedral coordination (3,4). The two waters of hydration occupy cis positions in the coordination sphere of Al. Metavariscite contains 4-, 6-, and 8- rings of alternating alumina octahedra and phosphate tetrahedra. The partial removal of the waters of hydration from metavariscite or variscite is reversible but complete removal results in structural collapse. In addition to these hydrated forms of  $\text{AlPO}_4$ , the dense phase  $\text{AlPO}_4$ 's can also be synthesized hydrothermally.

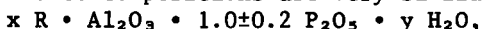
## Synthesis

The choice of a synthesis regime was followed by the selection of a synthesis strategy that included the use of the same types of templating agents so useful in the synthesis of high-silica zeolites and the silica molecular sieves. The synthesis procedure developed typically consists of first combining equimolar amounts of a reactive hydrated alumina, such as boehmite, and phosphoric acid in water. An aluminophosphate gel is formed, to which is added the templating agent R, an organic amine or a quaternary ammonium salt. This mixture is digested quiescently in the preferred temperature range of 125-200°C. A crystalline product is formed which is worked up using procedures typical of zeolite synthesis.

These crystalline products are the aluminophosphate molecular sieves. The large number of different structure-types, as determined by X-ray diffraction, made it necessary to assign each new structure-type a number. Thus the family of  $\text{AlPO}_4$  molecular sieves

was born. About 20 three-dimensional structures have been reported, of which 14 are microporous. These 20 include structural analogs of three zeolites: erionite ( $\text{AlPO}_4$ -17), sodalite ( $\text{AlPO}_4$ -20), and analcime ( $\text{AlPO}_4$ -24). Some of the novel structures are  $\text{AlPO}_4$ -5, -11, -14, -18, -31, and -33. The  $\text{AlPO}_4$ -5 structure has been solved by single crystal methods. Six two-dimensional layer-type structures have also been observed.

Despite the remarkable structural diversity in the  $\text{AlPO}_4$  family, the product compositions are very similar:



where R is an amine or quaternary ammonium ion. Each product as synthesized consists of a crystalline framework composed of essentially equimolar amounts of  $\text{Al}_2\text{O}_3$  and  $\text{P}_2\text{O}_5$ . The organic R and the  $\text{H}_2\text{O}$  are trapped or clathrated within the framework. The presence of R intact within the framework is implied by retention of the C/N ratio of the starting organic. The quantities x and y represent the amounts needed to fill the microporous voids within the neutral  $\text{AlPO}_4$  framework. The voids are freed of both organic and  $\text{H}_2\text{O}$  by calcination at 400-600°C.

#### Product X-ray Analysis and Morphology

Four  $\text{AlPO}_4$  molecular sieves, 5, 11, 17 and 20, typify the range of structure-types, pore sizes and pore volumes observed for the family as a whole. The first two are novel structure-types while the last two appear to be structural analogs of zeolites. X-ray powder diffraction data for these four materials are given in Table I.

$\text{AlPO}_4$ -5 was the first  $\text{AlPO}_4$  molecular sieve synthesized. It was immediately noted that its X-ray diffraction pattern (Figure 1) was unique and represented a novel structure. The pattern is quite simple and is easily indexed in the hexagonal system. This sample is well crystallized and was made with tetrapropylammonium cation ( $\text{Pr}_4\text{N}^+$ ) as template. It also exhibits an Al:P ratio of 1.0. The scanning electron micrographs of a typical  $\text{AlPO}_4$ -5 made with  $\text{Pr}_4\text{N}^+$  show barrel-like growth aggregates with platy growth steps (Figure 2). These aggregates are approximately 10-20 $\mu\text{m}$  across. When viewed end-on these barrels have a distinctly hexagonal cross-section and some of the barrels appear to be hollow. There also appear to be a few single crystal hexagonal prisms. The scanning electron micrographs in Figure 3 show single crystals of  $\text{AlPO}_4$ -5, also made with  $\text{Pr}_4\text{N}^+$ . These are large hexagonal prisms, approximately 50 $\mu\text{m}$  in diameter and 150 $\mu\text{m}$  long. The structure of  $\text{AlPO}_4$ -5 was determined using a crystal from this preparation (5).

The X-ray powder diffraction pattern of  $\text{AlPO}_4$ -11 (Figure 4) is also unique and represents a novel structure. Although the structure has not been determined, it appears to possess lower symmetry than hexagonal. This sample made with di-n-propylamine has an Al:P ratio of 1.0. The scanning electron micrographs of a typical  $\text{AlPO}_4$ -11 (Figure 5) show large growth aggregates composed

Table I

Typical X-ray Powder Diffraction Data for  $\text{AlPO}_4$  Molecular Sieves and Zeolites in Figures (Major Lines Only)

| <u><math>\text{AlPO}_4\text{-5}</math></u> |          | <u><math>\text{AlPO}_4\text{-11}</math></u> |          |             |          |
|--|----------|---|----------|-------------|----------|
| <u>d(A)</u>                                | <u>I</u> | <u>d(A)</u>                                 | <u>I</u> | <u>d(A)</u> | <u>I</u> |
| 11.8                                       | 100      | 10.85                                       | 34       | 3.59        | 11       |
| 6.84                                       | 11       | 9.31  | 49       | 3.38        | 13       |
| 5.93                                       | 28       | 6.66  | 16       | 3.34        | 17       |
| 4.50                                       | 66       | 5.64  | 30       | 3.13        | 15       |
| 4.24                                       | 63       | 4.32  | 50       | 3.11        | 10       |
| 3.97                                       | 94       | 4.23  | 100      | 2.84        |          |
| 3.43                                       | 37       | 4.00  | 58       | 2.71        | 15       |
| 3.08                                       | 21       | 3.93  | 75       | 2.61        | 11       |
| 2.97                                       | 22       | 3.83  | 67       | 2.39        | 14       |
| 2.60                                       | 19       | 3.62  | 10       | 2.37        |          |
| 2.40                                       | 13       |   |          |             |          |

| <u><math>\text{AlPO}_4\text{-17}</math></u> |          | <u>Erionite (15)</u> |          | <u><math>\text{AlPO}_4\text{-20}</math></u> |          | <u>Zeolite HS (16)</u> |          |
|---|----------|----------------------|----------|---|----------|------------------------|----------|
| <u>d(A)</u>                                 | <u>I</u> | <u>d(A)</u>          | <u>I</u> | <u>d(A)</u>                                 | <u>I</u> | <u>d(A)</u>            | <u>I</u> |
| 11.55                                       | 100      | 11.41                | 100      | 6.33  | 51       | 6.28                   | 80       |
| 9.12  | 41       | 9.07                 | 11       | 4.46  | 44       | 4.44                   | 30       |
| 6.63  | 39       | 6.61                 | 73       | 3.99  | 16       | 3.97                   | 5        |
| 6.24  | 13       | 6.28                 | 5        | 3.63  | 100      | 3.63                   | 100      |
| 5.75  | 62       | 5.72                 | 16       | 3.16  | 25       | 3.13                   | 5        |
| 5.34  | 33       | 5.34                 | 14       | 2.83  | 18       | 2.81                   | 60       |
| 4.93  | 20       | -                    | -        | 2.59  | 18       | 2.56                   | 80       |
| -   | -        | 4.595                | 8        | -   | -        | 2.37                   | 30       |
| 4.53  | 67       | 4.551                | 12       | 2.24  | 4        | 2.09                   | 80       |
| 4.33  | 93       | 4.322                | 67       | 2.10  | 5        | -                      | -        |
| 4.15  | 50       | 4.156                | 24       | -   | -        | 1.99                   | 5        |
| 3.95  | 15       | -                    | -        | 1.903                                       | 4        | 1.888                  | 9        |
| 3.82  | 34       | 3.813                | 37       | -   | -        | 1.81                   | 30       |
| 3.74  | 39       | 3.746                | 65       | 1.752                                       | 10       | 1.737                  | 40       |
| 3.52  | 55       | 3.570                | 24       |   |          |                        |          |
| 3.38  | 35       | 3.402                | 4        |   |          |                        |          |
| -   | -        | 3.303                | 39       |   |          |                        |          |
| -   | -        | 3.276                | 25       |   |          |                        |          |
| 3.26  | 20       | 3.271                | 25       |   |          |                        |          |
| 3.11  | 20       | 3.106                | 12       |   |          |                        |          |
| 2.92  | 17       | 2.923                | 12       |   |          |                        |          |
| -   | -        | 2.910                | 10       |   |          |                        |          |
| 2.87  | 29       | 2.860                | 60       |   |          |                        |          |
| -   | -        | 2.839                | 50       |   |          |                        |          |
| 2.81  | 68       | 2.812                | 52       |   |          |                        |          |

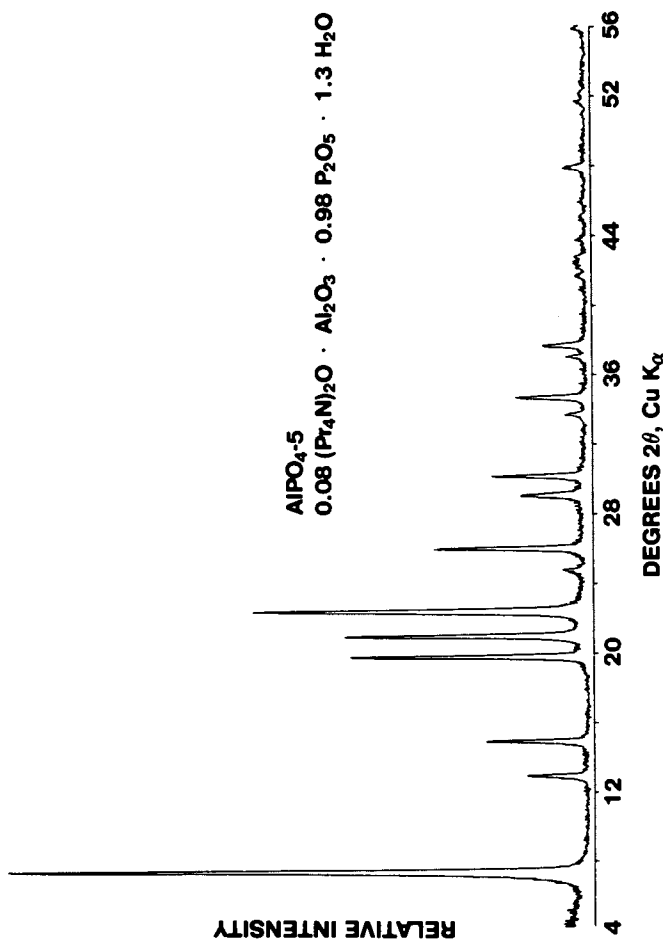
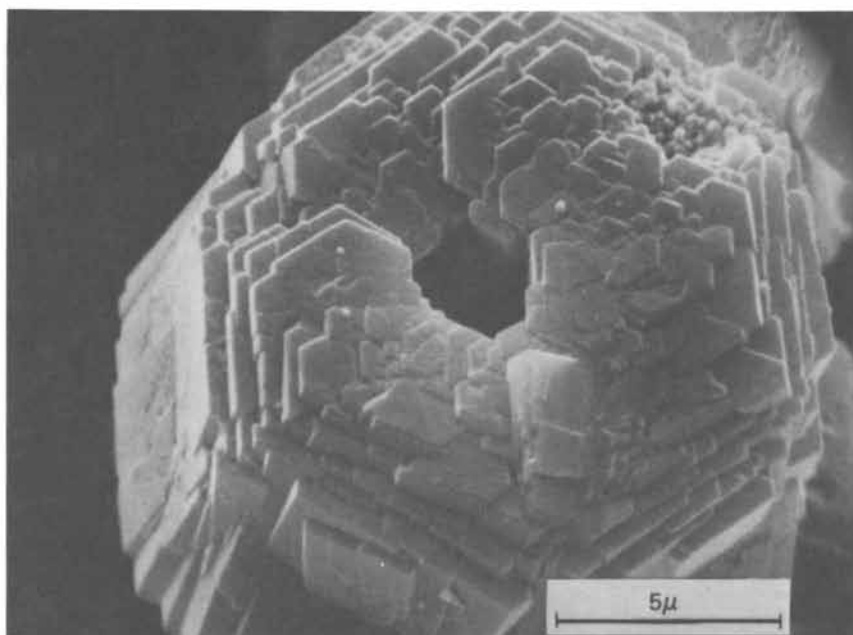
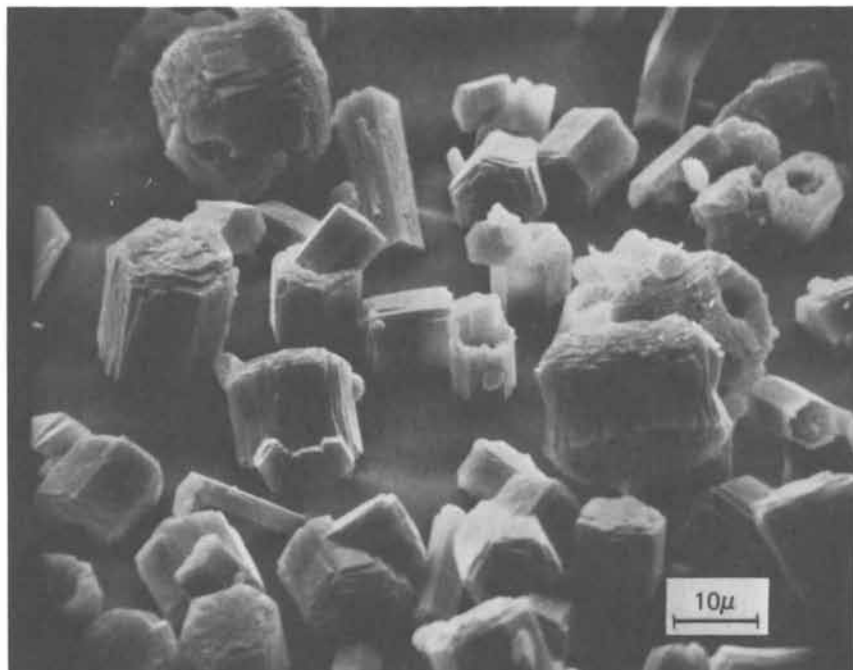
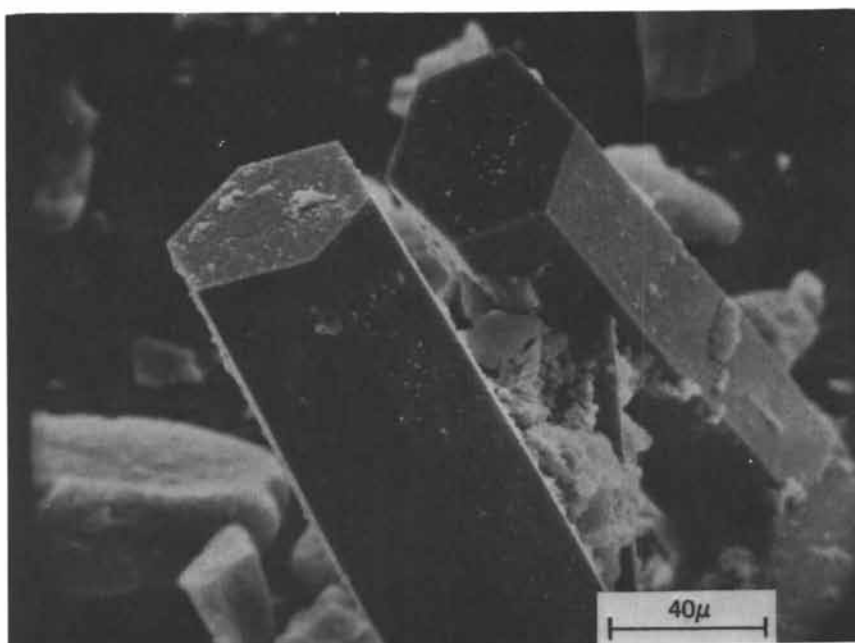
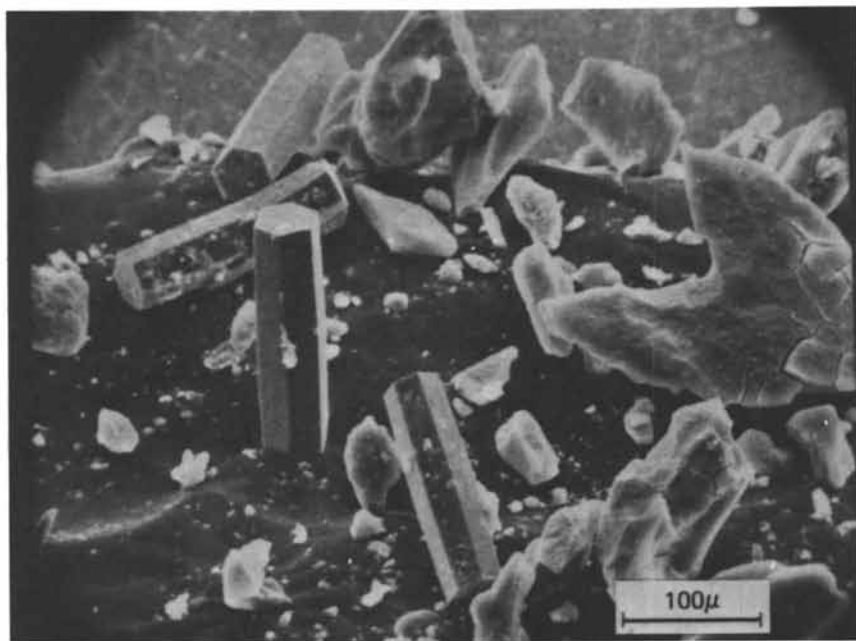


Figure 1.  
x-Ray Powder Diffraction Pattern of AlPO<sub>4</sub>-5.





**Figure 2.**  
SEM of AlPO<sub>4</sub>-5 Made With Pr<sub>4</sub>N<sup>+</sup>.



**Figure 3.**  
SEM of AlPO<sub>4</sub>-5 Single Crystals.

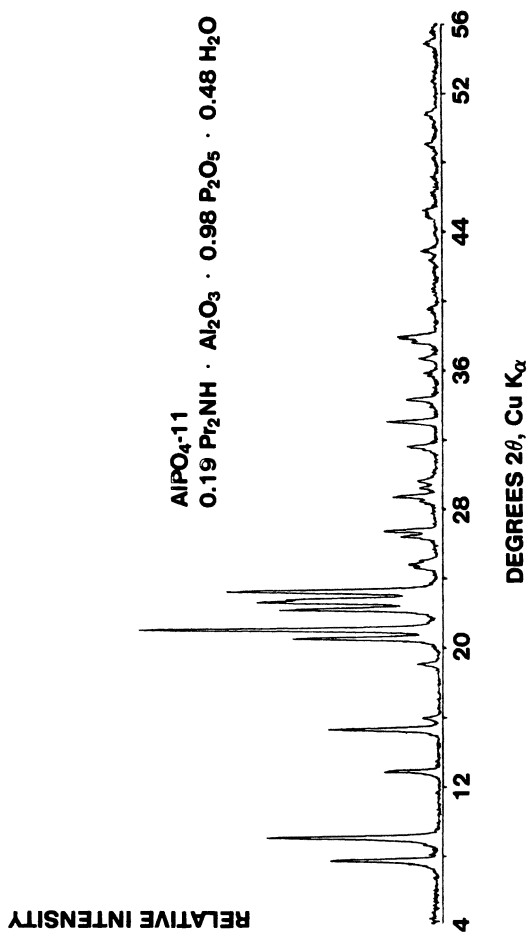
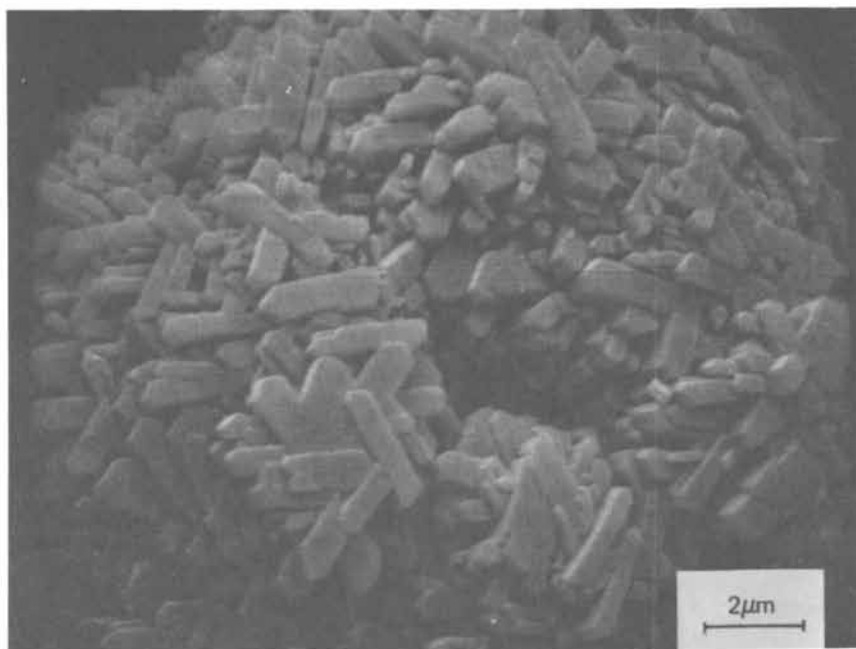
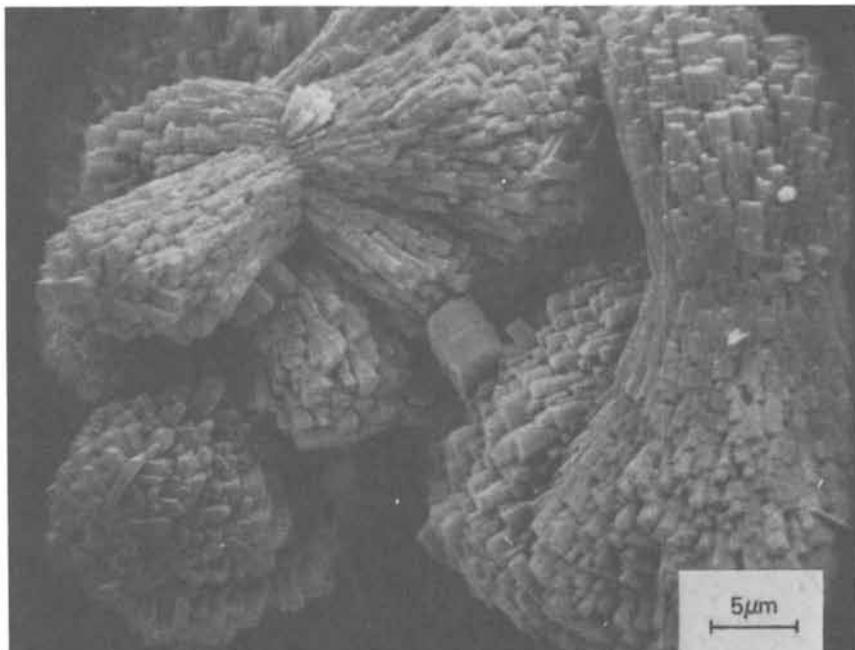


Figure 4.  
x-Ray Powder Diffraction Pattern of AlPO<sub>4</sub>-11.



**Figure 5.**  
SEM of AlPO<sub>4</sub>-11 Made with n-Pr<sub>2</sub>NH.

of small prisms. The aggregates vary in size from 25 up to 150 $\mu\text{m}$  across and often assume a wheat-sheaf habit. The individual prisms are approximately 1-2 $\mu\text{m}$  in length.

A comparison of the X-ray powder diffraction patterns of  $\text{AlPO}_4\text{-17}$  and a typical sedimentary erionite (Figure 6) suggests a framework structure analogy. Although there are some variations in relative intensities, many of the major lines match quite closely in d-spacings. There are differences, however, and these may be due to ordering of the Al and P in the  $\text{AlPO}_4\text{-17}$  framework and the quite different extra-framework constituents in the two compositions. The adsorption properties of  $\text{AlPO}_4\text{-17}$  are consistent with an erionite-type structure and neutron powder diffraction data confirm this framework structure (6). The scanning electron micrographs of  $\text{AlPO}_4\text{-17}$  made with quinuclidine (Figure 7) show growth aggregates with a hexagonal habit. Some are almost single crystal hexagonal prisms, 2-4 $\mu\text{m}$  across. Like  $\text{AlPO}_4\text{-17}$  erionite also assumes a hexagonal habit.

Comparison of the X-ray powder diffraction patterns of  $\text{AlPO}_4\text{-20}$  and a TMA-sodalite (Figure 8) strongly supports a structural analogy. The rather large line widths in the  $\text{AlPO}_4\text{-20}$  pattern are due to the submicron crystallite size. Both compositions were made with the template, TMA, and both can be indexed in the cubic system.

### Organic Templates as Structure-Directing Agents

The typical  $\text{AlPO}_4$  synthesis gel contains four components: an alumina source, a phosphate source, water, and an organic amine or quaternary ammonium salt. The relative concentrations and, of course, the individual characteristics of these reactants are important factors in the preparation of  $\text{AlPO}_4$  molecular sieves. One factor is particularly evident, namely, without the organic no  $\text{AlPO}_4$  molecular sieves are formed. The concept of a template in molecular sieve synthesis is not new (7,8). A template is a species which seems to exert a unique structure-directing influence during crystallization of the molecular sieve. The action of a template appears to have both electronic and steric components. In  $\text{AlPO}_4$  molecular sieve synthesis the steric component appears to dominate.

The synthesis of  $\text{AlPO}_4\text{-20}$ , -17, and -5 shows the range of structure-template specificity observed with  $\text{AlPO}_4$  molecular sieves. Only one template, tetramethylammonium (TMA), is known to make  $\text{AlPO}_4\text{-20}$ . As shown earlier, the X-ray powder pattern of  $\text{AlPO}_4\text{-20}$  matches that of TMA-sodalite. Elemental analysis of  $\text{AlPO}_4\text{-20}$  indicates approximately one TMA per sodalite cage. The framework structure of sodalite consists entirely of sodalite units packed together. Each sodalite cage is bounded by 4-rings and 6-rings. Figure 9 shows a scale model of the sodalite framework with TMA in one of the sodalite cages. In this and subsequent models, each black segment represents an Al-O-P bond con-

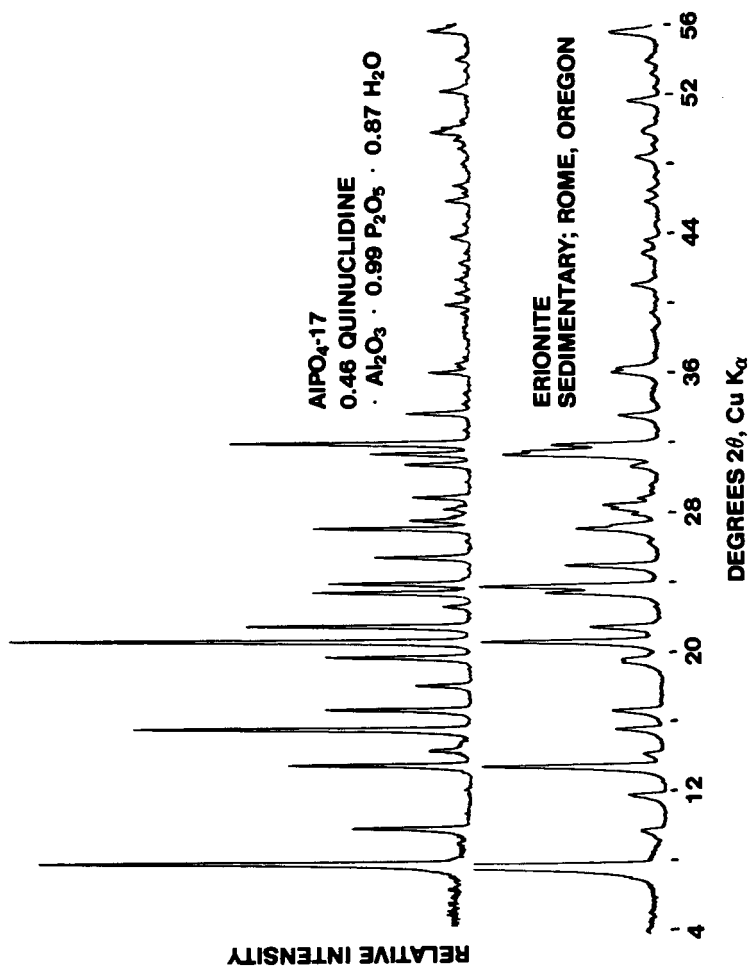
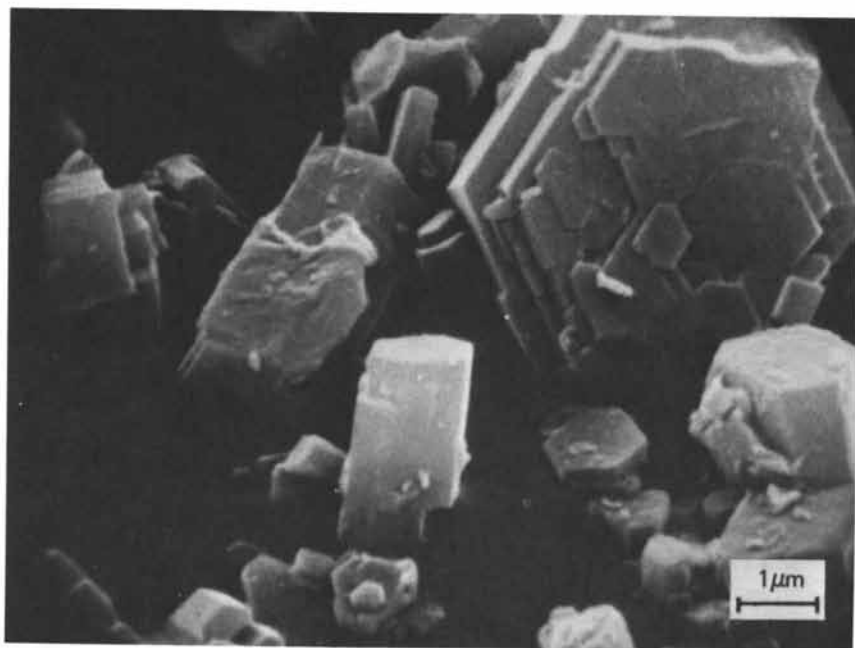
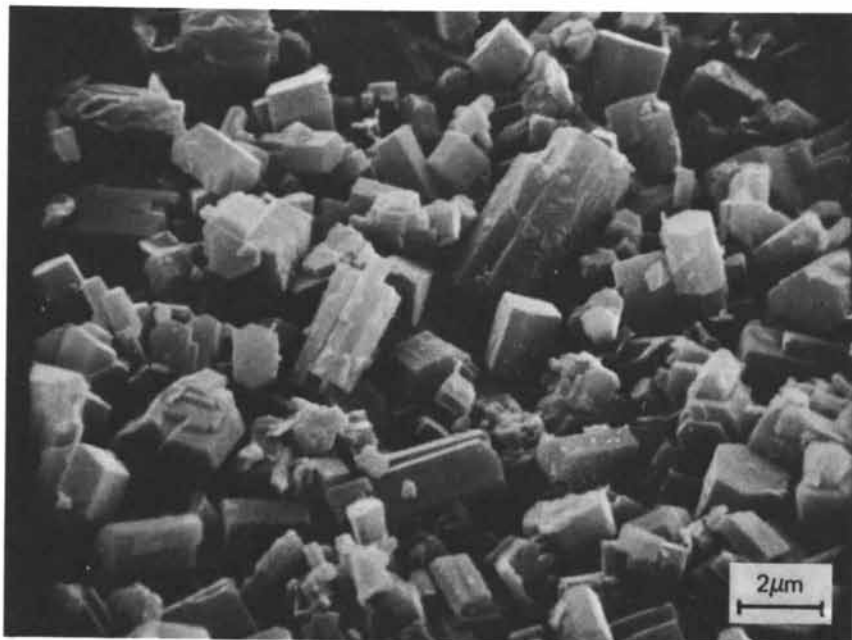


Figure 6.  
x-Ray Powder Diffraction Patterns of AlPO<sub>4</sub>-17 and  
Typical Erionite.



**Figure 7.**  
SEM of AlPO<sub>4</sub>-17 Made With Quinuclidine.

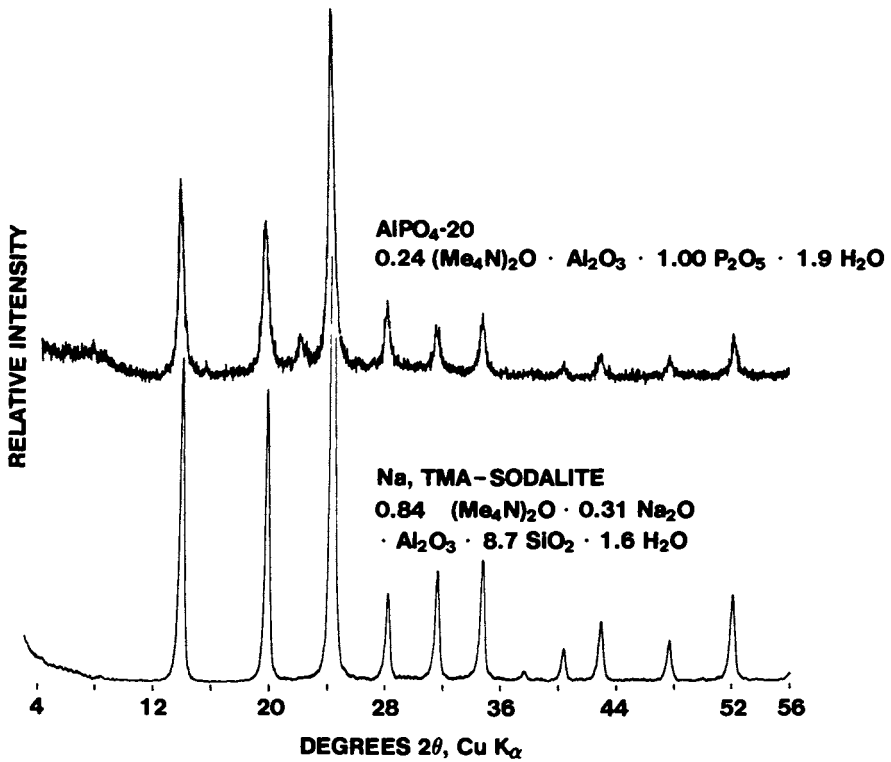
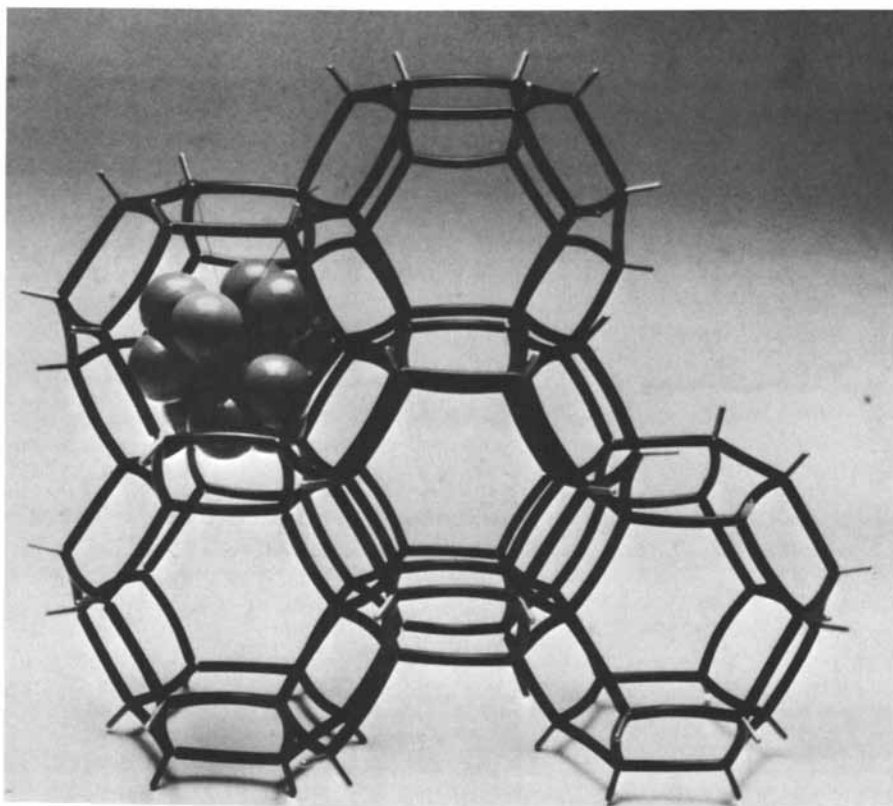


Figure 8.  
x-Ray Powder Diffraction Patterns of AlPO<sub>4</sub>-20 and  
TMA-Sodalite.






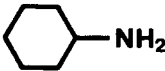
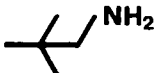
**Figure 9**  
**Framework Model of Sodalite Structure Containing TMA**

necting an Al tetrahedron and a P tetrahedron, assuming that Al and P tetrahedra alternate throughout the structure. The TMA template fits snugly inside the sodalite cage. An oxygen packing model would show the TMA completely surrounded by oxygens. The TMA had to be trapped by the crystallizing sodalite cages since it is much too large to enter the framework after crystallization.

AlPO<sub>4</sub>-17 is readily synthesized with three different templates: quinuclidine, cyclohexylamine, and neopentylamine. The X-ray powder patterns of each AlPO<sub>4</sub>-17 suggest an erionite structure-type. Elemental analyses of the three compositions as synthesized show approximately the same number of templates per unit cell (Figure 10). Assuming the same unit cell as erionite, i.e., 36 tetrahedral oxide units (TO<sub>2</sub>), there are approximately 4 template molecules per unit cell. The framework structure of erionite (Figure 11) consists of two types of columns running parallel to the c-axis. One column consists of alternating cancrinite cages and double 6-rings. The other consists of large cages, with internal dimensions 15.1Å by 6.3Å. Access to the large cages is controlled by 8-rings whereas access to the cancrinite cages is controlled by 6-rings. There are two of these large cages per unit cell of erionite. The elemental analysis of AlPO<sub>4</sub>-17 is consistent with 4 template molecules per unit cell, or 2 per large cage. Scale models show that the templates, such as quinuclidine in Figure 11, can only fit in the large cages, and that each cage can accommodate at most 2 templates. As in AlPO<sub>4</sub>-20, the AlPO<sub>4</sub>-17 templates had to be incorporated within the structural voids during crystallization of the framework since they are too large to diffuse through the 8-rings. If one approximates the space-filling capability of each template on the basis of its carbon and nitrogen content, each template contributes approximately 30 C+N atoms per unit cell or 15 per cage (Figure 10).

The rather selective structure-template relationship of AlPO<sub>4</sub>-20 and AlPO<sub>4</sub>-17 contrasts with the large number of templates that make AlPO<sub>4</sub>-5 (Figure 12). Among these templates are quaternary ammonium cations, primary amines, secondary amines, tertiary amines, cyclic amines, diamines, and alkanolamines. Individual templates contain as many as 13 C+N atoms to as few as 5. There seems to be no common thread connecting these templates, not size, not shape, not solubility, and not pK<sub>b</sub>.

AlPO<sub>4</sub>-5 crystallizes in the hexagonal system with a=13.7Å and c=8.5Å (5). The unit cell contains 24 tetrahedral oxide units, 12 Al and 12 P, with strict alternation of Al and P throughout the framework. Unlike the structures of AlPO<sub>4</sub>-20 and AlPO<sub>4</sub>-17, the AlPO<sub>4</sub>-5 structure has no cages containing the trapped organic template (Figure 13). It has a unidimensional pore system consisting of cylindrical channels bounded by 12-rings and running parallel to the c-axis. The remainder of the structure consists of columns of 6-rings and columns of 4-rings, with each column axis parallel to the c-axis (Figure 14a and b). The 6-ring columns consist of individual 6-rings of alternating Al and P tetra-

| <u>TEMPLATE</u>   | <u>TEMPLATE/U.C.*</u> | <u>C+N/U.C.*</u> |
|---|-----------------------|------------------|
|  | 4.1                   | 33               |
|  | 4.1                   | 29               |
|  | 4.7                   | 28               |

\* BASED ON 36 TO<sub>2</sub>/U.C. IN ERIONITE-TYPE STRUCTURE

Figure 10.

Three Templates Make AlPO<sub>4</sub>-17 (Erionite-Type).

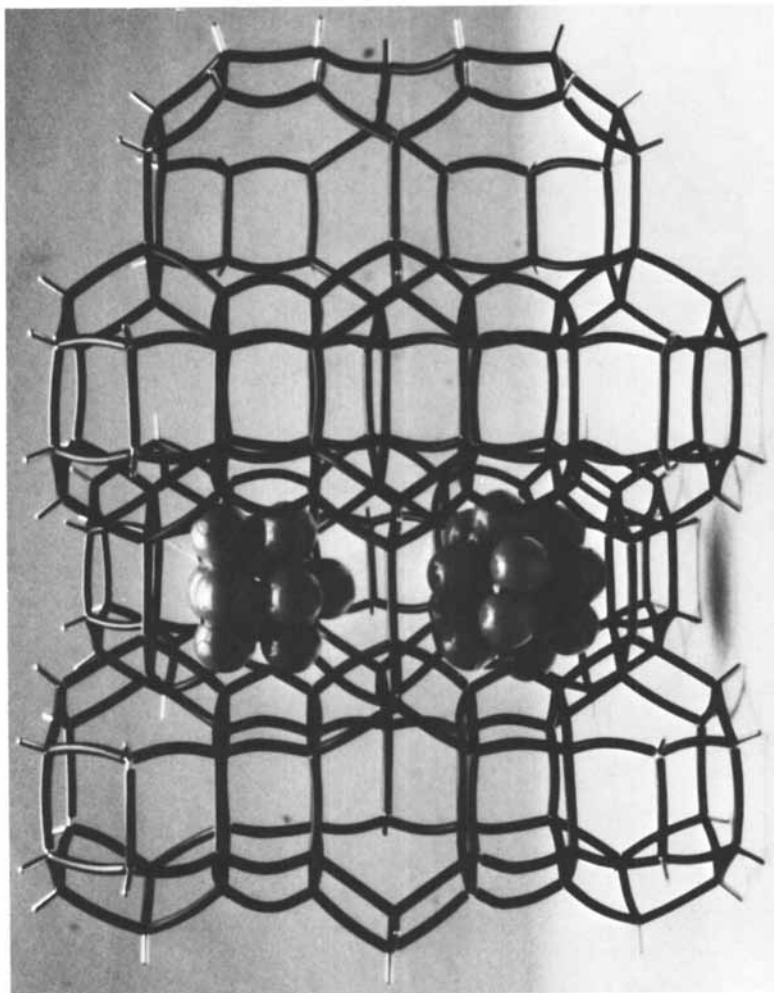


Figure 11  
Framework Model of Erionite Structure Containing Two  
Quinuclidine Molecules

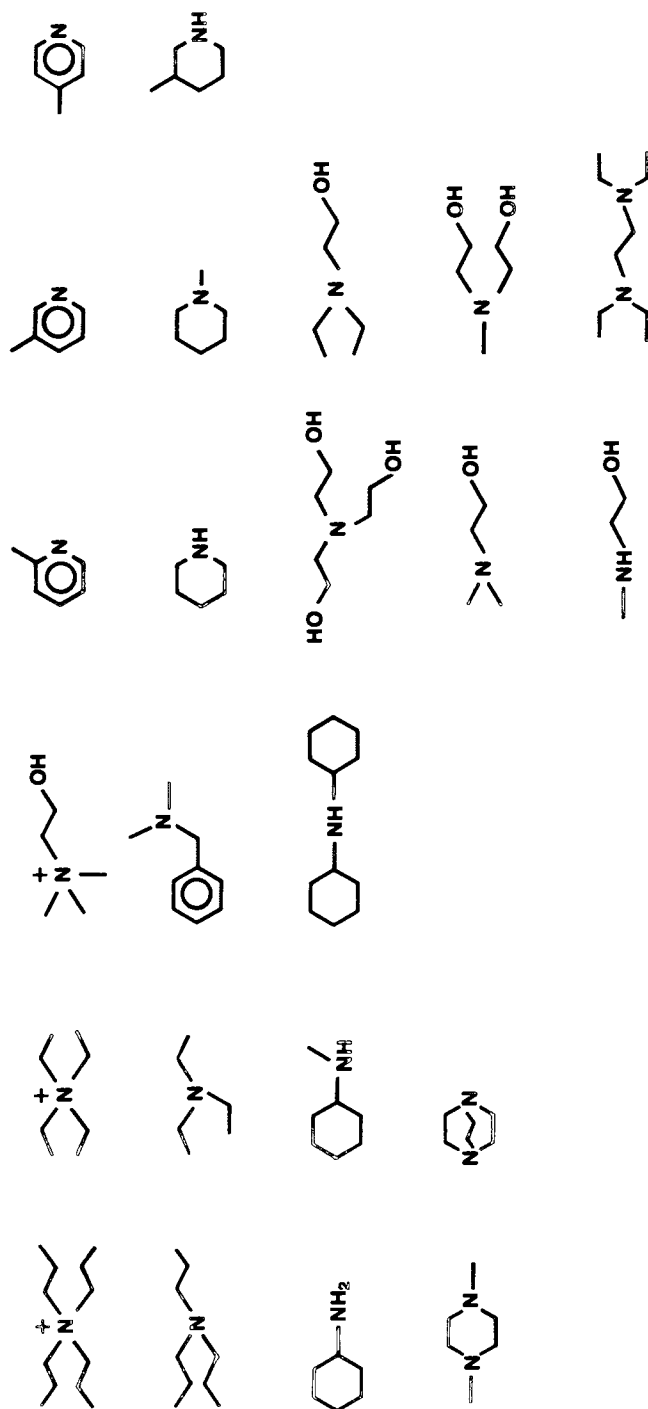


Figure 12  
Twenty-three Templates That Make AlPO<sub>4</sub>-5

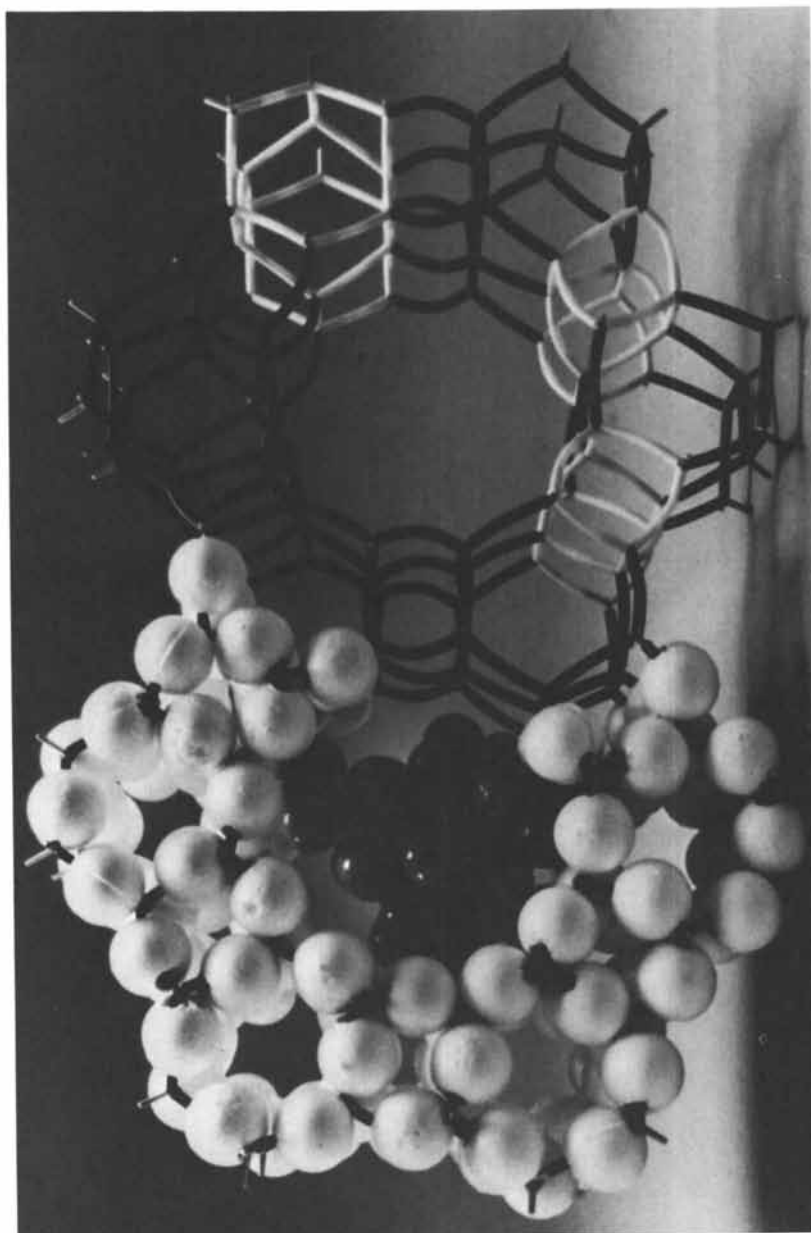


Figure 13  
Oxygen-Packing Model of  $\text{AlPO}_4\text{-5}$  Structure Containing TPA

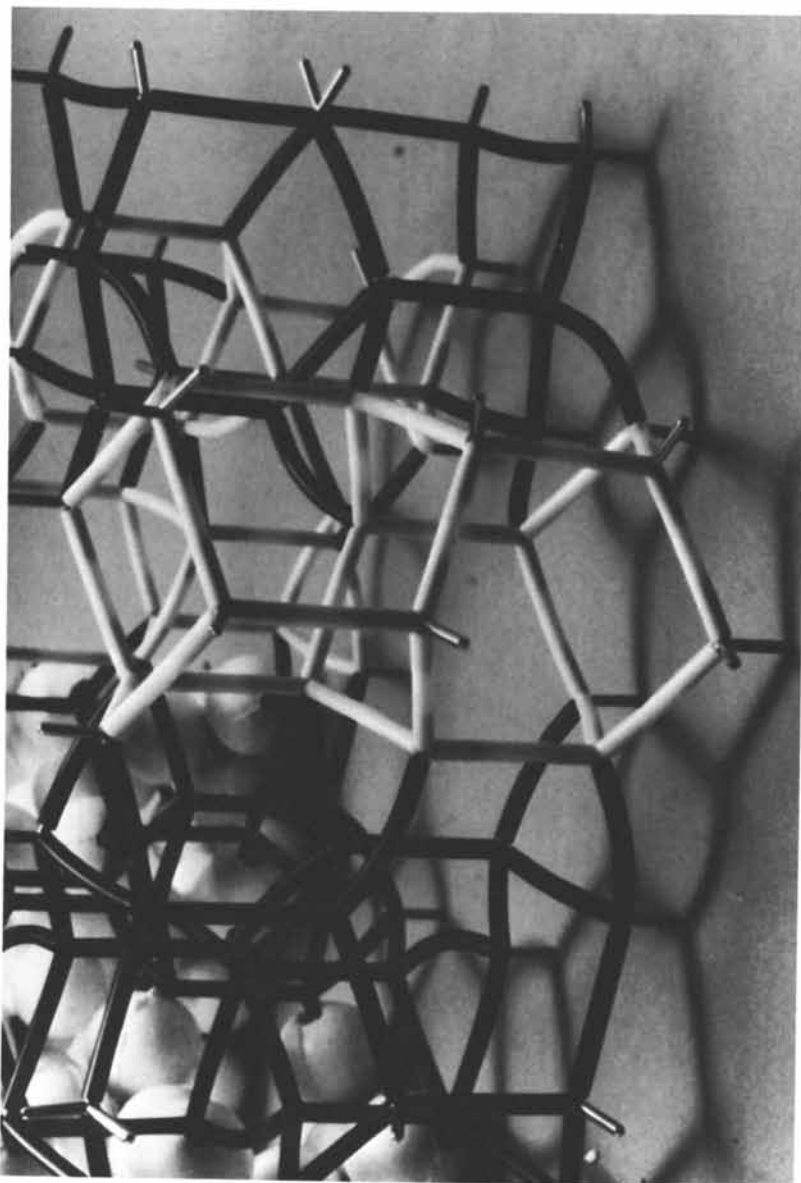


Figure 14a  
Detail of  $\text{AlPO}_4\text{-5}$  Structure: 6-Ring Column

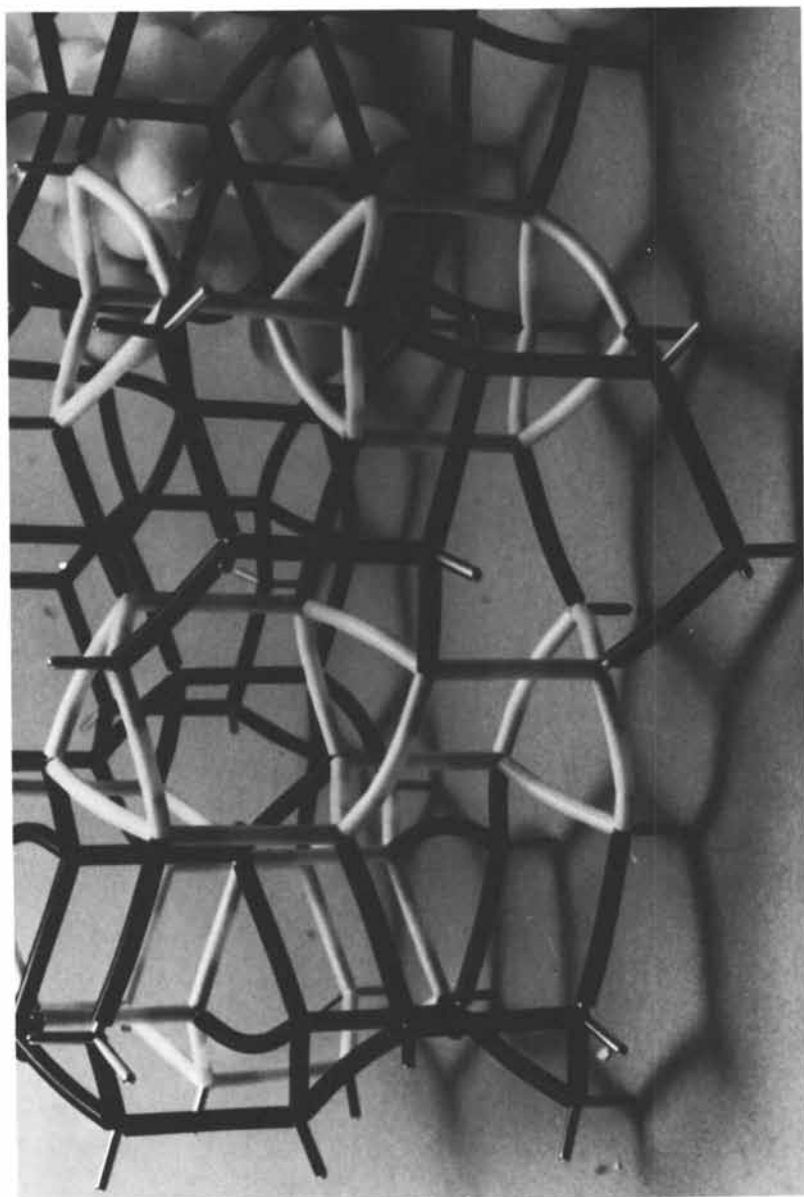


Figure 14b  
Detail of  $\text{AlPO}_4\text{-5}$  Structure: 4-Ring Column



hedra, each ring in a chair conformation. Every tetrahedron possesses one bond in a direction parallel to the c-axis. This bond can be designated up or down depending on its direction along the c-axis. Thus each 6-ring has an alternating up-down arrangement of tetrahedral atoms. Each 6-ring is bonded to the ring below it by 3 bonds and similarly to the ring above it. This bonding pattern is also found in the tridymite structure. The 4-ring column shows a similar bonding pattern. Each 4-ring is twisted into a boat-like conformation, and is bonded to a 4-ring above by 2 bonds and to one below by 2 bonds. There is also strict up-down alternation of the tetrahedra in the 4-ring parallel to the c-axis.

Since the  $\text{AlPO}_4\text{-5}$  framework contains no cages and the pore structure is essentially a cylinder of uniform cross-section, the only steric requirement placed on a template molecule is that its width not exceed ca. 8Å. The oxygen packing model in Figure 13 contains one of the largest templates that makes  $\text{AlPO}_4\text{-5}$ , tetrapropylammonium. The lack of framework charge means that the template nitrogen, positively charged or not, need play no role in determining the packing density of the various templates in the pore. The elemental analyses of eight  $\text{AlPO}_4\text{-5}$  products as synthesized illustrates the apparently steric nature of the template packing (Figure 15). The largest templates take up the most room. Three of these, tetrapropylammonium, tripropylamine, and tetraethylammonium, occupy one unit cell length, about 8.5Å. At the other extreme, Dabco, a particularly compact bicyclic, packs to give 1.8 templates per unit cell. Most of the templates show packing densities equivalent to about 8-10 C+N's per unit cell.

### Thermal Stability and Adsorption Properties

The  $\text{AlPO}_4$  molecular sieves show excellent physical properties. Many are thermally stable and resist loss of structure at 1000°C. Those studied for hydrothermal stability, including  $\text{AlPO}_4\text{-5}$ , -11, and -17, show no structure loss when treated with 16% steam at 600°C. The layer structures undergo structural collapse when the organic interlayer propanol is removed thermally at 200-400°C.

The adsorption properties of selected  $\text{AlPO}_4$  molecular sieves are summarized in Table II. All measurements were performed by standard gravimetric techniques on samples calcined at 500-600°C to remove the organic template. The different structure-types are arranged in order of decreasing pore size. Pore size was determined by using so-called "plug gauge" molecules of known kinetic diameter (9). The ring size refers to the number of tetrahedral atoms (Al or P) in the ring that controls pore size. For the 12-ring structures,  $\text{AlPO}_4\text{-5}$  and  $\text{AlPO}_4\text{-31}$ , adsorption of neopentane is observed. The 10- or puckered 12-ring of  $\text{AlPO}_4\text{-11}$  adsorbs cyclohexane but not neopentane. This pore size is similar to that of ZSM-5. Two of the 8-ring structures,  $\text{AlPO}_4\text{-17}$  and  $\text{AlPO}_4\text{-18}$ , sorb

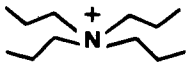
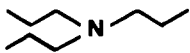
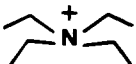
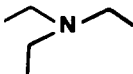
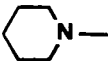
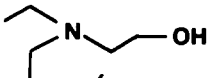
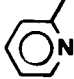

| <u>TEMPLATE</u>   | <u>TEMPLATE/U.C.</u> | <u>C+N/U.C.</u> |
|---|----------------------|-----------------|
|    | 1.0                  | 12              |
|    | 1.0                  | 9.1             |
|    | 1.0                  | 8.7             |
|    | 1.2                  | 8.4             |
|    | 1.3                  | 9.0             |
|   | 1.3                  | 9.2             |
|  | 1.3                  | 9.9             |
|  | 1.8                  | 15              |

Figure 15.  
Template Packing in  $\text{AlPO}_4\text{-5}$  Structure.

butane but not isobutane. Two,  $\text{AlPO}_4$ -14 and  $\text{AlPO}_4$ -33, sorb xenon but not butane, indicating a somewhat puckered 8-ring structure. Finally, the 6-ring structures of  $\text{AlPO}_4$ -16 and  $\text{AlPO}_4$ -20 adsorb only  $\text{H}_2\text{O}$ . The pore volumes are the near saturation values,  $\text{O}_2$  at  $-183^\circ\text{C}$  and  $\text{H}_2\text{O}$  at ambient temperature.

Table II

Adsorption Properties of  $\text{AlPO}_4$  Molecular Sieves

| $\text{AlPO}_4$ - | Pore Size,<br>nm | Ring Size            | Pore Vol.,<br>$\text{cm}^3/\text{g}$ |                      |
|-------------------|------------------|----------------------|--------------------------------------|----------------------|
|                   |                  |                      | $\text{O}_2$                         | $\text{H}_2\text{O}$ |
| 5                 | 0.8              | 12                   | 0.18                                 | 0.3                  |
| 31                | 0.8              | 12                   | 0.09                                 | 0.17                 |
| 11                | 0.61             | 10 or<br>puckered 12 | 0.11                                 | 0.16                 |
| 17                | 0.46             | 8                    | 0.20                                 | 0.28                 |
| 18                | 0.46             | 8                    | 0.27                                 | 0.35                 |
| 14                | 0.41             | 8                    | 0.19                                 | 0.28                 |
| 33                | 0.41             | 8                    | 0.23                                 | 0.23                 |
| 16                | 0.3              | 6                    | 0                                    | 0.3                  |
| 20                | 0.3              | 6                    | 0                                    | 0.2                  |

The  $\text{H}_2\text{O}$  and  $\text{O}_2$  pore volumes of  $\text{AlPO}_4$ -17 compare very closely with the best of the mineral erionites (10), while the  $\text{H}_2\text{O}$  pore volume of  $\text{AlPO}_4$ -20 is comparable to the theoretical value for an unstuffed sodalite framework (11). In general, the  $\text{H}_2\text{O}$  pore volumes are usually greater than the  $\text{O}_2$  pore volumes, reflecting the presence of additional pore volume accessible to  $\text{H}_2\text{O}$  but not to  $\text{O}_2$ . This additional volume is presumably reached through 6-rings. For example, the additional volume in the cancrinite cages of the erionite structure is accessible only to  $\text{H}_2\text{O}$ . The model of the framework structure of  $\text{AlPO}_4$ -5 (Figure 13) shows the large pore voids capable of adsorbing  $\text{O}_2$  or  $\text{H}_2\text{O}$ . The small voids, outlined by columns of twisted chains of 4- and 6-rings parallel to the c-axis (Figure 14a,b), adsorb  $\text{H}_2\text{O}$  only. In  $\text{AlPO}_4$ -5 these small voids apparently sorb about  $0.12 \text{ cm}^3/\text{g}$ .

The  $\text{O}_2$  isotherms for these  $\text{AlPO}_4$  molecular sieves are essentially Type I, typical of micropore filling (12,13). In Figure 16 the  $\text{O}_2$  isotherms of  $\text{AlPO}_4$ -5, -11, -17 are compared with those of a typical zeolite, NaX, and a silica molecular sieve, silicalite.  $\text{AlPO}_4$ -5 and -17 have saturation pore volumes of approximately  $0.2 \text{ cm}^3/\text{g}$  similar to that of silicalite, while  $\text{AlPO}_4$ -11 has a relatively small  $\text{O}_2$  pore volume (ca.  $0.1 \text{ cm}^3/\text{g}$ ).

The  $\text{H}_2\text{O}$  adsorption isotherms for  $\text{AlPO}_4$ -5, -11, -17, and -20 are shown in Figure 17. For comparison, the hydrophilic NaX and the hydrophobic silicalite are included. The isotherm shape for  $\text{AlPO}_4$ -11 and  $\text{AlPO}_4$ -17, like that of NaX and silicalite, is Type I, typical of micropore filling. The isotherm shape of the  $\text{AlPO}_4$ -20

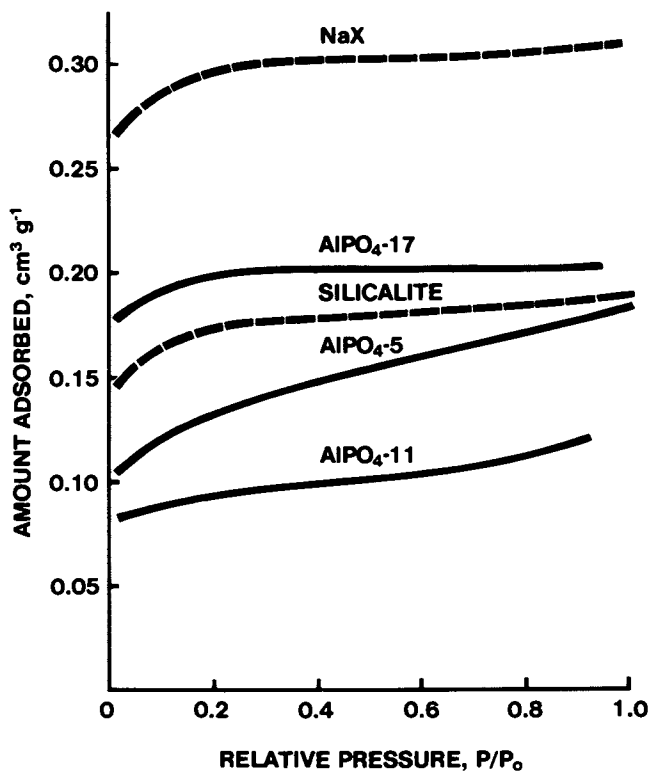


Figure 16.

O<sub>2</sub> Adsorption Isotherms for Selected AlPO<sub>4</sub> Molecular Sieves (-183 C).

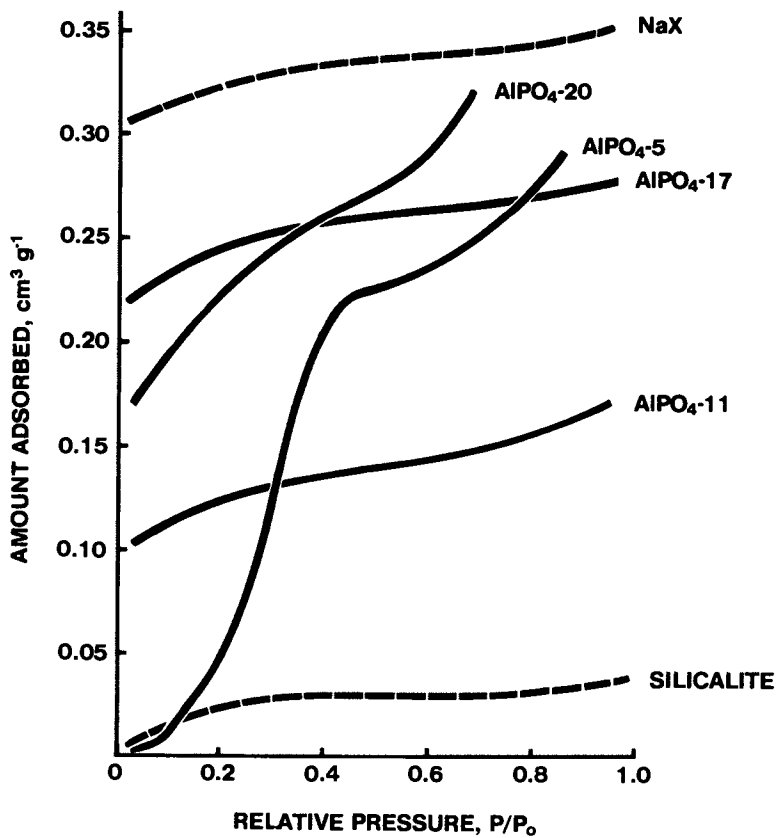


Figure 17.

H<sub>2</sub>O Adsorption Isotherms for Selected AlPO<sub>4</sub> Molecular Sieves (24 C).

is Type IV, indicating both micropores and appreciable transition pores. Although  $\text{AlPO}_4\text{-5}$  exhibits Type I adsorption for  $\text{O}_2$  and paraffins,  $\text{H}_2\text{O}$  sorption follows a Type V isotherm shape (12,13). This shape, unusual for a microporous solid, has been observed on all  $\text{AlPO}_4\text{-5}$  materials studied regardless of synthesis. Water sorption at values of  $P/P_0$  less than 0.2 is unusually low, and there is a large increase between  $P/P_0 = 0.2$  and 0.4. More recently this type of adsorption has been observed with  $\text{H}_2\text{O}$  on  $\text{AlPO}_4\text{-31}$ . Although significantly different in pore volume (Table II),  $\text{AlPO}_4\text{-5}$  and -31 share a similar large pore size, a factor which may be influencing  $\text{H}_2\text{O}$  sorption in an unexpected way.

The surface character of the  $\text{AlPO}_4$  molecular sieves differs from that of the silica molecular sieves even though both framework types are neutral with no extra-framework cations. The molecular sieve silicalite is hydrophobic and the  $\text{AlPO}_4$  molecular sieves are moderately hydrophilic. Zeolites are hydrophilic due to the interaction of the dipole of the  $\text{H}_2\text{O}$  molecule with the electrostatic fields of the anionic aluminosilicate framework and the balancing nonframework cations. The hydrophilicity of the  $\text{AlPO}_4$  materials is apparently due to the difference in electronegativity between Al(1.5) and P(2.1). Neither mechanism is possible with silica molecular sieves. The  $\text{AlPO}_4$  molecular sieves do exhibit less affinity for  $\text{H}_2\text{O}$  than the hydrophilic zeolites such as Type A and Type X.

### Summary and Conclusion

$\text{AlPO}_4$  molecular sieves have been synthesized using a wide variety of organic amine and quaternary ammonium cations. In each case the organic appears to behave as a templating agent directing structure formation. Each crystalline product as synthesized contains the templating agent trapped within structural voids. The wide variety of templating agents has yielded almost as wide a variety of structure types. Every framework structure, however, exhibits the same composition, with Al and P in equimolar proportion. Each framework is thus neutral with nil iron exchange capacity. The various structure-types include a broad range of pore sizes and volumes, as broad as that found among synthetic zeolites. The  $\text{AlPO}_4$  frameworks have excellent thermal and hydrothermal stability.

The diversity of pore sizes coupled with the essentially cation-free framework make  $\text{AlPO}_4$  molecular sieves potentially applicable in separations of molecules and other adsorption applications. A broad screening program in air drying has shown many  $\text{AlPO}_4$  molecular sieves with performance characteristics similar to those of Linde Type A and X. The hydrophilic surface character has also been demonstrated in the selective removal of  $\text{H}_2\text{O}$  from solutions of 2-butanone containing 4 vol.%  $\text{H}_2\text{O}$ . The hydroxyl infrared region ( $4000\text{-}3400\text{ cm}^{-1}$ ) for several  $\text{AlPO}_4$  molecular sieves contains weak  $\nu_{\text{OH}}$  absorptions at  $3680\text{ cm}^{-1}$  attributed by Peri (14)

to  $\nu(\text{P-OH})$ . This feature coupled with the hydrophilic surface character appears to account for the weakly acidic catalytic properties observed in this new family of materials.

#### Literature Cited

1. Shannon, R. D. Acta. Cryst. 1976, A32, 751-767.
2. Dietzel, A.; Poegel, H. J. Die Naturwissenschaften 1953, 40, 604.
3. Kniep, R.; Mootz, D. Acta. Cryst. 1973, B29, 2292-4.
4. Kniep, R.; Mootz, D.; Vegas, A. Acta. Cryst. 1977, B33, 263-5.
5. Bennett, J. M.; Cohen, J. P.; Flanigen, E. M.; Pluth, J. J.; Smith, J. V. in this symposium.
6. Bennett, J. M.; Cox, D. E. to be published.
7. Flanigen, E. M. "Molecular Sieves, Advances in Chemistry Series. Number 121"; American Chemical Society: Washington, DC, 1973; pp. 119-39.
8. Daniels, R. H.; Kerr, G. T.; Rollman, L. D. J. Amer. Chem. Soc. 1978, 100, 3097-3100.
9. Breck, D. W. "Zeolite Molecular Sieves"; John Wiley and Sons: New York, NY, 1974; p. 636.
10. ibid., p. 622.
11. ibid., p. 155.
12. Brunauer, S.; Deming, L. S.; Deming, W. S.; Teller, E. J. Amer. Chem. Soc. 1940, 62, 1723.
13. Brunauer, S.; Emmett, P. H.; Teller, E. J. Amer. Chem. Soc. 1938, 60, 309.
14. Peri, J. B. Discuss. Faraday Soc. 1971, 52, 55-65.
15. Breck, D. W. op. cit., p. 217.
16. ibid., p. 360.

RECEIVED November 16, 1982

## Crystal Structure of Tetrapropylammonium Hydroxide–Aluminum Phosphate Number 5

J. M. BENNETT, J. P. COHEN, and EDITH M. FLANIGEN

Union Carbide Corporation, Tarrytown Technical Center, Tarrytown, NY 10591

J. J. PLUTH and J. V. SMITH

The University of Chicago, Department of Geophysical Sciences, Chicago, IL 60637

A new family of aluminophosphate molecular sieves with zeolite-like properties has potential as adsorbents, catalysts, and catalyst supports. Number 5 of the family (hexagonal,  $a$  13.726,  $c$  8.484Å, P6cc) contains alternating Al and P atoms on the tetrahedral nodes of hypothetical framework #81. Non-connecting parallel channels spanned by 12-rings in the as-synthesized material contain tetrapropylammonium hydroxide species in a tripod-shaped conformation, which possibly acted as polar templates during crystallization. Removal of the TPA(OH) by calcination yields a one-dimensional channel theoretically capable of polar diffusion. Framework oxygens in the as-synthesized material show strong displacements analogous to those in high-cristobalite and high-tridymite: mean distances respectively uncorrected and corrected for displacement of oxygen from its centroid of electron density are: P-O 1.49 and 1.53Å; Al-O 1.71 and 1.74Å. Uncorrected P-O-Al angles of 148 to 178° become more equal when adjusted for oxygen displacements.

0097-6156/83/0218-0109\$06.00/0

© 1983 American Chemical Society



A new family of crystalline molecular sieves(1, 2) having aluminophosphate frameworks was synthesized. Strict alternation of Al and P on the tetrahedral nodes yields neutral oxygens in contrast to the aluminosilicate zeolites, and non-framework cations are not needed for charge balance. Whereas a microporous silica (silicalite, 3) with neutral oxygens is hydrophobic, the aluminophosphate sieves are moderately hydrophilic.

The precursor to the  $\text{AlPO}_4$  #5 molecular sieve crystallizes at  $150^\circ\text{C}$  from a hydrothermal system containing an aluminophosphate gel and tetrapropylammonium hydroxide. Its ideal chemical composition is  $\text{TPAOH}\cdot 12\text{AlPO}_4$ . Removal of the TPAOH by calcination at  $400\text{--}600^\circ\text{C}$  produces a molecular sieve for which absorption studies are consistent with unconnected pores bounded by 12-rings. The  $\text{AlPO}_4$  #5 sieve is thermally stable to  $1000^\circ\text{C}$  above which it transforms to the  $\text{AlPO}_4$  analog of tridymite.

### Experimental

The first synthetic crystals were very small hexagonal prisms. Electron diffraction patterns showed hexagonal symmetry with  $a \approx 13.7$ ,  $c \approx 8.5\text{\AA}$ . Sections tilted around  $a^*$  indicated a  $c$  glide plane, but the systematic absences around  $a$  were not determined. The X-ray powder pattern (Figure 1a) was completely indexed with the hexagonal cell (Table I). Later results have shown that the cell dimensions of an uncalcined  $\text{AlPO}_4$  #5 sample vary slightly depending on the organic phase used in the synthesis.

A later batch of large crystals range in size from hexagonal barrels to smaller hexagonal prisms. The initial crystal structure analysis on a hexagonal barrel was complicated by much greater broadness of (00 $l$ ) than (hk0) diffractions, as also was observed in X-ray patterns of several powders. Transmission electron micrographs of crushed fragments by G.D. Price of Cambridge University revealed no structural inhomogeneities, and it is concluded that each large barrel consists of a stack of hexagonal plates.

Single-crystal photographs yielded systematic absences consistent with  $P6/mcc$  or  $P6cc$ , and the latter was chosen because of the expected alternation of Al and P over tetrahedral nodes. A data set with  $2^\circ < 2\theta < 140^\circ$   $\text{CuK}\alpha$  was collected for a barrel-shaped crystal on an Enraf Nonius CAD4 diffractometer with a  $3.5^\circ$  variable-speed  $\theta$ - $2\theta$  scan to accommodate the broad diffractions. From 196 unique diffractions above background ( $2\sigma$ ) out of 2170 measured diffractions, the structure was solved independently by the Multan direct method and a search of hypothetical structures. The resulting framework (Figure 2) is #81 predicted by J.V. Smith(4). Refinement to  $R = 16\%$  yielded the framework geometry, but the T-O distances did not correspond satisfactorily to Al, P alternation, and the TPAOH was not located. Nevertheless the framework topology appeared correct, and the calculated powder pattern (Figure 1b) was satisfactory.

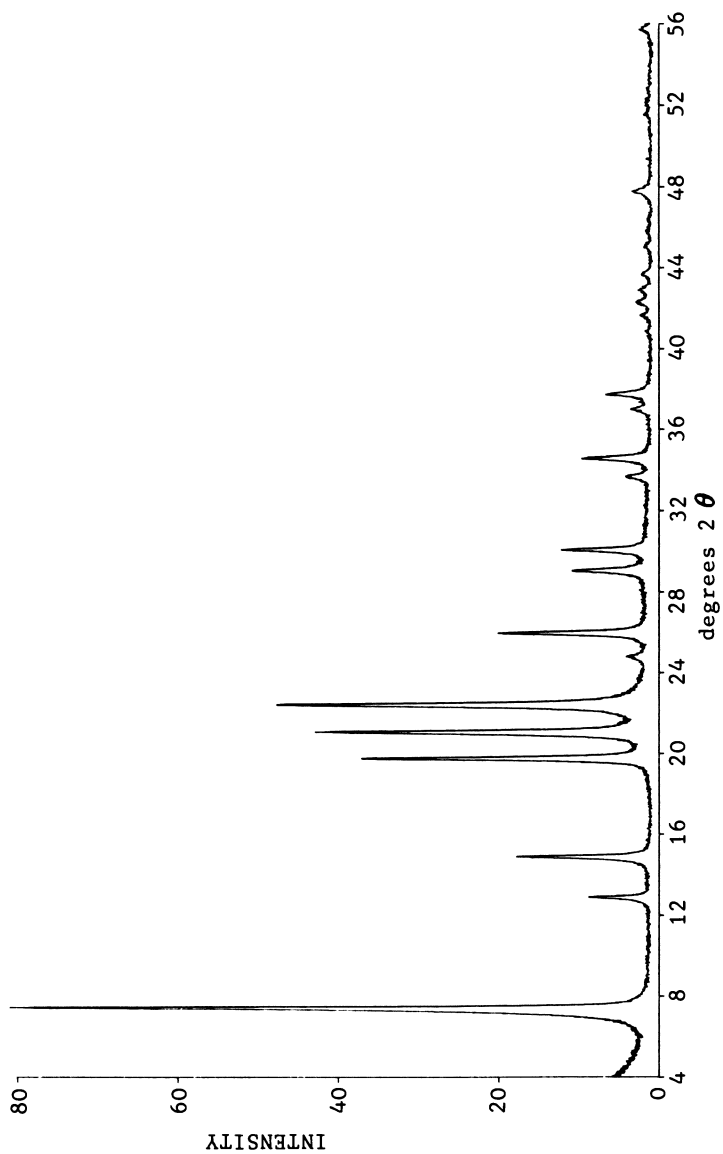


Figure 1a. Observed powder diffractometer patterns

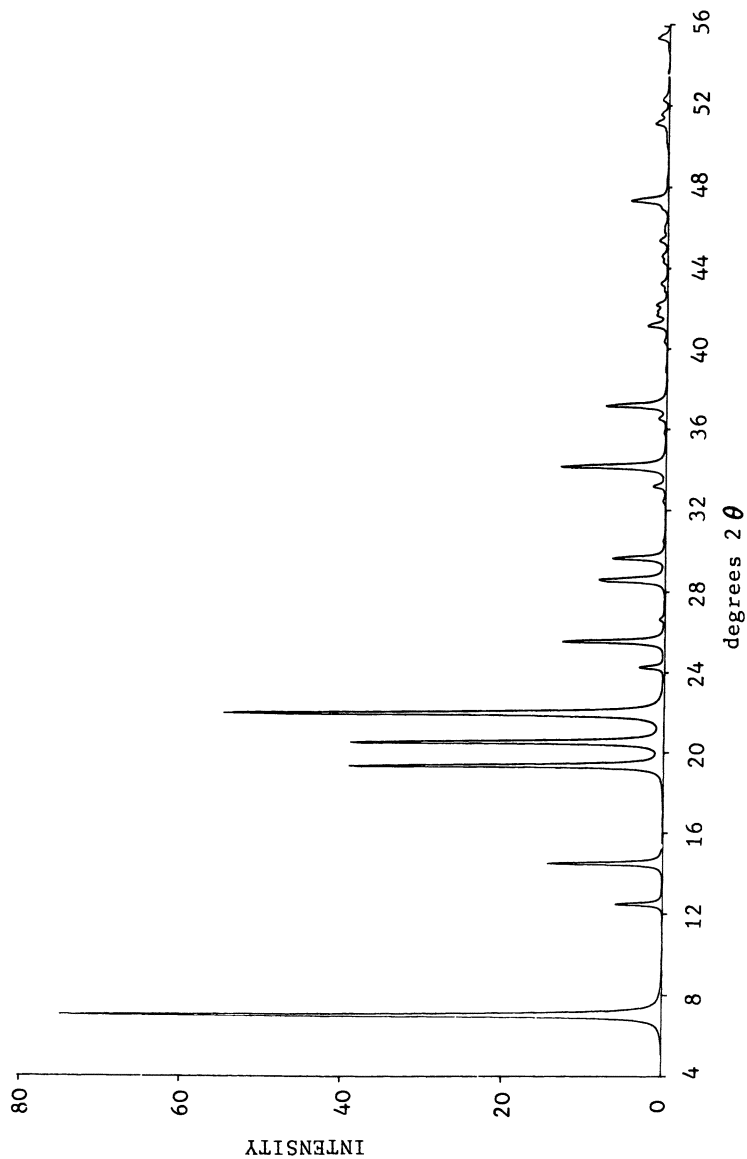


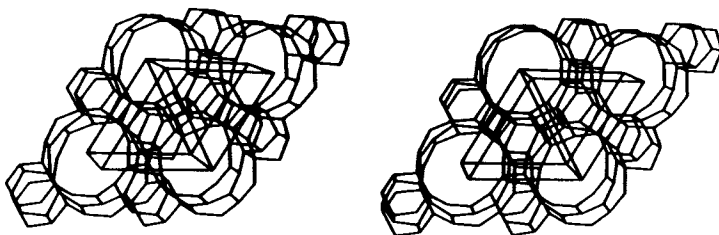
Figure 1b. Calculated powder diffractometer patterns

Table IObserved and Calculated d-spacings for  $\text{AlPO}_4$  #5

| $2\theta$ | $d_{\text{obs}}$ | $d_{\text{cal}}$ | index |
|-----------|------------------|------------------|-------|
| 7.457     | 11.844           | 11.876           | 100   |
| 12.917    | 6.847            | 6.857            | 110   |
| 14.917    | 5.933            | 5.938            | 200   |
| 19.775    | 4.486            | 4.489            | 210   |
| 21.090    | 4.209            | 4.213            | 002   |
|           |                  | 3.971            | 102   |
| 22.434    | 3.959            | 3.962            | 211   |
|           |                  | 3.959            | 300   |
| 24.803    | 3.587            | 3.590            | 112   |
| 25.968    | 3.428            | 3.428            | 220   |
|           |                  | 3.294            | 310   |
|           |                  | 3.072            | 212   |
| 29.053    | 3.071            | 3.068            | 311   |
| 30.071    | 2.969            | 2.969            | 400   |
| 33.655    | 2.660            | 2.659            | 222   |
|           |                  | 2.592            | 321   |
| 34.572    | 2.592            | 2.592            | 410   |
| 37.020    | 2.426            | 2.427            | 402   |
| 37.734    | 2.382            | 2.381            | 213   |
| 47.768    | 1.903            | 1.903            | 512   |

Cell dimensions:  $a = 13.713$   $c = 8.427$   $\gamma = 120^\circ$ 

These data were collected on a Siemens D500 diffractometer, using monochromatic  $\text{CuK}\alpha$  radiation, 6 seconds count time and a  $0.01^\circ$   $2\theta$  step size. The receiving slit was  $0.05^\circ$  and the apertures were  $0.3^\circ$ . The data were processed using programs written at Union Carbide Corporation.

Figure 2.

Stereoplot showing branches linking tetrahedral nodes of framework #81.

After careful search, a small hexagonal prism 30  $\mu\text{m}$  across and 180  $\mu\text{m}$  long with a sharp parallel extinction was found to give sharp diffractions throughout reciprocal space. It was attached to a glass fiber and sprayed with polyurethane to control the humidity. Diffraction intensities were collected with graphite-monochromatized  $\text{CuK}\alpha$  radiation on a Picker diffractometer. Centering of 20 diffractions ( $56^\circ < 2\theta < 65^\circ$ ;  $1.5418\text{\AA}$ ) each the average of the 8 possible settings, gave a 13.7258(12), b 13.7253(13), c 8.4835(5) $\text{\AA}$ ,  $\alpha$  89.997(6),  $\beta$  90.010(6),  $\gamma$  120.004(5) $^\circ$ . Intensities out to  $\sin \theta/\gamma = 0.58$  were measured at fixed  $\theta$ - $2\theta$  scanning ( $2^\circ/\text{min}$ ) for a range of 2.0-2.2 $^\circ$  with background measured for 25 seconds. Weighted averages(5) of 5112 intensities yielded 404 unique diffraction intensities, 393 ( $2\sigma$ ) with  $I \geq 2\sigma(I)$  were used for the structure refinement. All diffraction intensities obeyed the assumed space group P6cc except (13,0,1)  $92 \pm 28$ , (11,0,5)  $89 \pm 26$ , (229)  $78 \pm 28$  and (557)  $69 \pm 27$  ( $1\sigma$ ).

Refinement of the framework coordinates was difficult because of the acentricity and pseudosymmetry. A stable least-squares solution was obtained for the framework atoms in which the T-O distances indicate alternation of Al and P atoms. However, the O atoms showed large displacements from the centroid, particularly O(2) for which a difference-Fourier map indicated three separate peaks (Figure 3). Because there is no optical or X-ray evidence for symmetry lower than hexagonal, it is assumed that there are microdomains with tilted tetrahedra, as proposed for high-cristobalite(6) and high-tridymite(7). For convenience, the displacements of the oxygen atoms are approximated by ellipsoids.

Residual electron density in the channels was not well enough defined to give a precise position for the TPA(OH) complex. The peaks were consistent with a tripod shape (Figure 4) in which the (OH) is suspended between the three feet of one tripod and the head of the next tripod to form a polar array. (Polar is used in the crystallographic sense for an axis whose properties are different depending on the direction of travel along the axis.) To fit the 6-fold symmetry, the tripod is disordered between two orientations. Addition of fixed atomic positions for the TPA(OH) complex reduced the weighted R from 0.14 to 0.06, mainly because of changes in calculated intensities for low-angle intensities. Tables II and III give the atomic coordinates and interatomic distances. A listing of the observed and calculated structure factors is available as supplementary material. Ordering information is given on any current masthead page of J. Am. Chem. Soc.

The alternation of Al and P atoms over the tetrahedral nodes of framework #81 reduces the space group symmetry from P6/mcc to P6cc. All rings in framework #81 are of even number to accommodate the strict alternation of equal numbers of Al and P.

Table II  
Atomic Positions and Displacements of TPAOH-ALPO<sub>4</sub> #5

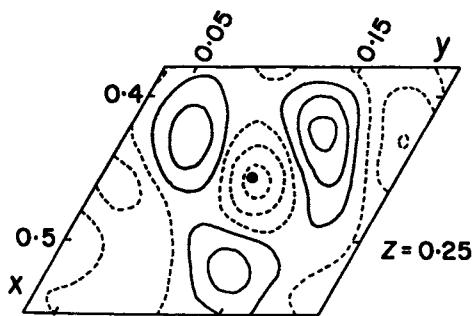
| Atom | Position | Popu-<br>lation | x         | y          | z        | U <sub>11</sub> | U <sub>22</sub> | U <sub>33</sub> | U <sub>12</sub> | U <sub>13</sub> | U <sub>23</sub> |
|------|----------|-----------------|-----------|------------|----------|-----------------|-----------------|-----------------|-----------------|-----------------|-----------------|
| P    | 12(d)    | 12              | 0.4524(3) | 0.3283(2)  | 0.078(3) | 35(2)           | 39(2)           | 44(3)           | 20(2)           | -3(3)           | 1(2)            |
| Al   | 12(d)    | 12              | 0.4577(4) | 0.3377(3)  | 0.450(3) | 43(3)           | 38(3)           | 46(4)           | 22(2)           | -9(3)           | -7(2)           |
| O(1) | 12(d)    | 12              | 0.4210(5) | 0.2137(7)  | 0.028(4) | 53(4)           | 37(5)           | 103(8)          | 24(4)           | 12(10)          | -14(7)          |
| O(2) | 12(d)    | 12              | 0.4555(8) | 0.3312(10) | 0.25*    | 128(9)          | 160(10)         | 30(10)          | 75(9)           | -9(10)          | -2(8)           |
| O(3) | 12(d)    | 12              | 0.3670(7) | 0.3584(8)  | 0.026(4) | 56(6)           | 63(6)           | 105(9)          | 40(4)           | 2(10)           | 20(9)           |
| O(4) | 12(d)    | 12              | 0.5684(7) | 0.4126(8)  | 0.014(4) | 38(5)           | 46(5)           | 123(9)          | 18(4)           | 20(7)           | 10(7)           |
| N    | 2(a)     | 1               | 0         | 0          | 0.350    | 787(83)         |                 |                 |                 |                 |                 |
| C(1) | 2(a)     | 1               | 0         | 0          | 0.106    | 787(83)         |                 |                 |                 |                 |                 |
| C(2) | 12(d)    | 1               | 0.000     | 0.106      | 0.106    | 787(83)         |                 |                 |                 |                 |                 |
| C(3) | 12(d)    | 1               | 0.999     | 0.105      | 0.923    | 787(83)         |                 |                 |                 |                 |                 |
| C(4) | 12(d)    | 3               | 0.122     | 0.079      | 0.409    | 787(83)         |                 |                 |                 |                 |                 |
| C(5) | 12(d)    | 3               | 0.126     | 0.177      | 0.504    | 787(83)         |                 |                 |                 |                 |                 |
| C(6) | 12(d)    | 3               | 0.150     | 0.166      | 0.679    | 787(83)         |                 |                 |                 |                 |                 |
| O    | 2(a)     | 1               | 0         | 0          | 0.620    | 787(83)         |                 |                 |                 |                 |                 |

Estimated standard deviation given in brackets to same significance level as parameter. x, y, z given as decimal fraction of cell edge. Anisotropic displacement factor given as  $10^3 \exp - 2\pi \sum U_{ij} a_i^* a_j^* h_i \cdot h_j$ . #Fixed to define origin.

The x, y, and z for the TPAOH complex were chosen from the structural model and not refined by least squares.

Table IIIInteratomic Distances ( $\text{\AA}$ ) and Angles ( $^\circ$ )

|                          | <u>centroid</u> | <u>riding*</u> |              |            |
|--------------------------|-----------------|----------------|--------------|------------|
| P-0(1)                   | 1.472(16)       | 1.501(16)      | 0(1)-P-0(2)  | 108.1(1.7) |
| 0(2)                     | 1.456(25)       | 1.530(25)      | 0(3)         | 110.9(1.2) |
| 0(3)                     | 1.492(18)       | 1.523(18)      | 0(4)         | 110.1(1.3) |
| 0(4)                     | 1.525(16)       | 1.558(17)      | 0(2)-P-0(3)  | 107.9(1.7) |
| mean                     | 1.486           | 1.528          | 0(4)         | 109.3(1.5) |
|                          |                 |                | 0(3)-P-0(4)  | 110.5(1.3) |
| Al-0(1)                  | 1.729(19)       | 1.751(19)      | 0(1)-Al-0(2) | 109.8(1.4) |
| 0(2)                     | 1.700(26)       | 1.760(26)      | 0(3)         | 104.2(1.2) |
| 0(3)                     | 1.726(21)       | 1.752(21)      | 0(4)         | 108.6(1.2) |
| 0(4)                     | 1.683(16)       | 1.707(16)      | 0(2)-Al-0(3) | 112.8(1.4) |
| mean                     | 1.710           | 1.742          | 0(4)         | 110.3(1.4) |
|                          |                 |                | 0(3)-Al-0(4) | 111.0(1.3) |
| *oxygen riding on T atom |                 |                | P-0(1)-Al    | 150.2(0.7) |
|                          |                 |                | 0(2)         | 178.1(1.2) |
|                          |                 |                | 0(3)         | 148.8(0.7) |
|                          |                 |                | 0(4)         | 151.0(0.9) |

Figure 3.

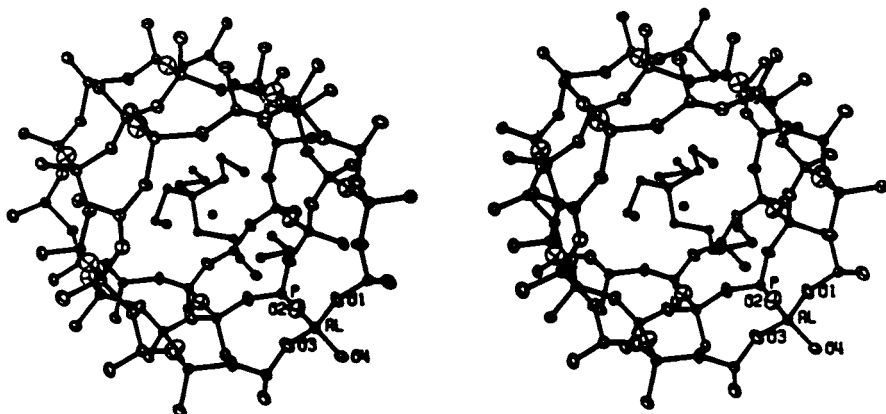
Difference-Fourier section through 0(2) showing perturbation from the ellipsoidal approximation (Figure 4) to the electron density. Contour levels at 0.12e/Å : dashed, negative; continuous, zero-level and positive.

frameworks with odd numbers of tetrahedra in rings are inconsistent with a strictly alternating  $\text{AlPO}_4$  composition. The strict up down alternation of all tetrahedra in the  $\text{AlPO}_4$  #5 structure causes all vertical P-O-Al bands to be aligned in one direction. This vertical alignment may be the cause of the polar nature of the structure.

The 6-fold axis in  $\text{AlPO}_4$  #5 is crystallographically polar. The sequence of tripod-shaped TPA(OH) complexes down each channel is also polar, and the concept of a polar template may be appropriate. Furthermore, the concept of polar diffusion should be explored: at low temperature, polar molecules should adopt a specific orientation during diffusion down a polar channel.

Interpretation of the distances and angles in the framework in TPAOH- $\text{AlPO}_4$  #5 is complicated by the large displacements of the oxygens. Distances between centroids of electron density are low (mean P-O 1.49Å, mean Al-O 1.71Å), but when adjusted by a simple model for riding of the oxygen about the tetrahedral atom, the distances (mean P-O 1.53Å, mean Al-O 1.74Å) are consistent with those in berlinite, the  $\text{AlPO}_4$  analog of quartz (mean P-O 1.516Å, mean Al-O 1.739Å; 8). The wide range of bond angles (148 to 178°) between centroids in TPAOH- $\text{AlPO}_4$  is reduced by the displacements of the oxygens. In particular, a displacement in the (001) plane of 0.4Å for O(2) would reduce the Al-O(2)-P angle from 178° to about 150°. Hence it appears that all the Al-O-P angles are near the 150° for the microdomain model(6), except at the boundary between microdomains. Such a restricted range of angles near 150° is consistent with partial covalency, as deduced for the  $\text{AlPO}_4$  form of quartz from charge-density refinements(9).

The TPAOH complex fits neatly into the channel when folded into the tripod configuration (Figure 4). This configuration is quite different from the tetrahedral shape of the TPAF complex



**Figure 4.**

Stereoplot of channel and TPAOH complex with ellipsoidal approximation to the electron density (20% level).



in the precursor to fluoride-silicalite(10) and the spread-eagle shape found in the crystal structure of tetra-n-propyl ammonium bromide(11). Speculations about template action must take into account these geometrical possibilities consequent upon bond rotation. Further crystal structure work at low temperature will be necessary to determine the detailed geometry of the TPAOH complex in  $AlPO_4$  #5.

### Acknowledgments

J.J. Pluth and J.V. Smith thank NSF for grant CHE 80-23444 and general support to the Materials Research Laboratory (DMR 79-24007).

### Literature Cited

1. Wilson, S.T.; Lok, B.M.; Flanigen, E.M. U.S. Patent 4,310,440, January 1982.
2. Wilson, S.T.; Lok, B.M.; Messina, C.A.; Cannan, T.R.; Flanigen, E.M. J. Am. Chem. Soc. 1982, 104, 1146-1167.
3. Flanigen, E.M.; Bennett, J.M.; Grose, R.W.; Cohen, J.P.; Patton, R.L.; Kirchner, R.M.; Smith, J.V. Nature 1978, 271, 512-516.
4. Smith, J.V. Am. Mineral 1978, 63, 960-969.
5. Pluth, J.J.; Smith, J.V. J. Am. Chem. Soc. 1980, 102, 4704-4708.
6. Wright, A.F.; Leadbetter, A. J. Phil. Mag. 1972, 31, 1391
7. Kihara, K. Z. Krist. 1966, 152, 95-101.
8. Schwarzenbach, D. Z. Krist. 1966, 123, 161-185.
9. Thons, N.; Schwarzenbach, D. Acta Cryst. 1979, A35, 658-664.
10. Price, G.D.; Pluth, J.J.; Smith, J.V.; Bennett, J.M.; Patton, R.L. J. Am. Chem. Soc. in press.
11. Zalkin, A. Acta Cryst. 1957, 10, 557-560.

RECEIVED November 4, 1982

## x-Ray Structural Refinements of Zeolite A and Silicalite

J. J. PLUTH and J. V. SMITH

The University of Chicago, Department of Geophysical Sciences,  
Chicago, IL 60637

Dehydrated Sr- and Ca-A have mean tetrahedral-oxygen distances near 1.60 and 1.73Å consistent with earlier evidence from dehydrated Na- and K-A for alternation of Si and  $\sim\text{Al}_{0.9}\text{Si}_{0.1}$ , and in complete disagreement with the 3:1 ordering model. All Sr and Ca atoms lie near the centers of 6-rings in disagreement with earlier determinations of unanalyzed crystals in which one atom was placed in an 8-ring: perhaps this latter position corresponds to K scavenged during ion exchange. Approximately 4/5ths of the Sr and Ca project into the large cage, and 1/5th into the sodalite unit. The latter position is puzzling from a simple electrostatic model, and the effect of local charge unbalance from the  $\text{Al}_{0.9}\text{Si}_{0.1}$  substitution and cation vacancies is being investigated. Electron density at the center of the sodalite unit and at  $\sim 1.7\text{\AA}$  along the triad axes is attributed to Al in a tetrahedron of oxygen species, disordered into two orientations. Such electron density is found in most varieties exchanged with divalent cations, but not with monovalent ones. Ion exchange with Rb gave complex results, and there was no evidence for zero coordination. A tetrapropylammonium fluoride complex was located at the channel intersections of a precursor to fluoride-silicalite. Each propyl group points down a channel towards another propyl group and there is insufficient room for a butyl group unless every other channel intersection is unoccupied. The position of the TPAF group is consistent with a template model of crystallization.

0097-6156/83/0218-0119\$06.00/0  
© 1983 American Chemical Society

This review summarizes some highlights of recent X-ray structural analyses of varieties of zeolite A and of fluoride-silicalite.

### Zeolite-A

Because of the chemical implausibility of some speculations about zeolite A, high-precision X-ray analyses were made of dehydrated crystals whose chemical composition was checked by electron microprobe analysis. Data were collected for the 24 Å superstructure. All diffractions are consistent with space group  $Fm\bar{3}c$  except for a few weak ones. Unpublished measurements by J.J. Pluth and G.D. Price of a hydrated Na-A (i.e. as-synthesized) showed strict obedience of  $Fm\bar{3}c$  except for a very weak (111) diffraction, and the inconsistent diffractions of the dehydrated crystals are attributed tentatively to minor positional disorder of extra-framework cations (1).

Framework The framework positions for the following dehydrated varieties of zeolite A are consistent within the experimental errors with alternation of Si and  $\sim Al_{0.9}Si_{0.1}$  over the tetrahedral nodes for the particular batch of crystals used for structure analysis: K- (2), Na- (3), Sr- (4), Ca- (5), Rb- (6), and AgH- (7). This confirms the original determination of Si/Al alternation for hydrated Na-A (8), and refutes the interpretation (9-12) of magic-angle-spinning-nuclear-magnetic-resonance data in terms of a 3:1 ordering scheme. The 4:0 alternation model has been reaffirmed by powder diffraction techniques (e.g. 13, 14; see detailed references in other papers of this symposium), and it is quite certain that the  $^{29}Si$  chemical shift of MASNMR depends on both the geometrical properties of an aluminosilicate framework and the types of extra-framework species as well as on the nearest tetrahedral neighbors (e.g. 15). Although the crystal structure of dehydrated Na-A was refined satisfactorily with cubic geometry, diffraction measurements at 4.5K and 296K have demonstrated rhombohedral geometry (11). An inversion to the cubic structure was found at 335K (16), and the effect of the degree of dehydration on the inversion temperature should be investigated. Single-crystal measurements at low temperature are in progress to determine the structural changes from cubic symmetry.

Cation positions New refinements of dKA (2), dNaA (3) and dRb-exchanged A (6) have shown that all the exchangeable cations are within bonding distance of framework oxygens thus invalidating the concept of zero coordination (17). The prefix d means dehydrated. Complete exchange of Na by Rb was not obtained even after considerable experimentation, and scavenging of Ba was demonstrated by electron microprobe analysis. Crystals became amorphous before complete Rb exchange was obtained, even for basic conditions.

Interest now is focused on the distribution of the cations among the various possible sites, and a complex model will be needed. For an ideal framework  $Al_{12}Si_{12}O_{24}$  with 8 six-ring, 3 eight-ring and various wall sites, a simple electrostatic model would lead to the following predictions: (a) six small divalent cations (e.g. Ca, Sr) should be associated only with the six-rings, and project into the large cage rather than the sodalite unit in order to minimize cation repulsion, (b) twelve monovalent cations should occupy all eleven of the six-rings and eight-rings while the remaining cation would be forced into a one-sided coordination opposite a four-ring. Interpretation of the experimental data is complicated by the electron microprobe and X-ray diffraction evidence for a framework composition near  $Al_{11.5}Si_{12.5}O_{48}$ .

New X-ray structure refinements for dSrA (4) and dCaA (5) show that the 5.7 Sr and 5.6 Ca atoms are associated only with the six-rings. Earlier X-ray evidence that one atom lies in an eight-ring (18, 19) is believed to result from scavenging of K from impure solution, and the original crystals should be checked by electron microprobe analysis. Although the Sr and Ca atoms are associated only with the six-rings, about one-fifth of them (1.2 Sr, 1.2 Ca) project into the sodalite unit rather than the supercage. Calculations are in progress in association with R. Catlow to test whether the observed cation distribution is related to (a) perturbations of electric charge balance associated with substitution of Si for Al in the  $Al_{0.9}Si_{0.1}$  site, or (b) inter-cation interactions resulting from occupancy of only ~6 out of the 8 six-ring sites, or both (a) and (b).

The monovalent cations Na and K (Table I) occupy almost all of the six- and eight-ring sites, and about two-thirds of an atom lies opposite a four-ring. However the details are unexplained. For dKA, 0.15 and 0.5 K atoms respectively project from four-rings into the sodalite unit (4S) and the supercage (4L) whereas 0.8 Na project only into the supercage. The Na atom is small enough to lie near the center of a six-ring, but the K atom is considerably displaced with 1.5 atoms pointing into the sodalite unit (6S) and 6.3 atoms into the supercage (6L); the total of 7.8 K corresponds exactly with 7.8 Na in the six-rings and is less than the theoretical limit of 8.

Interpretation of the distribution of Ag atoms (Table I: 21-26) is ambiguous from the crystallographic viewpoint (26) and it is not profitable to pursue here the controversy whether the Ag atoms form charge-exchange clusters or a piece of metal.

The  $NH_4$  cation also shows a complex distribution (27), and there can be no doubt that it will be difficult to produce a convincing explanation of the details. One factor will be steric hindrance between the 4S and 6S positions, and between the 4L and the 6L positions.

Table I Comparison of Site Occupancies and Coordinates

| Specimen   | Number of atoms in sites |     |                                  |                                     |        |
|--|--------------------------|-----|----------------------------------|-------------------------------------|--------|
|  | 4S                       | 4L  | 6S                               | 6L                                  | 8      |
| dK-A <sup>3</sup>                                  | 0.15<br>(x 0.176)        | 0.5 | 1.5<br>(x 0.162)                 | 6.3<br>(x 0.230)                    | 3.0    |
| dNa-A <sup>2</sup>                                 |                          | 0.8 |                                  | 7.8<br>(x 0.199 $\beta_{12}$ 21)    | 2.8    |
| dAg-A (oxidized) <sup>21</sup>                     | 0.5<br>(x 0.173)         |     |                                  | +8.0+<br>(x 0.194 $\beta_{12}$ 91)  | 3.0    |
| dAg-A (375°C) <sup>22</sup>                        | 1.8<br>(x 0.178)         |     | 3.5<br>(x 0.172)                 | 3.4<br>(x 0.207)                    | 2.1    |
| dAg-A (430°C) <sup>22</sup>                        | 1.1<br>(x 0.19)          |     | 2.6<br>(x 0.173)                 | 4.7<br>(x 0.201)                    | 1.8    |
| dAg-A (400°C) <sup>23,24</sup>                     | 2.1<br>(x 0.171)         |     |                                  | +7.3+<br>(x 0.191 $\beta_{12}$ 136) | 1.6    |
| dAg-A (425°C) <sup>23,24</sup>                     | 3.6<br>(x 0.168)         |     |                                  | +8.0+<br>(x 0.191 $\beta_{12}$ 148) | 0.9    |
| dAg-A (450°C) <sup>24</sup>                        | 3.5<br>(x 0.168)         |     |                                  | +7.8+<br>(x 0.189 $\beta_{12}$ 130) |        |
| C <sub>2</sub> H <sub>2</sub> ·dAg-A <sup>25</sup> | 2.6<br>(x 0.165)         |     | 2.6*<br>(x 0.188)                | 4.0<br>(x 0.240)                    | 1.7    |
| dHAg-A <sup>26</sup>                               | 0.7<br>(x 0.170)         |     | 1.1<br>(x 0.169)                 | 5.5<br>(x 0.192)                    | 0.9    |
| dNH <sub>4</sub> -A <sup>27</sup>                  |                          | 0.5 | 3.2<br>(x 0.106)                 | 5.4<br>(x 0.258)                    | 2.7    |
| dAgTl-A <sup>28</sup>                              | 0.6 Ag<br>(x 0.151)      |     | 3.8 Ag <sup>+</sup><br>(x 0.188) | 2.4 Tl<br>(x 0.260)                 | 3.0 Tl |

Based on pseudocell. 4 opposite four-ring; 6 near center of six-ring; 8 near center of eight-ring; S displaced into sodalite unit; L displaced into large cage. \*also 0.6 Ag(1) at .134, .134, .134. †also 2.0 Ag(2) at .129, .129, .129. Atomic coordinates and displacement factors ( $\times 10^4$ ) given for some positions.

Aluminum-oxygen complex An electron density peak has been observed at the center of the sodalite unit in dehydrated varieties exchanged with divalent cations (4, 5, 29-36) but not with monovalent ones. Another electron density peak was observed near  $\pm 0.08$ ,  $\pm 0.08$ ,  $\pm 0.08$  on the eight triad axes approximately 1.7Å away from the origin peak for dSrA and dCaA (4, 5). The peaks for two separate crystals of dSrA (Figure 1) are fairly well defined, and can be explained by angular disorder of two  $TO_4$  tetrahedra related by inversion through a center of symmetry (Figure 2). The non-circularity of the peaks for  $O^*$  in Figure 2 may result from some angular misorientation caused by interaction with framework oxygens and strontium atoms. Because there is considerable evidence (37) for removal of Al from zeolite frameworks by various processes it is assumed that the peaks correspond to  $AlO_4$  rather than  $SiO_4$ . The X-ray data could not distinguish between an  $AlO_4$  and an  $Al(OH)_4$  complex. Because the aluminum-oxygen complex is not found in the as-synthesized NaA zeolite, the n.m.r. evidence (38) for occluded aluminum compounds does not apply to the species found here for dehydrated varieties exchanged with divalent cations. Although an octahedral complex can apparently be ruled out because the electron density peaks for its O species should lie along cubic [100] rather than tetrahedral [111] directions, an  $^{27}Al$  n.m.r. study should be made: perhaps some of the angular deviation in Figure 2 might result from an octahedral complex in a disordered arrangement.

#### Tetrapropylammonium fluoride silicalite

The silicalite polymorph of  $SiO_2$  (39) and the ZSM5 molecular sieve (40) have the same type of four-connected framework characterized by ten-ring channels which have four-fold intersections of the straight and zigzag channels (Figure 3). Refinement of X-ray data for a twinned crystal of the TPAF-containing precursor to fluoride-silicalite (41, 42) revealed electron density (Figure 4) consistent with one TPAF complex at each channel intersection (Figure 5). Each propyl group fits neatly down a channel, and the end carbon atom lies at 2.7Å (C9 to C9) or 3.1Å (C3 to C6) from the end carbon atom of a propyl group of the next TPAF complex. It was not possible to replace each propyl group by a butyl group even with considerable twisting of the complex when account was taken of van der Waals bonding to framework oxygens. There would be sufficient room, of course, for occupation of every other channel intersection by a TBAF complex.

The crystallization of silicalite species containing tetrapropylammonium complexes is consistent with a template mechanism of crystallization (39). Nevertheless, caution is needed in proposing a specific template role for TPA because the zeolite LZ-105 (42) with apparently the same framework topology as silicalite can be synthesized in the absence of any organic

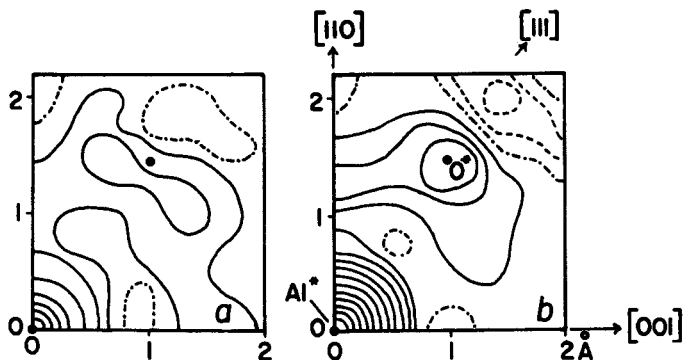


Figure 1. Electron density in (110) plane passing through the origin for two crystals of dSrA. Zero and negative contours, dot-dash and dash respectively. Contours at  $0.2e/\text{Å}^3$ , except for origin peak with  $0.4e/\text{Å}^3$ .

(Reproduced from Ref. 4. Copyright 1982, American Chemical Society.)

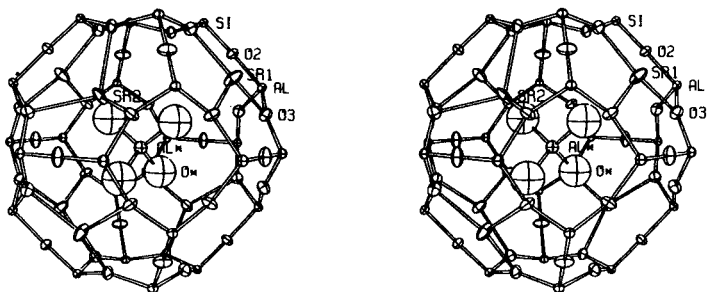


Figure 2. Stereoplot of sodalite unit and one of the  $\text{AlO}_4^*$  tetrahedral units in dSrA. Invert through the center to obtain the second orientation. Ellipsoids at 30% probability level.

(Reproduced from Ref. 4. Copyright 1982, American Chemical Society.)

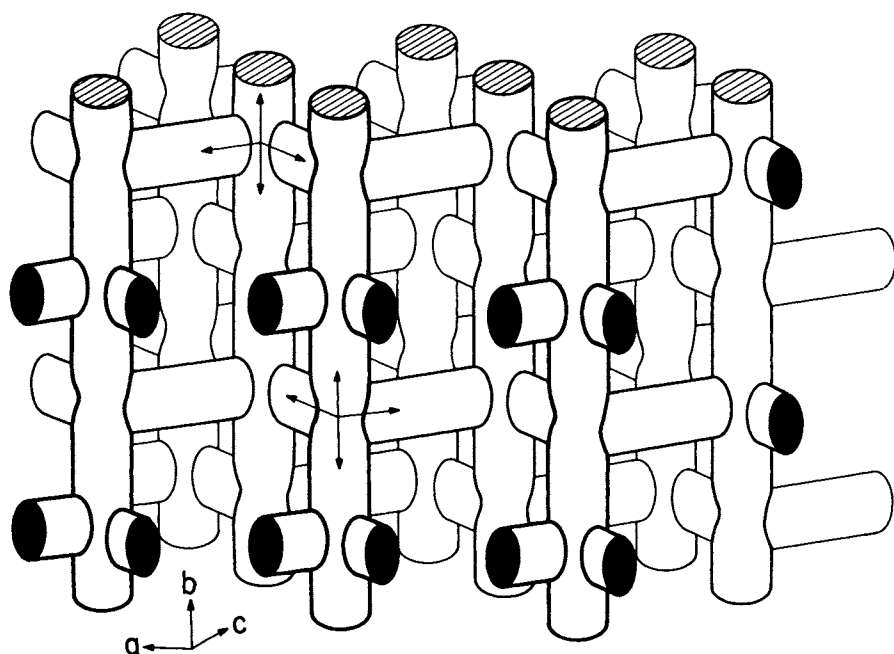


Figure 3. Channel system of silicalite with arrows showing two of the intersections



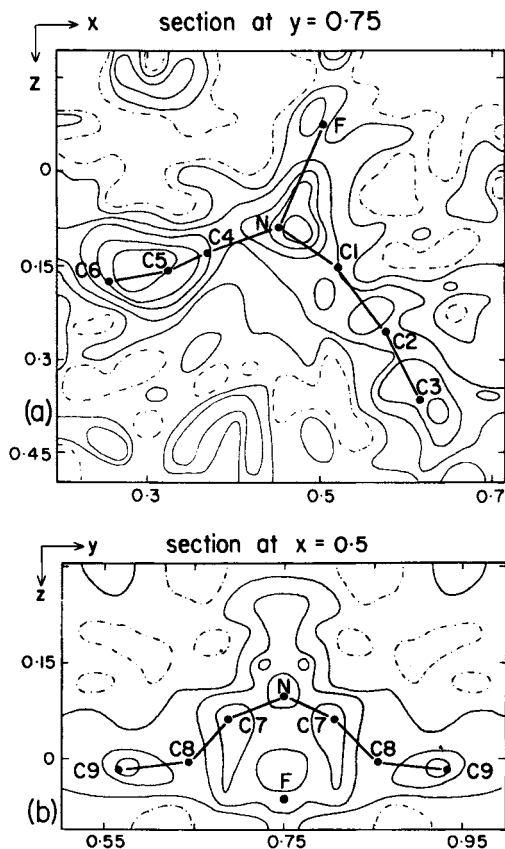


Figure 4. Difference-Fourier maps of electron density associated with non-framework atoms in the precursor to fluoride-silicalite: (a) section in mirror plane at  $y$  0.75; (b) section normal to mirror plane. The projections of the refined positions of the atoms in the TPAF complex are  $\sigma_{-3}$  projected onto the sections. Contours spaced at  $0.2e/\text{\AA}^3$ . Zero contour is dot-dashed. (Reproduced from Ref. 4. Copyright 1982, American Chemical Society.)

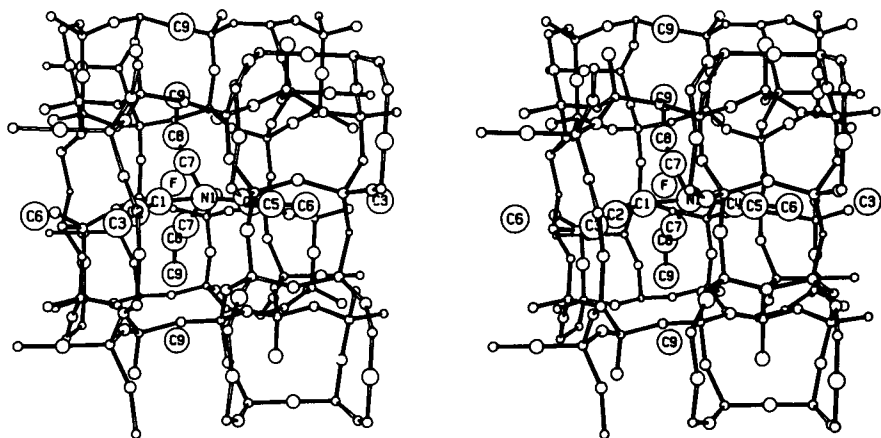


Figure 5. Stereoview of the refined positions of one TPAF complex and its relation to the surrounding portion of the silica framework and end C atoms of adjacent complexes. The N atom lies near the origin of the four arrows at the upper left of Figure 4, and the C8 and C9 atoms lie nearly in the center of a straight channel parallel to *b*. The C1-C6 atoms lie in a mirror plane and the C1-C3 and C4-C6 limbs point along adjacent zig and zag portions of a zigzag channel. (Reproduced from Ref. 4. Copyright 1982, American Chemical Society.)

template or seed material. The role of butyl complexes in the synthesis of ZSM-11 is speculative (42) until further data are published on the allowable range of crystallization conditions, and until a detailed crystal structure analysis is presented to augment the structural model (43) obtained from X-ray powder data. Finally, it should be emphasized that the tetrapropylammonium complex in the precursor to  $\text{AlPO}_4\text{-5}$  (J.M. Bennett et al., this symposium) has a tripod shape quite different from the near-tetrahedral shape in the precursor to fluoride silicalite. Hence any model for a template mechanism must take into account the change of shape consequent upon bond rotation.

**Acknowledgments** We thank T. Araki, J.M. Bennett, A.K. Cheetham, E. Flanigen, R.L. Patton, I.M. Steele and J.M. Thomas for their collaboration and support, and NSF for grant CHE 80-23444 and general support to the Materials Research Laboratory (DMR 79-24007). This paper is dedicated to the late Donald W. Breck whose pioneering work on zeolite A (44, 45) has stood the test of time. A grant from Union Carbide Corporation in his memory is gratefully acknowledged.

#### Literature Cited

1. Pluth, J.J.; Smith, J.V. Nature 1981, 291, 265.
2. Pluth, J.J.; Smith, J.V. J. Phys. Chem 1979, 83, 741-749.
3. Pluth, J.J.; Smith, J.V. J. Am. Chem. Soc. 1980, 102, 4704-4708.
4. Pluth, J.J.; Smith, J.V. J. Am. Chem. Soc. 1982, in press.
5. Pluth, J.J.; Smith, J.V. J. Am. Chem. Soc. 1982, in press.
6. Pluth, J.J.; Smith, J.V. J. Am. Chem. Soc. 1982, submitted.
7. Gellens, L.R.; Smith, J.V.; Pluth, J.J. J. Am. Chem. Soc. 1982, in press.
8. Gramlich, V.; Meier, W.M. Z. Kristallogr. 1971, 133, 134-149.
9. Lippmaa, E.; Magi, M.; Samoson, A.; Engelhardt, G.; Grimmer, A.-R. J. Am. Chem. Soc. 1980, 102, 4889-4893.
10. Lippmaa, E.; Magi, M.; Samoson, A.; Tarmak, M.; Engelhardt, G. J. Am. Chem. Soc. 1981, 103, 4992-4996.
11. Bursill, L.A.; Lodge, E.A.; Thomas, J.M.; Cheetham, A.K. J. Phys. Chem. 1981, 85, 2409-2421.
12. Klinowski, J.; Thomas, J.M.; Fyfe, C.A.; Hartman, J.S. J. Phys. Chem. 1981, 85, 2590-2594.
13. Melchior, M.T.; Vaughan, D.E.W.; Jarman, R.H.; Jacobson, A.J. Nature 1982, 298, 455-456.
14. Cheeham, A.K.; Eddy, M.M.; Jefferson, D.A.; Thomas, J.M. Nature 1982, 299, 24-26.
15. Cheetham, A.K.; Fyfe, C.A.; Smith, J.V.; Thomas, J.M. J. Chem. Soc. Chem. Comm. 1982, 823-825
16. Cox, D.E.; Blackwell, C.S.; Bennett, J.M., this symposium.
17. Firor, R.L.; Seff, K. J. Am. Chem. Soc. 1976, 98, 5031-5033.

18. Firor, R.L.; Seff, K. J. Am. Chem. Soc. 1978, 100, 3091-3096.
19. Firor, R.L.; Seff, K. J. Am. Chem. Soc. 1978, 100, 978-980.
20. Ogawa, K.; Nitta, M.; Aomura, K. J. Phys. Chem. 1979, 83, 1235-1236.
21. Kim, Y.; Seff, K. J. Phys. Chem. 1978, 82, 921-924.
22. Gellens, L.R.; Mortier, W.J.; Schoonheydt, R.A.; Uytterhoeven, J.B. J. Phys. Chem. 1981, 85, 2783-2788.
23. Kim, Y.; Seff, K. J. Am. Chem. Soc. 1977, 99, 7055-7057.
24. Kim, Y.; Seff, K. J. Am. Chem. Soc. 1978, 100, 6989-6997.
25. Kim, Y.; Seff, K. J. Am. Chem. Soc. 1978, 100, 175-180.
26. Gellens, L.R.; Smith, J.V.; Pluth, J.J. J. Amer. Chem. Soc. 1982, in press.
27. McCusker, L.; Seff, K. J. Am. Chem. Soc. 1981, 103, 3441-3446.
28. Kim, Y.; Seff, K. J. Phys. Chem. 1978, 82, 1307-1311.
29. Yanagida, R.Y.; Vance, T.B.; Seff, K. Inorg. Chem. 1974, 13, 723-727.
30. Riley, P.E.; Seff, K. Inorg. Chem. 1974, 13, 1355-1360
31. Riley, P.E.; Kunz, K.B.; Seff, K. J. Am. Chem. Soc. 1975, 97, 537-542.
32. Riley, P.E.; Seff, K. Inorg. Chem. 1975, 14, 714-721.
33. Raghavan, N.V.; Seff, K. J. Phys. Chem. 1976, 80, 2133-2137
34. McCusker, L.B.; Seff, K. J. Am. Chem. Soc. 1979, 101, 5235-5237
35. McCusker, L.B.; Seff, K. J. Phys. Chem. 1980, 84, 2827-2831
36. McCusker, L.B.; Seff, K. J. Phys. Chem. 1981, 85, 405-410.
37. McDaniel, C.V.; Maher, P.K. in J.A. Rabo, "Zeolite Chemistry and Catalysis," Am. Chem. Soc. Monog. 1976, 171, 285-331.
38. Basler, W.D.; Miawald, W. J. Phys. Chem. 1979, 83, 2148-2151.
39. Flanigen, E.M.; Bennett, J.M.; Grose, R.W.; Cohen, J.P.; Patton, R.L.; Kirchner, R.L.; Smith, J.V. Nature 1978, 271, 512-516.
40. Olson, D.H.; Kokotailo, G.T.; Lawson, S.L.; Meier, W.M. J. Phys. Chem. 1981, 85, 2238-2243.
41. Price, G.D.; Pluth, J.J.; Smith, J.V.; Araki, T.; Bennett, J.M. Nature 1981, 292, 818-819.
42. Price, G.D.; Pluth, J.J.; Smith, J.V.; Bennett, J.M.; Patton, R.L. J. Am. Chem. Soc. 1982, in press.
43. Kokotailo, G.T.; Chu, P.; Lawton, S.L.; Meier, W.M. Nature 1978, 275, 119-120.
44. Breck, D.W.; Eversole, W.G.; Milton, R.M.; Reed, T.B.; Thomas, T.L. J. Am. Chem. Soc. 1956, 78, 5963-5971.
45. Reed, T.B.; Breck, D.W. J. Am. Chem. Soc. 1956, 78, 5972-5977.

RECEIVED November 4, 1982

## Neutron Diffraction Studies of Zeolite-A and Synthetic Faujasite

A. K. CHEETHAM and M. M. EDDY

University of Oxford, Chemical Crystallography Laboratory, 9, Parks Road,  
Oxford OX1 3PD, England

A range of synthetic zeolites has been studied by high resolution, powder neutron diffraction at the high flux beam reactor, ILL Grenoble. Thallium and silver derivatives of zeolite-A are cubic,  $Fm\bar{3}c$ , and exhibit alternation of Si and Al. The sodium derivatives, however, are rhombohedral, space group  $R\bar{3}c$ . Measurements on sodium ZK-4, with Si/Al = 1.65, indicate that long range ordering of Si and Al is absent at this composition. Similarly, sodium zeolite-Y, with Si/Al = 2.61, also shows no apparent ordering of Si and Al, and has been refined in  $Fd\bar{3}m$ .

The resurgence of interest in the field of zeolite chemistry, which has been stimulated by the appreciation of their enormous potential as catalysts, has led to the application of several sophisticated physical methods in the study of their structural properties. Important advances have already been made using high resolution, solid state NMR (1,2) and electron microscopy (3), and in this paper we discuss the scope and limitations of neutron diffraction studies with powder samples, with some specific applications to zeolite-A and synthetic faujasite.

While it is indisputable that single-crystal X-ray techniques will continue to provide the bulk of the definitive structural information on zeolites, neutron diffraction does have an important role to play. First, neutrons are intrinsically more sensitive than X-rays to silicon, aluminium ordering since the neutron scattering lengths of Si and Al are significantly different;  $b_{Si} = 0.42$ ,  $b_{Al} = 0.35$  ( $\times 10^{-14}$  m) (4). Second, and perhaps more important, the use of neutrons opens up the possibility of refining complex structures using powder data in combination with the Rietveld profile analysis technique (5). This procedure has already been used to study a wide range of other inorganic systems including complex, low symmetry materials with

0097-6156/83/0218-0131\$06.00/0

© 1983 American Chemical Society

up to 100 variable parameters (6). The possibility therefore arises of determining the structure of zeolites that cannot be obtained in single-crystal form suitable for X-ray work.

There are, of course, difficulties associated with the use of neutrons in this area; in particular, the high level of incoherent (background) scattering that can arise from occluded water molecules in the zeolite cages. For this reason, our work so far has focused on dehydrated samples. Since this leaves approximately 50 percent of the unit cell volume unoccupied, the scattering is rather weak, a factor that is aggravated by the small neutron scattering lengths of Si, Al, and O; counting times are therefore long. Nevertheless, the results presented below will demonstrate that significant progress has been made and some interesting discoveries have emerged from neutron work in this area.

### Experimental

All the neutron data were collected on the high-resolution powder diffractometer, D1A, at the Laue-Langevin Institute, Grenoble. A neutron wavelength of approximately 2.9 Å was used for all measurements and a typical scan was obtained in 12 hours. Data from the bank of ten counters were collated using the programs of Hewat (7) and refined using the POWDER system (8) on the S.E.R.C.'s Interactive Computing Facility. The samples were kindly provided by Prof. J. M. Thomas (Cambridge).

### Results

Thallium and Silver Zeolite-A The zeolite-A structure is constructed from simple aluminosilicate cubeoctahedra, connected to form a three-dimensional, cubic network by so-called 'double-4' rings (Figure 1). This arrangement leads to the formation of large  $\alpha$ -cages whose internal diameter is approximately 11 Å. The chemical composition of the sodium derivative in its hydrated form is approximately  $\text{Na}_{12}\text{Si}_{12}\text{Al}_{12}\text{O}_{48}\cdot 27\text{H}_2\text{O}$ , and the Si/Al ratio typically falls in the range 1.0 - 1.1.

Single-crystal X-ray results (9) point to strict alternation of Si and Al (the 4:0 ordering scheme) in accordance with Loewenstein's rules (10), but this model was recently challenged on the basis of  $^{29}\text{Si}$  NMR measurements (1,2) and our discovery that the sodium derivative can be rhombohedral (11,12). However, the controversy has now been resolved and the correctness of the X-ray model reaffirmed (13,14). A consequence of the Si, Al ordering is that the lattice parameter of the cubic cell is ca. 24.6 Å, not 12.3 Å as reported in earlier work, a feature reflected in weak superlattice reflections. The space group is  $\text{Fm}\bar{3}\text{c}$ .

Our neutron study of the thallium and silver derivatives was stimulated by two factors. First, Tl and Ag are excellent neutron

scatterers ( $b_{Tl} = 0.89$ ,  $b_{Ag} = 0.60$ ), thereby affording accurate determinations of the cation positions. Second, they represent our attempts to obtain results, using powder techniques, approaching the precision obtained with single-crystal X-ray methods.

The thallium-A sample was prepared by ion exchange (15) from a rhombohedral, sodium sample with Si/Al = 1.10. The neutron data show no hint of a rhombohedral distortion, and the structure refines to a final R-factor (based upon profile intensities) of 11.3 percent using the model of Pluth and Smith (9):

$$R_{pr} = \frac{\sum |y_i(\text{obs}) - \frac{1}{c} y_i(\text{calc})|}{\sum |y_i(\text{obs})|}$$

where  $y_i(\text{obs})$  and  $y_i(\text{calc})$  are the observed and calculated intensities, respectively, at the  $i$ th point on the profile, and  $c$  is a scale factor. The atomic coordinates and occupancy factors are given in Table 1, and the observed and calculated profiles are shown in Figure 2. The bimodal distribution of bond lengths in the  $SiO_4$  and  $AlO_4$  tetrahedra confirms that Si and Al are strictly alternating and are in good agreement with the single-crystal X-ray results (Table 2). It is worth noting that we are comparing our results with a very precise X-ray determination and that, even quite recently, single-crystal studies in which Si, Al ordering was undetected have been reported (for example, reference 16).

The thallium atoms, Tl(1) and Tl(3), are found in trigonal positions on each side of the 6-ring (Figure 3), with the site projecting into the large  $\alpha$ -cage having the larger occupancy. The distances to the three O(3) atoms are 2.715 Å and 2.923 Å for Tl(1) and Tl(3), respectively. Tl(2) is located in the 8-ring window at 2.982 Å and 2.694 Å from O(1) and O(2), respectively (Figure 4). Difference Fourier calculations clearly reveal a fourth cation site, close to the center of the 6-ring at 2.256 Å from O(3) (Figure 3). This position is very close to that of the cation site with the highest occupancy in sodium zeolite-A and must correspond to some unexchanged sodium, a conclusion affirmed by analytical electron microscopy measurements. When the scattering length of Na (0.35) is substituted for that of Tl at this site, the total cation occupancy for the structure increases from 0.72(3) to 0.91(3); the expected value based upon the Si/Al ratio is 0.95(2). The sum of the occupancies of the sites in the 6-ring also increases to 0.69(3), compared with the theoretical maximum of 0.67. In detailed studies of ion-exchange at 25°C, 64 percent conversion of the sodium to the thallium form was achieved; our results correspond to 66 percent conversion. The zero-coordinated Tl site reported by Firor and Seff (16) was not found in the present work.

The above results augur well for the efficacy of neutron diffraction as a tool for studying zeolites. The sensitivity to

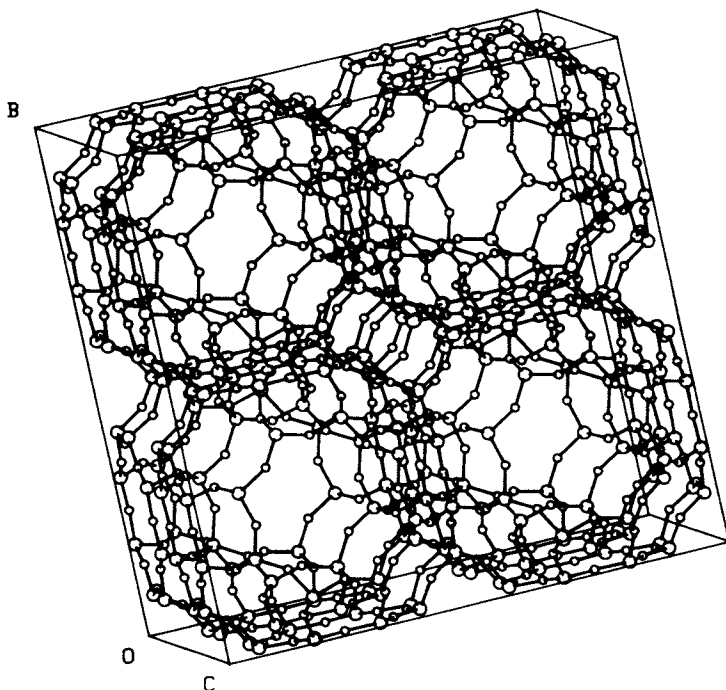


Figure 1.  
The cubic ( $a \sim 12.3 \text{ \AA}$ ) sub-cell of zeolite-A; Si(Al) and oxygen atoms are shown as large and small spheres, respectively.

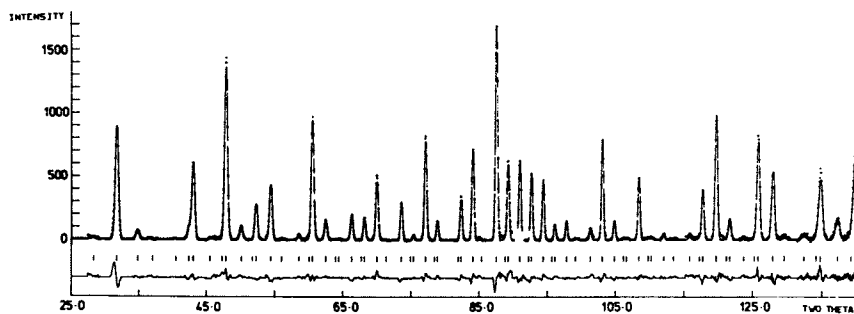


Figure 2.  
The observed (dots), calculated (solid curve), and difference profiles for Tl zeolite-A in  $Fm\bar{3}c$ ; reflection positions are also indicated.



TABLE I  
FINAL ATOMIC COORDINATES FOR  
T1 ZEOLITE-A IN SPACE GROUP Fm3c

| Atom  | Position | x         | y         | z         | Occupancy | B(Å <sup>2</sup> ) |
|-------|----------|-----------|-----------|-----------|-----------|--------------------|
| Si(1) | 96(1)    | 0.0       | 0.0906(5) | 0.1826(5) | 1.0       | 0.11(11)           |
| Al(1) | 96(1)    | 0.0       | 0.1852(5) | 0.0884(6) | 1.0       | 0.11(11)           |
| O(1)  | 96(1)    | 0.0       | 0.1069(2) | 0.2468(4) | 1.0       | 0.68(7)            |
| O(2)  | 96(1)    | 0.0       | 0.1486(3) | 0.1503(3) | 1.0       | 0.68(7)            |
| O(3)  | 192(j)   | 0.0532(2) | 0.0589(2) | 0.1676(1) | 2.0       | 0.68(7)            |
| T1(1) | 64(g)    | 0.1301(3) | 0.1301(3) | 0.1301(3) | 0.330(10) | 3.10(45)           |
| T1(2) | 96(1)    | 0.0       | 0.2273(3) | 0.2273(3) | 0.222(5)  | 3.10(45)           |
| T1(3) | 64(g)    | 0.0485(9) | 0.0485(9) | 0.0485(9) | 0.053(4)  | 3.10(45)           |
| Na(1) | 64(g)    | 0.1025(9) | 0.1025(9) | 0.1025(9) | 0.307(26) | 5.33(153)          |

TABLE 2  
SILICON-OXYGEN AND ALUMINIUM-OXYGEN BOND  
LENGTHS (Å) IN ZEOLITE-A, SPACE GROUP Fm3c\*

(a) Single crystal X-ray results on dehydrated Na zeolite-A: \*\*

|             |          |             |          |
|-------------|----------|-------------|----------|
| Si-O(1)     | 1.595(4) | Al-O(1)     | 1.723(4) |
| Si-O(2)     | 1.586(4) | Al-O(2)     | 1.717(4) |
| 2 X Si-O(3) | 1.604(3) | 2 X Al-O(3) | 1.741(2) |
| Av. Si-O    | 1.597    | Av. Al-O    | 1.731    |

(b) Powder neutron diffraction results on dehydrated T1 zeolite-A:

|             |           |             |           |
|-------------|-----------|-------------|-----------|
| Si-O(1)     | 1.608(14) | Al-O(1)     | 1.702(14) |
| Si-O(2)     | 1.628(14) | Al-O(2)     | 1.755(14) |
| 2 X Si-O(3) | 1.560(13) | 2 X Al-O(3) | 1.726(13) |
| Av. Si-O    | 1.589     | Av. Al-O    | 1.727     |

\*E.S.D.'s are given in parentheses.

\*\*Reference 9.

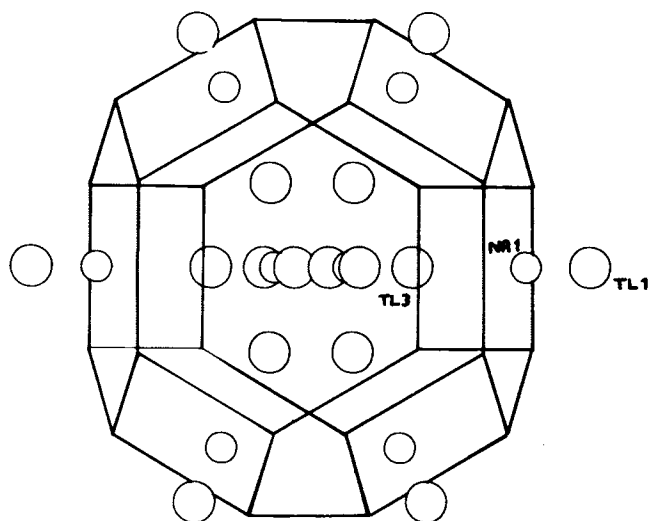


Figure 3.  
The location of Tl(1), Tl(3), and Na(1) close to the 6-rings of the cubeoctahedra in Tl zeolite-A.

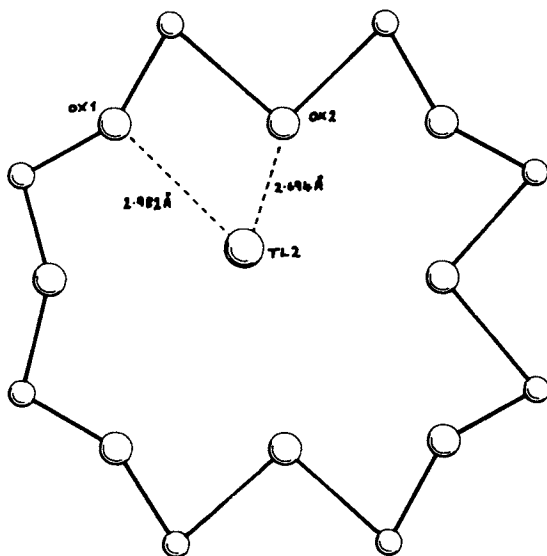


Figure 4.  
The location of Tl(2) in the 8-ring in Tl zeolite-A.

Si, Al ordering is clearly demonstrated and the ability to detect unexchanged sodium is reassuring. Zeolite-A, with its unit cell volume of  $15,000 \text{ \AA}^3$ , represents perhaps the largest cell to be studied by neutron powder methods up to the present time, though structures involving substantially larger numbers of parameters have been refined. The detection of Si, Al ordering stems from the ability to observe the weak superlattice reflections associated with the doubling of the unit cell, a feature made possible by the use of a very long neutron wavelength ( $2.98 \text{ \AA}$ ) in these experiments; Figure 5 shows the 531 superlattice peak on the leading edge of the 600 substructure reflection. When the Si and Al scattering lengths are inverted following convergence of the refinement to  $R_{pr} = 11.3$  percent, the R-factor increases to 12.4 percent. There is, therefore, some intrinsic sensitivity to Si, Al ordering, but in part our observations must reflect the different bond lengths to oxygen around Si and Al.

A corresponding  $Fm\bar{3}c$  refinement of the silver zeolite-A structure, using a sample with a Si/Al ratio of 1.02, has also been achieved. The final profile R-factor is 12.3 percent and a bimodal distribution of Si-O and Al-O bond lengths is again obtained, confirming once more the alternation of Si and Al. Our analysis of the cation positions is not yet complete and we are examining the results for evidence of silver clusters, as reported by Uytterhoeven and co-workers (17).

Rhombohedral Sodium Zeolite-A Our neutron data on three samples of sodium zeolite-A show clear evidence for a rhombohedral distortion of the structure that is most apparent with Si/Al = 1.0. The lattice parameters are set out below (12):

| Si/Al | Temperature | $a=b=c$ (Å) | $\alpha=\beta=\gamma$ (degrees) |
|-------|-------------|-------------|---------------------------------|
| 1.10  | 5           | 17.352      | 59.84                           |
| 1.02  | 290         | 17.365      | 59.82                           |
| 1.02  | 5           | 17.375      | 59.72                           |
| 1.00  | 290         | 17.392      | 59.62                           |
| 1.00  | 5           | 17.401      | 59.53                           |

Since we have demonstrated above that thallium and silver derivatives prepared from these rhombohedral samples are cubic with 4:0 ordering in the aluminosilicate framework, it is reasonable to assume that this distribution must be present in the sodium compounds. The structure can be described using space group  $R\bar{3}c$  and our efforts have recently concentrated on obtaining good refinements with this model. If no constraints are applied, a final R-factor of 13.6 percent is obtained using the 5K data (Si/Al = 1.0), but unfortunately the spread of Si-O and Al-O bond lengths is larger than would seem chemically reasonable.

Essentially, the structure is undetermined with powder data since lowering the symmetry from cubic to rhombohedral increases the number of variable atomic coordinates from 15 to approximately 50, whilst a high degree of pseudosymmetry persists. A variety of constrained models has been tested, including one in which the  $\text{SiO}_4$  and  $\text{AlO}_4$  units were held rigidly tetrahedral using coordinates determined from a distance least-squares (DLS) analysis (18). This gave an  $R_{\text{pr}}$ -factor of 22 percent, confirming, as we already know from the cubic derivatives, that significant deviations from  $T_d$  symmetry do occur. We are currently writing a version of the profile analysis programs in which flexible constraints will hold the structure within chemically reasonable limits using the procedure described by Waser (19).

Sodium ZK-4 Kerr and Kokotailo (20) have described the preparation of the zeolite ZK-4, a variant of zeolite-A in which the Si/Al ratio can be as high as 3, and we have studied a sample with a Si/Al ratio of 1.65 (determined by  $^{29}\text{Si}$  NMR) using a neutron wavelength of 2.98 Å. The most striking feature of the neutron powder pattern is the apparent absence of the superlattice reflections arising from the Si, Al ordering; this is illustrated in Figure 6, where the 531 reflection, normally seen on the low angle side of the 600 (Figure 5), is now absent. All the data can now be indexed using a primitive cubic cell,  $a_0 \sim 12.3$  Å, and we have carried out refinements in the space group Pm3m. Ironically, this is the space group originally proposed for zeolite-A at a time when it was thought that the Si, Al distribution was random (21). Our results therefore imply that Si and Al are no longer alternating in ZK-4 when Si/Al  $\sim 1.65$ , even though local ordering in obedience to Loewenstein's rules, is probably still present (high resolution,  $^{29}\text{Si}$  NMR results (14,22) suggest that this is the case). This conclusion is consistent with the results of Monte Carlo calculations which predict that superlattice ordering will be absent when the Si/Al ratio exceeds 1.70 (23).

A good refinement of the data with  $R_{\text{pr}} = 14.5$  percent has been obtained in Pm3m (Figure 7). Most of the discrepancies between the observed and calculated profiles stem from our inability to simulate the peak shapes for the low angle reflections, a problem that arises from the large vertical acceptance angle of the counters on the D1A diffractometer. Since we have now established that the superlattice is absent, this experiment could usefully be repeated with a shorter neutron wavelength.

In the Pm3m description there is only one tetrahedral Si, Al site in the aluminosilicate framework, and our mean Si, Al-O bond length (1.642 Å) is in good agreement with the weighted average of Si-O and Al-O bond lengths (1.653 Å) at this Si/Al ratio. The neutron study also reveals that the site in the 8-ring window, occupied by T1(2) in the thallium compound (see above) is unoccupied in ZK-4 because the sodium content is reduced as the Si/Al ratio increases. This structural feature has previously been

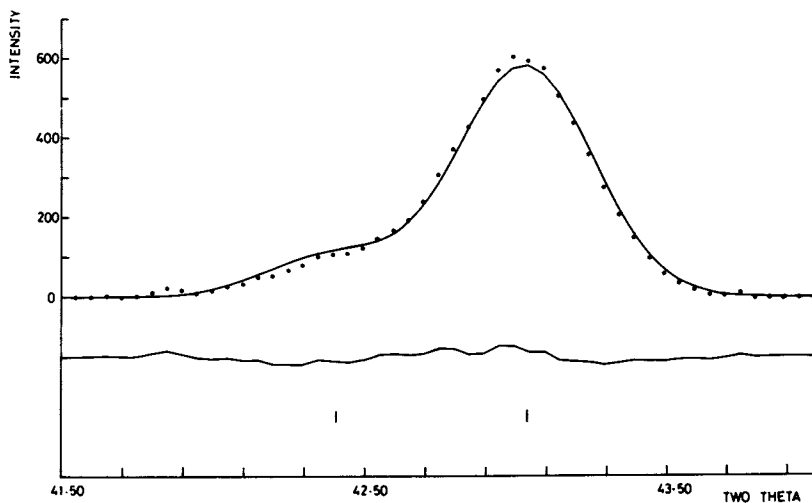


Figure 5.  
The 531 superlattice reflection on the low angle side of the 600 sub-structure reflection in Tl zeolite-A (observed and calculated models, as in Figure 2).

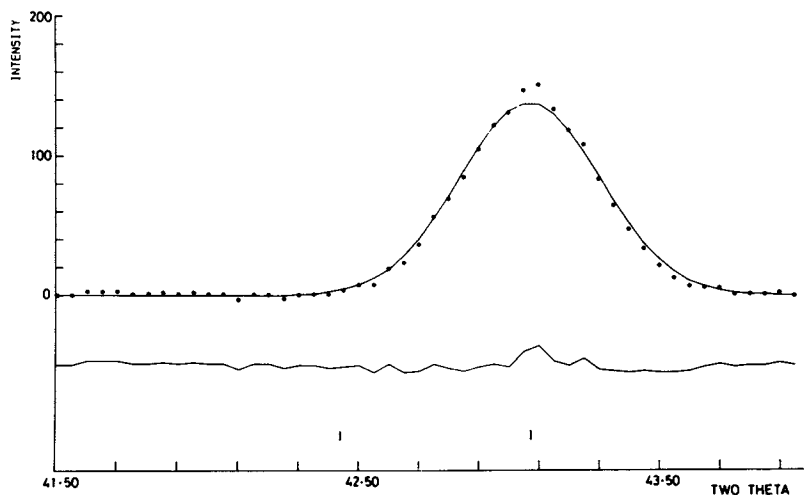


Figure 6.  
The 531 superlattice peak is absent in ZK-4 (compare with Figure 5).

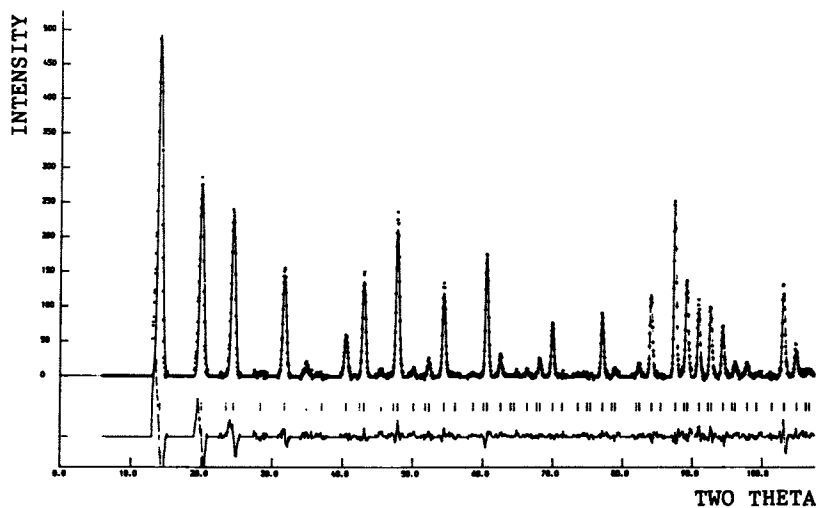


Figure 7.  
The observed, calculated, and difference profiles of  
sodium ZK-4.

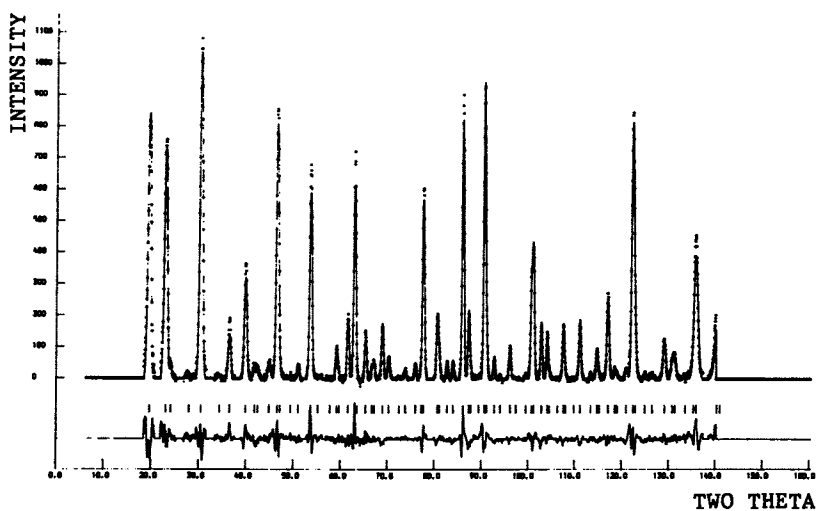


Figure 8.  
The observed, calculated, and difference profiles of  
sodium zeolite-Y.

suggested (24) in order to account for the ability of sodium ZK-4, but not sodium-A, to absorb long-chain hydrocarbons such as n-hexane (20). On the other hand, our final difference Fourier maps reveal some occupancy of sites in the  $\alpha$ -cage for which we have no facile explanation. This unexpected feature may be related to the frequent observations of an extra line in the NMR spectra of ZK-4 that is normally ascribed to metasilicate impurity (22).

Sodium Zeolite-Y (Faujasite) The faujasite structure is constructed from the same cubeoctahedral units that form the basis of zeolite-A, but in this instance they are connected through the 6-rings rather than the 4-rings. The crystal system is again cubic, and Olsen (25) has demonstrated that Si and Al are ordered in an alternating manner in a sample with Si/Al = 1.18. The space group is Fd3 and the lattice parameter is approximately 24.6 Å. Samples with higher Si/Al ratios have previously been examined by neutron diffraction, but Si, Al ordering was not considered and the space group Fd3m was assumed (26).

We have examined a sample with Si/Al = 2.61 and obtained a good refinement using the centrosymmetric space group and an apparently random Si, Al arrangement. The profile R-factor converged to 13.3 percent and the observed and calculated neutron patterns are illustrated in Figure 8. The mean Si, Al-O bond length, 1.64 Å, is once more in good agreement with the expected value (1.639 Å). As in ZK-4, we can again argue that Loewenstein's rules could be observed without overall Si, Al alternation at such high Si/Al ratios. Refinements in which the non-centric space group, Fd3, is assumed give a better fit ( $R_{pr} = 12.4$  percent) than in Fd3m, following an increase in the number of variable atomic coordinates from 12 to 20, but yield chemically unacceptable Si-O and Al-O bond lengths. We conclude that the higher symmetry description is correct for our sample. The sodium distribution is in good agreement with that of the previous neutron study, showing depletion of the site SI'.

### Conclusions

The results that we have obtained to date using neutrons are very encouraging and confirm that reliable structural information can be derived from powder studies. The extension of the work to more complex zeolites is certainly merited, although more sophisticated computational methods, for example the utilization of flexible constraints, may be necessary. The location of exchangeable cations should be feasible using Fourier methods and we can also look forward to studies in which absorbed molecular species are probed. On the other hand, we should not overestimate the sensitivity of neutrons to Si, Al ordering, bearing in mind that the difference between the neutron scattering lengths of Si and Al is modest, and the location of small concentrations of Al in low symmetry structures, for example ZSM-5, will clearly be difficult.

### Acknowledgments

We are grateful to the SERC for the provision of neutron facilities at the ILL, Grenoble, to the Exxon Research and Engineering Co. for a grant, and to Prof. J. M. Thomas and his group at Cambridge for their valuable collaboration.

### Literature Cited

1. Lippmaa, E.; Magi, M.; Somosen, A.; Engelhardt, G.; Grimmer, A. H. R. J. Am. Chem. Soc. 1980, 102, 4889.
2. Klinowski, J.; Thomas, J. M.; Fyfe, C. A.; Hartman, J.S. J. Phys. Chem. 1981, 85, 2590.
3. Bursill, L. A.; Lodge, E. A.; Thomas, J. M. Nature 1980, 286, 111.
4. Bacon, G. E. "Neutron Diffraction Third Edition"; Oxford University Press, Oxford, 1975.
5. Rietveld, H. M. J. App. Cryst. 1969, 2, 65.
6. Cheetham, A. K.; Taylor, J. C. J. Solid State Chem. 1977, 21, 253.
7. Hewat, A. W. "Powder Rietveld and Refinement System," I.L.L. Grenoble Report 1978.
8. Rae-Smith, A. R.; Cheetham, A. K.; Skarnulis, A. J. J. App. Cryst. 1979, 12, 485.
9. Pluth, J. J.; Smith, J. V. J. Am. Chem. Soc. 1980, 102, 4704.
10. Loewenstein, W. Am. Miner 1954, 39, 92.
11. Thomas, J. M.; Bursill, L. A.; Lodge, E. A.; Cheetham, A. K.; Fyfe, C. A. J. Chem. Soc. Chem. Comm. 1981, 276.
12. Bursill, L. A.; Lodge, E. A.; Thomas, J. M.; Cheetham, A. K. J. Phys. Chem. 1981, 85, 2409.
13. Cheetham, A. K.; Fyfe, C. A.; Smith, J. V.; Thomas, J. M. J. Chem. Soc. Chem. Comm. 1982, 823.
14. Melchior, M. T.; Vaughan, D. E. W.; Jarman, R. H.; Jacobson, A. J. Nature 1982, 298, 455.
15. Sherry, H. S.; Walton, H. F. J. Phys. Chem. 1967, 71, 1457.
16. Firor, R. L.; Seff, K. J. Am. Chem. Soc. 1977, 99, 1112.
17. Gellens, L. R.; Mortier, W. J.; Schoonheydt, R. A.; Uytterhoeven, J. B. J. Phys. Chem. 1981, 85, 2783.
18. Meier, W. M.; Villiger, H. Z. Kristallographie 1969, 129, 411.
19. Waser, J. Acta Cryst. 1963, 16(11) 1091.
20. Kerr, G. T.; Kokotailo, G. T. J. Am. Chem. Soc. 1961, 83, 4675.
21. Reed, T. B.; Breck, D. W. J. Am. Chem. Soc. 1956, 78, 5972.
22. Thomas, J. M.; Fyfe, C. A.; Ramdas, S.; Klinowski, J.; Gobbi, G. C. J. Phys. Chem. 1982, 86, 3061.
23. Gaunt, D. S.; Fisher, M. E. J. Chem. Phys. 1965, 43, 2840.
24. Kerr, G. T. J. Phys. Chem. 1962, 66, 2271.
25. Olsen, D. H. J. Phys. Chem. 1970, 74, 2758.
26. Bosacek, V.; Beran, S.; Jirak, Z. J. Phys. Chem. 1981, 85, 3856.

RECEIVED November 4, 1982



# A High Resolution Silicon-29 NMR and Neutron Powder Diffraction Study of Na-A Zeolite: Loewenstein's Rule Vindicated

J. M. BENNETT and C. S. BLACKWELL  
Union Carbide Corporation, Tarrytown, NY 10591

D. E. COX  
Brookhaven National Laboratory, Physics Department, Upton, NY 11973

The structure of dehydrated Na-A zeolite has been re-examined by magic angle spinning  $^{29}\text{Si}$ -NMR and neutron powder diffraction techniques. This is in light of recent proposals by Bursill et al., that the Si:Al ordering is different from the simple alternating scheme generally accepted, and violates Loewenstein's rule. The  $^{29}\text{Si}$ -NMR chemical shifts observed for Na-A zeolite and a series of nitro-geneous-A zeolites with varying Si:Al contents demonstrate conclusively that in the former each Si is surrounded by four Al and no Si near neighbors. This 4:0 ordering scheme is consistent with previous X-ray structure determinations and does not violate Loewenstein's rule. Neutron diffraction data confirm the results of Bursill et al. that Na-A zeolite has rhombohedral symmetry at 4.5K and 296K. However, there is a transition to the cubic symmetry at about 335K. Structural analyses at selected temperatures between 4.5K and 603K were carried out by Rietveld refinement of the neutron data. Above the transition, the results are in good agreement with recent X-ray single crystal refinements by Pluth and Smith. Below the transition, constrained refinement strongly indicates that ordering of Na atoms in partially occupied sites takes place, with a consequent lowering of the symmetry to at least  $R\bar{3}c$ . There is no necessity for the 3:1 ordering scheme proposed by Bursill et al. to be invoked to account for this lowering of symmetry.

0097-6156/83/0218-0143\$06.00/0  
© 1983 American Chemical Society

Since the original determination of the crystal structure of Linde zeolite 4A(1), the refinement of the structure of the hydrated variety in space group Fm3c with a unit cell edge of 24.6Å instead of space group Pm3m with a pseudo-cell edge of 12.3Å(2) showed that the Si and Al alternate in the framework.

Further accurate single crystal X-ray determinations of the structures of potassium and sodium zeolites by Pluth and Smith, (3, 4) contained alternating tetrahedra with mean tetrahedral cation-oxygen distances of about 1.60Å and 1.73Å, consistent with occupation by Si and Al respectively.

In a series of recent papers the structure of zeolite A has been re-examined with particular reference to the Si and Al ordering, and a different arrangement has been proposed,(5, 6,) based mainly upon results from three different techniques, electron diffraction,(5, 7) <sup>29</sup>Si-NMR(5, 7, 8) and neutron diffraction,(5, 9) and is at variance with Loewenstein's rule.(10)

Magic angle spinning (MAS) <sup>29</sup>Si-NMR is a valuable tool for revealing details of the structural environment in silicates, aluminosilicates and zeolites(11, 12) and can give valuable information about the Si:Al distribution in any zeolite framework. It is essential if the data are to be used for evaluation of Si:Al ordering that the <sup>29</sup>Si-NMR lines be quantitative such that their respective areas are proportional to the number of Si atoms of each type. A correct assignment of the identity of each line to its Si type is also crucial. In the case of Linde A zeolite, which has a chemical Si:Al ratio of unity, it was originally concluded from <sup>29</sup>Si-NMR results that Al-O-Al linkages are present,(7, 8) in violation of Loewenstein's rule. This finding was based upon the observation of a <sup>29</sup>Si chemical shift of -88.9 ppm which was assigned to an Si:Al ordering scheme of 3:1. A similar conclusion was reached on the basis of neutron powder diffraction experiments, which revealed a small rhombohedral distortion at 290 K and 5 K, and were interpreted in terms of a 3:1 ordering scheme with R<sub>3</sub> symmetry.(5)

This rather unexpected result stimulated a number of other investigations, including the present one, with the conclusion that the 4:0 ordering scheme is correct.(13) In addition, the NMR and neutron diffraction data reported in reference(5) have been re-interpreted in favor of 4:0 rather than 3:1 order,(14, 15) and it is concluded that the rhombohedral distortion observed in the neutron pattern is strongly dependent upon the identity of the exchangeable cations. However, in an independent neutron study of Na-A zeolite(16), Adams and Haselden reported no evidence for such a distortion, and conclude that the symmetry must depend subtly upon the method of preparation.

The present work was undertaken to investigate the structure of Na-A zeolite in more detail, particularly with respect to the

Si:Al ordering.  $^{29}\text{Si}$ -NMR experiments have been carried out on a series of nitrogenous-A zeolites and show clearly that the -88.9 ppm shift in Na-A zeolite should be assigned to Si surrounded by four Al near neighbors. In addition, neutron powder diffraction data have been collected as a function of temperature between 4.5 and 600 K, and these are also consistent with the 4:0 ordering scheme. Structural analysis by the Rietveld refinement technique (17) reveals that the rhombohedral symmetry is a consequence of ordering of the Na ions in 8-rings at a temperature of about 335K.

### Experimental

NMR Experiments  $^{29}\text{Si}$ -NMR spectra were obtained on a Bruker CXP-200 solid state high power and high resolution spectrometer equipped with the Bruker  $^{13}\text{C}$ -CPMAS accessory. Chemical shifts are reported relative to tetramethylsilane (TMS), to an accuracy better than can be justified from the line-widths (about 2.5 ppm) in these materials. The sample spinning rate was usually between 3 and 4 kHz, and no spinning side bands were observed.

A typical spectrum was acquired with Bloch decays excited by 4  $\mu\text{sec}$  pulses separated by 10 second recovery delays, and the data should give a reasonably quantitative estimate of the Si content. Previous work on other types of zeolites has demonstrated the importance of checking for complete relaxation if the spectra are to be used for quantitative studies.

The samples used were a standard Na-A zeolite and five nitrogenous types of zeolite A, or N-A. (18) The N-A zeolites are siliceous analogues of zeolite A, synthesized with tetramethylammonium cation. The Si:Al ratio varied from 0.94 (NaA) to 3.54 for the most siliceous N-A sample.† The ratios were determined by wet chemical analysis, and the structure type and absence of impurity phases were confirmed by X-ray powder diffraction techniques. Adsorption measurements (oxygen,  $-183^\circ\text{C}$ ) showed a zeolite A content of greater than 90%.

Neutron Diffraction Experiments The sample of Na-A zeolite used in the neutron diffraction studies was prepared by the standard technique and had a Si:Al ratio slightly greater than unity (1.06), corresponding to the composition  $\text{Na}_{0.97}\text{Si}_{1.03}\text{Al}_{0.97}\text{O}_4$ . The sample was dehydrated by slowly heating in air in a shallow dish up to  $300^\circ\text{C}$ , maintained at  $300^\circ\text{C}$  for 16 hours, rapidly transferred to a desiccator and allowed to cool. This procedure does not yield a completely anhydrous material. The sample was finally loaded into a cylindrical aluminum holder under an atmosphere of dry helium.

†These samples were furnished by Miss E.M. Flanigen's Group, Molecular Sieve Department, Engineering Products Division, Union Carbide Corporation, Tarrytown, New York 10591

Data were collected with 2.385 $\text{\AA}$  neutrons from the (002) reflection of a pyrolytic graphite monochromator and an analyzing crystal at two different settings, at various times over a period of several months. The analyzing crystal yields a significant improvement in peak-to-background ratios. In both cases a pyrolytic graphite filter was used to remove higher order wavelengths. The angular step interval was 0.05 $^{\circ}$ .

### Results and Discussion

$^{29}\text{Si-NMR}$ . The  $^{29}\text{Si-NMR}$  chemical shifts observed for various samples are:

Table I

|                                    | Sample No.   |        |        |        |        |        |
|------------------------------------|--|--------|--------|--------|--------|--------|
|                                    | A  | B      | C      | D      | E      | F      |
| Si:Al ratio from chemical analysis | 0.94   | 1.32   | 1.54   | 1.79   | 2.73   | 3.54   |
|                                    | $^{29}\text{Si-NMR}$ Chemical Shifts ( $\delta$ ) <sup>*</sup> |        |        |        |        |        |
| Assignments                        |  |        |        |        |        |        |
| $\text{SiO}_4^{-\dagger}$          | --   | -77.1  | -77.2  | --     | --     | --     |
| $\text{Q}^4(4:0)$                  | -89.6  | -88.8  | -89.4  | -89.3  | -89.2  | --     |
| $\text{Q}^4(3:1)$                  | --   | -93.6  | -94.2  | -94.4  | -94.4  | -94.6  |
| $\text{Q}^4(2:2)$                  | --   | -99.2  | -100.1 | -100.3 | -100.5 | -101.0 |
| $\text{Q}^4(1:3)$                  | --   | -105.2 | -106.0 | -106.0 | -106.2 | -107.0 |
| $\text{Q}^4(0:4)$                  | --   | --     | --     | -111.5 | -111.7 | -112.5 |

\*ppm with respect to TMS (tetramethylsilane)

$\dagger$ the assignment  $\text{SiO}_4^{-}$  in samples 2 and 3 is for an impurity phase.

Na-A zeolite has a single sharp line at -89.6 ppm, in agreement with data from numerous previous investigations. The data for the Na-A samples provide conclusive evidence with respect to the Si:Al ordering. If the Na-A resonance at -89.6 ppm were assigned to 3:1 ordering as previously suggested, (7, 8) then the chemical Si:Al ratio of unity would require the presence of Al-O-Al bridges, in formal violation of Loewenstein's rule. With this assumption, the regular progression of  $^{29}\text{Si-NMR}$  resonances to high field upon removal of Al from neighboring tetrahedra allows the positions of the resonances of Si in the other configurations to be predicted. If the shift  $\delta(3:1)$  is -89.6 ppm, and the decrease in shift for each Si substitution is taken to be 5.5 ppm on average, then one would expect  $\delta(2:2) = -95.1$ ,  $\delta(1:3) = -100.6$  and  $\delta(0:4) = -106.1$  ppm. The latter would therefore be the largest shift observed. If, on the other hand, -89.6 ppm corresponds to the 4:0 configuration, the progression to 0:4 order would cover five peaks out to a  $\delta(0:4)$  of -111.6 ppm. The data and the spectra in Figures 1-2 show an orderly progression with the growth of Si-rich peaks and the decrease of Al-rich peaks. The appearance of lines at -111.5,

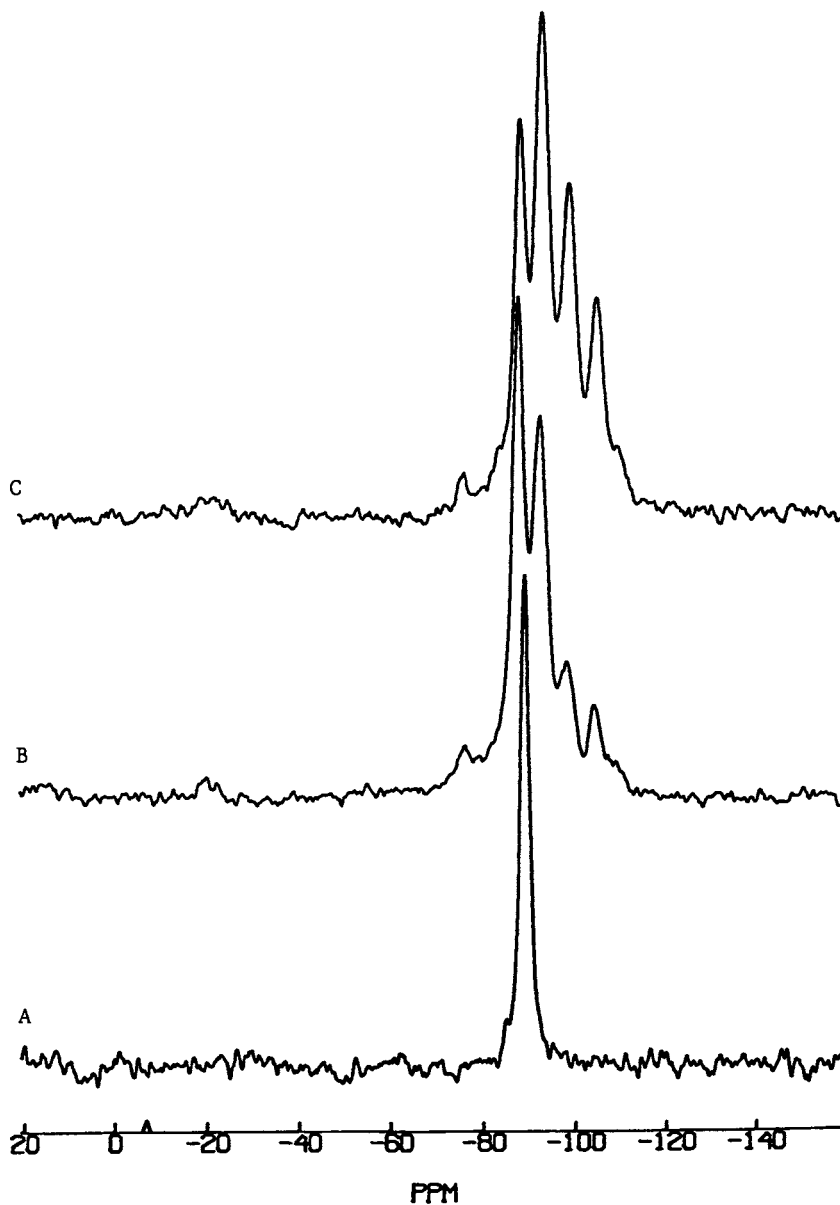


Figure 1.

$^{29}\text{Si}$ -NMR MAS Spectrum from:

A. NaA (Si:Al = .94) C. N-A (Si:Al = 1.54)

B. N-A (Si:Al = 1.32)

**American Chemical  
Society Library**

1155 16th St. N. W.

Washington, D. C. 20036

In Intrazeolite Chemistry; Stucky, G., et al.;

ACS Symposium Series; American Chemical Society: Washington, DC, 1983.

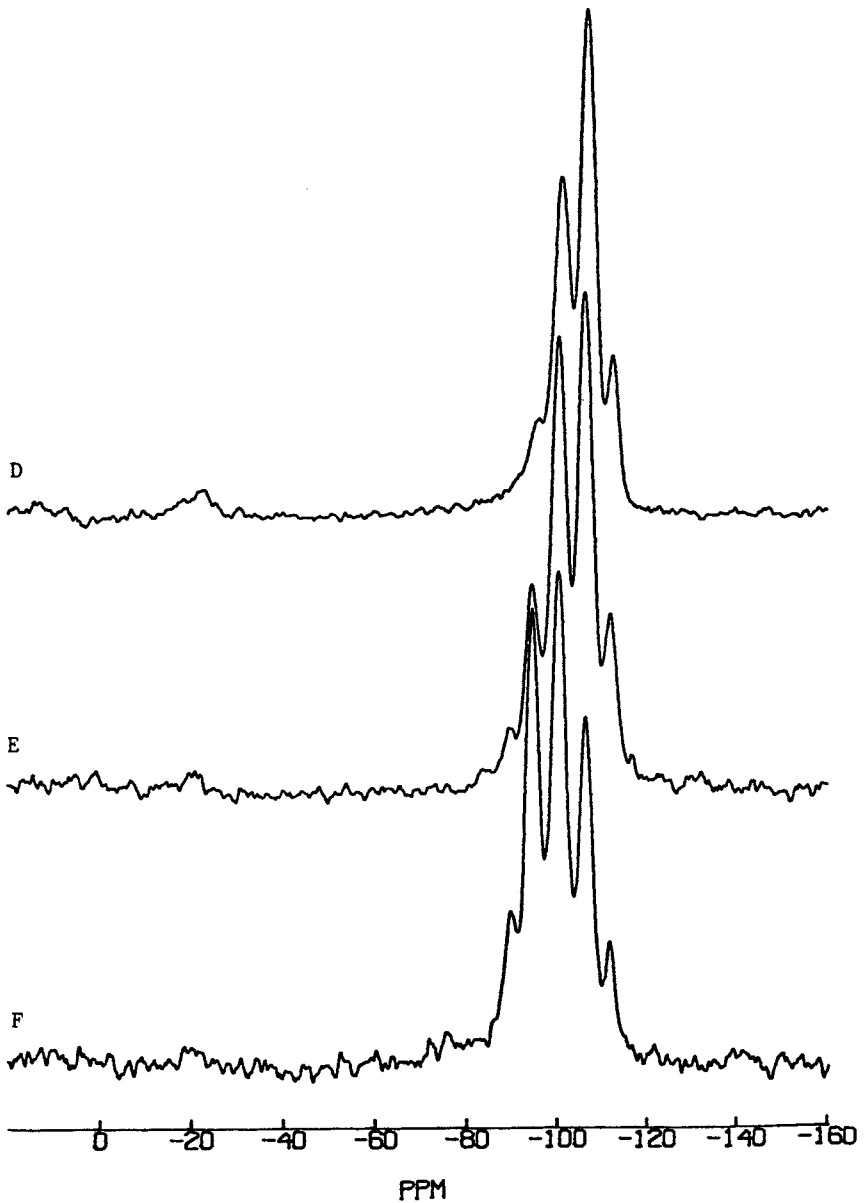


Figure 2.

$^{29}\text{Si}$ -NMR MAS Spectrum from:

D. N-A (Si:Al = 1.79) F. N-A (Si:Al = 3.54)

E. N-A (Si:Al = 2.73)

-111.7, and -112.5 ppm in samples D, E and F demonstrates the existence of the 0:4 configuration at  $\delta = -112$  ppm, and it therefore follows from the progression of lines to low field that the line at -89.6 ppm corresponds to the 4:0 configuration. Deconvolution of the peaks with a Dupont 310 Curve Resolver, measurement of their areas, and a calculation for Si:Al using the peak assignment as herein discussed yields Si:Al calculated values in good agreement with chemical analysis. Thus Loewenstein's rule is not violated in Na-A zeolite, and the NMR results are consistent with the previous X-ray studies.

We believe the probable explanation for the unusual  $^{29}\text{Si}$ -NMR shift in zeolite A for the 4:0 configuration lies in geometrical and steric effects. Early interpretations of  $\delta(^{29}\text{Si})$  shifts in zeolites have recognized only the effect of Al substitution. It is well known that other factors can influence the chemical shifts. The structures of A type zeolites and N-A are unique in having a double-four-ring building unit, and this is probably responsible for the unusual changes in  $\delta(^{29}\text{Si})$  in these materials. Moreover, the chemical shifts for a given type of configuration, e.g. 0:4, show a general slight shift towards greater shielding as a function of increasing Si content. A possible explanation for this is that the general shrinkage of zeolite unit cells with increasing ratios of Si:Al results in stronger Si-O bonds and increased shielding (a secondary geometrical effect).

### Neutron Diffraction

The neutron data collected at 4.5K and room temperature show that the symmetry is no longer cubic, in agreement with Bursill, et al.(5). This is most clearly seen by inspection of the (880) reflection, which is found to be asymmetric and considerably broadened with respect to the (12,0,0) reflection. Although (12, 0,0) in fact occurs in combination with (884), the latter has a negligibly small intensity and thus the true symmetry may be assumed to be rhombohedral, as confirmed by subsequent profile analysis.

As the temperature is increased from 293 K, the (880) peak width decreases steadily and attains the resolution-limited value slightly above 335 K, while the (12,0,0) peak width stays essentially unchanged. The rhombohedral distortion derived from the peak positions is shown in Figure 3 as  $\Delta\alpha$ , the deviation from the  $90^\circ$  angle of the face-centered unit cell. Above 315 K the distortion is too small for least-squares fitting to two peaks, but fits to a single peak showed definite broadening up to about 335 K, which is therefore taken to be the transition temperature to the cubic phase in Figure 3.

A careful scan was performed at 367 K in order to check whether the cubic phase had Fm3c symmetry. The (600,442) peak showed a distinct shoulder on the low angle side corresponding to

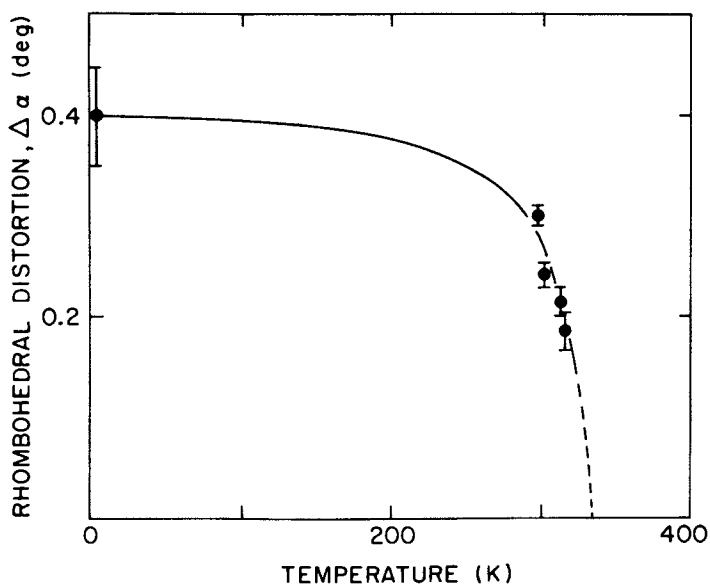


Figure 3.

Rhombohedral distortion of Na-A zeolite as a function of temperature expressed as the deviation  $\Delta\alpha$  from  $90^\circ$  of the face-centered cell. The solid line is drawn as a guide to the eye.



the (531) position within an uncertainty of  $0.05^\circ$ . Thus the rhombohedral symmetry does not appear to be associated with ordering of the Si and Al ions.

Additional scans performed between 293–385 K showed that the transition was reversible over this range. However, after the sample was maintained for about two days at 603 K, a subsequent room temperature pattern showed considerably less broadening, with a deviation  $\delta\alpha$  of about  $0.1^\circ$ .

**Structural Analysis** A logical initial choice for the rhombohedral space group is  $R\bar{3}c$  (which is the highest symmetry rhombohedral sub-group of  $Fm\bar{3}c$ ). However, for ease of comparison, the face-centered rhombohedral space group  $R_F\bar{3}c$  is used with  $a_R \approx a_C$  and  $\alpha_R \approx 90^\circ$ .

The  $96(i)$  sites of  $Fm\bar{3}c$  split into two sets of 48(f), and the 192(i) sites split into four. The Na(1) 64(g) sites split into a set of special 16(c) sites and a general set, while the Na(3) 96(h) sites split into two sets of special 24(e) sites and one general set. The number of variable positional parameters thus increases from 15 to 51. This represents a formidable problem and therefore the structural analysis is reduced to refinement of the occupancies of the seven possible Na sites in  $R_F\bar{3}c$ , while all the other positional parameters are constrained by the higher symmetry of  $Fm\bar{3}c$ .

603 K Data were collected at  $0.05^\circ$  intervals over the angular range  $7-137^\circ$  with the graphite analyzer in the (004) configuration. In the first stages of refinement, Si and Al were assumed to be ordered, but the atomic positions were constrained to  $Pm\bar{3}m$ , the Na occupancies were allowed to vary, subject to the constraint that the total amounted to 0.97 atoms per formula unit. The results are listed in column 1 of Table II:

When the  $Pm\bar{3}m$  constraints were removed, convergence was quickly obtained, with  $R_I = 0.086$  and  $R_{WP} = 0.169$ . Although the decrease in  $R_{WP}$  is quite small, there are some significant shifts in the parameters in reasonable agreement with the X-ray determination.

The refined values of the parameters are listed under column 2 of Table II, together with the X-ray values. The profile fit, which includes contributions from 176 reflections, is shown in Figure 4, together with the difference plot. The only striking discrepancy between the neutron and X-ray values is in the position of Na(3), which would correspond to a Na-O near neighbor distance of about  $4.7\text{\AA}$  instead of  $2.4\text{\AA}$  and clearly lacks physical meaning.

One additional set of refinements was performed to test the sensitivity of the neutron profile technique to the ordering of Si and Al, which have scattering amplitudes of 0.415 and  $0.345 \times 10^{-12}$  cm respectively. (19) When the occupation factor  $f$  (defined as the fraction of "right" atoms on Si and Al sites) was allowed to vary,

Table II

Results of Rietveld refinement of neutron powder data for Na-A zeolite at various temperatures above and below the cubic-rhombohedral transition. The space group used in each refinement is as shown. In the rhombohedral refinements, the positional parameters were constrained to satisfy Fm3c symmetry as discussed in text. f is the fractional occupancy and N the number of reflections included in this refinement. Also shown in columns I and II are the X-ray single crystal results of Pluth and Smith(†), but with their anisotropic temperature factors converted to the average isotropic values. Neutron scattering amplitudes taken as 0.415, 0.345, 0.5805 and 0.363 x 10<sup>-12</sup>cm for Si, Al, O and Na respectively. The precision in the unit cell edge is not a measure of the real accuracy, since these are small uncertainties in the neutron wavelength under different conditions.

|         | I         |                            | II        |                            | III           |                         | IV                      |  | V |  |
|---------|-----------|----------------------------|-----------|----------------------------|---------------|-------------------------|-------------------------|--|---|--|
|         | 603 K     | Pm3m<br>293 K <sup>†</sup> | 603 K     | Fm3c<br>293 K <sup>†</sup> | Fm3c<br>367 K | R $\bar{F}$ 3c<br>296 K | R $\bar{F}$ 3c<br>4.5 K |  |   |  |
| Si:y    | 0.0913(2) | 0.0918(1)                  | 0.0935(6) | 0.0932(1)                  | 0.0915(20)    | 0.0860(13)              | 0.0892(11)              |  |   |  |
| Si:z    | 0.1861(2) | 0.1861(1)                  | 0.1833(5) | 0.1850(10)                 | 0.1869(18)    | 0.1880(15)              | 0.1846(12)              |  |   |  |
| Al:y    | 0.1861    | 0.1861                     | 0.1891(6) | 0.1872(1)                  | 0.1848(19)    | 0.1806(16)              | 0.1870(14)              |  |   |  |
| Al:z    | 0.0913    | 0.0918                     | 0.0880(7) | 0.0904(1)                  | 0.0907(24)    | 0.0955(17)              | 0.0937(13)              |  |   |  |
| O(1):y  | 0.1131(2) | 0.1138(2)                  | 0.1132(2) | 0.1137(1)                  | 0.1129(4)     | 0.1122(6)               | 0.1147(4)               |  |   |  |
| O(1):z  | 0.25      | 0.25                       | 0.2475(5) | 0.2466(2)                  | 0.2469(6)     | 0.2519(14)              | 0.2458(8)               |  |   |  |
| O(2):y  | 0.1458(1) | 0.1455(2)                  | 0.1462(5) | 0.1446(1)                  | 0.1451(10)    | 0.1388(6)               | 0.1512(6)               |  |   |  |
| O(2):z  | 0.1458    | 0.1455                     | 0.1455(5) | 0.1459(1)                  | 0.1471(11)    | 0.1550(6)               | 0.1435(5)               |  |   |  |
| O(3):x  | 0.0564(1) | 0.0560(1)                  | 0.0550(2) | 0.0538(1)                  | 0.0548(9)     | 0.0546(8)               | 0.0518(5)               |  |   |  |
| O(3):y  | 0.0564    | 0.0560                     | 0.0577(3) | 0.0587(1)                  | 0.0571(8)     | 0.0561(7)               | 0.0576(5)               |  |   |  |
| O(3):z  | 0.1712(1) | 0.1719(2)                  | 0.1711(1) | 0.1715(6)                  | 0.1702(3)     | 0.1711(3)               | 0.1710(3)               |  |   |  |
| Na(1):x | 0.1004(3) | 0.0996(1)                  | 0.1001(3) | 0.0996(1)                  | 0.1033(5)     | 0.1007(7)               | 0.1021(3)               |  |   |  |
| Na(2):y | 0.2228(9) | 0.2145(4)                  | 0.2234(8) | 0.2165(6)                  | 0.2277(13)    | 0.2293(16)              | 0.2315(12)              |  |   |  |
| Na(2):z | 0.2228    | 0.2145                     | 0.2234    | 0.2111(6)                  | 0.2277        | 0.2293                  | 0.2315                  |  |   |  |

Table II, Continued

|                            | I          |                    | II         |                    | III         | IV             | V              |
|----------------------------|------------|--------------------|------------|--------------------|-------------|----------------|----------------|
|                            | Pm3m       | Fm3c               | Fm3c       | Fm3c               | Fm3c        | R $\bar{F}$ 3c | R $\bar{F}$ 3c |
|                            | 603 K      | 293 K <sup>†</sup> | 603 K      | 293 K <sup>†</sup> | 367 K       | 296 K          | 4.5 K          |
| Na(3):x                    | 0.1772(17) | 0.1044(15)         | 0.1778(16) | 0.1060(7)          | 0.1683(26)  | 0.1875(17)     | 0.1745(23)     |
| Na(1):f                    | 0.88(2)    | 0.91(1)            | 0.87(2)    | 0.97(1)            | 0.88(2)     | 0.96(16)       | 0.86(10)       |
| Na(11):f                   |            |                    |            |                    |             | 0.82(6)        | 0.96(4)        |
| Na(12):f                   |            |                    |            |                    |             | 0.51(3)        | 0.46(2)        |
| Na(2):f                    | 0.26(1)    | 0.37(1)            | 0.26(1)    | 0.24(1)            | 0.24(1)     | 0.0            | 0.0            |
| Na(21):f                   |            |                    |            |                    |             | 0.04(5)        | 0.14(4)        |
| Na(22):f                   | 0.13(1)    | 0.07(1)            | 0.13(1)    | 0.07(1)            | 0.14(1)     | 0.24(4)        | 0.09(4)        |
| Na(3):f                    |            |                    |            |                    |             | 0.24           | 0.09           |
| Na(31):f                   |            |                    |            |                    |             | 0.04(4)        | 2.1(2)         |
| Na(32):f                   |            |                    |            |                    |             | 0.7(2)         | 1.9(1)         |
| Na(33):f                   |            |                    |            |                    |             | 2.0(8)         | -1.2(3)        |
| Si,Al:B(R <sup>2</sup> )   | 1.1(1)     | 2.0                | 0.9(1)     | 2.0                | 1.9(2)      | 0.04(4)        | 2.1(2)         |
| O:B(R <sup>2</sup> )       | 2.6(1)     | 3.4                | 2.6(1)     | 3.2                | 2.4(1)      | 0.7(2)         | 1.9(1)         |
| Na:B(R <sup>2</sup> )      | 3.3(3)     | 6.3                | 3.0(3)     | 4.5                | 1.9(2)      | 2.0(8)         | -1.2(3)        |
| $\alpha$ (R <sup>2</sup> ) | 24.5693(5) | ---                | 24.5692(5) | ---                | 24.6226(10) | 24.6143(17)    | 24.5613(17)    |
| $\alpha$ (deg)             | 90         | ---                | 90         | ---                | 90          | 89.698(5)      | 89.585(6)      |
| R <sub>I</sub>             | 0.091      | ---                | 0.086      | ---                | 0.097       | 0.080          | 0.116          |
| R <sub>WP</sub>            | 0.174      | ---                | 0.169      | ---                | 0.221       | 0.207          | 0.201          |
| R <sub>E</sub>             | 0.102      | ---                | 0.102      | ---                | 0.191       | 0.188          | 0.160          |
| N                          | 176        | ---                | 176        | ---                | 142         | 292            | 625            |

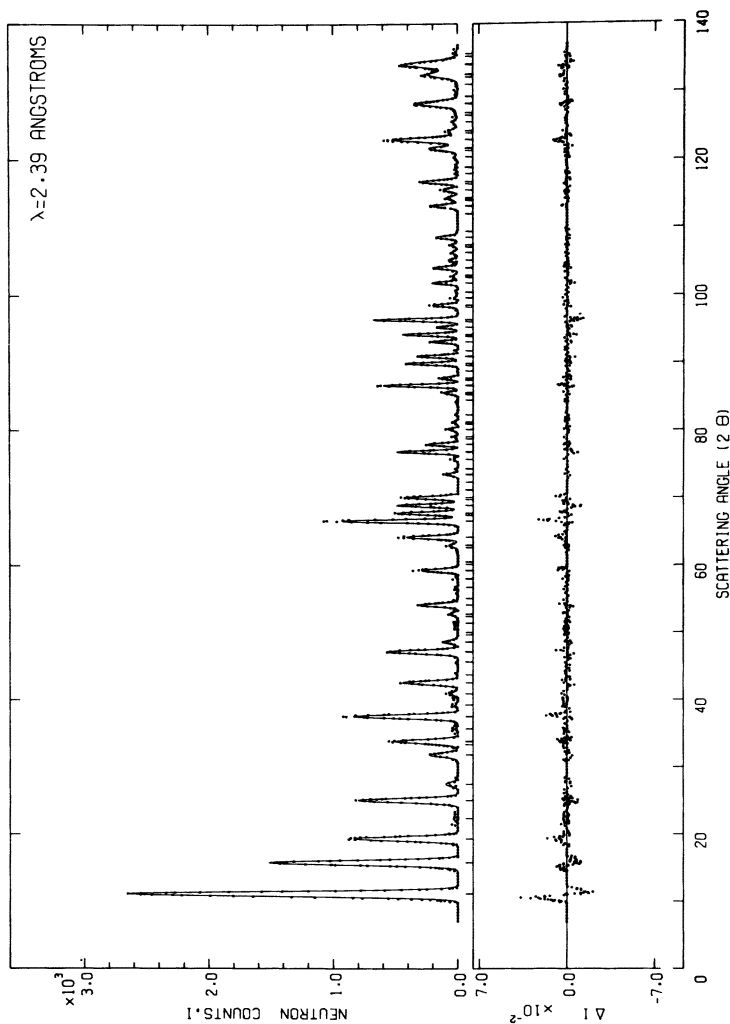


Figure 4.

Profile and difference plot for Na-A zeolite at 603 K. The short vertical markers below the pattern represent allowed reflections. Background intensities were about 400 at  $9^\circ$ , 300 at  $14^\circ$ , 200 at  $24^\circ$ , 100 at  $45^\circ$  and 50 at  $100^\circ$ . Small regions in the vicinity of  $61^\circ$ ,  $72^\circ$  and  $111^\circ$  were excluded because of overlap with Al peaks from the sample holder.

a value of 1.2(1)†† was obtained, with  $R_{WP}$  remaining at 0.169. A refinement with Si and Al fixed in the "wrong" sites gave an  $R_{WP}$  of 0.171.

367 K The final results for Fm3c with variable Na occupancies are listed in column 3 of Table II. The esd's are noticeably higher than at 603 K, but otherwise there do not appear to be any systematic differences. In particular, the Na occupancies are essentially unchanged.

296 K This data set was collected over the angular range  $7-91^\circ$ , and showed clear signs of a distortion, but no indication of any intensity at the (hhl) positions with  $l$  odd.

In the first stages of refinement, the positional parameters were constrained to Fm3c symmetry, the Na occupancies were fixed at the X-ray values, but the rhombohedral angle was allowed to vary. Then the three sets of Na sites were split into seven with  $R\bar{F}3c$  symmetry, i.e. Na(11) and Na(12) in 16(c) and 48(f) sites, Na(21) and Na(22) in two sets of 48(f) sites, and Na(31), Na(32) and Na(33) in a further set of 48(f) sites and two sets of 24(e) sites respectively. The Na(21) and Na(22) occupancies changed from initial values of 0.25 in each case to values of 0.59(8) and -0.09(8) respectively. The latter was therefore fixed at zero. In view of the large esd's for the Na(32) and Na(33) sites, and a high correlation coefficient of -0.96, these occupancies were constrained to be equal in the final cycles of refinement.

We therefore conclude that there is strong evidence for interpreting the cubic-rhombohedral transition in terms of ordering of Na(2) ions. The decrease in  $R_{WP}$  is small, but the ordered model contains only two additional parameters and the improvement in  $R_{WP}$  is comparable to those which follow from relaxation of the more restrictive constraints described above.

4.5 K These data were collected with the analyzer in the (004) position over the angular region  $5 - 135^\circ$ . The occupancy of the Na(22) site again refined to a small negative value, and was therefore set to zero in the final cycles of refinement. Some idea of the intrinsic complexity of the pattern can be gained from the fact that there are 625 reflections. The refined value of the rhombohedral angle  $\alpha$  is  $89.585(6)^\circ$ , in good agreement with the two-peak fit to (880).

Interpretation The results obtained for the cubic phase are less accurate than but generally consistent with the single crystal X-ray results.(4) The one obvious discrepancy involving the position of the Na(3) ions appears to be an artifact connected

---

††Here and elsewhere in the paper, the figure in parentheses is the esd referred to the least significant digit(s).

with the presence of water molecules in the channels as already mentioned. The neutron data also provide direct confirmation of ordering of Si and Al. The occupancy factors of the three sets of Na sites also agree well with the X-ray values, and do not change as a function of temperature in the range studied.

In the rhombohedral region, the small distortion and high degree of overlap, the rather poor peak-to-background intensity ratio, and the large number of additional parameters lead us to conclude that a full structure refinement would give ambiguous results. However, some progress in this direction has been achieved with a simple model involving ordering of Na ions on sites with rhombohedral  $R\bar{3}c$  symmetry but otherwise no relaxation of Fm $\bar{3}c$  positional constraints on any of the framework atoms.

The most important conclusion is that the cubic-to-rhombohedral transition is associated with ordering of Na(2) ions. There is basically no change in the overall distribution of Na ions among the three types of ring in the zeolite structure below the transition temperature. There is roughly one Na ion for each of the 6-rings and 8-rings, with the remainder statistically distributed over the 4-rings. However there is ordering of Na(2) into two of the four positions associated with an 8-ring which are equivalent in Fm $\bar{3}c$  but not in  $R\bar{3}c$  (Figures 5a and 5b). Complete ordering of Na(2) on one of these two sites can be achieved within space groups  $R\bar{3}c$  or  $R\bar{3}2$ , but not  $R\bar{3}$  (Figures 5c, 5d and 5e).

Comparison of the positional parameters above the transition with those obtained at 296 K and 4.5 K reveals some rather large differences and these parameters can be regarded as only approximate, nevertheless, it is worth noting that the average Si-O and Al-O bond lengths are 1.60 and 1.73Å at 296 K, and 1.62 and 1.70Å at 4.5 K, in reasonable agreement with those obtained in the cubic phase.

### Conclusion

There are thus two main conclusions to the present study of NaA. The  $^{29}\text{Si}$ -NMR data demonstrate unequivocally that the ordering scheme for Si and Al is 4:0 and the neutron diffraction data show that the rhombohedral symmetry observed at room temperature and below can be attributed to ordering of Na(2) ions with  $R\bar{3}c$  symmetry. The transition to cubic symmetry occurs at about 335K.

### Acknowledgments

We would like to acknowledge the provision of the NMR samples and encouragement in this work by E.M. Flanigen and R.L. Patton of Union Carbide Corporation. We would also like to thank S.M. Shapiro of Brookhaven National Laboratory for helpful discussions. The work performed at Brookhaven National Laboratory was supported by the Division of Materials Sciences U.S. Department of Energy under contract DE-AC02-76CH00016.

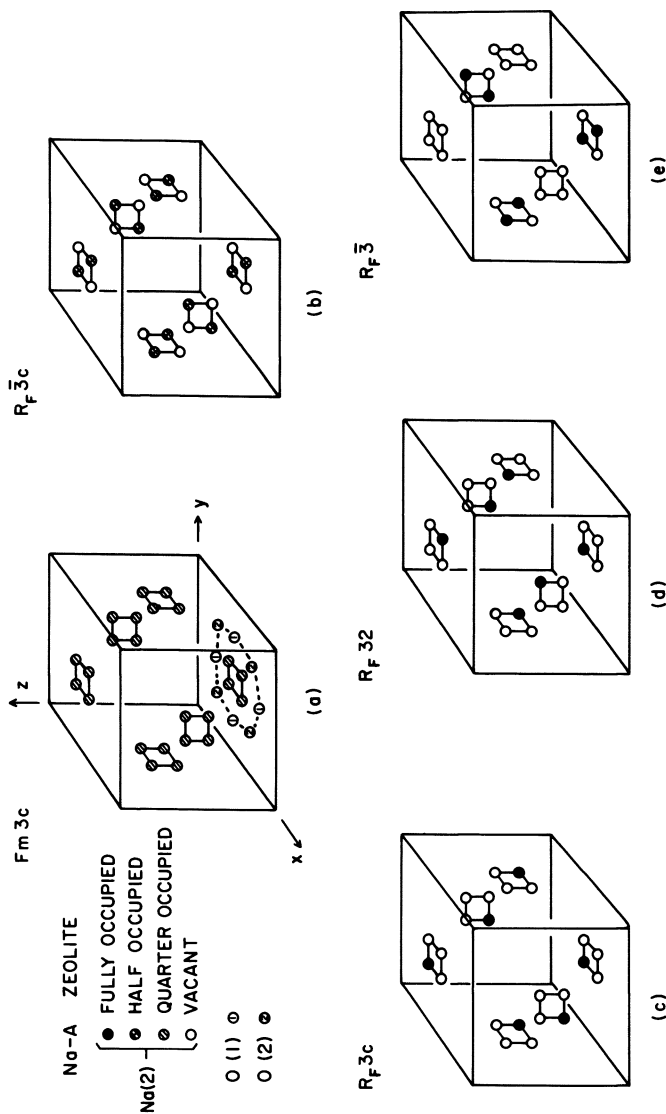


Figure 5.  
Schematic illustration of ordering of Na(2) ions in Na-A zeolite with an  $Fm\bar{3}c$  symmetry. The four equivalent off-center sites associated with an 8-ring are shown as shaded circles. The O(1) and O(2) atoms of the ring are shown as open circles joined by the cross-hatched circles. The sites represented by open circles joined by the cross-hatched circles are now unoccupied. Examples of complete ordering are shown by the full circles in (c)  $R_{F\bar{3}c}$  (d)  $R_{F32}$  and (e)  $R_{F\bar{3}}$ .

Literature Cited

1. Reed, T.B.; Breck, D.W. Am. Chem. Soc. **78**, 5972 (1956).
2. Gamlich, V.; Meier, W.M. Z. Krist. **133**, 134 (1971).
3. Pluth, J.J.; Smith, J.V. J. Phys. Chem. **83**, 741 (1979).
4. Pluth, J.J.; Smith, J.V. J. Am. Chem. Soc. **102**, 4704 (1980).
5. Bursill, L.A.; Lodge, E.A.; Thomas, J.M.; Cheetham, A.K. J. Phys. Chem. **85**, 2409 (1981).
6. Bursill, L.A.; Lodge, E.A. Thomas, J.M. Nature **286**, 113 (1980); Thomas, J.M.; Millward, G.R.; Bursill, L.A. Phil. Trans. Roy. Soc. London A300, 43 (1981).
7. Engelhardt, G.; Zeigan, D.; Lippmaa, E.; Magi, M.Z. Anorg. Allgem. Chem. **468**, 35 (1980).
8. Klinowski, J.; Thomas, J.M.; Fyfe, C.A.; Hartman, J.S. J. Phys. Chem. **85**, 2590 (1981).
9. Thomas, J.M.; Bursill, L.A.; Lodge, E.A.; Cheetham, A.K.; Fyfe, C.A. J. Chem. Soc., Chem. Commun. **276** (1981).
10. Loewenstein, W. Am. Mineral. **39**, 92 (1954).
11. Lipmaa, E.; Magi, M.; Samoson, A.; Engelhardt G.; Grimmer, A.R. J. Am. Chem. Soc. **102**, 4889 (1980).
12. Lipmaa, E.; Magi, M.; Samoson, A.; Tarmak, M.; Engelhardt, G. J. Am. Chem. Soc. **103**, 4992 (1981).
13. For short accounts of these investigations, see Jarman, R.H.; Melchior, M.T.; Vaughan, D.E.W. Symposium on Intrazeolite Chemistry, Amer. Chem. Soc. National Meeting, Kansas City, September (1982), to be published; Bennett, J.M.; Blackwell, C.S.; and Cox, D.E.; *ibid*; Melchior, M.T.; *ibid*; Vaughan, D.E.W.; Melchior, M.T.; and Jacobson, A.J.; *ibid*.
14. Thomas, J.M.; Fyfe, C.A.; Ramdas, S.; Klinowski, J. and Gobbi, G.C. J. Phys. Chem **86**, 3061 (1982); Klinowski, J.; Ramdas, S.; Thomas, J.M.; Fyfe, C.A. and Hartman, J.S. J. Chem. Soc., Faraday Trans. II, **78**, 1025 (1982); Anderson, M.W.; Klinowski, J.; Ramsack, S.; Thomas, J.M.; Fyfe, C.A. and Gobbi, G.C. Symposium on Intrazeolite Chemistry, Amer. Chem. Soc. National Meeting, Kansas City, September (1982), to be published.
15. Cheetham, A.K.; Fyfe, C.A.; Smith, J.V.; Thomas, J.M. J. Chem. Soc., Chem. Commun. **823** (1982); Cheetham, A.K.; Eddy, M.M., Symposium on Intrazeolite Chemistry, Amer. Chem. Soc. National Meeting, Kansas City, September (1982), to be published.
16. Adams, J.M.; Haselden, D.A. J. Chem. Soc., Chem. Commun. **822** (1982).
17. Rietveld, H.M. J. Appl. Cryst. **2**, 65 (1969).
18. Barrer, R.M.; Denny, P.J.; Flanigen, E.M. U.S. Patent 3,306, 922 (1967).
19. Koester, L.; Rauch, H. "Summary of Neutron Scattering Lengths"; International Atomic Energy Agency Contract 2517/RB,

RECEIVED November 4, 1982



## New Approaches to the Structural Characterization of Zeolites: Magic-Angle Spinning NMR (MASNMR)

J. M. THOMAS, J. KLINOWSKY, S. RAMADAS, and M. W. ANDERSON

University of Cambridge, Department of Physical Chemistry, Cambridge  
CB2 1EP, England

C. A. FYFE and G. C. GOBBI

University of Guelph, College of Physical Science, Guelph-Waterloo Centre for  
Graduate Work in Chemistry, Guelph, Ontario N1G 2W1, Canada

The advantages and successes achieved by the application of  $^{29}\text{Si}$  and  $^{27}\text{Al}$  high-resolution solid state NMR to the study of zeolites are briefly reviewed. In particular the ease with six-fold coordination of either Si or Al is distinguished from tetrahedrally coordinated analogues is illustrated.  $^{29}\text{Si}$  MASNMR can readily distinguish crystallographically distinct  $\text{Si}(\text{OSi})_4$  groups in highly siliceous solids such as silicalite; it enables the framework Si/Al ratio to be quantitatively and conveniently determined; it yields the number of neighbouring Al atoms bound to a central Si, via oxygen, and this, in turn, throws light on Si,Al ordering. Specific ordering schemes can thus be proposed for zeolites X and Y covering a range of Si/Al ratios.  $^{29}\text{Si}$  MASNMR measurements on zeolite ZK-4 confirm that the  $^{29}\text{Si}$  spectrum of zeolite A points to there being strict alternation of  $\text{SiO}_4$  and  $\text{AlO}_4$  tetrahedra in this framework when the Si/Al ratio is unity.  $^{27}\text{Al}$  MASNMR shows that the Al present in silicalite is bonded tetrahedrally and possesses an isotropic chemical shift close to that of Al in ZSM-5. A few results, and the structural conclusions to which they lead of  $^{13}\text{C}$ -,  $^{71}\text{Ga}$ - and  $^{17}\text{O}$ - MASNMR are also presented.

Physicists have long been aware of the power and usefulness of high-resolution solid-state NMR. Even prior to the development of cross-polarization, in the early to mid-seventies, it was clear that, by recording the nuclear magnetic resonance spectrum when the sample was spun at the magic angle ( $54^\circ 44'$ ) to the magnetic field, chemical shifts could be readily identified

0097-6156/83/0218-0159\$06.50/0

© 1983 American Chemical Society

(1) using solid samples. This meant that structural information, akin to that routinely inferred from solution ( $^1\text{H}$  and  $^{13}\text{C}$  NMR) measurements by organic chemists, could now be derived from spectra obtained with polycrystalline and non-crystalline specimens. The chemical shift values are characteristic of crystallographically and chemically distinct environments. An admirable summary of the advances achieved in the study of non-zeolitic solids using MASNMR, with nuclei other than  $^{29}\text{Si}$  and  $^{27}\text{Al}$ , has been given recently by Andrew (2), the discoverer of the technique.

On the basis of the pioneering work of Lippmaa *et al* (3) on  $^{29}\text{Si}$  MASNMR, and that of Engelhardt *et al* (4) on  $^{29}\text{Si}$  NMR of silicate solutions, it became apparent that  $^{29}\text{Si}$  chemical shifts are sensitive to the substituents present in the second coordination sphere. Correlations between chemical shift and structure were established, and these were soon utilized (5-7) for the structural studies of both soluble and insoluble silicates and aluminosilicates. A wide variety of zeolitic solids has by now been investigated (6-18) using  $^{29}\text{Si}$ ,  $^{27}\text{Al}$  and several other nuclei. The degree of structural insight achievable with MASNMR is exceptional, since it probes the immediate environment of a particular nucleus (provided it has a finite magnetogyric ratio) more or less irrespective of whether the sample itself is crystalline or amorphous. A measure of the practical value of this approach is reflected by the fact that most of the major commercial manufacturers and users of aluminosilicates have recently undertaken MASNMR studies for research and development purposes (12, 19). The scepticism expressed in some quarters as to the validity of the approach seems to have evaporated, and the techniques of  $^{29}\text{Si}$  and  $^{27}\text{Al}$  MASNMR have now gained general acceptance.

From the outset, it was clear that  $^{29}\text{Si}$  MASNMR resonances were, to some degree, structure-sensitive. The correlation charts of Lippmaa *et al* (5, 9) and our own (7, 10) show a range of values at which a  $^{29}\text{Si}$  nucleus in a particular environment ( $\text{Si}(\text{OAl})_{4-n}(\text{OSi})_n$  with  $n = 0, 1, 2, 3,$  or  $4$ ) was expected to resonate: this point emerges clearly from Table 1. In this respect MASNMR is similar to IR, UV and Raman and solution NMR spectroscopies for which there are comparable charts that are constructed, as in  $^{29}\text{Si}$  MASNMR, solid-state spectroscopy, largely on the basis of accumulated practical experience, rather than on theoretical calculations.

Although good MASNMR  $^{29}\text{Si}$  spectra may be obtained at ( $^1\text{H}$ ) frequencies of 90, 200, 250 and 300 MHz, we have found (17) the advantages that accrue from utilizing the highest fields to be most valuable. Improvements in sensitivity alone justify the recording of spectra under these conditions.

#### Studies of Faujasitic Zeolites (Zeolites X and Y)

The general usefulness and novelty of  $^{29}\text{Si}$ , and, to a lesser

TABLE 1

Ranges of  $^{29}\text{Si}$  MASNMR Chemical Shifts for Zeolitic Aluminosilicates (TMS as reference)

| Primary Coordination   | Notation | Results of the Tallin-Berlin Group <sup>a,b</sup> | Results of the Guelph-Cambridge Group <sup>c,d,e</sup> |
|--|----------|---|--|
| $\begin{array}{c} \text{Al} \\   \\ \text{O} \\   \\ \text{AlOSiOAl} \\   \\ \text{O} \\   \\ \text{Al} \end{array}$ | Si(4Al)  | -83 to -87  | -80 to -90.5   |
| $\begin{array}{c} \text{Al} \\   \\ \text{O} \\   \\ \text{AlOSiOAl} \\   \\ \text{O} \\   \\ \text{Si} \end{array}$ | Si(3Al)  | -88 to -94  | -88 to -97   |
| $\begin{array}{c} \text{Al} \\   \\ \text{O} \\   \\ \text{SiOSiOAl} \\   \\ \text{O} \\   \\ \text{Si} \end{array}$ | Si(2Al)  | -92 to -99  | -93 to -102  |
| $\begin{array}{c} \text{Al} \\   \\ \text{O} \\   \\ \text{SiOSiOSi} \\   \\ \text{O} \\   \\ \text{Si} \end{array}$ | Si(1Al)  | -97 to -105                                       | -97.5 to -107  |
| $\begin{array}{c} \text{Si} \\   \\ \text{O} \\   \\ \text{SiOSiOSi} \\   \\ \text{O} \\   \\ \text{Si} \end{array}$ | Si(0Al)  | -103 to -114                                      | -101.5 to -116.5                                       |

<sup>a</sup> E. Lippmaa, A. Mägi, G. Samoson, G. Engelhardt, A.-R. Grimmer, *J. Amer. Chem. Soc.*, **102**, 4889 (1980).

<sup>b</sup> G. Engelhardt, U. Lohse, E. Lippmaa, M. Tarmak, M. Mägi, *Z. Anorg. Allg. Chem.*, **482**, 49 (1981).

<sup>c</sup> J. Klinowski, J. M. Thomas, C. A. Fyfe and J. S. Hartman, *J. Phys. Chem.*, **85**, 2590 (1981).

<sup>d</sup> J. M. Thomas, C. A. Fyfe, S. Ramdas, J. Klinowski and G. C. Gobbi, *J. Phys. Chem.*, **86**, 3061 (1982).

<sup>e</sup> C. A. Fyfe, J. M. Thomas, J. Klinowski and G. C. Gobbi, *Angewandte Chemie* (in press).

degree,  $^{27}\text{Al}$ , MASNMR in the study of zeolites is perhaps best illustrated by citing the results obtained with and conclusions drawn from faujasitic zeolites (8, 9, 11, 17). When we embarked on these studies they were intended to serve both as a test of the validity of the MASNMR approach and as a vehicle for probing hitherto uncharted depths in the structural and analytical chemistry of zeolites. Our studies proceeded independently of, and essentially simultaneously with, those of Engelhardt *et al.* Our results concur in all major respects: they also agree in most principal respects with those of subsequent studies (12).

The advantages in selecting faujasitic zeolites merit enumeration here.

- (i) First, the Si/Al ratio may be altered (by suitable choice of conditions of growth) in small increments between the extrema of 1.0 and 3.0 while the framework structure — the topology and geometry of the T-O network ( $T = \text{Si/Al}$ ) in tetrahedral coordination — remains unchanged. This enables the spectral characteristics to be monitored as a function of Si/Al ratio, thereby permitting a test of the sensitivity of a given  $^{29}\text{Si}$  environmental resonance upon composition. It also throws light on the question of Si,Al ordering (see below) as this is reflected in the intensity ratios of the respective Si( $n\text{Al}$ ) peaks ( $n = 1, \dots, 4$  being the number of Al's tetrahedrally linked, via oxygen, to a central Si).
- (ii) Second, the enigmatic, and catalytically important process of ultrastabilization in which zeolite Y is converted (20) by suitable heat treatment, to an ultra-stable form, may be directly investigated.
- (iii) Third, the consequences of vapour phase dealumination, effected by using gaseous  $\text{SiCl}_4$ , and to a less effective degree by gaseous  $\text{PCl}_3$ , may be explored.
- (iv) Simple, but useful, point-charge calculations of electrostatic repulsions (between  $^+\text{Al}^{3+}$  ions within the aluminosilicate framework) are readily carried out (11) with the faujasite structure since, in this structure, unlike those of many others, zeolites and protecto-silicates, there is only one type of tetrahedral site.
- (v) Zeolitic gallosilicates possessing the faujasite (as well as the sodalite and analcite) structure may be readily prepared so that, in principle, by recording the appropriate  $^{29}\text{Si}$ ,  $^{27}\text{Al}$  and  $^{71}\text{Ga}$  MASNMR spectra information may be obtained pertaining to Si,Al and Si,Ga ordering schemes.

Some of our results have been presented and interpreted elsewhere others are still in the course of assessment. A few

typical spectra, along with computer-simulated analogues (based on Gaussian peak shapes) are shown in Figure 1, from which it is seen that there is a gradual evolution in the pattern of the peaks. The 4:0 peak (i.e. Si(0Al), otherwise designated Si(4Al)) dominates at low Si/Al; indeed at Si/Al = 1.0, there is but a single peak, centred at -84.0 ppm w.r.t. tetramethylsilane (TMS). These facts disclose that there is strict Si,Al alternation in zeolite X of composition 1.0 and, that Loewenstein's rule (21) which forbids the occurrence of Al-O-Al linkages in tetrahedrally bonded aluminosilicates is obeyed. Many other conclusions also stand out. They are as follows:

- (a) Whenever two or more resolvable Si(nAl) peaks occur in  $^{29}\text{Si}$  MASNMR spectra (with  $n \neq \text{zero}$ ), it is possible to compute quantitatively from the peak intensities the Si/Al ratio of the aluminosilicate (i.e. of the tetrahedrally bonded framework) provided that Loewenstein's rule is obeyed. As this rule is obeyed, it follows that each Si-O-Al linkage in a Si(nAl) structural units is equivalent to Al/4 atoms so that the Si/Al ratio in the tetrahedrally bonded anionic framework is given by:

$$(\text{Si/Al})_{^{29}\text{Si MASNMR}} = \frac{\sum_{\underline{n}=0}^4 I_{\text{Si}(\underline{n}\text{Al})}}{\sum_{\underline{n}=0}^4 0.25 \underline{n} I_{\text{Si}(\underline{n}\text{Al})}}$$

where  $I_{\text{Si}(\underline{n}\text{Al})}$  stands for the  $^{29}\text{Si}$  intensity for the peak in which a central Si atom is surrounded by  $\underline{n}\text{Al}$  and  $(4-\underline{n})$  Si atoms via oxygen linkages. This equation is exceptionally useful and reliable (9, 11). Inter alia, it enables a direct determination of the framework Si/Al ratio, unencumbered by uncertainties introduced (as they invariably are in wet chemical and other non-discriminatory techniques) by the presence of either occluded aluminous cations, detrital silica and other impurities such as silica-alumina gels or cristobalite. Neither X-ray fluorescence nor neutron activation analysis, because each is global, in the sense that it encompasses all the atoms present irrespective of their state of chemical combination, possesses the discriminatory analytical power of  $^{29}\text{Si}$  MASNMR.

- (b) Information about Si,Al ordering in the aluminosilicate framework, emerges from the quantitative values of the Si(nAl) intensities (such as those shown in Figure 1). It transpires that the tendency to order is less pronounced the higher the value of the Si/Al ratio. By matching the computed intensities for a possible ordering scheme with those observed taking due recognition of other constraints, such as unit cell repeat distances and crystallographic space group, we may arrive at plausible ordering schemes for a given Si/Al ratio. Thus, while both ordering schemes are

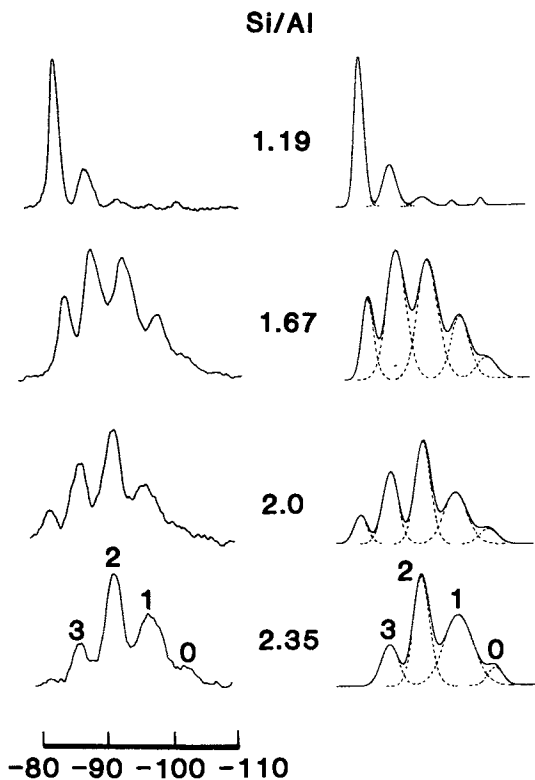


Figure 1.

A selection of the high resolution  $^{29}\text{Si}$  MASNMR spectra of synthetic NaX and NaY at 79.80 MHz. The left-hand columns show the observed spectra, those on the right are the computer-simulated analogues, with the deconvolution drawn as dotted lines. Si(nAl) peaks are identified by the n above the peak.

compatible with  $^{29}\text{Si}$  MASNMR spectra, we favour the model shown in Figure 2(a) over that in Figure 2(b), as the former retains translational periodicity between sodalite cages A and C or B and D whereas the latter does not.

As the Si/Al ratio increases further the tendency for ordering of the Si and Al in the framework diminishes progressively. There are even indications that, beyond Si/Al of ca 2.0, a random model (subject to the proviso of Loewenstein's rule) is applicable. In this connection it is noteworthy that, in a sample of 17-year old synthetic faujasite which had crystallized out at room temperature from a nutrient aluminosilicate gel prepared by Dr. C. V. McDaniel of the W. R. Grace & co., no strong preference for a well-defined, Si/Al ratio (representing 'integral' values of Si and Al ratios in the unit cell) was observed (Figure 3).

- (c) MASNMR spectra yield information pertaining to the coordination of Al in zeolites since the  $^{27}\text{Al}$  shifts corresponding to 4- and 6- coordination are widely separated from one another (see Figure 4). This fact is turned to good advantage in monitoring the progress of dealumination of zeolites either by exposure to  $\text{SiCl}_4$  vapour (22, 23) or by hydrothermal treatment. Identifying the coordination of Al in this way is a much more sensitive technique than other available methods such as those based on shifts in  $\text{AlK}\beta$  X-ray emission lines (24) or on XPS measurements (25).
- (d) Our knowledge of the atomic rearrangements that take place during the process of ultrastabilization of zeolite Y (see refs 14, 20) has been greatly enlarged by the application of  $^{29}\text{Si}$  and  $^{27}\text{Al}$  MASNMR. Fig. 5 shows how it has proved possible to monitor the changes in the environment of Si and the coordination of Al during the course of dealumination. Similar, but less dramatic changes have been observed in studies of the dealumination of mordenite by exposure to  $\text{SiCl}_4$  (26). The build up of a six-coordinated aluminium is seen clearly when mordenite is subjected to prolonged exposure to  $\text{SiCl}_4$  at high temperature. Likewise, when  $\text{PCl}_3$  vapour is used (27) in place of  $\text{SiCl}_4$  (for the dealumination of zeolites Y) we see clear evidence, from  $^{27}\text{Al}$  MASNMR, of the removal of aluminium from the framework and a build-up of six coordinated aluminium. The resulting phosphorus-rich faujasitic zeolite is, however, rather less ordered than the samples correspondingly dealuminated by  $\text{SiCl}_4$  (Fig. 6).

#### Studies of Zeolites A and ZK-4

The earliest indications (5, 6, 28) from  $^{29}\text{Si}$  MASNMR were that, contrary to what had emerged from X-ray studies, zeolite A

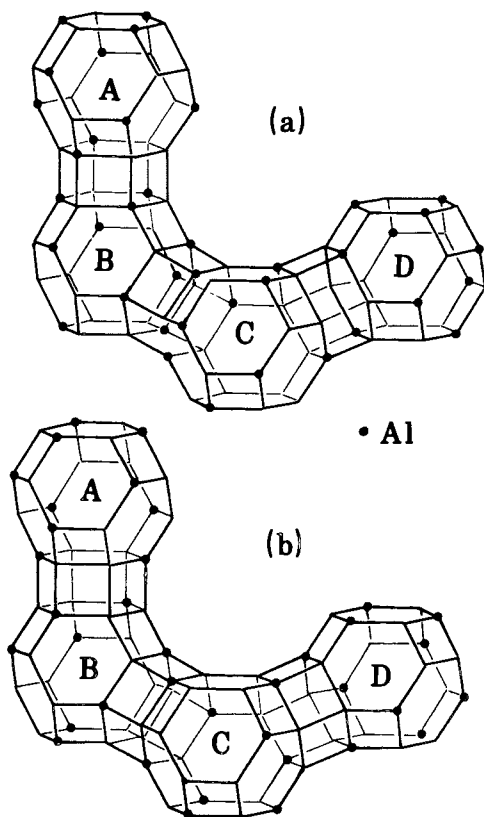


Figure 2.

Schematic illustration of two possible Si,Al ordering schemes for zeolite X with Si/Al = 1.4, both compatible with the observed  $^{29}\text{Si}$  MASNMR spectrum. Based on the observed intensities of Si( $n$ Al) peaks and other arguments — see text — we favour the first of these two alternatives.



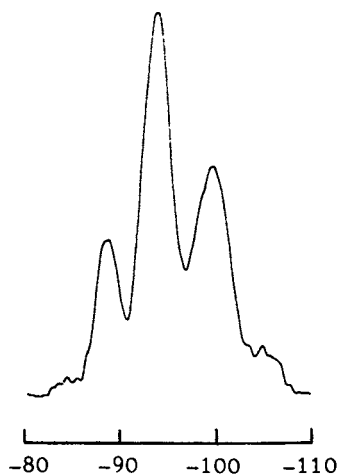


Figure 3.

$^{29}\text{Si}$  MASNMR spectrum of a sample of synthetic Na-Y which had crystallized slowly (over a period of 17 years) at room temperature. Using the equation given in the text we calculate the (Si/Al) framework to be 2.28. This does not correspond to a unique composition, so that the framework must consist of patches or domains of different local composition (e.g. of Si/Al = 16/8, 17/7, 18/6 etc.) Detailed electron microscopic analyses (using microdiffraction and microanalysis) may clarify the nature of the Si,Al disorder. It is clear, however, from results obtained to date that there is no strong tendency for Si,Al ordering otherwise a ratio of 2.28 would not have been obtained.

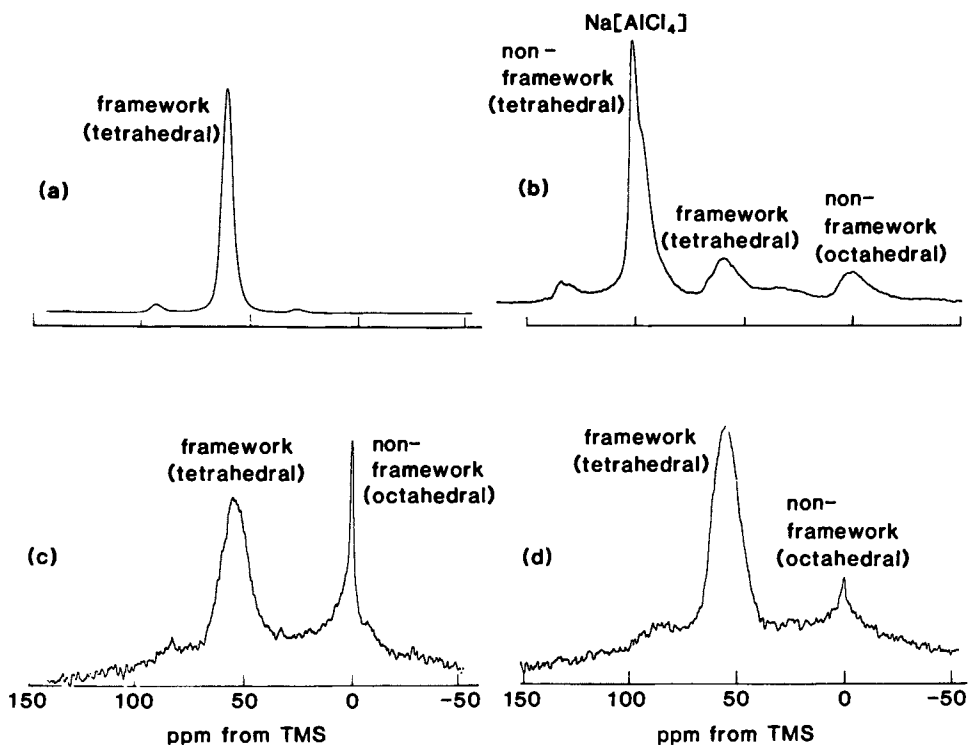


Figure 4.

Dealumination of zeolite NaY using  $\text{SiCl}_4$  vapour studied by  $^{27}\text{Al}$  MASNMR at 104.22 MHz.

- (a) Parent NaY zeolite.
- (b) Dealuminated material before washing.
- (c) After washing with dilute acid.
- (d) After repeated washing.

Note that the aluminium jettisoned from the zeolitic framework is first of all bound tetrahedrally (as  $\text{Na}^+\text{AlCl}_4^-$ ) but after washing adopts octahedral coordination. Note also that, as expected from electroneutrality considerations, the octahedral peak intensity is close to a third of the tetrahedral peak intensity.

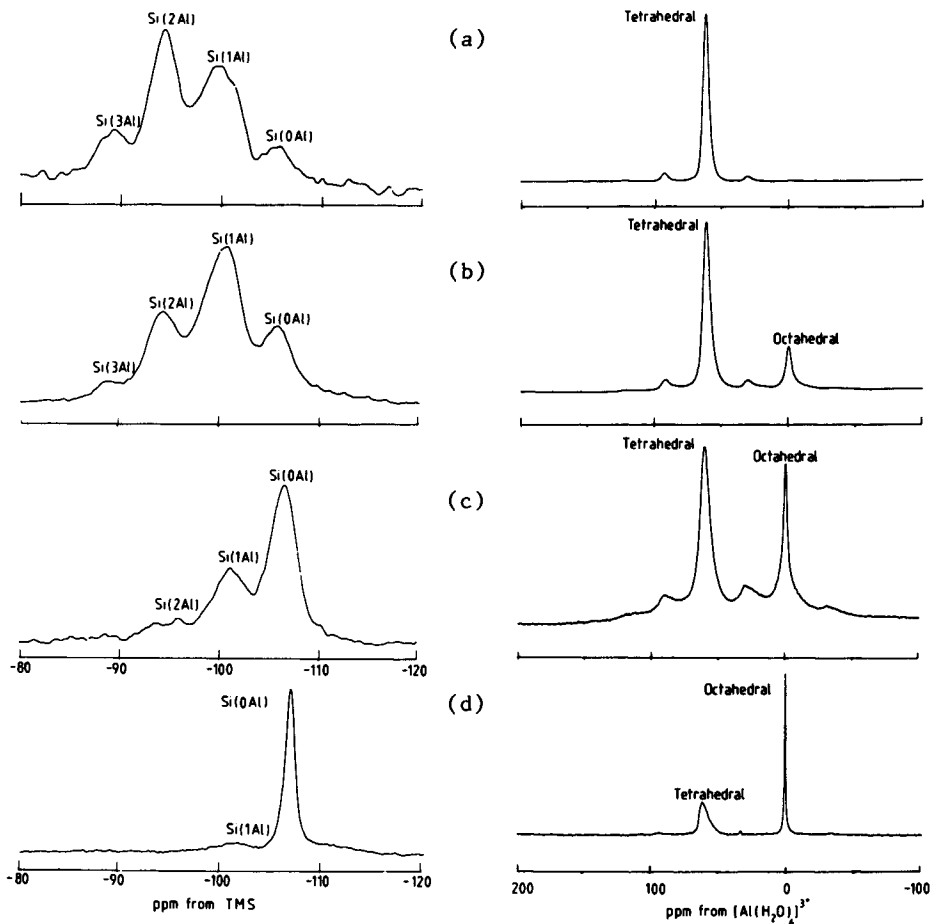


Figure 5.

High-resolution  $^{29}\text{Si}$  (79.80 MHz) and  $^{27}\text{Al}$  (104.22 MHz) MASNMR studies of ultrastabilization of zeolite Y.

- Parent  $\text{NH}_4\text{-Na-Y}$  zeolite.
- After calcining in air for 1 hr at  $400^\circ\text{C}$ . Note changes in  $I_{\text{Si}(n\text{Al})}$  relative intensities.
- After heating to  $700^\circ\text{C}$  for 1 hr in the presence to steam.
- After repeated ion exchange, heating and prolonged leaching with nitric acid. This material is evidently very crystalline (see ref (14) for a fuller discussion).

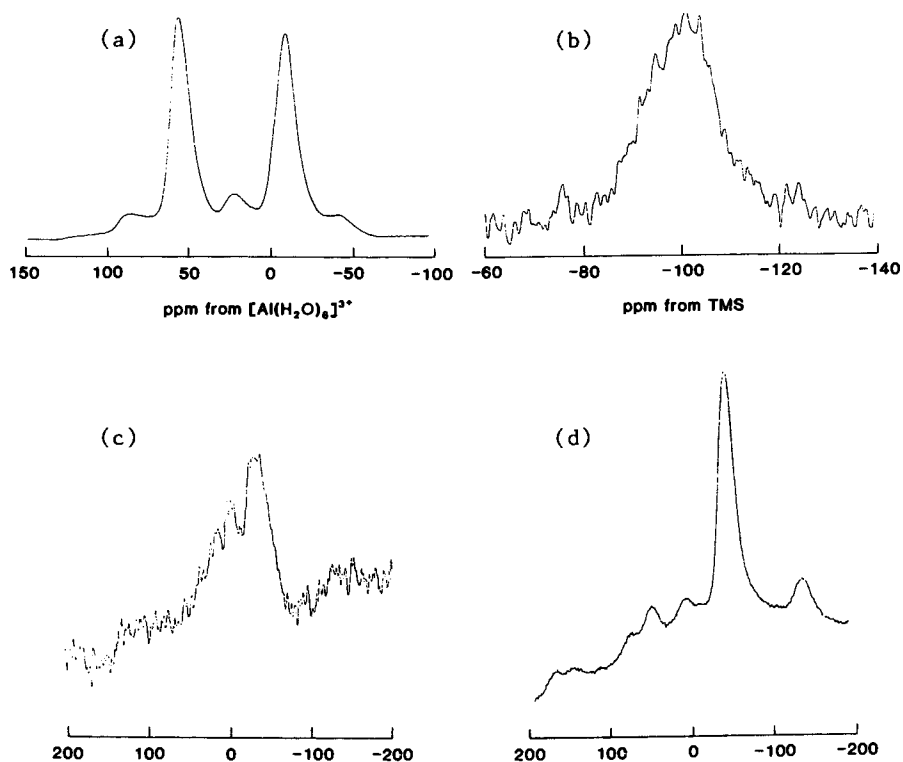


Figure 6.

- (a)  $^{27}\text{Al}$  MASNMR of  $\text{PCl}_3$ -treated Na-Y. The 'octahedral' peak at ca 0.0 ppm signifies that dealumination is effected by  $\text{PCl}_3$ .
- (b)  $^{29}\text{Si}$  MASNMR of  $\text{PCl}_3$ -treated Na-Y, washed with DMSO. The broadened line implies some loss of crystallinity.
- (c)  $^{31}\text{P}$  MASNMR of Na-Y after exposure to  $\text{PCl}_3$  at  $200^\circ\text{C}$  (without washing).
- (d)  $^{31}\text{P}$  MASNMR of Na-Y after exposure to  $\text{PCl}_2$  at  $200^\circ\text{C}$  and after washing with water.

had an ordering scheme in which Si(3Al) predominated. Subsequent work (10, 16) has shown that the single peak in the solid-state spectrum of zeolite A arises from the Si(4Al) not the Si(3Al) environment. One proof that this is so comes from measurements on a series of samples of zeolite ZK-4 where the aluminosilicate framework topology is exactly the same as it is in zeolite A, but the Si/Al ratio may vary from 1.0 to 2.7. Just as the evolution of the spectra in faujasitic zeolites (see Fig. 1) enabled us to pinpoint the peaks corresponding to the five distinct environments (see Table 1), so also do our experiments with ZK-4 lead to similar conclusions. Our results (Fig. 7) leave little doubt that the Si(4Al) peak in this family of zeolites is centred at -88.6 ppm w.r.t. TMS. A resonance at this value of the chemical shift in faujasitic and most other zeolitic structures corresponds to a Si(3Al) environment.

Additional confirmation that the peak at  $-88.5 \pm 1.5$  in the  $^{29}\text{Si}$  resonance for various cation-exchanged forms of zeolite-A ( $\text{Na}^+$ ,  $\text{K}^+$ ,  $\text{Ag}^+$ ,  $\text{Tl}^+$ ,  $\text{Ca}^{2+}$ ,  $\text{Mg}^{2+}$ ,  $\text{Ba}^{2+}$ ,  $\text{La}^{3+}$ ) is correctly assigned to Si(4Al) comes also from our NMR measurements of  $^{17}\text{O}$ -exchanged  $\text{Na}^+$ -A. As only one environment is detected (29) for the  $^{17}\text{O}$  it must follow that there are no significant quantities of Al-O-Al or Si-O-Si bonds in zeolite-A. Al-O-Si bonds clearly predominate. Neutron diffraction (Rietveld refinement) also confirms the 4:0 ordering in zeolite A (30, 31).

The reason why zeolite A has a resonance corresponding to Si(4Al) at  $-88.5 \pm 1.5$  stems from the unique feature of the structure: strained double four-membered rings, with T-O-T angles of  $129^\circ$ ,  $152^\circ$ ,  $152^\circ$  and  $177^\circ$ . We believe that the presence of linear or nearly linear T-O-T linkages modifies the bonding characteristic for a central Si atom in a  $\text{Si}(\text{OAl})_4(\text{OSi})_{4-n}$  unit (10, 32). It is very likely that there are other zeolites in which the chemical shift corresponding to the  $\text{Si}(\text{OAl})_4$  group occurs close to -90 ppm.

When Na-A is heated to beyond  $675^\circ\text{C}$  a marked shift is noted in the Si(4Al) peak. (Another, relatively minor peak also develops) - see Fig. 8. Separate diffraction experiments indicate that Na-A is converted principally to carnegieite, a closer packed structure. When Cs-A is heated in this fashion it, too, shows a marked shift in the  $^{29}\text{Si}$  resonance.  $^{133}\text{Cs}$  MASNMR measurements indicate that there are significant changes in cation environment brought about by heating: the main  $^{133}\text{Cs}$  peak at -89.3 (ppm relative to aqueous  $\text{Cs}_2\text{CO}_3$ ) in the as-prepared Cs-A solid changes to -137 ppm after heating to  $700^\circ\text{C}$  and to -221.5 after a further 8 hr at  $800^\circ\text{C}$ . Conceivably the "burial" of  $\text{Cs}^+$  cations by heat-treatment of  $\text{Cs}^+$ -exchanged zeolite A proceeds in broadly the same fashion as the burial of  $\text{Cs}^+$  ions in phillipsite which, on heating to very high temperatures, takes up a Cs-feldspar structure.

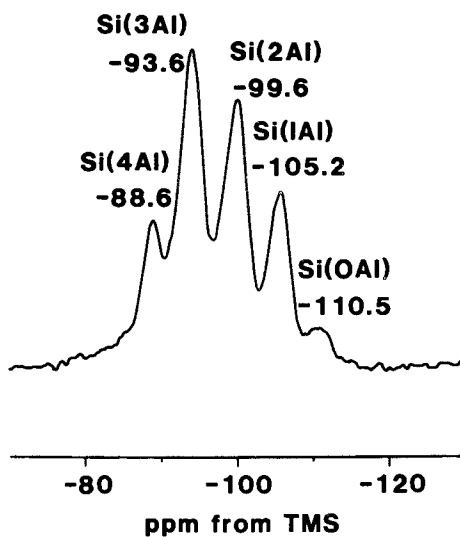


Figure 7.

$^{29}\text{Si}$  MASNMR at 79.8 MHz of zeolite ZK-4 showing five peaks at the chemical shift values indicated corresponding to the silicon environments in the figure. Compare Fig. 1 (for zeolites X and Y) where the Si(3Al) peak has a chemical shift at the value corresponding to Si(4Al) here.

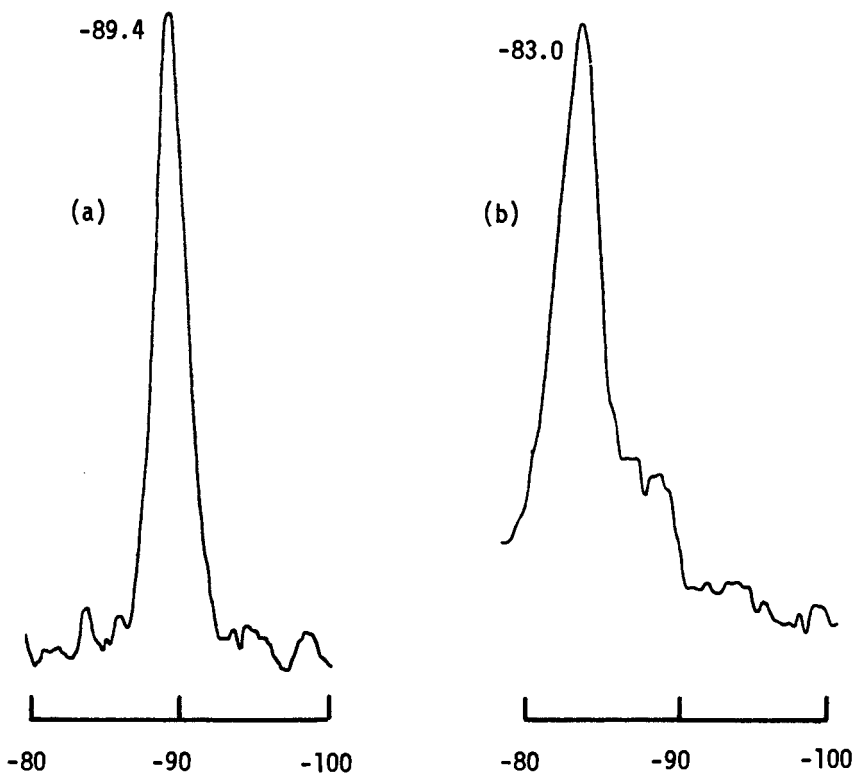


Figure 8.

$^{29}\text{Si}$  MASNMR spectra of zeolite Na-A after heat-treatment at (a) 450°C and (b) 675°C. In (b) the zeolite A has been converted to carnegieite (as identified by diffraction measurements). The Si(4A1) resonance has shifted significantly during this conversion and another resonance has also appeared.

### Zeolitic Gallosilicates

It is relatively easy to replace  $\text{Al}^{3+}$  ions in zeolitic framework by  $\text{Ga}^{3+}$ . K hl *et al* (33) showed that discontinuities in unit cell versus Si/Ga plots were more distinct than corresponding ones in unit cell versus Si/Al plots for the analogous structures (zeolites X and Y in particular). This is clearly indicative of the presence of Si,Ga ordering. This is one reason why MASNMR measurements on gallosilicates possessing open frameworks are timely. Another is bound up with the general understanding of the factors responsible for the observed magnitude of  $^{29}\text{Si}$  MASNMR chemical shifts. As may be seen from Figure 9(a) well-resolved  $^{29}\text{Si}$  peaks are obtained with Ga-Y, but the  $^{27}\text{Al}$  spectrum (Fig. 9(b)), of the residual Al, in line with other  $^{27}\text{Al}$  MASNMR peaks (34) is, in relative terms, less informative. Likewise, gallosodalite (Fig. 9(c)) shows a rich, informative  $^{29}\text{Si}$  spectrum, but the  $^{71}\text{Ga}$  MASNMR spectrum (Fig. 9(d)) is rather too broad for ready interpretation. We are currently engaged in exploring further the structural properties of gallozeolitic structures using multi-nuclear MASNMR spectroscopy. In Figure 9(c) the first peak (at -64.8 ppm) arises from an impurity. The most prominent peak at -75.5 corresponds to the  $\text{Si}(\text{OGa})_4$  group, that at -81.8 to  $\text{Si}(\text{OGa})_3(\text{OSi})$ , and so on. The correctness of this assignment is proven by the fact that the Si/Ga ratio, calculated as described earlier from MASNMR intensities, is found to be 1.23, in excellent agreement with the chemically determined ratio (also 1.23). (There was no detectable Al in this sample of gallosodalite, kindly provided by Dr. M. Barlow).

### Six-coordinated Silicon

In a few naturally occurring silicon-containing structures it is believed that there is six-fold coordination of Si. Stishovite (a high pressure form of  $\text{SiO}_2$ ) is one such material, thaumasite is another. Using samples of stishovite retrieved from Meteor Crater, Arizona, we have found (35) that the  $^{29}\text{Si}$  MASNMR resonance is  $-191.3 \pm 0.2$  ppm from TMS (Figure 10). For comparison quartz has a resonance at -107.4 ppm and low cristobalite at -109.9 ppm. Recently Lippmaa *et al* (36) have reported a  $^{29}\text{Si}$  resonance at -179.5 ppm for thaumasite. Clearly a broad range of structure-sensitive  $^{29}\text{Si}$  MASNMR chemical shifts exists for 6-coordinated, as for 4-coordinated silicon (see work on silicalite reported below). High pressure is used increasingly as a means of synthesizing novel silicates — the production of  $\text{MgSiO}_3$  as a perovskite from clinoenstatite or fosterite is one recent noteworthy example — and it is likely that, in the near future, a much wider range of solids containing 6-coordinated silicon will become available. In due course, knowing the range of chemical shifts taken up by  $\text{Si}(\text{OSi})_6$  groups in slightly different environments,  $^{29}\text{Si}$  MASNMR spectroscopy will serve as a



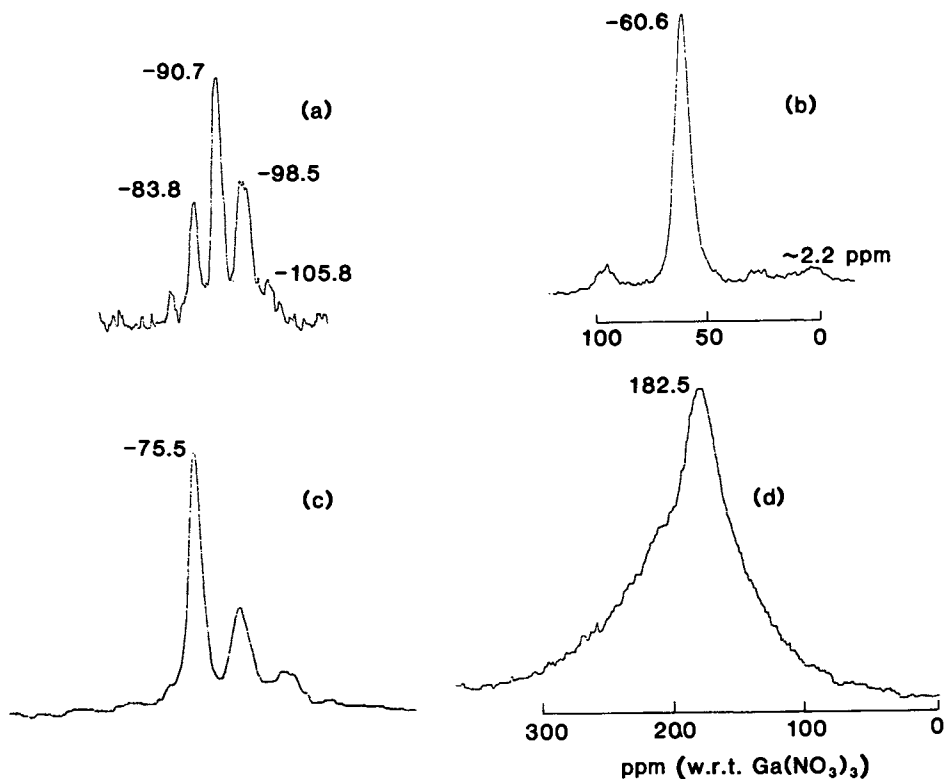


Figure 9.

- (a)  $^{29}\text{Si}$  MASNMR spectrum of a sample of Ga-Y.
- (b)  $^{27}\text{Al}$  MASNMR spectrum of the residual Al in the same Ga-Y sample as in (a).
- (c)  $^{29}\text{Si}$  MASNMR spectrum of a sample of gallosodalite. (No  $^{27}\text{Al}$  MASNMR signal was detectable with this sample).
- (d)  $^{71}\text{Ga}$  MASNMR spectrum of the same gallosodalite as in (c).

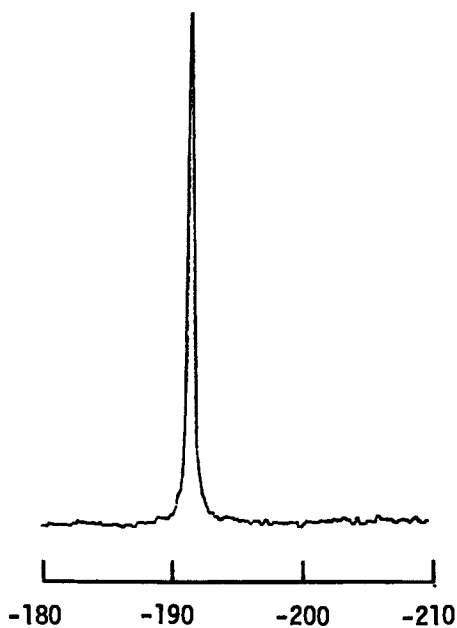


Figure 10.

$^{29}\text{Si}$  MASNMR spectrum of stishovite in which the silicon is in 6-fold coordination. Compare the position of the  $\text{Si}(\text{OSi})_6$  resonance seen here with the range of values found for  $\text{Si}(\text{OSi})_4$  in silicalite (Fig. 11).

useful structural probe for both crystalline (and quasicrystalline) siliceous materials, just as for silicalite discussed below.

Detecting Crystallographically Distinct Tetrahedral Sites in Silicalite: Detection of Aluminium in Tetrahedral Coordination

In many of the uncalcined samples of silicalite, kindly provided by Drs. B. Nay and M. Barlow of B.P. Sunbury, high-resolution  $^{29}\text{Si}$  MASNMR of exceptional quality have been obtained (without resolution enhancement)— see Figure 11. All the peaks and shoulders in this spectrum correspond to distinctly different  $\text{Si}(\text{OSi})_4$  environments. To ascertain how many non-equivalent tetrahedrally bonded Si atoms there are in this protectosilicate we use the intensities of the well-resolved lowest and highest field signals as a base unit for deconvolution. It transpires that there are 24 non-equivalent  $\text{Si}(\text{OSi})_4$  environments in the repeat unit of the structure. Crystallographic determinations of the silicalite structure need to take account of this fact. A space group such as Pnma, favoured in some circles, is not compatible with the MASNMR spectrum.

The original description of silicalite claims that no aluminium exists in the framework structure. Our  $^{27}\text{Al}$  MASNMR spectra are inconsistent with such a claim.  $^{27}\text{Al}$  NMR spectra for both a stationary and a magic-angle-spun sample yield a doublet. Moreover the position of these two peaks are close to the position of the  $^{27}\text{Al}$  resonance of numerous samples of ZSM-5 and well removed from the resonance of  $\text{Ca}_8(\text{Al}_{18}^{0,24})\text{O}_2$ , the "pure aluminium" analogue of sodalite (37). We, therefore, conclude that the aluminium readily detectable in so-called, high purity silicalite resides in the pentasil framework, just as it does in ZSM-5. We cannot, as yet, stipulate the precise tetrahedral sites occupied by the Al, but it is tempting to interpret the doublet as indicating that they are located in the four-membered rings present in the structure. More sophisticated MASNMR studies, preferably at even higher fields, should shed light on this question.

Acknowledgments

We acknowledge support of different kinds from the Universities of Cambridge and Guelph, the S.E.R.C., the B.P. Research Centre, Laporte Industries, W. R. Grace, Exxon and the N.S.E.R.C. of Canada. The spectra were recorded at the South-Western Ontario High-Field Facility, Manager Dr. R. E. Lenkinski.

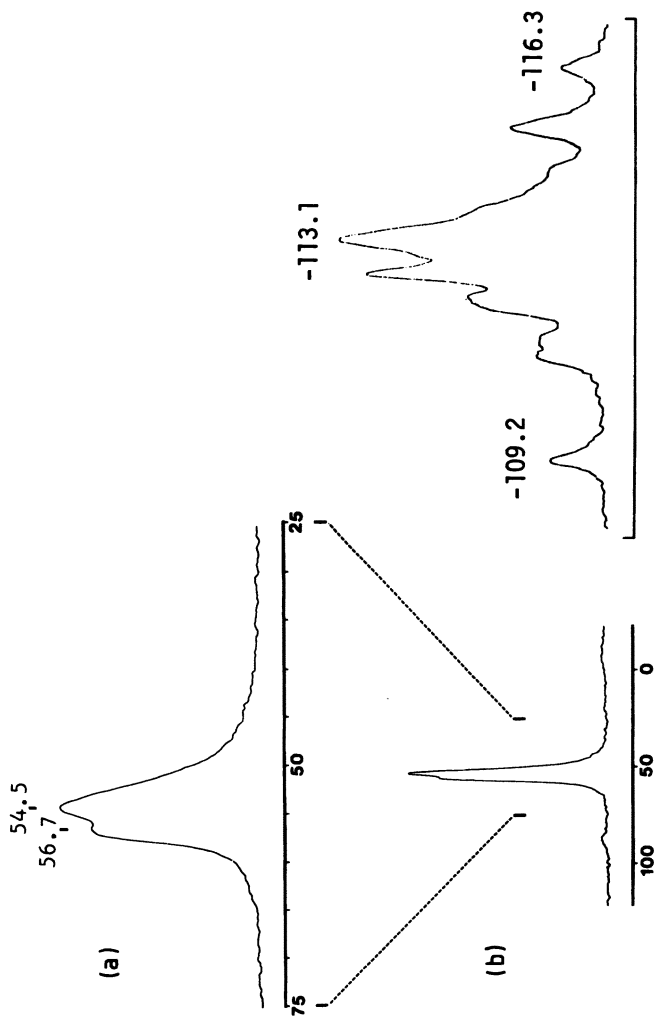


Figure 11.

$^{29}\text{Si}$  MASNMR spectrum of silicalite at 79.80 MHz. (Chemical shifts, as with all other  $^{29}\text{Si}$  MASNMR shown here, are in ppm from TMS). The inset shows a doublet in the  $^{29}\text{Al}$  MASNMR of silicalite attributable to two distinct tetrahedrally bonded Al.

Literature Cited

1. Andrew, E. R. in "Progress in NMR Spectroscopy" ed. by J. Emsley, J. Feeney and L. Sutcliffe, Pergamon Press, London, 1971, 8, 2.
2. Andrew, E. R. *International Reviews in Physical Chemistry* (Butterworths, London) 1981, 1, 195.
3. Lippmaa, E., Alla, M. A., Pehk, T. J. and Engelhardt, G., *J. Am. Chem. Soc.*, 1978, 100, 1929.
4. Engelhardt, G., Altenburg, W., Hoebbel, D. and Wieker, W., *Z. Anorg. Allg. Chemie*, 1977, 437, 249.
5. Lippmaa, E., Mägi, M., Samoson, A., Engelhardt, G. and Grimmer, A.-R., *J. Am. Chem. Soc.*, 1980, 102, 4889.
6. Lippmaa, E., Mägi, M., Samoson, A., Tarmak, M., Engelhardt, G., *J. Am. Chem. Soc.*, 1981, 103, 4992.
7. Klinowski, J., Thomas, J. M., Fyfe, C. A., and Hartman, J. S., *J. Phys. Chem.*, 1981, 85, 2590.
8. Ramdas, S., Thomas, J. M., Klinowski, J., Fyfe, C. A. and Hartman, J. S., *Nature*, 1981, 292, 228.
9. Engelhardt, G., Lohse, U., Lippmaa, E., Tarmak, M., and Mägi, M., *Z. Anorg. Allg. Chemie*, 1981, 482, 49.
10. Thomas, J. M., Fyfe, C. A., Ramdas, S., Klinowski, J. and Gobbi, G. C., *J. Phys. Chem.*, 1982, 86, 3061.
11. Klinowski, J., Ramdas, S., Thomas, J. M., Fyfe, C. A. and Hartman, J. S., *J. Chem. Soc. Faraday Trans 2*, 1982, 78, 1025.
12. Melchior, M. T., Vaughan, D. E. W., Jacobson, A. J., *J. Am. Chem. Soc.*, 1982, 104, 4859.
13. Fyfe, C. A., Gobbi, G. C., Klinowski, J., Thomas, J. M. and Ramdas, S., *Nature*, 1982, 296, 530.
14. Klinowski, J., Thomas, J. M., Fyfe, C. A. and Gobbi, G. C., *Nature*, 1982, 296, 533.
15. Thomas, J. M., Ramdas, S., Millward, G. R., Klinowski, J., Audier, M., Gonzalez-Calbet, J. and Fyfe, C. A., *Journal of Solid State Chemistry* (in press).
16. Melchior, M. T., Vaughan, D. E. W., Jarman, R. H. and Jacobson, A. J., *Nature*, 1982, 298, 455.
17. Engelhardt, G., Lohse, U., Samoson, A., Mägi, M., Tarmak, M. and Lippmaa, E. T., *Zeolites*, 1982, 2, 59.
18. Fyfe, C. A., Thomas, J. M., Klinowski, J. and Gobbi, G. C., *Angewandte Chemie*, 1983 (in press).
19. Vega, A. L., in this book.
20. McDaniel, C. V., and Maher, P. K., "Molecular Sieves", *Soc. Chem. Ind.*, London, 1968, p. 186.
21. Loewenstein, W., *Amer. Mineral.*, 1954, 39, 92.
22. Beyer, H. K. and Belenykaja, I., in "Catalysis by Zeolites" (ed. B. Imelik et al.), Elsevier, Amsterdam, 1980, p.203.

23. Klinowski, J., Thomas, J. M., Audier, M., Vasudevan, S., Fyfe, C. A. and Hartman, J. S., *J. Chem. Soc., Chem. Comm.*, 1981, 570.
24. K $\ddot{u}$ hl, G. H., *J. Phys. Chem. Solids*, 1977, 38, 1259.
25. Adams, I., Thomas, J. M. and Bancroft, G. M., *Earth and Planetary Science Letters*, 1972, 16, 429.
26. Klinowski, J., Thomas, J. M., Anderson, M. W., Fyfe, C. A. and Gobbi, G. C., *Zeolites*, 1983 (in press).
27. Anderson, M. W., Certificate of Post Graduate Studies, Thesis, University of Cambridge, June 1982.
28. Bursill, L. A., Lodge, E. A., Thomas, J. M. and Cheetham, A. K., *J. Phys. Chem.*, 1981, 85, 2409.
29. Klinowski, J., Thomas, J. M., Fyfe, C. A. and Gobbi, G. C. unpublished work.
30. Cheetham, A. K., Eddy, M. N., Jefferson, D. A. and Thomas, J. M., *Nature*, 1982, 299, 24.
31. Cheetham, A. K., Fyfe, C. A., Smith, J. V. and Thomas, J. M. *J. Chem. Soc., Chem. Comm.*, 1982, 823.
32. Ramdas, S. and Thomas, J. M., unpublished work.
33. K $\ddot{u}$ hl, G. H., private communication, 1982; see also Dempsey, E., K $\ddot{u}$ hl, G. H. and Olson, D. H., *J. Phys. Chem.*, 1969, 73, 387.
34. Fyfe, C. A., Gobbi, G. C., Hartman, J. S., Klinowski, J., and Thomas, J. M., *J. Phys. Chem.*, 1982, 86, 1247.
35. Thomas, J. M. Gonzalez-Calbet, J. M., Fyfe, C. A., Gobbi, G. C. and Nicol, M. F. (submitted).
36. Lippmaa, E. T., Samoson, A. V., Brei, V. V. and Gorlov, Yu. I., *Doklady A.N. SSSR*, in press.
37. Ponemarev, V. I., Kheiker, D. M. and Belov, N. V., *Kristallografiya*, 1970, 15, 918.

RECEIVED December 13, 1982

# **New Approaches to the Structural Characterization of Zeolites: High Resolution Electron Microscopy and Optical Diffractometry**

J. M. THOMAS, G. R. MILLWARD, and S. RAMADAS

University of Cambridge, Department of Physical Chemistry,  
Cambridge CB2 1EP, England

M. AUDIER

Institute National Polytechnique de Grenoble, Ecole Nationale Supérieure  
d'Electrochimie et d'Electrometallurgie, Laboratoire d'Adsorption et Reaction  
de Gas sur Solides, ERA CNRS No. 368, Saint-Martin-d'Herès, France

We discuss the combined use of high-resolution electron microscopy, electron diffraction, optical diffractometry and computer graphics for investigating zeolitic structure. Particular attention is given to twinned faujasitic materials and to intergrowth structures in ZSM-5 and ZSM-11 catalysts.

The strength of electron microscopy as a characterization technique lies not only in its ability to probe at near atomic resolution, the internal structure of minute amounts of material, but also in its capacity to reveal directly structural imperfections of the most subtle kind.(1-4) Other investigative methods such as x-ray or neutron diffraction as well as many spectroscopic techniques possess their own individual merits; but they utilize procedures which provide only spatially averaged information. And this is often far less suitable for the characterization of defective, multi-phasic or heterogeneous crystalline (or quasi-crystalline) materials.

In this paper we shall describe how high resolution electron microscopy (HREM) can be used in conjunction with selected area electron diffraction (SAED) to probe the local structure of zeolitic solids (2, 5-8) which are often microcrystalline, multi-phasic or twinned. We shall also refer to the application of optical diffractometry (4, 9-11) as a supplemental procedure either for interpretation of electron micrographs, or for analogue diffraction studies of model systems.

Two years have elapsed since we first reported the rather exacting experimental conditions required to record high-quality,

0097-6156/83/0218-0181\$06.00/0  
© 1983 American Chemical Society

structural images of zeolites. The reader is referred to refs. 5, 6, 7 for specific details. Other than to emphasize the beam sensitivity of zeolitic materials in general, and the need to operate rapidly (e.g. expose specimens for no more than a few minutes to low currents), and to emphasize the advantages of using an image intensifier, we shall concentrate here on some specific results and their interpretation.

One of the advantages that optical diffractometry confers is that it permits, in effect, a further enhancement in spatial resolution. Thus a portion of a micrograph, itself recorded at the highest magnification, can be optically averaged (using a laser beam as source and the region of the micrograph as an object) so as to produce a diffraction pattern from an area of as little  $10^4 \text{ \AA}^2$ .

## RESULTS AND DISCUSSION

### Faujasitic Zeolites

The framework structure of Zeolite-Y is well known (12), consisting of a face-centred cubic array of truncated octahedra (so-called  $\beta$ -cages) linked by T-O-T ( $T \equiv \text{Si}$  or  $\text{Al}$ ) bonds between opposing hexagonal faces. Fig. 1 illustrates a structure image of Zeolite -NaY viewed along the  $[\bar{1}10]$  zone-axis. The large white dots correspond to a projection of the 12-membered apertures of supercages (i.e.  $\alpha$ -cages), and the smaller white dots which constitute an inter-penetrating lattice, are the projections of 6-membered apertures of  $\beta$ -cages (compare this image with the projected skeletal structural drawing shown in the inset).

HREM is particularly suitable for determining the nature and extent of twinning in faujasite crystals which are prone (8) to twinning by reflection across  $\{111\}$  planes as shown in Fig. 2. Multiple twinning (not necessarily on the same member of the family of  $\{111\}$  planes) is common; and in Fig. 3 we show a crystal ( $[\bar{1}10]$  zone-axis orientation) exhibiting the consequences of simultaneous twinning on  $(111)$  and  $(\bar{1}\bar{1}\bar{1})$  planes. In such a situation two further twin planes inclined to  $[\bar{1}10]$  are theoretically possible (i.e.  $(111)$  and  $(\bar{1}\bar{1}\bar{1})$ ), but these twinned individual would be projected along a  $\langle 114 \rangle$  type zone-axis. Fig. 4 shows such a twinned crystal. The optical diffraction patterns of selected regions of the micrograph (black circles) indicate a  $\langle 100 \rangle$  zone-axis for the bottom right area and  $\langle 114 \rangle$  for the top left.

If the twin boundaries constitute true mirror planes, it can be shown that, across these planes Loewenstein's rule must be contravened. If, however, the mirror planes merely reflect the tetrahedral sites of the faujasitic framework and not the actual tenants of such sites Loewenstein's rule need not be



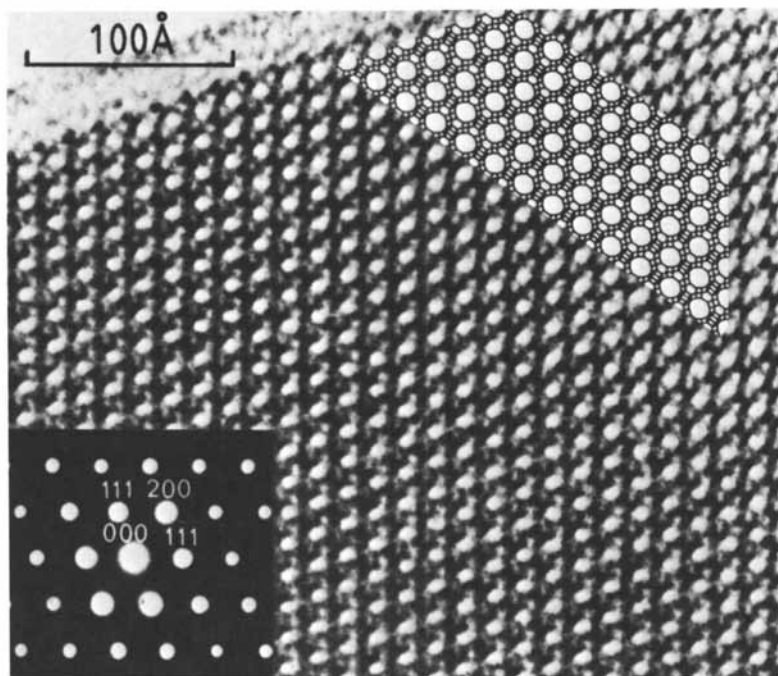


Figure 1.  
High resolution image of Zeolite Na-Y [110] projection.  
Inset shows corresponding electron diffraction pattern  
and a schematic illustration of the skeletal framework.

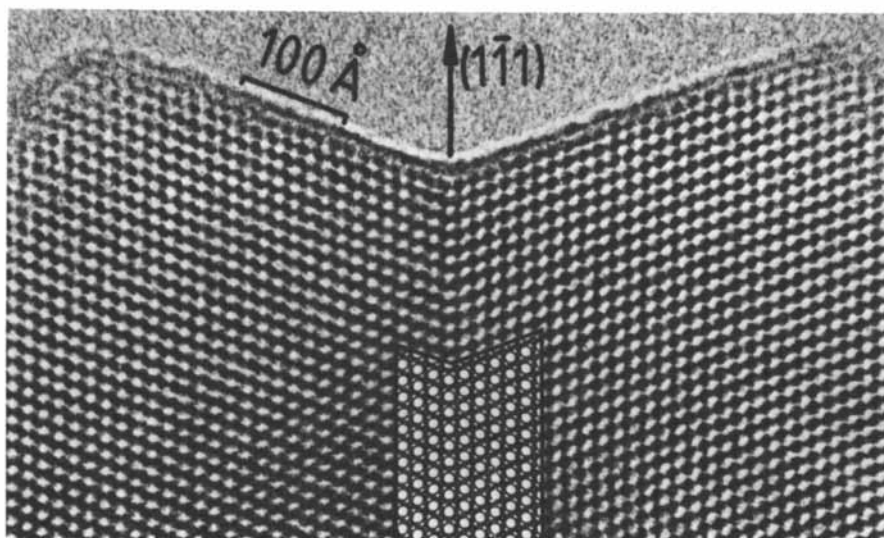


Figure 2.

A twinned, zeolite Na-Y crystal, [110] projection. Twinning across a  $(1\bar{1}1)$  plane is illustrated.

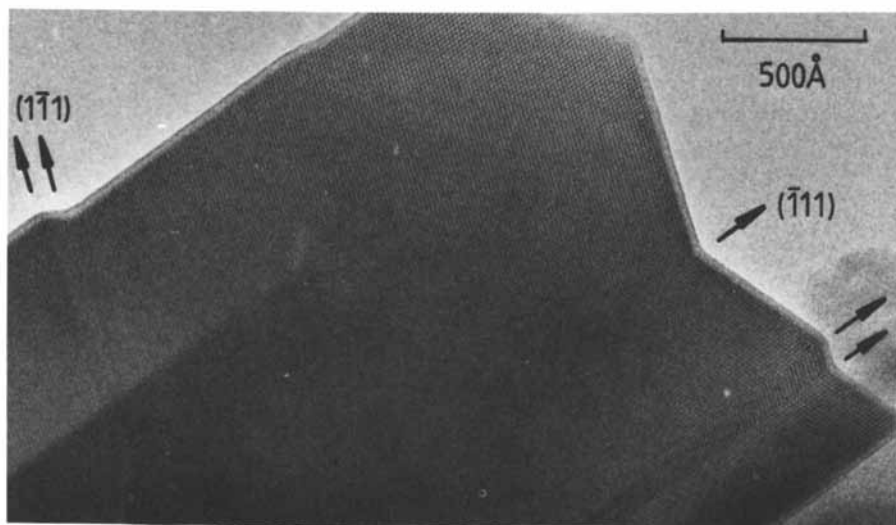


Figure 3.

Twinning on  $(1\bar{1}1)$  and  $(\bar{1}11)$  planes in a crystal of zeolite Na-Y.

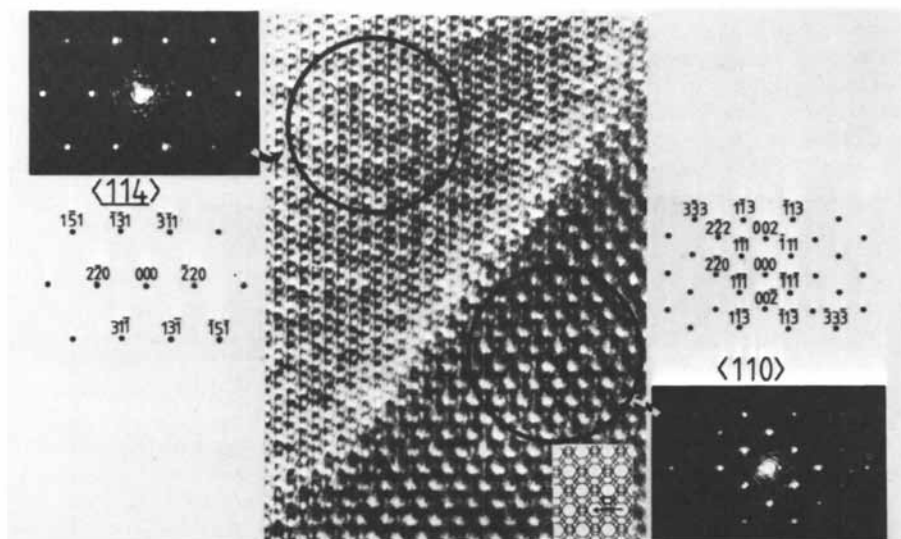


Figure 4.  
 Twinned crystal of zeolite Na-Y. The twin plane is inclined to the direction of viewing. Optical transforms originating from the circled regions are shown and indexed. See text for full explanation.

vitated. A 'local' technique (e.g. FABS) could be of value to ascertain what precisely happens across such boundaries.

### ZSM-5, ZSM-11 and related materials (13-16)

It is widely appreciated that ZSM-5 and ZSM-11 are, structurally, closely related, one being made up of sheets related by inversion the other related by mirror reflection (Fig. 5). ZSM-5 and ZSM-11 readily intergrow (Fig. 5d), and it has been postulated (17,18) that an almost infinite series of intermediate structural types exist. There is circumstantial evidence for such intergrowths.

[010] and [100] zone-axis orientations of ZSM-5 are readily recognized by electron diffraction (Fig. 6): the former yields an essentially rectangular lattice of diffraction spots, the latter a triangular one, as expected from the traditionally accepted space-group assignment (13) of Pnma. Distinction of the two zone-axes by HREM is not altogether so straightforward because of the adverse influence of structural degradation by the electron beam intensities required for satisfactory imaging. Thus, in Fig. 7, insufficient resolution is retained for it to be clear, from a direct inspection of the images, which micrograph corresponds to either of the two possible orientations. However, subsequent optical diffraction analysis (see inset Fig. 7) reveals that the images do, indeed, possess sufficient subtle information for the two zone-axes to be identified; thus emphasizing the strength and attraction of optical diffractometry as a clarifying technique.

By paying considerable attention to the imaging conditions employed and, in particular, by utilizing procedures designed to minimize exposure of the specimen to the electron beam, we have recently been able to improve significantly the attainable resolution. Fig. 8 illustrates the success of this approach. Here the [010] and [100] zone-axis projections of ZSM-5 are now distinguishable by direct visual inspection. Of particular significance is the ability to observe the inversion ( $i$ ) symmetry characteristics of ZSM-5 projected along [010] (compare, very carefully, the fine interchannel image detail of Fig. 8a with the small 5-membered interchannel apertures shown in Fig. 5a). This point is better illustrated in Fig. 9, which shows a high resolution image of a region of ZSM-5 (projected along [010]) containing two "defect" planes exhibiting mirror ( $\sigma$ ) rather than inversion symmetry. In regions of  $i$ -symmetry lines joining the larger of the interchannel 5-membered apertures (marked p in the schematic drawing of Fig. 9) trace a zig-zag path in the a direction, a pattern which can also be discerned in the image below. The presence of a plane of  $\sigma$  symmetry causes a change in "phase" of the zig-zag trace, thus enabling such defects to be readily identified.

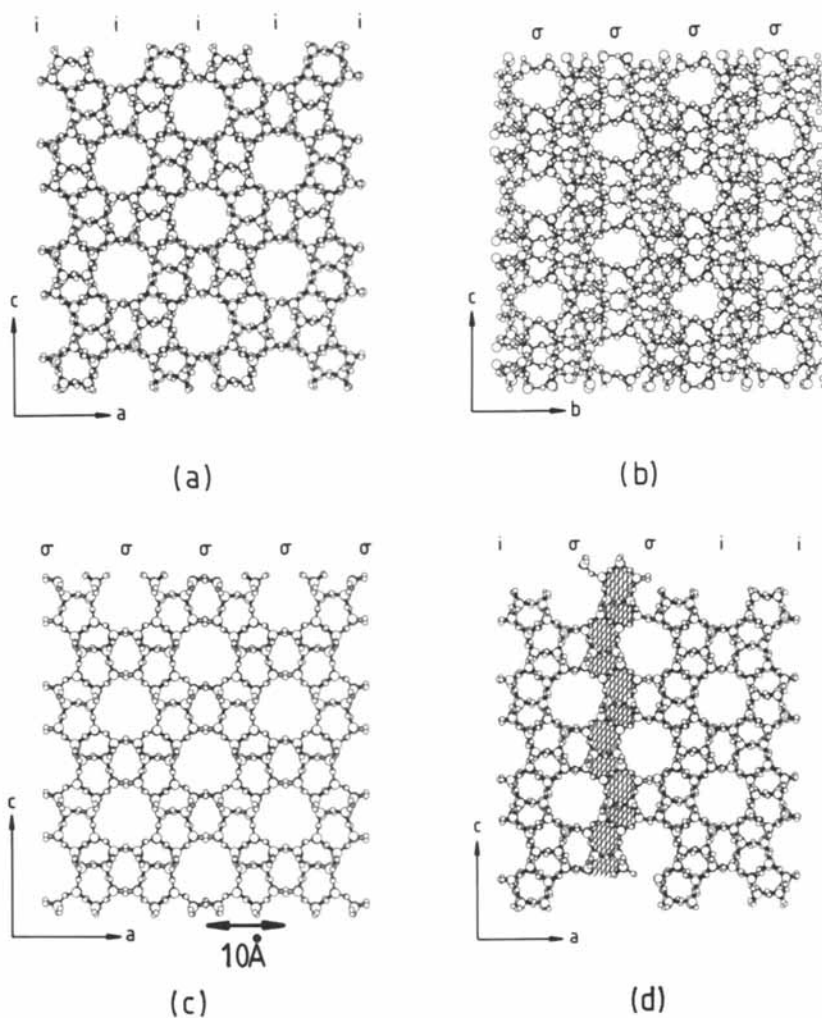
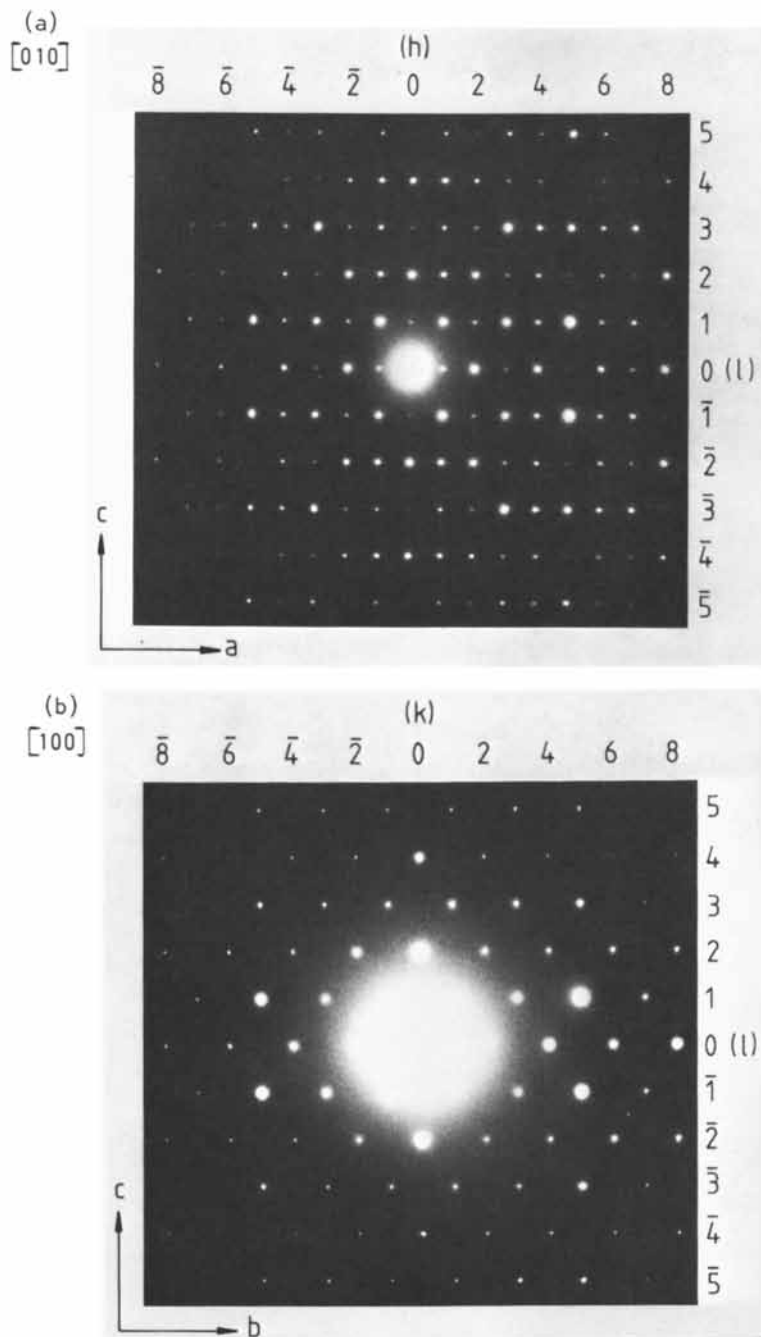


Figure 5. Structure projections of (a) ZSM-5 along  $[010]$ , (b) ZSM-5 along  $[100]$ , (c) ZSM-11 along  $[010]$ , (d) ZSM-5/ZSM-11 intergrowth, along  $[010]$ . Planes of mirror symmetry ( $\sigma$ ) and planes containing centres of inversion ( $i$ ) are indicated. ZSM-11  $[100]$  is identical to ZSM-11  $[010]$ .



**Figure 6.**  
**Selected area electron diffraction patterns of ZSM-5**  
**from circular region of diameter 3,500Å**

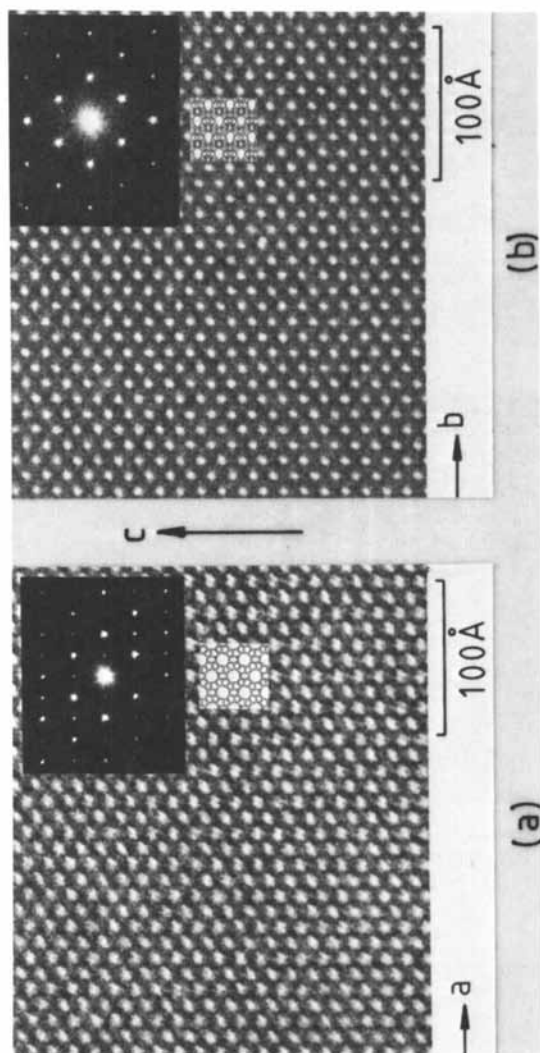


Figure 7.  
Electron micrographs of ZSM-5 projected along  
(a) [010], (b) [100]. Optical diffraction patterns  
(inset) exhibit the rectangular and triangular arrays  
of spots expected for the respective zone-axes. This  
distinction is not directly apparent by mere inspection  
of the images.

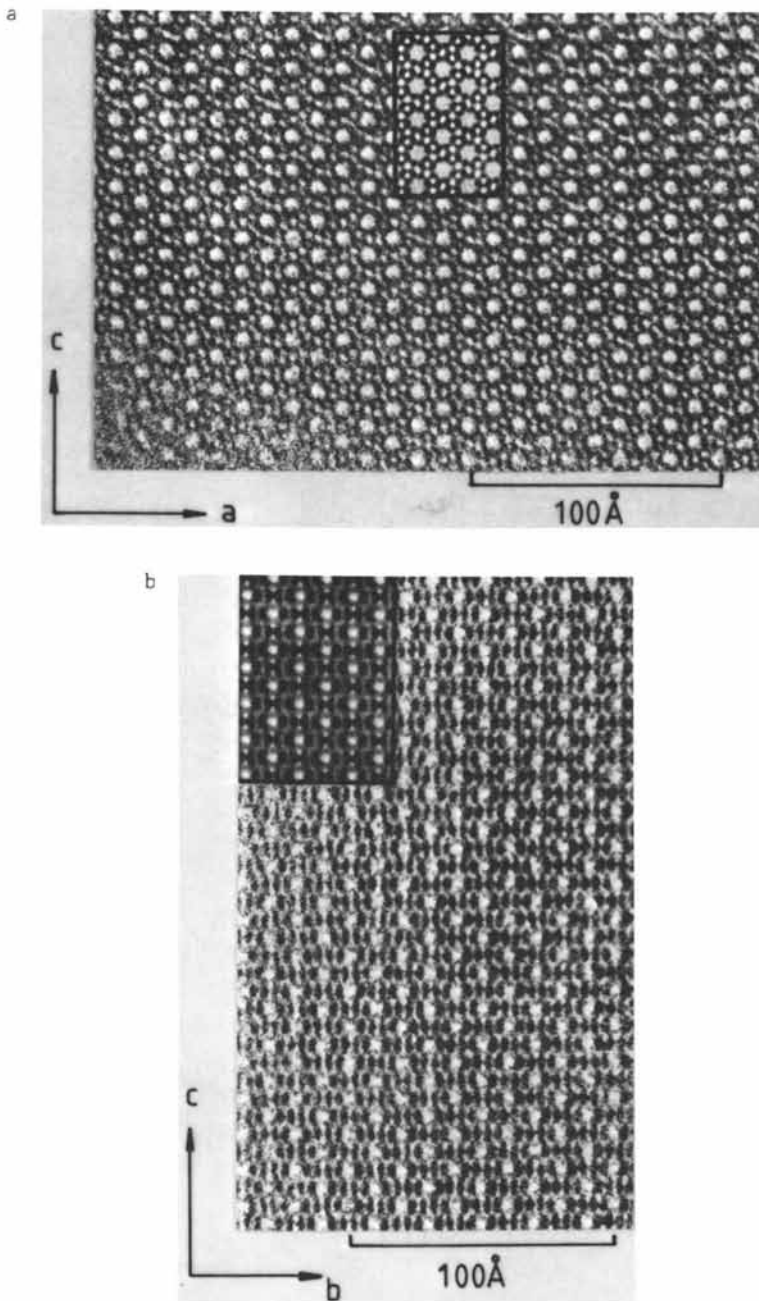


Figure 8. High resolution structure images of ZSM-5 showing the differences exhibited by (a)  $|010|$  zone-axis and (b)  $|100|$  zone-axis, projections. Inset are computer simulated images.



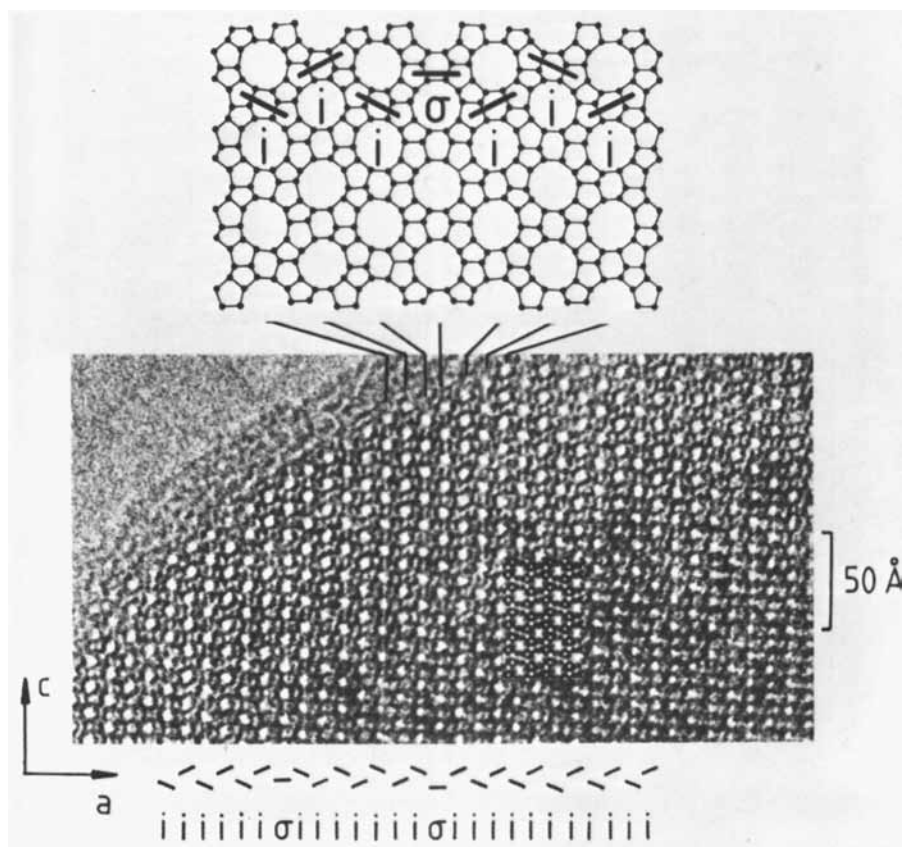


Figure 9.  
 High resolution image of a region of ZSM-5 ( $|010|$  projection) containing two  $\sigma$ -defect planes. The explanatory schematic drawing is discussed in the text.

We have examined a number of samples, prepared in slightly different ways, some being designated either as ZSM-11 or ZSM-5 or of structures intermediate between ZSM-5 and ZSM-11. In most cases electron diffraction patterns similar to Fig. 10a were observed with diffraction spots streaked along  $\underline{a}$ . Streaking of this kind, combined with intensity maxima in positions where  $h + k = \text{odd}$  indicate that  $\underline{\sigma}$  planes are included at irregular intervals in an essentially ZSM-5 ( $\underline{i}$ -symmetry) structural framework. However, one particular sample yielded some evidence of (non-integral  $h$ ) superlattice intensity maxima in the diffraction pattern (Fig. 10b) consistent with a degree of ordering of  $\underline{\sigma}$ ,  $\underline{i}$  sequences at a periodicity of about  $70\text{\AA}$ . Nevertheless the presence of significant streaking along  $\underline{a}$  suggests that any such periodicity is not constant throughout the area contributing to the diffraction pattern.

In order to ascertain how such a  $70\text{\AA}$  superlattice periodicity could arise, we have investigated a number of possible model systems by optical diffractometry. The method is illustrated in Fig. 11. Computer-simulated, graphical projections of the crystal structure are prepared onto 35mm photographic film as black and white transparency masks, which then serve as the object for optical diffraction. As can be seen, the technique faithfully yields the required rectangular (Fig. 11d) and triangular (Fig. 11e) diffraction patterns for simulated ZSM-5 and ZSM-11 ( $[010]$  projection), respectively. Further the  $40\text{\AA}$  periodicity along the  $\underline{a}$  axis for the particular  $\underline{\sigma}$ ,  $\underline{i}$ -sequence shown in Fig. 11c is clearly reflected in the appropriate transform (Fig. 11f).

To reproduce superlattice spots of the type observed in Fig. 10b, we found it necessary to assume a basic  $\underline{i}$ -symmetry framework (ZSM-5) with  $\underline{\sigma}$ -planes introduced at intervals (in multiples of  $10\text{\AA}$ ). A close simulation (see Fig. 12) was found for a model with a repeat sequence of:  $\underline{i i i i i i \sigma i i i i i i \sigma}$ , (i.e.  $\underline{\sigma}$  planes every  $70\text{\AA}$ ). This sequence has a repeat of  $140\text{\AA}$ , but yields a 'pseudo-periodic' superlattice spacing of  $70\text{\AA}$ . Other types of regular sequences yielded incorrect positioning or spacing of the superlattice spots. We have also considered models of irregular sequences. Thus the one based on a total sequence  $\underline{i i \sigma i i i i i \sigma i i i i i i \sigma i i i i i i \sigma i i}$ , i.e.  $\underline{\sigma}$  planes inserted at successive separation of 50, 60 and  $70\text{\AA}$  (median  $60\text{\AA}$ ), gave the required type of superlattice maxima (see Fig. 13) of reciprocal spacing equivalent to a periodicity along  $\underline{a}$  of  $66\text{\AA}$ ; whilst a model sequence  $\underline{i i \sigma i i i i i \sigma i i i i i i i i \sigma i i}$  ( $\underline{\sigma}$  every 50, 70 and  $90\text{\AA}$  - median  $70\text{\AA}$ ) yielded (Fig. 14) superlattice maxima equivalent to  $77\text{\AA}$  along  $\underline{a}$ .

Consequently, we can interpret the superlattice maxima exhibited in the electron diffraction pattern of Fig. 10b as originating from a framework with essentially the ZSM-5 structure (successive planes along  $\underline{a}$  are related by  $\underline{i}$ ) but with  $\underline{\sigma}$

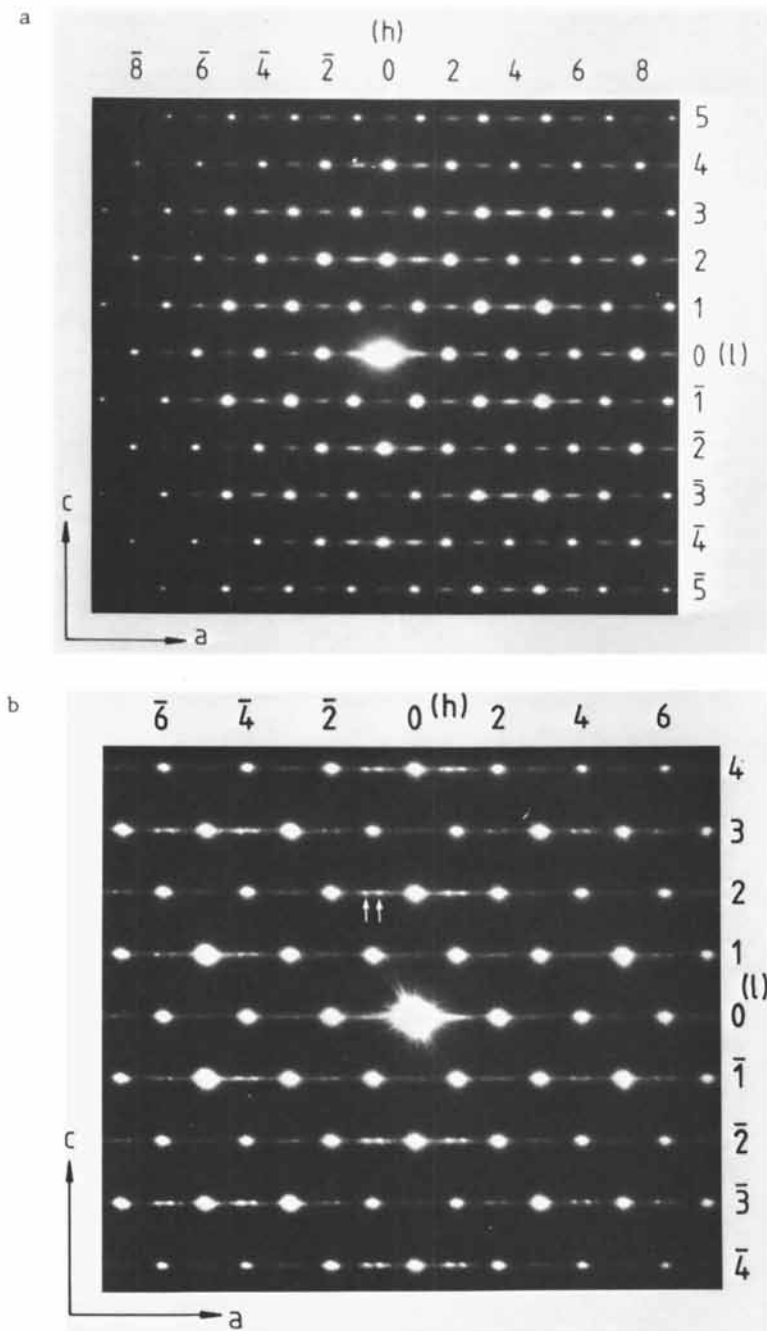


Figure 10. Selected area diffraction patterns of ZSM-5/ZSM-11 intergrowths. The arrowed superlattice maxima in 10(b) suggest a periodicity of about 70Å.

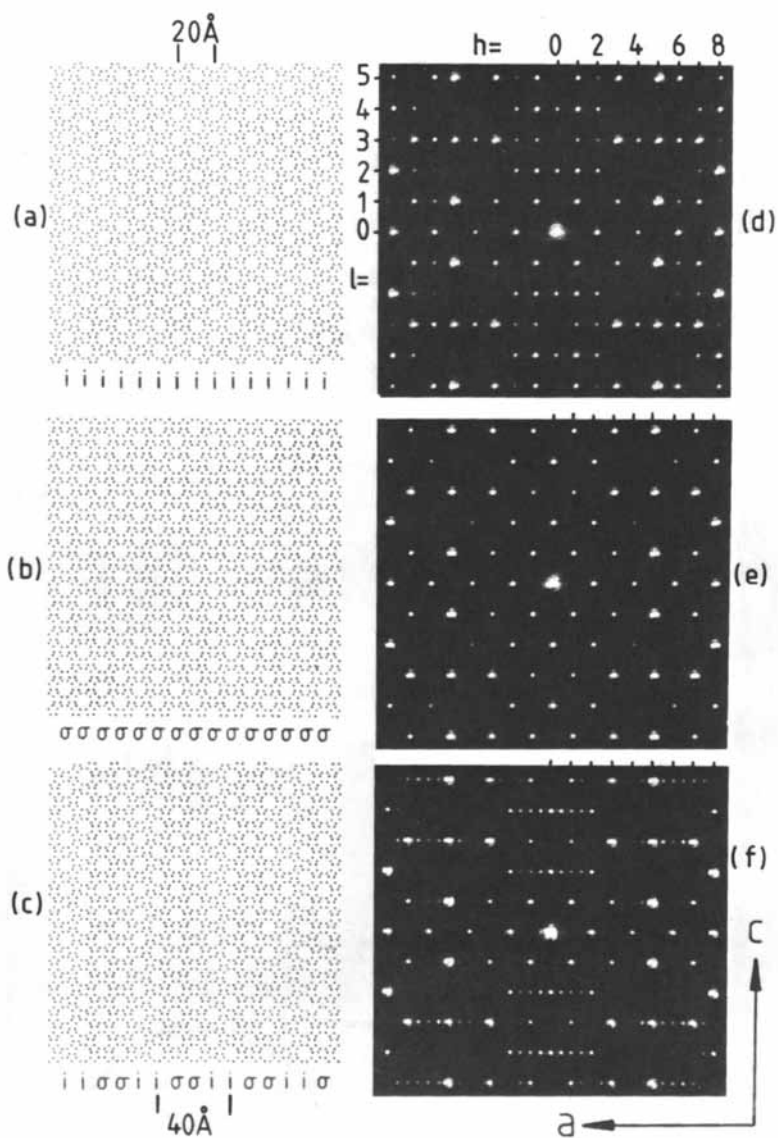


Figure 11.

Computer graphic  $[010]$  projections of model structures: (a) ZSM-5, (b) ZSM-11 and (c) ZSM-5/ZSM-11 intermediate compound with a unit cell repeat distance of  $40\text{\AA}$  along the  $a$ -axis. (d), (e) and (f) are the respective optical transforms. The black dots in (a)-(c) represent the projected positions of Si atoms.

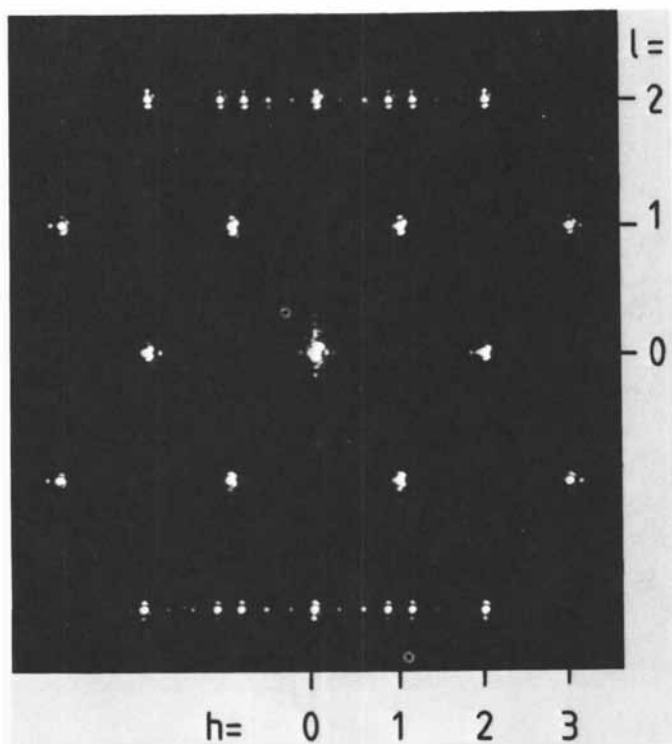


Figure 12.  
 Optical transforms of model ZSM-5/ZSM-11 intermediate  
 structures with repeated sequence along  $a$  of  
 $iiiiii\sigma iiiiii\sigma$ .

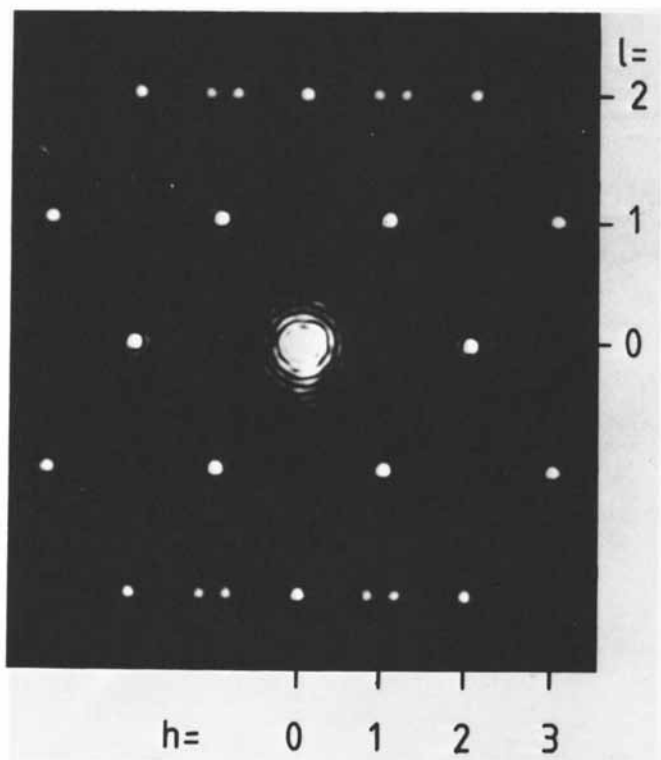


Figure 13.

Optical transform of model ZSM-5/ZSM-11 intermediate structures with a sequence along a of  $\underline{i\ i\ \sigma\ i\ i\ i\ i\ \sigma\ i\ i\ i\ i\ i\ \sigma\ i\ i\ i\ i\ i\ i\ \sigma\ i\ i}$  ( $\sigma$  inserted at 50, 60 and 70Å intervals).

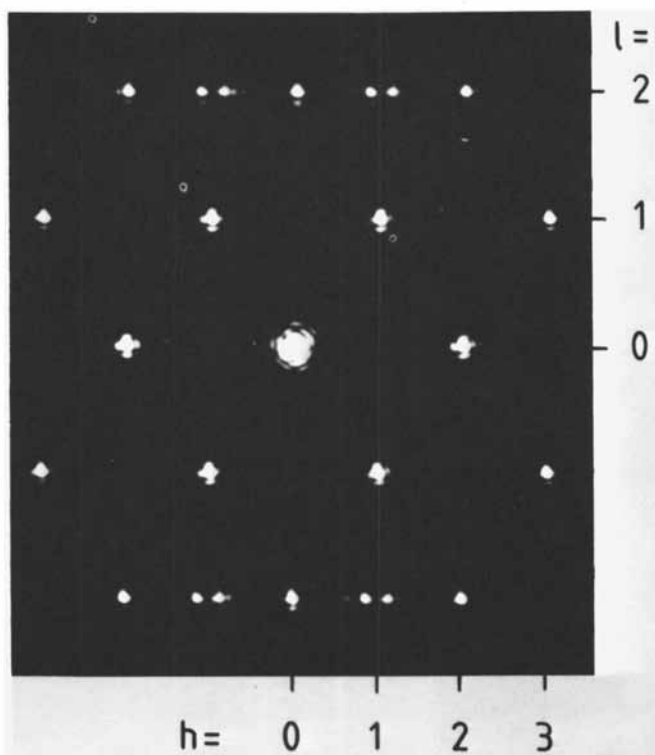


Figure 14.

Optical transform of model ZSM-5/ZSM-11 intermediate structures with a sequence along  $\underline{a}$  of  $\underline{i\ i\ \sigma\ i\ i\ i\ i\ i\ \sigma\ i\ i\ i\ i\ i\ i\ i\ \sigma\ i\ i\ i\ i\ i\ i\ i\ i\ i\ \sigma\ i\ i}$  ( $\underline{\sigma}$  inserted at 50, 70 and 90Å intervals).

planes being included, on average, at every sixth or seventh layer. We must assume considerable deviation from the average separation of  $\underline{\sigma}$  planes in order to account for the observed streaking of spots along  $\underline{a}$ . Preliminary HREM evidence lends some support to these conclusions.

The 'averaging' procedure inherent in optical diffractometry, as well as the direct, real-space crystallographic power of high resolution electron microscopy combine to yield a uniquely powerful set of techniques for structural characterisation. There are other problems, currently under investigation, in zeolite structural chemistry which may be resolved by adopting the twin approaches outlined here.

### Acknowledgments

We thank SERC and BP (Sunbury) for financial support, Drs. D. A. Jefferson and José Gonzalez-Calbet for helpful discussions, Drs. L. A. Bursill and A. Wilson for computer image simulation, and Drs. P. B. Weisz (Mobil), D. Stewart and M. Barlow (BP) for kindly providing us with samples of ZSM-5/ZSM-11.

### Literature Cited

1. Thomas, J. M., *Ultramicroscopy*, 1982, 8, 13.
2. Thomas, J. M., Jefferson, D. A. and Millward, G. R., *J. Micro. Spectr. Electronique*, 1982 - in press.
3. Thomas, J. M. and Jefferson, D. A., *Endeavour (New Series)*, 1978, 2, 127.
4. Millward, G. R. and Jefferson, D. A., *Chemistry and Physics of Carbon*, 1978, 14, 1.
5. Bursill, L. A., Lodge, E. A. and Thomas, J. M., *Nature*, 1980, 289, 111; Thomas, J. M., *New Scientist*, August 1980, 580.
6. Thomas, J. M., Millward, G. R., Ramdas, S., Bursill, L. A. and Audier, M., *Faraday Discussion*, 1981, 72, 345.
7. Thomas, J. M., Millward, G. R. and Bursill, L. A., *Phil. Trans. Roy. Soc.*, 1981, A300, 43.
8. Audier, M., Thomas, J. M., Klinowski, J., Jefferson, D. A. and Bursill, L. A., *J. Phys. Chem.*, 1982, 86, 581.
9. Millward, G. R. and Thomas, J. M., in "Proc. 4th Int. Lond. Carbon and Graphite Conf. 1974", *Soc. Chem. Ind., London*, 1976, 492.
10. Taylor, C. A. and Lipson, H., "Optical Transforms", G. Bell and Sons Ltd., London, 1964.
11. Mulvey, T., *J. Microscopy*, 1973, 98, 232.
12. Meier, W. M. and Olson, D. H. "Atlas of Zeolite Structure Types", Structure Commission of the Int. Zeolite Association 1978, 37.
13. Olson, D. H., Kokotailo, G. T., Lawton, S. L. and Meier, W. M., *J. Phys. Chem.*, 1981, 85, 2238.
14. Kokotailo, G. T., Chu, P., Lawton, S. L. and Meier, W. M., *Nature*, 1978, 275, 119.
15. Meisel, S. L., *Phil. Trans. Roy. Soc.*, 1981, A300, 157.
16. Weisz, P. B., *Pure and Appl. Chem.*, 1980, 52, 2091.
17. Kokotailo, G. T. and Meier, W. M., *Chem. Soc. Spec. Pub.* 1980, 33, 133.
18. Kokotailo, G. T., *Europ. Pat. Appl. No. 8030067, Pub. No. 0018090 A1* (1981).

RECEIVED December 13, 1982



## Compositional Variations Across Zeolite Particles

C. E. LYMAN, P. W. BETTERIDGE<sup>1</sup>, and E. F. MORAN  
E. I. du Pont de Nemours and Company, Experimental Station,  
Wilmington, DE 19898

The silicon-to-aluminum atomic ratio was measured in 30-50nm steps across individual zeolite particles in the size range 0.1-2 $\mu$ m. For NaA zeolite the composition was found to be nearly unity across the crystal. For Na-ZSM-5, three types of chemical profiles were found. Small particles of Si:Al=10 showed either enrichment of Si near the surface or a nearly homogeneous composition. Large particles of Si:Al=40 exhibited more Al near the particle surface than in the particle center. These results indicate that the overall Si-to-Al ratio from bulk chemical analysis should not be taken as the analysis at each point in the particle.

Zeolite catalytic selectivity is usually related to channel size, but for many reactions catalytic activity is influenced by the number of acid sites that contact reactant molecules. Since the acidity of a region within a zeolite crystal is directly related to the aluminum concentration in that region(1), it is important to know how the Al content varies across individual zeolite particles. Using the electron microprobe, von Ballmoos and Meier(2) showed that for 100 $\mu$ m long single crystals of ZSM-5 a gradient in aluminum concentration exists from the center to edge of the crystal with up to 5-10 times more Al near the edge. Derouane et al.(3) used x-ray photoelectron spectroscopy and proton-induced x-ray emission to compare the surface and bulk

<sup>1</sup>Current address: University of Oxford, Chemical Crystallography Laboratory, Oxford OX1 3PD, England

compositions of ZSM-5. They found that large ( $>5\mu\text{m}$ ) particles tend to be enriched in aluminum at the surface, whereas small particles ( $0.1\text{--}0.5\mu\text{m}$ ) could be either homogeneous in composition or enriched in Si at the surface. However, neither of these investigations provides actual concentration profiles across small zeolite particles of the size used in practical catalysis.

This paper describes chemical analyses at points across individual zeolite crystals in the size range  $0.1\text{--}2.0\mu\text{m}$ . The technique employed was x-ray emission spectroscopy in the scanning transmission electron microscope (STEM). Two ZSM-5 preparations were made with Si:Al ratios about 10 and 40. Many particles were examined carefully to detect chemical segregation. To check the analysis procedure, particles of NaA zeolite were examined as a control.

### Experimental

Zeolite Synthesis Two preparations of Na-ZSM-5 with different Si:Al ratios were made following the procedures of Rollmann and Valyocsik(4). Synthesis runs were carried out in a 1 gallon stirred titanium autoclave for 24 hours at  $160^\circ\text{C}$  and autogeneous pressure. The materials used were sodium aluminate (Fisher), sodium hydroxide, tetrapropylammonium bromide (TPABr) (Eastman Kodak), Ludox® HS-30 colloidal silica (Du Pont), and distilled water. These reagents were mixed to yield aluminosilicate gels having the molar ratios ( $\text{H}_2\text{O}/\text{SiO}_2=20$ ,  $\text{OH}^-/\text{SiO}_2=0.13$ , and  $\text{TPABr}/\text{SiO}_2=0.1$  as specified(4)). The Si:Al ratio was modified by varying the NaAlO content. After cooling, the solid product was filtered, water washed, and dried overnight at  $95^\circ\text{C}$ .

Zeolite A was made following a procedure also described by Rollmann and Valyocsik(4). A solution of sodium aluminate and sodium hydroxide was added to a solution of sodium meta-silicate and stirred at  $90^\circ\text{C}$  for 2 to 5 hours. The suspension was then filtered hot, washed, and dried.

Bulk chemical analyses of the products were determined by atomic absorption spectroscopy (Al) and gravimetric analysis (Si). The two samples of ZSM-5 were distinguished by noting the nominal Si:Al ratio in parentheses as shown in Table I. The average particle sizes measured by electron microscopy are also shown in Table I.

Microanalysis Specimens for microanalysis were prepared by dispersing the powder ultrasonically in ethanol, placing a drop of this suspension on a thin carbon support film, and allowing the solvent to evaporate. X-ray absorption effects are negligible for particles on the order of  $0.1\mu\text{m}$  thick allowing analysis of these particles without absorption corrections. For

Table I

| <u>Specimen</u> | <u>Bulk Si:Al</u> | <u>Particle Size</u> |
|-----------------|-------------------|----------------------|
| Na-ZSM-5(9)     | 9.3               | 0.3 $\mu$ m          |
| Na-ZSM-5(40)    | 39.5              | 1.9 $\mu$ m          |
| NaA zeolite     | 0.985             | 2.2 $\mu$ m          |

small particles analyzed directly on the support film, the particle thickness was assumed to be roughly the same as the lateral dimension of the particle. For particles on the order of 1 $\mu$ m in thickness or thicker, the absorption correction is significant and must be applied to each analysis point. Thin specimens of these larger particles were prepared by embedding the particles in epoxy resin and microtoming 80nm thick sections with a diamond knife.

Microanalysis was done in a Vacuum Generators HB-501 scanning transmission electron microscope equipped with a Kevex lithium-drifted silicon x-ray detector. The electron beam used for analysis was about 1-3nm in diameter and carried about  $10^{-10}$  to  $10^{-9}$  amperes. The vacuum in the specimen chamber was about  $5 \times 10^{-9}$  torr. X-ray counting times on the order of 100 seconds per analysis point were required to obtain adequate statistics especially for the ZSM-5 preparation with the higher Si:Al ratio. Conversion of the x-ray intensity ratios to chemical composition ratios was by the Cliff-Lorimer technique(5). An aluminum-silicon Cliff-Lorimer k-value of  $k=1.31$  was obtained from the mineral albite. Particles up to 0.15 $\mu$ m in thickness met the "thin film criterion"(6) indicating that absorption and fluorescence corrections to the data may be neglected.

## Results

Stability of Zeolites Under the Electron Beam Zeolites are generally unstable under electron bombardment(7,8). This electron beam damage may be divided into two levels of severity: loss of crystallinity and loss of mass. Evidence of damage to the crystal structure can be seen in Figure 1. This structure image along the 010 projection of H-ZSM-5 was photographed by scanning a single 20 second frame. The crystalline channel structure is lost at the top of the frame where the previous exposure was taken. This specimen was not fully dehydrated at 400-500°C(7), but was outgassed in the microscope specimen chamber overnight at

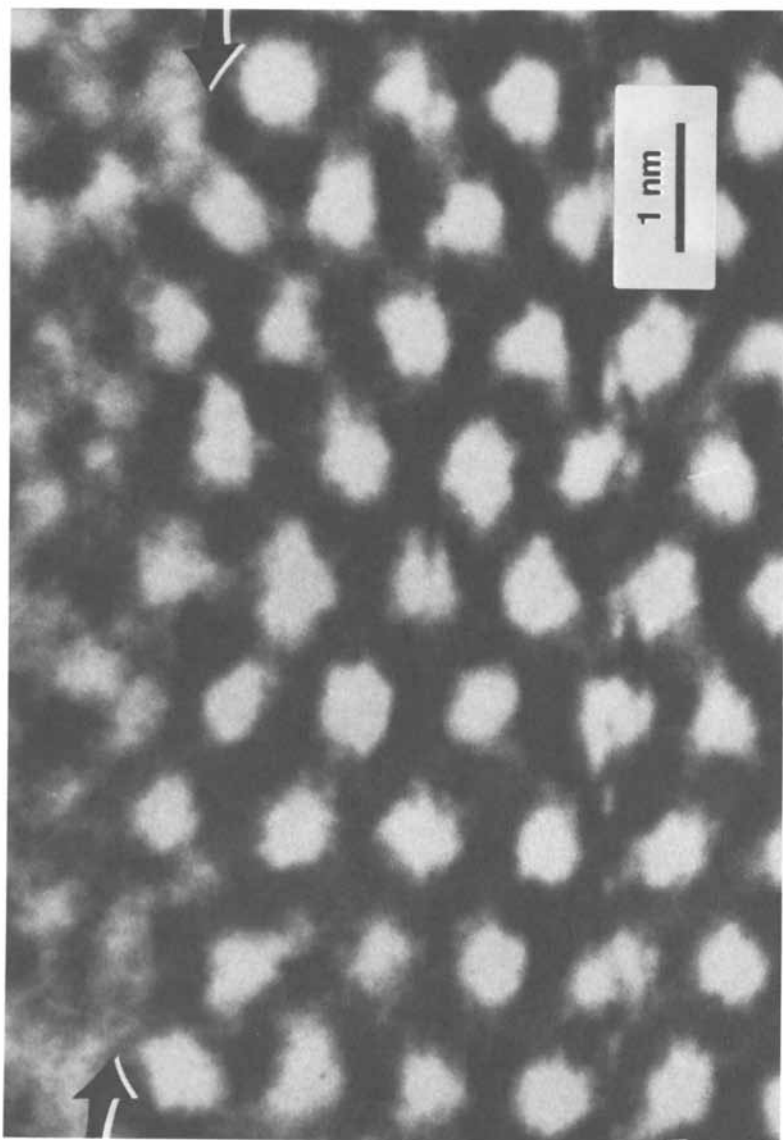


Figure 1. Electron beam damage to ZSM-5 after a brief exposure to the focused electron beam. Crystal orientation is probably such that [010] zone axis is parallel to the optical axis of the microscope.

$5 \times 10^{-9}$  torr. This type of damage, producing a loss of crystallinity, can occur at very low beam currents.

For the higher beam currents necessary for microanalysis in a reasonable time, mass-loss damage at analysis points is likely to occur. For zeolite crystals with low Si:Al ratios, mass loss was evident as holes in the specimen at high beam currents (see Figure 2). For such specimens very low beam currents were required for analysis. However, even in cases where mass loss is evident, the trends in compositional variations across particles will still be valid.

Particle Morphology Typical shapes of zeolite particles from these preparations are shown in Figures 3, 4, and 5. Crystals of NaA zeolite showed strong cubic habits typical of these structures (Figure 3). The surface morphology of the  $0.3 \mu\text{m}$  crystals of ZSM-5(9) was usually irregular (Figure 4) and seldom exhibited crystal facets. The  $2 \mu\text{m}$  crystals of ZSM-5(40) showed facets typical of ZSM-5 of moderate aluminum content (Figure 5).

Chemical Profiles Across Particles It is well known that NaA zeolite has a Si:Al ratio close to unity because it is considered a stoichiometric compound with little, if any, range in solid solubility. Since the chemical profile across the NaA zeolite crystal in Figure 6 is flat and near unity, this profile is in effect a control specimen for the analysis of the ZSM-5 particles.

Chemical profiles across particles of ZSM-5(9) reveal two characteristic types of particles. One type of particle has more aluminum in the center than near the surface (Figure 7). This particle had facets suggesting that it was a single crystal. The other type of particle in the same preparation exhibited no detectable compositional variation (Figure 8). High resolution images taken in the conventional transmission electron microscope (TEM) showed that the latter type of particle is composed of 20-40nm crystals stacked together in nearly the same orientation to form a  $0.3 \mu\text{m}$  particle (Figure 9). This composite particle apparently gives an average Si:Al ratio with no gradient.

As shown in Figure 4, a different particle morphology was observed in ZSM-5(40). A compositional profile across a thin section taken near the center of the particle thickness (Figure 10) reveals that there is more aluminum near the surface than in the particle interior. This compositional change appears to be abrupt at about  $0.4 \mu\text{m}$  into the particle from the surface.

Note that the point analyses shown in Figures 6, 7, 8 and 10 represent average compositions through the thickness of the particle or thin section. At each analysis point the composition was sampled in a cylindrical volume of material whose diameter is roughly  $10 \text{nm}$ , beam diameter plus beam spreading(6), and whose height is the specimen thickness. Thus, for the particle

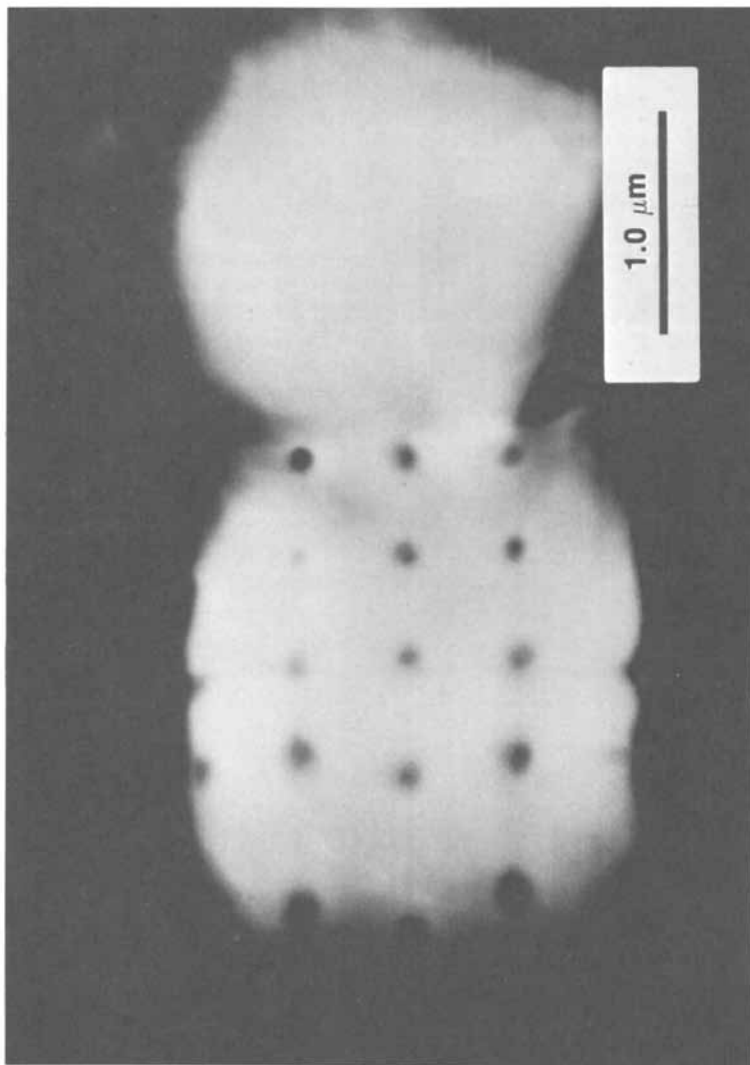
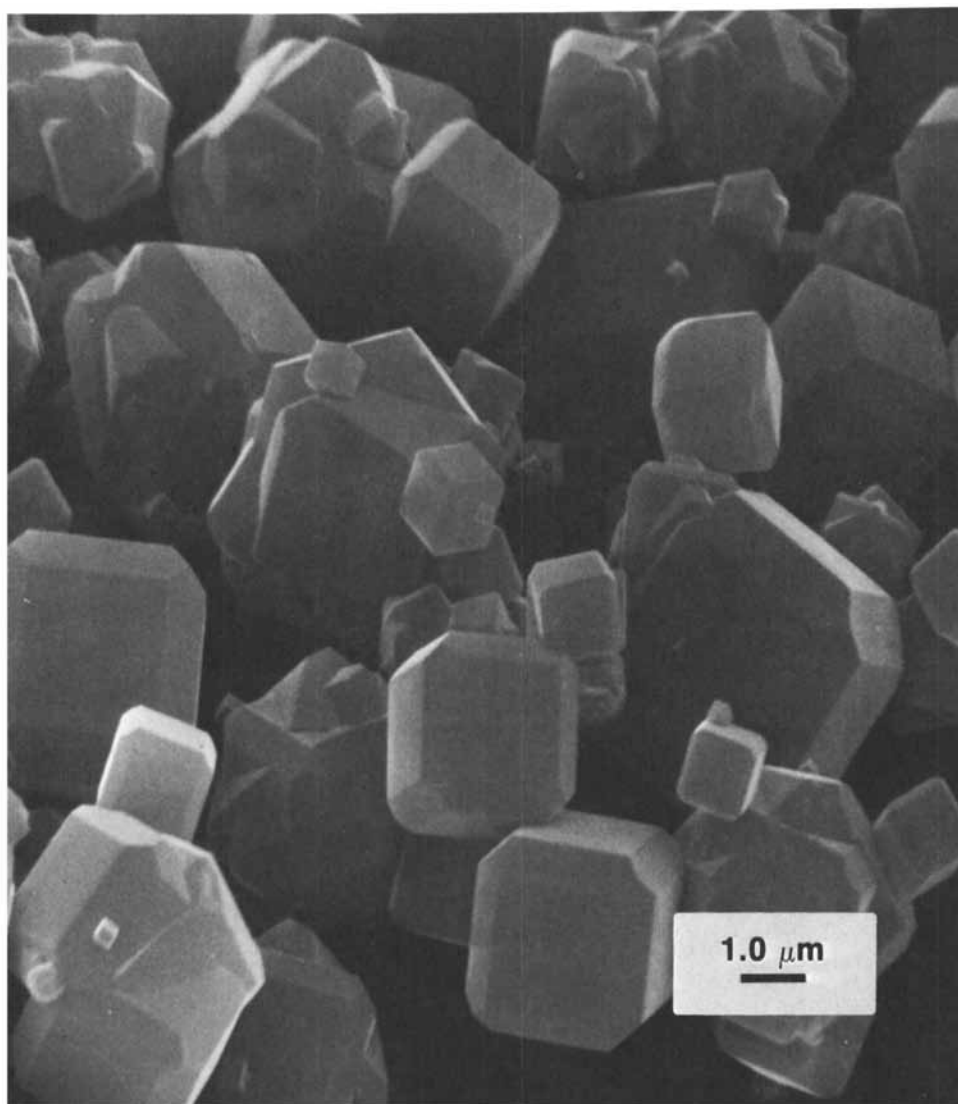


Figure 2. Evidence of beam damage in NaA zeolite at high beam currents. Mass loss is evident at places where a high intensity electron beam was stationary for several minutes.



**Figure 3.** Surface scanning electron microscope (SEM) image of NaA zeolite crystals showing a cubic habit.

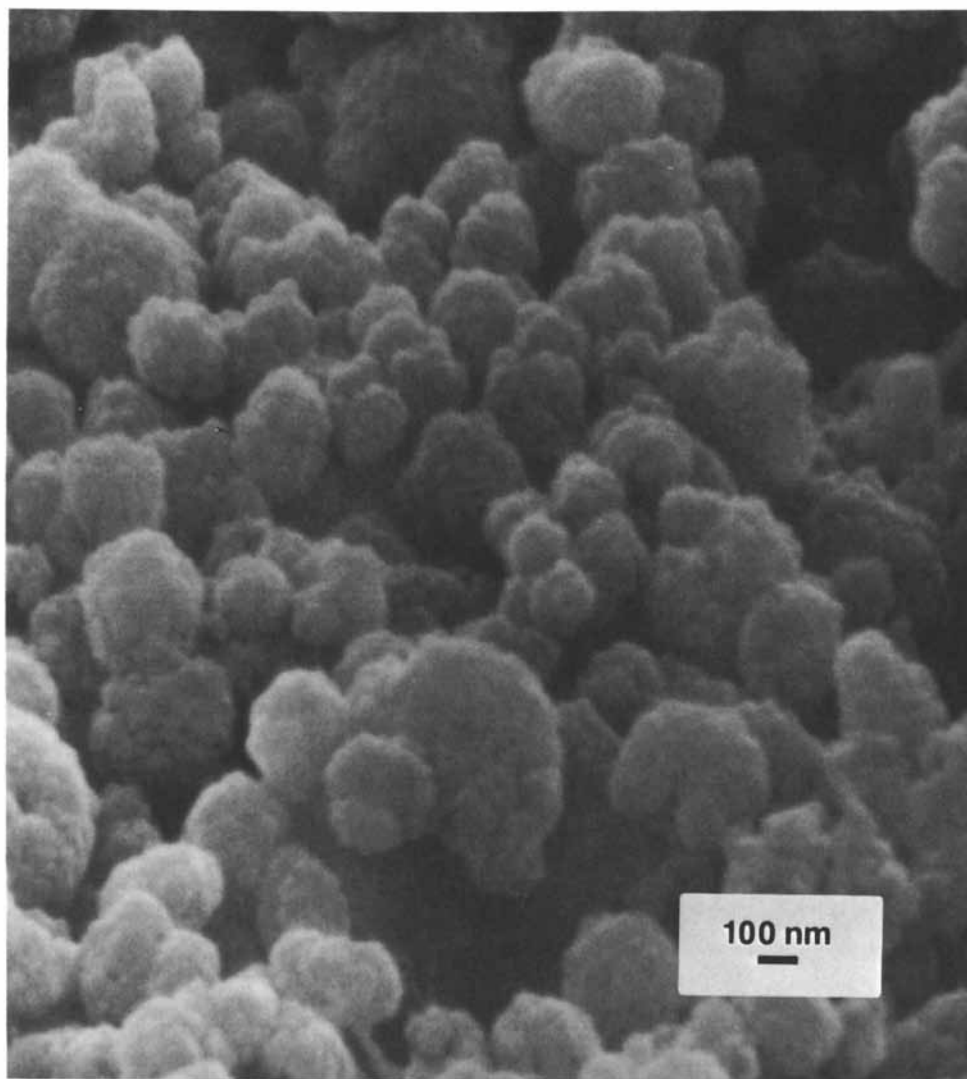
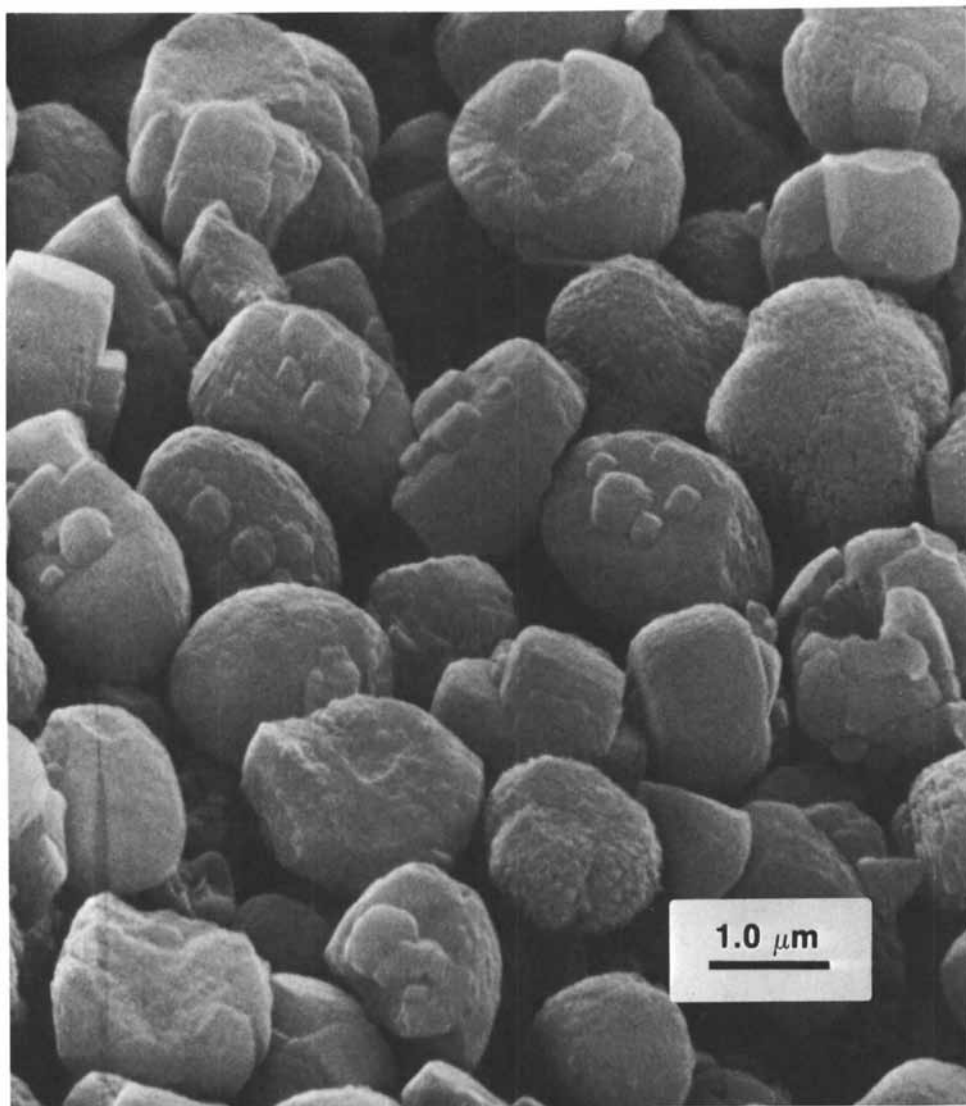


Figure 4. Surface SEM image of crystals of ZSM-5(9).





**Figure 5.** Surface SEM image of ZSM-5(40) showing faceted crystals with interpenetrating twins.

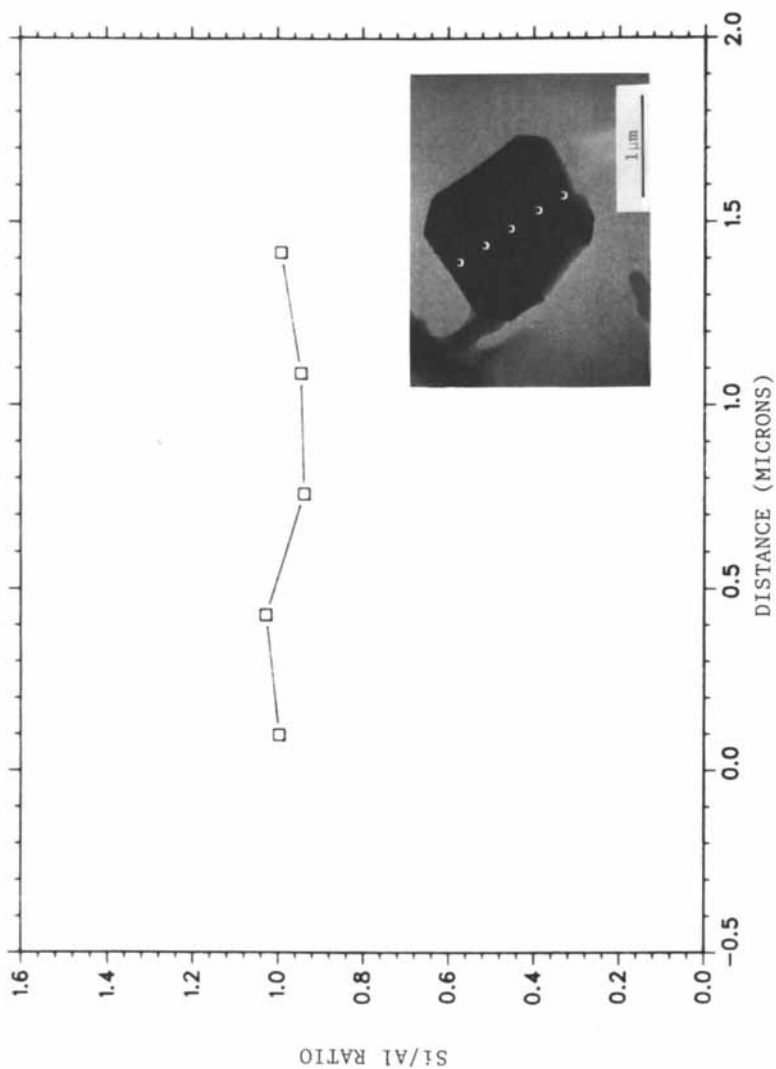


Figure 6. Chemical profile across a particle of NaA zeolite. This zeolite should give a stoichiometric Si:Al ratio of unity. Analysis points shown in inset.

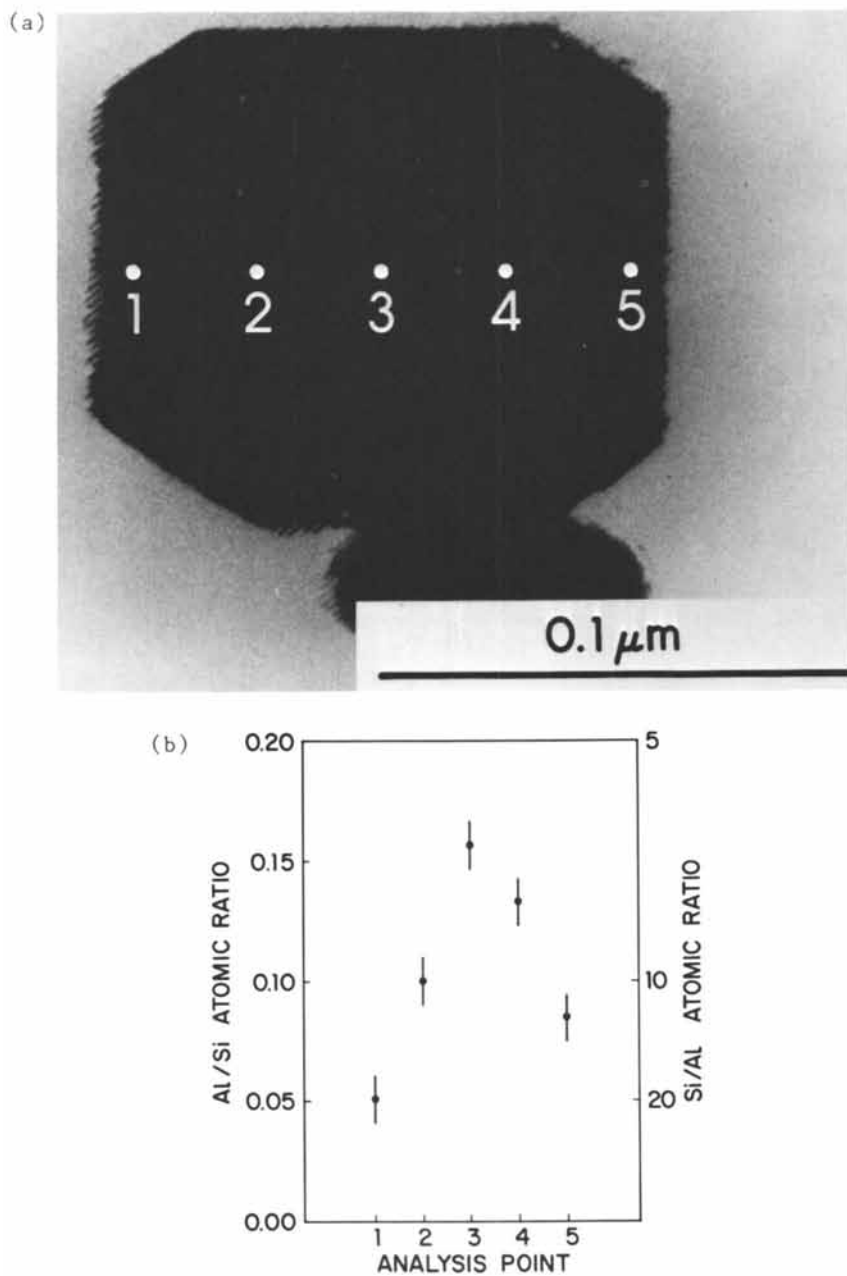
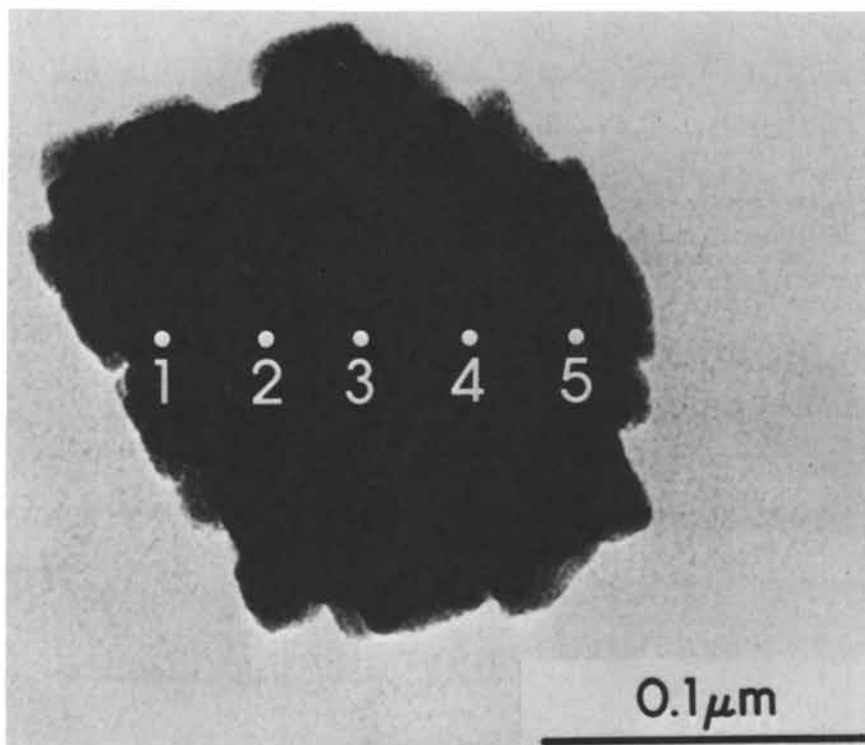
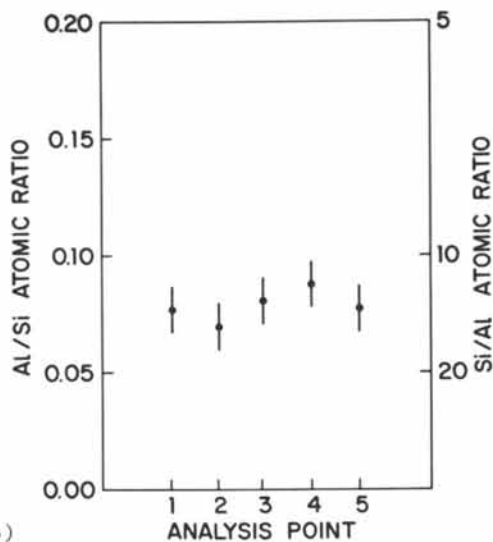


Figure 7. Chemical profile across a single crystal particle of ZSM-5(9). More aluminum is present in the crystal interior. a) image, b) profile of Al/Si ratio.



(a)



(b)

Figure 8. Chemical profile across a stack of small single crystals in ZSM-5(9). The chemical profile indicates a homogeneous composition. a) image, b) profile of Al/Si ratio.

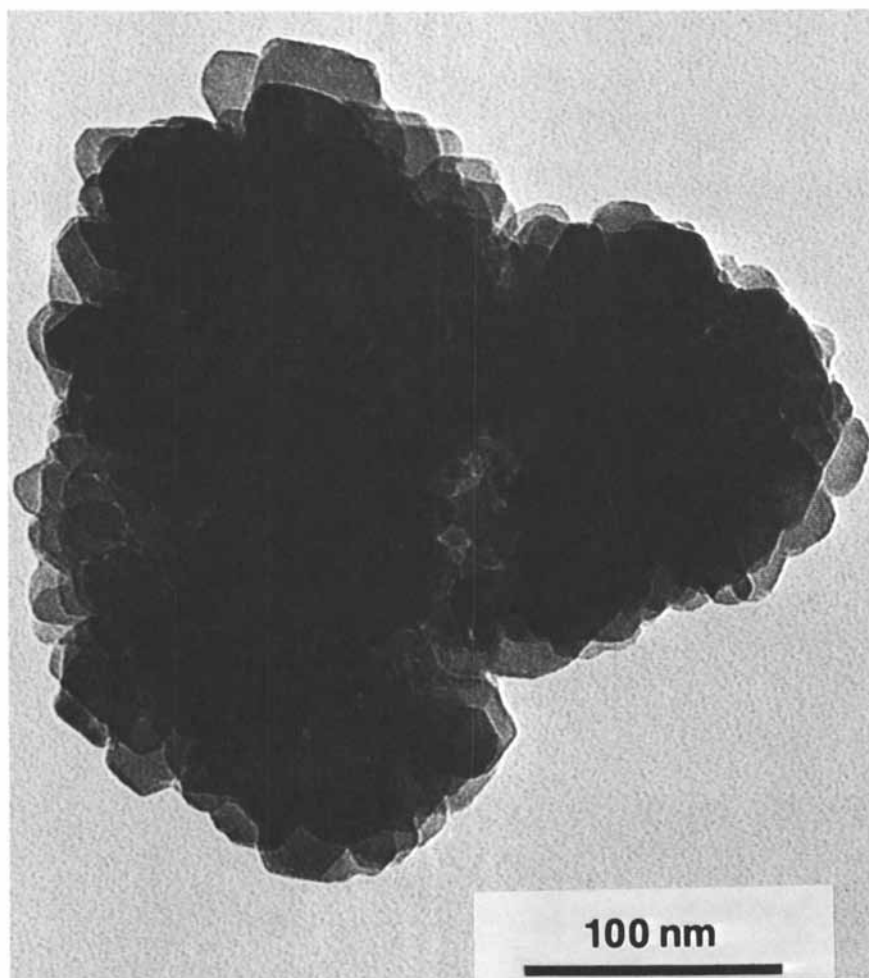


Figure 9a. High resolution TEM micrograph of a stack of small crystals of ZSM-5(9) similar to Figure 8. Some crystals show lattice fringes while one crystal in Figure 9b shows a structure image of the channels in the crystal.

Continued on next page.

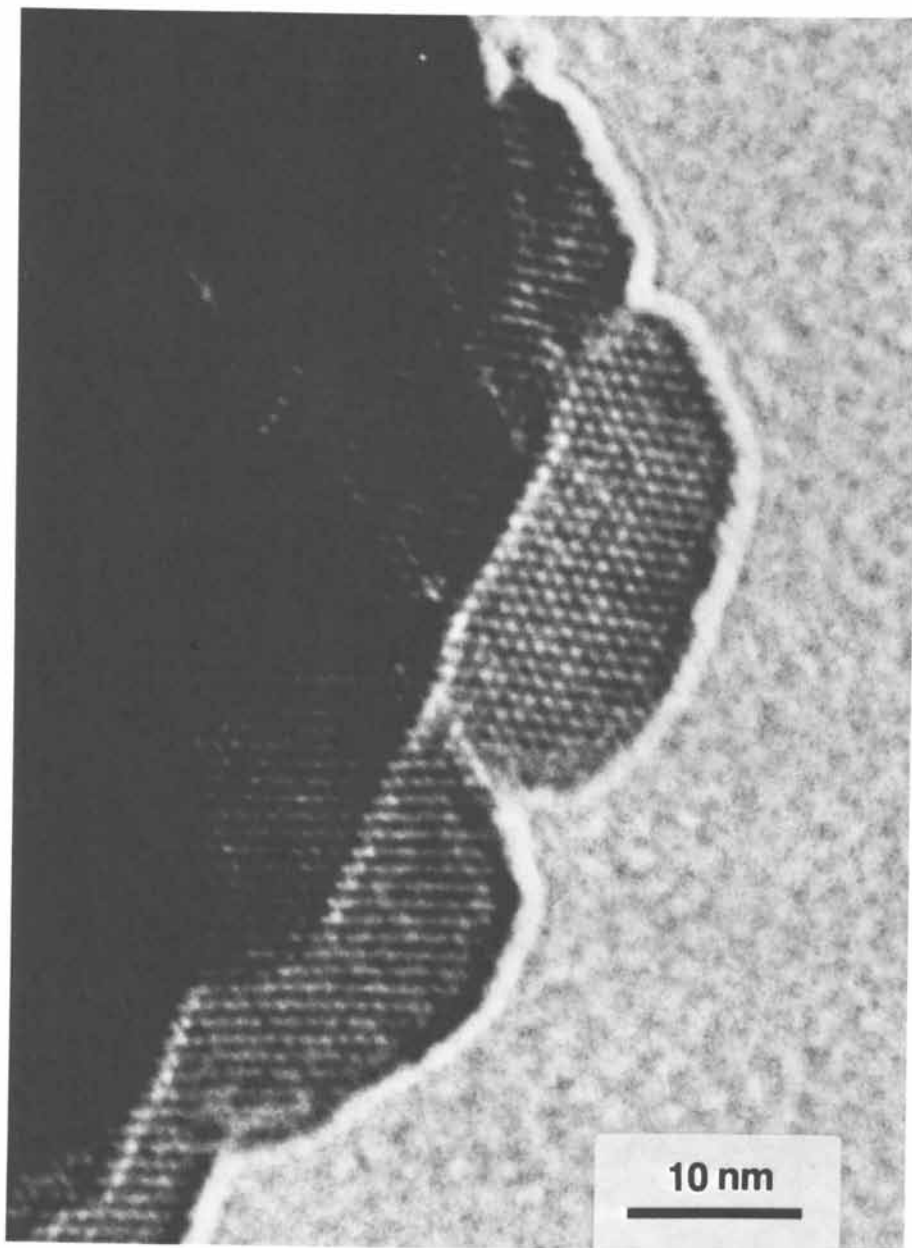
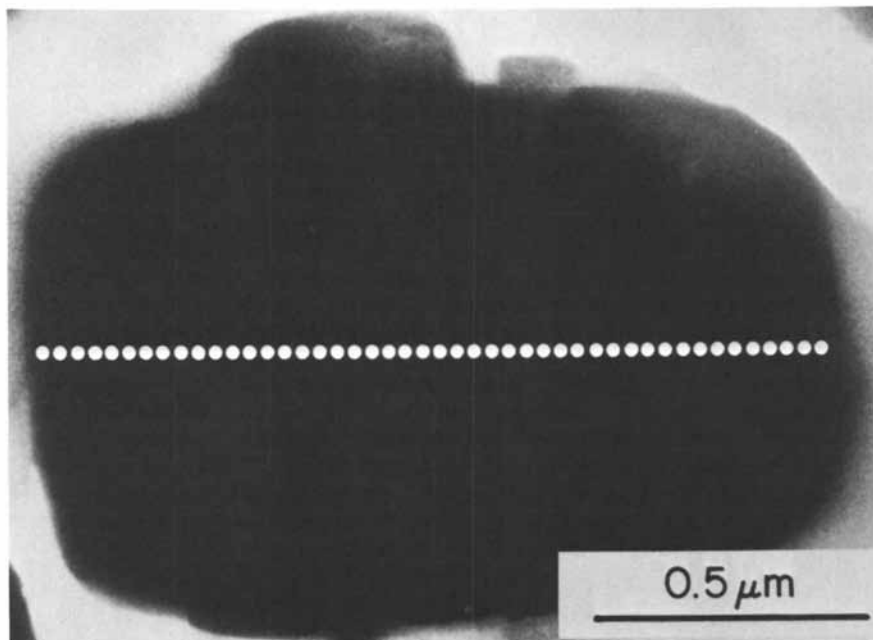
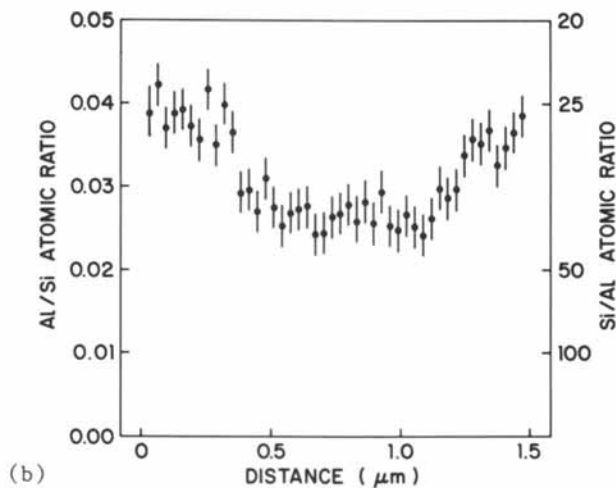


Figure 9b.



(a)



(b)

Figure 10. Chemical profile across a particle of ZSM-5(40) shows more aluminum near the surface than in the interior. a) image, b) profile of Al/Si ratio.

analyzed in Figure 7, the compositional variation from center to surface may be even greater than indicated by this type of analysis. Mass loss from the surface during analysis would also change the chemical composition measured in the analyzed volume. In the present case mass loss was believed to be small and no corrections were made. A final qualification for this work concerns the location of the aluminum measured in these studies. Some of the aluminum detected in these crystals may not be in the framework structure but rather in the channels as amorphous material. However, the presence of amorphous material containing aluminum does not invalidate the analysis technique presented here as a method to determine chemical profiles across small zeolite particles.

### Discussion

These results show that ZSM-5 zeolites of supposed uniform Si:Al ratio actually exhibit gradients in aluminum concentration within individual particles. This implies that the distribution of catalytically active sites is not necessarily uniform throughout a zeolite crystal. The activity and selectivity for a reaction should be most favorable where the Al sites have a particular average separation distance.

For the sample of ZSM-5(9) with a low Si:Al, two types of particles were observed. The single crystal particles had more aluminum in the center than near the surface. Other particles in the same preparation were actually stacks of smaller crystals aligned in nearly the same orientation and thus giving no chemical gradient across the entire composite particle. Each small crystal may possess a chemical gradient but this was not measured. These results support the work of Derouane et al.(3) who reported that small, low Si:Al ZSM-5 particles could be either homogeneous in composition or enriched in Si at the surface.

One may speculate from these results that zeolite crystal growth may take place in two ways within the same preparation. Possibly the ZSM-5(9) particle with the aluminum gradient nucleates first on an aluminum-rich inhomogeneity of the gel (e.g.  $\text{Al}_2\text{O}_3$ ) depleting the gel of aluminum. Particles consisting of stacks of 30nm crystals may nucleate homogeneously in regions of gel free of inhomogeneities.

Large ZSM-5(40) crystals with higher Si:Al ratios exhibit more aluminum near the particle surface than in the interior. von Ballmoos and Meier(2) found the same trend in the chemical profile, but their particles were 100 times larger. Derouane et al.(3) also noted higher aluminum content on the surface of this type of particle. This reversal in the Al chemical profile from the ZSM-5(9) case may indicate a third growth mechanism. Crystals of high Si/Al may nucleate on Si-rich inhomogeneities



and tend to reject Al into the liquor as they grow. At the end of the synthesis period zeolite of lower Si/Al may grow epitaxially on the surface from the remaining solution. Another possibility for the higher aluminum content near the surface is the penetration of amorphous gel high in Al into the zeolite channels. Further experiments are required to test these speculations about zeolite crystal growth.

### Conclusions

Particles of ZSM-5 with different Si:Al ratio may have different chemical profiles across the particle. Small (0.3 $\mu$ m) particles of low Si:Al may either be composed of 30nm crystals stacked together or be a single crystal with more aluminum in the center. Large 2 $\mu$ m particles of higher Si:Al exhibit a chemical profile showing more aluminum near the particle surface than in the interior. Therefore, the overall Si:Al ratio from bulk chemical analysis should not be taken as the analysis at each point in each particle.

### Acknowledgement

The authors are grateful to R. D. Shannon, L. Abrams, and G. D. Stucky for many helpful discussions, to B. F. Burgess and W. F. Farquhar for chemical analysis, and to I. R. Hartmann and M. L. van Kavelaar for assistance in electron microscopy. R. D. Shannon synthesized the sample of NaA zeolite.

### Literature Cited

1. Olson, D. H., Haag, W. O., and Lago, R. M., J. Catal. 1981, 61, 390.
2. von Ballmoos, R. and Meier, W. M., Nature 1981, 389, 782.
3. Derouane, E. G., Gilson, J. P. Gabelica, Z. Mousty-Desbuquoit, C. and Verbist, J., J. Catal. 1981, 71, 447.
4. Rollmann, L. D. and Valyocsik, E. W., to be published in Inorganic Syntheses, 22, Holt, S. L., (ed.).
5. Cliff, G. and Lorimer, G. W., J. Microsc. (Oxford) 1975, 103, 203.
6. Goldstein, J. I., in Introduction to analytical Electron Microscopy, Hren, J. J., Goldstein, J. I., and Joy, D. C. (eds.), Plenum, New York, 1979 p. 83.
7. Bursill, L. A., Lodge, E. A., and Thomas, J. M., Nature 1980, 286, 111.
8. Hirsch, E. H., Nature 1981, 293, 759.

RECEIVED November 4, 1982

## A Statistical Approach to the Interpretation of Silicon-29 NMR of Zeolites

A. J. VEGA

E. I. du Pont de Nemours and Company, Central Research and Development  
Department, Experimental Station, Wilmington, DE 19898

A moment analysis of  $^{29}\text{Si}$  MAS spectra of zeolites is shown to provide direct information on the number of second-nearest-neighbor Al-Al pairs. Monte Carlo computer calculations are described of randomized Al distributions in zeolite frameworks, under restrictions of Loewenstein's and Dempsey's rules. The method is applied to a hypothetical square planar lattice which allows the various Al distribution patterns to be visualized in simple displays, and to the zeolite X and Y framework. The results are compared with experimental data taken from the literature.

Several research groups have recently made extensive use of  $^{29}\text{Si}$  magic-angle-spinning NMR to obtain information on aluminum ordering in the zeolite framework (1-4). The basis for the spectral analysis is the observation that the  $^{29}\text{Si}$  chemical shifts fall into five nearly distinct regions corresponding to the number of Al neighbors attached via oxygen bridges. Assuming that the relative intensities of these five peaks can be accurately determined, one can proceed and identify particular Si/Al arrangements in the crystal network which agree with the observed intensities. However, while there is a very large number of possible distributions of Al atoms with a given Si/Al ratio, there are only four experimental quantities to be fit (the relative intensities of 5 NMR lines).

One way to simplify the problem is to consider only a small structural unit (e.g., one or two sodalite cages) and to assume that all other units in the crystal are identical and/or related through symmetry. In several publications (2, 3, 4), this approach led to specific patterns of Al occupancies which had excellent agreement with experimental NMR data. Other theoretical investigations considered random Al distributions of

0097-6156/83/0218-0217\$06.00/0  
© 1983 American Chemical Society

small structural units with no restrictions imposed on translational ordering (5-8).

This paper describes a statistical analysis that is not confined to small clusters. The method involves a moment analysis of the NMR spectra and Monte Carlo calculations of simulated spectra.

Thereby, two simplifying assumptions have been made: The Si/Al ratio is taken to be constant throughout the sample, and exterior surface effects are neglected. A nonuniform Al density highly complicates the interpretation of  $^{29}\text{Si}$  NMR data. Although this problem is not explicitly addressed in this discussion, some of the following results are also applicable to inhomogeneous samples in so far as they relate to average properties. The effect of external surfaces is probably not severe if the crystallites have a diameter of at least  $0.1\mu\text{m}$ .

### Definitions

First, we define a few quantities related to the distribution of Al and Si in the zeolite network.

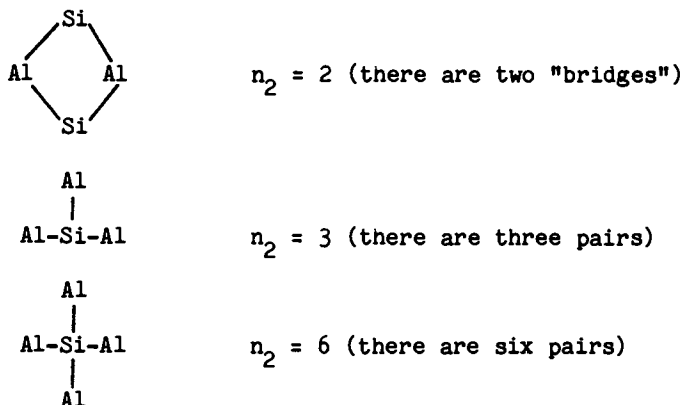
- N: Total number of T sites in the sample
- n: Total number of Al sites in the sample
- $n_1$ : Total number of nearest Al-Al neighbor pairs in the sample
- $n_2$ : Total number of Al-Si-Al second-nearest neighbor linkages in the sample

These quantities can also be expressed as densities or frequencies:

- $x = n/N$ : fraction of sites occupied by Al
- $x_1 = n_1/N$ : density of Al-Al pairs
- $x_2 = n_2/N$ : density of Al-Si-Al linkages

Obviously,  $x$  is another way to define the Si/Al ratio, which is equal to  $(1-x)/x$ . When  $x_1$  vanishes, Loewenstein's rule is obeyed, otherwise it is violated. The quantity  $x_2$  is related to the electrostatic energy rules of Dempsey's (9, 10), which state that the number of second-nearest Al neighbors is minimized, first in 4-rings, and subsequently in the meta-positions of 6-rings. We quantify this notion by assigning an  $n_2$  value of 1 to every "bridge" or "linkage" between two second-nearest neighbor Al's. Examples:





This definition recognizes the fact that the electrostatic repulsion in a 4-ring is about twice as strong as in larger rings. However, the main reason of choosing this particular definition is its usefulness in the interpretation of NMR data (see below).

Finally, we define the intensities of the  $^{29}\text{Si}$  NMR peaks:

$$I_k \quad (k = 0, \dots, 4): \text{ intensity of the Si } (k\text{-Al}) \text{ peak,}$$

$$I_{\text{tot}} = I_0 + I_1 + I_2 + I_3 + I_4: \text{ total intensity,}$$

and the first and second moments:

$$M_1 = \sum_k k I_k / I_{\text{tot}}$$

$$M_2 = \sum_k (k - M_1)^2 I_k / I_{\text{tot}}$$

#### Test of Loewenstein's Rule

Engelhardt, et al., (3) and Melchior, et al., (4) have pointed out that the first moment of the NMR spectrum is equal to  $4/(\text{Si}/\text{Al})$ , provided Loewenstein's rule is obeyed. We can extend this important relationship to the following:

$$x_1 = 2x - (1/2) (1-x)M_1 \quad (1)$$

The proof goes as follows:

For each Al-Al pair, there are two Al's with an Al neighbor. Thus all the Al's in the sample have a total of  $2n_1$  Al neighbors. Since the total number of all the neighbors of Al atoms is  $4n$ , we have  $4n - 2n_1$  Si-Al bonds. Thus, the total number of Al neighbors of all Si's is also  $4n - 2n_1$ . The ratio of this number to the total number of Si atoms,  $N - n$ , should be equal to the spectral ratio  $(I_1 + 2I_2 + 3I_3 + 4I_4)/I_{\text{tot}}$ . This directly leads to the above expression for  $x_1$ . Q.E.D.

Loewenstein's rule implies that  $x_1 = 0$ , which substituted in Equation (1) gives (3, 4)

$$M_1 = 4x/(1-x) = 4/(Si/Al) \quad (2)$$

### Test of Dempsey's Rules

The following relationship allows direct calculation of the density of second-nearest-neighbor Al pairs in a zeolite obeying Loewenstein's rule:

$$x_2 = (1-x)m_2 \quad (3)$$

where

$$m_2 = (I_2 + 3I_3 + 6I_4)/I_{tot} \quad (4)$$

The proof is straightforward: Referring to the examples given in the Definitions Section, it is readily seen that each Si contributing to  $I_2$  represents one Al-Si-Al pair; each Si contributing to  $I_3$  represents three Al-Si-Al pairs; and each Si contributing to  $I_4$  represents six Al-Si-Al pairs. Thus, the ratio of  $(I_2 + 3I_3 + 6I_4)$  and  $I_{tot}$ , equals the ratio of  $n_2$  and the total number of Si atoms. Q.E.D.

Notice that although  $m_2$  is not the proper second moment of the NMR spectrum, it is closely related to the second and first moments by

$$m_2 = (1/2) (M_2 + M_1^2 - M_1) \quad (5)$$

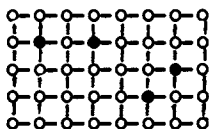
This relationship predicts that the NMR spectrum of a zeolite behaving according to Loewenstein's rule, while obeying Dempsey's rules with increasing degree, will exhibit an increasingly narrow intensity distribution around a constant center of gravity. This implies that if we can devise an experiment where Si and Al can rearrange to minimize electrostatic Al-Al interactions, the progress of such a process can be monitored by NMR.

### Simulation of NMR Spectra

Unlike Loewenstein's rule which predicts a vanishing  $x_1$  for Si/Al ratios larger than 1, Dempsey's rules do not directly provide an exact value of  $x_2$  except at the lowest Al concentrations (Si/Al  $\gtrsim$  5) where next-nearest neighbors can completely be avoided to give  $x_2=0$ . In fact,  $x_2$  as well as the finer details of the NMR intensity distribution, depend on the particular topology (i.e., the connectivity scheme) of the zeolite under consideration. The following sections describe a method to simulate NMR spectra for any zeolite topology with the

following three levels of randomness: (i) completely random; (ii) random with the restriction of vanishing  $x_1$  (Loewenstein's rule); (iii) random with vanishing  $x_1$  and the additional condition of minimum  $x_2$  (Dempsey's rules). The only other condition we must require is that the Si/Al structure be compatible with an extended three-dimensional network; i.e., we must avoid creating relatively small structural units which cannot be combined into a large crystal lattice. This does not necessitate strict translational symmetry. Therefore, the model must involve a relatively large cluster of lattice sites. In this work, the problem is approached by Monte-Carlo computer calculations on structural units containing more than 1000 T sites. Edge effects are avoided by assuming periodic boundary conditions. It turns out that for this cluster size, the results become essentially independent of the number of sites.

This paper reports the results obtained for two actual connectivity schemes: Zeolite X or Y and the square planar lattice. The latter can be viewed as a hypothetical zeolite because it has the same topological features as real zeolites. The coordination is four fold, and two next-nearest-neighbors are connected by either one or two lattice positions:



The planar lattice is particularly interesting as a model system because it allows the various patterns of Al distributions to be visualized in simple graphic displays.

#### Completely Random Al Distribution

In this model, where no preference of Si-Al over Al-Al pairing is assumed, the NMR spectrum is determined by the simple probabilities of uncorrelated occupancies of the four nearest neighbors. Therefore, the peak intensities for the completely random model are independent of the details of the zeolite framework topology. They are

$$\begin{aligned}
 I_0 &= (1-x)^4 \\
 I_1 &= 4x(1-x)^3 \\
 I_2 &= 6x^2(1-x)^2 \\
 I_3 &= 4x^3(1-x) \\
 I_4 &= x^4
 \end{aligned}
 \tag{6}$$

From these expressions, we derive  $M_1 = 4x$ . Thus the center of gravity,  $M_1$ , deviates substantially from Loewenstein's  $M_1 = 4x/(1-x)$ , as has been pointed out by Melchior, et al. (4) A computer simulation of the completely random Al occupation on the square planar lattice and the zeolite X lattice resulted in the NMR intensities predicted by Equation (6).

### Square Planar Lattice

The procedure that we followed to simulate a random occupation of sites by Al's under Loewenstein's restriction was to first randomly occupy sites at the desired concentration and then letting the Al's move to minimize  $x_1$ . This was done by choosing a Si and an Al at random and having them exchange positions only if the exchange would either decrease  $n_1$  or leave  $n_1$  unchanged. The latter condition was added to ensure rapid convergence and to allow a large degree of mobility thus ensuring optimum randomization. This procedure was continued well beyond the point where  $n_1$  vanished. The required number of "tosses" was as high as  $10^6$  for  $x=0.5$  and a square array of  $32 \times 32$  points but orders of magnitude less for lower  $x$  values. Dempsey's rules were implemented by allowing the randomization process to continue long after  $n_1$  had vanished, with the additional restriction that Si-Al exchanges were forbidden if they would increase  $n_2$ .

The results of eight runs on a  $20 \times 20$  square are shown in Figures 1 and 2. The figures show the actual sites occupied by Al's (Si's are left blank) together with the NMR spectra and the  $x_2$  values. The latter do not exactly correspond to the displayed Al/Si matrices but are the average results of 20 trials on a  $32 \times 32$  square. One sees clearly that second-nearest-neighbor avoidance changes the patterns and the spectra at  $x < 0.35$ , but that at higher Al concentration only minor effects are observed. The effect of Dempsey's rules is towards a more uniform distribution of the Al's in the lattice. This is most pronounced at  $x$  between 0.15 and 0.25 (Si/Al between 3 and 6). The NMR spectra are seen to narrow around the center of gravity when  $x_2$  decreases, in accordance with Equation (5). It should be noted that the Dempsey patterns of Figures 1 and 2 are not the ones with the very lowest attainable  $x_2$  value. Convergence is too slow to reach this limit. For instance, for  $x=0.25$ , there is a variety of ways to fill the square having  $x_2$  as low as 0.25. Thus the  $x=0.25$  result shown in Figure 1 ( $10^5$  tosses), having  $x_2=0.28$ , did not reach full convergence, although an extended run with  $10^6$  tosses brought  $x_2$  down to 0.26.

When  $x$  approaches 0.5, the patterns show large domains of long range "checker-board" order, separated by boundaries and containing vacancies. The domains quickly become smaller as  $x$  decreases below 0.35 and dissolve into a disordered structure.

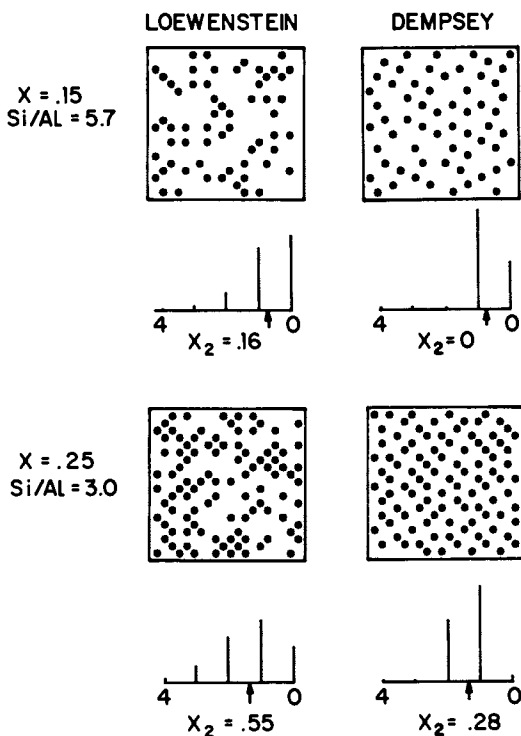


Figure 1.  
Random distributions in a 20 x 20 square planar lattice according to Loewenstein's rule and Dempsey's rules. The Al's are indicated by dots; the Si's are left blank. Also shown are simulated  $^{29}\text{Si}$  spectra and  $x_2$  values obtained from 32 x 32 square planar lattices.



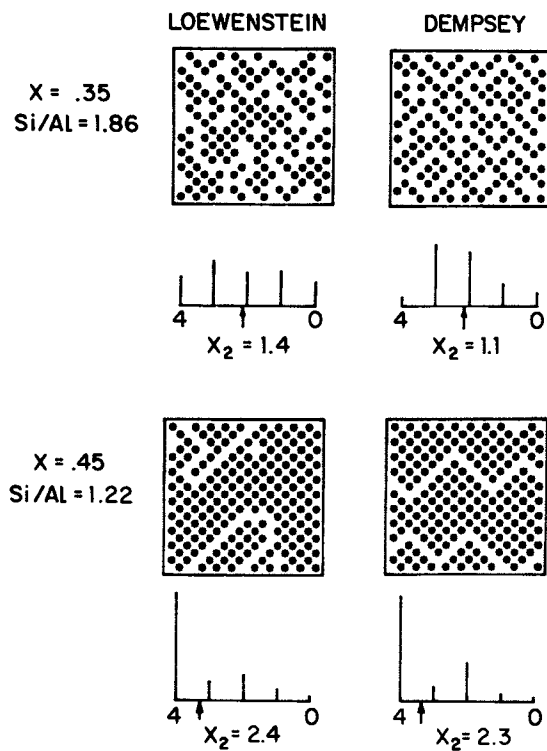


Figure 2.  
Same as Figure 1; for different Si/Al ratios.

This is shown quantitatively in Figure 3 where the pair correlation function is plotted for a few Si/Al ratios. Note that for  $x > 0.25$  the next-nearest-neighbor restriction partially destroys ("frustrates") the long range order, while at low Al content it tends to enhance the order. In any case, the correlation length is never much longer than a few bond lengths, unless the Si/Al ratio is very close to 1. Consequently, there is no reason to assume that a zeolite structure will result with identical unit cells to such an extent that Al ordering can be picked up by X-ray diffraction, unless  $\text{Si/Al} \sim 1$ .

### Zeolite X and Y

The zeolite X and Y framework is considered to be topologically built up out of basic units consisting of two sodalite cages that can be connected to other units through double six-rings into 6 directions. In this way, a three dimensional network of T-site connectivities can easily be constructed. Each unit contains 48 T-sites. Most calculations were done on a cluster of 27 ( $3 \times 3 \times 3$ ) units, i.e., 1296 sites. The computational procedure was the same as described for the square lattice. The results of the five calculated NMR intensities are plotted versus  $x$  in Figure 4. The plots are characterized by the appearance of maxima in the  $I_1$ ,  $I_2$ , and  $I_3$  curves. Thus, comparison between the positions, heights, and widths of these maxima is one way to distinguish the various computational models. The following observations can be made:

- The  $x$  values, at which maximum peak intensities are observed, are the same for Loewenstein's and Dempsey's models.
- The maximum peak intensities are significantly higher for site distributions according to Dempsey's rules. This follows from the minimization of the second moment.
- The onset of  $I_2$ ,  $I_3$ , and  $I_4$ , with increasing Al content occurs at higher  $x$  values in Dempsey's model.

The most significant diagnostic parameter for distinguishing between Loewenstein's and Dempsey's models should be  $x_2$ , because it directly measures the number of second-nearest Al-Al pairs. The  $x_2$  values are plotted in Figure 5. Also shown in Figure 5 are experimental data taken from the literature (vide infra). The difference between Loewenstein's and Dempsey's  $x_2$  values is most pronounced around  $x=0.2$ , as we have also seen in<sup>2</sup> Figures 1 and 2. At higher Al content, the distinction between the two models becomes less pronounced.

### Comparison with Experimental Data

The computational results of this work are compared in Figure 6 with the results of three publications (2, 3, 4) that provide experimental data on Si NMR intensities of zeolites X and

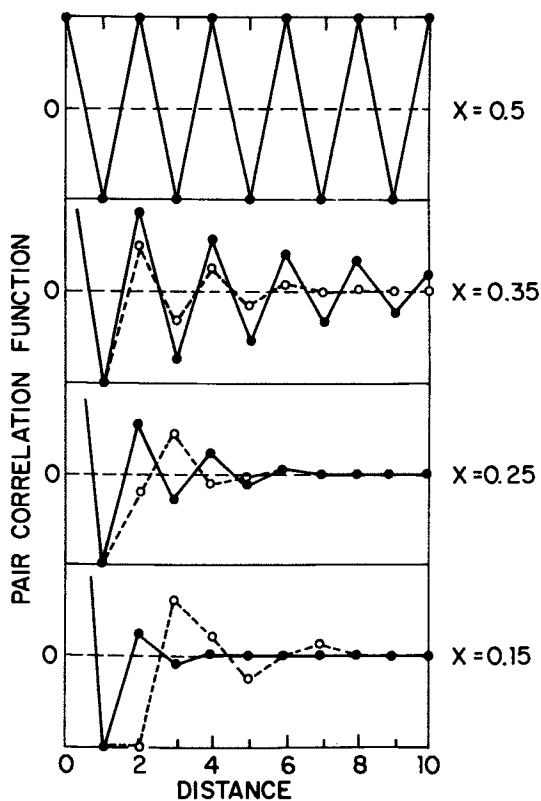


Figure 3.  
 Pair correlation function of Si/Al site occupancies in a square planar lattice with randomized Al distribution according to Loewenstein's rule (—●—) and Dempsey's rules (---○---).

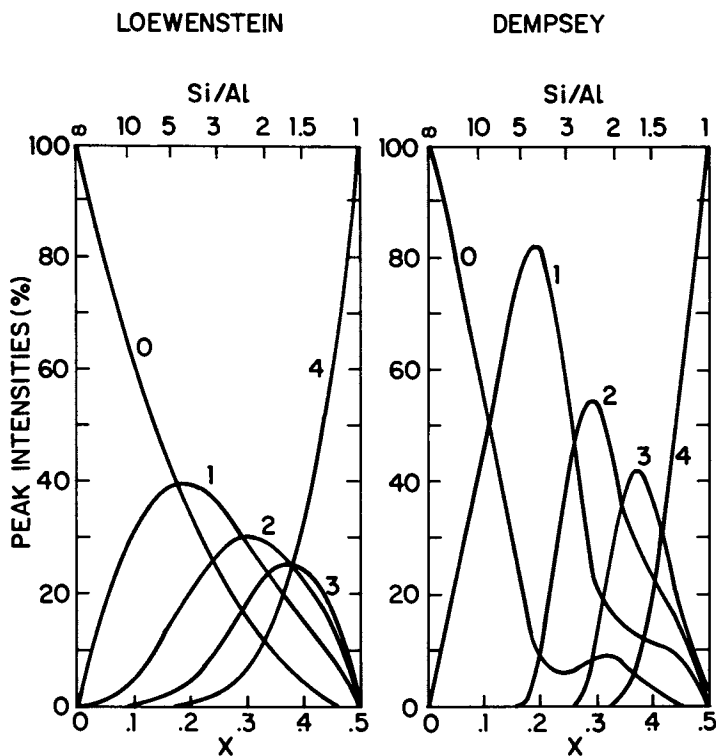


Figure 4.

Computer predicted  $^{29}\text{Si}$  NMR peak intensities for zeolites X and Y with randomized Al occupation restricted to Loewenstein's and Dempsey's rules, plotted versus the Al concentration,  $x$ . The corresponding Si/Al ratios are indicated above the figures.

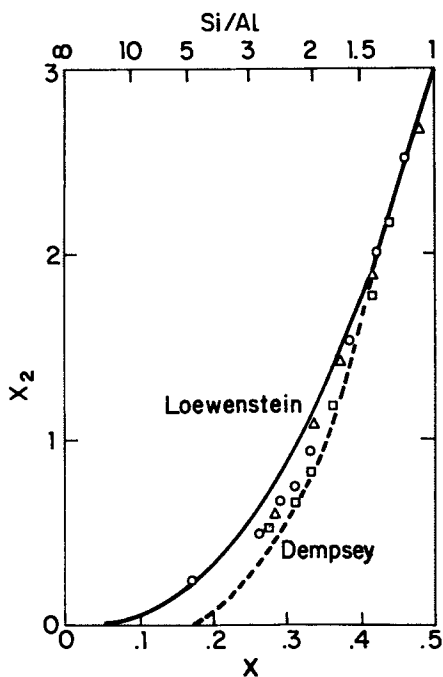


Figure 5.

Density of Al-Si-Al linkages ( $x_2$ ) in zeolites X and Y. Experimental results taken from:  $\Delta$  - Ramdas et al. (2); o - Engelhardt et al. (3);  $\square$  - Melchior et al. (4). The curves are the theoretical predictions of this work.

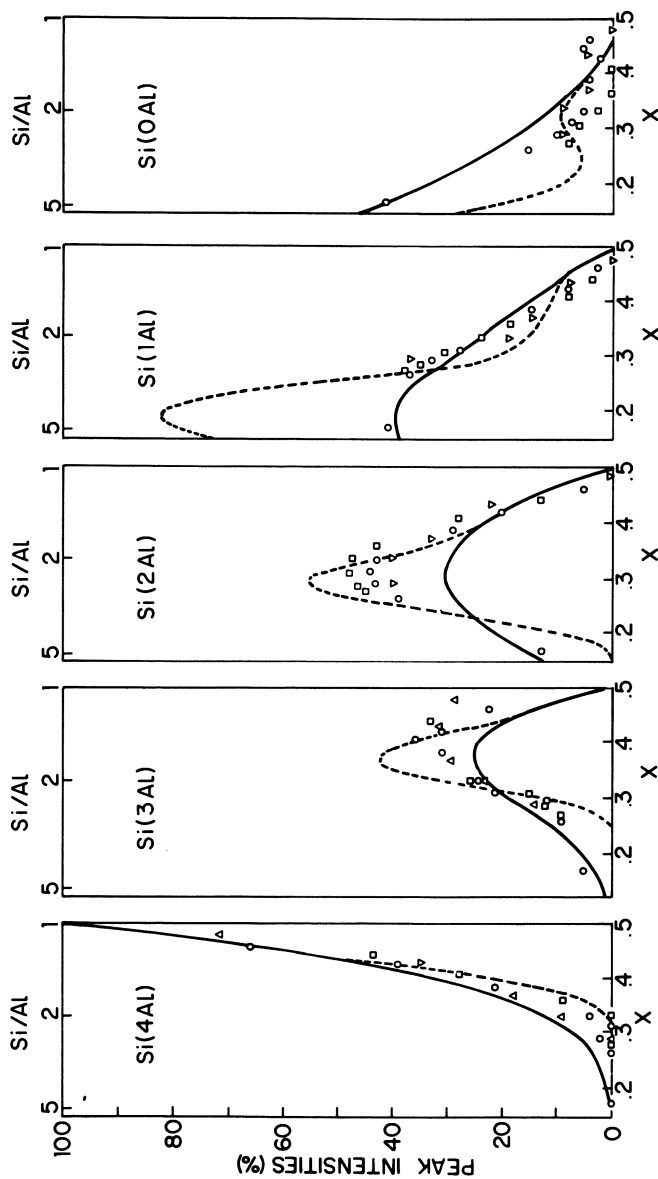


Figure 6.  
 The five relative  $^{29}\text{Si}$  peak intensities of zeolites X and Y.  
 Experimental results taken from:  $\Delta$  - Ramdas et al. (2);  $\circ$  -  
 Engelhardt et al. (3);  $\square$  - Melchior et al. (4). The curves  
 are the theoretical predictions of this work (—, Loewenstein  
 model; ---, Dempsey model).

Y with varying Al content. In Figure 6 are shown five separate plots of the relative intensities of the five spectral peaks versus the Al content,  $x$ . For each experimental spectrum,  $x$  was determined from the first moment according to Equation (2), whereby we assumed that Loewenstein's rule is obeyed for all samples. Inspection of Figure 6 gives the general impression that the actual spectra follow the predicted random models rather closely with a tendency to comply with Dempsey's rules, although not completely. However, when the Si/Al ratio approaches 1 ( $x > .4$ ), the experimental points fall substantially outside the theoretical range, notably Si (3 Al) and Si (0 Al). This probably indicates that at those compositions the Al distribution is more ordered than our model implies.

Our random approach is apparently more adequate at the higher Si/Al ratios ( $x < .35$ ). While most samples in that region clearly tend to avoid second-nearest-neighbor Al pairs, the sample with a Si/Al ratio of 5 shows perfect agreement with the random Loewenstein model. It should be noted that this sample differs from the others in that it was not directly synthesized, but was prepared by dealumination of a lower Si/Al ratio sample (3).

The most direct information concerning compliance with Dempsey's rules is found in Figure 5 where the experimental  $x_2$  values are compared with computed results. Again, the dealuminated  $x = .17$  sample (3) exhibits total randomization under Loewenstein's restrictions, while the other samples indicate limited compliance with Dempsey's rules.

#### Acknowledgement

The author thanks Drs. S. Reich, A. Suna, P. Meakin, and E. B. Caruthers for helpful discussions.

#### Literature Cited

1. Lippmaa, E.; Magi, M.; Samoson, A.; Tarmak, M.; Engelhardt, G. *J. Am. Chem. Soc.*, 1981, **103**, 4992.
2. Ramdas, S.; Thomas, J. M.; Klinowski, J.; Fyfe, C. A.; Hartman, J. S. *Nature*, 1981, **292**, 288.
3. Engelhardt, G.; Lohse, U.; Lippmaa, E.; Tarmak, M.; Magi, M. *Z. Anorg. Allg. Chem.*, 1981, **482**, 49.
4. Melchior, M. T.; Vaughan, D. E. W.; Jacobson, A. J. *J. Am. Chem. Soc.*, in press.
5. Mikovsky, R. J.; Marshall, J. F. *J. Catal.*, 1976, **44**, 170.
6. Mikovsky, R. J.; Marshall, J. F. *J. Catal.*, 1977, **49**, 120.
7. Mikovsky, R. J.; Marshall, J. F.; Burgess, W. P. *J. Catal.*, 1979, **58**, 489.
8. Peters, A. W. *J. Phys. Chem.*, 1982, **86**, 3489.
9. Dempsey, E.; Kuhl, G. H.; Olson, D. H. *J. Phys. Chem.*, 1969, **73**, 387.
10. Dempsey, E. "Molecular Sieves"; *Soc. Chem. Ind.*: London, 1968; p 293.

RECEIVED November 4, 1982

## High Resolution Silicon-29 NMR Studies of Gallium Faujasites and a Gallium Sodalite

D. E. W. VAUGHAN, M. T. MELCHIOR, and A. J. JACOBSON  
Exxon Research and Engineering Company, Linden, NJ 07036

High resolution silicon-29 NMR measurements have been made for three gallium faujasites and a gallium sodalite with Si/(Al + Ga) ratios of 1.14, 1.42, 2.17 and 1.28, respectively. The relative NMR peak intensities for the gallium faujasites are closely similar to their aluminum analogues indicating similar distributions of T atoms in the structure but the peaks are deshielded by an amount proportional to the number of nearest neighbor gallium atoms. The gallium sodalite sample shows similar chemical shift behavior but the relative peak intensities are different to those observed for either Na-X or ZK-4 with the same framework composition.

High resolution solid state silicon-29 NMR is being extensively investigated as a technique for probing the structure of zeolites and other aluminosilicates. The technique was first introduced by Lippmaa and coworkers (1,2,3) who showed that high resolution  $^{29}\text{Si}$  NMR gives well resolved absorptions with chemical shifts characteristic of the local silicon environment. For example, in zeolite Na-X with Si/Al = 1.18, five peaks are observed in the NMR spectrum which are associated with silicons surrounded by from 0 to 4 aluminum nearest neighbors (Si - nAl, n = 0 to 4). From measurements of a number of different zeolites and framework compositions, Lippmaa et al. (3) proposed ranges of chemical shifts characteristic of the five different Si-nAl environments. These ranges are relatively narrow (Table I) and increasingly overlap with decreasing aluminum substitution. For a given framework type, for example faujasite (3,4,5,6), the chemical shifts vary little with framework Si/Al ratio, the largest shift being observed for the Si-OAl peak (4ppm).

While this generalization initially has proved useful in interpreting data, several recent results have shown the

0097-6156/83/0218-0231\$06.00/0  
© 1983 American Chemical Society



TABLE I  
Chemical Shift Ranges for  $^{29}\text{Si}$  NMR of Aluminosilicates (3)

| <u>Si-nAl</u> | <u>Chemical Shift (ppm vs. TMS)</u> |
|---------------|-------------------------------------|
| 4             | -83 to -87                          |
| 3             | -88 to -94                          |
| 2             | -93 to -99                          |
| 1             | -97 to -105                         |
| 0             | -103 to -114                        |

sensitivity of chemical shifts to other than the nearest neighbor aluminum distribution. For example, Thomas and coworkers (7) measured the spectra of several zeolites not reported by Lippmaa et al. (3) and found similar chemical shift ranges. They did, however, extend the lower bound for Si-4Al to -80 ppm in order to include the zeolites Li-A(BW) at -80.1 ppm and a partially lithium exchanged cancrinite hydrate at -82.0 ppm. It has been assumed by most groups, with some experimental support, that the non-framework cations have little effect on chemical shifts. However, it is likely that the above shifts are to be associated with the lithium cations in the structure. Support for this hypothesis comes from the observation of large shifts in both zeolites A and X when sodium is exchanged for lithium (8,9).

It has also been observed that zeolite A (10,11,12) and Losod (7) both with Si/Al = 1 have chemical shifts of -88.9 ppm, outside of the range proposed for Si-4Al. At first, this was attributed to Si-3Al ordering in violation of Lowenstein's rule. However, recent neutron diffraction work on zeolite A (14) and NMR studies of its high silica analogue ZK-4, (8,13) have shown that the single resonance in zeolite A does correspond to Si-4Al. The unusual chemical shift for zeolite A may be a consequence of the strained double four rings in the structure and the presence of one nearly linear T-O-T angle.

The structural information contained in the chemical shift data is perhaps best illustrated by the recent results for high silica ZSM-5 (15). In this almost pure silica system, the Si-0Al resonance is resolved into nine components arising from crystallographically non-equivalent tetrahedral silicon environments.

In order to further extend our understanding of the origin of chemical shift variations in zeolites, we have examined the effects of gallium substitution for aluminum in the framework on the silicon NMR spectra of sodalite and faujasite. Gallium substitution in zeolites is well known though most preparations

have been made in the presence of major amounts of aluminum. Gallium analogues of faujasite and sodalite were reported by Selbin and Mason (16) and gallium thomsonite by Barrer et al. (17). The gallium containing zeolites analcime and nepheline hydrate II have also been described (18). Only the silicon NMR of gallium thomsonite (-82.9 ppm (7); c.f. thomsonite, -83.5 ppm (3)) has, to our knowledge, been previously described.

### Experimental

Faujasites with a low Si/Ga ratio were synthesized using a slurry composition:  $2.1 \text{ Na}_2\text{O} : \text{Ga}_2\text{O}_3 : 2-4 \text{ SiO}_2 : 60 \text{ H}_2\text{O}$  and seeded with aluminosilicate seeds (19); 1% Al relative to the gallium in the synthesis. Gallium was used as sodium gallate made by dissolution of  $\text{Ga}_2\text{O}_3$  in NaOH; the source of silica was sodium silicate ( $\text{SiO}_2/\text{Na}_2\text{O} = 1.32$ ). After thorough mixing the reaction slurry was heated at  $100^\circ\text{C}$  for 3 to 6 hrs in teflon bottles to give faujasite. Longer reaction times at the same temperature gave pure sodalite. Intermediate reaction times gave mixtures of sodalite and faujasite; the gallium analogue of zeolite A was not observed although comparable reactant compositions in the aluminum system give A at short (1-2 hrs) reaction times. Synthetic gismondine (Barrer P, Linde B) is replaced by gallium sodalite over a wide composition range.

Higher Si/Ga faujasites were synthesized using similarly seeded compositions in the range  $2-3 \text{ Na}_2\text{O} : \text{Ga}_2\text{O}_3 : 5-9 \text{ SiO}_2 : 140 \text{ H}_2\text{O}$ . Reactions were again carried out at  $100^\circ\text{C}$  without stirring in teflon bottles. Reaction times to well crystallized faujasites were typically 20 hrs. The general pattern of these syntheses parallels those for the pure sodium aluminosilicate system with gallium oxide completely replacing aluminum oxide except for the contribution from the seeds. Attempts to make gallosilicate seed solutions by the procedure of reference (19) by replacing  $\text{Al}_2\text{O}_3$  with  $\text{Ga}_2\text{O}_3$  were unsuccessful. Exclusion of seeds from the high silica synthesis gave no crystalline products in reasonable (<4 days) reaction times.

Chemical compositions were determined by plasma emission spectroscopy using a Jarrel-Ash Atomcom III inductively coupled plasma spectrometer (Table II). Samples were checked for purity by X-ray diffraction using a Siemens D500 diffractometer and  $\text{CuK}\alpha$  radiation and by scanning electron microscopy. No other crystalline phases or amorphous material were detected. For the gallium faujasites, nitrogen surface areas were in the range  $600-650 \text{ m}^2/\text{g}$ .

Silicon NMR measurements were made at 39.5 MHz on a Jeol FX200WB spectrometer using the combined techniques of magic-angle sample spinning and proton dipolar decoupling. All samples were examined in the fully hydrated state. Chemical shifts were referenced to sodium 4,4-dimethyl-4 silapentane sulfonate taken to

TABLE II

## Chemical Compositions of Gallium Sodalite and Faujasites

| Sample   | Na <sub>2</sub> O | Al <sub>2</sub> O <sub>3</sub> | Ga <sub>2</sub> O <sub>3</sub> | SiO <sub>2</sub> | Si/(Al+Ga) |
|----------|-------------------|--------------------------------|--------------------------------|------------------|------------|
| Sodalite | 1.03              | 0.03                           | 0.97                           | 2.56             | 1.28       |
| Na-GaX   | 1.00              | 0.05                           | 0.95                           | 2.28             | 1.14       |
| Na-GaX   | 0.95              | 0.03                           | 0.97                           | 2.84             | 1.42       |
| Na-GaY   | 0.97              | 0.02                           | 0.98                           | 4.33             | 2.17       |

have a <sup>29</sup>Si chemical shift of -1.30 ppm vs. tetramethylsilane (TMS).

### Results and Discussion

The NMR results for three sodium faujasites and a gallium sodalite are shown in Figs. 1 and 2. The chemical shifts and relative peak intensities are given in Tables III and IV. The relative peak intensities are normalized to  $\sum I(\text{Si-nT}) = 1.0$ . NMR compositions were calculated from the relative peak intensities assuming Lowenstein's rule and using the relation

$$\text{Si/Ga} = 4 / \sum_0^n nI(\text{Si-nGa})$$

We have not considered, in calculating the NMR compositions, the small amount of Al (<5%) introduced into the samples from the seeds used in the synthesis.

Gallium-Sodalite The gallium sodalite sample prepared as described above has a Si/(Al+Ga) ratio of 1.28 determined by elemental analysis. The composition determined from the NMR spectrum, Si/Ga = 1.26, is in good agreement with the elemental analyses indicating that this gallium sodalite obeys Lowenstein's rule. In aluminum sodalites with Si/Al = 1 variations in chemical shifts have been observed (7,20) and it has been suggested that some sodalites show Si-3Al ordering. However, the gallium sodalite data, the first reported for a material with a Si/T > 1, suggest that sodalites obey Lowenstein's rule. We have observed significant variations in chemical shifts for aluminum sodalites as the unit cell size and presumably the T-O-T angles are changed by salt inclusion and this may be the origin of the previously reported differences.

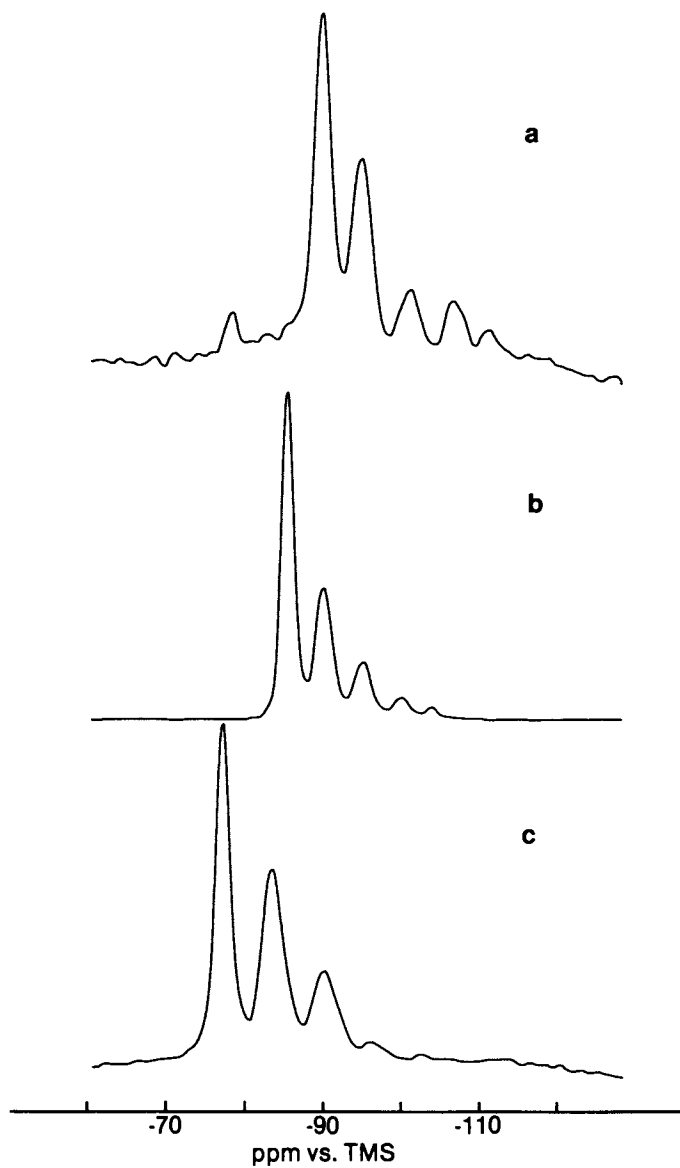


Figure 1.  
Silicon-29 NMR spectra of (a) ZK-4, (b) Na-X and (c) gallium sodalite.

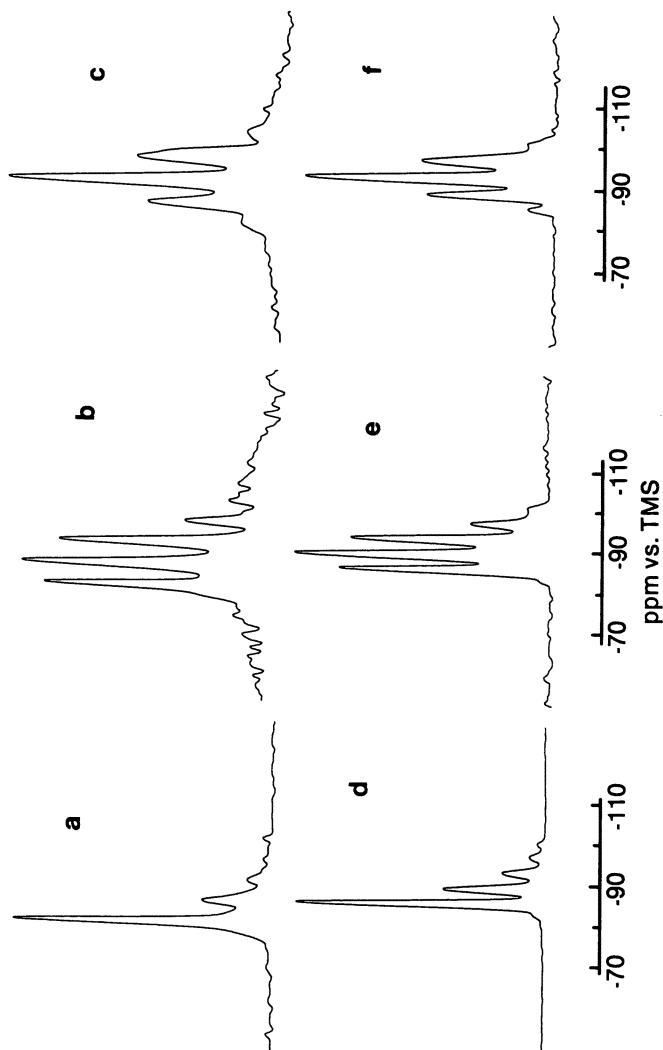


Figure 2.  
Silicon-29 NMR spectra of gallium faujasites with Si/(Al+Ga) ratios of (a) 1.11 (b) 1.26 and (c) 2.0 compared with their aluminum analogues with Si/Al ratios (d) 1.24 (e) 1.44 and (f) 1.95.

TABLE III

A Comparison of the Chemical Shifts and Relative Intensities in the Silicon NMR Spectra of ZK-4, Na-X and Gallium Sodalite

|             | Chemical Shift (ppm vs. TMS) for I(Si-nT), T = Al or Ga |                       |       |       |        |        |        |
|-------------|---|-----------------------|-------|-------|--------|--------|--------|
|             | (Si/T) <sub>E.A.</sub>                                  | (Si/T) <sub>NMR</sub> | Si-4T | Si-3T | Si-2T  | Si-1T  | Si-0T  |
| ZK-4* (21)  | 1.32  | 1.28                  | -89.2 | -94.1 | -100.3 | -105.7 | -110.4 |
| Na-X (22)   | 1.27  | 1.24                  | -84.4 | -88.9 | -93.9  | -98.7  | -102.6 |
| Ga-Sodalite | 1.28  | 1.26                  | -76.0 | -82.4 | -89.0  | -94.9  | -101.3 |
|             | Relative Intensities I(Si-nT), T = Al or Ga             |                       |       |       |        |        |        |
|             | Si-4T   | Si-3T                 | Si-2T | Si-1T | Si-0T  |        |        |
| ZK-4        | 0.430   | 0.350                 | 0.110 | 0.080 | 0.040  |        |        |
| Na-X        | 0.509   | 0.292                 | 0.135 | 0.032 | 0.032  |        |        |
| Ga-Sodalite | 0.436   | 0.350                 | 0.177 | 0.027 | 0.009  |        |        |

\*contains a small meta silicate impurity

TABLE IV  
 Chemical Shifts and Relative Intensities in the Silicon  
 NMR Spectra of Gallium Faujasites

|        | Chemical Shift (ppm vs. TMS) for I(Si-nGa) |                        |        |        |        |        |        |        |        |        |        |        |
|--------|--|------------------------|--------|--------|--------|--------|--------|--------|--------|--------|--------|--------|
|        | (Si/Al+Ga) <sub>EA</sub>                   | (Si/Ga) <sub>NMR</sub> | Si-4Ga | Si-3Ga | Si-2Ga | Si-1Ga | Si-0Ga | Si-4Ga | Si-3Ga | Si-2Ga | Si-1Ga | Si-0Ga |
| Na-CaX | 1.14                                       | 1.11                   | -77.7  | -84.2  | -90.3  | -96.4  | -102.8 |        |        |        |        |        |
| Na-CaX | 1.42                                       | 1.39                   | -78.0  | -84.2  | -90.9  | -97.4  | -104.2 |        |        |        |        |        |
| Na-CaY | 2.17                                       | 2.06                   | -78.3  | -84.6  | -91.4  | -98.2  | -105.8 |        |        |        |        |        |
|        | Relative Intensities I(Si-nGa)             |                        |        |        |        |        |        |        |        |        |        |        |
|        |  |                        | Si-4Ga | Si-3Ga | Si-2Ga | Si-1Ga | Si-0Ga |        |        |        |        |        |
| Na-CaX |  |                        | 0.681  | 0.222  | 0.059  | 0.022  | 0.015  |        |        |        |        |        |
| Na-CaX |  |                        | 0.318  | 0.348  | 0.242  | 0.076  | 0.015  |        |        |        |        |        |
| Na-CaY |  |                        | 0.047  | 0.219  | 0.411  | 0.274  | 0.049  |        |        |        |        |        |

In Fig. 1, the spectra for ZK-4 (21), Na-X (22) and gallium sodalite, all with similar compositions, are compared. Relative to Na-X, the Si-nAl peaks for ZK-4 are shielded by an amount which varies from 4.8 ppm for Si-4Al to 7.8 ppm for the Si-OAl peak. In comparing Na-X with gallium-sodalite, however, the opposite effect is observed; the Si-4Ga peak is deshielded by 8.4 ppm whereas the Si-OGa peak is only deshielded by 1.3 ppm. The first case illustrates the structure sensitivity of the chemical shift, whereas in the second case, substitution in the first coordination sphere by gallium evidently is the dominant effect. The comparison of aluminum and gallium faujasites below further illustrates this point.

It is also of interest to compare the relative peak intensities for these three materials. The differences between the peak intensities for Na-X and Y and ZK-4 as a function of composition have previously been discussed (22). Gallium sodalite with Si/Ga = 1.26 has a different intensity pattern to either faujasite or ZK-4. A comparison of the ratios of I(Si-4T)/I(Si-3T) and I(Si-3T)/I(Si-2T) for the three compounds shows the differences. The corresponding values are 1.23, 1.74, 1.25 and 3.18, 2.16, 1.98 for ZK-4, Na-X and gallium sodalite, respectively. Further discussion of the Si/Ga distribution in gallium sodalite requires data over a range of composition and this not yet available.

Gallium Faujasites In Table IV the data for three gallium faujasites are summarized. The agreement between the ratios calculated from the NMR spectra and determined by elemental analysis is good for the Na-GaX compounds and reasonable for Na-GaY, indicating that Lowenstein's rule is obeyed. The chemical shift range observed for the gallium faujasites is comparable to that observed for the gallium sodalite. An overall deshielding is observed as the Si/Ga ratio is increased, the effect being largest for the Si-OGa peak. Similar changes with composition are observed in aluminum faujasites, though the overall spread of chemical shifts is much smaller for aluminum faujasites (18.5 ppm at Si/Al = 1.16) than for their gallium analogues (25.1 ppm at Si/Ga = 1.14). The comparison of the spectra (Fig. 2) for the three gallium faujasites with aluminum analogues of closely similar composition clearly shows this effect. The Si-OGa peaks have comparable chemical shifts but the other peaks are deshielded by an amount which, within experimental error, is proportional to the number of gallium nearest neighbors. The differences in the mean chemical shifts for Na-X at Si/Al = 1.14 and Si/Al = 1.17 (refs. 5,23) and Na-GaX at Si/Ga = 1.1 are given in Table V to illustrate the point.

Finally, we note that the relative peak intensities for the three gallium faujasites are closely similar to those of their aluminum analogues indicating that the distributions of T atoms are similar in the two sets of materials.



TABLE V  
Comparison of the Chemical Shifts for Na-X and Na-GaX

| Sample | (Si/Al) <sub>NMR</sub> | Chemical Shift (ppm vs. TMS) for I(Si-nT), T = Al or Ga |       |       |       |        |    | Ref. |
|--------|------------------------|---|-------|-------|-------|--------|----|------|
|        |                        | Si-4T   | Si-3T | Si-2T | Si-1T | Si-0T  |    |      |
| Na-X   | 1.14                   | -83.9   | -88.1 | -93.1 | -97.9 | -102.4 | 5  |      |
| Na-X   | 1.17                   | -84.6   | -89.0 | -94.2 | -98.8 | -103.1 | 23 |      |
| Mean   |                        | -84.3   | -88.6 | -93.7 | -98.4 | -102.8 |    |      |
| Na-GaX | 1.11                   | -77.7   | -84.2 | -90.3 | -96.4 | -102.8 |    |      |
| Δ      |                        | 6.6   | 4.4   | 3.4   | 2.0   | 0      |    |      |

### Conclusions

High resolution  $^{29}\text{Si}$  NMR spectra of gallosilicates with the faujasite structure exhibit relative peak intensities similar to faujasite indicating similar distributions of T atoms. However, the peaks in the gallium containing zeolites are deshielded by an amount nearly proportional to the number of gallium atoms in the first neighbor shell.

There is evidence in the literature that chemical shift variations are related to variations in the average T-O-T angles. For example, Thomas et al. (8) have suggested that the unusual chemical shift for the Si-4Al peak in Na-A (~ 5 ppm shielded with respect to Na-X) is related to the unusually large average T-O-T angle of  $152.5^\circ$ ; the mean value for zeolites is about  $145^\circ$  (24). Additional support for this qualitative correlation comes from data on lithium containing zeolites. Exchange of lithium for sodium in Na-X is accompanied by a deshielding of the Si-4Al peak from -84 ppm to -80 ppm (9). Recent structural work on partially exchanged Li,Na-X showed that the average T-O-T angle is reduced to  $137.1^\circ$  in Li,Na-X from  $141.9^\circ$  in pure Na-X. Similarly, Li-A(BW) (27) has an average T-O-T angle of  $134.8^\circ$  and has a Si-4Al peak comparably deshielded to that observed in Li-X.

There is unfortunately little structural information for gallium substituted zeolites. However, the observed chemical shifts are compatible with the above general correlation with T-O-T angle. For example, the non-bonded or "one angle" radii approach of O'Keefe and Hyde (27) suggests that the Si-O-Ga angles would generally be smaller than Si-O-Al angles and consequently that gallium substitution would deshield the silicon resonances. More detailed studies of the relation of T-O-T angles to bond lengths and chemical shifts are in progress.

### Acknowledgments

We thank K. Strohmaier for assistance with sample preparation and analysis and C. F. Pictroski for his assistance in acquiring the NMR spectra.

### Literature Cited

1. Lippmaa, E. T.; Alla, M. A.; Pehk, T. J.; Engelhardt, G.; J. Am. Chem. Soc. 1978, 100, 1929.
2. Lippmaa, E.; Magi, M.; Samoson, A.; Engelhardt, G.; Grimmer, A. -R.; J. Am. Chem. Soc. 1980, 102, 4889.
3. Lippmaa, E.; Magi, M.; Samoson, A.; Tarmak, M.; Engelhardt, G.; J. Am. Chem. Soc. 1981 103, 4992.
4. Ramdas, S.; Thomas, J. M.; Klinowski, J.; Fyfe, C. A.; Hartman, J. S. Nature 1981, 292, 228..

5. Klinowski, J.; Ramdas, S.; Thomas, J. M.; Fyfe, C. A.; Hartman, J. S.; *J. Chem. Soc. Faraday Trans. 2*, 1982, 78, 1025.
6. Melchior, M. T.; Vaughan, D. E. W.; Jacobson, A. J.; *J. Am. Chem. Soc.* 1982, 104, 4859.
7. Klinowski, J.; Thomas, J. M.; Fyfe, C. A.; Hartman, J. S.; *J. Phys. Chem.* 1981 85, 2590.
8. Thomas, J. M.; Fyfe, C. A.; Ramdas, S.; Klinowski, J.; Gobbi, G. C.; *J. Phys. Chem.* 1982, 86, 3061.
9. Melchior, M. T.; Vaughan, D. E. W.; Jacobson, A. J.; to be published.
10. Engelhardt, G.; Zeigan, D.; Lippmaa, E.; Magi, M.; *Z. Anorg. Allg. Chem.* 1980, 468, 35.
11. Thomas, J. M.; Bursill, L. A.; Lodge, E. A.; Cheetham, A. K.; Fyfe, C. A.; *J. Chem. Soc. Chem. Commun.* 1981, 276.
12. Bursill, L. A.; Lodge, E. A.; Thomas, J. M.; Cheetham, A. K.; *J. Phys. Chem.* 1981, 85, 2409.
13. Melchior, M. T.; Vaughan, D. E. W.; Jarman, R. J.; Jacobson, A. J.; *Nature* 1982, 298, 455.
14. Cheetham, A. K.; Fyfe, C. A.; Smith, J. V.; Thomas, J. M.; *J. Chem. Soc. Chem. Commun.* 1982, 823.
15. Fyfe, C. A.; Gobbi, G. C.; Klinowski, J.; Thomas, J. M.; Ramdas, S.; *Nature* 1982, 296, 530.
16. Selbin J.; Mason, R. B.; *J. Inorg. Nucl. Chem.* 1961, 20, 222.
17. Barrer, R. M.; Baynham, J. W.; Bultitude, F. W.; Meier, W. M.; *J. Chem. Soc.* 1959, 195.
18. Ponomareva, T. M.; Tomilov, N. P.; Berger, A. S.; *Zh. Neorg. Khim* 1979, 24, 530.
19. Vaughan, D. E. W.; Edwards, G. C.; Barrett, M. G.; *U.S. Patent* 4,340,573, 1982.
20. Thomas, J. M.; Klinowski, J.; Fyfe, C. A.; Hartman, J. S.; Bursill, L. A.; *J. Chem. Soc. Chem. Commun.* 1981, 678.
21. Jarman, R. H.; Melchior, M. T.; Vaughan, D. E. W.; Chapter , in this book.
22. Melchior, M. T.; Chapter , in this book.
23. Engelhardt, G.; Lohse, U.; Lippmaa, E.; Tarmak, M.; Magi, M.; *Z. Anorg. Allg. Chem.* 1981, 482, 49.
24. Baur, W. H.; *Acta Cryst.* 1980, B26, 2198.
25. Herden, H.; Einicke, W. -D.; Schöller, R.; Mortier, W. J.; Gellens, L. R.; Uytterhoven, J. B.; *Zeolites* 1982, 2, 131.
26. Kerr, I. S.; *Z. Kristallogr.* 1974, 139, 186.
27. O'Keefe, M.; Hyde, B. G.; in "Structure and Bonding in Crystals" Vol. I, Eds. O'Keefe, M.; Navrotsky, A.; Academic Press, New York, 1981, p. 227.

RECEIVED November 4, 1982

# Silicon and Aluminum Ordering of Zeolites: Interpretation of Silicon-29 NMR Data for Faujasite and ZK4

M. T. MELCHIOR

Exxon Research and Engineering Company, Linden, NJ 07036

Silicon-29 NMR provides a direct measurement of the average Al neighbor distribution in zeolite frameworks, from which the nature of the Si,Al ordering can be inferred. Comparison of  $^{29}\text{Si}$  NMR data for synthetic faujasites and A-type (ZK4) zeolites shows that the Si,Al distribution is different for these frameworks despite their having a common structural element, the sodalite cage. It is shown that the Si,Al distribution in faujasite crystals can be understood in terms of an ordered sub-unit, the single 6-ring, combined randomly within the framework topology in accordance with Loewenstein's rule as the only constraint. It is hypothesized that the difference between faujasite and ZK4 ordering lies in nature of the fundamental sub-unit.

Silicon-29 Magic Angle Spinning NMR has become an important tool for characterizing silicates and aluminosilicates in general and zeolites in particular. Silicon-29 NMR provides a direct measurement of the average distribution of aluminum neighbors about silicon (1-4), from which it is hoped the nature of the Si,Al ordering can be inferred. Two zeolite framework systems have received the most attention, faujasite (2,3,4) and A-ZK4 (5,6,7). Until recently, only faujasite was available over a significant range of compositions. The recent synthesis and  $^{29}\text{Si}$  NMR study of A-type zeolites (ZK4) over the composition range  $1.0 < \text{Si/Al} < 2.7$  (7,8) provides the opportunity for comparison of  $^{29}\text{Si}$  NMR data for two closely related frameworks over a significant composition range. It has been noted (8) that the distributions of Si and Al atoms in the two structures are different over the entire composition range. This fundamental difference in Si,Al ordering is addressed in this paper, in which we show that the  $^{29}\text{Si}$  NMR data for faujasite, but not that for ZK4, is nicely accounted for in terms of short range order based on an ordered 6-ring building unit.

0097-6156/83/0218-0243\$06.75/0

© 1983 American Chemical Society

### The Ordered Sub-Unit Hypothesis

In our previous study of faujasite (4) we concluded that the Si,Al ordering is satisfactorily described by a simple hypothesis: the faujasite structure is built up, subject to Loewenstein's rule (9) (which excludes Al-O-Al linkages), from sodalite cage sub-units within which the number of Al, Al next nearest neighbors (Al-O-Si-O-Al) is minimized. This simple hypothesis leads to four ordering modes, each predominating over a particular composition range, typified by four sodalite cages X, XY, YX and Y shown in Figure 1. These four cages represent favored arrangements for 12, 14, 15, and 16 silicons per sodalite cage. Faujasite structures built from these ordered sodalite cage sub-units have predicted [Si(nAl)] distributions which have been shown to be in good agreement with the observed 11.9 MHz  $^{29}\text{Si}$  NMR spectra. (4) This agreement is evidence of a considerable local order, by which we mean there is a strong constraint on the Si,Al distribution in addition to Loewenstein's rule. To see this consider that the XY cage represents fewer than one in ten of the possible arrangements of 14 Si and 10 Al which are consistent with Loewenstein's rule. At higher values of Si/Al, the statistics are as unfavorable or more unfavorable toward the ordered sodalite sub-units.

While the essential agreement with the observed  $^{29}\text{Si}$  NMR data obtained with the ordered sodalite sub-unit hypothesis is strong evidence of local Si,Al order, it is important to realize there is no implication of long range order. The distributions predicted by this hypothesis are calculated by considering all choices of assembling the sub-units consistent with Loewenstein's rule as equally probable. Thus the hypothesized arrangements do not possess long range Si,Al order and application of a criterion such as "translational periodicity" (3) is irrelevant. [NOTE: Some of the theoretical distributions, most notably those for Si/Al = 1.67 and 2.43, in our previous publication (4) depend on a particular choice of hexagonal faces in constructing faujasite from ordered sodalite cages, that choice having been made by comparison with the observed NMR data. As is shown below, closely similar distributions result from considering all choices as equally probable.]

We find that the ordered sodalite cage model, which accounts for the faujasite  $^{29}\text{Si}$  NMR data quite well, does not account for the ZK4 data over the range  $1.0 \leq R \leq 3.0$ . Furthermore, as is shown below, high field  $^{29}\text{Si}$  NMR data (39.5 MHz) show small but significant deviations from the predicted distributions for ordered sodalite cages. In the following we consider ordering schemes based on smaller ordered sub-units. The basic hypothesis is that the Si,Al distribution in the zeolite crystal can be described in terms of some ordered sub-unit hooked together

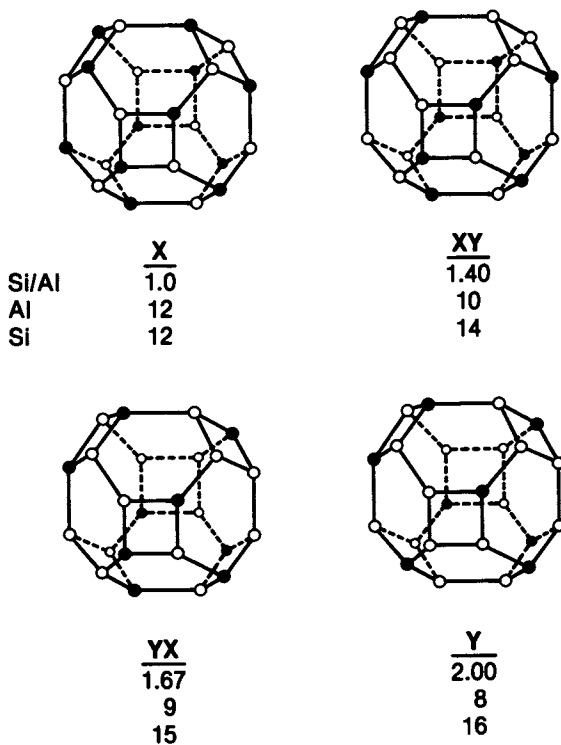


Figure 1.

Favored sodalite cage arrangements which minimize Al-O-Si-O-Al linkages for Si/Al = 1, 1.4, 1.67, 2.00.

statistically, in accordance with Loewenstein's rule as the only constraint. Within the sub-unit the Si,Al distribution is subject to Loewenstein's rule and an additional constraint reflecting a tendency toward reduction of the incidence of Al, Al next nearest neighbors.

Figure 2 depicts various pathways leading to the formation of faujasite and ZK4 from  $\text{SiO}_4$  and  $\text{AlO}_4$  tetrahedra. The various paths may be only conceptually different. Certainly if all steps are statistical (by which we mean subject only to the constraint of Loewenstein's rule) the pathway cannot matter to the final result. Similarly, if all steps are completely ordered, the pathway does not matter. On the other hand if each step is considered irreversible and if additional constraints come into play, we may be able to infer something of the pathway from the final ordering scheme. It will be seen that the success of the ordered sodalite cage description for faujasite, as well as its failure for ZK4, is well accounted for by choosing the 6-ring (6R) as the ordered sub-unit in faujasite but not in ZK4.

#### Experimental Results; Comparison of Faujasite and ZK4

Our previous study of Si,Al ordering in synthetic faujasite was based on  $^{29}\text{Si}$  NMR data obtained at 11.9 MHz (4). Silicon-29 NMR data for the same faujasites obtained at 39.5 MHz show greatly improved resolution of the five Si(nAl) components. Figure 3 shows a comparison of low and high field spectra for two compositions. The improved resolution at the higher field allows direct measurement of the intensities [Si(nAl)], not possible at 11.9 MHz. [NOTE: The striking difference in resolution is probably a consequence of the  $^{27}\text{Al}$  nuclear quadrupole interaction which causes the axis of quantization for  $^{27}\text{Al}$  to deviate from the applied magnetic field direction. At the lower magnetic field of 1.4T the magic angle sample spinning is unable to completely suppress the  $^{27}\text{Al}$ - $^{29}\text{Si}$  dipolar interaction which limits the resolution. This effect is strongly field dependent (10) and becomes negligible at the higher field of 4.7T.] The data is summarized in Table I and plotted as a function of Si/Al in Figure 4. This data was obtained under the same experimental conditions as the  $^{29}\text{Si}$  NMR data for ZK4 (8) and the differences between the distributions [Si(nAl)] for the two zeolites has already been noted.

Improved  $^{29}\text{Si}$  NMR data for these faujasite samples reveal small deviations from the ordered sodalite cage model described above. As illustrated in Figure 3, which shows spectra for Si/Al = 1.40 and 1.73, there is a small peak corresponding to Si(OAl) which is not evident in the low field spectra. The ordered sodalite cage model predicts that the Si(OAl) component vanishes for compositions in the range  $1.4 \leq \text{Si/Al} \leq 2.0$ . As shown in Figure 4, the intensity of Si(OAl) passes through a

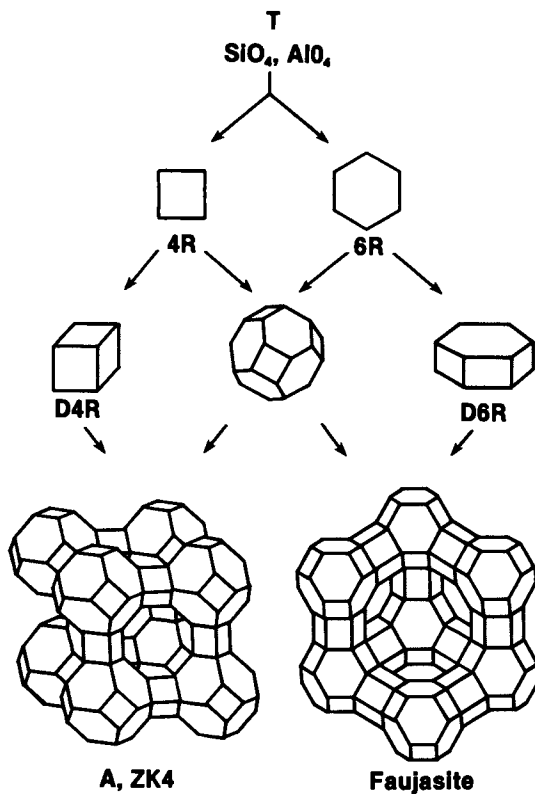


Figure 2.

Possible pathways for the formation of faujasite and A-type zeolites from SiO<sub>4</sub> and AlO<sub>4</sub> tetrahedra.

American Chemical  
Society Library  
1155 16th St. N. W.  
Washington, D. C. 20036



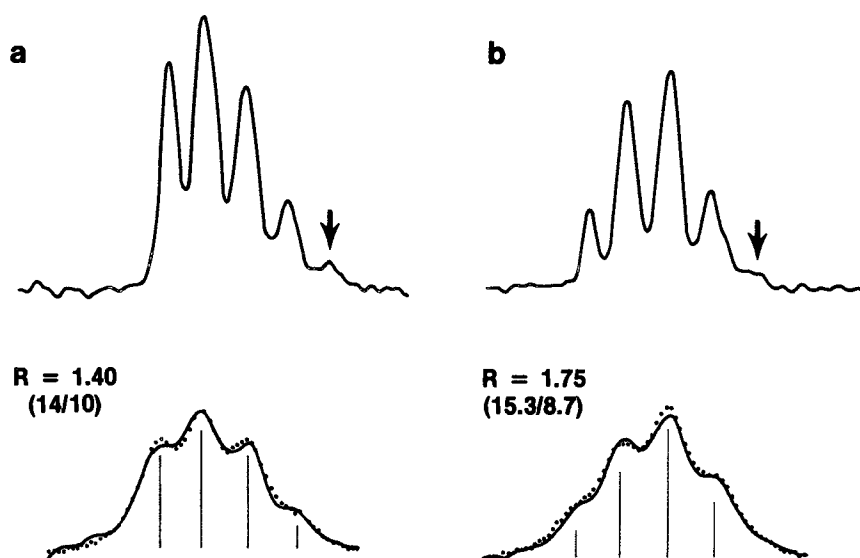


Figure 3.  
 Comparison of  $^{29}\text{Si}$  NMR spectra at 11.9 MHz (below) and 39.5 MHz (above) for faujasite at two compositions (a)  $R = 1.40$  and (b)  $R = 1.75$ . Also shown are the theoretical 11.9 MHz spectra predicted for ordered sodalite cages (points and solid lines) in previous work (4).

Table I

<sup>29</sup>Si NMR Data (39.5 MHz) for Na Faujasites

| Sample          | Si:Al<br>(elemental) | Si:Al<br>(NMR) | Relative Intensity |      |      |      |      |
|-----------------|----------------------|----------------|--------------------|------|------|------|------|
|                 |                      |                | 4Al                | 3Al  | 2Al  | 1Al  | 0Al  |
| 1               | 1.27                 | 1.24           | .509               | .292 | .135 | .032 | .032 |
| 2 <sup>+</sup>  | 1.33                 | 1.28           | .468               | .310 | .141 | .040 | .038 |
| 3               | 1.50                 | 1.48           | .255               | .344 | .266 | .112 | .023 |
| 4               | 1.53                 | 1.44           | .280               | .355 | .252 | .093 | .019 |
| 5               | 1.82                 | 1.74           | .103               | .310 | .388 | .181 | .017 |
| 6               | 2.41*                | 2.01           | .035               | .230 | .452 | .260 | .025 |
| 7               | 2.16                 | 2.12           | .034               | .200 | .425 | .298 | .043 |
| 8               | 2.24                 | 2.17           | .028               | .189 | .427 | .314 | .042 |
| 9 <sup>+</sup>  | 2.39                 | 2.37           | .016               | .139 | .426 | .352 | .066 |
| 10              | 2.49                 | 2.36           | .021               | .148 | .422 | .341 | .067 |
| 11              | 2.52                 | 2.45           | .020               | .126 | .394 | .384 | .076 |
| 12              | 2.52                 | 2.58           | .014               | .110 | .384 | .397 | .096 |
| 13 <sup>+</sup> | 2.53                 | 2.69           | --                 | .113 | .367 | .412 | .107 |
| 14              | 2.62                 | 2.61           | --                 | .093 | .421 | .414 | .071 |

\* Chemical analysis overestimates framework composition because this sample contained amorphous SiO<sub>2</sub>.

+ Samples 2, 9 and 13 are ASTM 2, 1 and 6, respectively.

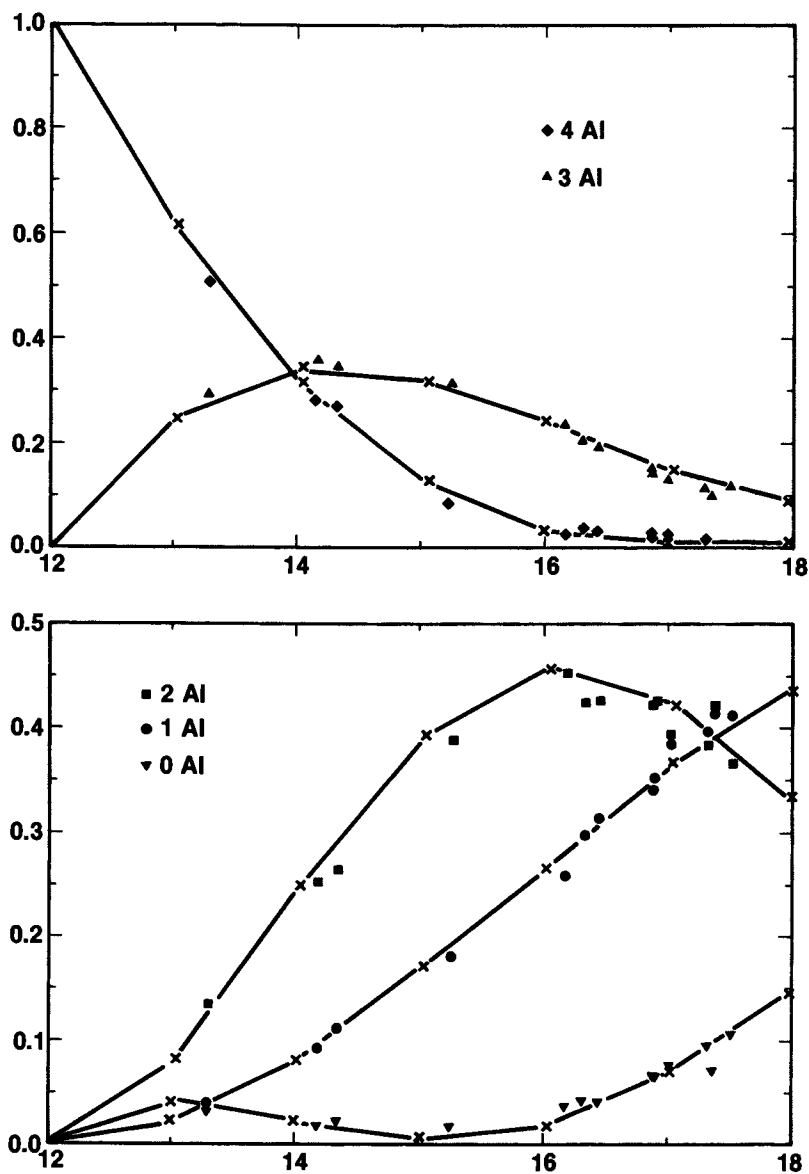


Figure 4.

Aluminum neighbor distributions  $[\text{Si}(n\text{Al})]_{n=4,3,2,1,0}$  for faujasite over compositions  $R = 1.0\text{--}3.0$ .

Experimental data from  $^{29}\text{Si}$  NMR at 39.5 MHz are shown as solid points. The points (x) connected by solid lines are the predictions of the theory described in the text.

minimum in this range but is clearly non-zero. This and other small discrepancies between the predicted distributions for ordered sodalite cages and the observed data may reflect macroscopic inhomogeneities in the framework composition. The predictions of the ordered sodalite cage model were calculated on the basis of a uniform  $N_{Al}$ , the number of Al atoms per sodalite cage (4). The result of allowing a distribution of  $N_{Al}$  about its sample average  $\bar{N}_{Al}$  is to bring theory and experiment into essential agreement on these minor features. We also find that differences between our data and that obtained in other laboratories (2,3) for faujasites in the same composition range can be rationalized by considering the other samples to contain somewhat broader distributions of  $N_{Al}$  about  $\bar{N}_{Al}$ .

The  $^{29}\text{Si}$  NMR data for faujasite and ZK4 (8) are compared in Figure 5 and Figure 6. Figure 5 is a plot of the first moment, or average number  $\bar{n}$  of aluminum neighbors per silicon as a function of  $R = \text{Si}/\text{Al}$ . The data for ZK4 and faujasite fall on the same line, namely  $\bar{n} = 4/R$ , a relationship which shows that Loewenstein's rule is obeyed for both structures within experimental error. Table I includes framework compositions calculated from the NMR data by assuming this functional relationship.

Figure 6 is a plot of the ratio  $\bar{s} = \overline{n^2}/\bar{n}$  where  $\overline{n^2}$  is the second moment of the  $\text{Si}(n\text{Al})$  distribution. The ratio  $\bar{s}$  provides a measure of the width of the distribution, hence the uniformity of the distribution of Al neighbors. The lower dashed line (a) in Figure 6 is the value of  $\bar{s}$  calculated for the minimum next nearest neighbor structures based on the favored sodalite cages X, XY, YX, and Y of Figure 1. The upper dashed line (b) is the result of a calculation of  $\bar{s}$  for structures based on X cages only. These limiting cases can be sharply differentiated in terms of 6R building units containing two  $\text{AlO}_4$  tetrahedra and four  $\text{SiO}_4$  tetrahedra, either meta ( $M^2$ ) or para ( $P^2$ ). Line (a) represents the limiting case in which only  $P^2$  6R's are used as building units, line (b) the case in which only  $M^2$  6R's are used. Figure 6 illustrates the difference in the Si,Al distribution in ZK4 and faujasite and shows that faujasite has a higher fraction of  $P^2$  6R's, particularly in the composition range  $1.4 \leq R \leq 2.4$ .

### Si,Al Ordering in Faujasite

We now proceed to the calculation of the Al neighbor distribution  $[\text{Si}(n\text{Al})]_{n=4,3,2,1,0}$  for faujasite with the assumption that the ordered sub-unit is the six T atom unit 6R. Loewenstein's rule is assumed to be strictly obeyed throughout. According to our hypothesis we consider an ensemble of 6R's within which the Si,Al distribution is constrained to reduce the number of Al,Al next nearest neighbors Al-O-Si-O-Al. The distribution we seek is that for faujasite formed from this 6R

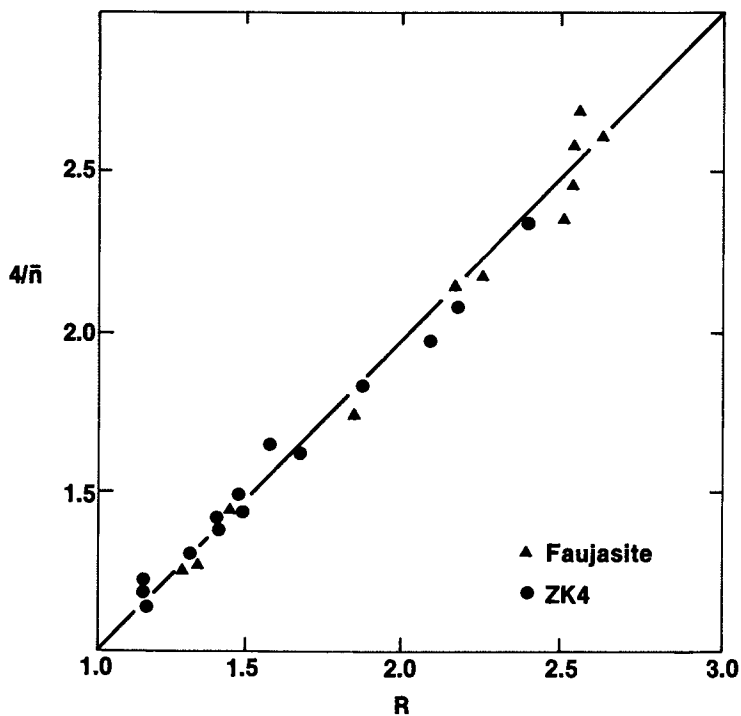


Figure 5.

Plot of  $4/\bar{n}$ , where  $\bar{n}$  is the average number of Al neighbors per silicon determined by  $^{29}\text{Si}$  NMR, as a function of composition. For frameworks subject to Loewenstein's rule  $4/\bar{n} = R$ .

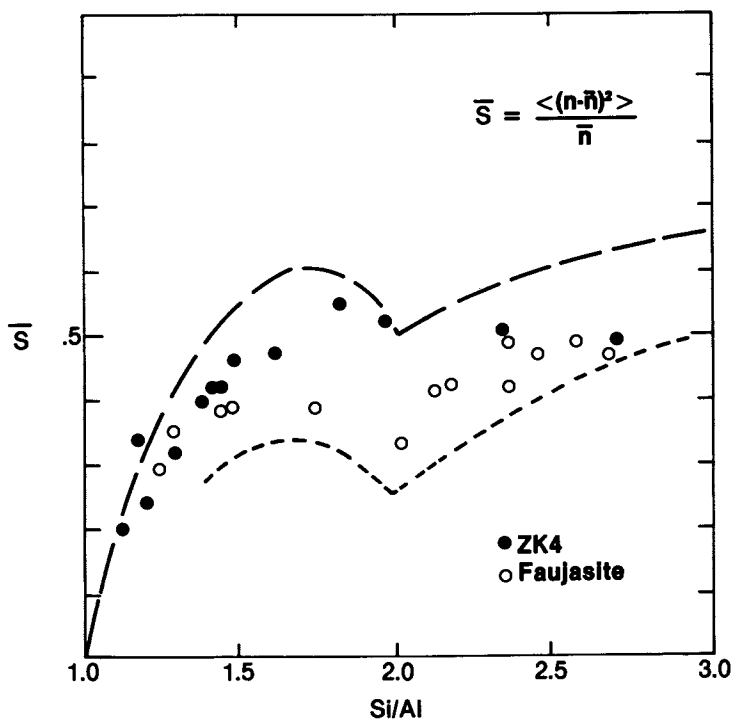


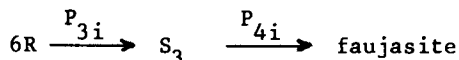
Figure 6.

Plot of the quantity  $\bar{s}$  which is the ratio of the second moment of the experimental Al neighbor distribution to the first moment  $\bar{n}$ . Dashed lines are  $\bar{s}$  predicted for  $P^2$  ordering (----) and for  $M^2$  ordering (- -) as described in the text.

ensemble subject only to Loewenstein's rule, assuming all combinations to be equally probable.

First note that the next nearest neighbor constraint controls both the distribution of Al atoms among 6R types and the arrangement of Al atoms in 6R's with two Al atoms ( $P^2$  vs.  $M^2$ ). The number of next nearest Al, Al pairs is minimized by taking the distribution to be as narrow as possible. Thus for  $1 < Si/Al < 2$ , only 6R's with 3 Al ( $M^3$ ) and 2 Al ( $M^2$  or  $P^2$ ) are considered and for  $2 < Si/Al < 3$ , only 6R's with 2 Al and 1 Al are considered. A single order parameter describes the 6R ensemble, namely the ratio of  $M^2$  to  $P^2$ , designated as  $K_{MP}$ . It is instructive to consider the formation of sodalite cages from this 6R ensemble. For instance, in the composition range  $1 \leq Si/Al \leq 2$ , sodalite cages may be formed with  $12 \leq N_{Al} \leq 8$ . Thus the notion of a distribution in  $N_{Al}$  arises quite naturally. Moreover, the topology of the sodalite cage is such that, if the ratio  $K_{MP}$  is zero, only the cages XY, YX and Y can be formed. Thus  $K_{MP} = 0$  for  $R \geq 1.4$  corresponds to the ordered sodalite cage description and to complete local order in the sense we have defined it.

The formation of faujasite from an ordered 6R ensemble can be represented schematically by



in which  $S_3$  is the appropriate 3-coordinate sub-unit and  $P_{Ni}$  is the probability that the  $i^{\text{th}}$  Si atom forms an Si-O-Al linkage when the N-coordinate structure is formed. As can be seen from Figure 2 there are two possible choices for  $S_3$ . For pathway II,  $S_3$  is taken to be a D6R unit and for pathway I,  $S_3$  is taken as an isolated sodalite cage (SC). The probabilities  $P_{Ni}$  are, of course, different for these pathways and are a function of the composition and the value of  $K_{MP}$  which characterizes the 6R ensemble. For a given step the ensemble average of probabilities is given by Loewenstein's rule and the composition as

$$\langle P_{Ni} \rangle_{\text{av.}} = \bar{P}(R) = 1/R$$

where  $R = Si/Al$ . For compositions in the range  $R > 2$  it is a good approximation to take  $P_{Ni}$  as equal to this average value but at lower values of  $R$  there is considerable dispersion in the individual probabilities within the set  $\{P_{Ni}\}$ . This is illustrated in Figure 7 which depicts the elements of  $\{P_{Ni}\}$  for the formation of sodalite cages from an ensemble of 6R's for which  $K_{MP} = 0.5$ , as a function of composition. Figure 7 was obtained by an explicit enumeration of all possible sodalite

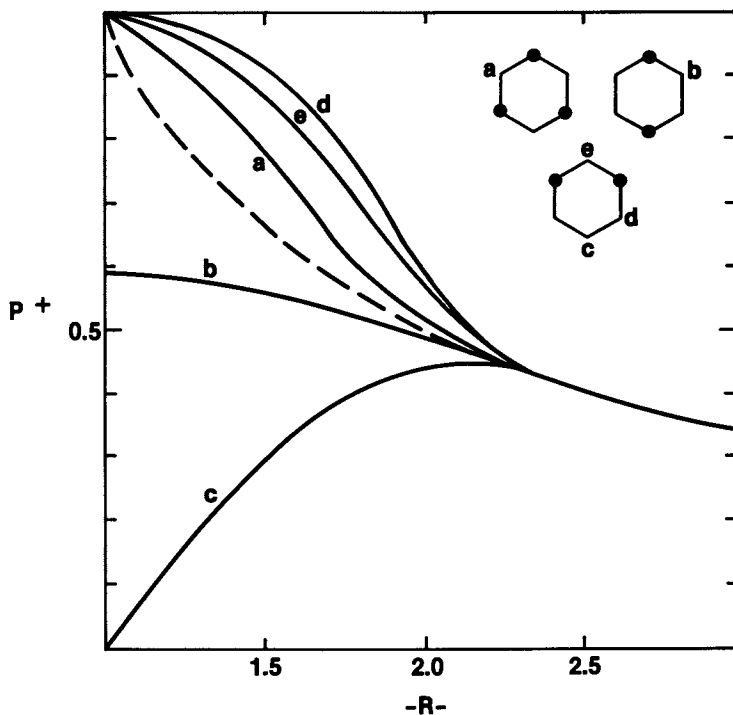


Figure 7.

Probabilities for formation of Si-O-Al linkages for various Si types upon formation of a sodalite cage from 6-ring sub-units, as a function of composition. The dashed line is the average for all sites  $\langle P_i \rangle = 1/R$ .



cage arrangements which can be formed from  $M^3$ ,  $M^2$ , and  $P^2$  6R's at Si/Al = 13/11, 14/10, and 15/9, together with the assumption that  $P_{Ni} = \bar{P}(R) = 1/R$  for  $R > 2$ . The dispersion within  $\{P_{Ni}\}$  is a reflection of the strong constraint represented by Lowenstein's rule when the connectivity of the sodalite cage is taken into account. In statistical terms, the probability  $P_{Ni}$  of adding an Si-O-Al linkage to the  $i$ th Si atom is strongly dependent on the linkages formed in the  $(N-1)$ th step.

The statistics of sodalite cage formation depicted in Figure 7 apply whether the 6R units are considered as isolated 6R's or as the hexagonal faces of a set of D6R units. Thus, the probabilities in Figure 7 represent  $P_{3i}$  for pathway I but  $P_{4i}$  for pathway II. The remaining step which must be considered for each of these pathways is the formation of D6R's from the 6-ring faces of a sodalite cage ( $P_{4i}$  for Pathway I) or from isolated 6R sub-units ( $P_{3i}$  for pathway II). Although the statistics for these two isolated steps are identical, given the same mixture of  $M^2$  and  $P^2$  6-rings, the steps differ in an important respect. The difference arises from the fact that the 6-ring faces involved in the step SC  $\rightarrow$  faujasite for pathway I are not simply the members of the 6R ensemble involved in the previous step 6R  $\rightarrow$  SC. Formation of a sodalite cage from four 6R's results in the formation of an additional set of four 6-ring faces which at some compositions may have a different mix of  $M^2$  and  $P^2$  arrangements. This can be seen most clearly by considering the composition Si/Al = 1.67. As has already been noted, for  $K_{MP} = 0$ , topological constraints force the arrangement designated as YX in Figure 1. Note that while YX is formed from one  $M^3$  and three  $P^2$  6R units, two of the four additional 6-ring faces have a  $M^2$  arrangement. These  $M^2$  6-ring faces must be included in the statistics of the subsequent step in which faujasite is formed. This expansion can be described by an effective ratio  $K_{MP}^*$  and must be reflected in the probabilities  $P_{4i}$  for pathway I. This point is crucial in that it provides the opportunity of distinguishing pathway I and pathway II.

Figure 8 shows the D6R arrangements which have been considered for the calculation of  $P_{4i}$  for pathway I and of  $P_{3i}$  for pathway II over the composition range  $1 \leq \text{Si/Al} \leq 3$ . Included in the figure are the number of next nearest neighbor Al, Al pairs across 4-rings ( $\bar{z}_4$ ) and across 6-rings ( $\bar{z}_6$ ) for each D6R unit. It is easily shown that for  $1 \leq R \leq 2$  the total number of next nearest neighbor pairs ( $\bar{z}_4$ ,  $\bar{z}_6$ ) at a given Si/Al ratio is a function of one parameter,  $K_{MP}^*$  for pathway I or  $K_{MP}$  for pathway II. It is the essence of our hypothesis of 6R's as the ordered sub-unit that we assume a distribution of D6R's determined only by the average composition, the ratio  $K_{MP}$  or  $K_{MP}^*$ , and simple statistical probabilities over the entire range of composition.

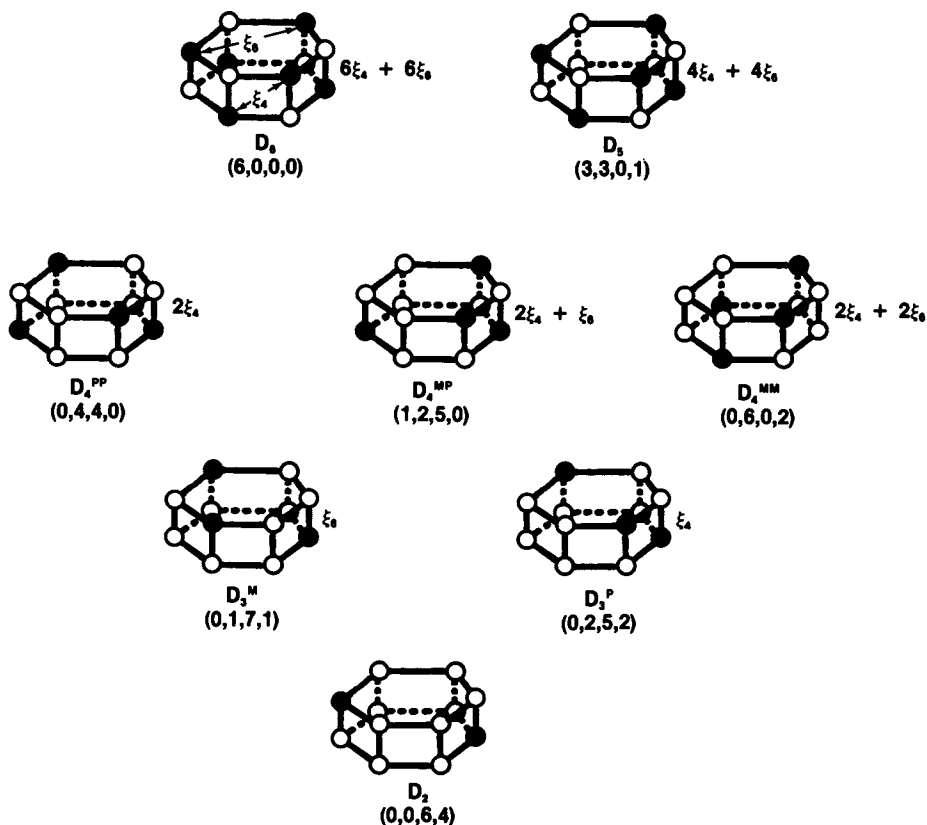


Figure 8.

Double 6-ring arrangements considered for the formation of a faujasite framework. Shown in the figure are the number of Al-O-Si-O-Al pairs across 4-rings ( $\xi_4$ ) and across 6-rings ( $\xi_6$ ) for each D6R moiety as well as the 3-neighbor distributions (Si(nAl))<sub>n=3,2,1,0</sub>\*

Consider first the formation of faujasite by pathway II,  $6R \rightarrow D6R \rightarrow$  faujasite. For a given composition and 6R order parameter  $K_{MP}$  straightforward statistical calculation gives the appropriate set of D6R populations. Figure 8 shows the 3-neighbor distributions  $(Si(nAl))_{n=3,2,1,0}$  for each D6R moiety. Calculation of the 4-neighbor distribution  $[Si(nAl)]$  for faujasite involves converting each 3-neighbor distribution to the corresponding 4-neighbor distribution through application of the probabilities  $P_{4i}$  for each Si site as exemplified by Figure 7 for  $K_{MP} = 0.5$ . The overall distribution of  $[Si(nAl)]$  is then obtained as the weighted average of the various D6R results. In order to simulate the expected dispersion in the number of Al atoms per sodalite cage, a binomial distribution (1:2:1) in  $N_{Al}$  is imposed on the results at each discrete composition. An extensive study of this pathway for faujasite formation has been made, the detailed results of which are not reported here. The conclusions are quite clear, however. Although the theoretical distributions for  $K_{MP}$  in the range 0-0.5 agree well with the experimental distributions determined by  $^{29}Si$  NMR (Figure 4) for compositions  $R > 2$ , there is significant deviation for compositions in the lower range  $R < 2$ . This deviation is most apparent for the composition  $R = 1.67$ . Table II gives the theoretical results at this composition for  $K_{MP} = 0$  and  $K_{MP} = 0.5$  as well as the distribution obtained by a least-squares interpolation of the experimental data.

#### Ordered Sodalite Building Units

Formulation of local Si,Al ordering in faujasite in terms of pathway I,  $6R \rightarrow SC \rightarrow$  faujasite, represents an extension and refinement of our previous treatment in terms of ordered SC sub-units (4). As we have noted, pathway I for  $K_{MP} = 0$  corresponds to formulation of faujasite from the SC arrangements of Figure 1. Actually the set of SC units specified by  $K_{MP} = 0$  is more exclusive than that specified previously (4) since there are minimum Al, Al next nearest neighbor SC units which cannot be formed using only  $M^3$  and  $P^2$  6R's. Moreover, consideration of 6R ensembles with  $K_{MP} \neq 0$  provides a straightforward approach to the study of deviations from complete local order.

Calculation of theoretical 4-neighbor distributions  $[Si(nAl)]$  for pathway I is a more involved task than for pathway II, especially for a 6R ensemble with  $K_{MP} \neq 0$ . The first step is to convert the 6R ensemble to a weighted average of sodalite cage sub-units by application of the probability set  $P_{3i}$  which for this pathway is exemplified by Figure 7 for  $K_{MP} = 0.5$ . Additional complexity arises because, in addition to the 3-neighbor distributions for each Si site, we require a calculation of the resultant  $M^2/P^2$  ratio  $K_{MP}^*$ , needed in the next step. This value of  $K_{MP}^*$  is then used to calculate

Table II

Theoretical and Experimental Al Neighbor  
Distributions for Faujasite at Si/Al = 1.67

Theoretical (R = 1.67) [Si(nAl)]<sub>n</sub> = 4, 3, 2, 1, 0

Pathway I 6R → SC → Faujasite

$K_{MP} = 0$  [.125, .318, .390, .167, 0]

$K_{MP} = 0.5$  [.161, .304, .345, .168, .023]

Pathway II 6R → D6R → Faujasite

$K_{MP} = 0$  [.142, .288, .400, .170, 0]

$K_{MP} = 0.5$  [.171, .285, .351, .172, .020]

Experimental (R = 1.67)\*

[.130, .324, .369, .163, .015]

---

\*Obtained by computer fit interpolation of data in Table I (11).

the statistical distribution of D6R linkages and the associated probabilities  $P_{4i}$  used to convert the weighted average 3-neighbor distributions to the 4-neighbor distributions for faujasite.

Theoretical Al neighbor distributions have been calculated for pathway I with  $K_{MP}$  in the range 0-0.5 for the compositions  $N_{A1} = 14$  and  $N_{A1} = 15$  ( $R = 1.40$  and  $1.67$ ). The results for  $R = 1.40$  are closely similar to those calculated for pathway II. For  $R = 1.67$ , however, significantly better agreement with experiment is obtained for pathway I. This can be seen in Table II which compares results for pathways I and II with the (interpolated) experimental distribution obtained by  $^{29}\text{Si}$  NMR. The crucial comparison is the relative intensities of Si(4A1) and Si(3A1) for the two pathways. Table II shows that good agreement is obtained for pathway I for  $K_{MP} \approx 0$ .

From these results we conclude that the observed  $^{29}\text{Si}$  NMR data are well accounted for by assuming pathway I and postulating essentially complete  $P^2$  ordering in the 6R ensemble, equivalent to assuming distributions calculated for the ordered sodalite cages in Figure 1. Table III summarizes the results of this calculation for the compositions  $R = 13/11, 14/10, 15/9, 16/8, 17/7,$  and  $18/8$ . The first line (a) for each composition in Table III is the distribution calculated for the "pure" compositions, with an infinitely narrow distribution in  $N_{A1}$ . For  $R = 13/11$ , sodalite cage X missing one Al atom is used, corresponding to a faujasite framework formed from  $M^3$  and  $M^2$  6R sub-units in the ratio 3:1. For compositions  $R = 14/10, 15/9,$  and  $16/8$ , respectively, only sodalite cages XY, YX, and Y are used, corresponding to frameworks formed from an ensemble of  $M^3$  and  $P^2$  6R units. For these compositions the effective  $M^2/P^2$  ratio  $K_{MP}^*$  must be used to calculate  $P_{4i}$  for the statistical distribution of D6R linkages. For XY at  $R = 14/10$ ,  $K_{MP}^* = K_{MP} = 0$  but, as noted above, for YX at  $R = 15/9$   $K_{MP}^*$  has the value 0.5. It is precisely this observation that distinguishes pathways I and II. For  $R > 2$  it has been assumed that the constraint of the framework connectivity is sufficiently weak that  $P_{Ni} \approx 1/R$ . It should be noted that even for  $R \gg 2$  local order persists despite this assumption because we have assumed ordered  $P^2$  6R sub-units. The theoretical distributions (a) for these pure compositions may be compared with the results in (4).

Even for integral values of  $N_{A1}$ , the associated 6R ensembles are composed of a mixture of 6R's with three, two, and one Al atoms and it is reasonable to assume a microscopic dispersion in  $N_{A1}$  about the average  $\bar{N}_{A1}$  at each composition. The theoretical distributions in line (b) for each composition are obtained by applying a binomial distribution (1:2:1) to the pure distributions, in order to simulate this microscopic dispersion. The expected local dispersion in  $N_{A1}$  would best be included in

Table III  
Theoretical Al Neighbor Distributions  
for Ordered Sodalite Cage Building Units

| <u>Si/Al</u> | <u>4 Al</u> | <u>3 Al</u> | <u>2 Al</u> | <u>1 Al</u> | <u>0 Al</u> |
|--------------|-------------|-------------|-------------|-------------|-------------|
| 1.18         | (a) .615    | .308        | .000        | .000        | .077        |
|              | (b) .615    | .250        | .077        | .019        | .038        |
|              | (d) (.605)  | (.253)      | (.087)      | (.023)      | (.030)      |
|              |             |             |             |             |             |
| 1.40         | (a) .286    | .357        | .286        | .071        | 0           |
|              | (b) .317    | .339        | .245        | .080        | .018        |
|              | (c) .306    | .344        | .263        | .076        | .013        |
|              | (d) (.317)  | (.345)      | (.234)      | (.081)      | (.024)      |
| 1.67         | (a) .117    | .333        | .383        | .167        | 0           |
|              | (b) .125    | .317        | .392        | .167        | 0           |
|              | (c) .131    | .328        | .363        | .165        | .013        |
|              | (d) (.130)  | (.324)      | (.369)      | (.163)      | (.015)      |
| 2.00         | (a) .000    | .250        | .500        | .250        | .000        |
|              | (b) .027    | .240        | .454        | .263        | .016        |
|              | (c) .014    | .237        | .479        | .257        | .013        |
|              | (d) (.026)  | (.243)      | (.442)      | (.263)      | (.032)      |
| 2.43         | (a) .000    | .139        | .429        | .371        | .061        |
|              | (b) .000    | .148        | .420        | .362        | .070        |
|              | (c) .005    | .245        | .416        | .364        | .071        |
|              | (d) (.013)  | (.134)      | (.412)      | (.370)      | (.073)      |
| 3.00         | (a) .000    | .074        | .333        | .444        | .148        |
|              | (b) .000    | .083        | .330        | .434        | .156        |
|              | (c) .002    | .079        | .326        | .435        | .158        |
|              | (d) (.000)  | (.058)      | (.356)      | (.468)      | (.123)      |

- 
- (a) Theory for sodalite cage sub-units, pure compositions.  
 (b) Theory for binomial distribution (1:2:1) of pure compositions.  
 (c) Theory for pure compositions with  $K_{MP} = 0.25$ .  
 (d) Interpolated experimental data (unnormalized).

the intermediate step  $6R \rightarrow SC$ , i.e., in the calculation of 3-neighbor distributions for the sodalite cage sub-units. Preliminary results suggest that the approximation used to obtain (b) in Table III may overestimate somewhat the effect of dispersion in  $N_{Al}$ . Therefore, we have included for comparison (line c, Table III) the theoretical results for  $1.4 < R < 3.0$  for an infinitely narrow distribution in  $N_{Al}$  but with a small value  $K_{MP} = 0.25$ , to illustrate the effect of slight deviations from complete  $P_2^2$  order in the 6R ensemble. The ideal theory would include both sources of local disorder, which refinement is left to a future publication.

Table III also includes on line (d) for each composition the interpolated experimental result obtained from a computer fit to the  $^{29}Si$  NMR data (11). The predicted distributions (b) in Table III are compared with the experimental data in Figure 4. The agreement of theory and experiment is very good across the entire composition range, lending strong support to the conclusion that faujasite is formed from an ordered 6R ensemble via the pathway  $6R \rightarrow SC \rightarrow$  faujasite.

#### Si,Al Ordering in ZK4

It has already been noted that the ordered sodalite cage model which describes the Si,Al distribution in faujasite quite well does not account for the ZK4  $^{29}Si$  NMR data over the range  $1 < R < 3$ . It has been shown that the consequences of considering ordered 6R sub-units are closely related to a description in terms of ordered sodalite cages. It seems reasonable, therefore, to consider the formation of ZK4 by one or another of the possible pathways involving 4R's (cf. Figure 2). In the following we discuss the ordering in ZK4 in terms of the pathway  $T \rightarrow 4R \rightarrow D4R \rightarrow ZK4$ . For the case of ZK4 no distinction can be made between this pathway and the alternative  $4R \rightarrow SC \rightarrow ZK4$ .

Calculation of the predicted  $[Si(nAl)]$  distribution for ZK4 constructed from an ensemble of 4R sub-units is formally similar to the foregoing treatment of faujasite based on 6R sub-units. The first step is to calculate the statistical mix of D4R units which can be formed over the composition range  $1 < R < 3$ . In order that the  $\xi_4$  next nearest neighbor interactions be minimized we exclude  $Si_4$  units from our 4R ensemble. The appropriate mixture of D4R's is then assembled to form a ZK4 crystal, subject to the constraint of Loewenstein's rule as it applies to the topology of sodalite cages formed from six D4R's. Figure 8 shows the calculated probabilities  $P_{4i}$  of adding an aluminum neighbor for the step  $D4R \rightarrow ZK4$ , a result obtained in the same manner as was Figure 7 for faujasite. For the present case the topological constraint is much less severe because the 4R sub-unit imposes no local order beyond Loewenstein's rule. The number of possible sodalite cage arrangements is much greater and the resulting distribution corresponds to what we might term

"Loewenstein statistical," subject to no additional constraint. We find that the distributions  $[(\text{Si}(n\text{Al}))]$  calculated in this manner deviate significantly from the observed distributions for ZK4 at low Si/Al.

That the detailed statistical application of Loewenstein's rule does not account for the observed ZK4 data implies that a further constraint must be imposed in the step  $\text{D4R} \rightarrow \text{ZK4}$ , i.e., there are next nearest neighbor interactions which have not been considered. On the other hand, reasonably good agreement is obtained over the composition range  $1.4 \leq R \leq 3.0$  by taking  $P_{4i}$  to be equal to its average  $\langle P_4 \rangle = 1/R$  for all Si sites (Figure 9, dashed line). It can be shown that the averaging of of

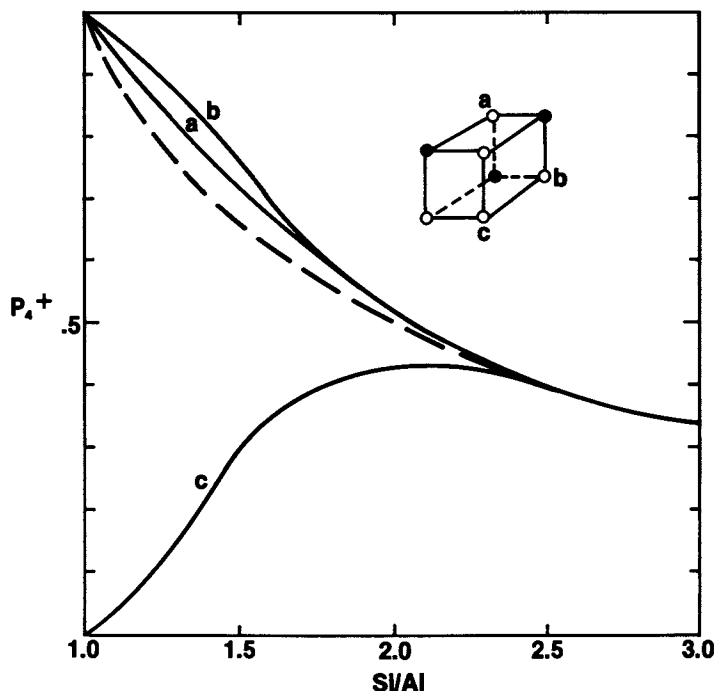


Figure 9. Probabilities for formation of Si-O-Al linkages for various Si sites upon formation of a sodalite cage from 4-ring sub-units in ZK4.



$P_{4i}$  corresponds to a nonstatistical mixture of sodalite cages formed by  $D4R \rightarrow ZK4$ . Not unexpectedly, this statistical bias can be expressed in terms of a preference for para arrangements of Al atoms in the eight 6-rings formed by the combination of six D4R units. Consider the following example for one composition  $Si/Al = 1.4$ . The statistical mixture of sodalite cages, that used to calculate  $P_{4i}$  in Figure 9 at this composition, can be characterized as having a  $M^2/P^2$  ratio of 5:1. As can be seen by Figure 9 the probabilities  $P_{4i}$  for different Si environments are significantly different from the average  $\langle P_4 \rangle = 1/R$ . However, for a non-random combination for which the resulting  $M^2/P^2$  is 1:1 it can be shown that all Si sites have  $P_{4i}$  within 5 percent of the average value of  $1/R$ . This result implies a significant next nearest neighbor constraint on the arrangements favored in ZK4 crystallization, comparable to that in faujasite. In principle at least we could carry out a detailed calculation of  $P_{4i}$  for  $D4R \rightarrow ZK4$  based on some formulation to express the preference for  $P^2$  6-rings leading to a ZK4 structure composed of partially ordered sodalite cages. As yet such calculation has not been achieved.

### Conclusions

The observed  $[Si(nAl)]$  distributions for faujasite have been satisfactorily accounted for by a model which assumes an ensemble of  $P^2$  ordered 6-rings assembled into a faujasite lattice via the pathway  $6R \rightarrow SC \rightarrow$  faujasite, subject only to the topological constraints imposed by strict adherence to Loewenstein's rule. Rationalization of the  $[Si(nAl)]$  distributions for ZK4 is less straightforward because the Al, Al next nearest neighbor interaction (responsible for the preference for  $P^2$  6-rings in faujasite) must be taken into account for the formation of sodalite cages from 4R or D4R sub-units. The data for ZK4 and, more importantly, comparison of the ZK4 data with the faujasite data leads to the conclusion that ZK4 is formed by a pathway involving 4-rings as the fundamental unit.

Both ZK4 and faujasite exhibit short range statistical order which can be rationalized in terms of a competition between the statistics of the step in which the sodalite cage is formed and the tendency of the system to avoid Al, Al next nearest neighbor interactions. The basic difference between the two systems can be understood in terms of the difference in the severity of the constraint imposed by Loewenstein's rule for the formation of a sodalite cage from four ordered 6R's in the case of faujasite or from six 4R's or D4R's in the case of ZK4. The local order in faujasite can be considered as "frozen in" by the topological constraint imposed by the ordered 6R sub-units. As such this order is more a property of the sub-unit than a manifestation of next nearest neighbor interactions in the faujasite crystal. By contrast the next nearest neighbor interaction in ZK4 cannot be

accommodated in a single ordered sub-unit and the resulting local order may be more appropriately considered a property of the zeolite framework.

#### Literature Cited

1. Lippmaa, E. T.; Alla, M. A.; Pehk, T. J.; Engelhardt, G. M.; J. Am. Chem. Soc., 1978, 100, 1929.
2. Englehardt, G.; Lohse, V.; Lippmaa, E.; Tarmak, M.; Magi, M.; Z. Anorg. Allg. Chem., 1982, 482, 49.
3. Klinowski, J.; Ramdas, S.; Thomas, J. M.; Fyfe, C. A.; Hartman, J. S.; J. Chem. Soc., Faraday Transactions, 1982, 78, 1025.
4. Melchior, M. T.; Vaughan, D. E. W.; Jacobson, A. J.; J. Am. Chem. Soc., 1982, 104, 4859.
5. Lippmaa E.; Magi M., Samoson; A., Tarmak; M., Englehardt, G.; J. Am. Chem. Soc., 1981, 103, 4992.
6. Bursill, L. A.; Lodge, E. A.; Thomas, J. M.; Cheetham, A. K.; J. Phy. Chem., 1981, 85, 2409.
7. Melchior, M. T.; Vaughan, D. E. W.; Jarman, R. H.; Jacobson, A. J.; Nature, 1982, 298, 455.
8. Jarman, R. H.; Melchior, M. T.; Vaughan, D. E. W.; Chapter \_\_, in this book.
9. Loewenstein, W.; Am. Miner., 1954, 39, 92.
10. Hexem, J. G.; Frey, M. H.; Opella, S. J.; J. Chem. Phys. 1982, 77, 3847.
11. Jarman, R. H., personal communication.

RECEIVED February 25, 1983

## Synthesis and Characterization of A-Type Zeolites

R. H. JARMAN, M. T. MELCHIOR, and D. E. W. VAUGHAN  
Exxon Research and Engineering Company, Linden, NJ 07036

The crystallization field of the A-type zeolite ZK4 in the system  $\text{TMA}_2\text{O}-\text{Na}_2\text{O}-\text{Na}_2\text{O}-\text{Al}_2\text{O}_3-\text{SiO}_2-\text{H}_2\text{O}$  was investigated and products characterized by chemical analysis, powder x-ray diffraction and  $^{29}\text{Si}$  NMR with magic-angle spinning. Modification of reaction conditions enabled pure materials to be prepared with Si/Al up to 2.74. A smooth decrease of unit-cell size with increasing Si content was observed, and the  $^{29}\text{Si}$  NMR data showed that Loewenstein's rule is obeyed over the entire composition range. Comparison of the relative intensities of the five components of the NMR spectra with similar data available for faujasite showed that the distributions of Si and Al atoms in the two structures are different over the whole composition range.

The application of high resolution solid state  $^{29}\text{Si}$  NMR spectroscopy with magic angle spinning to the study of zeolites (1,2) has generated much interest and discussion about the way Si and Al atoms are distributed among the tetrahedral framework sites of these materials. The observation that the isotropic chemical shift of  $^{29}\text{Si}$  is strongly dependent upon its local chemical environment, notably upon the number of neighboring Al atoms bound to it through bridging O atoms, has enabled assignment of the absorption peaks in  $^{29}\text{Si}$  NMR spectra to particular Si environments.

The system that has received the closest attention to date has been faujasite (2-5), synthetic samples of which (NaX and NaY) can be readily prepared over a wide range of composition. The observation of five distinct absorption peaks in spectra of samples with particular compositions enabled unambiguous

assignment of these peaks to the five Si environments Si(nAl, n-4Si) with  $4 > n > 0$ . From these spectra, and those of other zeolites, it was deduced that the chemical shifts of the five Si environments lay in the ranges shown in Table I. As will be seen later the ranges overlap and are actually much broader than shown

TABLE I

Chemical Shift Ranges vs. TMS For  
Four Coordinated Si Environments

|             | Chemical Shift/ppm |
|-------------|--------------------|
| Si(4Al)     | -83 to -87         |
| Si(3Al Si)  | -88 to -94         |
| Si(2Al 2Si) | -93 to -99         |
| Si(1Al 3Si) | -97 to -107        |
| Si(4Si)     | -103 to -114       |

Data taken from ref. 2.

indicating that spectra that contain only one peak cannot be assigned "a priori" to one Si environment. The apparent structural dependence of the chemical shifts provides information concerning the detailed geometry of the Si environment (6).

The data obtained from  $^{29}\text{Si}$  NMR spectra contain detailed information concerning the local ordering of Al and Si atoms independent of any long range crystallographic order that might exist in the structure. The precise nature of local order in faujasite is very much a topic of interest, and several different approaches to the interpretation of the NMR data have been presented (4,5,7,8,9).

X-ray diffraction has had limited application to the study of Si and Al distributions in zeolites because the scattering power of the two atoms are practically identical. Furthermore, such an experiment only presents a description of the average unit cell contents, and so is intrinsically unable to provide information concerning local order.

In cases where the Si and Al atoms are distributed in such a way that long range crystallographic order extends throughout the structure, Si and Al sites may be distinguished by the differences between the T-O bond lengths (Si-O~1.60Å, Al-O~1.73Å). One such example is zeolite A (Si/Al = 1) the structure of which consists of  $\text{T}_{24}\text{O}_{48}$  cuboctahedral "sodalite" cages linked in a cubic array via double 4-rings (10,11). The resulting three dimensional

channel system contains the charge balancing cations and, in the hydrated form, water molecules. The critical factor in detecting the strict alternation of Si and Al atoms in the structure was refinement of the X-ray data in the true unit cell of 24.6Å and space group Fm3c, rather than the pseudo cell with a=12.3Å and space group Pm3m(13). The latter again merely presents an average description of the structure. This result has recently been confirmed by a powder neutron diffraction study of T $\alpha$ -A (12).

Recently other evidence gained from  $^{29}\text{Si}$  NMR and electron and neutron diffraction studies (2,14-16) cast uncertainty upon the veracity of this description of zeolite A. The chemical shift of the single absorption peak in the  $^{29}\text{Si}$  NMR of Na-A lies outside the range originally prescribed for Si coordinated by 4Al (2) and was coincident with that of the Si(3Al) peak in a faujasite spectrum (2-5). A Si(3AlSi) environment and the stoichiometry of Si/Al=1.0 implies an Al environment of Al(3SiAl) meaning that zeolite A would stand in contravention of Loewenstein's rule (17) which states that Al-O-Al units in aluminosilicates are prohibited. The assignment of the peak to a particular Si environment where the spectrum contains but one peak is ambiguous. Subsequent study of samples of ZK4, the structural analogues of A with Si/Al>1.0, using  $^{29}\text{Si}$  NMR yielded spectra that contained five absorption peaks (18,19) which were assigned to the five possible Si environments. The chemical shift ranges are consequently actually much wider than previously supposed and the true assignment of the single  $^{29}\text{Si}$  NMR peak in A is almost certainly Si(4Al) as predicted by the original X-ray structure determination. Most probably the anomalies observed in diffraction data collected on Na-A, in particular the rhombohedral distortion of the cubic cell noticeable in powder neutron diffraction data (15,20), can be assigned to effects due to the cations rather than the framework. Indeed the cubic T $\alpha$ -A, spacegroup Fm3c, is prepared by simple ion-exchange of rhombohedral Na-A, probably space group R $\bar{3}c$  (12,20).

In this work we describe an extension of our previous work (18) to the synthesis of A-type zeolites over the range of composition  $1.0 < \text{Si}/\text{Al} < 3.0$  and report the results of  $^{29}\text{Si}$  NMR measurements made on these materials. We compare the data with those for faujasite over the same composition range and discuss the nature of the Si and Al distributions in these materials.

### Synthetic Methods

Our synthetic routes to ZK4 were modifications of those described by Kerr (21). An amorphous, basic aluminosilicate gel containing tetramethylammonium (TMA) ion was heated at 100°C to promote formation of ZK4 crystals. Preparation of the gel involved the vigorous mixing at room temperature of one component acting as a source of sodium and alumina, with another component acting as a source of TMA and silica. The alumina used was sodium

aluminate ( $1.45 \text{ Na}_2\text{O} \cdot \text{Al}_2\text{O}_3 \cdot 3\text{H}_2\text{O}$ , Baker) and the silica was a silica gel (Davison, #923) or colloidal silica sol (Ludox HS40, 40 wt%  $\text{SiO}_2$ , Dupont). The parent gel was then heated at  $100^\circ\text{C}$  in sealed teflon bottles for periods of several hours. Solid products were filtered, washed with distilled water and dried in air at  $100^\circ\text{C}$ .

Characterization of materials was achieved by powder X-ray diffraction, using a Siemens D500 diffractometer, and by scanning electron microscopy. Elemental analysis of pure single phase materials was carried out using a Jarrel Ash Inductively Coupled Plasma Atomic Emission Spectrometer.

### Results

The compositions of the parent gels, and products obtained, are given in Table II. It was found that modifications to the synthetic method were required to enable the preparation of pure ZK4 materials over the range of composition  $1.0 < \text{Si}/\text{Al} < 3.0$ .

$1.25 < \text{Si}/\text{Al} < 1.5$  Pure crystalline samples of ZK4 were prepared in this composition range by direct heating of the freshly prepared gels of appropriate composition at  $100^\circ\text{C}$ .

Figure 1 shows the compositions of the parent gels, and products obtained from them, plotted on a triangular component diagram. The dashed lines connecting the points of composition of starting material and product may be described as the "paths" of crystallization of ZK4 from the parent gel. In this region these paths appear to be parallel. Therefore, the products from #1-4, Table II, in which the concentrations of TMA and  $\text{SiO}_2$  are raised concomitantly, vary over only a narrow range. It was found that heating times of 16-30 hours were sufficient for crystallization of ZK4, and that agitation of the bottles during heating had no effect on the crystallization rate. Products of #1 and #2 always contained amorphous material at shorter times and, after extending heating periods (>40 hours), crystalline impurities of sodalite and zeolite "V" (22), also known as "N" (23) or "Z21" (24).

Seeding of the parent gels with a mixture of molar composition  $13.3\text{Na}_2\text{O}:\text{Al}_2\text{O}_3:12.5\text{SiO}_2:270\text{H}_2\text{O}$  to add 1 mole % of  $\text{Al}_2\text{O}_3$  served merely to reduce the particle size of the products; the compositions remained unchanged.

By increasing the concentration of  $\text{SiO}_2$  in the gel at an approximately constant concentration of TMA, more silicon rich products were obtained, (#5 Table II, Figure 1). The ranges of concentration of  $\text{SiO}_2$  and TMA that could be used to prepare pure ZK4 materials of composition  $1.4 < \text{Si}/\text{Al} < 1.5$  were reduced. No pure samples of ZK4 with  $\text{Si}/\text{Al} > 1.49$  were prepared by direct heating of the parent gel at  $100^\circ\text{C}$ . Lowering the  $\text{SiO}_2$  content of the gel (#6 and #7) always led to the co-crystallization of large sodalite and "V" impurities, the relative quantities of which were essentially independent of heating time. Therefore, no pure materials with  $\text{Si}/\text{Al} < 1.25$  were prepared by this method.

TABLE II  
Preparative Data For ZK4

| Prep. No. | (Na <sub>2</sub> O+TMA <sub>2</sub> O):<br>Al <sub>2</sub> O <sub>3</sub> | SiO <sub>2</sub> :Al <sub>2</sub> O <sub>3</sub> | Si:Al† product                             |
|-----------|---|--|--|
| 1         | 5.85  | 3.73   | 1.25                                       |
| 2         | 6.39  | 4.00   | 1.24                                       |
| 3         | 7.45  | 4.26   | 1.32                                       |
| 4         | 9.45  | 5.33   | 1.38-1.41†††                               |
| 5         | 7.50  | 5.50   | 1.44,1.49                                  |
| 6         | 5.85  | 3.14   | contained V, sodalite                      |
| 7         | 4.65  | 3.14   | contained V, sodalite                      |
| 8         | 6.91  | 3.14*  | 1.18                                       |
| **9       | 5.85  | 3.14   | 1.16                                       |
| 10        | 8.00  | 12.00  | contained "offretite"                      |
| 11        | 2.00  | 4.00   | contained chabazite<br>plus other impurity |
| **12      | 3.75  | 5.50   | 1.66                                       |
| **13      | 3.5   | 6.00   | 1.86                                       |
| **14      | 3.25  | 6.50   | 2.08                                       |
| **15      | 4.65  | 8.67   | 2.16                                       |
| **16      | 4.33  | 9.33   | 2.39                                       |
| **17      | 4.0   | 10.00  | 2.99††                                     |
| **19      | 3.33  | 11.33  | incomplete crystal-<br>lization            |

$$\text{H}_2\text{O}:\text{Al}_2\text{O}_3 = 320$$

$$\text{Na}_2\text{O}:\text{Al}_2\text{O}_3 = 1.45$$

\*source of silica = silica gel

\*\*aged reaction

†Si:Al as determined by elemental analysis

††contains small sodalite impurity

†††range of five samples

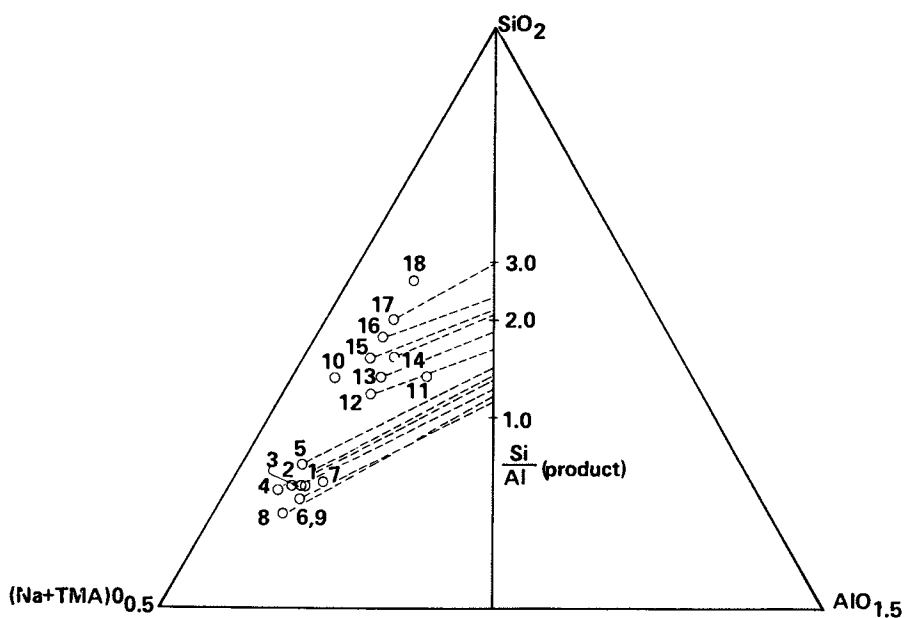


Figure 1.  
 Triangular component diagram for the synthesis of ZK4 materials. The numbers refer to the compositions in Table 2.



1.0 < Si/Al < 1.25 The two modifications of the method leading to successful preparations of pure materials with a low Si/Al ratio involved changing the source of silica to silica gel (#8), and "cold-aging" of the parent gels at room temperature for 2 days prior to heating at 100°C ((#9), Table II).

In both cases crystallization times were between 16-20 hours and the paths of crystallization were parallel to those of the higher silica products described in the last section.

1.5 < Si/Al < 3.0 No pure ZK4 materials could be prepared in this composition range by direct heating of the parent gels. Crystalline impurities were always observed; the amounts and types depending upon the gel composition. For example, the amounts of impurity observed in #10 and #11 were much greater than in #12 or #13, Figure 1. However, if these same gels were cold-aged for 2 days prior to heating, the level of impurities in the products was dramatically reduced. For example, the products of aged gels, (#12-17) were pure crystalline samples of ZK4 with crystallization times increasing from 24 hours to 60 hours with increasing SiO<sub>2</sub> content. At still higher SiO<sub>2</sub> concentrations complete crystallization did not occur, even after several weeks (#18). In all cases, if heating was continued after crystallization of ZK4 was complete, additional crystalline impurities were observed. Cold-aging prior to heating was also found (25,26) to promote crystallization of the A-type zeolite  $\alpha$  (27). In this work we recognize no structural distinction between  $\alpha$  and ZK4 and retain the name ZK4 to describe all our products.

The products with Si/Al > 2.0 displayed an unusual morphology for A-type materials where the cubes show an octahedral prism development.

### <sup>29</sup>Si NMR Measurements

<sup>29</sup>Si NMR spectra were obtained at 39.5 MHz on a JEOL FX200WB spectrometer using the combined techniques of magic-angle sample spinning and proton dipolar decoupling. The corresponding <sup>1</sup>H frequency was 199.5 MHz.

The spectrum of a sample with Si/Al = 1.66 as determined by elemental analysis is shown in Fig. 2. The five absorption peaks at -89.4, -94.6, -100.4, -106.3, -111.0 ppm from tetramethylsilane (TMS) are comparable with those reported for ZK4 in other work (18,19) and are assigned to the silicon environments Si(nAl) with  $4 > n > 0$ . It has been demonstrated for faujasite and ZK4 that, if the distribution of Si and Al atoms in the tetrahedral framework sites obeys Loewenstein's rule (16), then the Si/Al ratio of the material can be directly computed from the <sup>29</sup>Si NMR spectrum (4,5,18,19). The average number of Al neighbors about Si,  $\bar{Al}$ , is given by the relation,

$$\bar{Al} = \frac{\sum_0^4 nI_n}{\sum_0^4 I_n} \quad (1)$$

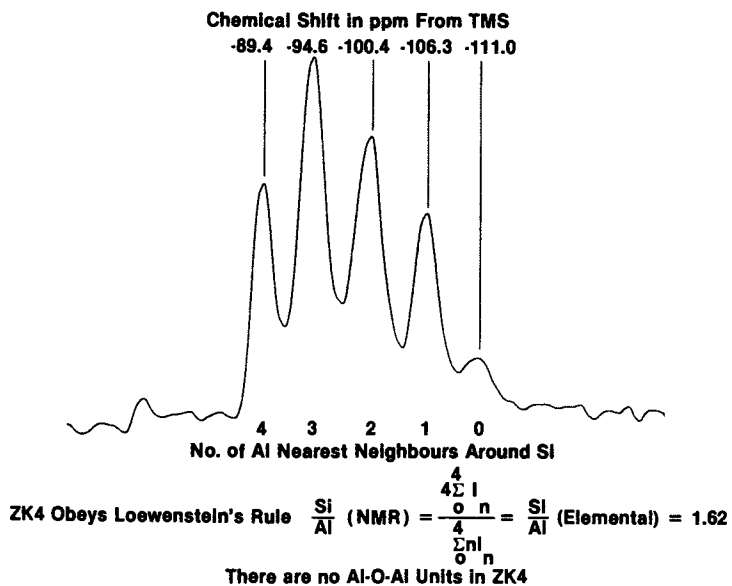


Figure 2.

$^{29}\text{Si}$  NMR spectrum at 39.5 MHz with magic angle spinning and proton dipolar decoupling of ZK4 with Si/Al (elemental) = 1.66.

where  $I_n$  is the integrated intensity of the Si(nAl) absorption peak. The Si/Al ratio is then  $4/I_n$  Al.

Application of (1) to the  $^{29}\text{Si}$  NMR spectra of materials prepared in this work show that Loewenstein's rule is valid over the entire range. The complete set of NMR data and values of Si/Al (NMR) are recorded in Table III.

#### Characterization of ZK4 by X-Ray and $^{29}\text{Si}$ NMR

Powder X-Ray Data. We believe that  $^{29}\text{Si}$  NMR provides a more accurate determination of framework composition than elemental analysis since the measurement is essentially independent of any impurities that may be occluded in the zeolite pores. Therefore, we used the values of Si/Al derived from the NMR data to follow the variation of unit-cell size with composition.

In order to obtain a good correlation of lattice parameter with composition, sodium-exchanged samples of several materials were obtained from the initial products by calcining them in air at  $520^\circ\text{C}$  to remove trapped  $\text{TMA}^+$  ion by oxidation to gaseous products and  $\text{H}^+$ ; followed by sodium-exchange with excess 2M NaCl (aq) at  $60^\circ\text{C}$ . Elemental analysis showed that this treatment was in fact inadequate for the exchange,



indicating that  $\text{H}^+$  is tightly bound in ZK4. The back exchange procedure was repeated successfully using 2M NaCl(aq) which was also 0.1M in NaOH(aq). The washed and dried final products were stored at controlled 56% relative humidity for 24 hours before powder X-ray data were collected. X-ray diffraction patterns were not recorded under controlled humidity, but at ambient humidity the materials are effectively saturated with  $\text{H}_2\text{O}$  (28). No variation of unit cell size with time was observed during the recordings. Refined lattice parameters obtained by a least squares iterative procedure are recorded in Table IV, and are shown as a function of composition in Figure 3. There is a smooth but non-linear variation of  $a_0$  with silicon content, the reduction in unit-cell size reflecting the shorter Si-O bond length compared to Al-O.

$^{29}\text{Si}$  NMR Data The  $^{29}\text{Si}$  NMR data for faujasite (2-5) and ZK4 show that the isotropic chemical shifts of the particular Si environments show a strong framework dependence. On the other hand, chemical shifts are almost independent of composition for both materials. It has been suggested previously (19,20) that variations in chemical shift may arise from changes in Si site geometry. The double 4-ring unit in A causes the T-O-T angles to be markedly different from those in faujasite, in particular one T-O-T linkage is almost linear. Presumably such angle changes are reflected in the hybridisation of the Si atomic orbitals which in turn affects the Si s-electron density.

TABLE III

<sup>29</sup>Si NMR data for ZK4 materials

| Si:Al<br>(elemental) | Si:Al(NMR) | I(4Al) | I(3Al) | I(2Al) | I(1Al) | I(0Al) |
|----------------------|------------|--------|--------|--------|--------|--------|
| 1.18                 | 1.13       | 0.703  | 0.195  | 0.050  | 0.030  | 0.022  |
| 1.16                 | 1.18       | 0.642  | 0.246  | 0.036  | 0.026  | 0.051  |
| 1.16                 | 1.21       | 0.567  | 0.247  | 0.095  | 0.041  | 0.023  |
| 1.32                 | 1.30       | 0.430  | 0.350  | 0.110  | 0.080  | 0.040  |
| 1.40                 | 1.38       | 0.333  | 0.383  | 0.164  | 0.092  | 0.027  |
| 1.40                 | 1.41       | 0.317  | 0.375  | 0.171  | 0.103  | 0.037  |
| 1.49                 | 1.44       | 0.279  | 0.391  | 0.190  | 0.108  | 0.032  |
| 1.47                 | 1.49       | 0.254  | 0.387  | 0.200  | 0.105  | 0.054  |
| 1.66                 | 1.62       | 0.185  | 0.337  | 0.277  | 0.162  | 0.040  |
| 1.57                 | 1.64       | 0.169  | 0.360  | 0.260  | 0.162  | 0.050  |
| 1.86                 | 1.83       | 0.121  | 0.285  | 0.316  | 0.220  | 0.058  |
| 2.08                 | 1.96       | 0.080  | 0.250  | 0.360  | 0.250  | 0.060  |
| 2.16                 | 2.08       | 0.025  | 0.211  | 0.395  | 0.301  | 0.068  |
| 2.39                 | 2.34       | 0.025  | 0.167  | 0.387  | 0.331  | 0.089  |
| * 2.99               | 2.74       | 0.0    | 0.106  | 0.368  | 0.407  | 0.119  |

\* includes small sodalite impurity

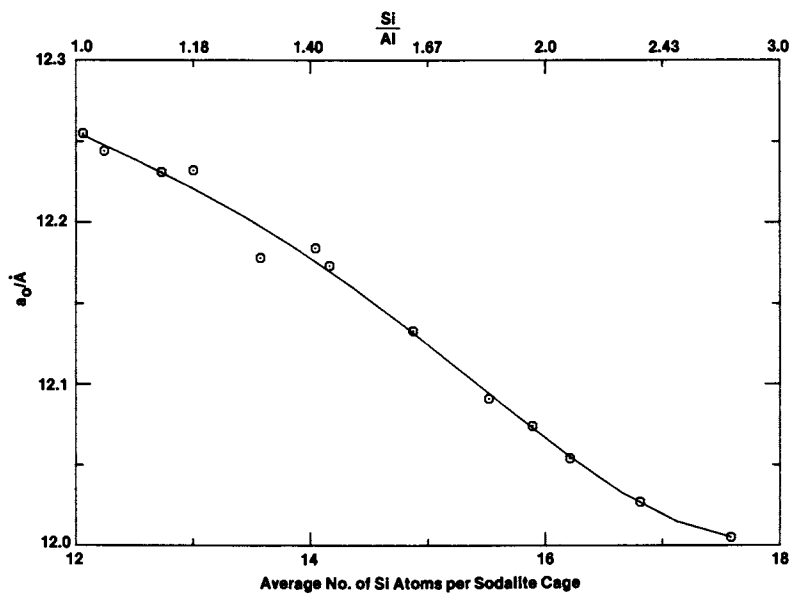


Figure 3.  
Cubic lattice parameter vs. composition for the hydrated sodium form of ZK4.

TABLE IV  
Unit Cell Data For Sodium Exchanged Samples of ZK4

| Si:Al ratio | Average No. of Si Atoms<br>per sodalite cage (24 atoms) | $a_0/\text{\AA}$ |
|-------------|---|------------------|
| *1.01       | 12.06   | 12.255(1)        |
| *1.04       | 12.24   | 12.244(1)        |
| 1.13        | 12.89   | 12.231(1)        |
| 1.18        | 13.00   | 12.232(2)        |
| 1.30        | 13.66   | 12.178(1)        |
| 1.41        | 14.04   | 12.184(1)        |
| 1.44        | 14.16   | 12.162(2)        |
| 1.62        | 14.98   | 12.133(2)        |
| 1.83        | 15.61   | 12.091(2)        |
| 1.96        | 16.21   | 12.074(3)        |
| 2.08        | 16.41   | 12.054(1)        |
| 2.34        | 16.92   | 12.027(1)        |
| 2.74        | 17.98   | 12.006(1)        |

\*Samples of synthetic NaA

The integrated intensity data of Table III are shown plotted as a function of composition in Figure 4. Each peak intensity shows a smooth variation over the whole range. These data contain information about the local order of Al atoms about Si. In the case of faujasite a structural model has been developed that successfully explains the NMR data over the whole range of composition (7). Comparison of the  $^{29}\text{Si}$  NMR spectra for ZK4 and faujasite at the same composition, Figure 5, shows that the relative intensities of the five peaks are different. Therefore, the local order of Al about Si is different in the two materials. This is true over the whole range of composition as demonstrated by comparison of the relative intensities of the Si(2Al) and Si(0Al) peaks in Figure 6.

No one structurally independent model can simultaneously describe the Si and Al distribution in ZK4 and faujasite. Furthermore, the structural model developed for faujasite (7) cannot, as it stands, be used for ZK4. We are at present developing a model to describe the Si and Al distributions in ZK4.

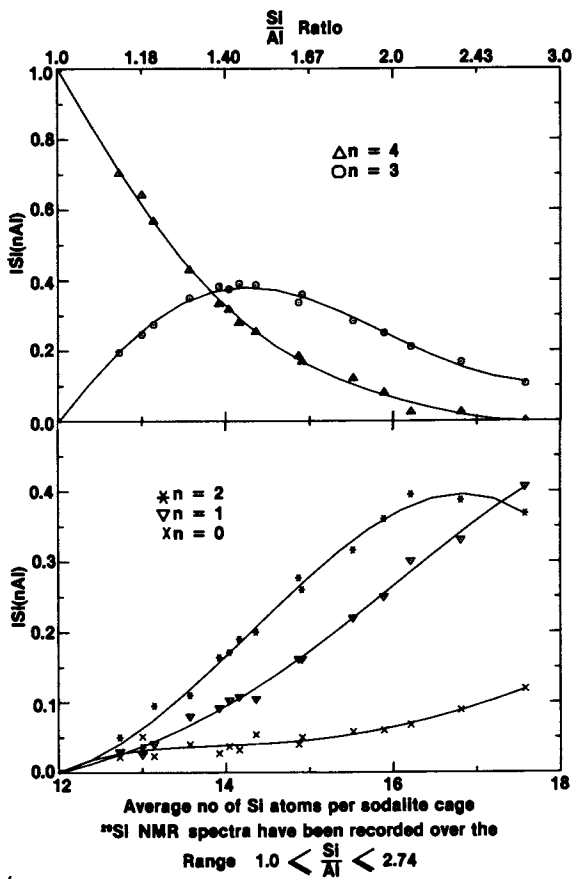


Figure 4.

$^{29}\text{Si}$  NMR peak intensities vs. composition for ZK4 in the range  $1.0 < \text{Si}/\text{Al} < 2.74$ .

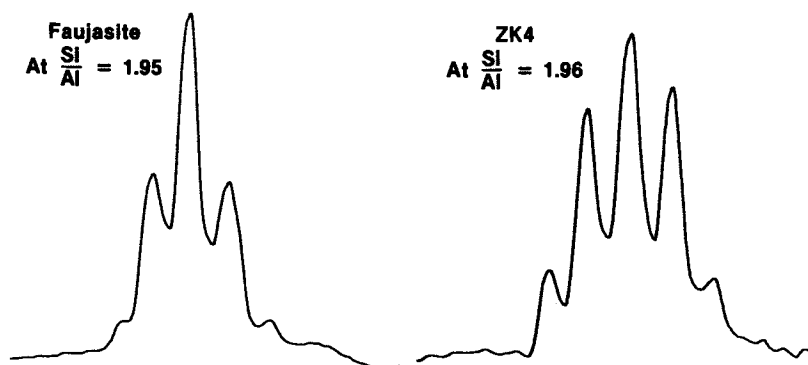


Figure 5.  
Comparison of  $^{29}\text{Si}$  NMR spectra of faujasite and ZK4 at the same composition.

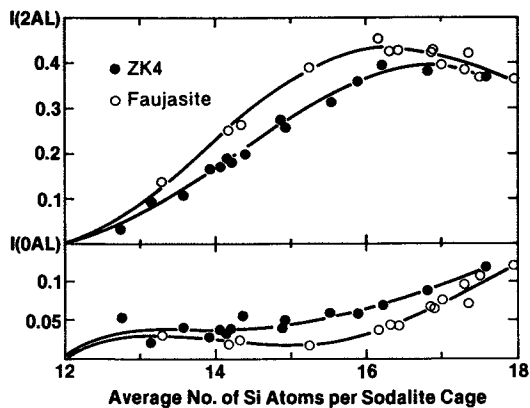


Figure 6.  
Differences in the  $^{29}\text{Si}$  NMR spectra of the faujasite and ZK4 systems as demonstrated by the relative intensities of the Si(2Al) and Si(0Al) peaks in the range  $1.0 < \text{Si/Al} < 3.0$ .



Literature Cited

1. Lippmaa, E.; Magi, M.; Samoson, A.; Englehardt, G.; Grimmer, A. R.; *J. Am. Chem. Soc.* 1980 102, 4889-4893.
2. Lippmaa, E.; Magi, M.; Samoson, A.; Tarmak, M.; Englehardt, G.; *J. Am. Chem. Soc.* 1981 103, 4992-4996.
3. Ramdas, S.; Thomas, J. M.; Klinowski, J.; Fyfe, C. A.; Hartman, J. S.; *Nature* 1981 292, 228.
4. Melchior, M. T.; Vaughan, D. E. W.; Jacobson, A. J.; *J. Am. Chem. Soc.* 1982.
5. Klinowski, J.; Ramdas, S.; Thomas, J. M.; Fyfe, C. A.; Hartman, J. S.; *J. Chem. Soc., Faraday Transactions* 1982 78, 1025.
6. Vaughan, D. E. W.; Melchior, M. T.; Jacobson, A. J.; Chapter , in this book.
7. Melchior, M. T.; Chapter , in this book.
8. Peters, A. W.; *J. Phys. Chem.* 1982, 86, 3489.
9. Englehardt, G.; Lohse, U.; Lippmaa, E.; Tarmak, M.; Magi, M.; *Z. Anorg. Allg. Chem.* 1981, 482, 49.
10. Gramlich, V.; Meier, W. M.; *Z. Kristallogr.* 1971 133, 134.
11. Pluth, J. J.; Smith, J. V.; *J. Am. Chem. Soc.* 1980 102, 4704.
12. Cheetham, A. K.; Eddy, M. N.; Jefferson, D. A.; Thomas, J. M.; *Nature*, 1982, 299, 24.
13. Reed, T. B.; Breck, D. W.; *J. Am. Chem. Soc.* 1956 78, 5972.
14. Englehardt, G.; Zeigan, D.; Lippmaa, E.; Magi, M.; *Z. Anorg. Allg. Chem.* 1980 468, 35.
15. Bursill, L. A.; Lodge, E. A.; Thomas, J. M.; Cheetham, A. K.; *J. Phys. Chem.* 1981 85, 2409.
16. Thomas, J. M.; Bursill, L. A.; Lodge, E. A.; Cheetham, A. K.; Fyfe, C. A.; *J. Chem. Soc. Chem. Comm.* 1981 276.
17. Loewenstein, W.; *Amer. Mineral.* 1954 39, 92.
18. Melchior, M. T.; Vaughan, D. E. W.; Jarman, R. H.; Jacobson, A. J.; *Nature* 1982 298, 455.
19. Thomas, J. M.; Fyfe, C. A.; Ramdas, S.; Klinowski, J.; Gobbi, G. C.; *J. Phys. Chem.*, 1982, 86, 3061.
20. Cheetham, A. K.; Fyfe, C. A.; Smith, J. V.; Thomas, J. M.; *J. Chem. Soc. Chem. Comm.* 1982 823.
21. Kerr, G. T.; *Inorganic Chemistry*, (1966) 5, 1537. Kerr, G. T.; *Canadian Patent No.* 817,322 1969.
22. Barrer, R. M.; Beaumont, R.; *J. Chem. Soc., Dalton*, 1973 405.
23. Acara, N. A.; *U.S. Patent*, 3,414,602 1968.
24. Duecker, H. C.; Weiss, A.; Guerra, C. R.; *U.S. Patent* 3,567,372 1971.
25. Kuehl, G. H.; *U. S. Patent*, 4,191,663 1980.
26. Kuehl, G. H.; *U. S. Patent*, 4,299,686 1981.
27. Wadlinger, R. L.; Rosinski, E. J.; Plank, C. J.; *U. S. Patent*, 3,375,205 1968.
28. Breck, D. W.; Eversole, W. G.; Milton, R. M.; Reed, T. B.; Thomas, T. L.; *J. Am. Chem. Soc.* 1956 78, 5963.

RECEIVED November 4, 1982

# Electron Spin Echo Studies of the Location and Adsorbate Interactions of Paramagnetic Metal Species in Zeolites

LARRY KEVAN and M. NARAYANA

University of Houston, Department of Chemistry, Houston, TX 77004

Electron spin echo spectrometry is a pulsed ESR technique that is able to resolve weak superhyperfine interactions even in powders and is thus becoming quite useful for elucidating the local structure of paramagnetic species in catalytic solids. In general the types, number, distance and isotropic hyperfine coupling of magnetic nuclei surrounding a paramagnetic species can be determined. We report how this spin echo technique can be used to give newly definitive information about the location and adsorbate interactions of paramagnetic metal species such  $\text{Ag}^0$  and  $\text{Cu}^{2+}$  in A, X and Y type zeolites. Of particular interest are the relocation of the metal species upon partial or complete dehydration, the dependence of location on the type of adsorbate and the effect of major cation like sodium vs potassium on the location of the paramagnetic metal species.

The class of aluminosilicates known as zeolites is widely used for sorption and catalytic purposes. Metal ions, typically sodium ion, are present in the zeolite lattices to compensate for the imbalance in charge between the valence states of aluminum and silicon. The charge balancing cation is relatively easily exchanged and a number of specific metal cation exchanged zeolites have been shown to be very useful catalysts for a wide range of chemical reactions. In many cases the metal cations are considered to be the active site for catalytic reaction. Consequently extensive work has been performed to elucidate the location of the cations and their interaction with adsorbed molecules (1). For example, various cupric ion exchanged zeolites have been implicated in the high efficiency of such catalytic reactions as the oxidation of propylene (2) and the cyclodimerization of butadiene (3). Likewise, partial exchange by silver ion affects the catalytic oxidation of ethylene on zeolites (4).

Paramagnetic transition metal ions partially exchanged into

0097-6156/83/0218-0283\$06.00/0

© 1983 American Chemical Society

zeolite lattices have been extensively studied by electron spin resonance (ESR) (5). The general focus of much of this work has been to measure hyperfine and g factor parameters of the paramagnetic ions in the presence and absence of adsorbed molecules and under various conditions of temperature treatment. The changes in the magnetic parameters observed have been used to infer the location of the paramagnetic cations in the zeolites and their interaction with adsorbed molecules. However, such studies have not generally led to detailed information about the specific location of the cations or about the specific orientation of adsorbed molecules relative to the cations because hyperfine interaction parameters with the lattice atoms or with the adsorbed molecules were not resolved. Since zeolites are crystalline materials it is, in principle, possible to use x-ray diffraction to determine information about the structure and site location of exchanged metal ions. However, the zeolite structure is so complex that x-ray diffraction often does not give definitive results except perhaps in the case of one of the structurally simplest zeolites known as A-zeolite (6).

In the last few years we have shown that the very weak hyperfine interactions characterizing the average surroundings of a paramagnetic species in a disordered matrix can often be quantitatively analyzed by a pulsed electron spin resonance technique called electron spin echo spectroscopy (7). In recent work we have shown how the utilization of this technique can lead to new and detailed structural information about the location and adsorbate interactions of paramagnetic species in zeolites. Here we discuss such studies with particular focus on silver atom and cupric ion probes. We first give a brief background of how electron spin echo spectroscopy can be used to obtain new structural information. Then follows a brief section on zeolite structure with respect to possible locations of metal cations before dealing with specific results involving silver atom and cupric ion probes.

It should be noted that these electron spin echo studies are in large part complimentary to x-ray diffraction results and to extended x-ray absorption fine structure (EXAFS) studies (8) since the spin echo experiment is a resonance technique which depends upon the magnetic moments of the surrounding atoms rather than on their scattering cross sections. Hence spin echo spectroscopy is well suited to look at the location of protons and deuteriums around a paramagnetic probe which have large magnetic moments but very low scattering cross-sections.

### Electron Spin Echo Modulation

The fundamentals and analysis of electron spin echo modulation have been described in some detail (9). Here the essential details will be summarized to aid in understanding the structural data to be presented. Electron spin echoes are generated in pulsed electron spin resonance experiments. The most common type

of pulse sequence consists of two pulses. The first is  $90^\circ$ , which flips the spins oriented along the magnetic field in the Z direction into the XY plane. The spins are allowed to precess in the XY plane where they are subject to time dependent magnetic interactions, including weak hyperfine interactions, for a time,  $\tau$ . Then a second  $180^\circ$  pulse is applied which flips the spins to the opposite direction in the XY plane so that the spins then precess together and refocus at a time  $2\tau$  after the original pulse to produce a burst of microwave energy called an echo. This echo intensity is then measured as a function of the time between the pulses to generate an echo decay envelope which is shown schematically in Figure 1.

The echo decay envelope is a product of two functions, a relaxation function and a modulation function. The relaxation function decreases monotonically with time and carries information about all of the spin relaxation processes that cause the electron spins to dephase. The modulation function carries structural information with which we are primarily concerned. The general analysis procedure is to analyze the spin echo modulation pattern in terms of a number of equivalent nuclei  $\underline{n}$ , located at a distance  $\underline{r}$  from the paramagnetic species which have a small overlap of the unpaired electron wavefunction to produce a small isotropic hyperfine coupling,  $\underline{a}_{iso}$ . Usually the physically reasonable assumption that  $\underline{n}$  is integral is made. For reasonably good quality data it is then typically possible to uniquely determine the value of  $\underline{n}$  to the nearest integer up to about  $\underline{n}=10$ . The parameters  $\underline{r}$  can be determined to about  $\pm 0.01$  nm and  $\underline{a}_{iso}$  to about  $\pm 15\%$ . For metal ion species such as silver atoms and cupric ions the unpaired electron wavefunction is highly localized and dipolar interactions with surrounding magnetic nuclei dominate, so the important parameters for interpretation are  $\underline{n}$  and  $\underline{r}$ .

It is also possible to carry out three pulse electron spin echo experiments in which the second  $180^\circ$  pulse is essentially divided up into two  $90^\circ$  pulses separated by another experimentally variable time,  $T$ . If simultaneous modulation from two different nuclei is encountered it is possible to suppress one of these by carrying out a three pulse experiment and selecting an appropriate value of the first pulse separation time,  $\tau$ , to suppress one of the modulation frequencies. This is found to be particularly valuable in studying zeolite systems where modulations from both aluminum nuclei in the zeolite lattice and deuterium nuclei from water adsorbate molecules are encountered.

It is also possible to Fourier transform the echo envelope modulation to obtain a frequency spectrum showing the various nuclear hyperfine frequencies. In practice there are some experimental difficulties and the intensities of the Fourier transformed spectrum which are related to the number of interacting nuclei are not well defined. However, the frequency spectrum does help to identify frequency components associated with specific nuclei and the presence of weak isotropic hyperfine interactions. In the

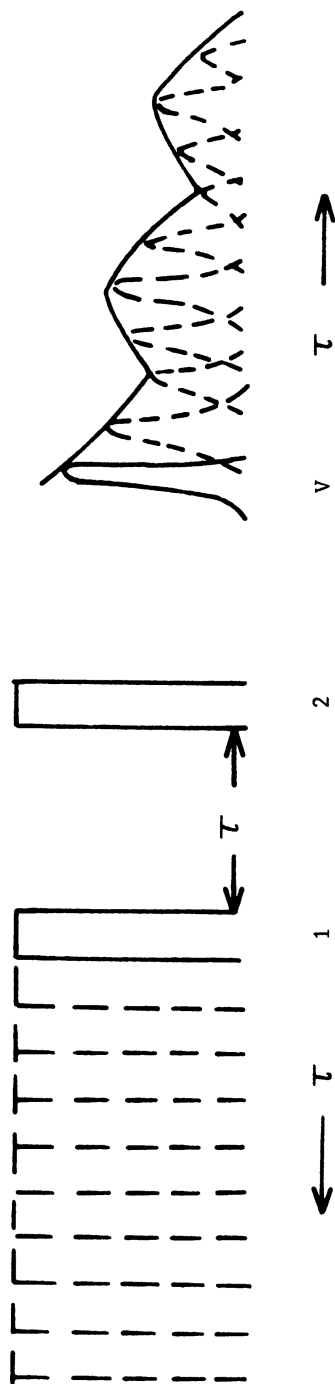


Figure 1.  
 Illustration of modulation of two pulse electron spin echo decay envelope. Microwave pulses 1 and 2 separated by the time  $\tau$  produce the echo signal at time  $\tau$  after pulse 2. As  $\tau$  is increased the echo amplitude changes and traces out an echo envelope which may be modulated.

case of complex modulation it is then effective to analyze the modulation by combining the techniques of Fourier transform and direct time domain spectral simulation (10a).

The simulations generally fit the experimental curves satisfactorily and uniquely within the indicated variation of parameters. Sometimes at longer delay times the fit is worse due to phase mismatch so the earlier delay time data is more heavily weighted. The analysis procedures and examples of the quality of fits obtainable have been thoroughly described (9,10).

### Zeolite Structure

We will be concerned with only the most common structural types of zeolites used for adsorptive and catalytic purposes, namely the so designated A, X and Y type zeolites. The A-zeolites have a relatively simple structure comprising a  $(Al_{12}Si_{12}O_{48})^{12-}$  anionic framework with charge balance being achieved by the presence of twelve exchangeable monovalent cations or six divalent ions or a mixture of both. The silica and alumina tetrahedra are coupled to form a truncated octahedron known as the sodalite unit. The sodalite units have square faces and hexagonal faces. When the sodalite units are interconnected by cubes on the square faces we have the A-zeolite structure which is shown in Figure 2 which shows about half of a unit cell. The void within the sodalite unit is called the  $\beta$ -cage. It can also be seen in Figure 2 that a larger cage is formed with octagonal, hexagonal and square faces; this is called the  $\alpha$ -cage. Possible site locations for exchangeable cations are at the center of hexagonal faces (S2), square faces (S3) and octagonal faces (S5). Other possible locations are at the centers of the  $\alpha$ -cages (S4) or  $\beta$ -cages (SU). Finally, an ion may be displaced from the hexagonal face towards the  $\alpha$ -cage (S2\*) or toward the  $\beta$ -cage (S2'). The cubes are too small to constitute an exchangeable ion site.

When the sodalite units are interconnected by hexagonal prisms on their hexagonal faces we have the X-zeolite structure also shown in Figure 2. Y-zeolite has essentially the same structure as X-zeolite except that Si:Al ratio is greater than 2. The site locations in X, Y zeolites are analogous to those in A-zeolite except that they are designated by Roman numerals. In addition the center of the hexagonal prisms constitute a new site, I. Displacement from site I towards the  $\beta$ -cage is designated site I'.

### Silver Species in Zeolites

Silver ion in zeolites is not paramagnetic however it may relatively easily be converted to silver atom by high energy irradiation reduction. Irradiation by gamma rays or x-rays typically converts only about 0.1% of the silver ions to silver atoms by electron reduction. Silver consists of two almost equally abundant isotopes ( $^{107}Ag$  and  $^{109}Ag$ ) both with nuclear spin  $I=\frac{3}{2}$ .

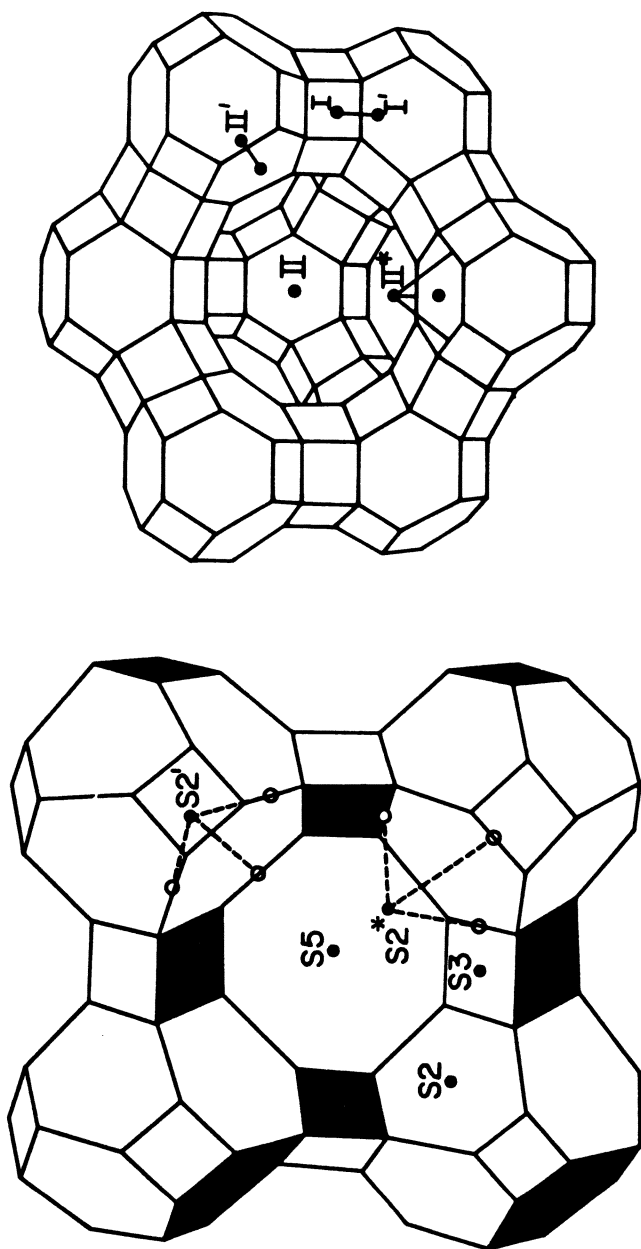


Figure 2.  
 The left side shows a structural model of A-zeolite composed of four octahedral sodalite units connected by cubes. Cation site locations are designated S2, S3, etc.; there is no S1 site. The right side shows a structural model of X-zeolite composed of sodalite units connected by hexagonal prisms. Cation site locations are designated I, II, etc.

The unpaired electron is a 5s electron and consequently the isotropic hyperfine splittings are quite large, are easily identified and are sensitively subject to local environmental perturbations.

### Ag<sup>0</sup> in A-Zeolites

Silver species have been studied in a variety of A-zeolites including Na<sub>12</sub>-A, K<sub>12</sub>-A, Li<sub>12</sub>-A, Cs<sub>7</sub>Na<sub>5</sub>-A and Ca<sub>6</sub>-A (11). Complete exchange of cesium ion for sodium ion cannot be achieved in the A-zeolites. Typically the major cation was exchanged by silver to an extent of about 0.7 ion per unit cell which is 6% of the exchangeable cations. After irradiation about 0.003 silver ions per unit cell were converted to atomic silver species.

Irradiation at 4 K gives a silver species designated as Ag<sup>0</sup>(B) in all of the hydrated A-zeolites studied. This particular silver species is characterized by a silver isotropic hyperfine coupling of about 1480 MHz and a g-factor of 1.991. For comparison the isotropic coupling constant of the silver atom in the gas phase is 1979 MHz, so species Ag<sup>0</sup>(B) shows considerable interaction with its environment. If the A-zeolites are dehydrated by heating to 400° C no silver species are formed by irradiation. Presumably the silver atoms that are formed are more mobile in the absence of water and form dimers or multimers. In addition, more prominent spectra of Ag<sup>2+</sup> are seen upon irradiation of the dehydrated A-zeolites. Thus it seems that species Ag<sup>0</sup>(B) is probably associated with some adjacent water molecules.

The electron spin echo of Ag<sup>0</sup>(B) has a very short phase memory time but relatively strong aluminum modulation can be identified. However, the phase memory time is too short to carry out a quantitative analysis of the modulation. This also precludes us from getting analyzable modulation from deuterated adsorbate molecules in a three pulse echo experiment. So the data is insufficient to locate Ag<sup>0</sup>(B) in the zeolite lattice without additional information.

Irradiation was therefore carried out on silver doped A-zeolites at 77 K and a new silver atom species was detected with a different hyperfine splitting than that of the one observed at 4 K. This species is designated as Ag<sup>0</sup>(A) with an isotropic hyperfine splitting of about 1985 MHz which is very close to that of the free atom value. Species Ag<sup>0</sup>(A) is the dominant species formed by irradiation at 77 K in all of the A-zeolites studied. In addition, species Ag<sup>0</sup>(B) is also visible at 77 K. However, upon warming above 77 K species Ag<sup>0</sup>(B) decays to apparently yield Ag<sup>0</sup>(A). The kinetics of this conversion have not been studied. Further thermal decay of species Ag<sup>0</sup>(A) yields an ESR spectrum which may be identified as the multimer species Ag<sub>4</sub><sup>3+</sup> and possibly other cluster species. Warming further to room temperature destroys all paramagnetic silver species. Dehydration at room temperature before irradiation at 77 K gives no monomeric silver species at all. Thus, Ag<sup>0</sup>(A) and Ag<sup>0</sup>(B) must be silver species involving some interaction with water molecules.



To locate species  $\text{Ag}^0(\text{A})$  in the zeolite lattice we turn to electron spin echo modulation spectroscopy. The phase memory time is longer than that for  $\text{Ag}^0(\text{B})$  and good two pulse and three pulse electron spin echo data can be obtained. The two pulse data shows that the aluminum modulation for  $\text{Ag}^0(\text{A})$  is significantly weaker than that for  $\text{Ag}^0(\text{B})$ . This suggests that species  $\text{Ag}^0(\text{A})$  is further away from aluminums in the zeolite lattice than is species  $\text{Ag}^0(\text{B})$ . However, the real breakthrough in analysis comes by looking at the three pulse ESE data. By using selective suppression of one modulation frequency the aluminum modulation can be suppressed and for silver zeolites hydrated with  $\text{D}_2\text{O}$  deuterium modulation from the water molecules can be detected. The analysis of this modulation indicates that there are four deuteriums at a distance of 0.33 nm from the silver nucleus. If we make the reasonable assumption that the negative end of the water dipole is oriented toward the silver nucleus we obtain a silver-oxygen distance of 0.26 nm and two interacting water molecules.

The experiments carried out in the lithium and cesium exchanged A-zeolites give additional information on the location of  $\text{Ag}^0(\text{A})$ . By hydrating with  $\text{H}_2\text{O}$  three pulse electron spin echo experiments can be used to suppress the aluminum modulation and to show up a weak modulation due to interactions with cesium nuclei. Although this modulation is too weak to analyze quantitatively a semiquantitative analysis indicates that the distance between the silver atom and the cesium nuclei must be  $\geq 0.6$  nm. The crystal structure of  $\text{Cs}_7\text{Na}_5\text{-A}$  zeolite has been studied and the cesium ion positions are well defined (12). Three are at S5 positions, three others are at S2\* positions and one is in the  $\beta$ -cage at an S2' position. See these site locations in Figure 2. Sorption and x-ray results show that  $\text{Ag}^+$  fills S2 type sites in preference to S5 sites (13,14). If the silver ion replaces the cesium ion at S2\* and then captures an electron to form silver atom at the same location it would have three nearest cesium ions in S5 sites at 0.43 nm. This would result in much stronger cesium nuclei modulation than is observed experimentally. Therefore we can eliminate this position. Similarly, if the silver atom is formed in site S2 in the hexagonal ring between the  $\alpha$  and  $\beta$ -cages it would still be too close to adjacent cesium nuclei to be compatible with the observed weak cesium modulation. However, if  $\text{Ag}^+$  replaces a  $\text{Na}^+$  at site S2' about 0.12 nm below the hexagonal ring, and subsequently captures an electron to form  $\text{Ag}^0$  which moves deeper into the  $\beta$ -cage to about 0.15 nm below the hexagonal window the nearest  $\text{Cs}^+$  positions are 0.6 nm away which is compatible with the observed weak  $\text{Cs}^+$  modulation. Thus we conclude that  $\text{Ag}^0(\text{A})$  is located in a S2' site about 0.15 nm below the hexagonal windows.  $\text{Ag}^0(\text{A})$  is coordinated to two water molecules in the  $\beta$ -cage and presumably also to two oxygens in the nearest hexagonal ring.

The nuclear modulation of lithium nuclei is stronger than that of cesium and an example is shown in Figure 3. Preliminary

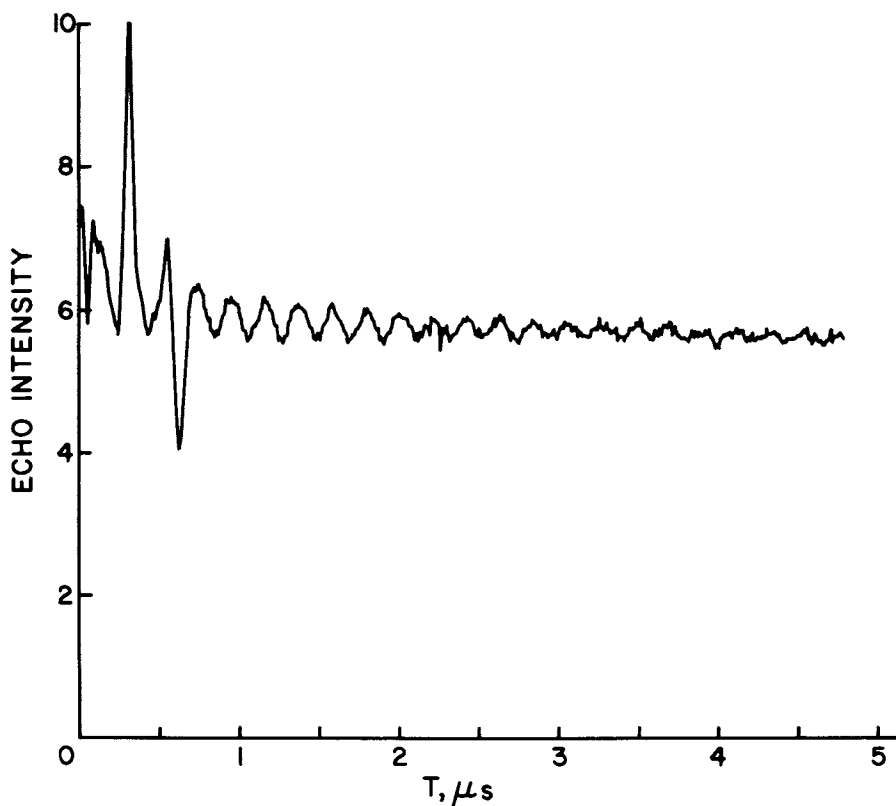


Figure 3.

Experimental three pulse electron spin echo spectra of  $\text{Ag}^0(\text{A})$  in  $\text{Li}_{12}\text{-A}$  zeolite. The two large sharper peaks below  $1 \mu\text{s}$  are due to two pulse interference.

analysis suggests that  $\text{Ag}^0(\text{A})$  interacts with 3  $\text{Li}^+$  at about 0.45 nm. Although the crystal structure of  $\text{Li}_{12}\text{-A}$  has not been reported one expects from a comparison of the cation locations in  $\text{Na}_{12}\text{-A}$  and  $\text{K}_{12}\text{-A}$  that the  $\text{Li}^+$  at  $\text{S2}^*$  positions are much closer to the hexagonal window than are the  $\text{Cs}^+$  ions. This is in semiquantitative agreement with the modulation analysis.

Both  $\text{Ag}^0(\text{A})$  and its apparent precursor,  $\text{Ag}^0(\text{B})$  are coordinated to water. The main difference is the stronger aluminum modulation for  $\text{Ag}^0(\text{B})$  which indicates that it is closer to the aluminums in the nearest hexagonal ring. We tentatively suggest that  $\text{Ag}^0(\text{B})$  is located at site  $\text{S2}'$  where  $\text{Ag}^+$  originally replaced  $\text{Na}^+$ , that is about 0.12 nm below the hexagonal ring, and that it is also coordinated to two waters in the  $\beta$ -cage. After electron capture at 4 K,  $\text{Ag}^+$  is converted to  $\text{Ag}^0$  but remains at nearly the same location. This, however, is a nonequilibrium environment and upon warming to 77 K and above  $\text{Ag}^0(\text{B})$  moves 0.03 to 0.04 nm further away from the hexagonal ring to become  $\text{Ag}^0(\text{A})$ .

#### $\text{Ag}^0$ in X- and Y-Zeolites

Silver species have been studied in  $\text{Ag}^+$  exchanged Na-X and Na-Y zeolites as well as in these zeolites 63% exchanged by cesium. X-irradiation at 4 K gives no paramagnetic silver species in contrast to the A-zeolites. The reason for this is unclear. However, at 77 K irradiation produces  $\text{Ag}^0(\text{D})$  with a silver isotropic hyperfine coupling of about 1850 MHz. The couplings are similar in the X and Y zeolites but are consistently about 15 MHz greater in the X zeolites. This silver hyperfine coupling is intermediate between those for  $\text{Ag}^0(\text{B})$  and  $\text{Ag}^0(\text{A})$  in the A-zeolites.

Electron spin echo studies of  $\text{Ag}^0(\text{D})$  show weak aluminum modulation in the two pulse spectra. This is weaker than observed for  $\text{Ag}^0(\text{A})$ . The three pulse echo spectra show strong deuterium modulation in  $\text{D}_2\text{O}$  hydrated samples when the aluminum modulation is suppressed. This can be analyzed in terms of eight interacting deuteriums at  $r=0.35$  nm which implies four adjacent water molecules with a  $\text{Ag}^0\text{-O}$  distance of 0.28 nm. Thus  $\text{Ag}^0(\text{D})$  in the X and Y zeolites is a fully solvated species. In the  $\text{Cs}^+$  exchanged X and Y zeolites three pulse electron spin echo spectra show quite weak  $\text{Cs}^+$  modulation. From the arguments used before in A zeolites this clearly indicates that the  $\text{Ag}^0(\text{D})$  species is not in the  $\alpha$ -cage. We therefore assign the location of  $\text{Ag}^0(\text{D})$  to site SU in the center of the  $\beta$ -cage where it is fully solvated by four waters.

The initial exchange site of  $\text{Ag}^+$  into X and Y zeolites is most probably SI in the hexagonal prisms or possibly  $\text{SI}'$  displaced into the  $\beta$ -cage (15,16) from the hexagonal prisms. When  $\text{Ag}^0$  is formed by electron reduction of  $\text{Ag}^+$  at 77 K the  $\text{Ag}^0$  does not seem to remain in the SI or  $\text{SI}'$  sites. Instead it appears to be able to move to site SU. Partial dehydration studies suggest that  $\text{Ag}^0$  moves toward  $\text{SI}'$  as dehydration occurs.

Cu<sup>2+</sup> in A-Zeolites

Divalent cupric ion has a  $3d^9$  electronic configuration with an effective spin of  $S=\frac{1}{2}$ . Copper consists of 69%  $^{63}\text{Cu}$  and 31%  $^{65}\text{Cu}$  isotopes both with nuclear spin  $I=3/2$ . The nuclear g-factors of these two isotopes are sufficiently close that no resolution of the two isotopes is typically seen in zeolite matrices. No Jahn-Teller effects have been observed for  $\text{Cu}^{2+}$  in zeolites. The spin-lattice relaxation time of cupric ion is sufficiently long that it can be easily observed by ESR at room temperature and below. Thus cupric ion exchanged zeolites have been extensively studied (5,17-26) by ESR, but ESR alone has not typically given unambiguous information about the water coordination of cupric ion or the specific location of cupric ion in the zeolite lattice. This situation can be substantially improved by using electron spin echo modulation spectrometry. The modulation analysis is carried out as described in the previous sections. The number of coordinated deuterated water molecules is determined from deuterium modulation in three pulse electron spin echo spectra. The location in the zeolite lattice is determined partly from aluminum modulation and more quantitatively from cesium modulation. The symmetry of the various copper species is determined from the water coordination number and the characteristics of the ESR spectra.

Seff et al. (27) have reported that 20% or greater exchange of  $\text{Cu}^{2+}$  in acidic media into A-zeolites results in the breakdown of the crystal structure. Our studies involve an exchange of 0.3%  $\text{Cu}^{2+}$  per unit cell for which low exchange level we did not observe significant structural breakdown. At this low exchange level  $\text{Cu}^{2+}$  populates only the most preferential sites.

We have found that the coordination and location of  $\text{Cu}^{2+}$  in A-zeolites depends sensitively on the nature of the major cocation, on the degree of hydration or dehydration and sometimes on the past history of dehydration. Several results on individual A-zeolites have been published (28-31). Here we concentrate on the overall picture with respect to the major cocation with the aid of additional data. This picture is summarized in Table I. Four different  $\text{Cu}^{2+}$  species corresponding to different degrees of water coordination have been identified. These are designated by a Roman numeral subscript denoting the number of waters in the first coordination shell.  $\text{Cu}_{\text{III}}$  is a distorted octahedron,  $\text{Cu}^{2+}(\text{O}_z)_3(\text{H}_2\text{O})_3$  where  $\text{O}_z$  denotes an oxygen in the zeolite lattice.  $\text{Cu}_{\text{II}}$  is a trigonal bipyramid  $\text{Cu}^{2+}(\text{O}_z)_3(\text{H}_2\text{O})_2$ ,  $\text{Cu}_{\text{I}}$  is a distorted tetrahedron  $\text{Cu}^{2+}(\text{O}_z)_3(\text{H}_2\text{O})$  and  $\text{Cu}_0$  is the trigonal species  $\text{Cu}^{2+}(\text{O}_z)_3$ .

Table I. Sites and Coordination of  $\text{Cu}^{2+}$  in A and X-Zeolites for Different Hydration/Dehydration Treatments

| Zeolite                           | Copper Species (Zeolite Site) <sup>a</sup> |                                     |                            |  |
|-----------------------------------|--|-------------------------------------|----------------------------|--|
|                                   | Hydrated                                   | Partially Hydrated                  | Dehydrated                 | Rehydrated   |
| $\text{Na}_{12}\text{-A}$         | $\text{Cu}_{\text{III}}(\text{S2}^*)$      | $\text{Cu}_{\text{II}}(\text{S2})$  | $\text{Cu}_0(\text{S2}')$  | $\text{Cu}_{\text{III}}(\text{S2}^*)$                              |
| $\text{K}_{12}\text{-A}$          | $\text{Cu}_{\text{I}}(\text{S2}')$         | $\text{Cu}_{\text{II}}(\text{S2})$  | $\text{Cu}_0(\text{S2}^*)$ | $\text{Cu}_{\text{III}}(\text{S2}^*)$                              |
| $\text{Cs}_7\text{Na}_5\text{-A}$ | $\text{Cu}_{\text{I}}(\text{S2}')$         | -                                   | $\text{Cu}_0(\text{S2}^*)$ | $\text{Cu}_{\text{I}}(\text{S2}')$                                 |
| $(\text{NH}_4)_{12}\text{-A}$     | $\text{Cu}_{\text{I}}(\text{S2}')$         | $\text{Cu}_{\text{II}}(\text{S2})$  | -                          | -  |
| $\text{Na-X}$                     | $\text{Cu}_0(\text{SI})$                   | $\text{Cu}_0(\text{SI})$            | $\text{Cu}_0(\text{SI}')$  | $\text{Cu}_0(\text{SI})$   |
| $\text{K-X}$                      | $\text{Cu}_{\text{III}}(\text{SII}^*)$     | $\text{Cu}_{\text{II}}(\text{SII})$ | $\text{Cu}_0(\text{SI}')$  | $\text{Cu}_{\text{III}}(\text{SII}^*)$                             |
| $\text{Ca-X}$                     | $\text{Cu}_{\text{II}}(\text{SII})$        | $\text{Cu}_{\text{II}}(\text{SII})$ | $\text{Cu}_0(\text{SI}')$  | $\text{Cu}_0(\text{SI}')$<br>$\text{Cu}_{\text{II}}(\text{SII})^b$ |

<sup>a</sup>The copper species are  $\text{Cu}_{\text{III}}=\text{Cu}^{2+}(\text{O}_2)_3(\text{H}_2\text{O})_3$ ,  $\text{Cu}_{\text{II}}=\text{Cu}^{2+}(\text{O}_2)_3(\text{H}_2\text{O})_2$ ,  $\text{Cu}_{\text{II}}'=\text{Cu}^{2+}(\text{O}_2)_3(\text{OH})_2$ ,  $\text{Cu}_{\text{I}}=\text{Cu}^{2+}(\text{O}_2)_3(\text{H}_2\text{O})$ ,  $\text{Cu}_0=\text{Cu}^{2+}(\text{O}_2)_3$ ,  $\text{Cu}_0'=\text{Cu}^{2+}(\text{O}_2)_6$ . The zeolite sites are defined in the text.

<sup>b</sup>Minor species

In freshly prepared, hydrated  $\text{Na}_{12}\text{-A}$  only  $\text{Cu}_{\text{III}}$  is observed which is located at  $\text{S2}^*$  sites above a hexagonal window in the  $\alpha$ -cage. This species is very sensitive to partial dehydration even at room temperature and a major portion of it readily converts into the trigonal bipyramidal  $\text{Cu}_{\text{II}}$  in site  $\text{S2}$  with one water in the  $\alpha$ -cage and one water in the  $\beta$ -cage. This is why Ichikawa and Kevan originally reported the formation of  $\text{Cu}_{\text{II}}$  in hydrated  $\text{Na}_{12}\text{-A}$  (28). Figure 4 shows a comparison of the electron spin echo deuterium modulation of  $\text{Cu}_{\text{III}}$  versus that for  $\text{Cu}_{\text{II}}$ . Another interesting feature is that rehydration of  $\text{Cu}_{\text{II}}$  and  $\text{Cu}_{\text{III}}$  at room temperature or slightly above does not restore  $\text{Cu}_{\text{III}}$  as the sole copper species. All of the coordinated water can be removed by dehydration under vacuum at  $400^\circ\text{C}$  for several hours. After this treatment all the copper is converted to a trigonal  $\text{Cu}_0$  species located at site  $\text{S2}'$  in the  $\beta$ -cage. Rehydration of  $\text{Cu}_0$  at room temperature does restore  $\text{Cu}_{\text{II}}$  as the sole copper species in the zeolite.

In contrast to the results for  $\text{Cu}^{2+}$  in  $\text{Na}_{12}\text{-A}$ , the major copper species in freshly prepared, hydrated  $\text{K}_{12}\text{-A}$  is tetrahedrally coordinated  $\text{Cu}_{\text{I}}$  coordinating to only one water molecule (31).  $\text{Cu}_{\text{I}}$  is located in site  $\text{S2}'$  in the  $\beta$ -cage. A small fraction of

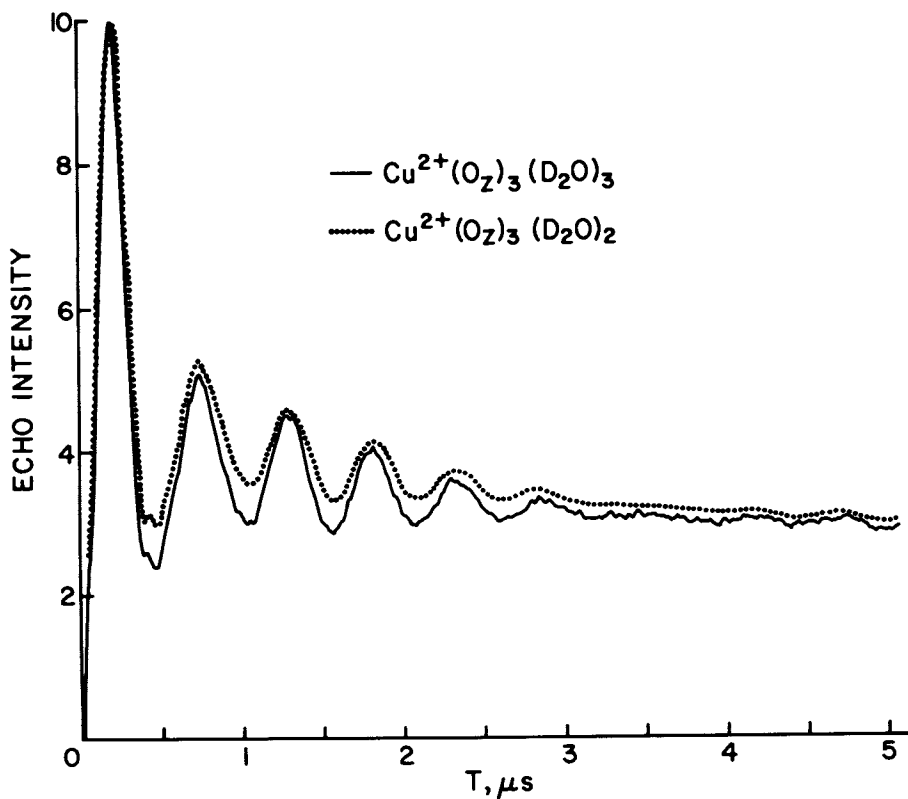


Figure 4.

Experimental three pulse electron spin echo spectra of two types of  $\text{Cu}^{2+}$  in  $\text{Na}_{12}\text{-A}$  zeolite.  $\text{Cu}^{2+}(\text{O}_2)_3(\text{D}_2\text{O})_3$  is the dominant copper species in site S2\* in freshly prepared, hydrated  $\text{Na}_{12}\text{-A}$  and  $\text{Cu}^{2+}(\text{O}_2)_3(\text{D}_2\text{O})_2$  in site S2 is the dominant species after partial dehydration under vacuum at room temperature. The different deuterium modulation depths characterize the different numbers of coordinated waters in these two  $\text{Cu}^{2+}$  species.

cupric ion is present as  $\text{Cu}_{\text{III}}$  but it can be converted completely into  $\text{Cu}_{\text{I}}$  by dehydration at 30–60° C followed by rehydration at room temperature. Partial dehydration at 30–60° C converts all of  $\text{Cu}_{\text{I}}$  and some  $\text{Cu}_{\text{III}}$  to  $\text{Cu}_{\text{II}}$ . Note that  $\text{Cu}_{\text{I}}$  can be converted to  $\text{Cu}_{\text{II}}$  by 'dehydration' because there is still considerable water in the zeolite at this temperature. Dehydration at 200 to 400° C converts all copper species to  $\text{Cu}_0$ . Subsequent rehydration at room temperature forms  $\text{Cu}_{\text{III}}$  as the dominant copper species while  $\text{Cu}_{\text{I}}$  is not formed. Thus, while  $\text{Cu}_{\text{I}}$  is dominant in freshly prepared, hydrated  $\text{K}_{12}\text{-A}$  it is not reformed after complete dehydration and subsequent hydration. This is an interesting anomaly not observed in other zeolites and experiments to better understand it are in progress.

The results in  $\text{Cs}_7\text{Na}_5\text{-A}$  and  $(\text{NH}_4)_{12}\text{-A}$  are basically similar to those for  $\text{K}_{12}\text{-A}$ . In freshly prepared, hydrated  $\text{Cs}_7\text{Na}_5\text{-A}$  only  $\text{Cu}_{\text{I}}$  is observed (30). Partial dehydration at 50–100° C gives a weak signal of  $\text{Cu}_{\text{II}}$  and mainly  $\text{Cu}_0$ . Complete dehydration to give  $\text{Cu}_0$  is readily achieved at 400° C and subsequent rehydration at room temperature reforms  $\text{Cu}_{\text{I}}$  as expected. Note the contrast here with the anomalous rehydration result in  $\text{K}_{12}\text{-A}$ . In hydrated  $(\text{NH}_4)_{12}\text{-A}$   $\text{Cu}_{\text{I}}$  is predominant with sometimes a little  $\text{Cu}_{\text{II}}$ . Partial dehydration at 50° C converts  $\text{Cu}_{\text{I}}$  to  $\text{Cu}_{\text{II}}$  as found in  $\text{K}_{12}\text{-A}$  and rehydration at room temperature restores  $\text{Cu}_{\text{I}}$ . Dehydration at higher temperatures than 100° C cannot be done because it results in the irreversible decomposition of this zeolite.

The main factor that seems to determine whether  $\text{Cu}_{\text{III}}$  or  $\text{Cu}_{\text{I}}$  is initially formed in the hydrated A-zeolites is the bulkiness of the major cocation. X-ray diffraction studies show that eight  $\text{Na}^+$  associated with the hexagonal windows of an  $\alpha$ -cage in  $\text{Na}_{12}\text{-A}$  project into the  $\alpha$ -cage by 0.05 nm (32) while in  $\text{K}_{12}\text{-A}$  the similar  $\text{K}^+$  project 0.15 nm into the  $\alpha$ -cage (33). In addition, the ionic radius of  $\text{K}^+$  (0.133 nm) is significantly larger than that of  $\text{Na}^+$  (0.099 nm). Thus, the  $\alpha$ -cage is more crowded in  $\text{K}_{12}\text{-A}$  than in  $\text{Na}_{12}\text{-A}$  and thus must cause the electrostatic and steric repulsion of  $\text{Cu}_{\text{III}}$  to be so great that the cupric ion moves into the  $\beta$ -cage and changes its water coordination accordingly. Similar arguments can be made for  $\text{Cs}_7\text{Na}_5\text{-A}$  and  $(\text{NH}_4)_{12}\text{-A}$  where x-ray studies also indicate  $\alpha$ -cage crowding (34,35). On partial dehydration in all these zeolites the monovalent ions move closer to the S2 sites in the hexagonal windows. This decreases the repulsion from the  $\alpha$ -cage in the  $\text{K}^+$ ,  $\text{Cs}^+$  and  $\text{NH}_4^+$  A-zeolites and allows  $\text{Cu}_{\text{I}}$  in site S2' in the  $\beta$ -cage to move to site S2 and adopt the trigonal bipyramidal geometry of  $\text{Cu}_{\text{II}}$  coordinating to one water in the  $\beta$ -cage and to an additional water in the  $\alpha$ -cage. In  $\text{Na}_{12}\text{-A}$  where  $\text{Cu}^{2+}$  is originally in site S2\* as  $\text{Cu}_{\text{III}}$  partial dehydration destroys this coordination possibility so  $\text{Cu}_{\text{III}}$  converts to  $\text{Cu}_{\text{II}}$ ; in this zeolite partial dehydration rather than  $\alpha$ -cage crowding appears to be the driving force for the  $\text{Cu}_{\text{III}}$  in S2\* to  $\text{Cu}_{\text{II}}$  in S2 conversion.

Cu<sup>2+</sup> in X-Zeolites

Our studies of Cu<sup>2+</sup> in X-zeolites are, as yet, less complete than in A-zeolites. However, a striking difference in site locations and water coordination between Na-X and K-X has been found (36). This appears to be primarily an effect of hydration energy instead of major cocation site location.

In hydrated Na-X exchanged with D<sub>2</sub>O only very weak deuterium modulation is seen which is consistent with one water molecule with a Cu<sup>2+</sup>-D(D<sub>2</sub>O) distance of 0.37 nm. This is 0.11 nm longer than for water directly coordinated to Cu<sup>2+</sup>. Thus it appears that a Cu<sub>0</sub> species is formed which is most logically associated with the hexagonal prism sites I and I' in X-zeolites. In site I (see Figure 2) Cu<sup>2+</sup> would be coordinated to six adjacent oxygens with approximately octahedral symmetry and should be given a new designation, Cu<sub>0</sub>'. At this point it is difficult to distinguish between trigonal (site SI') and octahedral (site SI) sites. Based on changes in the aluminum modulation on dehydration we tentatively assign Cu<sup>2+</sup> in hydrated Na-X to SI. Partial dehydration at 50° C has little effect but strong dehydration at 400° C changes the aluminum modulation consistent with Cu<sup>2+</sup> being closer to a hexagonal ring which we tentatively assign as SI' with trigonal coordination. Rehydration produces the original formed species assigned to SI.

In contrast, the major Cu<sup>2+</sup> species in hydrated K-X is clearly coordinated to three waters and can be assigned as Cu<sub>III</sub> in site SII\*. Partial dehydration at 30-60° C converts Cu<sub>III</sub> to the trigonal bipyramidal complex, Cu<sub>II</sub>. Rehydration at room temperature converts most of the Cu<sub>II</sub> to Cu<sub>III</sub> but traces of the former are still present. Cu<sub>III</sub> becomes the sole copper species on dehydration at 400° C and rehydration at room temperature. Complete dehydration at 400° C gives the same species as formed in Na-X which is assigned to Cu<sub>0</sub> in site SI'.

The major difference in Cu<sup>2+</sup> site locations in hydrated Na-X and K-X can be attributed to hydration energy differences and the ease with which the β-cage cations can be replaced by Cu<sup>2+</sup>. Let's assume that the Cu<sup>2+</sup> is initially located in SII\*. The migration of Cu<sup>2+</sup> from SII\* to SI requires the displacement of an alkali cation from SI (21,22). Since the hexagonal prism offers the same electrostatic field to both Na<sup>+</sup> and K<sup>+</sup>, the energy for removing an unhydrated alkali cation is the same for Na<sup>+</sup> and K<sup>+</sup>. However, the net energy gain for transferring an unhydrated alkali cation from SI to a more exposed site, where it will be hydrated, is greater for Na<sup>+</sup> because it has a larger hydration energy. So it is energetically more favorable for Cu<sup>2+</sup> to displace Na<sup>+</sup> from SI than to displace K<sup>+</sup>.

Only one divalent ion exchanged X-zeolite has been studied in detail thus far, namely Ca-X. It shows a surprise in that Cu<sup>2+</sup> is found to form a completely new species identified as Cu(O<sub>2</sub>)<sub>3</sub>(OH)<sub>2</sub> trigonal bipyramidal complex designated Cu<sub>II</sub>' (37). Its ESR spectra indicate trigonal bipyramidal symmetry and are distinctly different from those of Cu<sub>II</sub> in both resolution and dependence on the



dehydration temperature. The electron spin echo modulation indicates two protons close enough to be in the first coordination shell. Since the ESR spectrum indicates trigonal bipyramidal symmetry the two protons are assigned to two hydroxyl groups rather than to one water. The  $\text{Cu}_{\text{II}}$  species, unlike  $\text{Cu}_{\text{II}}$ , is extremely stable and shows no noticeable changes in the ESR as the sample is dehydrated up to  $120^{\circ}\text{C}$ . Above this temperature the resolution of the hyperfine components slowly decreases along with the intensity, presumably due to auto reduction of  $\text{Cu}^{2+}$  or  $\text{Cu}^0$ . In samples dehydrated at  $30\text{--}200^{\circ}\text{C}$ ,  $\text{Cu}_{\text{II}}$  can be completely restored as the sole  $\text{Cu}^{2+}$  species on rehydration at room temperature. If the dehydration temperature is  $200\text{--}400^{\circ}\text{C}$ , oxidation is necessary to regenerate  $\text{Cu}^{2+}$  and rehydration of such oxidized samples restores only a part of the original  $\text{Cu}_{\text{II}}$ . The rest of it is either in the reduced state or exists as  $\text{Cu}_0$  in the  $\beta$ -cage sites SI' and SII'. This unique copper species is not observed in several other divalent ion exchanged zeolites we have examined with the exception of Cd-X.

#### Acknowledgments

We thank the National Science Foundation and the Robert A. Welch Foundation for support of this work.

#### Literature Cited

1. Barrer, R.M. "Zeolites and Clay Minerals", Academic Press; New York, 1978.
2. Mochida, I.; Mayata, S; Kato, A. J. Catal. 1970, 19, 405.
3. Maxwell, I.E.; Downing, R.S.; Von Lauger, S.A.J. J. Catal. 1980, 61, 485.
4. Giordane, N.; Bart, J.C.J.; Maggiure, R. Z. Phys. Chem. 1981, 124, 97.
5. Tikhomirova, N.N.; Nikolaeva, I.V. Zh. Strukt. Khim. 1969, 10, 547.
6. Seff, K. Acct. Chem. Res. 1976, 9, 121.
7. Kevan, L. J. Phys. Chem. 1981, 85, 1628.
8. Morrison, T.I.; Shenoy, G.K.; Iton, L.E.; Stucky, G.D.; Suib, S.L. J. Chem. Phys. 1982, 76, 5665.
9. Kevan, L. in "Time Domain Electron Spin Resonance", Kevan, L; Schwartz, R.N., Eds.; Wiley-Interscience: New York, 1978; Chapter 8.
10. (a) Narayana, P.A.; Kevan, L. J. Magn. Res. 1982, 46, 84; (b) Ichikawa, T.; Kevan, L.; Bowman, M.K.; Dikanov, S.A.; Tsvetkov, Yu. D. J. Chem. Phys. 1979, 71, 1167; (c) Ichikawa, T.; Kevan, L. J. Phys. Chem. 1980, 84, 1955; (d) Narayana, M.; Kevan, L. J. Am. Chem. Soc. 1981, 103, 1618.
11. Narayana, M.; Kevan, L. J. Chem. Phys. 1982, 76, 3999.
12. Vance, T.B.; Seff, K. J. Phys. Chem. 1975, 79, 2163.
13. Nitta, M.; Ogawa, K.; Aomura, K. Bull. Chem. Soc. Japan 1975, 48, 1939.

14. Kim, Y.; Seff, K. J. Phys. Chem. 1978, 82, 1071.
15. Aldridge, C.P.; Pope, C.G. J. Inorg. Nucl. Chem. 1976, 36, 2097.
16. Maes, A.; Gremers, A. J. Chem. Soc. Faraday Trans. I 1978, 74, 136.
17. Leith, I.R.; Leach, H.F. Proc. Roy. Soc. Lond. 1972, A330, 247.
18. Conesa, J.C.; Soria, J. J. Chem. Soc. Faraday Trans. I 1978, 74, 406.
19. Conesa, J.C.; Soria, J. J. Chem. Soc. Faraday Trans. I 1978, 74, 423.
20. Conesa, J.C.; Soria, J. J. Phys. Chem. 1978, 82, 1575.
21. Conesa, J.C.; Soria, J. J. Phys. Chem. 1978, 82, 1847.
22. Conesa, J.C.; Soria, J. J. Magn. Reson. 1979, 33, 295.
23. Horser, H.; Primet, M; Vedrine, J.C. J. Chem. Soc. Faraday Trans. I 1978, 74, 335.
24. Iton, L.E.; Turkevich, J. J. Phys. Chem. 1977, 81, 435.
25. Kasai, P.H.; Bishop, R.J. J. Phys. Chem. 1978, 82, 279.
26. Herman, R.G. Inorg. Chem. 1980, 18, 995.
27. Lee, H.S.; Seff, K. J. Phys. Chem. 1981, 85, 397.
28. Ichikawa, T; Kevan, L. J. Chem. Soc. Faraday Trans. I 1981, 77, 2567.
29. Ichikawa, R.; Kevan, L. J. Am. Chem. Soc. 1981, 103, 5355.
30. Narayana, M.; Kevan, L. J. Chem. Phys. 1981, 75, 3269.
31. Narayana, M.; Kevan, L. J. Phys. C 1982, 00, 0000.
32. Pluth, J.J.; Smith, J.V. J. Am. Chem. Soc. 1980, 102, 4704.
33. Pluth, J.J.; Smith, J.V. J. Phys. Chem. 1979, 83, 741.
34. Firor, R.L.; Seff, K. J. Am. Chem. Soc. 1977, 99, 6249.
35. McCusker, L.B.; Seff, K. J. Am. Chem. Soc. 1981, 103, 3441.
36. Ichikawa, T.; Kevan, L. J. Am. Chem. Soc. 1982, 104, 0000.
37. Narayana, M.; Kevan, L. J. Chem. Phys. 1982, 78, 0000.

RECEIVED December 16, 1982

## Mössbauer Studies of Iron-Containing Zeolites

STEVEN L. SUIB, KERRY C. McMAHON, and DIMITRIOS PSARAS

University of Connecticut, Department of Chemistry, Institute of Materials Science,  
Storrs, CT 06268

The following paper reviews recent results in the field of Mössbauer studies of iron-containing zeolites, bimetallic iron-containing zeolites and some Fischer-Tropsch zeolite catalysts. Coordination complexes of iron, superparamagnetism, ion-exchanged zeolites and the reduction of iron-containing zeolites will all be discussed. Some preliminary results concerning the synthesis of coordination complexes of iron, organometallic compounds and bimetallic systems in zeolites are then presented. Structural properties and particle size of these systems as probed by X-ray diffraction and electron microscopy results have also been determined. Changes in these catalysts due to their interactions with controlled gas environments of 10% CO/H<sub>2</sub> are determined by Mössbauer spectroscopy using an in-situ pretreatment cell. The catalytic activity is continuously monitored by a gas chromatograph interfaced to the Mössbauer cell. The surface, structural, electronic and catalytic properties of these iron-containing zeolites will be discussed in relation to the changes in oxidation state of the iron species. These iron-containing zeolites are activated thermally, photochemically and chemically. The influence of the support, reaction temperature and sample pretreatment will also be discussed. In particular, this report outlines the use of photoactivation of Fe(CO)<sub>5</sub> in several zeolites for the isomerization of olefins. The shape selectivity of the zeolite controls the activity and selectivity of these systems. In the case of zeolite ZSM-5 the conversion of 1-pentene to trans 2-pentene is 100% selective showing that photoactivation of zeolites can remarkably affect the product distribution.

0097-6156/83/0218-0301\$06.00/0  
© 1983 American Chemical Society

Some of the first Mössbauer studies of zeolites that contained iron dealt with the ion-exchange of both ferric and ferrous ions into several different zeolites. From these studies much valuable information about the site location and the redox behavior of the iron ions was obtained. One of the earliest studies was that of Rees (1). Zeolites X, Y, mordenite, and clinoptilolite were investigated. Valency changes during dehydration of these materials and during rehydration were reported. Delgass, Garten and Boudart reported the Mössbauer absorption data for ferrous ions in Y zeolite (2) and concluded that the ferrous ions are solvated in the pores of the zeolite. The use of a nitrogen atmosphere, degassed solutions and pH adjustment of 4.0 were all important parameters in the synthesis of crystalline materials. Dehydration and rehydration phenomena were also reported. Further studies by the same researchers (3,4) dealt with the adsorption of several small molecules ( $\text{CO}$ ,  $\text{O}_2$ ,  $\text{N}_2$ ), bases (pyridine,  $\text{NH}_3$ ) and alcohols. These studies were important because they demonstrated that Mössbauer spectroscopy could be used as a diagnostic tool in the study of adsorption.

As time moved on, the Mössbauer studies of iron-containing zeolites started to involve different aspects of zeolite chemistry, most notably in the area of catalysis. In addition, other new preparations were revealed as well as experiments that were designed to obtain superparamagnetic iron oxide particles in zeolites. Garten, Gallard-Nechschein and Boudart (5) studied iron mordenites in the reverse of the water-gas shift reaction and the ammoxidation of propylene. Collins and Mulay (6) reported that  $\text{Fe}(\text{CO})_5$  and  $\text{FeCl}_3$  when thermally treated in air would form fine particles of  $\text{Fe}_2\text{O}_3$ .

Of particular interest to our research is the preparation of reduced iron species in zeolites. Several researchers (1, 7-10) have used different procedures to try to obtain reduced iron(0) species in zeolites. Kumer, et. al. (7) observed an Fe(0) line in the Mössbauer spectrum which appeared after dehydration of zeolite A. Huang and Anderson (8) have reported that bulk iron oxides could be reduced by hydrogen to metallic iron. They also present thermodynamic evidence that ferrous ions would be much more difficult to reduce. Gunser, Adolph and Schmidt (9) reported the reduction of ferrous ions in zeolite 4A by sodium vapor and conclude from magnetic susceptibility and Mössbauer experiments that superparamagnetic iron particles are formed. Lee (10) also used sodium vapor to reduce ferrous ions to  $\alpha\text{-Fe}$  and with electron microscopy learned that these particles were highly dispersed, on the order of 3.5 nm. Lee also attempted to reduce the ferrous ions with sodium borohydride. In this case, however, leaching

of the iron from the zeolite occurred. Rao and coworkers (11) have introduced iron ions into zeolite ZSM-5 via ion-exchange and  $\text{Fe}_3(\text{CO})_{12}$  impregnation, and have then reduced these catalysts at elevated temperature in hydrogen. These catalysts have been used in Fischer-Tropsch studies.

Other recent reports of the use of Mössbauer in the characterization of iron-containing zeolites involve the study of coordination complexes synthesized in zeolites. One such study carried out by Lunsford and coworkers (12) involved the study of tris(2,2' bipyridine) iron(II) complexes in zeolite Y. These materials were reacted with chlorine gas in order to oxidize the iron. Another study done by Banerjee (13) involved the Mössbauer analysis of iron(II)phenanthroline complexes sorbed on zeolite 3A. These are most of the Mössbauer studies of iron-containing zeolites that we have found, although some earlier work has not been included since reviews (14) are available.

### The Present Study

The research reported here is very much related to all of the above studies. Our goals are to develop new preparations of iron-containing zeolites, to stabilize iron in a highly dispersed and metallic state, and to explore the photochemical and thermal activation of these materials. Of major interest to us are the reports of Derouane and coworkers (15), Ballivet-Tkatchenko and Coudurier (16), Good (17), and Scherzer and Fort (18).

Photochemical activation (15) and thermal activation (11,16, 17) of iron carbonyl complexes in various zeolites have been reported. Part of our study is to use Mössbauer spectroscopy to investigate the behavior of  $\text{Fe}(\text{CO})_5$  on several zeolites when activated photochemically and thermally. Another part of our study is to investigate the novel preparation method of Scherzer and Fort (18) that introduces iron into (in their study) zeolite  $\text{NH}_4\text{Y}$  as an anionic complex. Finally, we will report the preparation of ferrocene sublimed onto zeolite ZSM-5. The photochemical and thermal activation of these systems will be reported as well as preliminary results of the photochemical isomerization of olefins by  $\text{Fe}(\text{CO})_5$  zeolites and the thermal activation of Fischer-Tropsch catalytic systems. It also should be noted here that our Mössbauer studies involve an in-situ pretreatment cell which can be heated to 500°C under various gaseous atmospheres.

### Experimental Procedure

Both  $\text{Fe}(\text{CO})_5$  and  $(\text{C}_5\text{H}_5)_2\text{Fe}$  were introduced into several zeolites by sublimation techniques employing a vacuum line. The zeolite and either of the two above-mentioned iron compounds were introduced into two separate ends of an inverted U-tube which was connected to a vacuum line. The iron compounds were frozen with

liquid nitrogen and the rest of the tube was evacuated to approximately  $1 \times 10^{-5}$  Torr. The tube was then isolated from the vacuum manifold and the liquid nitrogen was transferred from the iron complex to the zeolite and the transfer took place. The ferrocene was vacuum sublimed three times before use and the iron pentacarbonyl was kept cool during storage and initial synthesis conditions.

The mixed metal zeolites were prepared according to the procedure of Scherzer and Fort (18). There were, however, several additional preparations similar to those of Scherzer and Fort that we developed. First of all, ruthenium was introduced into zeolite Y and ZSM-5 as the cationic amine complex as reported by Jacobs and Uytterhoeven (19). Ruthenium was also added to the zeolite in an anionic complex form, either  $K_3Ru(CN)_6$  or  $K_2Ru(CN)_5NO$ . For these anionic preparations, either copper, zinc or cobalt exchanged zeolites Y or ZSM-5 were used.

The  $Fe(CO)_5$ ,  $(C_5H_5)_2Fe$  and mixed metal zeolites were reduced in hydrogen in our in-situ Mössbauer cell between temperatures of 300°C and 500°C for various times, 4 hours to 25 hours, depending on the form of iron introduced into the zeolites and depending on the particular zeolite.

The Mössbauer transmission spectra were recorded in the constant acceleration mode with an Elscint Mössbauer drive unit and a model MFG 3A Elscint function generator, an MVT-3 linear velocity transducer and an MD-3 transducer driving unit.  $\gamma$ -ray detection was done with a Reuter-Stokes Kv-CH4 proportional counter driven by an Ortec 401A/456 high voltage power supply. Voltage pulses were introduced into an Ortec 142 PC preamplifier and an Ortec 571 spectroscopy amplifier. Data were collected on a Tracor-Northern NS-701A multichannel analyzer. The data were later analyzed on an IBM 360/370 computer.

A Mössbauer transmission cell similar to that prepared by Delgass and coworkers (20) was used for all Mössbauer experiments. Zeolite pellets between 200 mg and 300 mg were used as samples. The cell was connected to thermal conductivity and flame ionization detectors so that products of the reactions in the Mössbauer cell could be analyzed. The Mössbauer data were collected in the flyback mode and deviations from a nonlinear background were corrected for by fitting the background to a parabola and subtracting out this effect. Computer fitting of all the iron Mössbauer data to Lorentzian lines was carried out with a modified version of a previous reported program (24). Attempts to fit the data to Gaussian lines were unsuccessful. The source used was an 85 mCi  $^{57}Co/Pd$  New England Nuclear source. All spectra are referenced with respect to iron foil.

X-ray powder diffraction data of the zeolite samples were collected before and after the catalytic reactions with a Diano-XRD 8000 X-ray powder diffraction apparatus. Electron paramagnetic resonance samples were sealed off in quartz tubes on a vacuum line after various treatments and analyzed with a Varian E-3 spectrometer at room temperature.

Transmission electron microscope samples were prepared by dispersing the zeolites into methanol in a vial. The vial was placed in an ultrasonic bath. After ultrasonic vibration, one drop was placed on carbon coated 300 mesh copper grids. A model HU200 Hitachi transmission electron microscope was used to analyze the samples.

Bulk photolyses were carried out using a Kratos 1000-W, variable power, high pressure, Xe lamp. This radiation was filtered first with a  $\text{CuSO}_4 \cdot 5\text{H}_2\text{O}$  aqueous solution and then an ultraviolet bandpass filter with maximum transmittance at 345 nm. For purposes of calibration and evaluation of power, 20 mW of power at 345 nm is produced at the sample surface of the test tube cell. This corresponds to  $3.4 \times 10^{15}$  photons/second. Iron carbonyl zeolite samples were loaded into ampoules with a magnetic stir bar and freeze-pump-thaw degassed three times before sealing off the pyrex tube. Sample tubes were opened just before the chromatographic analysis.

Gas chromatographic analyses were performed on a Hewlett Packard Model 5880 system equipped with a thermal conductivity detector with an injector temperature of 200°C, detector temperature of 250°C and an oven temperature of 35°C. All runs were isothermal. The columns used for the separation were 20 foot  $\text{AgNO}_3$ -ethylene glycol columns. Absolute retention times were 1.15 min (trans 2-pentene), 4.65 min (1-pentene), and 5.81 min (cis 2-pentene). Methods of automatic peak integration that were used during the analyses were peak height, peak area, area %, and internal standard experiments.

## Results

The results of the Mössbauer studies of ferrocene on zeolite ZSM-5 are shown in Figure 1. This spectrum shows a quadrupole split doublet and a broad non-quadrupole split singlet with an isomer shift of 0.53 mm/sec. It is also noted here that this material has a blue color which is quite different from the orange color of the ferrocene. On reduction of this material in hydrogen for 5 hours, a weak 6-line resonance occurs along with a central doublet as shown in Figure 2. It is noted here that the quadrupole splitting of this doublet has significantly changed from that shown in Figure 1.

The Mössbauer spectra for  $\text{Fe}(\text{CO})_5$  on zeolites A, X, Y, mordenite ( $\text{Na}^+$  and  $\text{H}^+$ ), and ZSM-5( $\text{Na}^+$ ) are all very similar with a quadrupole split doublet appearing at an isomer shift of 0.40 mm/sec. The  $\text{H}^+$  form of ZSM-5, however, shows a broad singlet centered at 0.40 mm/second. The quadrupole splitting for each of the iron carbonyl samples is between 0.8 mm/second and 1 mm/second.

The Mössbauer spectra for the mixed metal Scherzer-Fort type of preparation (18) are, on the other hand, quite different de-

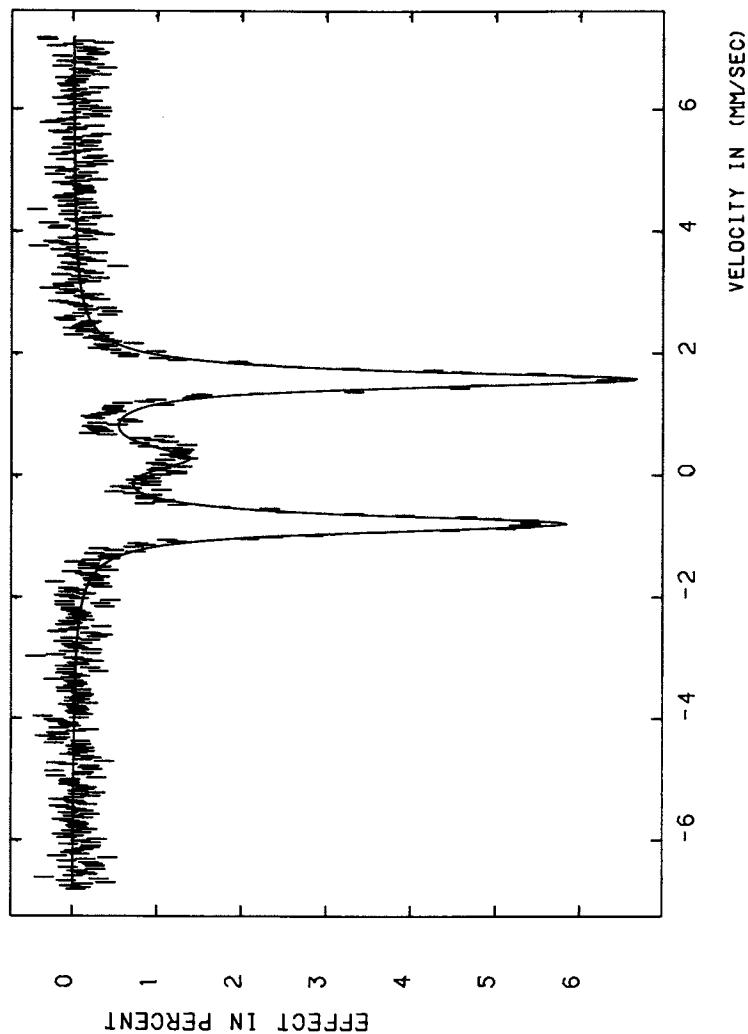


Figure 1. Mössbauer Spectrum of Ferrocene/ZSM-5.



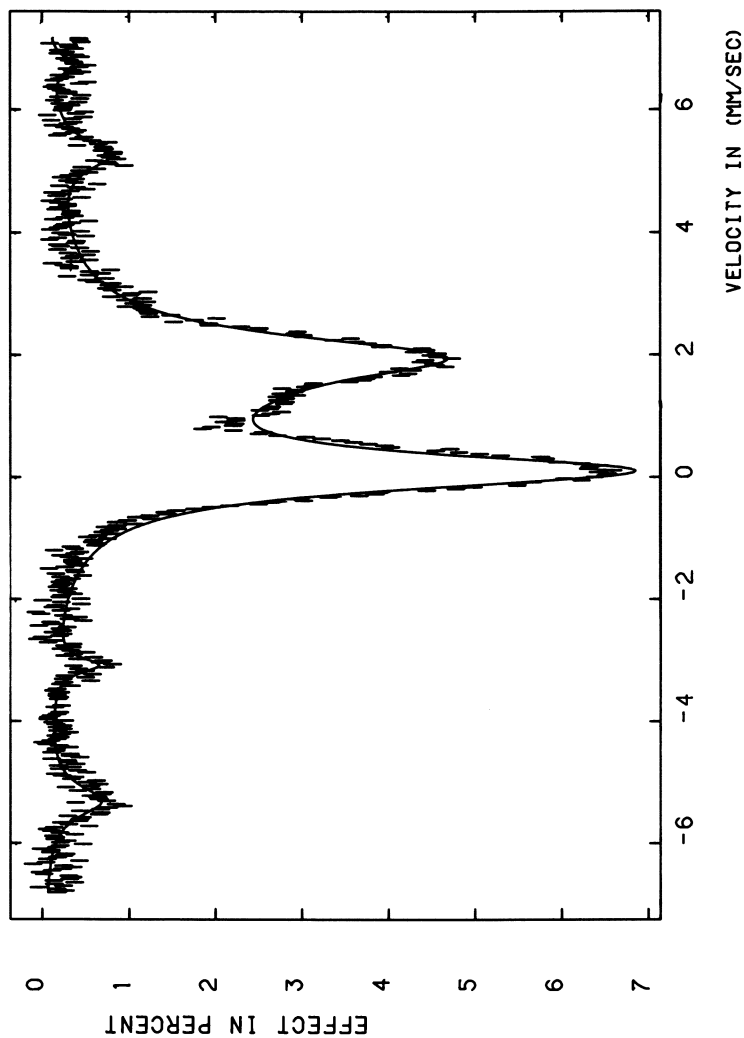


Figure 2. Mössbauer Spectrum of Reduced Ferrocene/ZSM-5.

pending on the nature of the cation in the zeolite, the particular zeolite, and the anionic form of the iron introduced into the zeolite. The data for these mixed metal zeolite systems are given in Tables I and II. Table I includes data for the unreduced samples. Table II incorporates data for these samples after reduction. Only the signals for the anionic iron species are included for clarity. Samples 9, 10, 18 also show a component in their Mössbauer spectra indicative of iron(II). Typical activation temperatures range from 300 to 400°C and the reduction in hydrogen is usually complete after 4 hours. The preparations developed in our laboratory are for samples 16 through 22. We note here that we have extended this method to include other zeolites (ZSM-5), other cations ( $\text{Ru}^{3+}$ ,  $\text{Pd}^{2+}$ ,  $\text{Pt}^{2+}$ ), and other anionic complexes ( $\text{K}_2\text{Ru}(\text{CN})_6$ ,  $\text{K}_2\text{Ru}(\text{CN})_5\text{NO}$ ).

Figure 3 shows a typical spectrum of the unreduced nitroprusside samples where iron is introduced only as the anionic  $\text{Na}_2\text{Fe}(\text{CN})_5\text{NO}$  complex. Zinc has been cation exchanged into  $\text{NH}_4\text{Y}$  before addition of the anionic complex. Figure 4 shows an example of samples similar to the zinc nitroprusside Y zeolite, shown in Figure 3, that are completely reduced to metallic iron by hydrogen.

The results of the photochemical isomerization of olefins by  $\text{Fe}(\text{CO})_5$  in zeolites X, ZSM-5, and mordenite are given in Table III. The conditions of lamp power, hours of illumination, and the results concerning the % conversion of 1-pentene to cis and trans-2-pentene are included. The thermodynamic ratio expected for trans to cis 2-pentene on photolysis of 1-pentene is about 3 to 1.

The X-ray powder diffraction data reveal that for the  $\text{Fe}(\text{CO})_5$  and the Scherzer-Fort preparations that bulk  $\alpha\text{-Fe}$  is present. Electron paramagnetic resonance experiments indicate in all cases that ferromagnetic iron is present in these reduced samples. The X-ray data also reveal that these samples are crystalline after each of these synthetic procedures and that crystallinity is not lost when these samples are photolyzed or thermally treated.

The details concerning the transient method which has been used to characterize Fischer-Tropsch reactions can be found elsewhere (21).

## Discussion

The ferrocene-exchanged ZSM-5 zeolite shows a Mössbauer spectrum that when analyzed gives a 40% ferrocinium ion signal with an isomer shift of 0.53 mm/second. It is likely that water in the zeolite is being reduced as the ferrocene is oxidized. Reduction of this sample in hydrogen causes a complete loss of both the ferrocinium ion and the ferrocene Mössbauer features and a new appearance of alpha iron(0) metal and a new quadrupole split doublet of 0.4 mm/second and a quadrupole splitting of

Table I  
MIXED METAL SYSTEMS, UNREDUCED

| Sample # | Cation           | Anion   | Zeolite           | $\delta$ , (mm/sec) | $\Delta E_Q$ , mm/sec |
|----------|------------------|---|-------------------|---------------------|-----------------------|
| 9        | Fe <sup>2+</sup> | K <sub>4</sub> Fe(CN) <sub>6</sub>                  | NH <sub>4</sub> Y | -0.1                | 2.45                  |
| 10       | Fe <sup>2+</sup> | (NH <sub>4</sub> ) <sub>4</sub> Fe(CN) <sub>6</sub> | NH <sub>4</sub> Y | -0.05               | -                     |
| 11       | Co <sup>2+</sup> | K <sub>3</sub> Fe(CN) <sub>6</sub>                  | NH <sub>4</sub> Y | 0.0                 | -                     |
| 12       | Co <sup>2+</sup> | (NH <sub>4</sub> ) <sub>4</sub> Fe(CN) <sub>6</sub> | NH <sub>4</sub> Y | -0.05               | -                     |
| 13       | Ni <sup>2+</sup> | (NH <sub>4</sub> ) <sub>4</sub> Fe(CN) <sub>6</sub> | NH <sub>4</sub> Y | -0.05               | -                     |
| 14       | Cu <sup>2+</sup> | Na <sub>2</sub> Fe(CN) <sub>5</sub> NO              | NH <sub>4</sub> Y | -0.20               | 1.8                   |
| 15       | Zn <sup>2+</sup> | Na <sub>2</sub> Fe(CN) <sub>5</sub> NO              | NH <sub>4</sub> Y | -0.20               | 1.8                   |
| 16       | Cu <sup>2+</sup> | Na <sub>2</sub> Fe(CN) <sub>5</sub> NO              | ZSM-5             | -0.15               | 1.5                   |
| 17       | Cu <sup>2+</sup> | Na <sub>2</sub> Fe(CN) <sub>5</sub> NO              | ZSM-5             | -0.20               | 1.6                   |
| 18       | Fe <sup>2+</sup> | Na <sub>2</sub> Fe(CN) <sub>5</sub> NO              | NH <sub>4</sub> Y | 0.0                 | 1.4                   |
| 19       | Co <sup>2+</sup> | Na <sub>2</sub> Fe(CN) <sub>5</sub> NO              | NH <sub>4</sub> Y | -0.20               | 1.9                   |
| 20       | Ni <sup>2+</sup> | Na <sub>2</sub> Fe(CN) <sub>5</sub> NO              | NH <sub>4</sub> Y | -0.20               | 1.8                   |
| 21       | Pd <sup>2+</sup> | Na <sub>2</sub> Fe(CN) <sub>5</sub> NO              | NH <sub>4</sub> Y | 0.35                | 0.7                   |
| 22       | Zn <sup>2+</sup> | K <sub>3</sub> Fe(CN) <sub>6</sub>                  | NH <sub>4</sub> Y | -0.10               | 0.7                   |

Table II  
MIXED METAL SYSTEMS, REDUCED

| Sample # | Cation           | Anion   | Zeolite           | $\delta$ , (mm/sec) | $H$ , (Koe) |
|----------|------------------|---|-------------------|---------------------|-------------|
| 9        | Fe <sup>2+</sup> | K <sub>4</sub> Fe(CN) <sub>6</sub>                  | NH <sub>4</sub> Y | -0.08               | 340.6       |
| 10       | Fe <sup>2+</sup> | (NH <sub>4</sub> ) <sub>4</sub> Fe(CN) <sub>6</sub> | NH <sub>4</sub> Y | -0.03               | 337.5       |
| 11       | Co <sup>2+</sup> | K <sub>3</sub> Fe(CN) <sub>6</sub>                  | NH <sub>4</sub> Y | -0.03               | 337.5       |
| 12       | Co <sup>2+</sup> | (NH <sub>4</sub> ) <sub>4</sub> Fe(CN) <sub>6</sub> | NH <sub>4</sub> Y | -0.09               | 336.5       |
| 13       | Ni <sup>2+</sup> | (NH <sub>4</sub> ) <sub>4</sub> Fe(CN) <sub>6</sub> | NH <sub>4</sub> Y | -0.05               | 331.3       |
| 14       | Cu <sup>2+</sup> | Na <sub>2</sub> Fe(CN) <sub>5</sub> NO              | NH <sub>4</sub> Y | -0.03               | 323.5       |
| 15       | Zn <sup>2+</sup> | Na <sub>2</sub> Fe(CN) <sub>5</sub> NO              | NH <sub>4</sub> Y | 0.03                | 320.4       |
| 16       | Cu <sup>2+</sup> | Na <sub>2</sub> Fe(CN) <sub>5</sub> NO              | ZSM-5(H)          | 0.00                | 318.9       |
| 17       | Cu <sup>2+</sup> | Na <sub>2</sub> Fe(CN) <sub>5</sub> NO              | ZSM-5(Na)         | 0.01                | 322.0       |
| 18       | Fe <sup>2+</sup> | Na <sub>2</sub> Fe(CN) <sub>5</sub> NO              | NH <sub>4</sub> Y | -0.01               | 322.0       |
| 19       | Co <sup>2+</sup> | Na <sub>2</sub> Fe(CN) <sub>5</sub> NO              | NH <sub>4</sub> Y | 0.00                | 331.3       |
| 20       | Ni <sup>2+</sup> | Na <sub>2</sub> Fe(CN) <sub>5</sub> NO              | NH <sub>4</sub> Y | -0.04               | 294.1       |
| 21       | Pd <sup>2+</sup> | Na <sub>2</sub> Fe(CN) <sub>5</sub> NO              | NH <sub>4</sub> Y | 0.03                | 312.7       |
| 22       | Zn <sup>2+</sup> | K <sub>3</sub> Fe(CN) <sub>6</sub>                  | NH <sub>4</sub> Y | -0.04               | 334.4       |

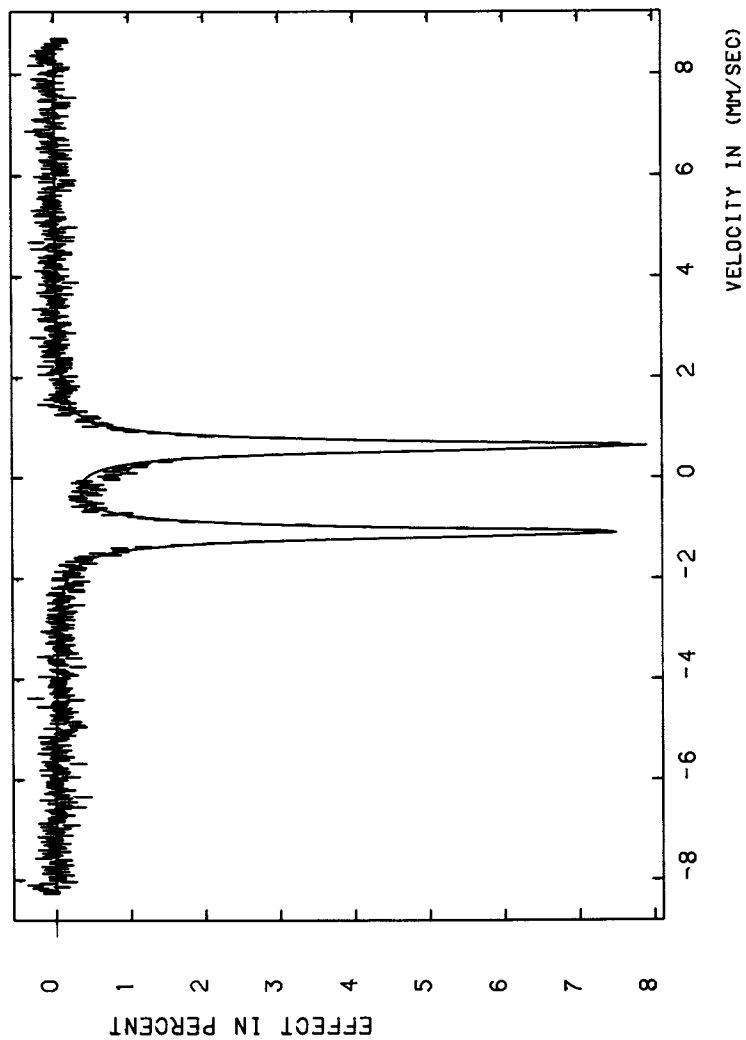


Figure 3. Mössbauer Spectrum of Zinc(II)Nitroprusside/ $\text{NH}_4\text{Y}$ .

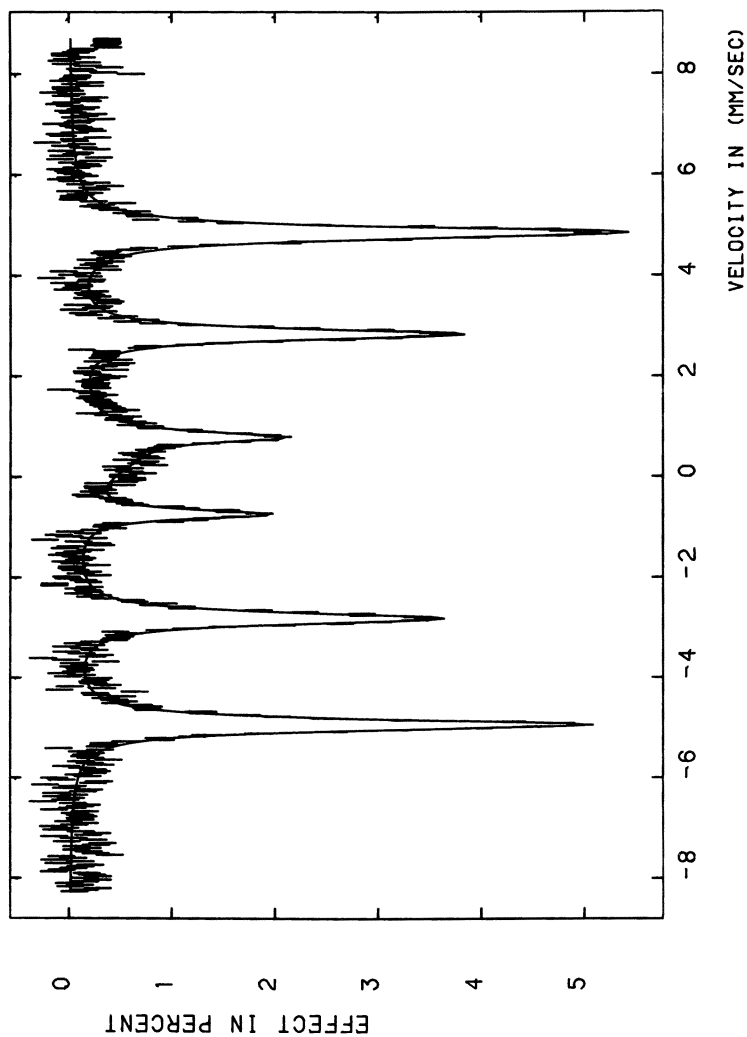


Figure 4. Mössbauer Spectrum of reduced Zinc(II)/Nitro-prusside/ $\text{NH}_4$ .

Table III  
Photoisomerization of 1-pentene

| <u>Zeolite<sup>a</sup></u> | <u>Lamp Power<sup>b</sup></u> | <u>Hrs. Illuminated</u> | <u>% Conversion<sup>c</sup></u> |
|----------------------------|-------------------------------|-------------------------|---------------------------------|
| NaX                        | 399                           | 1                       | 72%trans, 25%cis                |
| NaY                        | 399                           | 1                       | 74%trans, 15%cis                |
| NaZSM-5                    | 399                           | 1                       | 11%trans                        |
| NaMordenite                | 399                           | 1                       | 75%trans, 13%cis                |

a 0.2g zeolite, 0.11M 1-Pentene in Benzene, 5 weight % Fe(CO)<sub>5</sub>.

b Power in Watts.

c Analyzed by gas chromatography, 20' AgNO<sub>3</sub>/ethylene glycol/Chromosorb P.

1.1 mm/second. At this time, we are not sure to what this doublet may be attributed, and low temperature studies of this system are now in progress. Further reduction time and increased temperature treatment do not lead to more alpha iron(0). All of the iron carbonyl zeolite samples show very similar Mossbauer spectra. Infrared experiments by us and by others (16) and thermal decomposition of these samples in an in-situ IR cell have led to the belief that  $\text{Fe}(\text{CO})_5$  complexes retain a molecular structure during adsorption and that subsequent thermal treatment leads to loss of CO. The Mossbauer spectra of all the untreated samples show a quadrupole splitting and isomer shifts that are different from that reported by Herber and coworkers (26) for a low temperature matrix isolated  $\text{Fe}(\text{CO})_5$  system.  $^{13}\text{C}$ -NMR spectroscopy experiments by Derouane and coworkers (15) also suggest that the  $\text{Fe}(\text{CO})_5$  moiety is weakly interacting with the zeolite surface and that the framework remains unchanged on adsorption. This suggests that the Mossbauer parameters may shift from the low temperature measurement to our room temperature measurement. Further support for an intact  $\text{Fe}(\text{CO})_5$  species is given by our photochemical studies (vide infra). Reduction of the iron carbonyl systems does lead to complete reduction to alpha-iron, but the reduction conditions are quite severe and the particle sizes in most cases are fairly large, between 75 Å and 125 Å, on the basis of electron microscopy results. The  $\text{Fe}(\text{CO})_5$  zeolite Y system is a good Fischer-Tropsch catalyst with high activity for methane and it is stable for long periods of time and is regenerable. Further details of the catalytic activity of these samples are given elsewhere (23).

The data for mixed metal zeolites as first prepared by Scherzer and Fort (18) shown in Tables I and II are quite extensive. The reported isomer shifts and quadrupole splittings are for the iron atoms in the anionic state. Each of these unreduced samples show Mossbauer spectra that are in close agreement with literature values of the corresponding iron coordination complexes. Typical examples of unreduced and reduced samples are shown in Figures 3 and 4. We note here that preparations 16 through 22 are new and are developments of our laboratory and that 9 through 15 are preparations based on the work of Scherzer and Fort (18). Samples 16 and 17 show that this method can be extended to other zeolites like ZSM-5. If no transition metal cation is used in the synthesis, no Mossbauer spectrum for the corresponding anion is observed. Therefore, the nature of the cation is critical and complexation of the anion to a cation is necessary for anion inclusion. Certain transition metal cations ( $\text{Ru}^{3+}$  for instance) do not seem to bind the anion. On the other hand, we have introduced ruthenium as either the  $\text{K}_3\text{Ru}(\text{CN})_6$  or the  $\text{K}_2\text{Ru}(\text{CN})_5\text{NO}$  complex.

The reduction of these samples is extraordinary in two aspects. First of all, fairly low temperatures between 350°C and 400°C are needed to reduce the iron to the metallic state.



Secondly, only 4 hours of reduction with hydrogen is necessary to completely reduce these samples. The most easily reduced anion is  $[\text{Fe}(\text{CN})_5\text{NO}^{2-}]$  and for the corresponding  $\text{Zn}^{2+}$  and  $\text{Cu}^{2+}$  samples, complete reduction is noted in the Mössbauer spectrum. As indicated in Table II, the reported isomer shifts are all close to that of metallic iron and the hyperfine field strength,  $H$ , values are all very close to that of alpha iron. It should be noted here that whenever the cation was  $\text{Fe}^{2+}$  that reduction was never complete. We now believe that these ion-exchanged  $\text{Fe}^{2+}$  ions are strongly bonded to the lattice and are not easily reduced. This is also the belief of several other investigators (2-5, 8, 10).

These mixed metal systems have also been tested with the transient method for catalytic activity in the Fischer-Tropsch reaction. We would like to remark here that the nature of the cation, anion, and zeolite are all important factors in the Fischer-Tropsch reactions that we have studied. Further details of these catalytic studies can be found elsewhere (23). We do observe here, however, that some catalysts that are completely reduced to the metallic state are not necessarily the most active catalysts. Also, even though the Mössbauer experiments suggest that  $400^\circ\text{C}$  is sufficient for complete reduction, higher activation temperatures can increase the activity and selectivity of these reactions. We have also observed that the cation definitely changes the product distribution and the activity. For example, sample 15 which contains zinc and is totally reduced to the metallic state does not show good activity, but sample 19 which is not completely reduced does show high activity. Electron paramagnetic resonance experiments also support the existence of ferromagnetic iron particles. X-ray powder diffraction experiments, electron microscopy, and surface analysis measurements show the existence of both metals on the surface before and after reduction. We know the particle size again is quite large, although there is a wide distribution in these samples, ranging from 30 Å to about 150 Å.

The data in Table III for the photochemical isomerization of 1-pentene show that photochemical activation is also a viable means of sample activation. During these reactions, CO gas is given off and it is believed from solution studies that an  $\text{Fe}(\text{CO})_4\text{L}$  complex is initially formed. The  $\text{Fe}(\text{CO})_4\text{L}$  complex, where L is a bound pentene, can then undergo isomerization to the cis and trans isomers of 2-pentene. The data in Table III show that the incorporation of a zeolite not only changes the product distribution from a 2.0 ratio of the trans to the cis, as observed in solution studies, but that the photolysis time is relatively short. It should be recognized here that high energy ultraviolet radiation is used, but the photon flux is relatively low. The kinetics of this reaction are surely different from that of the solution reactions and it is not inconceivable that there are steric constraints administered by the zeolite

framework. Further studies concerning the mechanism of this reaction and the search for active intermediates by various techniques are in progress (25).

### Overview

We have reported here the preparations and treatment conditions that are needed to reduce iron ions to metallic iron in zeolites. Although we have not isolated highly-dispersed superparamagnetic iron particles in zeolites, we have shown that these iron-containing zeolites are active catalysts in Fischer-Tropsch and in olefin isomerization reactions. The added insight that stems from the use of in-situ Mössbauer experiments has led to the preparation of new active catalysts that can be selectively activated. We presently are studying photochemical reactions of other metal carbonyl complexes in zeolites and believe that increased selectivity is a major benefit in these types of reaction.

### Acknowledgments

We are grateful to the American Chemical Society Petroleum Research Fund, University of Connecticut Research Foundation, and the Atlantic Richfield Foundation of the Research Corporation for supporting this work. We would like to thank Professor .. Peter G. Debrunner for supplying us with a copy of the Mössbauer data fitting program. We also would like to acknowledge Professor C. O. Bennett and L. M. Tau as collaborators on the Fischer-Tropsch studies.

### Literature Cited

1. Morice, J. A.; Rees, L. V. C. Trans. Far. Soc. 1968, 64, 1388-1395.
2. Delgass, W. N.; Garten, R. L.; Boudart, M. J. Chem. Phys. 1969, 50, 4603-4606.
3. Delgass, W. N.; Garten, R. L.; Boudart, M. J. Phys. Chem. 1969, 73, 2970-2979.
4. Garten, R. L.; Delgass, W. N.; Boudart, M. J. Catal. 1970, 18, 90-107.
5. Garten, R. L.; Gallard-Nechschein, J.; Boudart, M. Ind. Eng. Chem. Fund. 1973, 12, 299-310.
6. Collins, D. W.; Mulay, L. N. I.E.E.E Trans. Magn. 1968, 4, 470-475.
7. Kumer, L.; Posch, H.; Kaltseis, J. Phys. Lett. 1972, 40A, 59-60.
8. Huang, Y. Y.; Anderson, J. R. J. Catal. 1975, 40, 143-153.
9. Gunsser, W.; Adloph, J.; Schmidt, F. J. Magn. Magn. Mat 1980, 15-18, 1115-1116.
10. Lee, J. B. J. Catal. 1981, 68, 27-32.

11. (a) Lo, C.; Rao, K.R.P.M.; Mulay, L. N.; Rao, V. U. S.; Obermeyer, R. T.; Gormley, R. J. 1981, "Mössbauer Spectroscopy and its Chemical Applications" (Advances in Chemistry Series, American Chemical Society, No. 194, J. G. Stevens, G. K. Shenoy, eds.), Chapter 27, 573-588.  
(b) Obermyer, R. J.; Mulay, L. N.; Lo, C.; Oskooie-Tabrizi, M.; Rao, V.U.S. J. Appl. Phys. 1982, 53, 2683-2685.
12. Quale, W. H.; Peeters, G.; Deroy, G. L.; Vansant, E. F.; Lunsford, J. H. Inorg. Chem. 1981, 21, 2226-2231.
13. Banerjee, S. P. Thermochim. Acta. 1982, 53, 369-374.
14. Gager, H. M.; Hobson, M. C., Jr. Catal. Rev. 1975, 11, 117-165.
15. Nagy, J. B.; vanEenoo, M.; Derouane, E. G. J. Catal. 1979, 58, 230-237.
16. Ballivet-Tkatchenko, D.; Coudurier, G. Inorg. Chem. 1979, 18, 558-564.
17. Chem. Eng. News. Oct. 26, 1981; 22-32.
18. Scherzer, J.; Fort, D. J. Catal. 1981, 71, 111-118.
19. Nijs, H. H.; Jacobs, P. A.; Uytterhoeven, J. B. J. Chem. Soc. Chem. Comm. 1979, 180-182.
20. Delgass, W. N.; Chen, L. Y. Rev. Sci. Instrum. 1976, 47, 968-972.
21. Bennett, C. O. ACS Symposium Series, No. 178, Catalysis Under Transient Conditions, A. J. Bell and L. L. Hegedus, eds. 1982, 1-32.
22. W. M. Reiff and S. L. Suib, unpublished data.
23. S. L. Suib, K. C. McMahon, L. M. Tau, and C. O. Bennett, manuscript in preparation.
24. Suib, S. L.; Zerger, R. P.; Stucky, G. D.; Emberson, R. M.; Debrunner, P. G.; Iton, L. E. Inorg. Chem. 1980, 19, 1858-1862.
25. S. L. Suib and J. C. Baxter, unpublished data.
26. Herber, R. H.; Kingston, W. R.; Wertheim, G. K. Inorg. Chem. 1963, 2, 153-158.

RECEIVED December 7, 1982

## Metal Ion Site Geometry and Oxidation State in Zeolites

T. I. MORRISON, P. J. VICCARO<sup>1</sup>, and G. K. SHENOY  
Argonne National Laboratory, Argonne, IL 60439

The combined results of EXAFS and Mössbauer effect spectroscopies have been used to deduce the oxidation state and local structure of iron in iron containing Na, K- and H-chabazites. In the mineral Na,K(Fe) chabazite iron is found to be present as oxo- or hydroxo-bridged Fe(III) oligomers, while in the H-chabazite it is found to be present as Fe(III) ions bridged by oxo- or hydroxo-groups to the zeolite framework.

Metal containing zeolites are of great interest as practical catalysts for petrochemical reactions. Such catalysts are usually considered to be bifunctional, with the zeolite framework acting as a support for the metal centers. In order to optimize reaction conditions and parameters in the processes for which metal-zeolite catalysts are used, it is necessary to understand the chemistry of the support and the metal and their interaction.

Much can be learned about the chemistry of the metal centers by a description of the environment of the cation. In broad terms, the task is to determine the location of the cation site or sites within the zeolite and thereby deduce its local site environment, or conversely to determine the local site environment of the cation and infer its position in the zeolite. The former task is often undertaken by x-ray or neutron scattering technique, and the latter by spectroscopic techniques.

<sup>1</sup>On leave from Instituto de Fisica, UFRGS, Porto Alegre RS, Brazil

This chapter not subject to U.S. copyright.  
Published 1983, American Chemical Society

A large number of x-ray scattering studies have been made on metal containing zeolites and have met with varying degrees of success (1). In cases where the number of cations per unit cell is high enough to give an appreciable (and unambiguous) signal, where suitably large single crystals can be grown, and when there is a degree of ordering among the cations, these studies have been able to provide complete and reliable descriptions of the cation environment. Nevertheless, there exists the possibility of misassignment of electron density peaks, attributing crystal coordination to wrong atoms or to "average sites" only partially filled (2, 3).

In cases where there is a low concentration of cation of interest, if the cations are highly disordered in the zeolite framework, or if good crystalline samples are unavailable, atom specific or environment-specific spectroscopic probes may be preferable to determine local structures about the cation in the zeolite. NMR (4), IR (5,6) ESR (7-10), optical (9,10), Mössbauer effect (11-15), and x-ray absorption studies (2,16,17,18) have been used to determine cation microenvironments. In particular, it has been shown that EXAFS (Extended X-ray Absorption Fine Structure) of the cation can often be used to give direct structure information about cation environments in zeolites, but EXAFS techniques, while giving radial distances and relative coordination numbers, are insensitive to site symmetry and cannot, in general, give both coordination numbers and relative site populations. Clearly it is desirable to use complementary spectroscopic techniques to fully elucidate the microenvironments in dilute, polycrystalline zeolite systems.

We have addressed the problem of determining the local environments of iron centers in iron containing chabazites by using two specifically short range probes, Mössbauer and EXAFS spectroscopies. The  $^{57}\text{Fe}$  Mössbauer effect can be used to obtain information on the oxidation states, magnetic states and the local symmetry of iron (19) while the EXAFS of the iron can be used to determine radial distances to near neighbors, near neighbor atomic type, and within limits the relative numbers of near neighbors. Of primary interest in this study is the change iron undergoes from its state in the freshly mined zeolite, through ion exchange, calcination, and framework protonation.

### Experimental

The natural mineral or "as mined" Na,K(Fe) chabazite samples were prepared by simply loading and resealing the zeolite powder in its sample cell. The protonated framework H(Fe) chabazite was prepared by ion exchange with ammonium nitrate, air drying, and calcination at 350 °C to drive off the ammonia. To determine separately the effects on the iron centers of ion exchange and heating, an  $\text{NH}_4(\text{Fe})$  chabazite sample was prepared by ion exchange of the Na,K(Fe) chabazite in 1 M  $\text{NH}_4\text{NO}_3$  for 16 hours at room

temperature with subsequent air drying of the sample. In addition, a sample of Na,K(Fe) chabazite was calcined for 16 hours at 350 °C to determine heating effects.

The Mössbauer effect experiments were performed using a  $^{57}\text{Co}/\text{Rh}$  source and a conventional electromechanical drive. Data were collected between 297 and 4.2 K on a Nuclear Data ND 6600 computer and were analyzed by least squares fitting of the appropriate line shapes to the spectra describing the hyperfine interactions. The amount of Fe in the chabazite was about 1 wt. %. Absorption path lengths were optimized in sample preparation by uniformly distributing 200 mg/cm<sup>2</sup> of the chabazite.

Iron K-edge EXAFS experiments were also performed on the Na,K(Fe) chabazite and H(Fe) chabazite samples. The experimental spectra were obtained at room temperature both in transmission and fluorescence mode at the Stanford Synchrotron Radiation Laboratory. Because of the dilution of Fe in the hosts, the fluorescence data were an order of magnitude better in statistics than the absorption data. Multiple runs were taken on each sample, and the incident and fluorescent intensities,  $I_0$  and  $I_f$ , were summed respectively to improve the signal-to-noise ratio.

### Results and Discussion

In Figure 1, we present the Mössbauer spectrum of Na,K(Fe) chabazite mineral measured at room temperature. The spectrum is composed of a symmetric doublet. The solid line in Figure 1 is a least squares fit to the data assuming a single quadrupole interaction. The quadrupole splitting of  $0.49 \pm 0.02$  mm/s and an isomer shift of  $0.35 \pm 0.02$  mm/s with respect to Fe metal obtained from this fit is typical for a high spin ferric ( $3d^5$ ) ion (20). The value of the isomer shift does not permit us to assign unambiguously either a tetrahedral or octahedral co-ordination for this ferric ion (21). It must be pointed out that although the above analysis assumes a unique crystallographic site for the ferric ion in the chabazite, the width of the resonance lines (which is nearly twice the minimum experimentally observable width) indicates some distribution in the neighboring environment of Fe ions on a microscopic scale.

The spectrum of Na,K(Fe) chabazite measured at 4.2 K does not differ from the room temperature spectrum. This is surprising since with the low concentration of Fe in the lattice, we expect to see some paramagnetic hyperfine structure or at least line broadenings (22) associated with slow relaxation of the  $\text{Fe}^{3+}$  electronic spin. This implies a fairly strong coupling of Fe spins to the lattice or to other Fe spins. Assuming the latter case, we expect Fe to have other Fe neighbors within about 4 Å.

The room temperature spectrum of  $\text{NH}_4(\text{Fe})$  chabazite was nearly identical to that of Na,K(Fe) chabazite, indicating that the process of ion exchange does not alter the environment of Fe atoms in this lattice.

The calcination of  $\text{NH}_4(\text{Fe})$  chabazite to produce  $\text{H}(\text{Fe})$  chabazite, however, drastically changes the Mössbauer spectrum. In Figure 2 we present the spectrum of  $\text{H}(\text{Fe})$  chabazite measured at room temperature. The solid line in Figure 2 is a least squares analysis assuming three distinct Fe sites with differing quadrupole interactions. The isomer shifts for each of the three sites is almost identical to that in  $\text{Na},\text{K}(\text{Fe})$  chabazite showing that iron is present in the high spin ferric state. The three quadrupole splittings are 1.90, 1.04 and 0.81 mm/s and the three inequivalent sites have an approximate population ratio of 1.3:3.0:2.0, respectively. The broad width of the resonances again indicates the presence of a distribution in the local surroundings of each of these sites. The dramatic increase in the quadrupole interaction on protonation is noteworthy. These interactions, which are among the largest measured for ferric compounds, are related to the local and near local charge dispositions around the iron sites. A large quadrupole interaction in the protonated chabazite is indicative of significant gradients in the charge distributions of the sites.

On cooling the sample to 4.2 K there are no indication of paramagnetic hyperfine splitting although the lines show some minor broadening. Again the Fe spins appear to be well coupled to the spin bath.

The spectrum of calcined  $\text{Na},\text{K}(\text{Fe})$  chabazite (Figure 3) is similar in every respect to that of  $\text{H}(\text{Fe})$  chabazite. This clearly indicates that the process of calcination is responsible for the large differences observed between the  $\text{Na}, \text{K}$ - and  $\text{H}$ -chabazite. Ion exchange alone produce little effect at the Fe site environment.

Both  $\text{Na},\text{K}(\text{Fe})$  chabazite and  $\text{H}(\text{Fe})$  chabazite after dehydration show the onset of paramagnetic hyperfine structure in their Mössbauer spectra at 77 and 4.2 K. It is tempting to suggest that dehydration reduces the coupling of the spins in a major way or that the Fe atoms form a superparamagnetic oxide (23).

We shall next discuss the EXAFS results and draw conclusions by comparing them with the Mössbauer results. In Figure 4 the EXAFS data are plotted in the wave-vector ( $k$ ) space. The oscillations were Fourier transformed to real space to resolve the major frequency components of the oscillations. The resulting phase-shifted radial distribution functions are shown in Figure 5. By backtransforming, or Fourier filtering, each peak representing a coordination shell, it is possible to determine from the backtransform envelope the type of near neighbor, and by least squares fitting the backtransformed oscillations it is possible to determine radial distances and relative coordination numbers about the iron (24).

Figure 6 shows the backscattering amplitude functions for the first coordination shells of Fe in  $\text{Na},\text{K}(\text{Fe})$  chabazite and  $\text{H}(\text{Fe})$  chabazite. The shape of this function, with the singularity at  $k = 0$ , is indicative of backscattering by first row elements and

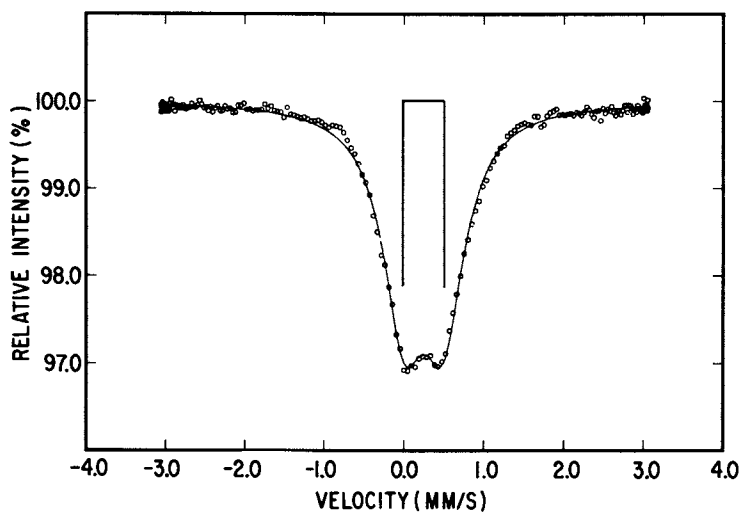


Figure 1. Room temperature Mössbauer spectrum of Na,K(Fe) chabazite.

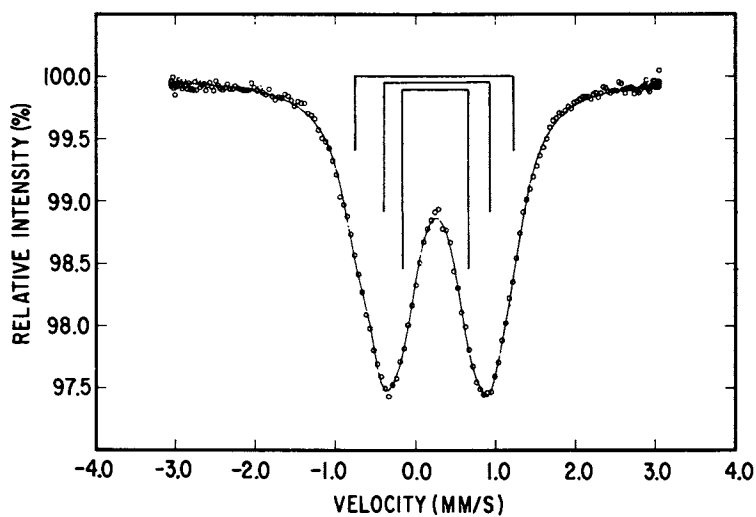


Figure 2. Room temperature Mössbauer spectrum of H(Fe) chabazite.



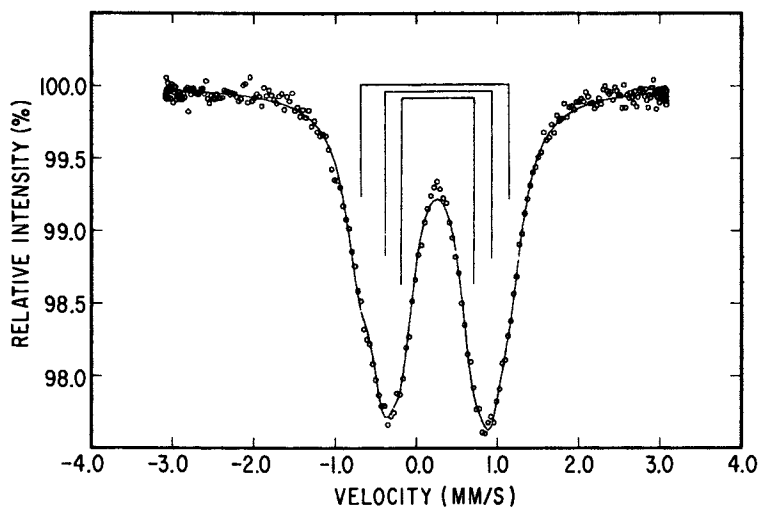


Figure 3. Room temperature Mössbauer spectrum of calcined Na,K(Fe) chabazite.

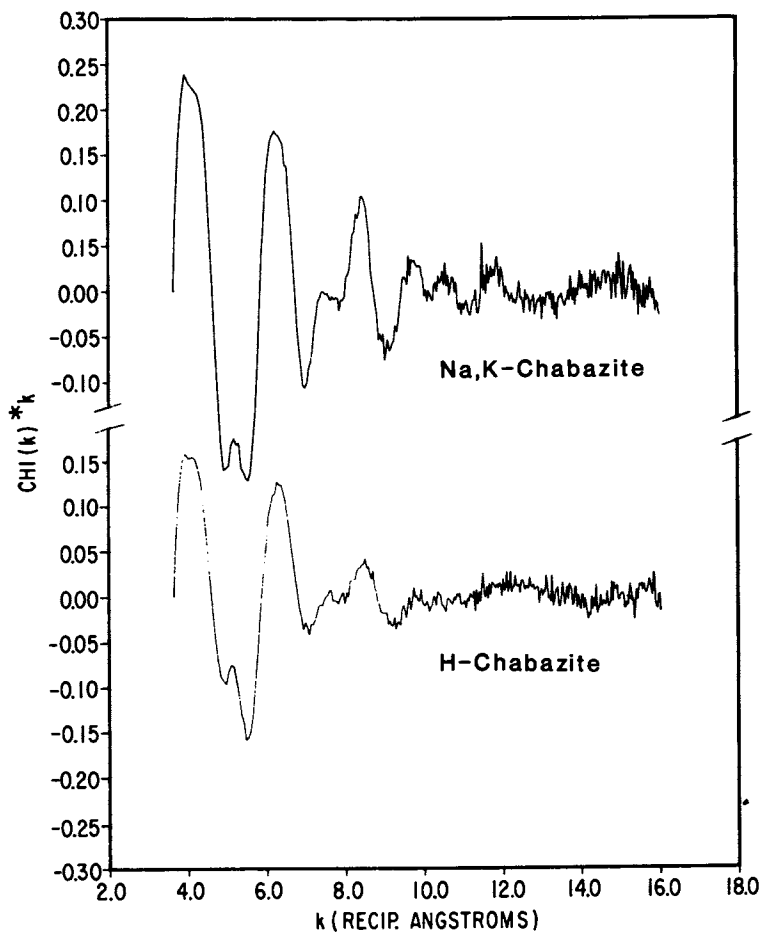


Figure 4.  
k-weighted iron K-edge EXAFS spectra of Na,K(Fe) chabazite and H(Fe) chabazite. Spectra obtained at room temperature.

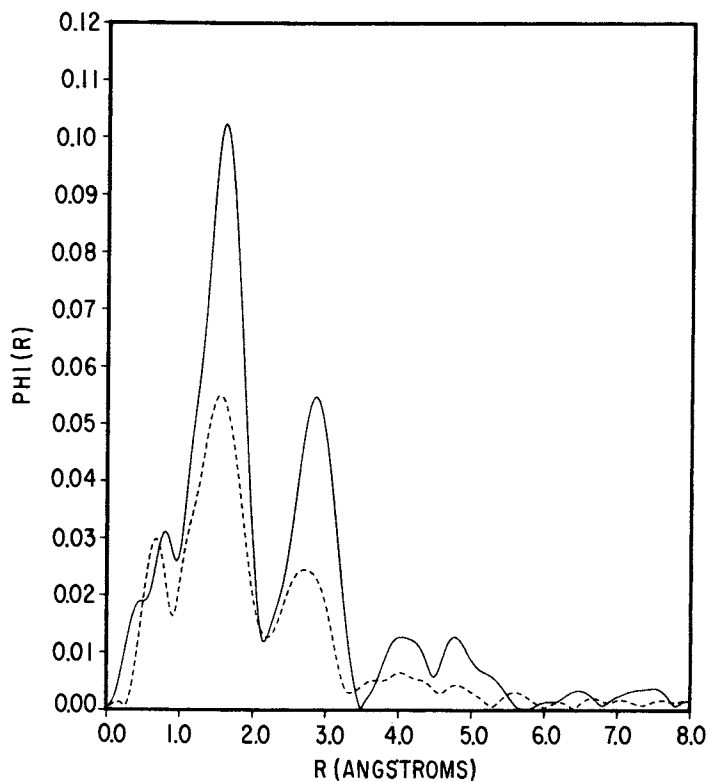


Figure 5.  
Fourier transforms of EXAFS spectra. Solid  
line  $\rightarrow$  Na,K(Fe) chabazite, dashed line  $\rightarrow$  H(Fe) chaba-  
zite.

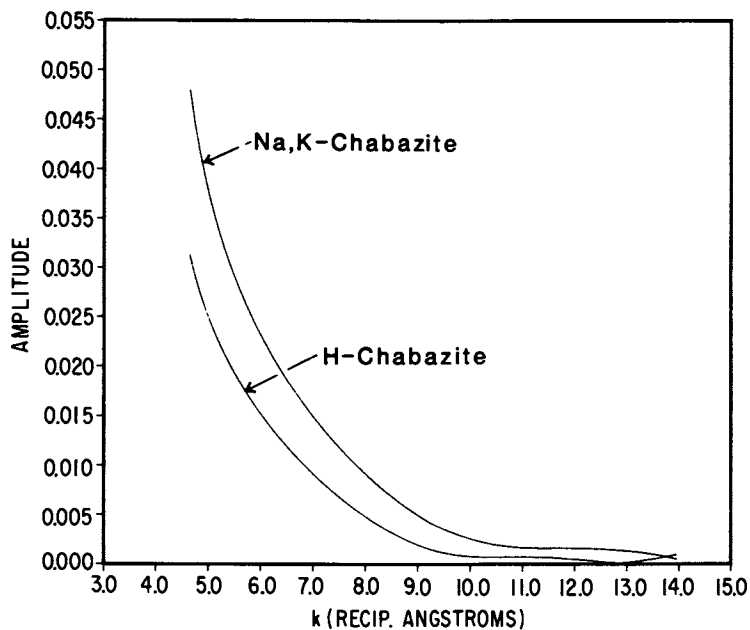


Figure 6.  
Backscattering amplitude functions for first coordination shells in Na,K(Fe) chabazite and H(Fe) chabazite.

we may conclude that the nearest neighbors to iron in both zeolites are oxygen atoms (25). This is further supported by the results of the least-squares fitting of the first peak in each spectrum, shown in Table I.

Figure 7 shows the backscattering amplitude functions for the second coordination shells of Fe in Na,K(Fe) chabazite and H(Fe) chabazite. The backscattering amplitude for the second shell of the Na,K(Fe) chabazite indicates that this shell is made up completely of iron, and the results of the least-squares fitting corroborate this. In H(Fe) chabazite on the other hand, the backscattering amplitude for the second shell indicates that this shell is composed of silicon and/or aluminum and oxygen. It was evident in the least squares fitting of this shell that the atoms were highly disordered relative to the absorbing iron, and reliable structural parameters could not be extracted.

TABLE I

EXAFS RESULTS

|                    | Na,K(Fe)-chabazite | H(Fe)-chabazite |
|--------------------|--------------------|-----------------|
| Z <sub>1</sub>     | 8                  | 8               |
| R <sub>1</sub> (Å) | 2.00 (.02)         | 2.00 (.01)      |
| A <sub>1</sub>     | 0.52 (.01)         | 0.32 (.04)      |
| σ <sub>1</sub> (Å) | 0.045 (.002)       | 0.043 (.011)    |
| Z <sub>2</sub>     | 26                 | 8               |
| R <sub>2</sub> (Å) | 3.12 (.03)         | 1.46 (.02)      |
| A <sub>2</sub>     | 0.09 (.03)         | 0.15 (.03)      |
| σ <sub>2</sub> (Å) | 0.045 (.029)       | 0.02 (.02)      |

Z<sub>i</sub> = ith backscatterer atomic number

R<sub>i</sub> = radial distance to ith backscatterer

A<sub>i</sub> = amplitude of oscillations due to ith backscatterer

σ<sub>i</sub> = (rms relative displacement)<sup>1/2</sup> of ith backscatterer

Conclusions

By combining results of Mössbauer and EXAFS spectroscopies we are able to draw certain conclusions about the iron sites in the chabazite samples. Considering first the iron in the Na,K(Fe) chabazite, we find that the iron is not exchangeable with the ammonium solutions used, indicating that the iron is either in an inaccessible site, is incorporated into the zeolite framework, or is present as species insoluble under exchange conditions used in the zeolite. The Mössbauer spectra tell us that all of the iron in the zeolite is in nearly identical environments, so only one of the above options is possible.

The EXAFS spectrum of iron in Na,K(Fe) chabazite shows that (within EXAFS resolution) each iron is surrounded equidistantly by

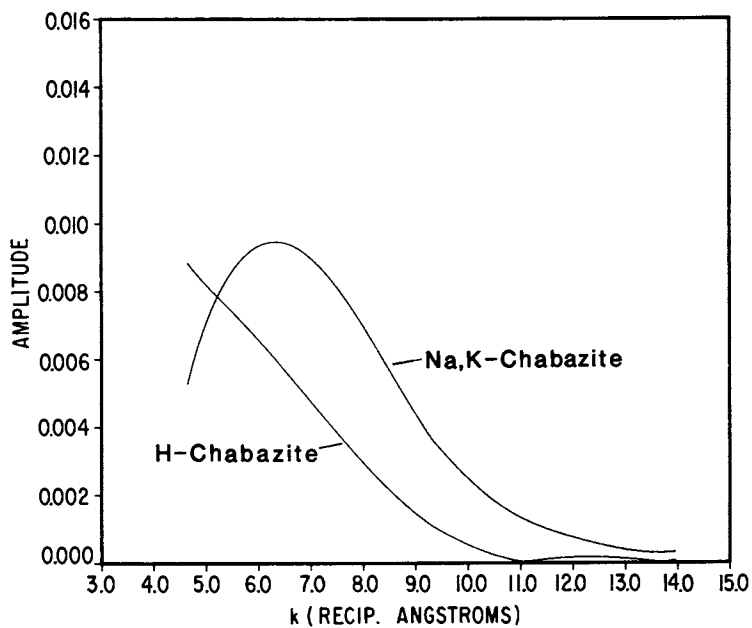


Figure 7.  
Backscattering amplitude functions for second coordination shells in Na,K(Fe) chabazite and H(Fe) chabazite.

oxygen with next near neighbors of iron. Since the Mössbauer data indicate that all irons are nearly identical, it is most plausible to suggest an aquo, hydroxo, or oxo bridged iron oligomer. It is doubtful that the irons are aquo bridged, since such a species should be soluble and subject to ion exchange. The dimensions of the chabazite supercage put an upper limit on the size of the iron multimer, since this cage would be the only reasonably sized host for the multimer. It can also be concluded that the closest approach of an iron atom to the cage wall cannot be less than approximately 3 Å, since no silicon, aluminum, or oxygen contributes coherently to the second shell backscattering.

The Mössbauer spectra of the H(Fe) chabazite show clearly that the iron environment changes on protonation of the framework by ammonium exchange and deammoniation. The similarity of the spectra of Na,K(Fe) chabazite and  $\text{NH}_4(\text{Fe})$  chabazite indicates that the change in iron environment is not due to the ion exchange. However, calcined Na,K(Fe) chabazite gives a spectrum very similar to the deammoniated H(Fe) chabazite, showing that the heating of the sample is responsible for the changes in the iron environment.

The Mössbauer spectrum of the H(Fe) chabazite shows three resolvable ferric iron sites, with large quadrupole interactions indicative of asymmetry in the positions of surrounding ions. The EXAFS data, indicating two disordered iron-oxygen distances, are consistent with the Mössbauer results. The EXAFS also shows that the iron multimer is completely disrupted after heating, since iron is no longer present in the second shell. Since the second shell is composed entirely of Si, Al, and O, we may conclude that the iron has moved closer to the zeolite framework.

The possible locations of the iron sites in the H(Fe) chabazite can be inferred by a process of elimination. It is improbable that the iron is located in the center of the prisms forming supercages, since the site is highly symmetric and there are no electric field gradients present that would give rise to the observed quadrupole splitting. It is also doubtful that the iron is located in the center of a six-ring, since this iron would be tetra- or penta-, rather than hexa-coordinate. It is most likely that the irons are coordinated to the walls of the supercage via oxo- or hydroxo-bridges with waters of hydration coordinatively saturating the irons jutting into the supercage.

The complementarity and interplay of the results of EXAFS and Mössbauer spectroscopies provide means by which crystal chemistry of certain cations in zeolites may be successfully studied. While neither technique is completely adequate as a "stand-alone" tool for such studies, the combination of the two can be used to map the chemical nature, environment and location of cations where this information would otherwise be inaccessible.

#### Acknowledgments

Work supported by the U.S. Department of Energy.

Literature Cited

1. Smith, J. V. Proceedings of the Fifth International Conference on Zeolites 1980, 194-204 and references cited therein.
2. Morrison, T. I.; Reis, A. H., Jr.; Gebert, E.; Iton, L. E.; Stucky, G. D.; Suib, S. L. J. Chem. Phys. 1980, 72, 6276-6282.
3. Pluth, Joseph J.; Smith, Joseph V. J. Chem. Phys. 1979, 83, 741-749.
4. Lechert, H.; Henneke, H. W. "Molecular Sieves - II"; Katzer, James R., Ed., American Chemical Society: Washington; 1977; p 53-63.
5. Brodskii, I. A.; Zhadanov, S. P. Proceedings of the Fifth International Conference on Zeolites 1980, 234-241.
6. Flanigen, Edith M. "Zeolite Chemistry and Catalysis"; Rabo, Jule A., Ed.; American Chemical Society: Washington; 1977; p 80-117.
7. Tikhomirova, N. N.; Nikolaeva, I. V. Proceedings of the Fifth International Conference on Zeolites 1980, 230-233.
8. Kasal, Paul H.; Bishop, R. J., Jr. "Zeolite Chemistry and Catalysis"; Rabo, Jule A., Ed.; American Chemical Society: Washington; 1977; p 350-391.
9. Peigneur, P.; Lunsford, J. H.; de Wilde, W.; Schoonheydt, R. A. J. Phys. Chem. 1977, 81, 1179-1187.
10. Garbowski, Edward; Primat, Michel; Mathieu, Michel-Vital "Molecular Sieves - II"; Katzer, James R., Ed.; American Chemical Society: Washington; 1977; p 281-290.
11. Schmidt, F.; Gussner, W.; Adolph, J. ibid., 291-301.
12. Fitch, Frank R.; Rees, Lovat V. C. Zeolites 1982, 2, 33-41.
13. Dickson, Bruce L.; Rees, Lovat V. C. J. Chem. Soc. Faraday Trans. 1 1974, 70, 2038-2050.
14. Suib, S. L.; Zenger, R. P.; Stucky, G. D.; Emberson, R. M.; DeBrunner, G.; Iton, L. E. Inorg. Chem. 1980, 19, 1858-1862.
15. Samuel, E. A.; DeGass, W. N. J. Chem. Phys. 1975, 62 1590-1592.
16. Morrison, T. I.; Reis, A. H., Jr.; Gebert, E.; Iton, L. E.; Stucky, G. D.; Suib, S. L. J. Chem. Phys. 1980, 73, 4705-4706.
17. Morrison, Timothy I.; Iton, L. E.; Shenoy, G. K.; Stucky, G. D.; Suib, S. L. J. Chem. Phys. 1981, 75, 4086-4089.
18. Morrison, T. I.; Shenoy, G. K.; Iton, L. E.; Stucky, G. D.; Suib, S. L. J. Chem. Phys. 1982, 76, 5665-5668.
19. See, for example "Chemical Applications of Mössbauer Spectroscopy"; Gol'danskii, V. I.; Herber, R. H., Ed.; Academic Press: New York; 1968 and Gütlich, P.; Link, R.; Trautwein, A. "Mössbauer Spectroscopy and Transition Metal Chemistry"; Springer-Verlag: Berlin; 1978.



20. Ingalls, R.; van der Woude, F.; Sawatzly, G. A. "Mössbauer Isomer Shifts"; Shenoy, G. K.; Wagner, F. E., Eds.; North-Holland: Amsterdam; 1978; p 361-429.
21. Nicholson, W. J.; Burns, G. Phys. Rev. A 1964, 133, 1568-1570.
22. Wickman, H. H. "Mössbauer Effect Methodology"; 2, Gruverman, I. J., Ed.; Plenum Press: New York; 1961.
23. Suzdalev, I. P.; Afanasev, A. M.; Plachinda, A. S.; Gol'danskii, V. I.; Makarov, E. F. Zhur. Eksp. Teor. Fiz. SSSR, 1968, 55, 1752.
24. Stern, E. A.; Sayers, D. E.; Lytle, F. W. Phys. Rev. B 1975, 11, 4836-4846.
25. Lee, P. A.; Beni, G. Phys. Rev. B 1977, 15, 2862-2883.

RECEIVED December 16, 1982

## Steric Effects in Nitrogen Adsorption by Mordenite

D. T. HAYHURST

Cleveland State University, Department of Chemical Engineering,  
Cleveland, OH 44115

M. D. SEFCIK

Monsanto Company, Corporate Research Department, St. Louis, MO 63166

Zeolites are well known for their ability to adsorb a large variety of gases, including even highly volatile nonpolar permanent gases (1, 2). Nitrogen is among the most strongly adsorbed non-polar gases; in fact, among some of the earliest observations on adsorptive separation of gaseous mixtures was the selectivity shown by several zeolites for nitrogen from air. Early work of Barrer (3), McKee (4) and Domine and Hay (5) showed that calcium A, calcium X, mordenite and several types of natural zeolites could be used to enrich air by a selective adsorption of nitrogen. Several pressure-swing-adsorption processes utilizing zeolite adsorbents have been developed which yield a product containing up to 95% oxygen at rates of 20 tons per day (6,7).

The selective adsorption of nitrogen over oxygen is not a true molecular sieving effect since nitrogen (3.64Å) is larger than oxygen (3.46Å). Thus, the increased affinity of many zeolites for nitrogen can be ascribed to a greater heat of adsorption for nitrogen than for oxygen (8). The initial heat of adsorption in zeolites adsorbents can be partitioned into contributions from repulsive and dispersive forces, polarization energy and electrostatic interactions arising from dipole and electric quadrupole moment interactions with electric fields in the zeolite (9). At higher concentrations of adsorbates, interactions between adsorbates must also be considered (10).

The physical constants of oxygen and nitrogen (11) suggest that the heat of adsorption due to repulsive, dispersive and polarization effects should be similar. Contributions to the heat of adsorption by the electric-quadrupole field-gradient interactions are expected to be greater for nitrogen whose quadrupole moment is three times larger than that of oxygen. Barrer (12) has estimated that the electrostatic energy contri-

bution to the initial heat of adsorption for nitrogen on Na-mordenite is 2.5 Kcal/mole and 3.4 Kcal/mole for adsorption on Na-faujasite. It is possible, however, that these results seriously underestimate the true interaction. The results of Barrer were calculated from experimental data obtained in a region where one may reasonably expect that adsorbed nitrogen is rotating isotropically (13, 14).

The electric-quadrupole field-gradient energy  $\phi_{F-Q}^{\cdot}$  is given by,

$$\phi_{F-Q}^{\cdot} = \frac{FQ}{4r} (3\cos^2\theta - 1) \quad (1)$$

where  $\dot{F}$  is the field gradient,  $Q$  the electric quadrupole moment,  $r$  is the separation between the quadrupole and charge and  $\theta$  is the angle between the quadrupole axis and the field gradient. If the molecule has some rotational mobility in its adsorption site, the expression  $(3\cos^2\theta - 1)$  in Equation 1 must be replaced by  $\langle 3\cos^2\theta - 1 \rangle_{\theta}$  where  $\langle 3\cos^2\theta - 1 \rangle_{\theta}$  is the average value of  $(3\cos^2\theta - 1)$  weighted overall all allowable orientations of the quadrupole axis. For a nonrotating molecule oriented so that  $\theta=0$ ,  $\langle 3\cos^2\theta - 1 \rangle_{\theta} = (3\cos^2\theta - 1) = 2$  and for an isotropically rotating molecule the value of  $\langle 3\cos^2\theta - 1 \rangle_{\theta}$  is zero. For anisotropically rotating molecules  $(3\cos^2\theta - 1)$  can have values between  $-1$  and  $2$  depending on the orientation of the rotation axis.

If nitrogen is adsorbed into sites which reduce or eliminate its rotational freedom and, if the nitrogen quadrupole is aligned with the cation field gradient, then a significant increase in the value of  $\phi_{F-Q}^{\cdot}$  may be expected. This was exactly the result observed for  $CO_2$  adsorbed on small-pore mordenite (19). At low coverages,  $CO_2$  molecules were adsorbed into the pore shaped side pockets and held with little rotational freedom. Zeolitic cations are located at the end of each of these side pockets (16), so  $\phi_{F-Q}^{\cdot}$  is a maximum and, consequently, the heat of adsorption is high. It is the objective of this research to demonstrate that for certain adsorption conditions, similar side-pocket adsorption is significant for nitrogen leading to high heats of adsorption.

## EXPERIMENTAL

### Materials

The samples used in this study were both natural and synthetic varieties of mordenite and are listed in Table I. Each material contained more than 95% pure zeolite with the remainder being amorphous material as measured by x-ray diffractometry. Before being used in experimentation, each sample was exchanged to the sodium form.

TABLE I

## ZEOLITE SAMPLES USED

| <u>Sample</u>                               | <u>Source (or supplier)</u>                              |
|---|--|
| Zeolon 900                                  | Norton Company Lot No. 40644                             |
| HB-33 (Si/Al=7.75)                          | Norton Company Lot No. 6EH                               |
| HB-33 dealuminated <sup>a</sup> (Si/Al=126) | Norton Company Lot No. 6EH                               |
| Alaskan Mordenite                           | Horn's Mountain<br>Area Site #45 D.B. Hawkins(18)        |
| ZE-502 Zeoharb <sup>b</sup>                 | Osaka Oxygen<br>Industries<br>Ltd. Japan Lot No. 6203738 |
| Zeolite NaA                                 | Union Carbide<br>Corp.                                   |

a. This sample was dealuminated using procedures outlined by Chang (17).

b. The Zeoharb is a natural mordenite mined in Japan. Deposit locality is unknown.

Ion exchange was performed by crushing and sieving the zeolite to between 70-200 mesh (Tyler standard). Approximately 50 grams was placed into an Erlenmeyer flask, 250 ml of 1N NaCl solution was added and the slurry was agitated for 16 hours. This procedure was repeated for a total of five exchanges.

After the final exchange, the slurry was washed several times with distilled water in a Buchner funnel and the filter cake was placed in a 110°C drying oven overnight. The dried cake was milled gently before use.

Each mordenite was treated using the same procedure except for the HB-33. Since this sample was received in the H<sup>+</sup>exchanged form, the sample was activated in vacuum and exposed to anhydrous ammonia at room temperature to insure each zeolitic cation was ammonium. The sample was then sodium exchanged using the procedure outlined above.

Adsorption

Adsorption isotherms were determined on a Cahn 1000 vacuum micro-balance system, using a Leybold-Heraeus Turbotronic TMP 120 turbomolecular pump for evacuation and a variable-leak valve for adsorbate gas injection. Approximately 0.3 grams of the sodium-exchanged zeolite was placed into a 1 cm. diameter hemispherical quartz sample pan within the adsorption chamber of the balance and activated. The activation was accomplished by heating the mordenite to 400<sup>±</sup>2 °C under a vacuum of < 5 x 10<sup>-6</sup> torr and maintaining these conditions for

16 hours. The adsorption run was initiated by allowing the sample to cool to run temperature and injecting the adsorbate gas. Adsorption equilibrium was assumed when the sample weight varied less than  $1 \times 10^{-5}$  grams in 30 minutes. The equilibrium nitrogen capacity was measured at pressures from 0.2 to 700 mmHg using a 170 series MKS Baratron high accuracy electronic manometer. When the final equilibrium pressure was reached, the sample was reactivated. Three replicates of the Alaskan mordenite sample were run to insure experimental accuracy and reproducibility.

#### N-15 NMR Analysis

Nitrogen-15 nmr spectra were obtained at 9.12 and 20.72 MHz on spectrometers using external  $^{19}\text{F}$  time-share, field-frequency lock. Details of the spectrometer modifications are published elsewhere (19).

Samples of approximately one gram of sodium-exchanged Alaskan mordenite were placed in 10 mm O. D. nmr tube fitted with o-ring seals and degassed under vacuum with a programmed temperature rise to 350°C. After cooling, the samples were allowed to equilibrate with a known pressure of  $^{15}\text{N}_2$  (Prochem Ltd.; 95%  $^{15}\text{N}$ ) and sealed. Spectra were obtained on samples equilibrated with 10, 72, 206, 760 and 792 mmHg  $^{15}\text{N}_2$  corresponding to 0.16, 0.54, 1.02, 2.26 and 2.32 gN<sub>2</sub> adsorbed/100 g mordenite.

### RESULTS AND DISCUSSION

#### Adsorption Isotherms

The equilibrium adsorption capacity for nitrogen was determined for each of the samples tested. Isotherms were measured in the range of 0.2 to 700 mmHg adsorbate gas pressure and at 22°, 40° and 65°C. Due to the amount of data taken, (and to reduce the number of figures presented) adsorption data were fitted to Freundlich isotherm model. This model was chosen after testing applicability of several models, including the Henry's Law, Langmuir and Temkin models. In each instance, the Freundlich isotherm was found to provide a significantly better agreement with the obtained data.

The Freundlich equation is an exponential relation of gas loading with adsorbate gas pressure. The form of the equation used for curve fitting is given below:

$$\frac{X}{m} = KP^{1/n} \quad 2)$$

where  $X/m$  is the grams of nitrogen adsorbed per 100 grams of anhydrous zeolite,  $K$  and  $n$  are the Freundlich constants and  $P$  is the equilibrium adsorbate gas pressure in mmHg. To determine the quality of fit for the adsorption model, a coefficient of determination,  $r^2$ , was calculated for each

isotherm. A value of  $r^2$  equal to 1.00 indicates a perfect fit. The Freundlich constants and the coefficient of determination for each zeolite are listed in Table II.

TABLE II

## FREUNDLICH CONSTANTS AND COEFFICIENT OF DETERMINATION

| <u>Sample</u>            | <u>T(C°)</u> | <u>Kx10<sup>3a</sup></u> | <u>1/n<sup>a</sup></u> | <u>r<sup>2</sup></u> |
|--------------------------|--------------|--------------------------|------------------------|----------------------|
| Zeolon 900               | 20           | 32.7                     | 0.65                   | 1.00                 |
| "                        | 43           | 11.6                     | 0.73                   | 1.00                 |
| "                        | 67           | 8.85                     | 0.68                   | 1.00                 |
| Zeolon HB33              | 26           | 8.46                     | 0.76                   | 0.98                 |
| "                        | 40           | 4.07                     | 0.84                   | 0.99                 |
| "                        | 64           | 2.82                     | 0.83                   | 1.00                 |
| Zeolon HB33 dealuminated | 26           | 7.51                     | 0.54                   | 0.91                 |
| "                        | 40           | 4.77                     | 0.57                   | 0.95                 |
| "                        | 64           | 1.32                     | 0.74                   | 0.95                 |
| Alaskan Mordenite        | 22           | 39.6                     | 0.61                   | 1.00                 |
| "                        | 41           | 26.7                     | 0.60                   | 0.99                 |
| "                        | 64           | 9.70                     | 0.70                   | 0.98                 |
| ZE-502 Zeoharb           | 22           | 12.2                     | 0.70                   | 0.99                 |
| "                        | 40           | 4.79                     | 0.80                   | 0.99                 |
| "                        | 65           | 2.68                     | 0.80                   | 0.99                 |
| Zeolite NaA              | 23           | 12.1                     | 0.56                   | 0.92                 |
| "                        | 42           | 1.58                     | 0.88                   | 1.00                 |
| "                        | 65           | 0.90                     | 0.88                   | 0.98                 |

a. From Equation 2.

Heats of Adsorption

The isosteric heats of adsorption,  $\Delta H_{ISO}$ , were calculated as a function of nitrogen loading for each of the samples tested. For each sample, the  $\Delta H_{ISO}$  was found to decrease logarithmically with increased loading and this functionality is consistent with the assumptions of the Freundlich adsorption equation. As before, the brevity of presentation, the heat of adsorption data were curve fitted to an equation of the form:

$$\Delta H_{ISO} = a + b \ln(X/m) \quad 3)$$

where a and b are constants and X/m is the loading as expressed in the isotherm equation. The equation constants for each of the samples tested are listed in Table III. Two typical heat of adsorption curves are presented in Figure 1.

Using these heats of adsorption curves, the initial heats  $\Delta H_{ISO}^0$ , were determined for the five mordenite samples. Values for the  $\Delta H_{ISO}$  were derived by a linear extrapolation of

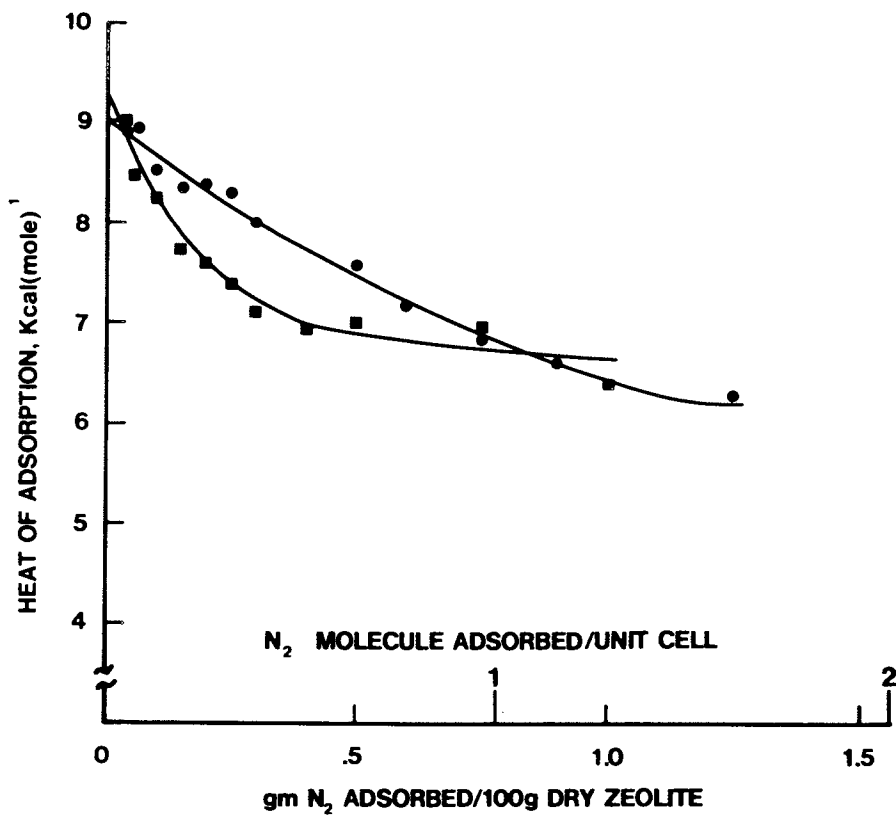


Figure 1. Heat of adsorption for Alaskan mordenite (●) and for Zeolon 900 (■).

data taken at low nitrogen loadings. The initial heats are plotted as a function of silicon to aluminum ratio in Figure 2 and are listed in Table III. These initial heats of adsorption are significant as they indicate the energies of interaction between the nitrogen and the most energetically favorable adsorption sites in the mordenite structure. At these low levels of nitrogen adsorption, the interaction energy due to adsorbate-adsorbate repulsion are negligible.

TABLE III  
HEAT OF ADSORPTION CONSTANTS,  
INITIAL HEATS AND SILICON ALUMINUM RATIOS

| Sample                     | Constants <sup>a</sup> |       | Coef.<br>Determ. | Range(gN <sub>2</sub> /100g) <sup>b</sup> |       |       | $\Delta H_{iso}^{\circ}$ |
|----------------------------|------------------------|-------|------------------|---|-------|-------|--------------------------|
|                            | a                      | b     |                  | Initial                                   | Final | Si/Al |                          |
| Zeolon 900                 | 6.41                   | -0.76 | 0.97             | 0.01                                      | 1.00  | 4.18  | 9.5                      |
| Zeolon HB33                | 4.44                   | -0.22 | 0.85             | 0.01                                      | 0.80  | 7.75  | 6.0                      |
| Zeolon HB33<br>(Si/Al=126) | 3.36                   | -0.30 | 0.91             | 0.01                                      | 0.20  | 126   | 5.5                      |
| Alaskan Mord.              | 6.72                   | -0.82 | 0.91             | 0.01                                      | 1.30  | 3.93  | 9.3                      |
| ZE502 Zeoharb              | 3.89                   | -1.08 | 0.91             | 0.01                                      | 0.75  | 4.68  | 9.3                      |
| Zeolite NaA                | 3.49                   | -0.11 | 0.82             | 0.01                                      | 0.25  | --    | 6.5                      |
| Barrer (19)                |                        |       |                  |   |       | 4.75  | 7.0                      |
| Takaishi (13)              |                        |       |                  |   |       | 5.05  | 6.6                      |

a. From Equation 3.

b. This is the range of nitrogen loadings (gN<sub>2</sub>/100 g mordenite) where this correlation is valid.

c. Determined by inductively-coupled argon plasmaoptical emission spectroscopy by Monsanto Company's Physical Science Center.

The initial heats of adsorption (Figure 2) of nitrogen on mordenite show a marked decrease as the silicon content of the zeolite increases. The resulting  $\Delta H_{iso}^{\circ}$  curve is not a continuous function, but rather has an abrupt discontinuity at Si/Al of 4.70. The curve consists of two approximately horizontal lines having  $\Delta H_{iso}$  equal to 9.3 to 9.5 at Si/Al below 4.70 and  $\Delta H_{iso}$  of 7.0 to 6.0 being obtained above the critical Si/Al ratio. These results indicated that the initial nitrogen adsorption in mordenite takes place at two sites energetically different by 2.5 Kcal/mole and the existence of the high energy sites require that the Si/Al be less than 4.70.

Zeolite pore diameters increase as aluminum is isomorphically substituted for silicon in the crystal structure. Given the relationship observed between the initial heat of adsorption and the silicon to aluminum ratio, we suggest that a sterically different adsorption site becomes available for nitrogen when the Si/Al is below the critical value of 4.70.



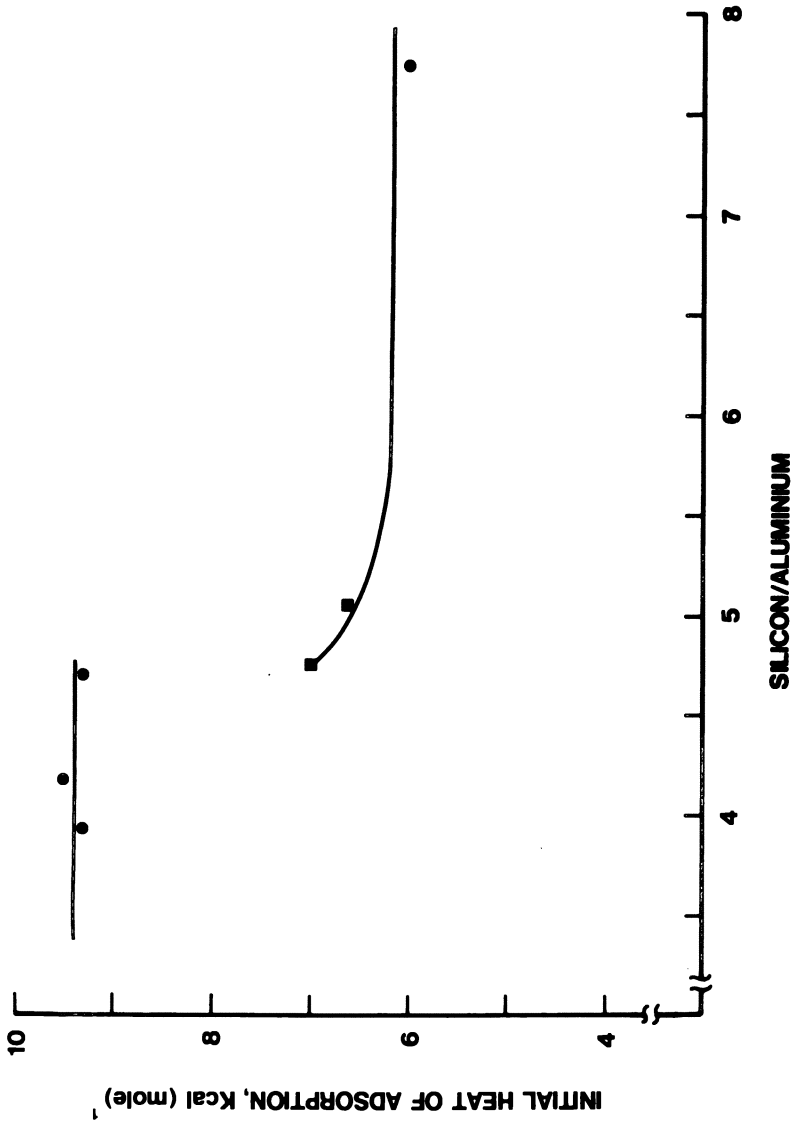


Figure 2. The initial heat of adsorption for various Si/Al. (●) This study and (■) literature values.

The availability of such a new site would most likely be the consequence of the mordenite structure undergoing a crystal lattice expansion, opening the 8-membered ring side pocket for adsorption.

In order to insure the validity of the results presented, heats calculated were found to be identical to those measured for NaA at near-ambient-temperature by other investigators (21, 22).

#### Nitrogen-15 NMR Analysis

The nitrogen-15 nmr spectra (Figure 3) of sodium exchanged Alaskan and HB33 mordenites were analyzed for the chemical shift anisotropy tensors. The chemical shift anisotropy tensors have been measured for solid nitrogen at 4.2K(23) and calculated to be  $603 \pm 28$  ppm for the static molecule. The observed chemical shift tensors can be used to calculate an orientational parameter  $\xi$ , where

$$\xi = \frac{\langle \sigma_{11} - \sigma_{12} \rangle}{\sigma_{11} - \sigma_{12}} \quad (4)$$

$\langle \sigma_{11} - \sigma_{12} \rangle$  is the observed, motionally averaged chemical shift anisotropy and  $\sigma_{11} - \sigma_{12}$  is the static anisotropy.

The orientational order parameter is the second Legendre polynomial of  $\cos\theta$  and, where the chemical shift dispersion is reduced by rotational averaging,  $\xi$  is given by

$$\xi = 1/2 \langle 3\cos^2\theta - 1 \rangle_{\theta} \quad (5)$$

where  $\theta$  depends on the angular amplitude of the rotation.

The same motion which reduces the chemical shift dispersion of the adsorbed nitrogen also reduces the field-gradient quadrupole interaction energy. For a molecule which is undergoing rotation we can combine Equations 1 and 5 to give

$$\delta_{F-Q} = -\frac{FQ}{2r} \xi \quad (6)$$

where  $\xi$  is directly measured from the nmr powder spectrum. Using the orientational order parameter from the motional narrowing of the chemical shift dispersion, we can calculate the field-gradient quadrupole interaction energy without any assumptions concerning the adsorbate motion.

For  $N_2$  adsorbed on Alaskan mordenite, the chemical shift dispersion from the chemical shift anisotropy is reduced to about 190 ppm and so  $\xi = 0.31$ . For sodium-exchanged Zeolon HB33  $\langle \sigma_{11} - \sigma_{12} \rangle = 90$  ppm and  $\xi = 0.19$ . From Equation 6, and assuming that  $\bar{r}$  of the adsorption sites are similar for the two zeolites, we estimate that the contribution of  $\delta_{F-Q}$  is about twice as large for the Alaskan mordenite as for HB33.

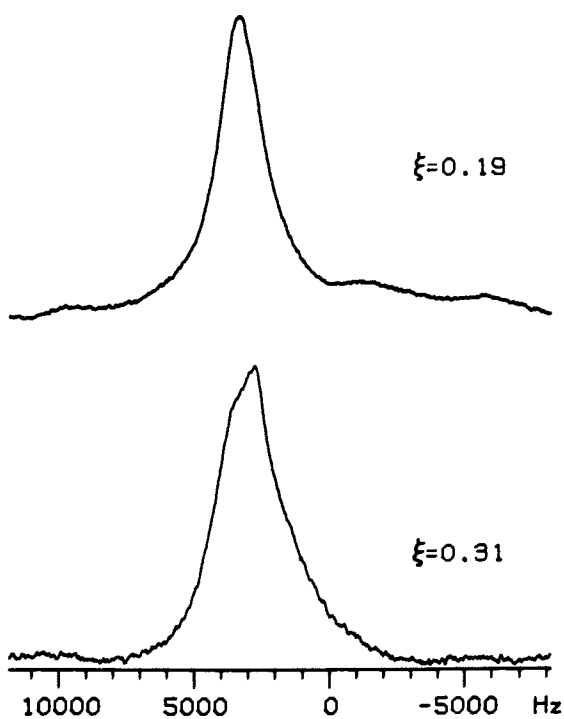


Figure 3.  $20.72\text{MHz}$   $^{15}\text{N}$ -NMR of adsorbed nitrogen on  $\text{Na}^+$  HB33 (upper) and Alaskan mordenite (lower).

## CONCLUSIONS

Both the heat of adsorption and the  $N^{15}$ -NMR results indicate that, for mordeinite samples with a Si/Al of less than 4.70, nitrogen is selectively adsorbed into the side-pocket adsorption site. In the sodium-exchanged form of mordeinite, the pore-shaped side pockets are accessible from the 12-membered ring main channel and a sodium cation is located at the opposite end effectively closing off this 8-membered ring channel (16). The shape of the side-pocket is such that adsorbed nitrogen molecules have restricted rotational freedom. Such a forced alignment of the quadrupole axis with the cation field gradient causes  $\langle 3\cos^2\theta - 1 \rangle_0$  to assume its maximum value resulting in an increase in the heat of adsorption.

The discontinuity in the initial heats of adsorption with decreasing Si/Al results from the isomorphic substitution of aluminum for silicon in the 8-membered side pocket ring structure. As the aluminum content of the zeolite increases, the size of the side-pocket increases correspondingly. This occurs to a degree where nitrogen can enter this adsorption site without steric hindrances. In mordeinites with Si/Al > 4.70, the side-pocket dimensions are reduced to the point where nitrogen can no longer enter these energetically favored sites and adsorption can only take place in the zeolite's 12-membered-ring main channel. Side-pocket nitrogen adsorption is therefore, considered to be unique to mordeinites with Si/Al of less than 4.70.

## LITERATURE CITED

- (1) Breck, D.W., "Zeolite Molecular Sieves", John Wiley and Sons, New York, New York (1974).
- (2) Nedderniep, R.J., *J. Colloid Interface Sci.*, 28, 293 (1968).
- (3) Barrer, R.M., *Proc. Roy. Soc., London*, 167A (1938).
- (4) McKee, D.W., U. S. Patent 3,140,932 (1964).
- (5) Domine, D. and Hay, L., *Molecular Sieves*, Soc. Chem. Industries, London (1968).
- (6) Breck, D.W., "Zeolite Molecular Sieves", John Wiley and Sons, New York, New York (1974).
- (7) Mumpton, F.A., *Mineralogy and Geology of Natural Zeolites*, M.S.A. Short Course Notes, Southern Printing Company (1977).
- (8) Breck, D.W., "Zeolite Molecular Sieves", John Wiley and Sons, New York, New York p. 645-659 (1974).
- (9) Barrer, R.M., *J. Coll. and Interface Sci.*, 21, 415 (1966)
- (10) Kingston, G.L. and MacLeod, A.C., *Trans. Faraday Soc.*, 55, 1799 (1959).
- (11) Breck, D.W., *Zeolite Molecular Sieves*", John Wiley and Sons, New York, New York p. 650 (1974).

- (12) Barrer, R.M., *J. Coll. and Interface Sci.*, 21, 415 (1966)
- (13) Takaishi, T., Yusa, A., Ogino, Y. and Ozawa, S., *Proc. 2nd. Int'l. Conf. Solid Surfaces* (1974).
- (14) Takaishi, T., Yusa, A., Ogino, Y and Ozawa, S., *J. Chem. Soc., Faraday Trans. I*, 70, 671 (1974).
- (15) Sefcik, M.D. and Yeun, H.K., *Thermochimico Acta*, 26, 297 (1978).
- (16) Meier, W.M., *Z. Krist.*, 115, 439 (1961).
- (17) Chang, H.D., Ph.D. Thesis, Worcester Polytechnic Institute, Worcester, Massachusetts (1970).
- (18) Hawkins, D.B., *Alaska Geological and Geophysical Surveys Special Report 9*, College, Alaska (1976).
- (19) Sefcik, M.D., Schaefer, J. and Skejskal, E.O., *ACS Symp. Series 40*, 344 (1977).
- (20) Barrer, R.M. and Peterson, D.L., *Proc. Roy. Soc.*, 40, 95 (1964).
- (21) Peterson, D., *ACS Symp. Series 135*, 118 (1980).
- (22) Habgood, H.W., *Can. J. Chem.*, 42, 2340 (1964).

RECEIVED November 16, 1982

## Diffusion in A, X, and Y Zeolites

DOUGLAS M. RUTHVEN

University of New Brunswick, Department of Chemical Engineering,  
Fredericton, N.B., Canada

Diffusion of hydrocarbons and other simple molecules in A, X and Y zeolites has been studied by a range of experimental methods including direct sorption rate measurements, chromatography and NMR. The advantages and limitations of these techniques are considered and results of recent experimental studies are reviewed with emphasis on the detailed microdynamic information obtainable by NMR.

Earlier studies of intracrystalline diffusion in zeolites were carried out almost exclusively by direct measurement of sorption rates but the limitations imposed by the intrusion of heat transfer and extra-crystalline mass transfer resistances were not always fully recognized. As a result the reported diffusivities showed many obvious inconsistencies such as differences in diffusivity between adsorption and desorption measurements<sup>(1-3)</sup>, diffusivities which vary with fractional uptake<sup>(4)</sup> and large discrepancies between the values measured in different laboratories for apparently similar systems. More recently other experimental techniques have been applied, including chromatography and NMR methods. The latter have proved especially useful and have allowed the microdynamic behaviour of a number of important systems to be elucidated in considerable detail. In this paper the advantages and limitations of some of the common experimental techniques are considered and the results of studies of diffusion in A, X and Y zeolites, which have been the subject of several detailed investigations, are briefly reviewed.

### Sorption Rate Measurements

Measurement of the transient adsorption or desorption curve for a sample of zeolite crystals exposed to a step change in ambient sorbate concentration (pressure) provides, in principle, a simple and direct method of measuring the intracrystalline diffusivity ( $D$ ). Such measurements are conveniently carried out by gravimetric, volumetric or piezometric methods. The

0097-6156/83/0218-0345\$06.50/0

© 1983 American Chemical Society

diffusional time constant ( $D/r^2$ ) is determined by matching the experimental uptake curve to the appropriate transient solution of the diffusion equation, which, for the simplest case of a set of uniform spherical crystals subjected to a step change in concentration at time zero, is given by:

$$m_t/m_\infty = 1 - (6/\pi^2) \sum_{n=1}^{\infty} \frac{1}{n^2} \cdot \exp(-n^2\pi^2D t/r^2) \quad (1)$$

This method depends on the implicit assumption that the uptake rate is controlled entirely by intracrystalline diffusion in an isothermal system, with all other resistances to either mass or heat transfer negligible. This is a valid approximation if diffusion is sufficiently slow or if the zeolite crystals are sufficiently large but the dominance of intracrystalline diffusional resistance should not be assumed without experimental verification. In many practical systems, particularly with small commercial zeolite crystals, the external heat and mass transfer resistances are in fact dominant. A detailed discussion of such effects has been given by Lee and Ruthven (5-7).

In order to minimize external (bed) diffusion resistance and maximize the heat transfer rate it is desirable to use a very small adsorbent sample with the crystals spread as thinly as possible over the balance pan or within the containing vessel. To minimize the effect of non-linearities, such as the strong concentration dependence of the diffusivity, measurements should be made differentially over small concentration changes. Variation of the step size and comparison of adsorption and desorption curves provide simple tests for linearity of the system. The large differences between adsorption and desorption diffusivities, reported in some of the earlier work, have been shown to be due to the concentration dependence of the diffusivity (8) and in differential measurements under similar conditions no such anomaly was observed.

Variation of the crystal size and/or the adsorbent sample bed configuration provide simple and direct experimental tests for intracrystalline diffusion control. As an example diffusional time constants for  $\text{CO}_2$  in several different size fractions of 4A crystals (9) are shown in figure 1. For the larger crystals the data confirm intracrystalline control in a near isothermal system since the values of  $D/r^2$  give consistent values of  $D$ . For the smallest ( $7.3\mu\text{m}$ ) crystals, however, analysis of the uptake curves according to eqn. 1 leads to apparent values of  $D/r^2$  which show an unusual concentration dependence and which are only slightly larger than the values for the  $21.5\mu\text{m}$  crystals. Detailed analysis reveals that in the smallest crystals heat transfer resistance is important. Re-analysis of the uptake curves according to the non-isothermal model of Lee and Ruthven (5) leads to diffusivity values which are entirely consistent with the data for the larger crystals.

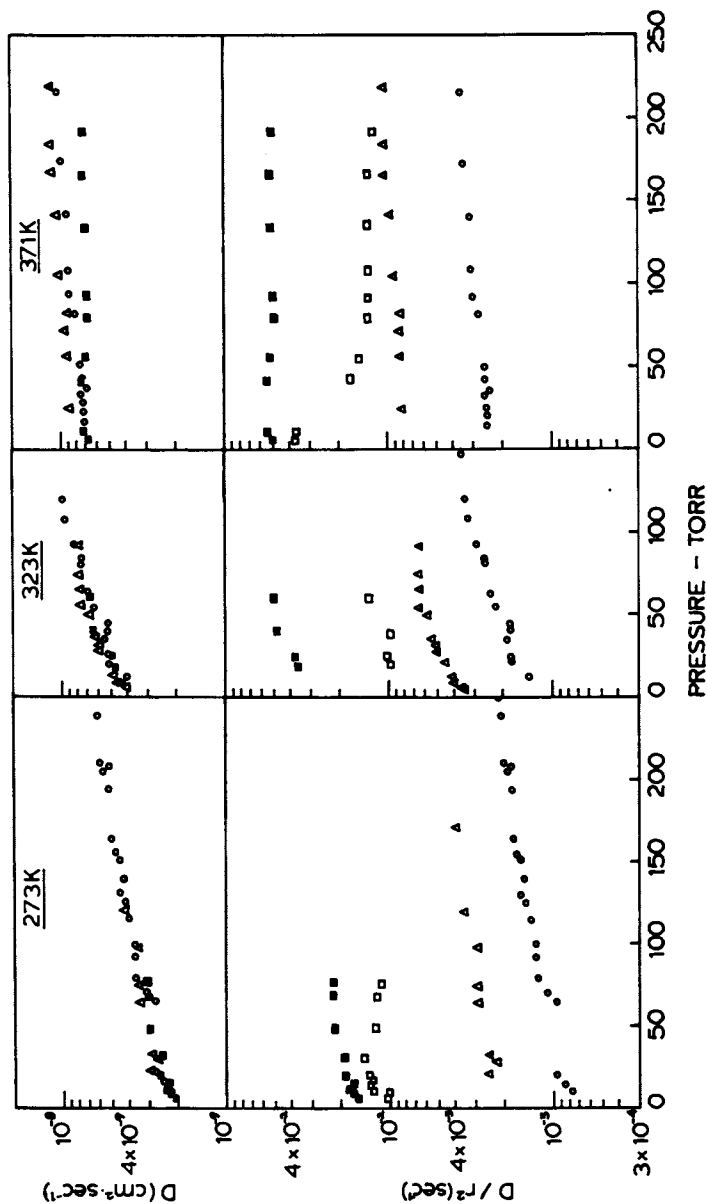


Figure 1.  
 Diffusion time constants and diffusivities for CO<sub>2</sub>-4A  
 calculated from uptake curves for crystals of different  
 size. 34µm, o; 21.5µm, Δ; 7.3µm □. Values calculated  
 for 7.3µm crystals from non-isothermal model ■.  
 (Reproduced with permission from Ref. 9. Copyright 1980,  
 J. Colloid Sci.)

American Chemical  
 Society Library  
 1155 16th St. N. W.  
 Washington, D. C. 20036



### Chromatography

In the chromatographic method a pulse or step change in sorbate concentration is introduced into the carrier stream at the inlet of a packed adsorption column and the diffusional time constant is determined from the dispersion of the response signal at the column outlet. Since heat transfer in a packed bed is much faster than in a closed system the chromatographic method may, in principle, be used to follow somewhat faster sorption processes. The choice between step or pulse inputs is governed solely by practical convenience since the same information may be obtained from either measurement. Although most commonly used with an inert carrier to measure the limiting diffusivity at low sorbate concentrations, the method may be extended to the study of diffusion at any concentration by using a mixed carrier stream(16,21).

The theory of chromatography depends on the assumption of a linear system with diffusivity independent of concentration over the relevant range. The validity of this assumption may be conveniently tested by varying the pulse (or step) size.

The analysis of chromatographic data is commonly carried out by determining the first and second moments of the response peak. This method is simple and convenient although somewhat more accurate results may be obtained by more sophisticated methods such as Fourier transform or direct matching of the response curves in the time domain(10-14).

The definitions of the moments and their relationship to the system parameters for a biporous (macropore-micropore) adsorbent such as a commercial pelleted molecular sieve are given by the following equations(15,16):

$$\mu \equiv \int_0^{\infty} c \cdot t \cdot dt / \int_0^{\infty} c \cdot dt = \left(\frac{L}{v}\right) \left[1 + \left(\frac{1-\epsilon}{\epsilon}\right) K_p\right] \quad (2)$$

$$\begin{aligned} \frac{\sigma^2}{2\mu^2} &= \frac{1}{2\mu^2} \int_0^{\infty} c (t-\mu)^2 dt / \int_0^{\infty} c \cdot dt \\ &= \frac{D_L}{vL} + \left(\frac{\epsilon}{1-\epsilon}\right) \left(\frac{v}{L}\right) \left[ \frac{R}{3k} + \frac{R^2}{150D_p} + \frac{r^2}{15K_p D} \right] \left[ 1 + \frac{\epsilon}{(1-\epsilon)K_p} \right]^{-2} \quad (3) \end{aligned}$$

where  $K_p \equiv \theta + (1-\theta)K_c$ . For a strongly adsorbed species ( $K_p \gg 1.0$ ) eqn. 3 reduces to the familiar form:

$$\frac{HETP}{2v} \equiv \frac{\sigma^2}{2\mu^2} \left(\frac{L}{v}\right) = \frac{D_L}{v^2} + \left(\frac{\epsilon}{1-\epsilon}\right) \left[ \frac{R}{3k_f} + \frac{R^2}{150D_p} + \frac{r^2}{15DK_p} \right] \quad (4)$$

In order to determine the intracrystalline diffusion time constant from a chromatographic measurement, it is necessary to ensure that the contributions from other mass transfer resistances (external film and macro diffusion) are not important. This can often be achieved by reducing the size of the adsorbent particles. Variation of the particle size provides a simple and convenient test for the significance of extracrystalline resistance. It is in principle possible to eliminate external mass transfer resistance by packing the column with unaggregated crystals rather than with pelleted material. In practice it is however difficult to obtain sufficiently large quantities of the larger crystals to pack any reasonable length of column.

The elimination or estimation of the axial dispersion contribution presents a more difficult problem. Established correlations for the axial dispersion coefficient are notoriously unreliable for small particles at low Reynolds number (17,18) and it has recently been shown that dispersion in a column packed with porous particles may be much greater than for inert non-porous particles under similar hydrodynamic conditions (19,20). One method which has proved useful is to make measurements over a range of velocities and plot  $(\sigma^2/2\mu^2)(L/v)$  vs  $1/v^2$ . It follows from eqn. 6 that in the low Reynolds number region where  $D_L$  is essentially constant, such a plot should be linear with slope  $D_L$  and intercept equal to the mass transfer resistance term. Representative data for several systems are shown plotted in this way in figure 2 (21).  $CF_4$  and  $iC_4H_{10}$  molecules are too large to penetrate the 4A zeolite and the intercepts correspond only to the external film and macropore diffusion resistance which varies little with temperature. For  $N_2$  which can penetrate the sieve the intercept is much larger and strongly temperature dependent, as a result of the dominance of intracrystalline diffusion resistance.

Several systems have been investigated by both gravimetric and chromatographic methods with consistent results (16,21). Since the extracrystalline resistances to both heat and mass transfer are certainly different in the gravimetric and chromatographic systems such agreement confirms in essence the validity of both experimental methods.

### NMR Methods

The application of NMR to the study of diffusion in zeolites involves the refinement and extension of methods originally developed to study self diffusion in liquids and low melting solids. The method is restricted to species such as hydrocarbons which contain a sufficiently high density of atoms such as H with unpaired nuclear spins. Authoritative reviews of the application of NMR to the study of adsorbed molecules have been given by Pfeifer (22,23) and only a brief outline is included here.

Relaxation Time Measurements The earlier NMR measurements depended on determining the correlation time for molecular re-orientation ( $\tau_c$ ) which was considered as equal to the average time

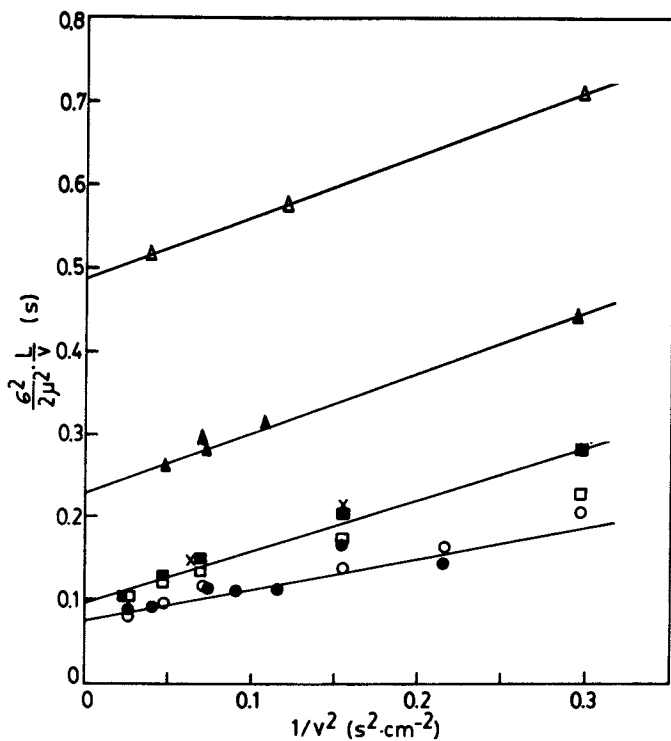


Figure 2.

Plots of  $(\sigma^2/2\mu^2)(L/v)$  vs  $v^{-2}$  from chromatographic data for 4A sieve. (iso-butane at 398K, o; 448K, ●; CF<sub>4</sub> at 333K, □; 353K, ○; 373K, x; N<sub>2</sub> at 308K, Δ; 363K, ▲.)

between molecular jumps. This quantity may be found from measurements of the longitudinal (spin-lattice) relaxation time as a function of temperature. The diffusivity is then estimated from Einstein's equation ( $D = \overline{\lambda^2}/6\tau$  for an isotropic cubic lattice) using a reasonable estimate for the mean square jump length ( $\overline{\lambda^2}$ ). Since the jump length generally cannot be estimated with confidence this represents a severe limitation of the method.

#### Pulsed Field Gradient (PFG) Self Diffusion Measurement (24)

This method, which was first developed by Stejskal and Tanner (25-26) for liquids, provides a more reliable measurement of the self diffusivity since the mean square molecular displacement, in a known time interval of a few ms, is measured directly.

A pulsed magnetic field gradient is applied to a sample prepared by a radio frequency pulse of suitable intensity and width. This starts the nuclear spins precessing with an angular velocity determined by the position of the molecule at time zero. After a known time interval the gradient pulse is reversed. If there were no diffusion the second gradient pulse would exactly counteract the effect of the first pulse, leaving all spins in phase. However, as a result of molecular migration the cancellation is incomplete and the attenuation of the signal provides a direct measurement of the mean square displacement during the known time interval between gradient pulses. A number of conditions concerning the duration of the time interval relative to the relaxation time must be fulfilled and the rms displacement must be less than the crystal diameter (24,27). The net result of these limitations is to restrict the method to relatively rapidly diffusing systems ( $D \sim 10^{-8} \text{cm}^2 \cdot \text{s}^{-1}$ ).

The variation in apparent diffusivity with temperature and crystal size is of the form illustrated in figure 3. At lower temperatures and in larger crystals the rms displacement is always smaller than the crystal diameter and under these conditions the intracrystalline diffusivity is measured directly. At higher temperatures and for smaller crystals the molecule escapes from the crystal during the time interval of the measurement and the apparent diffusivity corresponds to the long range effective extracrystalline or macro diffusivity. In the intermediate region there is a plateau region of restricted diffusion in which the molecules do not have sufficient energy to escape from the crystal and are reflected from the surface. The diffusivity at the plateau is simply related to the crystal size and this provides a direct check on the consistency of the method. Other simple tests such as blocking the intercrystalline space with  $\text{CCl}_4$  have also been performed in order to confirm that the signals are associated with intracrystalline rather than extracrystalline diffusion (27).

Combining the PFG self diffusion measurement with a measurement of the correlation time provides a means of determining directly the mean jump distance.

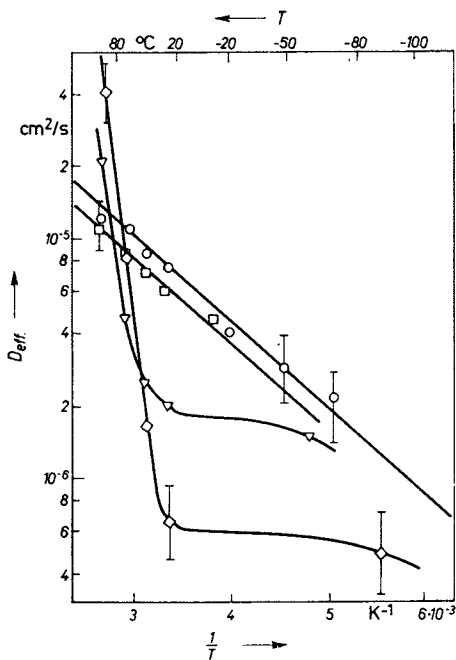


Figure 3.

Variation with temperature of effective diffusivity from NMR PFG experiment for n-hexane in NaX zeolite.  $r=0.9\mu\text{m}$ ,  $\Theta=0.49$ ,  $\diamond$ ;  $r=2\mu\text{m}$ ,  $\Theta=0.39$ ,  $\nabla$ ;  $r=9\mu\text{m}$ ,  $\Theta=0.35$ ,  $\square$  and  $r=25\mu\text{m}$ ,  $\Theta=0.29$ ,  $\circ$ . ( $\Theta$  = fractional saturation; saturation capacity 215 mg/g).

(Reproduced with permission from Ref. 24. Copyright 1976, Z. Chemie.)

Fast Tracer Desorption There are many zeolitic systems in which intracrystalline diffusion is too slow to measure directly by the PFG method. A modification of this method which makes it possible, under certain conditions, to measure much slower diffusion processes has recently been introduced by Karger (28,29). By increasing the time interval in a PFG experiment an increasing fraction of the molecules escapes from the crystal during the time interval of the measurement. If there is a sufficiently large difference between the intracrystalline and effective extracrystalline diffusivities it becomes possible to determine the fraction escaping during the time interval of the measurement from the variation of the signal attenuation with the intensity of the gradient pulse. By varying the time interval it is then possible to determine the desorption curve for the spin labelled molecules under equilibrium conditions. The diffusional time constant is found by matching this desorption curve to eqn. 1. Comparison with time constants measured directly by the PFG method provides direct evidence concerning the significance of any 'surface barrier' to mass transport.

#### Comparison of NMR and Sorption Diffusivities

The relationship between the transport diffusivity ( $D$ ), as measured under non-equilibrium conditions in an uptake experiment and the tracer self diffusivity ( $D_s$ ), measured under equilibrium conditions in an NMR experiment, has been discussed by Ash and Barrer (30) and Karger (31,32), who show that

$$D(c) = D_s(c) \cdot \left( \frac{\partial \ln p}{\partial \ln q} \right) [1-f]^{-1} \quad (5)$$

where  $f$  represents a positive function of the concentrations of marked and unmarked molecules and the straight and cross coefficients of irreversible thermodynamics. It follows that the corrected diffusivity ( $D_0$ ) and self diffusivity are related by:

$$D_0 = D(\partial \ln q / \partial \ln p) = D_s / (1-f) \quad (6)$$

At low sorbate concentrations  $f \rightarrow 0$  and eqn. 6 reduces to the familiar Darken equation (33). In comparing the results of sorption and NMR diffusivity measurements it is logical to compare  $D_0$  with  $D_s$ , even though exact agreement can be expected only at low sorbate concentrations. At higher concentrations one may expect  $D_0 \geq D_s / (1-f)$ .

#### Diffusion in Type A Zeolites

The channels of zeolite A are obstructed by 8-membered oxygen rings of free diameter  $\sim 4.2\text{\AA}$ . In the Ca form (5A) the windows are open whereas in the Na form (4A) or K form (3A) the windows are partially obstructed by  $\text{Na}^+$  or  $\text{K}^+$  ions. For all but the smallest

molecules, passage through the window is hindered by a significant repulsive energy barrier and diffusional activation energies of several kcal/mole are typical. As a consequence of the relatively high activation energy diffusivities are generally less than about  $10^{-8} \text{ cm}^2 \cdot \text{s}^{-1}$  at room temperature (except for very small molecules in 5A). Diffusivities of this magnitude are sufficiently low to permit reliable determination from uptake rate measurements, particularly in the larger crystals (20-50 $\mu\text{m}$ ) which are easily synthesized by Charnell's method(34). Measurement of diffusion of C<sub>1</sub>-C<sub>4</sub> alkanes in 5A is also possible by NMR methods but diffusion in 4A or of higher hydrocarbons in 5A is too slow to measure by the PFG method.

The behaviour of some representative systems is illustrated in figures 4-6. The differential diffusivity generally shows a strong increase with sorbate concentration but this is due mainly to the non-linearity of the relationship between activity and concentration, as defined by the equilibrium isotherm. Corrected diffusivities, calculated according to eqn. 6, are essentially constant within the limits of experimental uncertainty. The diffusional activation energy depends strongly on the diameter of the sorbate molecule relative to the sieve window, as is to be expected if the repulsive energy required to pass through the window is the major energy barrier. In figure 4 the van der Waals radius is used as a measure of molecular diameter but, although the correlation is good, it is clear that shape of the molecule is also important since molecules such as *i*C<sub>4</sub>H<sub>10</sub> ( $\sigma_0 \approx 4.48 \text{ \AA}$ ) and cyclohexane ( $\sigma_0 \approx 4.8 \text{ \AA}$ ) cannot penetrate the 5A lattice while linear paraffins with much larger van der Waals radius can penetrate easily.

The variation of diffusivity with ion exchange in the Na-CaA zeolites has been shown to be consistent with a simple model based on a random distribution of open (5A type) and partially closed (4A type) windows(36). The model predicts a sharp change in both diffusivity and activation energy at 33% Ca<sup>++</sup> exchange and this is confirmed by the experimental data.

Measurements for a given sorbate in several different 4A and 5A sieve samples show large differences in diffusivity but little variation in activation energy(9,35,36,41). Diffusion of n-butane and propane in large Charnell 5A crystals has been measured by both sorption and NMR (PFG) with consistent results (figure 5)(41). However, the NMR measurements showed little difference in diffusivity between the small Linde crystals and the large Charnell crystals whereas the uptake measurements show a very large difference in diffusivity. This and other similar observations led to the suggestion that the uptake rate in the small Linde crystals may be limited by a surface barrier rather than by a true diffusional resistance(27). In apparent support of this hypothesis measurements of uptake rates in 5A crystals showed a large decrease in apparent diffusivity with crystals size(42). This however appears to have been due to the intrusion of heat transfer resistance which becomes significant for the smaller crystals. A

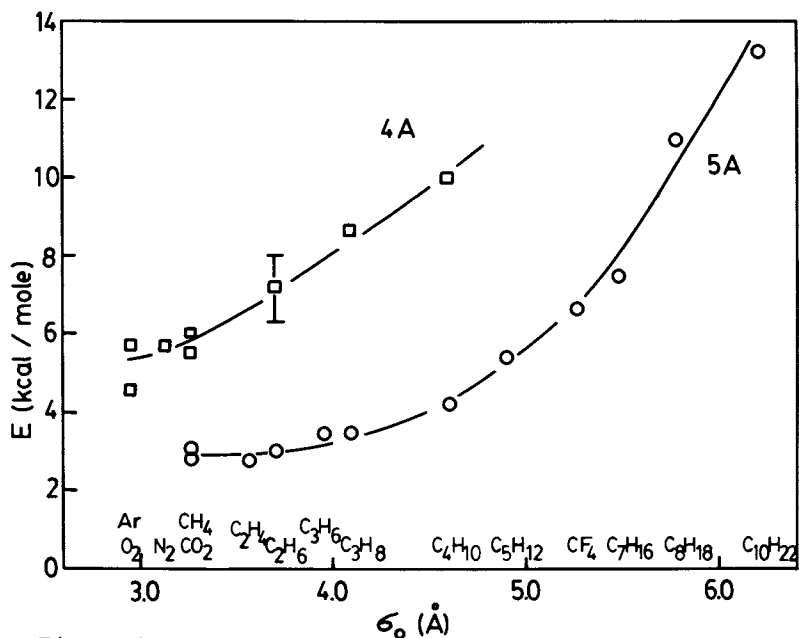


Figure 4.  
Variation of diffusional activation energy with van der Waals radius ( $\sigma_0$ ) for diffusion in 4A and 5A zeolites



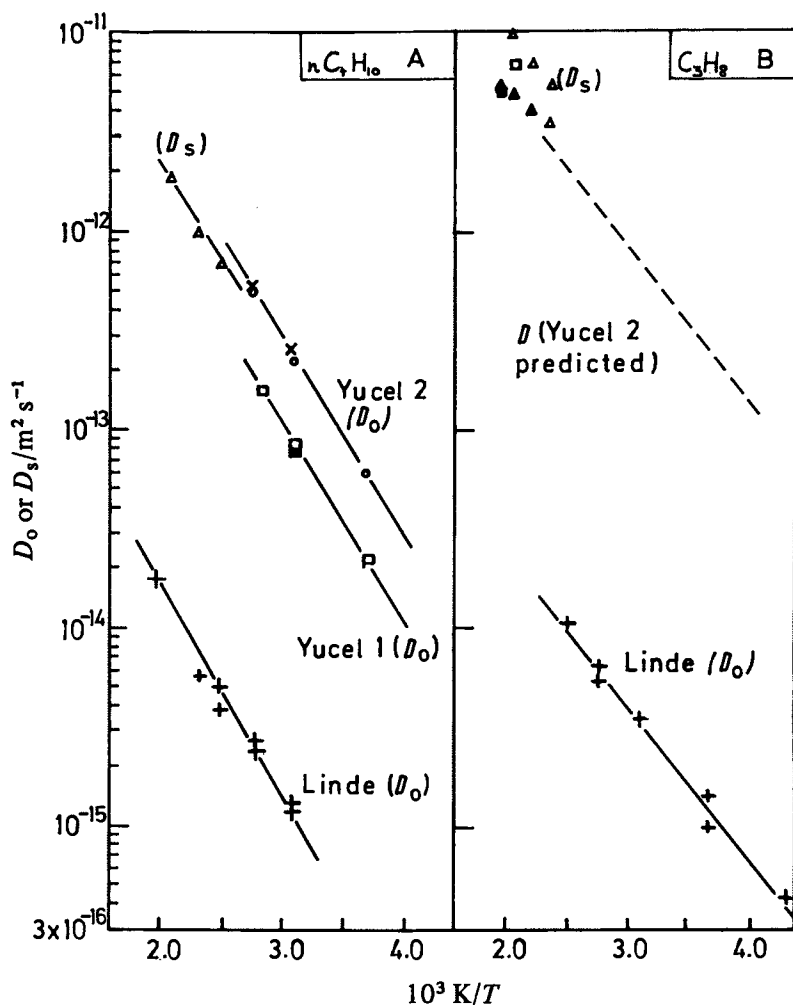


Figure 5.

Arrhenius plot showing comparison of corrected sorption diffusivities ( $D_o$ ) and NMR self diffusivities ( $D_s$ ) for A, butane and B, propane in 5A zeolite crystals. (x, o 55 $\mu$ m and 27 $\mu$ m Charnell crystals I.  $\square$ ,  $\blacksquare$  34 $\mu$ m and 7.3 $\mu$ m Charnell crystals II; +, 3.6 $\mu$ m Linde crystals;  $\blacktriangle$ ,  $\triangle$  21 $\mu$ m Charnell crystals III at 2.0 and 3.5 molecule/cage.)

(Reproduced with permission from Ref. 41. Copyright 1981, J. Chem. Soc.)

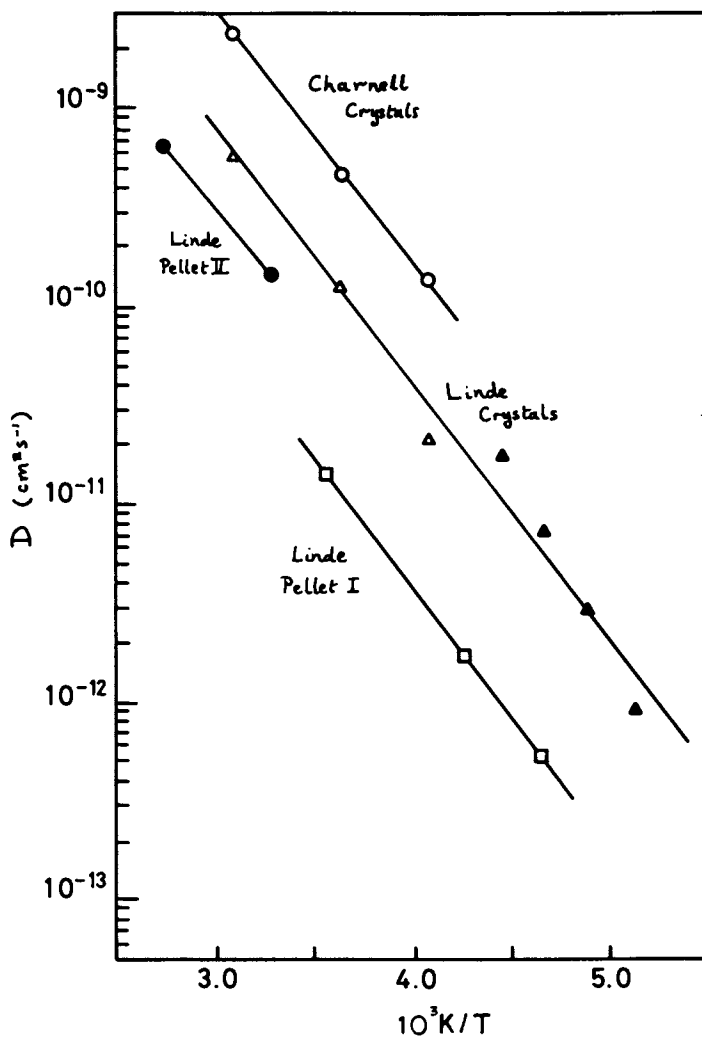


Figure 6. Arrhenius plot showing temperature dependence of corrected diffusivity for  $\text{N}_2$  in various different samples of 4A crystals. (Reproduced with permission from Ref. 35. Copyright 1980, J. Chem. Society.)

similar study carried out in this laboratory, in which heat transfer was allowed for in the analysis of the uptake curves (5) showed the diffusivity to be essentially independent of crystal size (35).

With the development of the fast tracer desorption NMR method a more detailed investigation of these systems became possible. A study of diffusion of  $C_2H_6$  in 5A by this method showed no significant surface barrier, even when the sieve was dehydrated at  $600^\circ C$  under conditions similar to those used commercially (28,29). The sorption capacity and x-ray pattern were essentially the same as for a similar sample dehydrated under milder conditions at  $400^\circ C$ . For the larger crystals the diffusivity was also essentially independent of the dehydration conditions but for the small ( $<1\mu m$ ) crystals the diffusivity was dramatically reduced by high temperature dehydration to within an order of magnitude of the previously reported sorption data for small Linde 5A crystals (29,39). Furthermore the reduction in diffusivity was accompanied by an increase in activation energy from 1.3 kcal/mole to 2.8 kcal/mole, very close to the value of 3.0 kcal/mole for the Linde crystals (39).

It seems clear that, at least in the case of 5A zeolite, the large differences in diffusivity between the uptake rate data for commercial crystals and the NMR data for laboratory synthesized crystals reflect a subtle difference in structure resulting from differences in the initial dehydration conditions. One can speculate that a redistribution of the exchangeable cations may be involved but this has not yet been proved. There seems to be no obvious explanation for the greater sensitivity to thermal treatment shown by the smaller crystals.

#### Diffusion in Type X Zeolites

The lattice of the faujasite zeolites (types X and Y) is much more open than that of zeolite A. The windows consist of 12-membered oxygen rings which are unobstructed by cations. The free diameter ( $\sim 7.5\text{Å}$ ) is large enough to admit quite large molecules such as naphthalene, mesitylene, neo pentane and tertiary amines. Diffusion is rapid and generally too fast to measure by conventional gravimetric or chromatographic methods except in large crystals. Recent experimental studies (43) and detailed theoretical analysis (6,7) reveal that earlier reported diffusivities for hydrocarbons in zeolite X, determined from uptake rate measurements (44-46), were almost certainly in error due to the intrusion of extracrystalline mass and/or heat transfer resistance. A significant repulsive energy barrier associated with passage through the sieve windows is observed only with very large molecules such as triethylamine or tributylamine and, in contrast to the hydrocarbons, diffusion of these species is slow enough to be determined from uptake rate measurements (57).

Saturated Hydrocarbons. A detailed study of the diffusion of a series of linear paraffin and cyclohexane in NaX has been reported by Karger, Pfeifer et al.<sup>(47)</sup>. The results of these investigations reveal a consistent pattern of behaviour which differs in several significant ways from diffusion in zeolite A. The general features are illustrated in figures 7-9. The self diffusivity in all cases decreases strongly with increasing sorbate concentration but this decrease in diffusivity is not due to an increase in diffusional activation energy which, in the case of the linear paraffins, is essentially independent of loading. Comparison of PFG self diffusion measurements and relaxation measurements shows that the reduction in diffusivity arises from a reduction in the rms jump distance which falls to about 1Å at high loadings (see figure 9), presumably as a result of the increasing importance of intermolecular collisions. The comparison of diffusivity and diffusional activation energy for the adsorbed phase and free liquid (figure 8) suggests that at higher loadings intracrystalline diffusion occurs by essentially the same mechanism as liquid diffusion. Indeed the free volume theory has been successfully extended to intracrystalline diffusion<sup>(47)</sup>.

The behaviour of cyclohexane<sup>(48)</sup> and iso-paraffins<sup>(41)</sup> is basically similar to that of the linear alkanes. Activation energies are somewhat lower than for the linear paraffin with the same carbon number and, in the case of cyclohexane, the activation energy decreases with loading (3.0-2.1 kcal/s).

Benzene Benzene diffuses much less rapidly than cyclohexane and the activation energy is higher ( $\sim 5$  kcal/mole). Detailed studies by Lechert and co-workers<sup>(49-51)</sup> reveal that in zeolite Y, which has no delocalized cations, the benzene molecules tend to occupy tetrahedrally disposed sites with the molecules oriented parallel to the six ring at a distance 3.2Å from the S<sub>2</sub> cation. Up to a coverage of 4 molecules/cage the rms jump distance remains reasonably constant (3-4Å) and is approximately consistent with the site-site distance.

Olefins The diffusivity in NaX zeolite decreases by about a factor of 10 in the sequence n-butane>t-butene>l-butene>cis-butene<sup>(52)</sup>. Activation energies for all these species are similar and increase somewhat with loading. Correlation times are also similar and the difference in diffusivity is due to a difference in the rms jump distance, which evidently varies as a result of different degrees of steric hindrance to passage through the 12-membered O ring. Thus for every jump between cages, the slowest diffusing species (cis-butene) makes, on average, about 8 jumps within a cage compared with only about two intra cage jumps for trans-butene. This difference is attributed to the orienting effect of the small but significant dipole moment of cis-butene.

Partial ion exchange of Na<sup>+</sup> for Ag<sup>+</sup> leads to a dramatic reduction in diffusivity for the olefins (more than two orders of

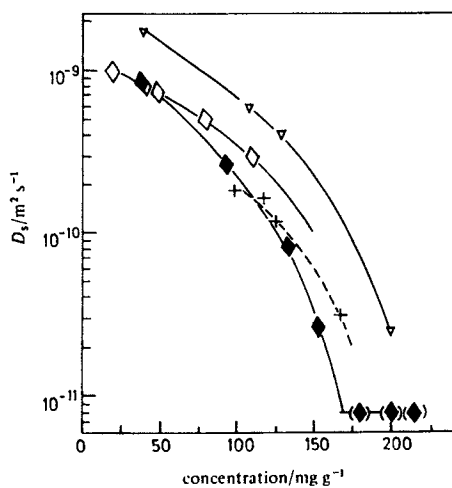


Figure 7.

Concentration dependence of self diffusivity for i-octane ◆, n-heptane ∇, n-octane, ◇ and n-decane at 358K. Points in parenthesis are for fully saturated sieve. (Reproduced with permission from Ref. 41. Copyright 1981, J. Chem. Soc.)

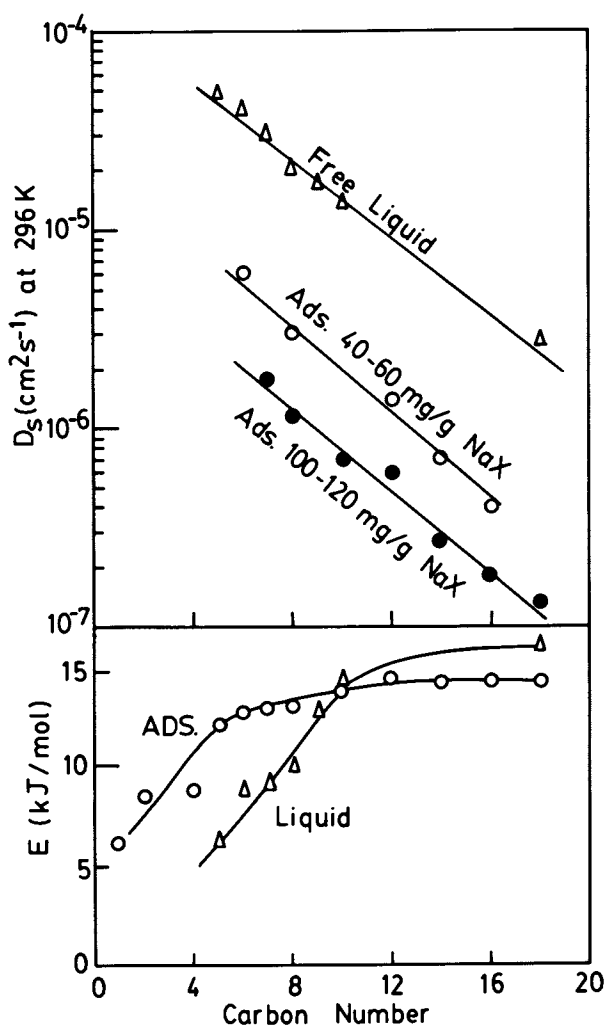


Figure 8.  
Comparison of diffusivities and diffusional activation energies for linear paraffins as free liquids and adsorbed on NaX zeolite.  
(Reproduced with permission from Ref. 47. Copyright 1980, J. Chem. Society.)

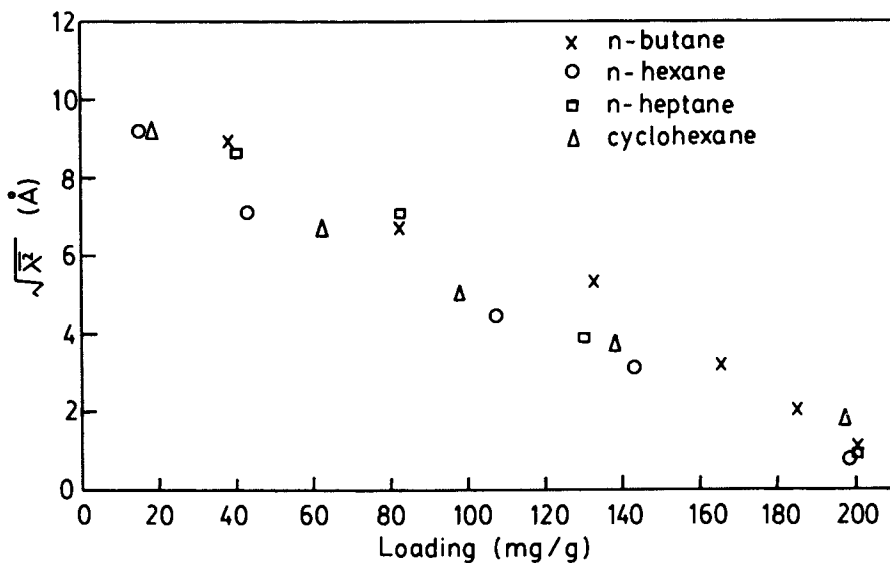


Figure 9.  
Variation of rms jump distance with sorbate concentration for saturated hydrocarbons on NaX zeolite.  
(Reproduced with permission from Ref. 47. Copyright 1980, J. Chem. Society.)

magnitude at 20% exchange) as a result of the strong olefin-Ag<sup>+</sup> interaction<sup>(53)</sup>. There is a parallel increase in correlation time, reflecting a dramatic increase in the mean residence time at an adsorption site rather than any change in rms jump distance. Ion exchange for Tl<sup>+</sup> has the opposite effect, increasing the diffusivity relative to the Na<sup>+</sup> form. The reasons are less obvious.

Theoretical Model As a simple model we may represent the potential field within the zeolite by a symmetric three dimensional sinusoidal function:

$$U = U_0 + \frac{1}{2}V_0(1 - \cos\frac{2\pi x}{a}) + \frac{1}{2}V_0(1 - \cos\frac{2\pi y}{a}) + \frac{1}{2}V_0(1 - \cos\frac{2\pi z}{a}) \quad (7)$$

From this model, following the analysis of Hill<sup>(54)</sup>, one may derive theoretical expressions for the Henry's Law equilibrium constant<sup>(55,56)</sup>.

$$K_C = K_0 \exp(-U_0/kT); \quad K_0 = [\exp(-\frac{V_0}{2kT}) \cdot I_0(\frac{V_0}{2kT})]^3 \left(\frac{v}{kT}\right) \quad (8)$$

and for the diffusivity at low concentration:

$$D = D_* \exp(-V_0/kT); \quad D_* = \frac{a}{\sqrt{2}} \left(\frac{V_0}{m}\right)^{\frac{1}{2}} \quad (9)$$

Using for  $V_0$  the experimental value of the diffusional activation energy one may estimate theoretical values for the pre-exponential factors  $D_*$  and  $K_0$ , which may then be compared with the experimental values. Such a comparison is shown in table 1 and it is evident that in spite of the obvious approximations, the model provides a good representation of the behaviour of these systems at low concentrations.

NMR Sorption Comparison Diffusion of the large triethylamine molecule is sufficiently slow that reliable diffusivities can be determined from uptake rate measurements in  $\sim 50\mu\text{m}$  crystals<sup>(57)</sup>, at least over a limited range of conditions. A comparative study, carried out with the same zeolite samples showed good agreement between the sorption and PFG NMR measurements, both as to the magnitude of the diffusivity ( $\sim 10^{-8}\text{cm}^2\text{s}^{-1}$  at 445K) and the trends with concentration and temperature<sup>(41)</sup>.

#### Acknowledgment

The kind cooperation of Prof. H. Pfeifer and Dr. J. Karger in reviewing the results of the NMR studies is gratefully acknowledged.



TABLE I

Comparison of Theoretical and Experimental Values of  $K_O$  and  $D_*$  for Hydrocarbons in NaX Zeolite  
(after Karger et al. (47))

|   | <u>Experimental Values</u> |  |   | $(D_*)_{\text{Theory}}$ | $(K_O)_{\text{Theory}}$ |
|---|----------------------------|--|---|-------------------------|-------------------------|
|   | $V_O$<br>(kcal/mole)       | $D_* \times 10^3$<br>( $\text{cm}^2 \cdot \text{s}^{-1}$ ) | $K_O \times 10^9$<br>(molecule/<br>cage.Pa) | $(D_O)_{\text{Expt}}$   | $(K_O)_{\text{Expt}}$   |
| CH <sub>4</sub>                         | 1.6                        | 3.5  | 7.6   | 1.3                     | 1.5                     |
| C <sub>2</sub> H <sub>6</sub>           | 2.3                        | 5.0  | 5.0   | 0.8                     | 1.2                     |
| nC <sub>4</sub> H <sub>10</sub>         | 2.5                        | 1.9  | 1.5   | 1.5                     | 3.9                     |
| nC <sub>6</sub> H <sub>14</sub>         | 3.5                        | 6.3  | 1.5   | 0.5                     | 1.9                     |
| nC <sub>7</sub> H <sub>16</sub>         | 3.0                        | 1.6  | 2.3   | 1.6                     | 1.6                     |
| cyclo<br>C <sub>6</sub> H <sub>12</sub> | 3.7                        | 6.4  | 1.5   | 0.5                     | 1.7                     |

(sorbate concentration 15-30 mg/g)

#### Notation

|       |   |             |   |
|-------|---|-------------|---|
| a     | lattice parameter   | L           | column length                             |
| c     | sorbate concentration<br>(fluid phase)                              | m           | mass of sorbate molecule                  |
| D     | intracrystalline diffusivity  | P           | sorbate pressure                          |
| $D_O$ | corrected diffusivity (eqn.6)                                       | r           | crystal radius                            |
| $D_L$ | axial dispersion coefficient  | R           | pellet radius                             |
| $D_p$ | macropore diffusivity   | t           | time                                      |
| $D_s$ | NMR self diffusivity  | T           | absolute temperature                      |
| $D_*$ | pre-exponential factor<br>(eqn. 9)                                  | $U, U_O$    | potential energy (eqn.6)                  |
| f     | function of concentration<br>and cross coefficients<br>(eqn. 5)     | $V_O$       | amplitude of potential                    |
| k     | Boltzmann's constant (eqn.8,9)                                      | V           | volume of super cage                      |
| $k_f$ | external mass transfer co-<br>efficient (eqn. 3)                    | v           | interstitial velocity                     |
| $K_C$ | dimensionless adsorption<br>equilibrium constant<br>(crystal basis) | x, y, z     | coordinates                               |
| $K_p$ | dimensionless adsorption<br>equilibrium constant (pellet<br>basis)  | $\mu$       | mean retention time                       |
|       |   | $\sigma^2$  | variance of chromato-<br>graphic response |
|       |   | $\epsilon$  | bed voidage                               |
|       |   | $\theta$    | particle porosity                         |
|       |   | $\lambda^2$ | mean square jump distance                 |
|       |   | $\tau$      | correlation time                          |
|       |   | $\sigma_O$  | van der Waals radius                      |

Literature Cited

1. Eberly, P.E.; Ind. Eng. Chem. Prod. Res. Develop. 1969, 8, 140-144.
2. Satterfield, C.N.; Frabetti, A.J.; AICHEJl. 1967, 13, 731-738.
3. Moore, R.M.; Katzer, J.R.; AICHEJl. 1972, 19, 816-824.
4. Satterfield, C.N.; Katzer, J.R.; Adv.Chem. 1971, 102, 193-205.
5. Lee, L.K.; Ruthven, D.M.; J. Chem. Soc. Faraday Trans I 1979, 75, 2406-2422.
6. Ruthven, D.M.; Lee, L.K.; Yucel, H.; AICHEJl. 1980, 26, 16-23.
7. Ruthven, D.M.; Lee, L.K.; AICHEJl. 1981, 27, 654-663.
8. Garg, D.R.; Ruthven, D.M.; Chem. Eng. Sci. 1972, 27, 417-423.
9. Yucel, H.; Ruthven, D.M.; J. Colloid Sci. 1980, 74, 186-195.
10. Haynes, H.W.; Chem. Eng. Sci. 1975, 30, 955.
11. Gangwal, S.K.; Hudgins, R.R.; Bryson, A.W.; Silveston, P.L.; Can. J. Chem. Eng. 1971, 49, 113.
12. Scott, D.S.; Lee, W.; Papa, J.; Chem. Eng. Sci. 1974, 29, 2155.
13. Chou, T.S.; Hedgedus, L.L.; AICHEJl. 1978, 24, 255.
14. Boersma-Klein, W.; Moulijn, J.A.; Chem. Eng. Sci. 1979, 34, 959.
15. Haynes, H.W.; Sarma, P.N.; AICHEJl. 1973, 19, 1043.
16. Shah, D.B.; Ruthven, D.M.; AICHEJl. 1977, 23, 804.
17. Edwards, M.F.; Richardson, J.F.; Chem. Eng. Sci. 1968, 23, 109.
18. Langer, G.; Roethe, A.; Roethe, K.P.; Gelbin, D.; Int. J. Heat Mass Transfer 1978, 21, 751-759.
19. Wakao, N.; Kaguei, S.; Nagai, H.; Chem. Eng. Sci. 1978, 33, 183-187.
20. Wakao, N.; Funazkri, T. Chem. Eng. Sci. 1978, 33, 1375-1384.
21. Kumar, R.; Ruthven, D.M.; Can. J. Chem. Eng. - in press.
22. Pfeifer, H.; "NMR, Basic Principles and Progress" Springer, 1972, 7, 53-153.
23. Pfeifer, H.; Phys. Reports (Physics Letters C) 1976, 26, 293-338.
24. Karger, J.; Pfeifer, H.; Z. Chemie 1976, 16, 85-90.
25. Stejskal, E.O.; Tanner, J.E.; J. Chem. Phys. 1965, 42, 288.
26. Tanner, J.E.; Stejskal, E.O.; J. Chem. Phys. 1968, 49, 1768.
27. Karger, J.; Caro, J.; J. Chem. Soc. Faraday Trans I 1977, 73,
28. Karger, J.; AICHEJl. 1982, 28, 417-423.
29. Karger, J.; Pfeifer, H.; Ranscher, M.; Bulow, M.; Sumewitc, N.; Shdanov, S.P.; Z. Phys. Chem. Leipzig
30. Ash, R.; Barrer, R.M.; Surface Sci. 1967, 8, 461.
31. Karger, J.; Surface Sci. 1973, 36, 797-801.
32. Karger, J.; Surface Sci. 1976, 59, 749-754.
33. Darken, L.; Trans. AIMME 1948, 175, 184.
34. Charnell, J.F.; J. Crystal Growth 1971, 8, 291.
35. Yucel, H.; Ruthven, D.M.; J. Chem. Soc. Faraday Trans I 1980, 76, 60-70 and 71-83.
36. Ruthven, D.M.; Can. J. Chem. 1974, 52, 3523-3528.
37. Vavlitis, A.P.; Ruthven, D.M.; Loughlin, K.F.; J. Colloid Sci. 1981, 84, 526-531.

38. Ruthven, D.M.; Derrah, R.I.; J. Chem. Soc. Faraday Trans I 1975, 71, 2031-2044.
39. Ruthven, D.M.; Derrah, R.I.; Loughlin, K.F.; Can. J. Chem. 1973, 51, 3514.
40. Doetsch, I.H.; Ruthven, D.M.; Loughlin, K.F.; Can. J. Chem. 1974, 52, 2717.
41. Karger, J.; Ruthven, D.M.; J. Chem. Soc. Faraday Trans I 1981, 77, 1485-1496.
42. Karger, J.; Caro, J.; Z. Chem. 1976, 16, 331-332.
43. Riekert, L.; Doelle, H.J.; Angew. Chem. 1979, 18, 266-272.
44. Lee, T.Y.; Ma, Y.H.; ACS Symp. Ser 1977, 40, 428.
45. Ma, Y.H.; Lee, T.Y.; AIChEJl. 1976, 22, 147-52.
46. Ruthven, D.M.; Doetsch, I.H.; AIChEJl. 1976, 22, 882-886.
47. Karger, J.; Pfeifer, H.; Rauscher, M.; Walter, A.; J. Chem. Soc. Faraday Trans I 1980, 76, 717.
48. Karger, J.; Lorenz, P.; Pfeifer, H.; Bulow, M.Z.; Z. Phys. Chem. Leipzig 1976, 257, 209-217.
49. Lechert, H.; Wittern, K.P.; Schweitzer, W.; Acta. Phys. Chem. 1978, 24, 201-206.
50. Lechert, H.; Schweitzer, W.; Kairek, H.; "Adsorption of Hydro-Carbons on Zeolites II" p 23-32 Academy of Sciences of GDR, Berlin 1979.
51. Wittern, K.P.; Ph.D. Thesis, University of Hamburg, W. Germany 1979.
52. Karger, J.; Michel, D.; Z. Phys. Chem. Leipzig 1976, 257, 983-992.
53. Karger, J.; Michel, D.; Petzold, A.; Caro, J.; Pfeifer, H.; Schollner, R.; Z. Phys. Chem. Leipzig 1976, 257, 1009.
54. Hill, T.L.; "Introduction to Statistical Thermodynamics", p Addison Wesley, Reading, Mass. 1960.
55. Ruthven, D.M.; Doetsch, I.H.; J. Chem. Soc. Faraday Trans I, 1976, 72, 1043-1050.
56. Karger, J.; Bulow, M.; Haberlandt, R.; J. Colloid Sci. 1977, 60, 386-388.
57. Ruthven, D.M.; Graham, A.M.; Vavlitis, A.; Fifth Internat. Conf. on Zeolites, Naples Proceedings p 535-544, Heyden, London 1980.

RECEIVED November 4, 1982

## Acidity in Zeolite ZSM-5

G. W. SKEELS and W. H. FLANK

Union Carbide Corporation, Tarrytown Technical Center, Tarrytown, NY 10591

Acidity in zeolite ZSM-5 was investigated via thermogravimetry and potentiometric titration measurements on  $\text{NH}_4^+$ - and  $\text{H}_3\text{O}^+$ -exchanged samples subjected to various thermal treatments. Stoichiometric decomposition of the  $\text{NH}_4^+$  moiety to  $\text{NH}_3$  and a hydroxylated zeolite occurs below  $400^\circ\text{C}$ , and is characterized by a first-order weight loss step that corresponds closely with changes observed in the infrared spectra. Weight loss due to dehydroxylation occurs over a temperature range from less than  $400^\circ\text{C}$  to about  $1100^\circ\text{C}$ , with a first-order dehydroxylation step over the interval  $750^\circ\text{C}$ - $1000^\circ\text{C}$ .

Results from the filtrate titrations of the calcined zeolite samples treated in salt solution show that a large fraction of the acidic hydroxyl groups have been lost at temperatures as low as  $400^\circ\text{C}$ . An additional 35% decrease in acidity occurs when the calcination temperature is increased from  $400^\circ\text{C}$  to  $700^\circ\text{C}$ , and almost no acidity remains after calcination at  $1000^\circ\text{C}$ . Maintenance of crystallinity in all samples was confirmed by X-ray powder diffraction data. The  $\text{NH}_4^+$ -exchanged ZSM-5 forms a minor amount of weaker acidity attributable to hydroxoaluminum cations, which is not found in the  $\text{H}_3\text{O}^+$ -exchanged material. Both forms exhibit substantial strong acidity due to the formation of  $\text{H}_3\text{O}^+$ .

These results are consistent with the generalized reaction scheme, initially presented by Rabo et al., in which both  $\text{NH}_4^+$ - and  $\text{H}_3\text{O}^+$ -exchanged zeolites decompose to produce an  $\text{H}^+$ -form that upon further heating becomes a decationized zeolite. This behavior is similar to that reported earlier for calcined ion-exchanged synthetic mordenites, where two distinct sources of acidity were found in the  $\text{NH}_4^+$ -form but not in the  $\text{H}_3\text{O}^+$ -form.

0097-6156/83/0218-0369\$06.00/0

© 1983 American Chemical Society

Acidity in zeolites, particularly Bronsted or proton acidity, was shown many years ago by Rabo, Pickert and co-workers (1) to be more complex than was originally proposed. Later it was shown that the thermal treatment of  $\text{NH}_4\text{Y}$  zeolite produces a zeolite containing hydroxoaluminum cations as the stable end product, rather than solely protons, in order to balance framework negative charges following the decomposition of the ammonium ions, as established by Breck and Skeels in 1976 (2). On the other hand, the acidity in acid-exchanged synthetic mordenite has been shown by Flank and Skeels in 1977 to arise from either  $\text{H}_3\text{O}^+$  or, following removal of adsorbed water at elevated temperatures,  $\text{H}^+$  species balancing framework negative charges (3). The same study showed that the acidity of calcined  $\text{NH}_4^+$ -mordenite arises from two separate and distinct acid centers. Nearly two-thirds of the acidity is due to the presence of  $\text{H}_3\text{O}^+$  or  $\text{H}^+$  species. The remaining third of the acidity is due to the formation of hydroxoaluminum cations during the thermal treatment.

The techniques used to determine acidity in zeolites can be briefly described. The calcined zeolite is treated in a slurry with concentrated NaCl solution. Hydroxoaluminum cations are exchanged and hydrolyzed, producing acid and a soluble aluminum species which, if not trapped in the zeolite, can be removed with the filtrate. Hydronium ions are exchanged in the slurry with no subsequent removal of aluminum. The acid strength, expressed as pKa, of the solutions containing exchanged  $\text{H}_3\text{O}^+$  is nearly two orders of magnitude greater than the pKa of the solutions containing exchanged hydroxoaluminum cations. When both hydronium ions and hydroxoaluminum cations are present, two separate and distinct steps are observed in the potentiometric titration curve.

In addition, from the equivalence point of the titration curve, it is possible to calculate whether the acidity in solution arises from the exchange of  $\text{H}_3\text{O}^+$  or from hydroxoaluminum cations. For example, if the equivalence point of a titration is 2.35 milli-equivalents per gram (meq./g) of zeolite and 2.00 g of sample were slurried in 50  $\text{cm}^3$  of NaCl solution, then the calculated pH of the initial slurry is 1.03, using the simple relation  $\text{pH} = -\log [\text{H}^+]$  and assuming all acidity is due to the exchange of hydronium ions. Clearly, then, if the initial slurry pH was measured as 3.25, this assumption is not correct and the acidity did not arise from the exchange of hydronium ions, but rather from some other species such as hydroxoaluminum cations. This type of chemistry is well-established. Equations and log K values involving hydroxoaluminum cations in zeolites were published by Breck in 1974 (4), and a generalized treatise on aluminum species in solution was published by Baes and Mesmer in 1976 (5).

The study of acidity in the  $\text{H}_3\text{O}^+$ - and  $\text{NH}_4^+$ -exchanged forms of ZSM-5, which is the subject of the

present paper, is part of an overall study, the objective of which is to define the source and nature of acidity in zeolites in general.

### Experimental

A sample of ZSM-5 was prepared, using the reactant compositions described in the patent literature (6). The synthesis was performed by Dr. R. L. Patton of Union Carbide's Tarrytown Technical Center. Part of the sample was exchanged three times for one hour each at reflux with a 10/1 (weight) ratio of 10%  $\text{NH}_4\text{Cl}$  solution to zeolite, washed chloride-free and dried at 100°C. Another part of the sample was treated three times with a 10/1 (weight) ratio of 1N HCl to zeolite, at 95°C for 1 hour, following which the acid-exchanged zeolite was washed chloride-free and dried at 100°C. The chemical analyses of the starting ZSM-5 and the two exchanged forms are shown in Table I.

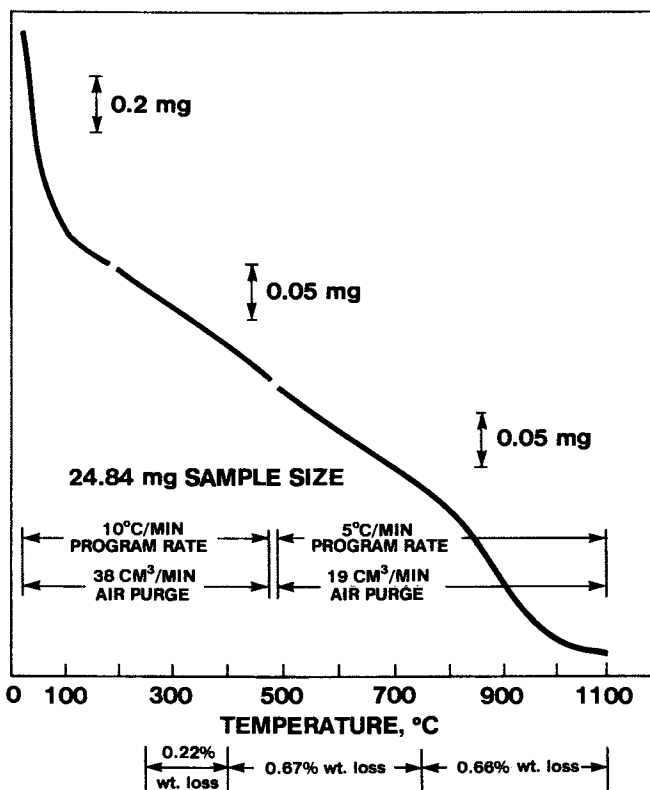
Thermogravimetry (TG) data were obtained on the  $\text{NH}_4^+$ - and  $\text{H}_3\text{O}^+$ -exchanged ZSM-5 samples, as well as on a separately prepared  $\text{NH}_4^+$ -exchanged sample of similar composition, for confirmation purposes. A duPont Model 951 thermogravimetric analyzer was used in conjunction with a Model 990 Recorder-Controller. The TG curves were obtained on approximately 25 mg samples, at a heating rate of 10°C per minute, and under flowing air at a rate of 38  $\text{cm}^3$  per minute. For some samples, the high-temperature portion of the curve was obtained at a heating rate of 5°C per minute and an air purge rate of 19  $\text{cm}^3$  per minute. The sensitivity was varied between 0.2 mg per inch in the lower temperature regions to 0.05 mg per inch at elevated temperatures. An example is shown in Figure 1. The results at the bottom are for this one curve. Overall means and standard deviations are discussed below.

It was ascertained from the TG data that: (a)  $\text{NH}_4^+$  ions were decomposed by 400°C, (b) for both the  $\text{NH}_4^+$ - and the  $\text{H}_3\text{O}^+$ -exchanged ZSM-5 samples, further weight loss due to dehydroxylation occurs in a temperature range from less than 400°C to about 1100°C, with a first-order dehydroxylation step over the interval 750-1000°C, and (c) dehydroxylation is essentially complete by 1000°C. Maximum hydroxyl concentration should be obtained subsequent to complete deamination and prior to dehydroxylation. Therefore, acidity measurements were made on samples calcined in a shallow bed under flowing dry air at temperatures of 400°C, 500°C, 700°C (where acidity should be at or near a maximum), and after calcination at 1000°C (where acidity should drop to nearly zero).

Acidity measurements were obtained either from the slurry or from the resulting filtrate of the calcined zeolite treated with concentrated NaCl solution. Approximately 3 g (anhydrous weight) of the calcined zeolite were treated in 50  $\text{cm}^3$  of 3.4 molar

Table I. Chemical Analysis Data for ZSM-5 Samples

| COMPONENT  | Na <sup>+</sup> -ZSM-5 | NH <sub>4</sub> <sup>+</sup> -ZSM-5 | H <sub>3</sub> O <sup>+</sup> -ZSM-5 |
|--|------------------------|-------------------------------------|--------------------------------------|
| Na <sub>2</sub> O, WT. %   | 0.89                   | <0.03                               | <0.03                                |
| (NH <sub>4</sub> ) <sub>2</sub> O, WT. %                         | —                      | 1.40                                | —                                    |
| Al <sub>2</sub> O <sub>3</sub> , WT. %                           | 3.0                    | 3.06                                | 2.77                                 |
| SiO <sub>2</sub> , WT %  | 83.1                   | 86.50                               | 86.50                                |
| <b>MOLAR RATIO</b>   |                        |                                     |                                      |
| SiO <sub>2</sub> /Al <sub>2</sub> O <sub>3</sub>                 | 47.04                  | 47.97                               | 53.02                                |
| Na <sub>2</sub> O/Al <sub>2</sub> O <sub>3</sub>                 | 0.49                   | —                                   | —                                    |
| (NH <sub>4</sub> ) <sub>2</sub> O/Al <sub>2</sub> O <sub>3</sub> | —                      | 0.90                                | —                                    |

Figure 1. Thermogravimetry curve for H<sub>3</sub>O<sup>+</sup>-ZSM-5 sample.

NaCl solution. In one set of experiments, the slurry was titrated with 0.1 normal NaOH solution in one  $\text{cm}^3$  increments to a pH of about 10. The samples of this set are referred to as the "slurry" samples (titration of the calcined zeolite - NaCl solution slurry). In another set of experiments, the calcined zeolite - NaCl solution slurry was filtered, the filter cake washed with about  $100 \text{ cm}^3$  distilled water, and the combined filtrates were titrated with 0.1 N NaOH solution, again to a pH of about 10. The samples of this latter set are referred to as the "filtrate" samples (the zeolite being removed by filtration prior to titration of the filtrate). In addition to the manual titrations, automated potentiometric titration curves were obtained with a Metrohm E636 Titroprocessor, which has an estimated pH measurement accuracy of  $\pm 0.001$  pH unit and an estimated volumetric addition accuracy of  $\pm 0.001 \text{ cm}^3$  ( $1 \mu\text{l}$ ). An example of the titration curves obtained is shown in Figure 2.

All of the treated zeolite solids, both "filtrate" samples and "slurry" samples, were further analyzed by X-ray powder diffraction. The chemical compositions were determined by standard wet chemical analysis, and the filtrates were analyzed for  $\text{SiO}_2$  and  $\text{Al}_2\text{O}_3$  following titration. The results show that crystallinity was fully maintained in the solids and that the chemical reactions described in this work are confirmed by the analytical data and mass balances.

### Results and Discussion

Two distinct weight loss steps are seen in the TG curve obtained on  $\text{NH}_4^+$ -exchanged ZSM-5, an example of which is shown in Figure 3. One step is observable between about  $250^\circ\text{C}$  and  $400^\circ\text{C}$ , and the other is observable between about  $750^\circ\text{C}$  and  $1000^\circ\text{C}$ . This can be compared to the TG curve obtained on  $\text{H}_3\text{O}^+$ -exchanged ZSM-5 shown in Figure 1. In the case of the  $\text{H}_3\text{O}^+$ -exchanged ZSM-5, only one weight loss step is observed, between about  $750^\circ\text{C}$  and  $1000^\circ\text{C}$ . The magnitude of these steps can best be measured by drawing straight lines tangent to the three segments of the curve that define the step. If that is done, it is obvious that the steps are superimposed on a background of continual weight loss due to dehydroxylation. Interpretation of these types of TG curve was described earlier with  $\text{NH}_4\text{Y}$  (7). In that study, a normal probability plot, like that shown in Figure 4, of weight loss data for 90% exchanged  $\text{NH}_4\text{Y}$  showed that the region of the rapid weight loss step is obviously different in slope from both the higher-temperature portion and the lower-temperature portion of the plot. A fairly straight, kinetically first-order, curve for kaolinite is shown for comparison. (The tail sticking straight down merely shows that nothing happens between removal of surface-adsorbed water at drying temperatures and initiation of decomposition



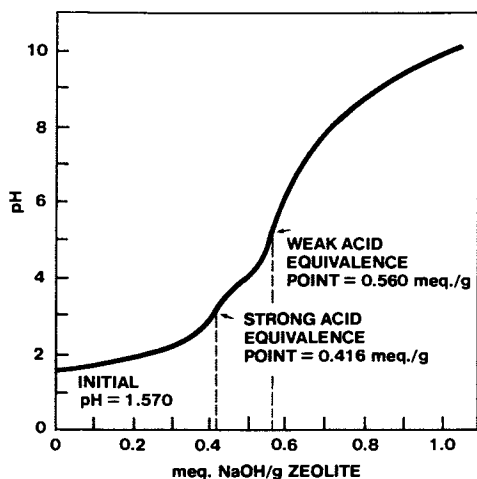


Figure 2. Potentiometric titration curve for 500<sup>o</sup> C calcined NH<sub>4</sub><sup>+</sup>-ZSM-5 slurry sample.

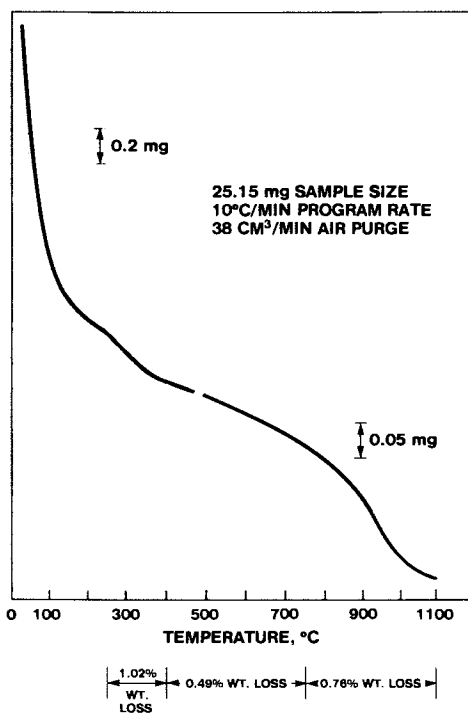


Figure 3. Thermogravimetry curve for NH<sub>4</sub><sup>+</sup>-ZSM-5 sample.

around 400°C.) The separate portions of the  $\text{NH}_4\text{Y}$  plot, with their distinctively different slopes, depict multiple independent processes overlapping each other over the entire temperature range.

A summary of the weight losses ascribed to deamination and dehydroxylation of the various samples is shown in Table II. The assumption that the weight loss in the region 250–400°C observed with the  $\text{NH}_4^+$ -ZSM-5 is due to decomposition of  $\text{NH}_4^+$ , is justified by infrared spectra taken of the samples over that temperature range. As the activation temperature increases to 400°C, the spectra show a decrease in the N-H stretching bands and the growth of an OH band at 3610  $\text{cm}^{-1}$ . All traces of  $\text{NH}_4^+$  bands are removed following air activation at 400°C. A decrease in the 3610  $\text{cm}^{-1}$  band is seen upon heating from 400°C to 800°C, quantitatively corresponding to dehydroxylation. The weight loss step observed on the TG curves of the  $\text{NH}_4^+$ -ZSM-5, in the region 250–400°C, is not observed on the TG curves of  $\text{H}_3\text{O}^+$ -ZSM-5, a further indication that the 250–400°C weight loss step is associated with deamination.

The TG data for  $\text{NH}_4^+$ -exchanged ZSM-5 show a stoichiometric evolution of  $\text{NH}_3$  in the temperature region associated with this weight loss step. The mean value and standard deviation for the weight loss step is 0.88 ( $\pm 0.07$ )  $\text{NH}_3/\text{Al}$ , which corresponds well with the  $\text{NH}_4/\text{Al}$  value of 0.90 obtained from chemical analysis and noted in Table I. While no comparable weight loss step is observed in the TG curves of  $\text{H}_3\text{O}^+$ -exchanged ZSM-5, it is presumed that the water associated with the proton is gradually lost, as the curves imply. From 400°C to 1100°C the TG curves of both samples are nearly identical. The mean value for the moles of  $\text{H}_2\text{O}$  evolved per formula weight of  $\text{Al}_2\text{O}_3$  in the zeolite in the first-order step over the interval 750–1000°C is 0.95 ( $\pm 0.06$ ). Note that the total moles of  $\text{H}_2\text{O}$  per mole of  $\text{Al}_2\text{O}_3$  that are lost between 400°C and 1100°C are about 2.4 for both  $\text{NH}_4^+$ - and  $\text{H}_3\text{O}^+$ -ZSM-5. All these data are consistent with the generalized reaction scheme presented earlier by Rabo et al. for the preparation of decationized zeolites (1,8) and illustrated in Figure 5 for ZSM-5. Comparable intermediates are formed by heating of both ion-exchanged forms, and further heating produces a decationized product.

It was ascertained from both TG and IR data that  $\text{NH}_4^+$  ions were decomposed by 400°C. Thus, the samples calcined at 400°C should contain a maximum concentration of Bronsted acid sites. In order to determine the changes in zeolite acidity occurring between deamination and just prior to the rapid weight loss step, samples were calcined for two hours at 700°C. Finally, in order to show that loss of acidity accompanies completion of dehydroxylation, samples were calcined for two hours at 1000°C.

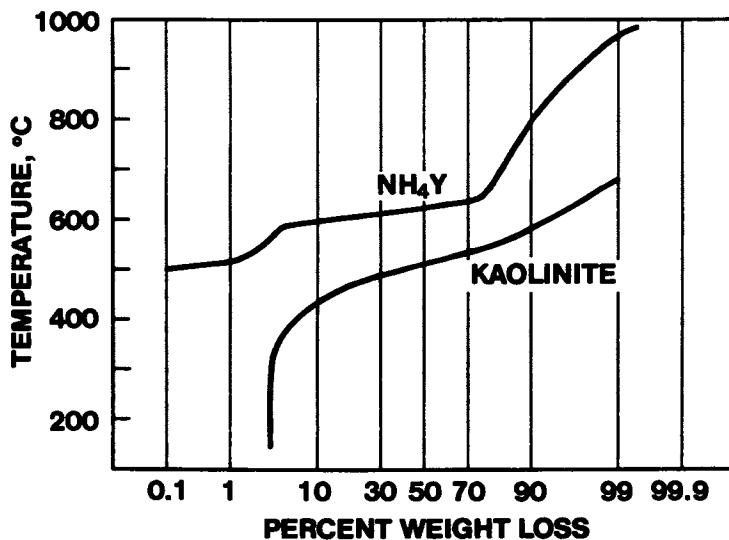


Figure 4. Normal probability plots of TG weight loss data for NH<sub>4</sub>Y and Kaolinite. (Reproduced with permission from Ref. 7. Copyright 1980, John Wiley and Sons, Ltd.)

Table II. Summary of Thermogravimetry Data for ZSM-5 Samples

|   | NH <sub>4</sub> <sup>+</sup> -ZSM-5 | H <sub>3</sub> O <sup>+</sup> -ZSM-5 |
|---|-------------------------------------|--------------------------------------|
| <b>STEP 1</b>   |                                     |                                      |
| TEMPERATURE RANGE, °C   | 250- 400                            | —                                    |
| PERCENT WEIGHT LOSS   | 0.97 (0.08)*                        | —                                    |
| MOLES NH <sub>3</sub> EVOLVED/AI IN ZEOLITE                               | 0.88 (0.07)                         | —                                    |
| <b>STEP 2</b>   |                                     |                                      |
| TEMPERATURE RANGE, °C   | 750-1000                            | 750-1000                             |
| PERCENT WEIGHT LOSS   | 0.55 (0.02)                         | 0.52 (0.03)                          |
| MOLES H <sub>2</sub> O EVOLVED/ AI <sub>2</sub> O <sub>3</sub> IN ZEOLITE | 0.95 (0.06)                         | 0.95 (0.05)                          |
| <b>ADDITIONAL DEHYDROXYLATION</b>   |                                     |                                      |
| TEMPERATURE RANGE, °C   | 400-1100                            | 400-1100                             |
| PERCENT WEIGHT LOSS   | 0.87 (0.13)                         | 0.77 (0.03)                          |
| MOLES H <sub>2</sub> O EVOLVED/ AI <sub>2</sub> O <sub>3</sub> IN ZEOLITE | 1.53 (0.23)                         | 1.42 (0.05)                          |
| <b>TOTAL DEHYDROXYLATION ABOVE 400°C</b>                                  |                                     |                                      |
| TEMPERATURE RANGE, °C   | 400-1100                            | 400-1100                             |
| PERCENT WEIGHT LOSS   | 1.42 (0.16)                         | 1.28 (0.05)                          |
| MOLES H <sub>2</sub> O EVOLVED/ AI <sub>2</sub> O <sub>3</sub> IN ZEOLITE | 2.48 (0.27)                         | 2.36 (0.09)                          |

\* VALUES IN PARENTHESES ARE STANDARD DEVIATIONS

Potentiometric titration curves obtained with the filtrates following NaCl treatment of these last samples (treated at 1000°C) are shown in Figure 6. Little acidity is observed. After 700°C, Figure 7 shows appreciable acidity, with two steps visible for the  $\text{NH}_4^+$ -form. (Note the inflection at about pH 4.) The most acidity is seen after 400°C calcination, and again two end-points are clearly noted for the  $\text{NH}_4^+$ -exchanged sample, as shown in Figure 8. The curves are fairly sharp for these filtrate samples because there are no hydrolysis reactions (9) to provide a buffering effect, as illustrated in the slurry sample curves of Figure 7. A summary of the titration end-points is shown in Table III for all the above-noted samples calcined at the three different temperatures.

The last column in Table III shows that, as expected, maximum zeolite acidity was measured with the samples calcined at 400°C. Acidity decreases as the calcination temperature is increased to 700°C, showing that the hydroxyl groups lost in this interval are also acidic. Following the rapid weight loss step, after 1000°C, very little acidity remains in the sample. Strong acidity, as evidenced by the low initial pH measurements, was obtained on all the samples. (Data are shown in the third column of Table IV and the last column of Table V.)

The calcined  $\text{H}_3\text{O}^+$ -exchanged samples all give a smooth S-shaped titration curve. This is indicative of the presence in the solution of a single strong acid species, presumably  $\text{H}_3\text{O}^+$ . The inflected titration curves of all of the calcined  $\text{NH}_4^+$ -exchanged samples, examples of which can be found in Figures 7 and 8, show the presence of two acidic species. The stronger one is attributable to  $\text{H}_3\text{O}^+$ , and the weaker one is attributable to hydroxoaluminum cation species. Slurry sample pH and titrated acidity data are shown in Table IV. The highly acidic pH of these samples can be noted, as well as the increasing contribution from hydroxoaluminum cations in the calcined  $\text{NH}_4^+$ -ZSM-5 samples as the temperature increases. Analytical data, however, show that the number of Al ions is not changing, so the effect must be ascribed to progressive thermal stripping of OH groups from the Al cations.

The relationships between measured pH, titrated meq.  $\text{H}_3\text{O}^+$  per gram and calculated pH values, for the filtrate samples, are shown in Table V. The molar  $\text{H}^+/\text{Al}$  ratio is also tabulated, demonstrating that a third of the proton sites are dehydroxylated by 400°C and another third by 700°C. This is further supported by the observation of decreased absorbance of the OH band at  $3610\text{ cm}^{-1}$  in the infrared spectrum as the temperature is increased from 400°C to 800°C. Assuming that all strong acidity is derived from the exchange of  $\text{H}^+$  in the zeolite by  $\text{Na}^+$  in the concentrated NaCl solution, the filtrate pH is a direct measure of that exchange, using the simple relation  $\text{pH} = -\log [\text{H}^+]$ . For  $\text{H}_3\text{O}^+$ -ZSM-5 calcined at 400°C, the filtrate sample titer is 0.431 meq.  $\text{H}_3\text{O}^+/\text{g}$  of

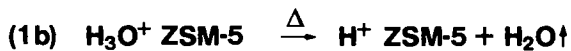
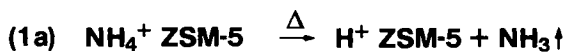


Figure 5. Reaction scheme for the preparation of decationized zeolite ZSM-5.

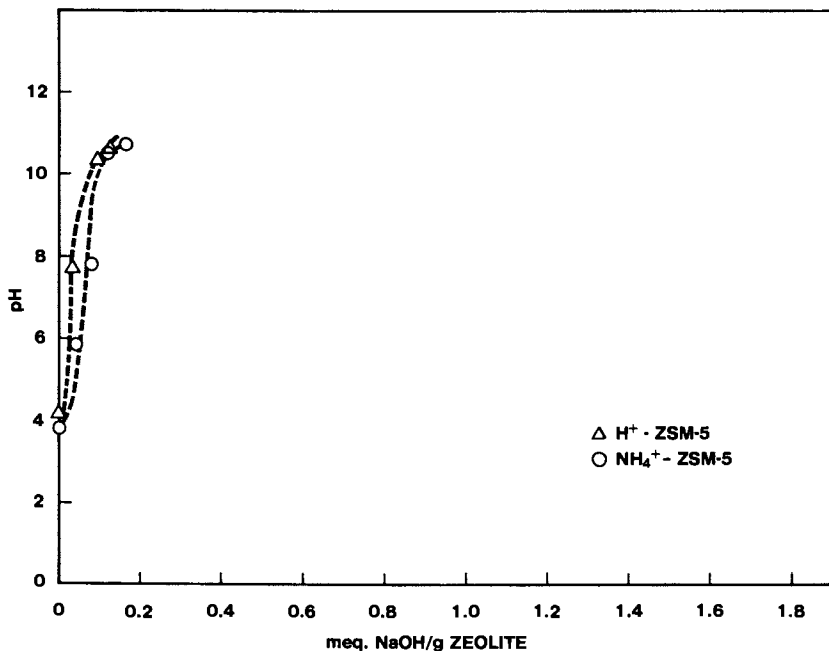


Figure 6. Potentiometric titration curves for 1000<sup>o</sup> C calcined NH<sub>4</sub><sup>+</sup> and H<sub>3</sub>O<sup>+</sup>-ZSM-5 filtrate samples.

Table III. Titration Endpoints for Calcined  $\text{NH}_4^+$ - and  $\text{H}_3\text{O}^+$ -ZSM-5 Samples

| ION EXCHANGED FORM     | CALCINATION TEMP., °C | SAMPLE TYPE | TITRATED ACIDITY, MEQ./GRAM |                                  |        |
|------------------------|-----------------------|-------------|-----------------------------|----------------------------------|--------|
|                        |                       |             | $\text{H}_3\text{O}^+$      | $\text{Al}(\text{OH})_x^{(3-x)}$ | TOTAL  |
| $\text{NH}_4^+$        | 400                   | SLURRY      | 0.387                       | 0.071                            | 0.458  |
| $\text{H}_3\text{O}^+$ | 400                   | SLURRY      | 0.565                       | —                                | 0.565  |
| $\text{NH}_4^+$        | 400                   | FILTRATE    | 0.243                       | 0.092                            | 0.335  |
| $\text{H}_3\text{O}^+$ | 400                   | FILTRATE    | 0.431                       | —                                | 0.431  |
| $\text{NH}_4^+$        | 700                   | SLURRY      | 0.213                       | 0.211                            | 0.424  |
| $\text{H}_3\text{O}^+$ | 700                   | SLURRY      | 0.389                       | —                                | 0.389  |
| $\text{NH}_4^+$        | 700                   | FILTRATE    | 0.140                       | 0.062                            | 0.202  |
| $\text{H}_3\text{O}^+$ | 700                   | FILTRATE    | 0.245                       | —                                | 0.245  |
| $\text{NH}_4^+$        | 1000                  | FILTRATE    | <0.015                      | —                                | <0.015 |
| $\text{H}_3\text{O}^+$ | 1000                  | FILTRATE    | <0.015                      | —                                | <0.015 |

Table IV. Titrated Acidity Data for Slurry Samples of Calcined  $\text{H}_3\text{O}^+$ - and  $\text{NH}_4^+$ -ZSM-5

| SAMPLE                        | CALCINATION TEMP., °C | EQUILIBRIUM pH OF NaCl SLURRY | TITRATED ACIDITY               |  |               |
|-------------------------------|-----------------------|-------------------------------|--------------------------------|--|---------------|
|                               |                       |                               | $\text{H}_3\text{O}^+$ meq./gm | $\text{Al}(\text{OH})_x^{(3-x)}$ meq./gm | TOTAL meq./gm |
| $\text{H}_3\text{O}^+$ -ZSM-5 | 400                   | 1.05                          | 0.565                          | —  | 0.565         |
| $\text{H}_3\text{O}^+$ -ZSM-5 | 500                   | 1.505                         | 0.507                          | —  | 0.507         |
| $\text{H}_3\text{O}^+$ -ZSM-5 | 700                   | 1.30                          | 0.389                          | —  | 0.389         |
| $\text{NH}_4^+$ -ZSM-5        | 400                   | 1.20                          | 0.387                          | 0.071                                    | 0.458         |
| $\text{NH}_4^+$ -ZSM-5        | 500                   | 1.570                         | 0.416                          | 0.144                                    | 0.560         |
| $\text{NH}_4^+$ -ZSM-5        | 700                   | 1.51                          | 0.213                          | 0.211                                    | 0.424         |

Table V. Titrated Acidity Data for Filtrate Samples of Calcined  $\text{H}_3\text{O}^+$ - and  $\text{NH}_4^+$ -ZSM-5

| SAMPLE                        | CALCINATION TEMP., °C | TITRATED ACIDITY meq./g | MOLAR $\text{H}^+/\text{Al}^{**}$ | INITIAL       | MEASURED pH |
|-------------------------------|-----------------------|-------------------------|-----------------------------------|---------------|-------------|
|                               |                       |                         |                                   | CALCULATED pH |             |
| $\text{H}_3\text{O}^+$ -ZSM-5 | 400                   | 0.431                   | 0.65                              | 2.14          | 2.08        |
| $\text{H}_3\text{O}^+$ -ZSM-5 | 700                   | 0.245                   | 0.37                              | 2.46          | 2.45        |
| $\text{NH}_4^+$ -ZSM-5        | 400                   | 0.243*                  | 0.63                              | 2.48          | 2.44        |
| $\text{NH}_4^+$ -ZSM-5        | 700                   | 0.140*                  | 0.30                              | 2.49          | 2.45        |

\* STRONG ACIDITY ONLY

\*\* CALCULATED FROM THE ANALYSIS OF THE FILTERED SOLIDS

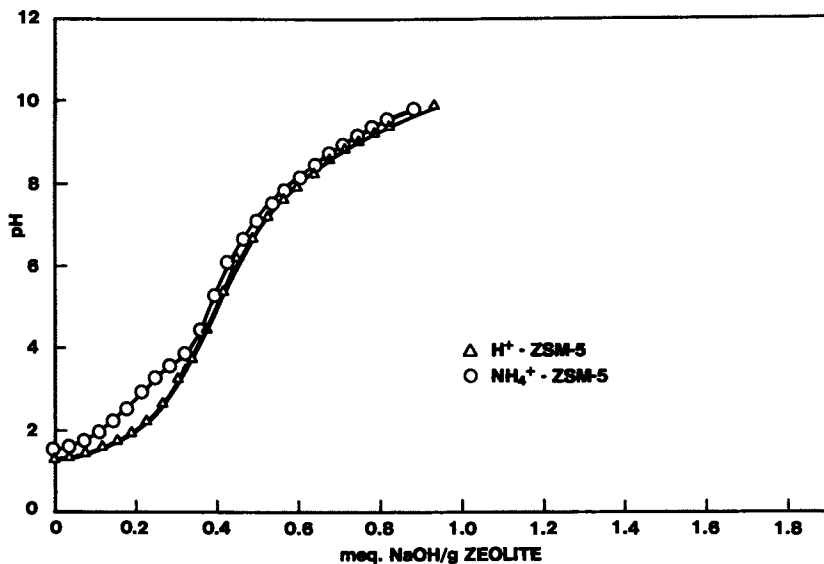


Figure 7. Potentiometric titration curves for 700 °C calcined  $NH_4^+$  and  $H_3O^+$ -ZSM-5 slurry samples.

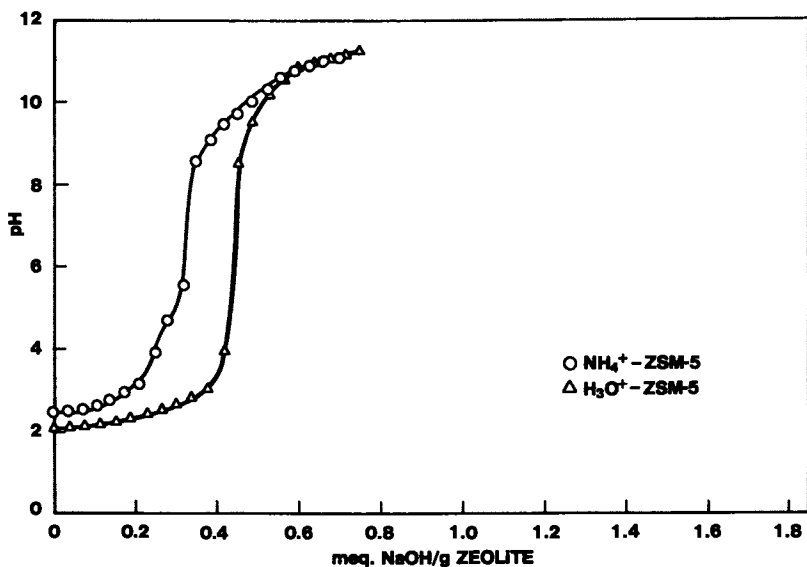


Figure 8. Potentiometric titration curves for 400 °C calcined  $NH_4^+$  and  $H_3O^+$ -ZSM-5 filtrate samples.

zeolite, which calculates out to a pH of 2.14. The initial pH measured on the filtrate was 2.08. With  $\text{H}_3\text{O}^+$ -ZSM-5 calcined at  $700^\circ\text{C}$ , the calculated pH and measured pH are even closer.

With the filtrate samples of the  $\text{NH}_4^+$ -ZSM-5, only the estimation of the first end-point, due to the strongest acid, was used in the calculations. For  $\text{NH}_4^+$ -ZSM-5 calcined at  $400^\circ\text{C}$ , the filtrate titer is 0.243 meq.  $\text{H}_3\text{O}^+$ /g of zeolite. The calculated pH is 2.48, compared to the initial pH measured on the filtrate of 2.44. For  $\text{NH}_4^+$ -ZSM-5 calcined at  $700^\circ\text{C}$ , the values are also quite close. The agreement in these measured and calculated numbers shown in Table V is quite satisfactory.

The only question that might be raised is whether any of the observations, particularly those relating to the use of concentrated NaCl solution, are an artifact of the procedures employed. To address this, it can be noted that the effect of 3.4 M NaCl is dramatically different from that of  $\text{H}_2\text{O}$  or even sub-molar NaCl solution, so that comparisons with effects seen in these media cannot be made. Furthermore, after undergoing all of the treatment chemistry described, the recovered solids still retain full crystallinity, as measured by X-ray powder diffraction and micropore sorption capacity.

It should also be remembered that the chemistry we are describing is kinetically very fast. It takes place in seconds, is a consequence of, and merely reflects what happened during the prior thermal treatment of the sample. If attack on framework Al were to commence only upon contact with the NaCl solution, the extent of hydrolysis apparently observed after just 10 seconds would be kinetically unlikely. Moreover, no further change can be seen over the next several hours. Given these circumstances, it is virtually inconceivable that some of the Al-O-Si bonds were not already ruptured when the calcined zeolite came in contact with the concentrated NaCl solution.

### Conclusions

We can conclude that the overall decationization of ZSM-5 proceeds in accord with the originally proposed scheme of Rabo et al.(1) depicted in Figure 5. With  $\text{NH}_4^+$ -ZSM-5, deamination is complete by  $400^\circ\text{C}$ , and the resulting zeolite product is essentially in the classical  $\text{H}^+$ -zeolite form. Formation of hydroxoaluminum cations is slight, and while the acidity attributed to the formation of these species appears to increase with increasing calcination temperature, as shown in Table IV, the analytical evidence suggests that the actual number of hydroxoaluminum cations remains constant at less than about 20%. The amount of Al coming out of the solid and appearing in the filtrate doesn't change with calcination temperature. Thus, the increase in acidity due to the aluminum species can be attributed to change in net charge on the aluminum cation, i.e.,

$$\text{Al}(\text{OH})_2^+ \rightarrow \text{Al}(\text{OH})_2^{2+} \rightarrow \text{Al}^{3+}.$$

The  $\text{H}^+$ -ZSM-5 produced from the calcination of both  $\text{H}_3\text{O}^+$ - and  $\text{NH}_4^+$ -ZSM-5, as shown in Figure 5, begins to dehydroxylate at temperatures even below  $400^\circ\text{C}$ , as judged by



the  $H^+/Al$  ratio of the 400°C-calcined samples. As the calcination temperature increases between 400°C and 700°C, a substantial number of protons are lost through dehydroxylation. From the acidity measurements, it can be deduced that about one-third dehydroxylation of the proton sites has occurred by 400°C, and another third has occurred by 700°C. This is quantitatively substantiated by the IR data.

The rapid weight loss step in the TG curves which occurs above 750-800°C, and whose temperature range is proportional to Si/Al ratio (10), cannot be attributed merely to the condensation of the  $H^+$  and lattice oxygens. Acidity measurements have already shown that more than two-thirds of the proton sites are dehydroxylated by heating to 700°C. The additional  $H_2O$  evolved during the rapid weight loss step must come from other, non-acidic, hydroxyl groups associated with the remaining proton sites in this silica-rich structure.

The behavior of  $NH_4^+$ -ZSM-5 is similar to that found earlier with calcined  $NH_4^+$ -mordenite (3), in that two distinct sources of acidity were found, with the major one being  $H_3O^+$ . This is in contrast to calcined  $NH_4Y$ , where hydroxoaluminum cations predominate, as was shown by Breck and Skeels (2). In mordenite nearly two-thirds of the measured acidity was due to  $H_3O^+$  and about a third was due to the hydrolysis of hydroxoaluminum cations. As in  $H_3O^+$ -mordenite, no hydroxoaluminum cation species were detected with  $H_3O^+$ -ZSM-5. We conclude that acidity in ZSM-5 conforms rather well to the classic protonic picture.

#### Literature Cited

1. J. A. Rabo, P. E. Pickert, D. N. Stamiros and J. E. Boyle, Actes Congr. Intern. Catalyse, 2e, Paris, 1960 (Publ. 1961), 2, 2055.
2. D. W. Breck and G. W. Skeels, Proc. Int. Congr. Catal., 6th, London, 1976 (Publ. 1977), 2, 645.
3. W. H. Flank and G. W. Skeels, presented at Fifth North American Meeting of the Catalysis Society, Pittsburgh, April 1977.
4. D. W. Breck, "Zeolite Molecular Sieves", Wiley-Interscience, New York, 1974.
5. C. F. Baes, Jr. and R. E. Mesmer, "The Hydrolysis of Cations", Wiley-Interscience, New York, 1976.
6. R. J. Argauer and G. R. Landolt, U.S. Patent 3,702,886 (1972).
7. W. H. Flank and G. W. Skeels, Fifth International Conference on Zeolites, Naples, 1980, p. 344.
8. J. A. Rabo, U.S. Patent 3,130,006 (1964).
9. D. W. Breck and G. W. Skeels, Fifth International Conference on Zeolites, Naples, 1980, p. 335.
10. A. P. Bolton and M. A. Lanewala, J. Catalysis 1970, 18, 154.

RECEIVED November 4, 1982

## Conversion of C<sub>2</sub>-C<sub>10</sub> to Higher Olefins over Synthetic Zeolite ZSM-5

W. E. GARWOOD

Mobil Research and Development Corporation, Paulsboro, NJ 08066

The phenomena of shape-selective polymerization is introduced and described as it applies to the conversion of C<sub>2</sub>-C<sub>10</sub> olefins over ZSM-5 to higher olefins up to C<sub>30</sub> and higher. Reaction conditions favoring higher molecular weight product are low temperature (200-260°C), high pressure (300-1500 psig), and long contact time (0.5-1 WHSV). The reaction under these conditions proceeds through the acid-catalyzed steps of (1) oligomerization, (2) isomerization-cracking to a mixture of intermediate carbon number olefins, and (3) copolymerization to give a continuous boiling product containing all carbon numbers. The intermediates of step 2 at sub-atmospheric pressure are an equilibrium mix of primarily C<sub>4</sub>-C<sub>7</sub> olefins. Amorphous silica alumina gives a product containing more aromatics, less total olefins, and more highly-branched olefins, confirming the shape-selective constraints of ZSM-5.

The activity of acid-type catalysts for polymerization of olefins to higher boiling product has long been known, as reviewed by Oblad et al. (1). Depending on reaction conditions, the product can be predominantly olefinic, or a mixture of olefins, paraffins, naphthenes and aromatics ("conjunct" polymerization).

Previous publications on ZSM-5 have described its shape selective properties (2, 3) and also its use for conversion of light olefins to both olefinic (4) and aromatic (5) mixtures of hydrocarbons boiling in the gasoline range. Further, methanol yields a C<sub>5</sub>-C<sub>11</sub> aromatic gasoline over HZSM-5 at moderate reaction conditions via an intermediate mixture of light olefins (MTG process) (6). More recently, conditions for obtaining a high yield of C<sub>2</sub>-C<sub>5</sub> olefins from methanol have been reported (7).

0097-6156/83/0218-0383\$06.00/0  
© 1983 American Chemical Society

The present paper describes the phenomena of shape-selective polymerization involved in converting  $C_2$ - $C_{10}$  olefins over HZSM-5 to higher boiling olefins and the similarities and differences compared to amorphous silica-alumina. The channel systems of ZSM-5 (8), Figure 1, impose shape-selective constraints on the shape of the large molecules accounting for the differences with amorphous catalysts.

### Experimental

The experiments were conducted in a high-pressure micro-reactor capable of operating up to 2000 psig. The reactor, enclosed in a three-zone heater, had an isothermal reaction zone holding up to 10 cm<sup>3</sup> of catalyst. Back pressure was maintained by an inverted Grove Loader.

The olefin feed stocks were all commercial grade of >95% purity, used without further purification. Light products  $<C_5$  were analyzed by both gas chromatography and mass spectrometry. Liquid analysis was done by gas chromatography and boiling point curves by ASTM method D-2887 (gas chromatography).

### Results and Discussion

#### Effect of Temperature on Propylene Conversion at Atmospheric Pressure

At 530°F, atmospheric pressure, 0.6 WHSV, propylene converts to a mixture of predominantly  $C_3$ - $C_{11}$  olefins (Table I) of the composition typical of that reported by Givens et al. (4).

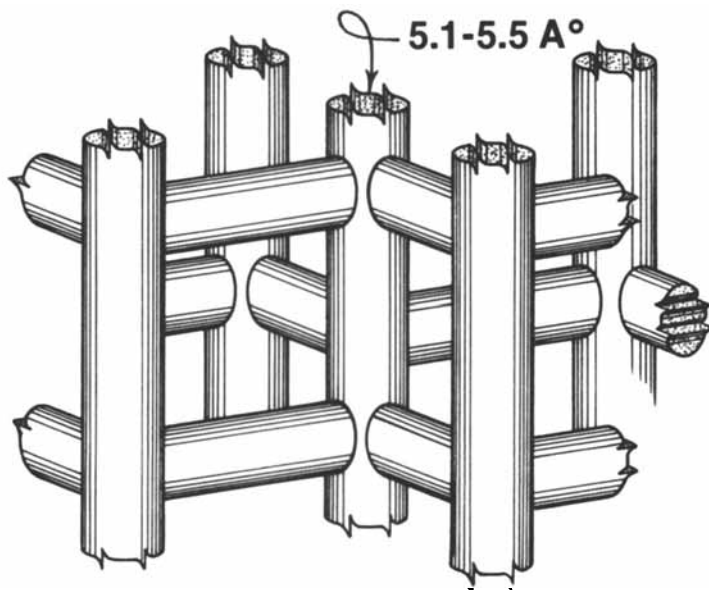
The products are 95% olefins, with the remainder mostly paraffins and some naphthenes in the higher carbon numbers. At higher temperature conjunct polymerization occurs (involving olefin cyclization to naphthene, followed by hydrogen transfer from naphthenes to olefin). The reaction proceeds essentially to completion at 730°F to give the mixture of paraffins and aromatics shown in Table II.

#### Effect of Pressure

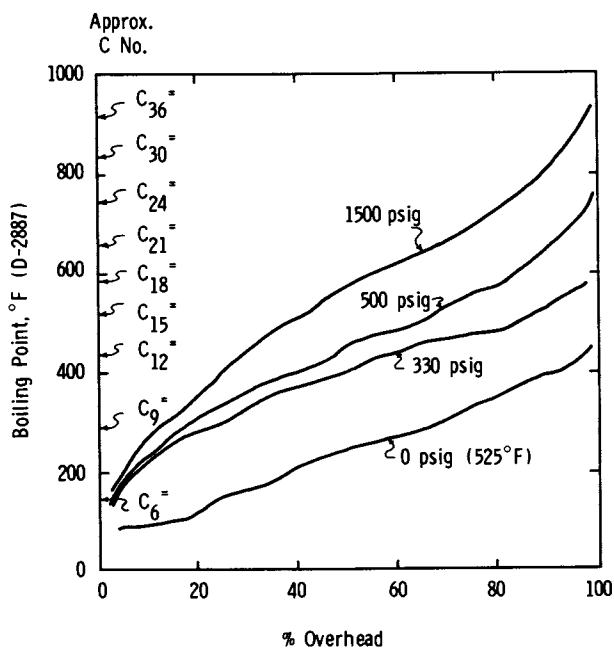
Figure 2 shows that the boiling range of the heavy products from propylene increases steadily with increasing pressure. Propylene conversion is essentially complete at 400°F, 330 psig and higher. The range of the product at 1500 psig includes all carbon numbers from  $C_6$  to about  $C_{36}$ .

#### Effect of Contact Time

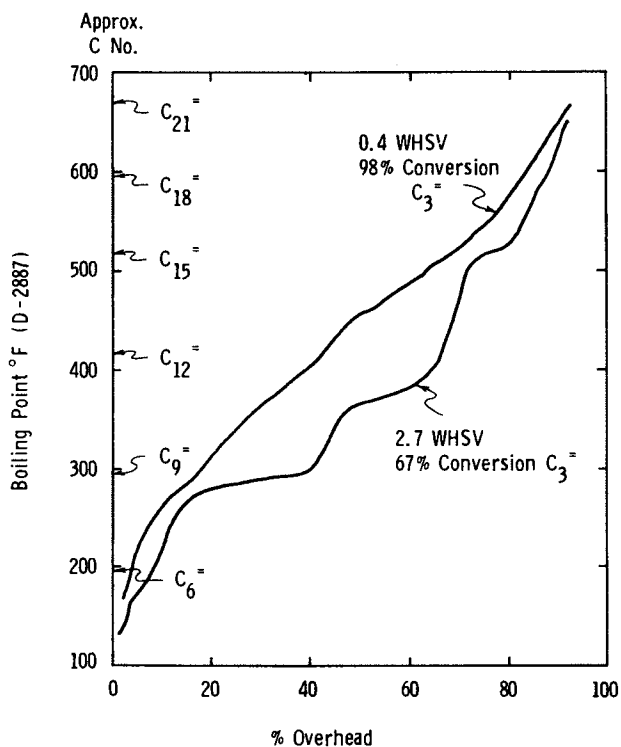
Evidence of oligomers appears at short contact time. Figure 3 shows plateaus corresponding to the trimer, tetramer and pentamer of propylene at conditions of 2.7 WHSV, 400°F, 500 psig at which propylene conversion is 67%. This contrasts with the smooth curve at 0.4 WHSV, 98% propylene conversion.



**Figure 1**  
**Channel System in ZSM-5**  
 Kokotailo, et al. (Ref. 8)



**Figure 2**  
**Effect of Pressure**  
 C<sub>3</sub> Charge 0.4 WHSV 400°F



**Figure 3**  
**Effect of Space Velocity**  
**C<sub>3</sub>= Charge 500 psig 400°F**

TABLE I

CONVERSION OF PROPYLENE AT 530°F, 0 PSIG, 0.6 WHSV

| <u>Product Olefin</u>        | <u>Wt %</u> |
|------------------------------|-------------|
| C <sub>2</sub>               | 0.1         |
| C <sub>3</sub>               | 2.0         |
| C <sub>4</sub>               | 8.6         |
| C <sub>5</sub>               | 16.6        |
| C <sub>6</sub>               | 15.5        |
| C <sub>7</sub>               | 16.6        |
| C <sub>8</sub>               | 13.6        |
| C <sub>9</sub>               | 12.3        |
| C <sub>10</sub>              | 10.0        |
| C <sub>11</sub> <sup>+</sup> | <u>4.7</u>  |
|                              | 100.0       |

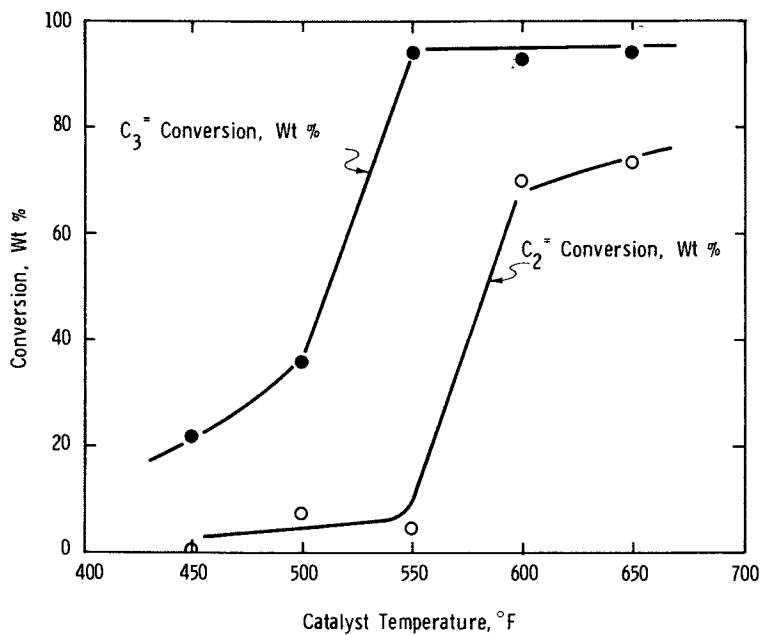
TABLE II

CONVERSION OF PROPYLENE AT 730°F, 0 PSIG, 0.5 WHSV

| <u>Carbon No.</u> | <u>Olefin</u> | <u>Isoparaffin</u> | <u>n-Paraffin</u> | <u>Aromatic</u> | <u>Total, Wt %</u> |
|-------------------|---------------|--------------------|-------------------|-----------------|--------------------|
| 1                 | -             | -                  | 0.2               | -               | 0.2                |
| 2                 | -             | -                  | 0.8               | -               | 0.8                |
| 3                 | 0.4           | -                  | 23.3              | -               | 23.7               |
| 4                 | 0.7           | 17.1               | 9.1               | -               | 26.9               |
| 5                 | 0.1           | 7.2                | 1.7               | -               | 9.0                |
| 6                 | 0.1           | 1.0                | 0.2               | 2.0             | 3.3                |
| 7                 | 0.1           | 0.9                | 0.2               | 10.7            | 11.9               |
| 8                 | -             | -                  | -                 | 12.8            | 12.8               |
| 9                 | -             | -                  | -                 | 6.3             | 6.3                |
| 10                | -             | -                  | -                 | 2.1             | 2.1                |
| 11+               | -             | -                  | -                 | <u>3.0</u>      | <u>3.0</u>         |
|                   | 1.4           | 26.2               | 35.5              | 36.9            | 100.0              |

Olefin Charge

Of the C<sub>2</sub>-C<sub>10</sub> olefins, ethylene is the least reactive. Figure 4 shows that charging a mixture of ethylene and propylene at 400 psig and increasing temperature from 400-600°F, propylene reacts before ethylene. At one "window" conversion of propylene is 95%, compared to 5% for ethylene; thus, providing a separation procedure for the two monomers. Ethylene finally converts also, at a higher temperature.



**Figure 4**  
Conversion of C<sub>2</sub>=/C<sub>3</sub>= Mixture  
400 psig 0.4-0.6 WHSV C<sub>2</sub>= 0.4 WHSV C<sub>3</sub>=

$C_5$  and  $C_6$  olefins convert at about the same rate (Figure 5), charging a mixture of the two. Also, 1-decene gives essentially the same boiling range product as propylene at 0.5 WHSV, 1500 psig, 450°F (Figure 6), ~98% conversion to liquid product. This shows conclusively that the final decene product is not a simple mixture of oligomers and suggests that the two widely different molecular weight charge olefins are going through a common intermediate stage.

### Reaction Steps

The data discussed above provide evidence for the following reaction steps:

1. Oligomerization (for example,  $C_3^=$  to  $C_6^=$ ,  $C_9^=$ ,  $C_{12}^=$ , etc.).
2. Isomerization-cracking of oligomer (or higher carbon no. olefin charge) to a mixture of intermediate carbon number olefins.
3. Copolymerization of the intermediate mixture of olefins.

An intermediate step similar to "2" is described in the literature (1), proceeding through carbenium ion species. However, isolation of the intermediates proving their existence has not been reported. Such isolation at the conditions used above was also not possible, suggesting that copolymerization "step 3" is very rapid.

### Equilibration of $C_2$ - $C_{10}$ Olefins at Sub-Atmospheric Pressure

Isolation of a common group of olefin isomers has now been accomplished, charging olefins from  $C_2$ - $C_{10}$  over HZSM-5 at sub-atmospheric pressure. Conditions used were:

|                         |  |
|-------------------------|--|
| Olefin partial pressure | 1-2 psia                                 |
| Total pressure          | 1 Atmosphere ( $H_2$ and $N_2$ dilution) |
| Temperature, °F         | 520-530°F                                |
| WHSV                    | 0.5 - 0.9                                |

Ethylene, propylene, a mixture of internal pentene isomers, 1-hexene and 1-decene all give a mixture of predominantly  $C_4$ - $C_7$  olefins (Table III).



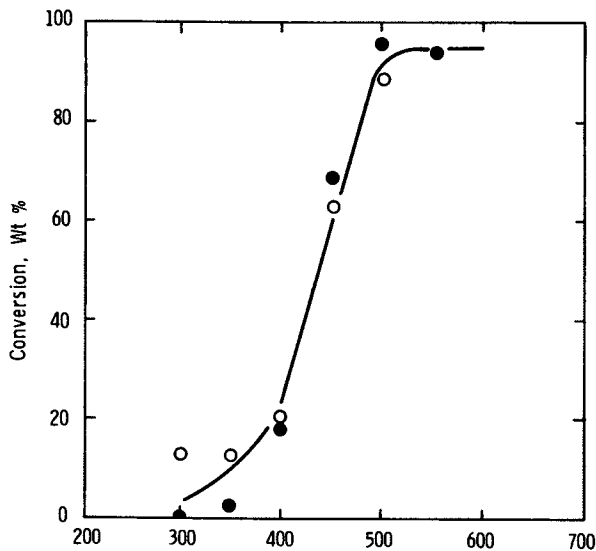


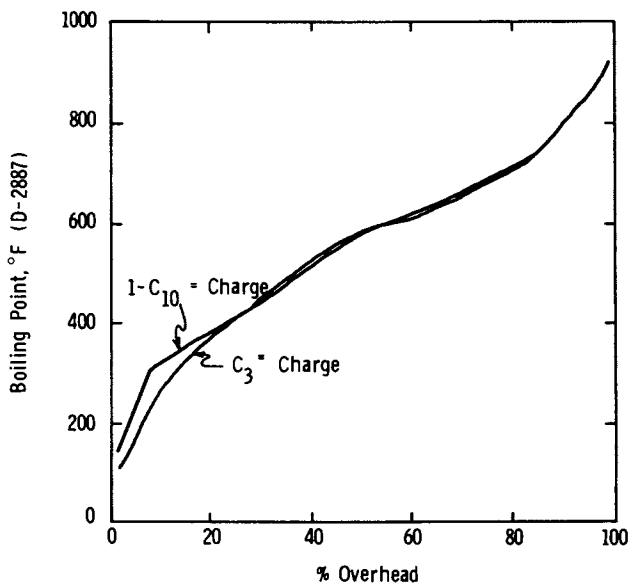
Figure 5

Conversion of  $C_5^= / C_6^=$  Mixture

700 psig 0.6 WHSV  $C_5^=$  (~80% 1-olefin, ~20% internal)

0.9 WHSV  $C_6^=$  (~80% 1-olefin, ~20% internal)

○  $C_5^=$  Conversion      ●  $C_6^=$  Conversion



**Figure 6**  
**Comparison of Propylene and 1-Decene Charge**  
**0.5 WHSV 1500 psig 450°F**

TABLE III  
OLEFIN EQUILIBRATION CARBON NUMBER DISTRIBUTION

| $C_2-C_{10}$ Olefin Charge | $C_2$ | $C_3$          | $C_5$<br>Mix <sup>b</sup> | $1-C_6$ | $1-C_{10}$ |
|----------------------------|-------|----------------|---------------------------|---------|------------|
| $C_2$ Product              | 47.5  | 0 <sup>a</sup> | <0.1                      | <0.1    | <0.1       |
| $C_3$ Product              | 5.6   | 11             | 8                         | 10      | 9          |
| $C_4$ Product              | 10.6  | 20             | 28                        | 20      | 20         |
| $C_5$ Product              | 11.3  | 21             | 30                        | 27      | 23         |
| $C_6$ Product              | 6.9   | 13             | 13                        | 15      | 16         |
| $C_7$ Product              | 6.2   | 12             | 11                        | 11      | 10         |
| $C_8$ Product              | 4.1   | 8              | 6                         | 7       | 8          |
| $C_9$ Product              | 4.3   | 8              | 3                         | 5       | 6          |
| $C_{10}^+$ (unidentified)  | 3.5   | 7              | 1                         | 5       | 8          |
|                            | 100   | 100            | 100                       | 100     | 100        |

a. Based on converted  $C_2$ .

b. 88% 2M2C4=, 8% 2M1C4=.

Ethylene again is less reactive than the higher olefins, but what is converted falls in the same carbon number range. The distribution of  $C_2-C_6$  olefins, normalized to 100%, is close to equilibrium (Table IV - equilibrium data are complete through  $C_6$  only (9)).

TABLE IV  
COMPARISON OF PRODUCT CARBON NUMBERS, WT%, WITH EQUILIBRIUM  
530°F

|       | Average of results<br>charging $C_2-C_{10}$ olefins,<br>1-2 psia | Equilibrium<br>1.3 psia |
|-------|--|-------------------------|
| $C_2$ | <1   | 2                       |
| $C_3$ | 12   | 11                      |
| $C_4$ | 29   | 35                      |
| $C_5$ | 36   | 38                      |
| $C_6$ | 23   | 14                      |
|       | 100  | 100                     |

The product pentene isomers from the C<sub>2</sub>-C<sub>10</sub> olefin charge stocks also all approach equilibrium, as shown in Table V.

TABLE V

COMPARISON OF PENTENE PRODUCT ISOMERS WITH EQUILIBRIUM  
530°F

| Charge →                       | C <sub>2</sub> <sup>=</sup> | C <sub>3</sub> <sup>=</sup> | C <sub>5</sub> <sup>=</sup> Mix | 1-C <sub>6</sub> <sup>=</sup> | 1-C <sub>10</sub> <sup>=</sup> | Equilibrium |
|--------------------------------|-----------------------------|-----------------------------|---------------------------------|-------------------------------|--------------------------------|-------------|
| Pentene Isomer, %              |                             |                             |                                 |                               |                                |             |
| 1-C <sub>5</sub> <sup>=</sup>  | 2                           | 2                           | 2                               | 2                             | 2                              | 2           |
| 2M1C <sub>4</sub> <sup>=</sup> | 18                          | 16                          | 18                              | 18                            | 17                             | 24          |
| 3M1C <sub>4</sub> <sup>=</sup> | 1                           | 2                           | 2                               | 2                             | 1                              | 2           |
| T2C <sub>5</sub> <sup>=</sup>  | 11                          | 10                          | 11                              | 12                            | 13                             | 9           |
| C2C <sub>5</sub> <sup>=</sup>  | 5                           | 5                           | 5                               | 5                             | 6                              | 7           |
| 2M2C <sub>4</sub> <sup>=</sup> | 63                          | 65                          | 62                              | 61                            | 61                             | 56          |

The common product distribution as established above at sub-atmospheric pressures is evidence that a similar common distribution also occurs at higher pressure, explaining the similarity of final products.

Comparison of HZSM-5 and 46 Al Silica Alumina

Amorphous 46 Al silica alumina is relatively inactive for the equilibration reaction charging propylene (Table VI).

TABLE VI

EQUILIBRATION REACTION - 46 Al Si/Al VS. HZSM-5  
C<sub>3</sub><sup>=</sup> CHARGE, 0.5 WHSV, 1.3 PSIA, 530°F

|   | <u>46 Al Si/Al</u> | <u>HZSM-5</u> |
|---|--------------------|---------------|
| C <sub>2</sub> <sup>=</sup>                 | <0.1               | <0.1          |
| C <sub>3</sub> <sup>=</sup>                 | 91                 | 8             |
| C <sub>4</sub> <sup>=</sup>                 | <1                 | 28            |
| C <sub>5</sub> <sup>=</sup>                 | 1                  | 30            |
| C <sub>6</sub> <sup>=</sup>                 | 4                  | 13            |
| C <sub>7</sub> <sup>=</sup>                 | 1                  | 11            |
| C <sub>8</sub> <sup>=</sup>                 | 1                  | 6             |
| C <sub>9</sub> <sup>=</sup>                 | 1                  | 3             |
| C <sub>10</sub> <sup>+</sup> (unidentified) | <u>1</u>           | <u>1</u>      |
|   | 100                | 100           |

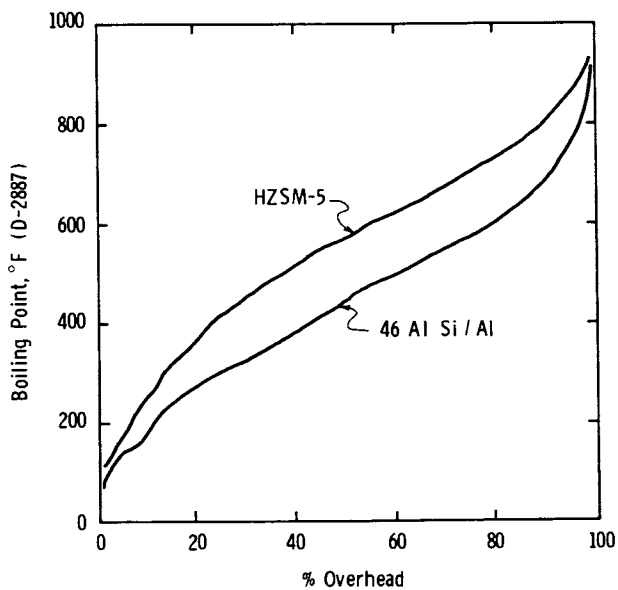
TABLE VII

INFRARED ANALYSIS - 46 AI Si/Al VS. HZSM-5 LIQUIDS  
FROM C3=, 0.5 WHSV, 1500 PSIG, 450°F

| Band, cm <sup>-1</sup> | Hydrocarbon  | Liquid Form |         |
|------------------------|--|-------------|---------|
|                        |  | 46 AI Si/Al | HZSM-5  |
| 980-965                | $\begin{array}{c} R_1 \quad H \\ \diagdown \quad / \\ C=C \\ / \quad \diagdown \\ H \quad R_2 \end{array}$   | Weak        | Medium  |
| 895-885                | $\begin{array}{c} R_1 \quad H \\ \diagdown \quad / \\ C=C \\ / \quad \diagdown \\ R_2 \quad H \end{array}$   | Weak        | V. Weak |
| 840-790                | $\begin{array}{c} R_1 \quad H \\ \diagdown \quad / \\ C=C \\ / \quad \diagdown \\ R_2 \quad R_3 \end{array}$ | Weak        | Absent  |
| 995-985<br>910-905     | $\begin{array}{c} R_1 \quad H \\ \diagdown \quad / \\ C=C \\ / \quad \diagdown \\ H \quad H \end{array}$     | Absent      | Absent  |
| 1600-1590              | Aromatics  | Weak        | V. Weak |

The activity of silica-alumina under these conditions is only sufficient to catalyze some dimerization of the propylene. As an acid catalyst, however, it has the potential for the same carbenium ion reactions at more drastic reaction conditions than needed for HZSM-5. It does make higher boiling product charging propylene at 1500 psig, as shown in Figure 7. It is significant that the shape of the curve is different from that of HZSM-5, showing more lower boiling product but a "tail" at the higher boiling range. Infrared analysis of the liquids showed less olefins and more aromatics in the silica-alumina product compared to HZSM-5 (Table VII).

The absence of the more highly branched olefins and less aromatics over ZSM-5 are both indicative of shape-selective constraints.



**Figure 7**  
**Comparison of HZSM-5 and 46 Al Si/Al**  
**C<sub>3</sub> Charge 0.5 WHSV 1500 psig**  
**450°F**

### Conclusions

The applications of the ZSM-5 family of zeolites for shape-selective cracking of paraffins in the gasoline (2, 10), distillate (11) and lube oil range (12) have all been reported. In this paper, we have established evidence of the converse reaction, shape-selective polymerization, to produce hydrocarbons in the same product range.

### Acknowledgments

The microunit operation by B. Bicknell, gas chromatography analysis by J. Stockinger, infrared interpretations by J. Ehlers and discussions with F. Krambeck on the equilibrium data are all acknowledged with thanks.

### Literature Cited

1. Oblad, A. G., Mills, G. A., and Heinemann, H., Chapter 4 of *Catalysis, VI*, Reinhold Publishing Co., NY, P. H. Emmett, ed. (1958).
2. Chen, N. Y., and Garwood, W. E., *J. Catal.* 1978, 52, 453-458.
3. Argauer, R. J., and Landolt, G. R., U. S. Patent 3,702,866 (1972).
4. Givens, E. N., Plank, C. J., and Rosinski, E. J., U. S. Patent 3,960,978 (1976).
5. Givens, E. N., Plank, C. J., and Rosinski, E. J., U. S. Patent 3,827,968 (1974).
6. Chang, C. D., and Silvestri, A. J., *J. Catal.* 1977, 47, 249.
7. Brennan, J. A., Garwood, W. E., Yurchak, S., and Lee, W., *Proc. Int'l. Seminar on Alternate Fuels*, Liege, Belgium, A. Germain, ed. (1981).
8. Kokotailo, G. T., Lawton, S. L., Olson, D. H., and Meier, W. M., *Nature* 1978, 272, 437. Also, Kokotailo, G. T., and Meier, W. M., *Proc. Int'l. Conf. Properties and Applications of Zeolites*, London, England, R. P. Townsend, ed. (1979).
9. Rossini, E. D., *The Science of Petroleum, V, Part 1*, Oxford University Press (1950).
10. Garwood, W. E., and Chen, N. Y., *PREPRINTS, Div. of Petrol. Chem., ACS*, 25(1), 84 (1980).
11. Chen, N. Y., Gorrington, R. L., Ireland, H. R., and Stein, T. R., *Oil and Gas J.* 6/6/77, 75, 165.
12. Smith, K. W., Starr, W. C., and Chen, N. Y., *Oil and Gas J.* 5/26/80, 78, 75.

RECEIVED November 16, 1982

## Evaluation of Some New Zeolite-Supported Metal Catalysts for Synthesis Gas Conversion

GORDON A. MELSON, JANET E. CRAWFORD, JAMES W. CRITES,  
and KETCHA J. MBADCAM

Virginia Commonwealth University, Department of Chemistry,  
Richmond, VA 23284

JOHN M. STENCEL and V. UDAYA S. RAO

U.S. Department of Energy, Pittsburgh Energy Technology Center,  
Pittsburgh, PA 15236

Series of zeolite-supported iron-containing catalysts with weight percent iron (% Fe) varying from ~1 to ~17% Fe have been prepared from  $\text{Fe}_3(\text{CO})_{12}$  and the synthetic zeolites ZSM-5, mordenite and 13X by an extraction technique. The zeolites ZSM-5 and mordenite were used in the acid form, 13X in the sodium form. The catalysts were characterized by a variety of techniques including infrared spectroscopy, X-ray powder diffractometry, X-ray photoelectron spectroscopy, ion-scattering spectrometry and Mössbauer spectroscopy. All catalysts contain highly dispersed, small particle-sized  $\gamma\text{-Fe}_2\text{O}_3$  with a small amount of the iron (0.6-1.5% Fe depending on the support) located in the pores of the support. Evaluation of the catalytic ability of some of these materials for synthesis gas conversion was conducted at 280°C and 300°C by using a fixed-bed continuous flow microreactor. All catalysts evaluated produce significant quantities of hydrocarbons. The distribution of hydrocarbons varies, depending upon the support used, for catalysts with similar weight percent iron. For the liquid hydrocarbons, Fe/ZSM-5 produces the highest percentage of aromatics, Fe/mordenite produces the highest percentage of olefins, and Fe/13X produces the highest percentage of saturates. The effect of support acidity and pore structure on hydrocarbon product distribution is discussed.

The use of bifunctional metal/zeolite catalysts for the conversion of synthesis gas (carbon monoxide and hydrogen) to gasoline range hydrocarbons has recently attracted much attention. For example, the combination of metal oxides with the medium pore (~6Å) zeolite ZSM-5 and the use of a metal nitrate impregnated ZSM-5 catalyst have been shown to produce gasoline range hydrocar-



bons containing a high percentage of aromatics from synthesis gas (1-3).

The efficiency and selectivity of a supported metal catalyst is closely related to the dispersion and particle size of the metal component and to the nature of the interaction between the metal and the support. For a particular metal, catalytic activity may be varied by changing the metal dispersion and the support; thus, the method of synthesis and any pre-treatment of the catalyst is important in the overall process of catalyst evaluation. Supported metal catalysts have traditionally been prepared by impregnation techniques that involve treatment of a support with an aqueous solution of a metal salt followed by calcination (4). In the Fe/ZSM-5 system, the decomposition of the iron nitrate during calcination produces  $\alpha$ -Fe<sub>2</sub>O<sub>3</sub> of relatively large crystallite size (>100 Å). This study was initiated in an attempt to produce highly-dispersed, thermally stable supported metal catalysts that are effective for synthesis gas conversion. The carbonyl Fe<sub>3</sub>(CO)<sub>12</sub> was used as the source of iron; the supports used were the acidic zeolites ZSM-5 and mordenite and the non-acidic, larger pore zeolite, 13X.

### Experimental

The zeolite supports were calcined in air prior to use. ZSM-5 (SiO<sub>2</sub>/Al<sub>2</sub>O<sub>3</sub> = 30) and mordenite (SiO<sub>2</sub>/Al<sub>2</sub>O<sub>3</sub> = 11.4) were used in the acid form (H-ZSM-5, H-Mord), and 13X (SiO<sub>2</sub>/Al<sub>2</sub>O<sub>3</sub> = 1) used in the sodium form. Series of zeolite-supported iron catalysts of weight percent iron (% Fe) varying from ~1% to ~17% Fe were prepared from Fe<sub>3</sub>(CO)<sub>12</sub> and the calcined zeolites with cyclohexane as solvent by an extraction technique developed in our laboratory (5). All materials were characterized by infrared spectroscopy, X-ray powder diffractometry (XRPD), X-ray photoelectron spectroscopy (XPS), ion-scattering spectrometry (ISS), and Mössbauer spectroscopy. The weight percent of iron was determined by atomic absorption spectroscopy.

For the catalytic activity evaluation, selected materials were pressed into 1/8 inch diameter pellets, reduced under H<sub>2</sub> at 300 psig (20.7 bar) and 450°C for 24 hours, and then treated with synthesis gas (H<sub>2</sub>/CO = 1/1) at 100 psig (6.9 bar) and 250°C for 24 hours. Catalytic data were obtained by using a fixed-bed continuous flow microreactor. Conditions employed were 300 psig (20.7 bar) pressure of 1/1 synthesis gas, GHSV ~1000 h<sup>-1</sup> and reactor temperatures of 280°C and 300°C. The products obtained over a 48 to 72 hour period from the microreactor were analyzed in two fractions. The gaseous effluent, including C<sub>1</sub>-C<sub>4</sub> hydrocarbons, was analyzed by use of a gas chromatograph that is an integral part of the microreactor. The liquid product was collected in an ice-cooled trap located after a heated (175°C) trap to collect high molecular weight (wax) products. The liquid product was separated into oil and aqueous fractions; analysis of the oil fraction was

accomplished by FIA chromatography on silica gel (6) and by simulated distillation (7).

### Results and Discussion

**Characterization** Infrared spectra of the prepared materials do not show the presence of  $\nu(\text{CO})$  bands; thus, it is concluded that decomposition of  $\text{Fe}_3(\text{CO})_{12}$  accompanies adsorption onto the supports during the preparative procedure. For catalysts with low (<10%) iron loading, only the support is detected by XRPD suggesting that the particle size of the iron-containing species is <50 Å. However, above ~10% Fe loading a diffraction pattern associated with  $\gamma\text{-Fe}_2\text{O}_3$  and/or  $\text{Fe}_3\text{O}_4$  is observed in addition to that for the support. The XPS data confirm the presence of iron oxide in all the prepared catalysts; a detailed study of the XPS data for a series of Fe/ZSM-5 catalysts has recently been described (8). Ion scattering spectrometry, with  $^4\text{He}^+$  sputtering, has been employed to study the surface of the iron/zeolite catalysts. For all samples studied, large Fe/Si intensity ratios are obtained in comparison with those ratios from iron/zeolite catalysts prepared by wet-impregnation techniques using an aqueous solution of iron nitrate. It is concluded that the iron oxide particles in the catalysts prepared from  $\text{Fe}_3(\text{CO})_{12}$  are considerably smaller than those obtained by using iron nitrate. Depth profiling studies (XPS and ISS) have demonstrated that some iron (~1%) is incorporated into, and is strongly interacting with, the zeolite support; data for the Fe/ZSM-5 catalysts have been reported (8). Recent studies (9) of the infrared spectra of chemisorbed pyridine on Fe/ZSM-5 catalysts prepared by the extraction technique from  $\text{Fe}_3(\text{CO})_{12}$  has suggested that, in the prepared form, the iron is not interacting with the support at the Brønsted acid sites whereas for iron nitrate impregnated Fe/ZSM-5 catalysts some ion exchange does take place. Mössbauer spectroscopy has identified the surface iron-containing species as small particle-sized  $\gamma\text{-Fe}_2\text{O}_3$  in a superparamagnetic form (10, 11). For Fe/ZSM-5 catalysts, (15% to 16% Fe) magnetic and Mössbauer studies (12) have concluded that the carbonyl-impregnated samples contain  $\gamma\text{-Fe}_2\text{O}_3$  particles of diameter 60-66 Å whereas the nitrate-impregnated samples contain  $\alpha\text{-Fe}_2\text{O}_3$  of ~100 Å diameter.

Characterization of the used catalysts (~15% Fe) has shown the presence of  $\chi\text{-Fe}_5\text{C}_2$  (Hägg carbide) and  $\text{Fe}_3\text{O}_4$  for all materials investigated. For an Fe/ZSM-5 catalyst, it is estimated that ~80% of the iron is in the metallic form after the reduction step (12). Following the carbiding step,  $\chi$ - and  $\epsilon$ -carbides are detected in addition to  $\text{Fe}_3\text{O}_4$ .

It is concluded from the characterization studies, that the extraction technique which we have employed for the preparation of zeolite-supported iron catalysts results in the formation of highly dispersed, small particle-sized  $\gamma\text{-Fe}_2\text{O}_3$  on the support surface and, in addition, a small amount (~1%) of iron present as a spe-

cies, possibly in a non-oxide form, that interacts strongly with the zeolite support. It is suggested that the strongly interacting iron may be incorporated into the pores of the zeolite. The iron component in the prepared catalysts is readily reduced to the metallic form which in turn forms iron carbides which are active for hydrocarbon synthesis.

Catalytic Evaluation In order to investigate support effects in these iron/zeolite catalysts prepared from  $\text{Fe}_3(\text{CO})_{12}$  by the extraction technique, three catalysts of similar weight percent iron loading were evaluated for their ability to catalyze synthesis gas conversion; these catalysts were 15.0% Fe/ZSM-5, 16.4% Fe/Mordenite and 15.0% Fe/13X. All catalysts were evaluated under similar conditions as described in the experimental section. Catalytic data is presented in the accompanying figures; in each figure the first three points for each catalyst are data obtained at 280°C, the second three points are data at 300°C.

The catalysts evaluated are active for synthesis gas conversion; the percent conversion of  $\text{H}_2$  and CO is shown for each catalyst in Figure 1 as a function of time under evaluation conditions and temperature. At 280°C the percent conversion of synthesis gas increases with time for the acidic zeolite-supported catalysts, Fe/ZSM-5 and Fe/Mordenite, but decreases for the larger pore, non-acidic zeolite-supported catalyst Fe/13X. The percent conversion increases for all catalysts at 300°C; for Fe/ZSM-5 and Fe/Mordenite the conversions remain constant at this temperature for several days, although for Fe/13X the conversion increases with time. The trends in % synthesis gas conversion, particularly % CO, are reflected in the weight % hydrocarbons, carbon dioxide and water obtained in the reactor effluent over the period of evaluation, see Figure 2. It is apparent that the catalysts are effective for the production of hydrocarbons from synthesis gas, but also catalyze the water gas shift reaction; the % hydrocarbons and %  $\text{CO}_2$  obtained are greater at the higher temperature (300°C) whereas the %  $\text{H}_2\text{O}$  is less at this temperature than at 280°C.

The distribution of the hydrocarbons is presented in Figures 3(a) through (d) and Figures 4(a) and (b) as a weight percent of the total hydrocarbon product. Figure 4(a) represents  $\text{C}_{5+}$  hydrocarbons obtained from the ice-cooled trap and Figure 4(b) the high molecular weight waxy products obtained from the heated trap. All catalysts produce a wide range of hydrocarbon products; the Fe/ZSM-5 catalyst produces the highest yield of methane and the lowest yield of oil of the three catalysts investigated. High methane and low oil yields may be related to the small particle size of the iron-containing species in this catalyst. Carbon monoxide chemisorption data on Fe/Mordenite catalysts have indicated the presence of larger particle sizes for the iron-containing species in these catalysts compared with those in the Fe/ZSM-5 catalysts (13). It has also been observed (14) that for the Fe/ZSM-5 catalyst, calcination in air (300°C and 500°C) leads to an increase in

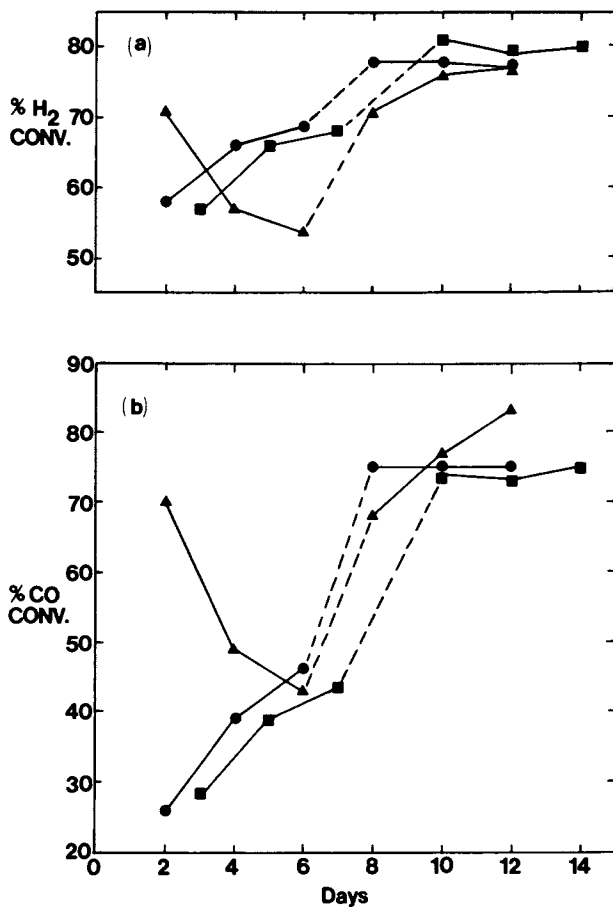


Figure 1.  
(a), % H<sub>2</sub> conversion; (b), % CO conversion. ■ = 15.0% Fe/ZSM-5; ● = 16.4% Fe/Mord; ▲ = 15.0% Fe/13X.

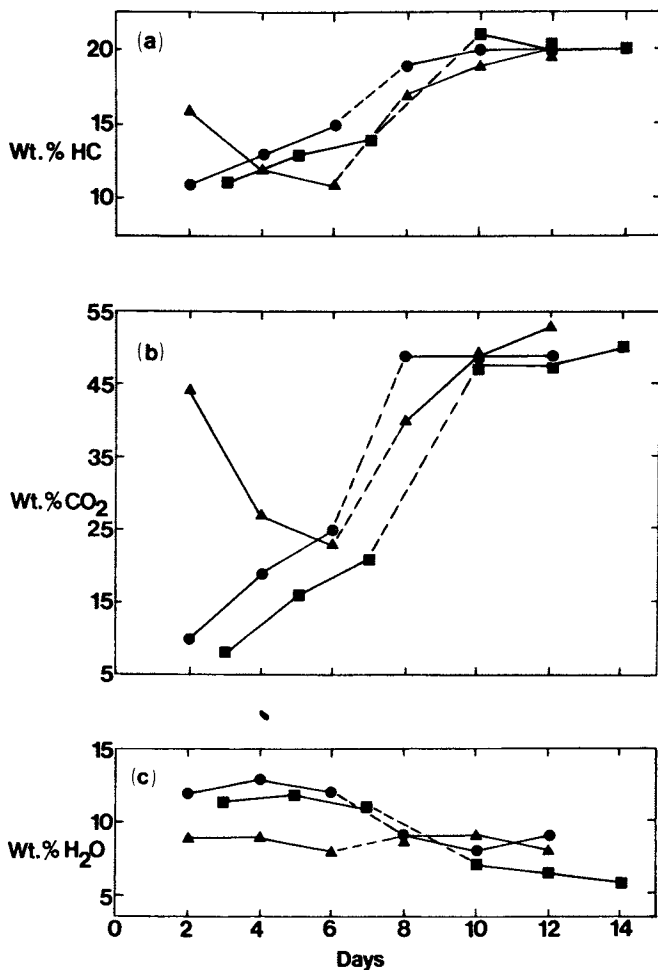


Figure 2.

(a), Weight % Hydrocarbons; (b), weight % Carbon Dioxide; (c), weight % water in the reactor effluent.  
Key same as Figure 1.

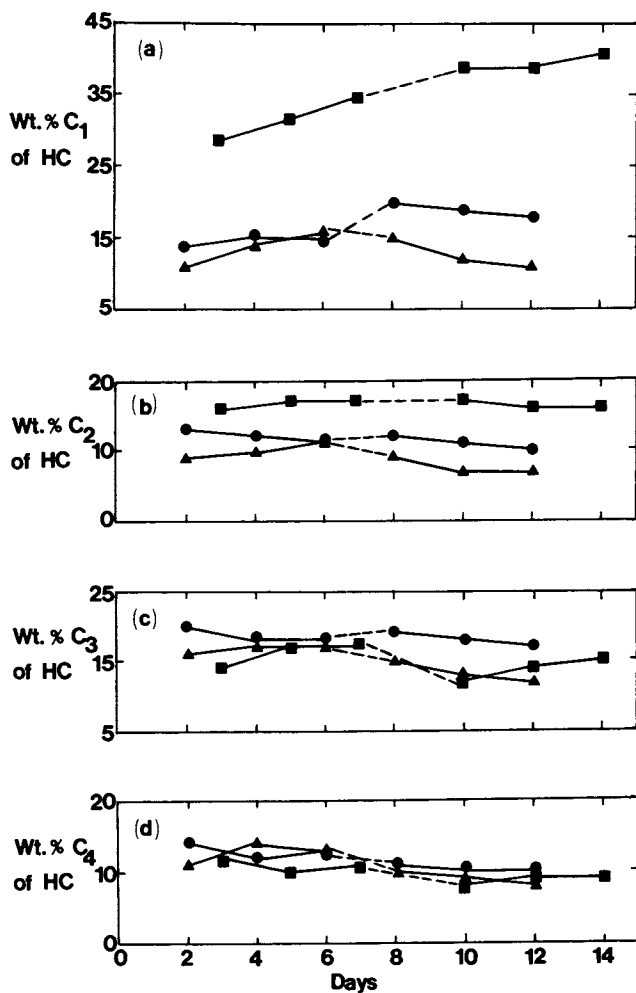


Figure 3.  
 (a), Weight % C<sub>1</sub>; (b), weight % total C<sub>2</sub>; (c), weight % total C<sub>3</sub> and (d), weight % total C<sub>4</sub> hydrocarbons of total hydrocarbons produced. Key same as Figure 1.

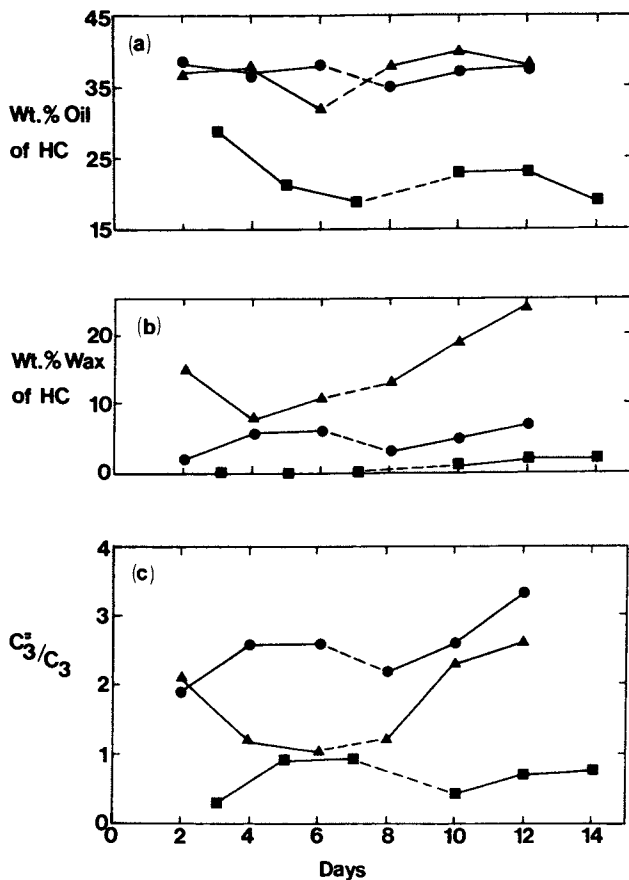


Figure 4.  
 (a), Weight % oil ( $C_{5+}$ ); (b), weight % wax of total hydrocarbons produced; (c), propene/propane ratio for  $C_3$  hydrocarbons. Key same as Figure 1.

particle size of the iron oxide which results in decreased methane and increased oil production for these catalysts compared with the as-prepared, uncalcined, catalyst. Simulated distillation data for the oil product ( $C_{5+}$  hydrocarbons) obtained by using Fe/ZSM-5 and Fe/Mordenite catalysts suggest that ~90% of the product boils in the gasoline range ( $<204^{\circ}C$ ) compared with ~70% for the oil obtained by using Fe/13X. The Fe/ZSM-5 and Fe/Mordenite catalysts produce only small amounts of wax whereas Fe/13X produces significant quantities, particularly at  $300^{\circ}C$ . It should be noted that for the Fe/13X catalyst, the increase in % CO conversion at  $300^{\circ}C$  with time is reflected in the increased production of high molecular weight hydrocarbons at this temperature. Thus, for synthesis gas conversion with the acidic zeolite-supported catalysts (Fe/ZSM-5 and Fe/Mordenite) a lower molecular weight distribution of hydrocarbons is obtained compared with that for the non-acidic, larger-pore zeolite-supported catalyst Fe/13X. It is apparent that the pores in the ZSM-5 and mordenite zeolites restrict the formation of high molecular weight hydrocarbon products and/or the presence of Brønsted acid sites in these zeolites results in the cracking of any high molecular weight products which may be formed. However, the 13X zeolite with larger-sized pores and the lack of Brønsted acid sites, does not have the ability to restrict the formation of high molecular weight products and thus a higher molecular weight distribution of hydrocarbons is obtained.

Fluorescence Indicator Absorption (FIA) chromatographic analysis of the  $C_{5+}$  hydrocarbon fraction was conducted on each sample obtained; the results are presented in Figures 5(a) through (c). Comparison of these results for the three catalysts studied shows that the use of the Fe/ZSM-5 catalyst results in the formation of the highest percentage of aromatics for all samples analyzed, for the Fe/Mord catalyst the highest percentage of olefins is obtained and for the Fe/13X catalyst, the highest percentage of saturates is obtained in the oil. The relatively high yield of aromatics for the Fe/ZSM-5 catalyst may be related to the low propene/propane ( $C_3^=/C_3$ ) ratio found by using this catalyst (see Figure 4(c)). This low ratio demonstrates the ability of the Brønsted acid sites in this catalyst to convert propene to aromatic products. It has previously been demonstrated that propene is readily converted into liquid hydrocarbons containing a high percentage of aromatics by the acidic form of ZSM-5 (15). For the Fe/Mordenite catalyst, it is concluded that the acid sites which are present catalyze the oligomerization of light olefins to heavier (liquid) olefins but are not as effective as those in the Fe/ZSM-5 catalyst for the production of aromatic hydrocarbons from propene. The absence of Brønsted acid sites in Fe/13X evidently allows the polymerization of hydrocarbon intermediates to occur resulting in the formation of higher molecular weight saturated hydrocarbons.

The effect of weight percent iron on the catalytic activity of Fe/ZSM-5 and Fe/13X catalysts was investigated by comparison of the catalytic data obtained for 7.0% Fe/ZSM-5 with that for 15.0%



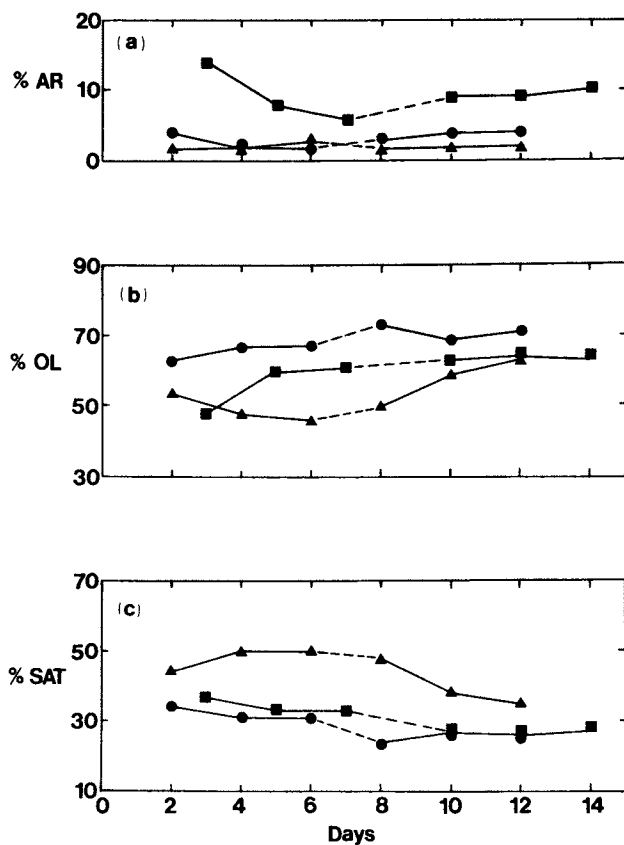


Figure 5.  
(a), Weight % aromatics; (b), weight % olefins; (c), weight % saturates in the oil ( $C_{5+}$  hydrocarbon) product. Key same as Figure 1.

Fe/ZSM-5 and for 7.0% Fe/13X with that for 15.0% Fe/13X. These data indicate that an increase in the weight percent iron loading results in an increase in the carbon monoxide and hydrogen conversions and an increase in the total amount of hydrocarbons in the effluent. However, there is no appreciable difference in the distribution of the hydrocarbons that are produced.

### Conclusions

This study was initiated in an attempt to produce highly-dispersed, thermally-stable, zeolite-supported metal catalysts and to investigate the effect of acidity and pore size of the zeolite on the products obtained from synthesis gas conversion. As a result of this study, several conclusions can be made.

First, the use of  $\text{Fe}_3(\text{CO})_{12}$  and an extraction technique for the preparation of zeolite-supported iron catalysts results in the formation of highly-dispersed, small particle-sized  $\gamma\text{-Fe}_2\text{O}_3$  on the zeolite surface with a small amount, ~1 Wt % Fe, present in a non-oxide form that interacts strongly with, and may be incorporated into the pores of, the zeolite.

Second, the iron oxide readily forms the iron carbide  $\chi\text{-Fe}_5\text{C}_2$  after reduction in hydrogen and subsequent carburizing in synthesis gas. The thermally stable, long-lived catalysts that are obtained are active for synthesis gas conversion.

Third, the acidity and pore structure of the zeolite support are important factors that influence the distribution of products obtained during synthesis gas conversion. The catalysts Fe/ZSM-5 and Fe/Mordenite contain Brönsted acid sites and medium-sized pores and result in the conversion of synthesis gas to gaseous and liquid hydrocarbons containing a high percentage of unsaturates. Approximately 90% of the liquid (oil) products obtained by using these catalysts are in the gasoline boiling range. The catalyst Fe/13X, which consists of a non-acidic, larger-sized pore zeolite leads to the conversion of synthesis gas to a higher molecular weight distribution of largely saturated hydrocarbons. For this catalyst, approximately 70% of the liquid (oil) product obtained is in the gasoline boiling range.

Fourth, by careful choice of the zeolite support in the preparation of a bifunctional catalyst for synthesis gas conversion, the product distribution, particularly for hydrocarbons, may be controlled. This conclusion is of importance in the design of catalysts for the production of liquid transportation fuels from synthesis gas.

### Acknowledgment

This work was supported in part by Grant No. DE-FG22-80PC30228 to G.A.M. from the office of Fossil Energy, U.S. Department of Energy.

Literature Cited

1. Dwyer, F. G.; Garwood, W. E. U.S. Patent. 1979, 4,172,843; Chang, C. D.; Lang, W. H. U.S. Patent. 1979, 4,180,516.
2. Chang, C. D.; Lang, W. H.; Silvestri, A. J. J. Catal. 1979, 56, 268.
3. Rao, V. U. S.; Gormley, R. J. Hydrocarbon Proc. 1980, 59 (11), 139.
4. Anderson, J. R.; "Structure of Metallic Catalysts"; Appendix II, Academic Press: London, 1975.
5. Melson, G. A.; Crawford, J. E.; Crites, J. W.; Mbadcam, K. J. to be published.
6. "Annual Book of American Society for Testing and Materials Methods" American Society for Testing and Materials: Philadelphia, 1977, ASTM # D1319-77.
7. "Annual Book of American Society for Testing and Materials Methods" American Society for Testing and Materials: Philadelphia, 1978, ASTM # D2887-73.
8. Stencel, J. M.; Diehl, J. R.; Douglas, L. J.; Spitler, C. A.; Crawford, J. E.; Melson, G. A. Colloids and Surfaces 1982, 4, 331.
9. Rhee, K. H.; Rao, V. U. S.; Stencel, J. M.; Melson, G. A.; Crawford, J. E. J. Catal. submitted.
10. Montano, P. A. private communication.
11. Mulay, L. N. private communication.
12. Obermyer, R. T.; Mulay, L. N.; Lo, C.; Oskooie-Tabrizi, M.; Rao, V. U. S. J. App. Phys. 1982, 53, 2683.
13. Goodwin, J. A.; Irwin, K. private communication.
14. Crawford, J. E.; Melson, G. A. unpublished results.
15. Butter, S. A.; Kaeding, W. W. U.S. Patent. 1979, 3,972,832.

RECEIVED November 16, 1982

# Intrazeolitic and Rare Gas Isolated Silver Atom and Silver Cluster Spectroscopy, Photoprocesses, and Support Interactions

GEOFFREY A. OZIN, FRANCOIS HUGUES, DOUGLAS F. McINTOSH,  
and S. MATTAR

University of Toronto, Lash Miller Chemistry Laboratories,  
Toronto, Ontario M5S 1A1, Canada

Guest-host interactions involving both ground and excited electronic states are shown to play a critical role in determining the energetic properties and dynamical processes of silver atoms and small silver clusters isolated in faujasite-type zeolites and rare gas matrices. An investigation of the spectroscopy and photoprocesses of these immobilized metal reagents indicates that although the ground state metal-support interactions can be classified as weak, the excited state interactions are exceptionally sensitive to the nature of the support. In fact they are of sufficient magnitude to result in a range of novel metal-support relaxation processes including cage-relaxed metal atomic fluorescence/photodiffusion/photoaggregation, metal cluster photofragmentation/cage-relaxed metal atomic fluorescence/cage-recombination and metal cluster photoisomerization. An appreciation of these kinds of interactions is important as they clearly bear a relationship to metal-support effects known to be operative in supported metal catalysts.

Experimental techniques for fabricating and spectroscopically probing specific naked metal clusters, with nuclearities spanning the range from atom to bulk have been the focus of intense scientific interest over the past decade. Molecular beam and matrix isolation methods have emerged as the premier approaches for studying ligand-free metal clusters in the gas and condensed phases respectively (1). In the ideal collision free environment of a molecular beam, the properties of a metal cluster can be considered to be truly isolated from cluster-substrate effects. Therefore, spectroscopic methods that can selectively extract information from metal cluster beams hold great promise for illuminating diverse size dependent properties of aggregates of metal atoms in their equilibrium configuration. Condensation of metal atoms and/or metal clusters, with rare gases at cryogenic

0097-6156/83/0218-0409\$08.25/0  
© 1983 American Chemical Society

temperatures, from either jets or beams represents the other main approach for observing nucleation phenomena from isolated metal atoms to bulk metal agglomerates in a weakly interacting solid support. In this way the metal dispersion as well as the thermal and photolytic behaviour of particular metal atomic and cluster reagents may be spectroscopically observed. The spectra obtained reflect not only the properties of the guest but also their interaction with the host. Because the size requirement of up to six metal atoms is of great practical significance to the spectroscopic, chemical and catalytic properties of supported metal clusters in both weakly and strongly interacting environments (2), it is important to study very small metal clusters in various types of substrate as well as in the gas phase. In this way, one can hope to develop a scale of metal-support effects (guest-host interactions) and evaluate the role that they play in diverse technological phenomena.

In the past five years, the field of metal-zeolite chemistry has developed to the point where a number of metal atomic and small cluster guests have been synthesized and unequivocally characterized by spectroscopic and crystallographic techniques. The silver-zeolite A, X and Y systems in particular have yielded a wealth of valuable structural and site information pertaining to silver guests in the size range of one to six atoms (3). The spectroscopy of these silver-zeolites can therefore be probed in detail and compared with the corresponding data for silver atoms and silver clusters immobilized in weakly interacting rare gas solid supports (4).

In this paper, we will concentrate on some of the more interesting photophysical properties observed for silver atomic and small cluster reagents entrapped in rare gas solid and faujasite-type zeolite substrates. Attention will be directed to matrix cage relaxation energetics and dynamics following uv and visible photoexcitation of specific silver guests. Metal-support interactions involving both ground and excited electronic states of the silver guest-cage unit will feature prominently throughout this discussion, as they play a critical role in controlling the spectroscopy and relaxation dynamics of the entrapped metal guests. These interactions clearly bear an important relationship to metal-support effects known to be operative in supported metal catalysts.

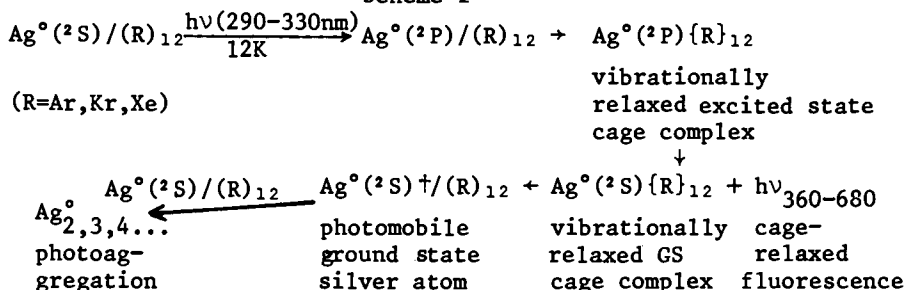
## Results and Discussion

(A) Silver Atoms and Clusters in Rare Gas Solids The fluorescence emission and excitation spectra of metal atomic and small clusters immobilized in cryogenic matrices exhibit a specificity which has for some time been recognized as a sensitive probe of the microscopic environment of the entrapped guest, signalling subtle changes in its surroundings as well as specific guest-host interactions operating in its ground and excited states (4, 5, 6, 7). In this context, a striking resemblance between the optical spectra of rare gas and zeolite Y isolated silver atoms and clusters has been previously noted and interpreted in

terms of a weak metal-support interaction for these silver guests in a zeolite Y host (4). An objective of this paper is to evaluate the spectroscopic consequences of large variations in guest-host interactions (metal-support effects) in the ground and optically excited states of silver atoms and low nuclearity clusters in rare gas and faujasite-type zeolites. As most of the photophysical and photochemical information for  $Ag_n$ /rare gas matrices ( $n = 1-6$ ) has been previously reported, and the corresponding zeolite X,Y data is new, we will present the rare gas solid information pertinent to this paper in a highly summarized form, where the original papers should be consulted for details. In Figure 1, typical uv-visible absorption spectra are shown which illustrate the isolation of  $Ag^{\circ}$  (Figure 1A), co-isolation of  $Ag^{\circ}/Ag_2^{\circ}$  (Figure 1B),  $Ag^{\circ}/Ag_2^{\circ}/Ag_3^{\circ}$  (Figure 1C) and  $Ag_n^{\circ}$  (where  $n = 1, 2, 3, 4, 5 \dots$  Figure 1D). The corresponding fluorescence emission and excitation profiles for isolated  $Ag^{\circ}$  and co-isolated  $Ag^{\circ}/Ag_2^{\circ}/Ag_3^{\circ}$  are displayed in Figures 2A, 2B, and 2C respectively.

When these atomic and cluster species are embedded in a solid rare gas, dramatic alterations in their spectroscopic and photolytic properties ensue which can be traced to specific ground and excited state interactions. These perturbations can be described in terms of attractive van der Waals interactions and short range repulsive forces due to overlap between charge clouds on the metal and matrix atoms. It is evident that the potential energy of interaction between a metal atom or cluster and a support will in general be different for distinct electronic states of the metal guest, since the polarizability, radial extent and symmetry of the electronic charge distribution will generally vary from one electronic state to another. Studies of the energetics and dynamics of  $Ag^{\circ}$ ,  $Ag_2^{\circ}$  and  $Ag_3^{\circ}$  in rare gas solids have been completed (4-9). The absorption and fluorescence spectra are indicative of strong guest-host interactions in the low lying states of  $Ag^{\circ}$ ,  $Ag_2^{\circ}$  and  $Ag_3^{\circ}$ . Rather than presenting the spectroscopic and photolytic details, a summary of the observed radiative and non-radiative relaxation processes of visible and uv-photoexcited  $Ag^{\circ}$ ,  $Ag_2^{\circ}$  and  $Ag_3^{\circ}$  in rare gas solids is shown below:

## Scheme I



The most pertinent feature of the spectroscopy and photoprocesses of rare gas isolated  $Ag^{\circ}$  atoms is the strong guest-host

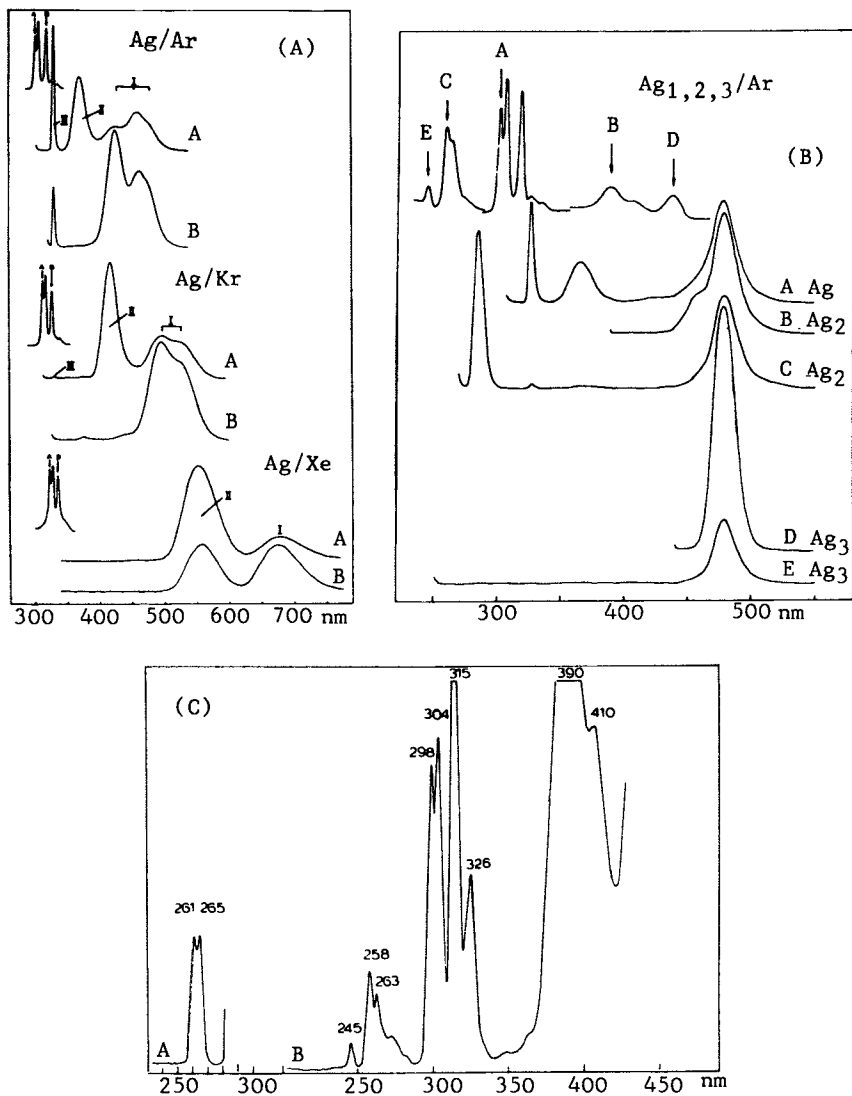


Figure 1.

Optical absorption spectroscopy for (A) Ag<sup>0</sup> in Ar, Kr, Xe at 12K (B) Ag<sup>0</sup>/Ag<sub>2</sub><sup>0</sup> in Ar, Kr, Xe at 12K, (C) Ag<sup>0</sup>/Ag<sub>2</sub><sup>0</sup>/Ag<sub>3</sub><sup>0</sup>/Ag<sub>4</sub><sup>0</sup> in Xe at 12K (D) Ag<sub>n</sub><sup>0</sup> (where n = 1, 2, 3, 4, 5, ... bulk) in Ar at 12K (5, 6, 8, 9).

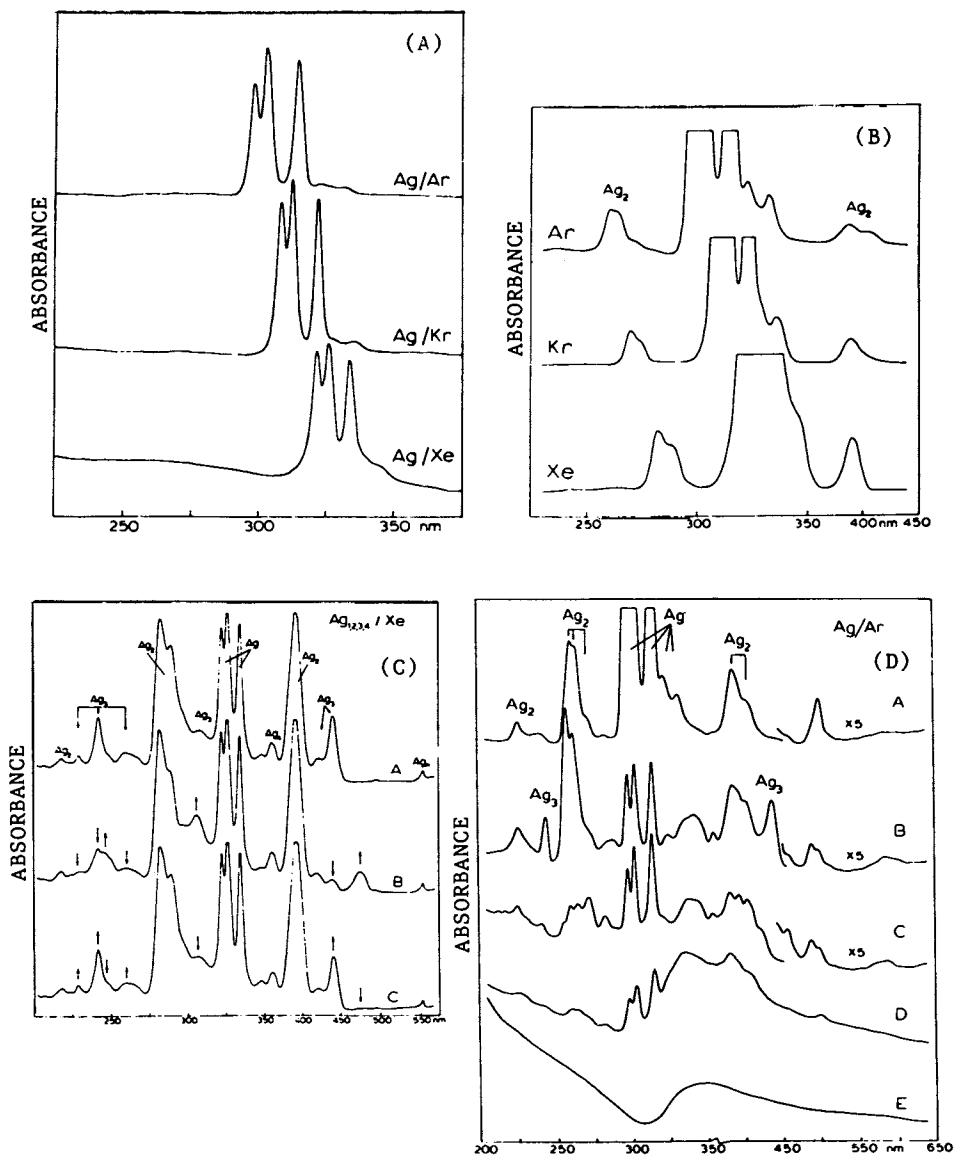


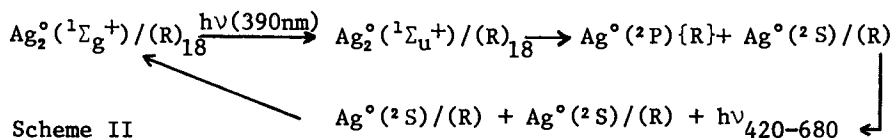
Figure 2.

(A) Fluorescence emission and absorption profiles for  $\text{Ag}^\circ$  in Ar, Kr, Xe at 12K (B) Optical absorption and emission spectra for  $\text{Ag}^\circ/\text{Ag}_2^\circ/\text{Ag}_3^\circ$  in Ar at 12K (C) Excitation profiles for  $\text{Ag}^\circ/\text{Ag}_2^\circ/\text{Ag}_3^\circ$  in Ar at 12K (4, 5, 9).



interactions in the optically excited Jahn-Teller active  $^2P$  state of  $Ag^\circ$ , which results in fast vibrational relaxation of the rare gas cage atoms around the  $Ag^\circ(^2P)$  atom, followed by cage-relaxed (strongly red shifted) atomic fluorescence. It is thought that the destabilization caused by producing a ground state  $Ag^\circ(^2S)$  in the relaxed excited state cage-configuration, provides the driving force for photoinduced diffusion of the Ag atoms which leads to photoaggregation. The phenomenon of photoaggregation has been found to be a sensitive function of the metal dispersion, nature and temperature of the support (5). A vibronic coupling model which focusses attention on a  $^2P$   $Ag^\circ$  atom in an  $O_h$  symmetry  $Ag\{R\}_{12}$  tetradecahedral rare gas substitutional site (quasi-molecule or cage-complex approximation) for the case of strong spin orbit and weak vibronic coupling, has been used to unify the absorption and emission spectra, fluorescence lifetime and depolarization values, and diffusion and aggregation properties (5), (see later).

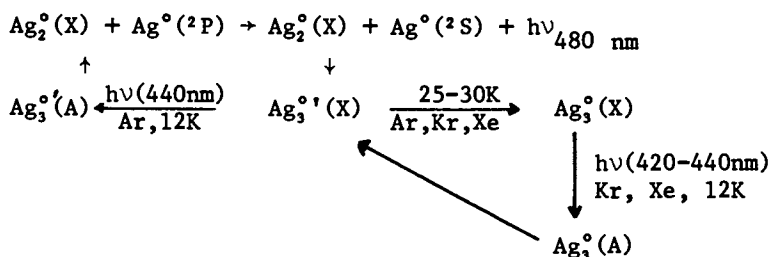
The absorption and fluorescence spectra of  $Ag_2^\circ$  in rare gas solids (6,10) are also clearly indicative of strong guest-host interactions involving the  $A, ^1\Sigma_u^+$  and  $C, ^1\Pi_u$  states of  $Ag_2$ , the former being summarized below:



The atomic emission spectrum produced by  $A \leftarrow X$ ,  $Ag_2^\circ$  excitation at 390nm in Ar, Kr, and Xe is interpreted in terms of an excited state  $Ag_2^\circ$  dissociation, involving strong destabilization of the A-state of  $Ag_2^\circ$  (bound in the gas phase) and strong stabilization of the  $^2P + ^2S$   $Ag^\circ$  fragments by matrix cage relaxation effects (as described in Scheme I for the  $^2P$  excited state of Ag itself). The net "cage-assisted" photofragmentation yield is quite small (around 10%) due to the short range repulsive constraints of the matrix cage, resulting in efficient recombination of the ground state  $Ag^\circ$  atomic fragments as illustrated in Scheme II.

The optical absorption, fluorescence and photochemical properties of  $Ag_3$  provide clear evidence for the occurrence of two distinct forms of  $Ag_3^\circ$  in each of the three rare gas matrices (4,8,9). This observation shows that the matrix environment can act to stabilize distinct isomeric forms of this species. It appears that a common form of  $Ag_3^\circ$  is produced during matrix formation in Ar, Kr and Xe and a structurally different yet common form of  $Ag_3^{\circ'}$  is produced by photoinduced aggregation of  $Ag^\circ$  atoms in Ar matrices and photoisomerization of  $Ag_3^\circ$  in Kr and Xe matrices. The results available for  $Ag_3^\circ, Ag_3^{\circ'}$  in rare gas matrices are summarized below:

Scheme III



In the case of the  $\text{Ag}_3^{\circ'}$  isomer in solid Ar, the spectroscopic and photochemical results indicate the operation of an efficient  $\text{Ag}_3 \rightarrow \text{Ag}_2 + \text{Ag}$  photodissociative-recombination process localized in the matrix cage. However, for the  $\text{Ag}_3^\circ$  isomer in solid Kr and Xe, the available data leans heavily in favour of a photoisomerization to the  $\text{Ag}_3^{\circ'}$  structural form within a deformable matrix cage. The observation of thermal and photolytic reversibility, amongst other things, argues in favour of a photoisomerization rather than a photodissociation or photoionization process for the  $\text{Ag}_3^\circ$  isomer in Kr and Xe matrices. These photoprocesses for  $\text{Ag}_3^\circ$  and  $\text{Ag}_3^{\circ'}$  in rare gas solids are summarized in Scheme III.

It is apparent that the effects discussed in the preceding paragraphs have a significance over and above that of the detailed form of the optical spectroscopy of  $\text{Ag}^\circ$  and  $\text{Ag}_n^\circ$  in rare gas matrices. The evidence for cage-relaxed atomic fluorescence and photoaggregation processes for  $\text{Ag}^\circ$ , cage-assisted photofragmentation/cage relaxed atomic emission/recombination processes for  $\text{Ag}_2^\circ$ , and the stabilization of distinct isomeric forms of  $\text{Ag}_3^\circ$  with characteristic photochemical and thermal properties is most significant because it represents a direct experimental indication that the rare gas matrix environment can exert a decisive influence on the energetic, dynamical and structural properties of entrapped metal atoms and molecular metal clusters (a similar idea has been proposed for  $\text{Ni}_2$  in solid Ar (11)). Thus in certain cases it may not be appropriate to make direct comparison of the results of spectroscopic and structural studies of entrapped metal clusters with predictions made on the basis of theoretical calculations on the corresponding atoms or clusters in the gas phase. Of course a great deal of very useful and interesting information can be obtained from such spectroscopic studies, even if the entrapped metal atoms and clusters are significantly perturbed by the matrix support. The elucidation of the spectroscopic and structural properties of entrapped or supported metal atoms and clusters is of interest from the point of view of the interaction between the cluster and the support, because such interactions, as described earlier, are expected to be of importance in most situations in which metal atoms and clusters are accessible for experimental studies and especially those situations where the clusters are involved in chemical or catalytic processes. The possibility that certain cluster spe-

cies can adopt more than one stable structural configuration in a rare gas matrix is an important consideration in spectroscopic, chemical and photochemical studies of entrapped cluster species. It is perhaps not surprising that this effect is important in the case of entrapped silver clusters, because molecular orbital calculations for these and related systems show that only small energy differences separate quite different structural forms of the clusters, such as straight chains and two and three dimensional structures. For example, on the basis of accurate SCF-CI calculations on the  $\text{Ag}_3$  molecule, Basch (12) has concluded that the energy difference between a linear and strongly bent form of  $\text{Ag}_3^0$  is only 0.14 eV or  $3.2\text{kcal.mol}^{-1}$ . This energy difference is of the same order of magnitude as the spectral shift of the  $\text{Ag}_3$  absorption bands from Ar to Xe matrices, which can be taken as a rough measure of the magnitude of the  $\text{Ag}_3$ -rare gas interaction energy (i.e. support effect). Thus it is reasonable to suggest that rare gas solid matrix effects, which might at first glance be categorized as weak support interactions, exert a significant influence on the energetic, dynamical and structural properties of entrapped silver atomic and cluster guests, and it is therefore of considerable interest to evaluate the nature of the metal-support effect for similar metal species in other supports. In the following section we present such data for silver atomic and low nuclearity silver cluster guests in well defined sites of faujasite zeolite hosts.

(B) Silver Atoms and Clusters in Faujasite Zeolites It has been shown recently by different techniques that small, charged silver clusters can be formed and stabilized in the cavities of zeolites A, X and Y. Uytterhoeven et al (3b) have shown that in completely silver exchanged zeolite X and Y, thermal treatment under vacuum followed by exposure to oxygen produced the clusters  $\text{Ag}_2^+ \text{q}^+$  and linear  $\text{Ag}_3^+ \text{p}^+$  (p and q not defined). The formation of these charged clusters arises from the simultaneous occupancy of the hexagonal prismatic site I and one or two adjacent sites I' in the sodalite cage. No optical data have been published concerning these charged clusters. Kellerman and Texter (13) have however, obtained optical spectroscopic evidence that isolated silver atoms are formed during the dehydration of low exchanged silver zeolite Y ( $\text{Ag}_8\text{NaY}$ ). The appearance of an absorption band at 306 nm, a fluorescence emission at 490 nm excited in the uv-range, as well as an excitation spectrum showing a maximum at 306 nm, constitute strong evidence for the existence of zeolite entrapped silver atoms by comparison with the corresponding data for gaseous and rare gas matrix isolated  $\text{Ag}^0$  atoms. The resistance of this species to oxidation by molecular  $\text{O}_2$  led the authors to conclude that the isolated silver atoms most probably reside in site I.

In this section we describe our diffuse optical reflectance and fluorescence emission/excitation spectra (14) related to the silver atoms and silver clusters  $\text{Ag}_2^+ \text{q}^+$  and  $\text{Ag}_3^+ \text{p}^+$  stabilized in

faujasite zeolites. We will attempt to elucidate the mechanism of formation of the clusters and, in particular compare the spectroscopy, photoprocesses and metal-support interactions of these zeolite entrapped silver guests with changing Si/Al ratio, as well as with the data for the corresponding guests immobilized in rare gas matrices.

The fully hydrated samples do not show any fluorescence or absorption in the wavelength ranges examined. However, when submitted to vacuum treatment at increasing temperature, the zeolite samples show fluorescence emission and excitation spectra whose intensity increases up to 500°C. In Figure 3A the excitation and emission profiles for  $Ag_xNaY_{500}$  are presented. These profiles remain essentially invariant after oxygen treatment at 400°C.

In the case of low loading samples ( $x = 3,6$ ) the excitation and emission bands at 308/312 nm and 483/490 nm respectively (Figure 3A,A; 3A,B) are in line with Kellerman and Texter's data (13) and are best interpreted as arising from isolated silver atoms residing in an inaccessible site of the zeolite lattice, most probably site I at the center of the hexagonal prism. The dynamic and energetic properties of intrazeolitic silver atoms in site I appear to be quite similar to those observed for silver atoms entrapped within the cubo-octahedral sites of the solid rare gases (5) and will be discussed in the next section. In the case of the completely exchanged sample ( $x = 55$ ), the reflectance spectrum taken after oxygen treatment at 300°C (Figure 3B, A) shows an intense and narrow absorption at 340 nm and the excitation spectrum shows a maximum at 340 nm associated with a broad emission centred around 544 nm (Figure 3A, F). At this level of exchange, Uytterhoeven's crystallographic results (3) indicate the probable presence of a charged cluster  $Ag_2^{q+}$  arising from the simultaneous occupancy (at least to a certain extent, measured by the excess of population in site I') of one site I and one adjacent site I' by a silver ion. Therefore, we associate the species giving rise to these optical spectra with the cluster  $Ag_2^{q+}$ , the spectroscopic properties of which will be described in a later section (where  $q$  is shown to be unity).

In the case of  $Ag_{13}NaY$ , the excitation and emission spectra (Figure 3A,C) indicate the presence of a mixture of isolated atoms (313 nm, 495 nm respectively, in line with the spectral properties of  $Ag_3NaY$  and  $Ag_6NaY$ ) as well as charged clusters  $Ag_2^+$  associated with the shoulder at 334 nm in the excitation spectrum giving rise to the 530 nm emission band (Figure 3A,D). The  $Ag_{35}NaY$  sample is found to contain mainly the species  $Ag_2^{q+}$  (excitation maximum at 338 nm, emission at 535 nm, Figure 3A,E) with a small amount of isolated silver atoms giving rise to a slight band broadening on the high energy side of the excitation band.

These results demonstrate that beginning with isolated silver atoms in the samples  $Ag_3NaY$ , an increase in silver ion concentration induces a growth in the population of  $Ag_2^{q+}$  species, via a progressive occupancy of site I' adjacent to site I. Taking into account the site occupancies obtained by Uytterhoeven (3) for

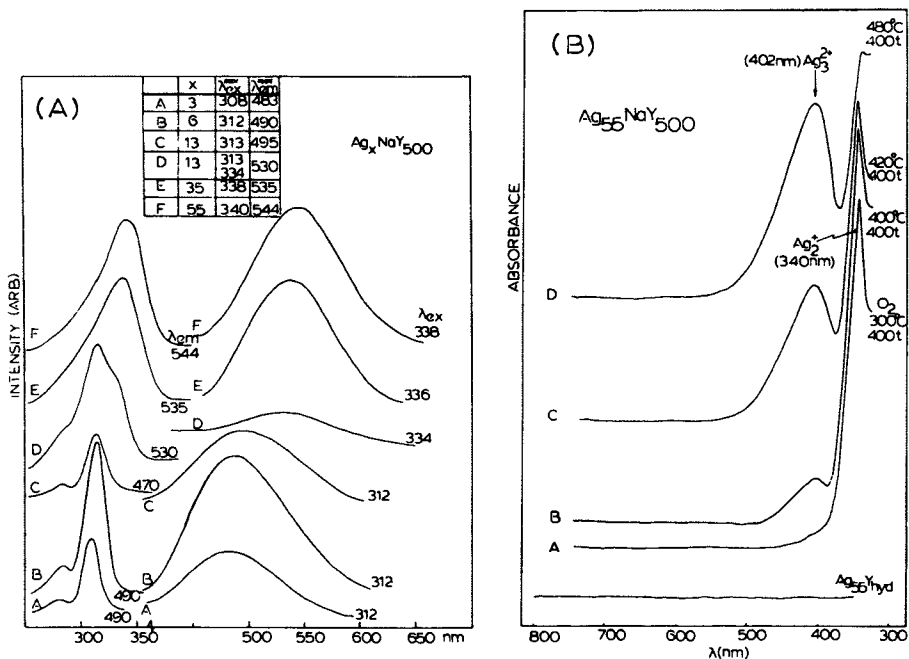


Figure 3.

(A) Fluorescence emission and excitation spectra of  $Ag_xNaY_{500}$ , where  $x$  varies from 3 to 55. (Ref. 14).

(B) Diffuse reflectance spectra of  $Ag_{55}NaY_{500}$  as a function of oxygen treatment (400 torr) at increasing temperature. Lower trace shows baseline of the hydrated sample

(Reproduced with permission from Ref. 14. Copyright, American Chemical Society.)

site I (12.8 Ag) and site I' (13.1 Ag) in  $\text{Ag}_{56}\text{Y}$ , together with our fluorescence results (14), we can deduce that in completely exchanged silver zeolite Y there exists a strong tendency for the silver ions to simultaneously occupy the site I and I' positions to form  $\text{Ag}_2^{\text{q+}}$ , up to a maximum of approximately 13  $\text{Ag}_2^{\text{q+}}$ /unit cell.

In Figure 3B are presented the diffuse reflectance spectra obtained after oxidation of  $\text{Ag}_{55}\text{NaY}$  under  $\text{O}_2$  at increasing temperature. When the temperature of  $\text{O}_2$  treatment is raised above  $300^\circ\text{C}$  up to  $480^\circ\text{C}$ , the sample turns yellow and one observes the progressive increase of a new band at 402 nm with a concomitant decrease of the 340 nm band associated with  $\text{Ag}_2^{\text{q+}}$ . The behaviour of these two bands indicates that the new species giving rise to the 402 nm absorption is generated at the expense of the  $\text{Ag}_2^{\text{q+}}$  clusters. Moreover, the position of the new band suggests that it corresponds to a small silver cluster (4-10). Unlike  $\text{Ag}^\circ$  and  $\text{Ag}_2^{\text{q+}}$ , fluorescence emission could not be excited for this new silver cluster species anywhere in the range 200-700 nm (c.f.  $\text{Ag}_3^{\circ}$  in Ar described earlier). Taking into account that the linear cluster  $\text{Ag}_3^{\text{P+}}$  stabilized in the sodalite cage of zeolite A has been shown to absorb at 446 nm (3) and that  $\text{Ag}_3^\circ$  and  $\text{Ag}_3^{\circ}$  isomers isolated in rare gas solids absorb in the range 400-440 nm and 440-474 nm respectively (8,9), we tentatively attribute our new 402 nm absorption to an  $\text{Ag}_3^{\text{P+}}$  cluster. Such a cluster could be envisaged to form from  $\text{Ag}_2^{\text{q+}}$  by simply filling the vacant site I' adjacent to a filled site I. It would in fact correspond to the  $\text{Ag}_3^{\text{P+}}$  cluster identified by Uytterhoeven by x-ray diffraction analysis (3). The spectral shift from 402 nm to 446 nm probably reflects the different environment of  $\text{Ag}_3^{\text{P+}}$  in the  $\beta$ - cage of zeolite A compared to site I + 2 site I' of  $\text{Ag}_3^{\text{P+}}$  in zeolite Y, and/or the slightly different silver-silver bond lengths (2.85 - 3.00Å in zeolite A, 3.08 - 3.17Å in zeolite X and Y). The formation of  $\text{Ag}_3^{\text{P+}}$  from  $\text{Ag}_2^{\text{q+}}$  requires the filling of a vacant site I' adjacent to a filled site I - site I' pair (illustrated in Figure 4), which implies the migration of a silver ion from another lattice site (I, II, II') to site I under the influence of  $\text{O}_2$  treatment at elevated temperatures, which is consistent with Uytterhoeven's recent X-ray observations (3). Because site II shows the highest occupancy among the available sites, it is likely that the migration preferentially depletes this site, defining the  $\text{Ag}_3^{\text{P+}}$  nucleation process as a migration from the supercage (II) to the sodalite cage (I') sites. Without going into detail it should be noted that similar experiments to those described for  $\text{Ag}_x\text{NaY}$  have been performed for  $\text{Ag}_x\text{NaX}$  and the results are summarized, for low and high silver exchanged samples, in Figures 5 and 6. In the context of this and the following discussions, the most important features to notice for  $\text{Ag}^\circ$ ,  $\text{Ag}_2^{\text{q+}}$  and  $\text{Ag}_3^{\text{P+}}$  are (i) red spectral shifts in the  $\text{Ag}^\circ$  emission and excitation band maxima on passing from ZY to ZX (ii) red spectral shifts for the  $\text{Ag}_2^{\text{q+}}$  emission and excitation band maxima on passing from ZY to ZX (iii) red spectral shifts for the emission and excitation band maxima of  $\text{Ag}_2^{\text{q+}}$  relative to  $\text{Ag}^\circ$  for ZY and (iv)

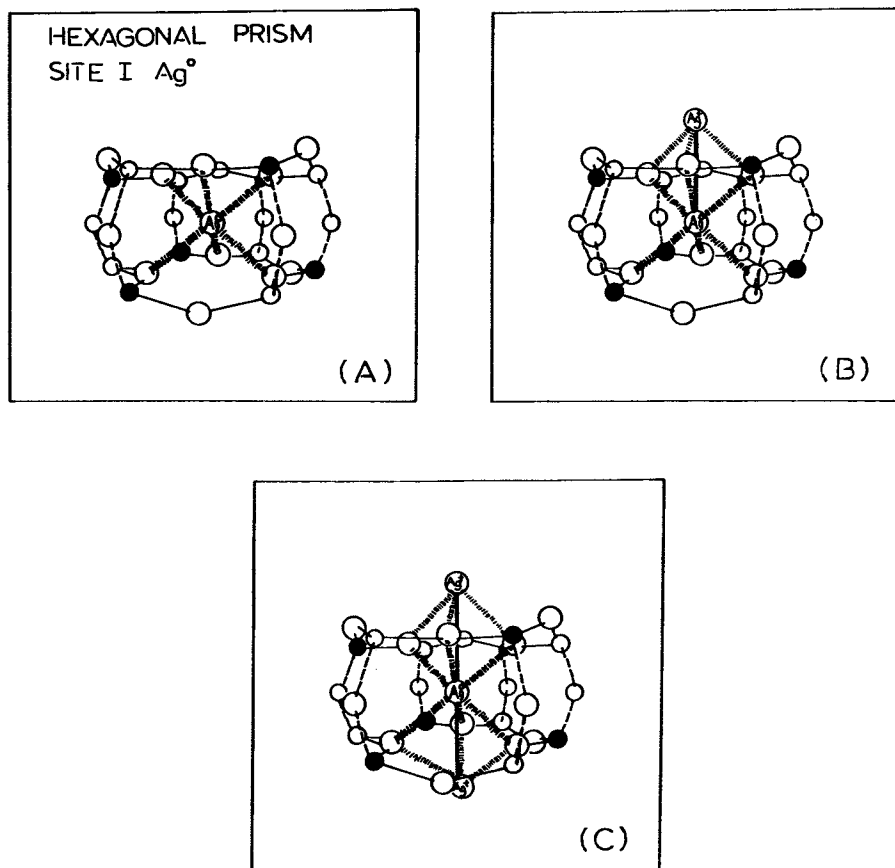


Figure 4.  
Perspective drawing of the location and coordination  
of (A):  $\text{Ag}_1^\circ$ , (B):  $\text{Ag}_2^+$ , (C):  $\text{Ag}_3^+$ , in X and Y zeolites,  
where  $\text{Ag}^\circ$  occupies site I (centre of the hexagonal  
prism) and  $\text{Ag}^+$  one (or two) adjacent site I'  
(Reproduced with permission from Ref. 3b.)

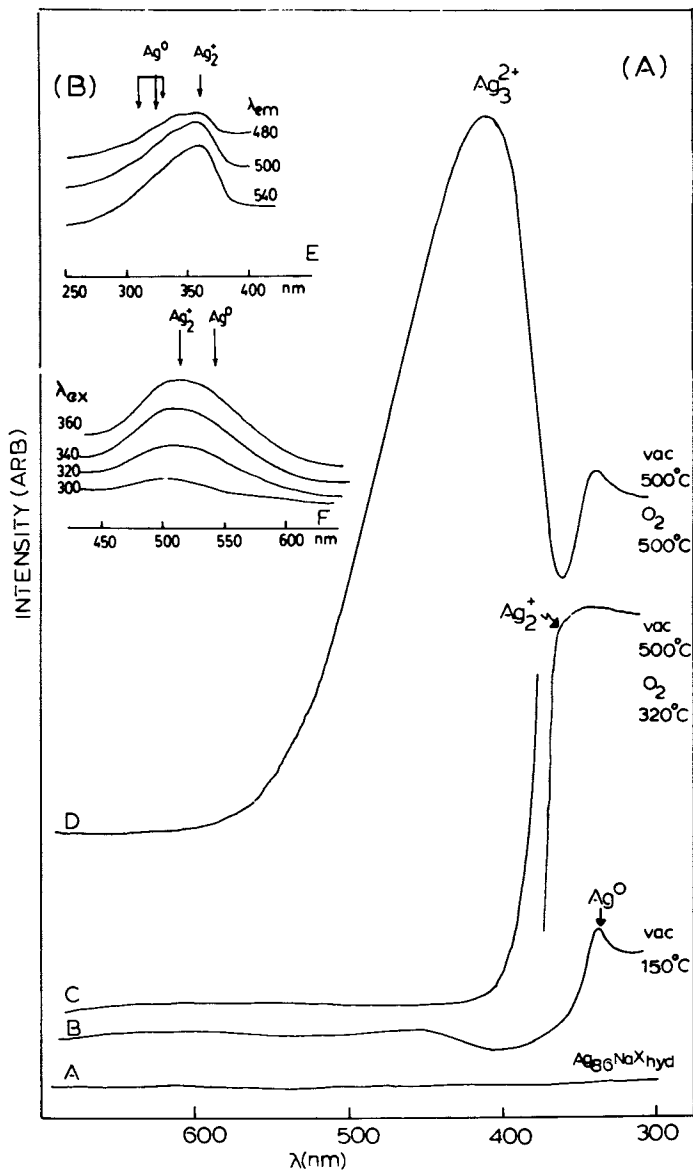


Figure 5. Diffuse reflectance spectra (A) of  $\text{Ag}_{86}\text{NaX}$  taken during dehydration under vacuum and oxygen treatment<sup>86</sup> (400 torr). Fluorescence emission and excitation profiles (B) corresponding to stage C in Figure 5(A) (15).



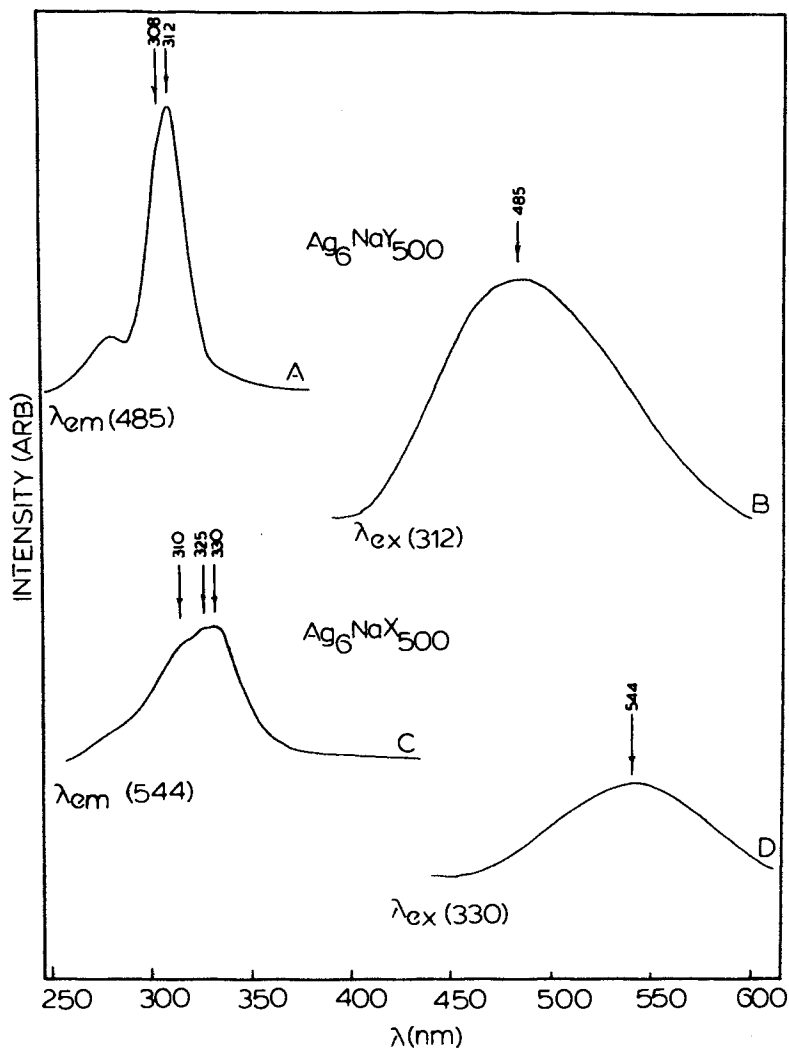


Figure 6.  
 Fluorescence emission and excitation spectra of  $\text{Ag}_6\text{NaY}_{500}$  and  $\text{Ag}_6\text{NaX}_{500}$ . Note that the weak shoulder seen around 280 nm for the excitation spectra is probably due to  $\text{Ag}^+$  (15).

a red spectral shift for the emission maximum but a blue spectral shift for the excitation maximum for  $\text{Ag}_2^{\text{q}+}$  relative to  $\text{Ag}^\circ$  in ZX (see later sections). In view of the consistency between the crystallographic data and the electronic absorption and emission spectroscopy for the proposed intrazeolitic silver guests  $\text{Ag}^\circ$ ,  $\text{Ag}_2^{\text{q}+}$  and  $\text{Ag}_3^{\text{p}+}$  it is surprising that on the one hand there is no observable epr signal attributable to these paramagnetic species (at least  $\text{Ag}^\circ$ , the charges p and q for  $\text{Ag}_2^{\text{q}+}$  and  $\text{Ag}_3^{\text{p}+}$  being not precisely known) and on the other hand, considering the extensive previous epr work done, that no spectra have been reported for the vacuum dehydrated forms of  $\text{AgNaX}$  and  $\text{AgNaY}$  zeolites. Note that the epr spectra of similar species ( $\text{Ag}_1^\circ$  and  $\text{Ag}_{n+1}^\circ$  for  $n = 1, 2, 3, \dots$ ) have been observed in hydrated or partially dehydrated silver exchanged zeolites A, X and Y following  $\gamma$ - or X-ray irradiation (16). The epr silence for these species may be due to several factors, such as saturation of the paramagnetic species at low microwave powers, due to spin-lattice relaxation effects, coupled with broadening effects due to the existence of other paramagnetic species in the vicinity of the silver guests.

At this point we note that the overall form of the absorption, fluorescence emission and excitation profiles for  $\text{Ag}_1^\circ$ ,  $\text{Ag}_2^{\text{q}+}$  and  $\text{Ag}_3^{\text{p}+}$  for  $\text{Ag}_x\text{NaX}$  and  $\text{Ag}_x\text{NaY}$  is superficially reminiscent of those observed for  $\text{Ag}^\circ$ ,  $\text{Ag}_2^\circ$ , and  $\text{Ag}_3^\circ$  entrapped in rare gas solids (4-10). However, a number of important differences are also apparent. These details are discussed for each silver guest as a necessary prelude to the subject of metal-support interactions.

(C) Intrazeolitic  $\text{Ag}^\circ$  Spectroscopy and Photoprocesses In all discussions of the spectroscopy, photoprocesses and support-interactions of immobilized metal atoms (or clusters) a knowledge of the local structure and symmetry of the trapping site is mandatory. For the particular case of faujasite zeolites containing site I isolated  $\text{Ag}^\circ$  atoms, the first coordination sphere is comprised of six oxygen atoms, three from each hexagonal six-ring (17). As the crystallographic data for  $\text{Ag}_3^{\text{p}+}$  in faujasite zeolites demonstrates that all of the site I<sub>0</sub>Ag-O bond lengths are approximately equal ( $\text{Ag}(\text{I}) - 60(3) = 2.67\text{\AA}$  for  $\text{Ag}_{56}\text{NaY}$ ) conveying near perfect octahedral symmetry to the central Ag atom, it is reasonable to assume that the "gross" features of the electronic and optical properties of site I isolated  $\text{Ag}^\circ$  atoms in faujasite zeolites will be governed by a model in which the local symmetry of the six oxygen atoms is cubic. By taking into account the Si/Al distribution, the effects of the full symmetry of the hexagonal prism (illustrated in Figure 7, based on MASNMR and Dempsey's rules (18, 19)) can probably be treated as a non-cubic

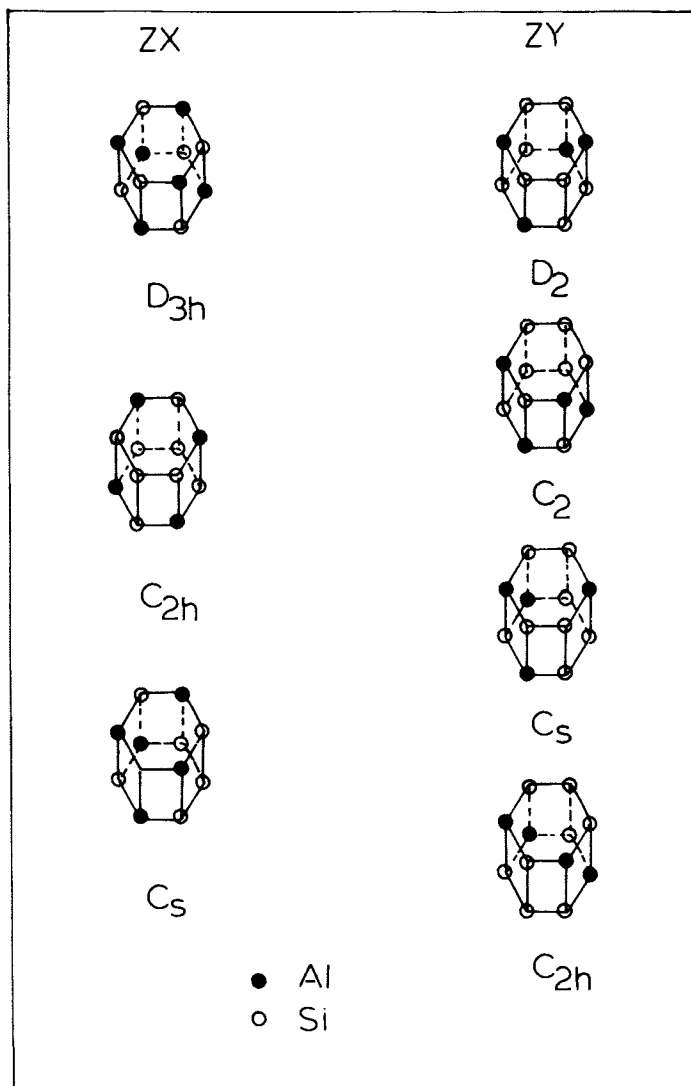


Figure 7. Distribution of aluminium atoms in the hexagonal prism of faujasite-type zeolites. According to  $^{29}\text{Si}$  Magic-Angle-Spinning NMR data (Ref. 18) and Dempsey's rules (Ref. 19) for zeolite X (Si/Al = 1.18) and zeolite Y (Si/Al = 2.0), the site distribution for zeolite X is  $D_{3h}$ : 9,  $C_{2h}$ : 1,  $C_s$ : 6, and for zeolite Y the centrosymmetric site  $C_{2h}^s$  is strongly favoured (15).

perturbation on the model used to interpret the optical spectroscopy (see later).

The overall form, but not the detail, of the fluorescence emission and excitation profiles for  $\text{Ag}^\circ$  atoms in site I of X and Y zeolites is similar to those observed for  $\text{Ag}^\circ$  atoms isolated in the cubo-octahedral site of rare gas solids. The observation of multiple structure on the  $^2\text{P} \leftarrow ^2\text{S}$  absorption and large red spectral shifts for the  $^2\text{P} \rightarrow ^2\text{S}$  emission of site I entrapped  $\text{Ag}^\circ$  atoms, indicates that the guest-host interactions are markedly different for the  $^2\text{S}$  and  $^2\text{P}$  states and can be explained in terms of site I relaxation effects, using a vibronic coupling model similar to that described in detail for  $\text{Ag}^\circ$  atom rare gas cage complexes (5).

In brief, the form of the potential energy surface in the simplest theory (20) for a  $^2\text{P}$   $\text{Ag}^\circ$  atom in an  $\text{O}_h$  symmetry  $\text{AgO}_6$  "quasi-molecule", for the case of strong spin-orbit and weak vibronic coupling, is illustrated in the configuration coordinate diagram of Figure 8. If the non-cubic perturbations arising from the Si/Al distribution around the  $\text{AgO}_6$  coordination sphere are small compared to the Jahn-Teller interactions, then the model should be still applicable with some slight modification (see later). The  $U_1$  and  $U_2$  branches of the potential energy surface represent the two electronic states which replace the original  $^2\text{P}_{3/2}$  state ( $^2\text{G}_{3/2u}$  in the  $\text{O}_h'$  double group) where the separation at any point in the ( $Q_2, Q_3$ ) coordinate space represents the vibronic splitting of the  $^2\text{G}_{3/2u}$  state. The curve labelled  $U_3$  represents the potential energy surface for the  $^2\text{P}_{1/2}$  state ( $^2\text{E}_{1/2u}$  in the double group  $\text{O}_h'$ ) in which account has been taken of the effects of  $^2\text{P}_{1/2} - ^2\text{P}_{3/2}$  mixing of the spin-orbit components (20).

Thus optical excitation of  $\text{AgO}_6$  into the  $U_1, U_2$  or  $U_3$  surfaces should be followed by rapid vibrational relaxation to the respective minimum points and subsequent radiative decay to the  $^2\text{S}_{1/2}$  ( $^2\text{A}_{1g}$  in the double group  $\text{O}_h'$ ) ground state surface, as illustrated in Figure 8. The large spectral shifts of the emission bands of site I  $\text{Ag}^\circ$  atoms can therefore be seen to be the consequence of the tendency for Jahn-Teller distortion of the excited state  $\text{Ag}^\circ$  site I cage complex. The red shifts arise both from the stabilization of the excited state and accompanying destabilization of the ground state (Figure 8).

With the configuration coordinate diagram of Figure 8 which is applicable to perfect  $\text{O}_h$  symmetry one can begin to interpret the major splittings and shifts in the emission/excitation spectra of  $\text{Ag}^\circ$  in  $\text{Ag}_6\text{NaX}_{500}$  and  $\text{Ag}_6\text{NaY}_{500}$ . However, to take into account the Si/Al distribution in X and Y zeolites, it is necessary to first consider how the model predictions would be altered for  $\text{Ag}^\circ$  trapping sites exhibiting different actual site symmetries, remembering that the first coordination sphere of a site I  $\text{Ag}^\circ$  atom in faujasite zeolites is perfectly octahedral no matter what the Si/Al ratio.

If the non-cubic perturbation is small compared to the vibronic interactions (which probably applies to the present case of

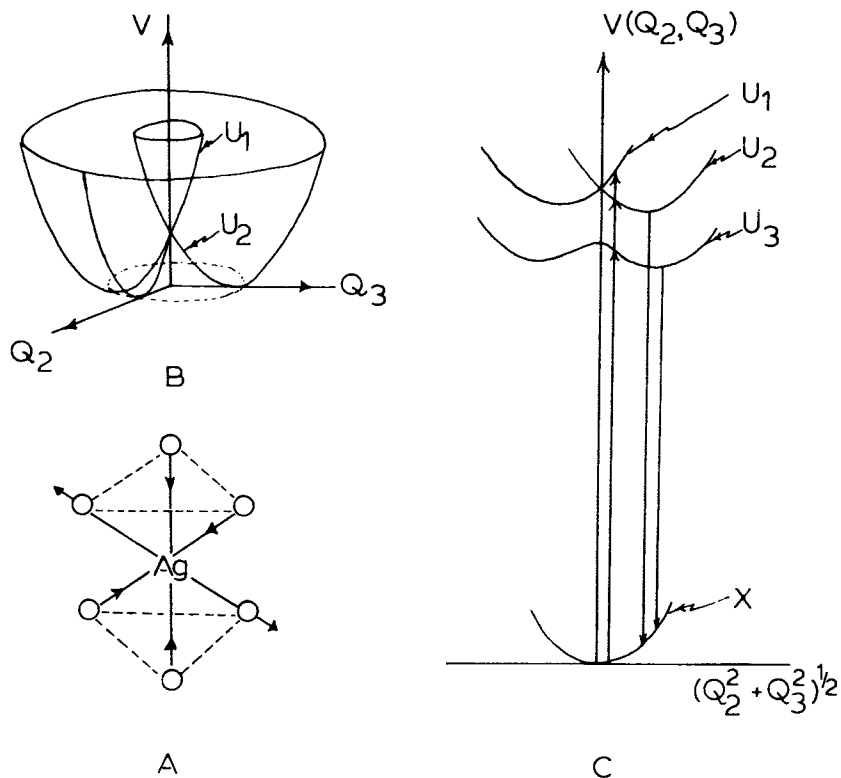


Figure 8. Vibronic coupling model used to explain the dynamic and energetic properties of the octahedral  $\text{Ag}^{\text{O}}_6$  cage complex (A), appropriate for a silver atom in site I of faujasite-type zeolites (5).

a next-nearest neighbour Si/Al perturbation on the  $\text{AgO}_6$  quasi-molecule) then the model should still be applicable, since the Jahn-Teller effect can operate also in the case of near degeneracy (20). However, the potential energy surfaces would no longer be expected to be symmetrical for tetragonal distortions along the x, y, z directions, since these directions would be rendered inequivalent by the non-cubic perturbations. This could cause a splitting or broadening of certain emission bands into two or more components because the accessible distorted configurations would be energetically inequivalent in Figure 8. Furthermore, it is expected that the energetic positions of the emission bands would be different for distinct types of trapping sites. Considerations of this type could account for the appearance of broad structureless emission bands of site I  $\text{Ag}^\circ$  atoms in  $\text{Ag}_6\text{NaX}_{500}$  and  $\text{Ag}_6\text{NaY}_{500}$ , where there clearly exists a distribution of site I types with less than cubic symmetry.

One may conclude that the optical emission and excitation spectra for site I  $\text{Ag}^\circ$  atoms are probably best interpreted in terms of a strong spin-orbit and weak vibronic coupling model for the  $^2\text{P}$  excited state of  $\text{Ag}^\circ$  in an  $\text{AgO}_6$  cage, in which weaker interactions arising from the Si/Al distribution in the second coordination sphere of  $\text{AgO}_6$  are seen in X zeolite as two major emissions from the high abundance  $\text{D}_{3d}$  and  $\text{C}_s$  sites, and in Y zeolite as one major emission from the dominant  $\text{C}_{2h}$  site (15), both with superimposed non-cubic perturbations (Figure 7).

(D)  $\text{Ag}^\circ$  - Support Interactions Recall that the major absorption and emission processes of gaseous Ag atoms in the uv-range are rather straightforwardly interpreted in terms of electronic transitions between an isotropic  $4d^{10}5s^1$ ,  $^2\text{S}_{1/2}$  ground state and a spin-orbit split  $4d^{10}5p^1$ ,  $^2\text{P}_{3/2, 1/2}$  excited state (21). However, when implanted into a solid support, dramatic alterations in the spectroscopic properties of  $\text{Ag}^\circ$  atoms are expected as described earlier.

In the specific case of  $\text{Ag}^\circ$  atoms in site I of faujasite type zeolites, one can qualitatively rationalize the red shifts observed for the  $^2\text{P} \leftrightarrow ^2\text{S}$  emission (485 to 544 nm)/ excitation (308/312 to 310/325/330 nm) bands with increasing Al content on passing from Y to X zeolite, in terms of the anticipated increasing electronic charge density on the oxygen atoms of the  $\text{AgO}_6$  first coordination sphere. Short range repulsive interactions between the electronic charge clouds of the low lying valence  $2s/2p$  orbitals of these oxygen atoms and the valence  $5s/5p$  orbitals of an  $\text{Ag}^\circ$  atom at the centre of site I, would tend to destabilize the  $^2\text{S}$  state with respect to the  $^2\text{P}$  state of  $\text{Ag}^\circ$ , the higher charge density on oxygen causing the greater reduction in the  $^2\text{S} \leftrightarrow ^2\text{P}$  energy separation. With this simple model one can satisfactorily account for the red shift of the emission and excitation bands of site I  $\text{Ag}^\circ$  atoms on passing from Y to X zeolite.

Another way of viewing these metal-support effects described above is in terms of a site I effective cage polarizability which

is sensitive to the Si/Al ratio. An increasing charge density on the first coordination sphere oxygen atoms in the  $\text{AgO}_6$  cage-complex is accompanied by an increasing cage polarizability. One might therefore envisage that a correlation between cage polarizability and the  $^2\text{P} \leftrightarrow ^2\text{S}$  emission and excitation energies should exist for  $\text{Ag}^\circ$  isolated in a variety of matrices, in which the metal-support interaction can be categorized as weak. In practice, one finds that a plot of the polarizability of the solid rare gases Ar, Kr and Xe (measured at 20K) versus the energies of the observed  $^2\text{P} \leftrightarrow ^2\text{S}$  emission and absorption bands (employing average values of the energies of the spin-orbit/vibronic components) for the major (thermally stable) cubo-octahedral trapping site of atomic silver, is remarkably linear as seen in Figure 9A, 9B. As a first approximation, these correlations can be considered to provide a calibration of effective cage polarizability with respect to the  $^2\text{S}$  and  $^2\text{P}$  electronic states of  $\text{Ag}^\circ$  atoms in a range of substrates. On placing the emission and excitation energies of site I  $\text{Ag}^\circ$  atoms in X and Y zeolites on the appropriate  $\alpha$  versus  $\Delta E(^2\text{P} \leftrightarrow ^2\text{S})$  plots of Figure 9A, 9B, one finds that the effective cage polarizability for both the ground ( $^2\text{S}$ ) and excited ( $^2\text{P}$ ) states of atomic silver is greater for zeolite X than for zeolite Y. This observation is consistent with the charge density arguments presented earlier. For the  $\text{Ag}^\circ(^2\text{S})$  atom the  $\alpha$  value for ZX lies between those of Xe and Kr and for ZY between Kr and Ar (Figure 9A). The apparent increase in the effective cage polarizability of  $\text{Ag}^\circ(^2\text{P})$  compared to  $\text{Ag}^\circ(^2\text{S})$  in X and Y zeolites as seen in Figure 9A, 9B is most likely due to the use of an  $\alpha$  vs  $\Delta E(^2\text{P} \rightarrow ^2\text{S})$  correlation based on the averaging of the emission energies of the  $U_1/U_2$  and  $U_3$  surfaces (Figure 8) for  $\text{Ag}^\circ$  in rare gas matrices. This discrepancy indicates that the  $\text{Ag}^\circ$  emissions in X and Y zeolites probably originate entirely from the lower  $U_3$  surface and that a more appropriate  $\alpha$  vs  $\Delta E(^2\text{P} \rightarrow ^2\text{S})$  correlation should employ the lower energy rare gas emission components of  $\text{Ag}^\circ$  also graphed in Figure 9D. These data yield effective cage polarizabilities for  $\text{Ag}^\circ(^2\text{P})$  which are in line with those obtained for  $\text{Ag}^\circ(^2\text{S})$  in Figure 9A, for which averaging of the  $\Delta E(^2\text{P} \leftrightarrow ^2\text{S})$  excitation energies is more acceptable.

(E) Support Interactions in the Spectroscopy and Photo-processes of  $\text{Ag}_2^+$  in Zeolite X and Y It is interesting to compare the spectroscopic properties of site I, I' isolated  $\text{Ag}_2^+$  in ZY with those for  $\text{Ag}_2$  entrapped in rare-gas solids (6). In the latter one finds a strongly blue shifted gas to matrix X,  $^1\Sigma_g^+ \rightarrow A, ^1\Sigma_u^+$  transition which appears as a broad, structureless absorption band, and for which, photoexcitation produces atomic fluorescence as a result of an excited state  $\text{Ag}_2$  dissociation process. The blue shift is due mainly to strong destabilization of the excited A-state of  $\text{Ag}_2$  (bound in the gas phase) where the energetics is such that the optically prepared state is unstable with respect to dissociation to excited atomic fragments.

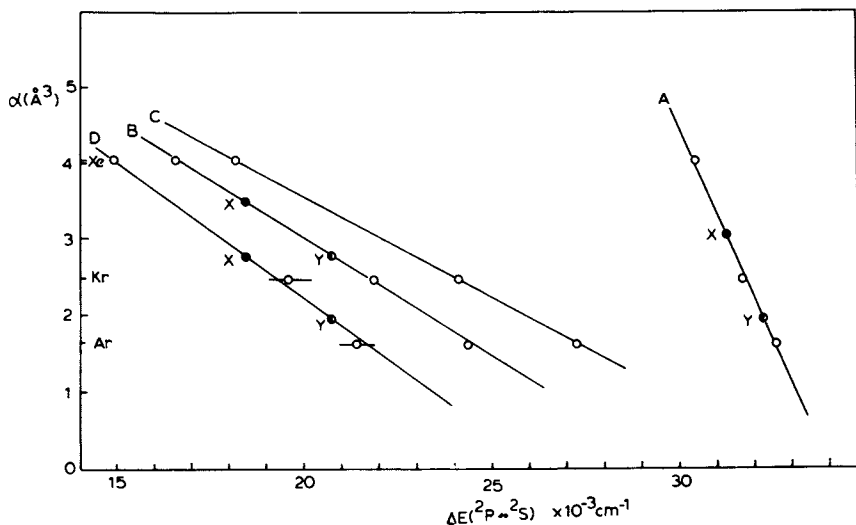


Figure 9.

Plot of fluorescence emission and excitation (absorption) band energies ( $\text{cm}^{-1}$ ) versus polarizability ( $\text{\AA}^3$ ) for  $\text{Ag}^0$  atoms isolated in solid Ar, Kr, and Xe (5, 22). In this case of the excitation process, average energies of the extremal spin-orbit component bands have been plotted in graph (A). For the emission process, the average energies of the  $U_1/U_2$  and  $U_3$  component bands (see Figure 8) as well as the actual energies of the individual  $U_1/U_2$  and  $U_3$  component bands have been plotted in graphs (B), (C) and (D) respectively. The observed excitation and emission energies for  $\text{Ag}_6\text{NaX}_{500}$  and  $\text{Ag}_6\text{NaY}_{500}$  have been placed on graphs (A), (B) and (D) (see text for details).



On the other hand, the ground state of  $\text{Ag}_2$  is found not to be strongly perturbed in the rare-gas matrix. The instability with respect to excited state dissociation arises from two factors. Firstly, there are repulsive (destabilizing)  $\text{Ag}_2$ -rare gas interactions in the excited state of  $\text{Ag}_2$  which originate from electronic repulsion effects due to the diffuse charge density associated with the A-state (i.e. resulting in blue gas to matrix shifts). Secondly, the  $^2\text{S} + ^2\text{P}$  atomic fragments, which correlate with the optically prepared A-state of  $\text{Ag}_2$ , are strongly stabilized by matrix-cage relaxation effects in a manner analogous to that described in detail for  $^2\text{P}$  atomic  $\text{Ag}^\circ$  in rare gas solids (5). The extent to which the destabilization of the photoexcited  $\text{Ag}_2$  is successful in promoting net dissociation is determined by the detailed relaxation dynamics of the excited  $\text{Ag}_2$ -rare gas cage-complex (6). This idea is illustrated schematically in Figure 10.

Compared to gaseous  $\text{Ag}_2$ , the gaseous cation  $\text{Ag}_2^+$  is expected to have a less strongly bound X-state ( $^2\Sigma_g^+$ ) and a dissociative (or weakly bound) A-state ( $^2\Sigma_u^+$ ) which correlate with the separated atom and ion limits  $^2\text{S}(\text{Ag}^\circ) + ^1\text{S}(\text{Ag}^+)$  and  $^2\text{P}(\text{Ag}^\circ) + ^1\text{S}(\text{Ag}^+)$  respectively (Figure 10). For zeolite Y isolated  $\text{Ag}_2^+$ , repulsive interactions with the O(3) atoms at site I, I' will act to further destabilize the A-state of  $\text{Ag}_2^+$  with respect to dissociation to excited  $\text{Ag}^\circ$   $^2\text{P}$  atomic fragments (Figure 10), where the latter will be strongly stabilized by site I cage-relaxation effects primarily involving the six O(3) oxygen atoms. One therefore expects the energetic and dynamical properties of  $\text{Ag}_2^+$  in ZY to be such that the A  $\leftarrow$  X transition should be blue shifted compared to that of  $\text{Ag}_2$  in rare-gas solids ( $\text{Ag}_2^+$ , 340 nm, ZY;  $\text{Ag}_2$ , 389 nm, Ar; 390 nm, Kr; 391 nm, Xe; 435 nm, gas phase (6)) and for which photoexcitation should produce cage-relaxed  $^2\text{P}$   $\text{Ag}^\circ$  atomic fluorescence as a result of either an intrinsic/and or cage-assisted excited state dissociation process of  $\text{Ag}_2^+$  in site I, I'. This  $\text{Ag}^\circ$  emission from  $\text{Ag}_2^+$  in ZY is expected to be somewhat red shifted (544 nm) compared to the emission from cage-relaxed  $^2\text{P}$   $\text{Ag}^\circ$  atoms isolated in site I (483/490 nm) as a result of short range repulsive interactions with the neighbouring site I',  $\text{Ag}^+$  ion, the latter destabilizing the  $^2\text{S}$  state to a greater extent than the  $^2\text{P}$  state of  $\text{Ag}^\circ$  thereby reducing the  $^2\text{P} \rightarrow \text{S}$  energy separation. Overall therefore, a net charge of +1 seems quite reasonable and hence an  $\text{Ag}_2^+$  formulation for the binuclear charged cluster in zeolite Y.

The sensitivity of the  $^2\text{P} \leftrightarrow ^2\text{S}$  transition energy of  $\text{Ag}^\circ$  atoms isolated in rare gas and faujasite zeolite matrices described in section D, proved to be a valuable probe of the  $\text{Ag}^\circ$ -support interaction. This suggests that similar concepts might be applied to site I, I' isolated  $\text{Ag}_2^+$  cations in ZX and ZY. In practice one finds that the uv-absorption band for  $\text{Ag}_2^+$  red shifts (340  $\rightarrow$  360nm) whereas the visible emission band blue shifts (544  $\rightarrow$  510nm) on passing from ZY to ZX. By considering  $\text{Ag}_2^+$  to have a bound X,  $^2\Sigma_g^+$  ground electronic state and a dissociative (or weakly bound) A,  $^2\Sigma_u^+$

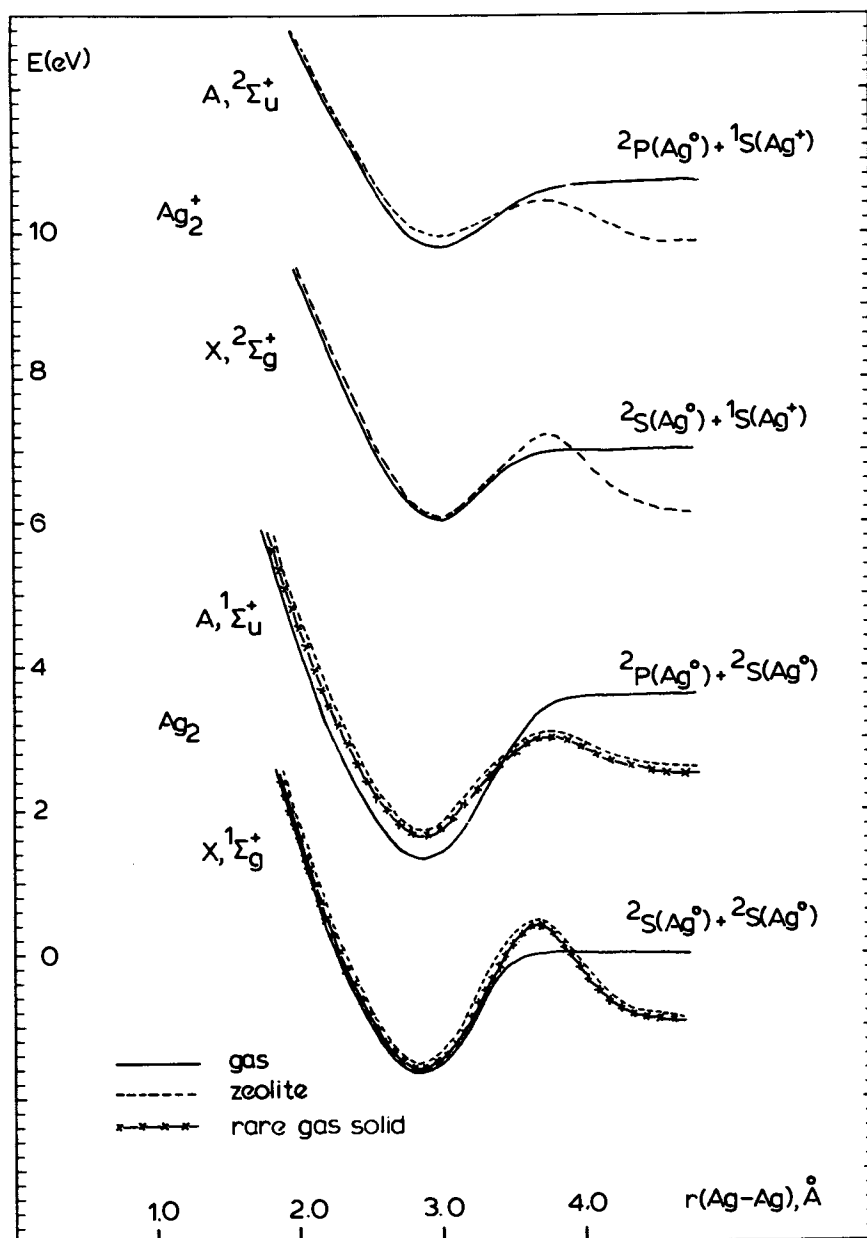


Figure 10.

Illustration of the X and A-state potential energy curves for gaseous, rare gas solid, and zeolite Y isolated  $\text{Ag}_2$  and  $\text{Ag}_2^+$  (15).

excited state (Figure 10) one can rationalize the spectral trends for  $\text{Ag}_2^+$  on passing from ZY to ZX simply in terms of a greater  $\text{Ag}^+(\text{I}')\text{-O}(3)$  interaction. This will lead to a reduction in the repulsive interactions between the  $\text{O}(3)$  oxygens and the diffuse charge density of the A-state of  $\text{Ag}_2^+$ , thereby resulting in stabilization of the A-state relative to the X-state and an explanation for the observed red spectral shift in the absorption energy of  $\text{Ag}_2^+$  on passing from ZY to ZX. However, the greater  $\text{Ag}^+(\text{I}')\text{-O}(3)$  interaction in ZX than in ZY will also have the effect of reducing the repulsive interactions between the  $\text{O}(3)$  oxygens and the site I  $\text{Ag}^\circ$  atom the latter being produced following the photoexcitation of  $\text{Ag}_2^+$  into the A-state. Overall, this will be manifest as a blue spectral shift in the  $^2\text{P} \rightarrow ^2\text{S}$  emission energy on passing from ZY to ZX, in agreement with the observations.

At this point one can conclude that like  $\text{Ag}_2$  in rare gas matrices, the absorption and fluorescence spectra of  $\text{Ag}_2^+$  in X and Y zeolites are also clearly indicative of strong guest-host interactions involving the low lying electronic states. In particular, the absorption, fluorescence and excitation bands for  $\text{Ag}_2^+$  show energy shifts on passing from ZY to ZX which are consistent with the expected increasing charge density on the site I, I'  $\text{O}(3)$  oxygen atoms arising from the lower Si/Al ratio. Furthermore, photoexcitation of the A-X absorption band of  $\text{Ag}_2^+$  produces intense emission bands characteristic of  $\text{Ag}^\circ$  atoms in site I, as a result of an excited-state dissociation process. This involves strong stabilization of the  $^2\text{P}$  atomic fragment by site I cage relaxation effects, analogous to those described for  $\text{Ag}_2$  in rare gas matrices (6). The quantum yield for fluorescence is probably near unity but the net  $\text{Ag}_2^+$  photodissociation yield is zero probably because of the rigidity of the hexagonal prismatic site I in faujasite zeolites and the close proximity of the  $\text{Ag}^\circ$  and  $\text{Ag}^+$  photofragments in adjacent sites I, I' respectively. This should be contrasted with the small, but observable, net photodissociation of  $\text{Ag}_2$  trapped in the more deformable cages of the solid rare gases (6).

(F)  $\text{Ag}_3^{2+}$  in Zeolite X and Y. The  $\text{Ag}_3^{2+}$  cluster cation has been crystallographically characterized as the yellow chromophore in silver exchanged, vacuum and oxygen pretreated A, X and Y zeolites (3). From Uytterhoeven's work,  $\text{Ag}_3^{2+}$  isolated in the sodalite cage of ZA absorbs at 446 nm (3a). The present study defines the corresponding electronic transitions for  $\text{Ag}_3^{2+}$  entrapped in site I, I' of ZX and ZY at 410 and 402 nm respectively. As described earlier, trisilver isolated in rare gas matrices exists in two structurally distinct forms denoted  $\text{Ag}_3^\circ$  absorbing at 400, 420, 440 nm and  $\text{Ag}_3^{\circ'}$  absorbing at 440, 470, 474 nm in Ar, Kr and Xe respectively (8, 9).

It is apparent from the support sensitivity of these low lying electronic transitions that guest-host interactions play a significant role for  $\text{Ag}_3^\circ$  and  $\text{Ag}_3^{\circ'}$  in rare gas

matrices, as well as for  $\text{Ag}_3^{2+}$  in ZA, ZX and ZY. Before one can draw meaningful comparisons between the optical spectra of  $\text{Ag}_3$  and  $\text{Ag}_3^{2+}$  in rare gas and zeolite matrices and evaluate support-interactions, it is important to first elucidate the electronic state(s) responsible for the low energy absorption (yellow colour). Although it has previously been assumed to originate from a transition common to both the neutral and cationic trisilver clusters(3), as discussed below this need not necessarily be the case.

From the rare gas isolation studies of trisilver (8,9), it is thought that the  $\text{Ag}_3^{\circ}$  structural isomer has an equilateral triangular form (trapped in a  $60^\circ$  trisubstitutional vacancy site) with an  $E'$  electronic ground state. Its spectroscopy is best described in terms of a vibronically active, pseudo rotating triatomic, as calculated for  $\text{Li}_3$  (23) and observed for  $\text{K}_3$  (24). The  $\text{Ag}_3^{\circ}$  isomer, on the other hand, probably has either a linear or bent form and in the context of the present discussion is thought to be the most appropriate triatomic cluster for comparison with zeolite entrapped  $\text{Ag}_3^{2+}$ .

When comparing the optical spectroscopy of the linear forms of  $\text{Ag}_3^{\circ}$  and  $\text{Ag}_3^{2+}$ , one must examine the effect of gradually depleting the valence electron density from  $\text{Ag}_3^{\circ}$  on such properties as the electronic ground state, the ordering and spacing of the molecular orbital energy levels, the number, energy and intensity of dipole allowed electronic transitions, the orbital ionization potentials and the  $g$  and hyperfine tensors. In this brief discussion, we will address only those points directly related to the identification of the low lying electronic transition(s) responsible for the yellow hue in  $\text{Ag}_3^{\circ}$  and  $\text{Ag}_3^{2+}$ . Our approach to this problem is to compute the molecular orbitals for linear  $\text{Ag}_3^{\circ}$ ,  $\text{Ag}_3^+$  and  $\text{Ag}_3^{2+}$  within the framework of  $X\alpha$  theory (25) and to examine which electronic transitions are likely candidates for the  $\text{Ag}_3^{\circ}$  and  $\text{Ag}_3^{2+}$  optical absorptions in question. As a first approximation we decided to neglect the effects of the rare gas and zeolite supports (see for example (26)) and to compute the electronic structure of naked  $\text{Ag}_3^{q+}$  ( $q = 0, 1, 2$ ). Furthermore, the Ag-Ag bond lengths were held equal at the bulk metallic distance of 2.88 Å, and the calculations were performed with 10% overlapping spheres. Relativistic effects were not included at this level of calculation. Preliminary ground state molecular orbital schemes for  $\text{Ag}_3^{q+}$  ( $q = 0, 1, 2$ ) are displayed in Figure 11. The effect of an increasing positive charge on linear trisilver can be seen as an overall relaxation of all valence levels, with corresponding energy spacings generally becoming more pronounced (similar effects seen for  $\text{Ag}_2^{\circ}$  and  $\text{Ag}_2^+$ , (27)). The latter effect is more noticeable for the 5s and 5p derived valence levels compared with the more tightly bound, mainly 4d-valence levels (Figure 11). The SCF- $X\alpha$ -SW MO calculations show the presence (12, 26) of a three level valence orbital set ( $3\sigma_g^+$ ,  $2\sigma_u^+$ ,  $4\sigma_g^+$ ) for  $\text{Ag}_3^{\circ}$ ,  $\text{Ag}_3^+$  and  $\text{Ag}_3^{2+}$  derived mainly from the 5s atomic

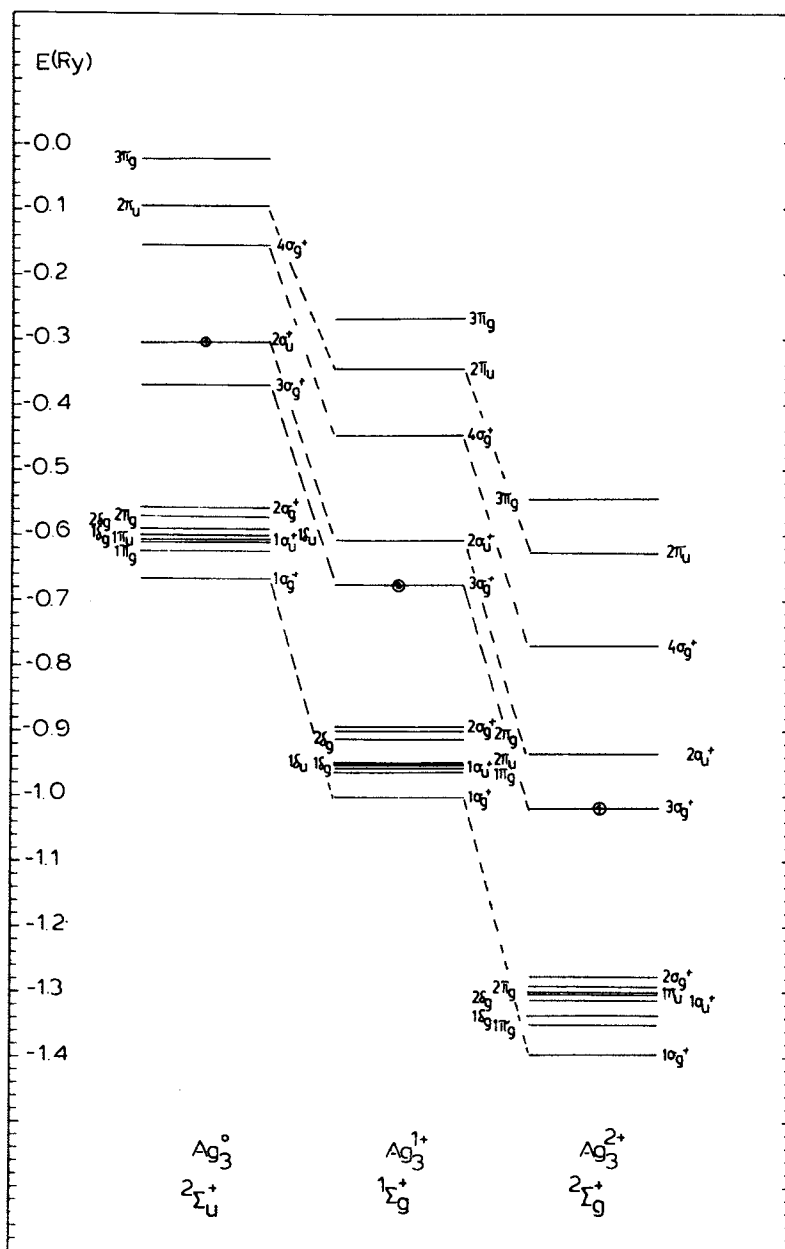


Figure 11.  
 SCF-X $\alpha$ -SW cluster model MO calculations for isolated  
 linear  $Ag_3^{q+}$  ( $q = 0, 1, 2$ ). (21).

orbitals, producing  $(3\sigma_g^+)^2(2\sigma_u^+)^1, {}^2\Sigma_u^+$ ;  $(3\sigma_g^+)^2, {}^1\Sigma_g^+$ ; and  $(3\sigma_g^+)^1, {}^2\Sigma_g^+$  electronic ground state configurations and terms for the 3, 2 and 1 electron trisilver clusters respectively (12,26).

On the basis of these calculations one can tentatively associate the low energy absorption of  $\text{Ag}_3^{\circ'}$  (440-474 nm) with the  ${}^2\Sigma_g^+ \leftarrow {}^2\Sigma_u^+$  dipole allowed electronic transition, i.e.,  $(3\sigma_g^+)^2(2\sigma_u^+)^1 \rightarrow (3\sigma_g^+)^2(4\sigma_g^+)^1$  calculated to occur around 600 nm. The other candidate  $(3\sigma_g^+)^2(2\sigma_u^+) \rightarrow (3\sigma_g^+)^1(2\sigma_u^+)^2$  is calculated to occur in the near ir around 1500 nm and therefore seems to be a less likely assignment for the 440-474 nm band of rare gas isolated  $\text{Ag}_3^{\circ'}$ . This observation has great significance, since the corresponding  $(3\sigma_g^+)^2(2\sigma_u^+)^1 \rightarrow (3\sigma_g^+)^2(4\sigma_g^+)^1$  transition cannot occur for  $\text{Ag}_3^{2+}$  (Figure 11) and the  $(3\sigma_g^+)^1 \rightarrow (2\sigma_u^+)^1$  transition still occurs at energies around 1300 nm which are too small to represent an acceptable assignment for the yellow band 402-446 nm of linear  $\text{Ag}_3^{2+}$  in A,X and Y zeolites. A more plausible assignment from these X $\alpha$  calculations would appear to be a transition from the  $1\sigma_u^+$  or  $1\pi_u$  levels of the completely filled d-type valence levels to the half filled  $3\sigma_g^+$  level, computed to be around 350-310 nm (Figure 11). On these grounds, it therefore does not seem to be justified to assume that an electronic transition, common to both  $\text{Ag}_3^{\circ'}$  and  $\text{Ag}_3^{2+}$  is responsible for the low energy absorption, even though spectroscopically they appear very similar (3). Some additional support for this idea comes from the observation that photo-excitation into the 440 nm band of  $\text{Ag}_3^{\circ'}$  in solid Ar results in a photofragmentation/cage recombination process as seen by cage-relaxed  ${}^2\text{P Ag}^\circ$  atomic fluorescence (8,9). However, no such process has so far been observed for 400-410 nm photoexcitation of  $\text{Ag}_3^{2+}$  in site I, I' of ZX or ZY. These observations are consistent with the population of the antibonding  $4\sigma_g^+$  excited state for  $\text{Ag}_3^{\circ'}$  which could lead to  $\text{Ag}_2^\circ + \text{Ag}^\circ$  dissociation, whereas the proposed  $1\sigma_u^+$ ,  $1\pi_u$  to  $3\sigma_g^+$  low energy excitation for  $\text{Ag}_3^{2+}$  increases the population of the  $3\sigma_g^+$  molecular orbital, which could lead to a strengthening of the metal-metal bond (Figure 11). Further studies will clearly be required to confirm these proposals.

### Conclusion

Rather dramatic alterations in the electronic properties and relaxation dynamics of supported silver atoms and clusters have been traced to extremely subtle differences in ground and excited state guest-host interaction potentials. For  $\text{Ag}^\circ$  and  $\text{Ag}_2^+$  in faujasite zeolites, pronounced changes in their optical absorption and emission profiles are observed with increasing Si/Al ratio, which are attributed to increasing electronic charge density on the O(3) oxygens of the sites I, I'. For zeolite isolated  $\text{Ag}^\circ$  atoms, these metal-support interactions are described in terms of an "effective cage polarizability" for site I, which is sensitive to the Si/Al distribution. In conjunction

with the corresponding data for rare gas solid supports, a calibration of effective cage polarizability with respect to the  $^2P - ^2S$  energy gap of atomic  $Ag^{\circ}$  and a scale of  $Ag^{\circ}$ - support interactions is proposed. Photo-excitation of the A-state of  $Ag_2^+$  in ZX and ZY is best described in terms of a photofragmentation/ cage-recombination process, as determined by the observation of site I cage-relaxed  $Ag^{\circ}$  atomic fluorescence, analogous to, but not identical in detail with that observed following photoproduction of the A-state of  $Ag_2^{\circ}$  in rare gas matrices. In the case of tri-silver clusters, spectroscopic and X $\alpha$  electronic structure calculations for linear  $Ag_3^q$  ( $q = 0,1,2$ ) alert one to the care that should be exercised when attempting to correlate optical absorptions of matrix isolated  $Ag_3^{\circ}$  and zeolite entrapped  $Ag_3^{2+}$ . This relates to the complications associated with the existence of at least two structurally distinct forms of  $Ag_3^{\circ}$  in rare gas solids and the likelihood of confusing optical transitions, which appear spectroscopically to be similar in origin but which likely correspond to excitations between entirely different electronic states.

The results of this study suggest that silver atom and cluster optical absorption and fluorescent probes offer a very sensitive method for assessing the strength of a metal support interaction and a way of monitoring subtle alterations in electronic charge density at the trapping site of a metal guest.

#### Acknowledgments

Financial assistance from the Natural Sciences and Engineering Research Council of Canada's Strategic Energy Programme and a Special Research Grant from the Connaught Foundation of the University of Toronto are both greatly appreciated.

#### Literature Cited

1. Proceedings of the Second International Meeting on Small Particles and Inorganic Clusters, Lausanne, Switzerland, 1980; Surf. Sci., 1981, 106,1; Ozin, G.A., Cat. Rev. Sci. Eng., 1977, 16, 191; Coord. Chem. Rev., 1979, 28, 117; J. Macromol. Sci., 1981, A16,167 (and references cited therein).
2. "Growth and Properties of Metal Clusters; Applications to Catalysis and the Photographic Process", Proc. 32nd Int. Meeting of Soc. de Chim. Phys., Ed. Bourdon, J.; Elsevier, New York, 1980 (and references cited therein).
3. (a) Gellens, L.R.; Mortier, W.J.; Schoonheydt, R.A.; Uytterhoeven, J.B.; J. Phys. Chem., 1981, 85, 2783; (b) Gellens, L.R.; Mortier, W.J.; Uytterhoeven, J.B.; Zeolites, 1981, 1, 11; 1981, 1, 85 (and references cited therein).
4. Ozin, G.A., Faraday Symp. Chem. Soc., 1980, 14, 7 (and references cited therein).
5. Ozin, G.A.; Mitchell, S.A.; Farrell, J.; Kenney-Wallace, G., J. Amer. Chem. Soc., 1980, 102, 7702.

6. Ozin, G.A.; Farrell, J.; Kenney-Wallace, G.; Mitchell, S.A., J. Amer. Chem. Soc., 1981, 103, 6030.
7. Ozin, G.A.; Garcia-Prieto, J.; Mitchell, S.A., J. Phys. Chem., 1982, 86, 473.
8. Ozin, G.A.; Mitchell, S.A.; Huber, H.X., Inorg. Chem., 1979, 18, 2932.
9. Ozin, G.A.; Huber, H.X., Inorg. Chem., 1978, 17, 155; Mitchell, S.A., Ph.D. Thesis, University of Toronto, 1982.
10. Ozin, G.A.; Huber, H.X.; McIntosh, D.F.; Mitchell, S.A.; Norman, J.G. Jr.; Noodleman, L., J. Amer. Chem. Soc., 1979, 101, 3504.
11. DiLella, D.P.; Moskovits, M., "Metal Bonding and Interactions in High Temperature Systems", A.C.S. Symp. Series, 179, Ed. Cole, J.L.; Stwalley, W.C., ACS Washington.
12. Basch, H., J. Amer. Chem. Soc., 1981, 103, 4657.
13. Kellerman, R.; Texter, J., J. Chem. Phys., 1979, 70, 1562.
14. Ozin, G.A.; Hugues, F., J. Phys. Chem., (in press).
15. Ozin, G.A.; Hugues, F., (manuscript in preparation).
16. A. Abou-Kais, J.C. Vedrine and C. Naccache, J. Chem. Soc. Faraday T1, 1978, 74, 759. N. Narayana, A.S.W. Li and L. Kevan, J. Phys. Chem., 1981, 85, 132; N. Narayana and L. Kevan, J. Chem. Phys., 1982, 76, 3999.
17. "Zeolite Molecular Sieves", Breck, D.W., Wiley-Interscience, New York, 1974.
18. Lippmaa, E.; Mägi, M.; Samoson, A.; Tarmak, M.; Engelhardt, G., J. Amer. Chem. Soc., 1981, 103, 4992; Engelhardt, G.; Lippmaa, E.; Mägi, M., J. Chem. Soc. Chem. Comm., 1981, 712.
19. Dempsey, E., in "Molecular Sieves", Soc. of Chem., Ind., 1969, 293; J. Catal, 1975, 39, 155..
20. Engleman, R., "The Jahn Teller Effect in Molecules and Crystals", Wiley, New York, 1972; Moran, D.R.; Phys. Rev., 1965, 137; Fulton, T.A.; Fitchen, D.B., Phys. Rev., 1969, 179, 846; Sturge, M.D.; Solid State Phys., 1967, 20, 91; Liehr, A.D., J. Phys. Chem., 1963, 67, 389; Öpic, U; Pryce, M.H.L., Proc. Roy. Soc., 1957, A238, 425; (and references cited therein).
21. Moore, C.E.; Natl. Bur. Stand. (US), Circ. 1958, No.467, Vol.2,3.
22. "Cryochemistry", Ed. M. Moskovits; Ozin, G.A., Pub. John Wiley and Sons, New York, 1976.
23. Gerber, W.H.; Schumacher, E., J. Chem. Phys., 1978, 69, 1962.
24. Thompson, G.P.; Lindsay, D.M., J. Chem. Phys., 1981, 74, 959; Thompson, G.A.; Tischler, F.; Garland, D.; Lindsay, D.M., Surf. Sci., 1981, 106, 408.
25. "Cluster Model Theory", Messmer, R.P., in "Nature of the Chemical Bond", Ed., Rhodin, T.N.; Ertl, G., Pub., North Holland, N.Y. 1979.
26. Gellens, L.R.; Mortier, W.J.; Lissillour, R.; LeBeuze, A., J. Phys. Chem., 1982, 86, 2509 (and references cited therein).
27. Ozin, G.A.; Hugues, F.; McIntosh, D.F., (manuscript in preparation).

RECEIVED November 4, 1982



## Low Temperature Water Gas Shift Activity of Ruthenium in Zeolites in Relation to Its Chemistry

P. A. JACOBS, R. CHANTILLON, P. De LAET, J. VERDONCK,  
and M. TIELEN

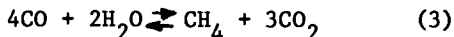
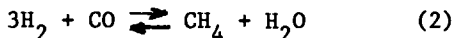
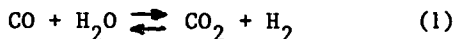
Katholieke Universiteit Leuven, Centrum voor Oppervlaktescheikunde en  
Colloïdale Scheikunde, de Croylaan 42, B-3030 Leuven (Heverlee), Belgium

The chemical transformation of Ru-complexes in faujasite-type zeolites in the presence of water and of carbon monoxide-water mixtures is reviewed and further investigated by IR, UV-VIS spectroscopic and volumetric techniques. The catalytic activity of these materials in the watergasshift reaction was followed in a parallel way. The major observations could be rationalized in terms of a catalytic cycle involving Ru(I)bis and triscarbonyl intermediates stabilized in the supercages of the faujasite-type zeolite. The turnover frequency of this cycle is found to be determined by the nature, number and position of the charge compensating cations, as well as by the nature of the ligands present in the Ru-coordination sphere. If these factors increase the electron-donor capability of the Ru-cationic intermediate, an increase in activity results.

It has been reported earlier (1, 2) that upon activation of ruthenium(III)hexamine complexes exchanged in faujasite-type zeolites, a very active low-temperature watergasshift (WGS) catalyst was formed. The geometry of the faujasite-supercage was found to be a prerequisite for the formation of the active intermediate. The catalysis was of a redox nature and a tentative mechanism was advanced, taking into account the major observations (1). These catalysts at low activation and reaction temperature (1), are selective since no methane is formed. When the same zeolite is reduced at higher temperatures, a highly dispersed metal phase is formed (3), which is active as high temperature WGS catalyst (1, 2, 4) but is less selective since methane is always formed. This is the result of the successive occurrence of the WGS reaction (equation 1) and the methanation (equation 2). The over-

0097-6156/83/0218-0439\$06.00/0  
© 1983 American Chemical Society

all reaction is known as the Kölbel-Engelhardt synthesis (equation 3) (4).



The chemistry of Ruthenium in Y zeolites has been extensively investigated (5), and seems to parallel in many respects its behavior in homogeneous media. More particularly, the chemistry of Ru(III)(NH<sub>3</sub>)<sub>6</sub> in the supercages of Y-type zeolites has received considerable attention (1,6-10), either in vacuum, inert atmosphere, or in presence of O<sub>2</sub>, CO and NO.

In view of what precedes, it has been the aim of the present work to identify the Ru-species present in faujasite-type zeolites activated under WGS-conditions, making use of the available literature data. The activation procedure of Ru(III)hexammine in NaY has been related to its catalytic performance as low temperature WGS-catalyst. Subsequently, the basicity of the material was related to its catalytic behavior in the same reaction, by changing the nature of the parent complex, of the charge compensating cations and of the aluminum content of the faujasite-type zeolite.

### Experimental

Faujasite-type zeolites with different Al content were from Union Carbide. NH<sub>4</sub>-exchanged Y-zeolite was dealuminated using gaseous SiCl<sub>4</sub> (13) or via a steaming treatment at 550°C. Ru was exchanged into the zeolites by an ion exchange procedure using the chloride salts of: [Ru(III)(NH<sub>3</sub>)<sub>6</sub>]<sup>3+</sup>, [Ru(II)(NH<sub>3</sub>)<sub>5</sub>Cl]<sup>2+</sup>, [Ru(III)(NH<sub>3</sub>)<sub>5</sub>O], Ru(IV)(NH<sub>3</sub>)<sub>4</sub>O, Ru(III)(NH<sub>3</sub>)<sub>5</sub><sup>6+</sup>, [Ru(I)(NH<sub>3</sub>)<sub>4</sub>OHC1]<sup>+</sup>. In one case Ru<sub>3</sub>(CO)<sub>12</sub> was impregnated on NaY from a n-pentane solution. The amount of Ru in weight % precedes the sample notation.

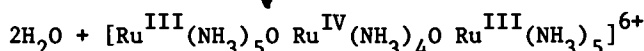
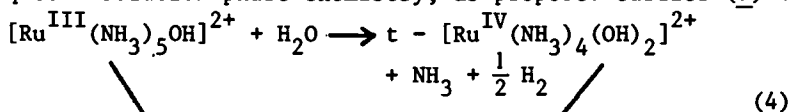
The sample characterization techniques consisted of static and dynamic volumetric methods, IR and VIS-UV spectroscopy and have been described in detail (7, 8). Catalysis was done in a continuous flow reactor (2).

### Results and discussion

Influence of pretreatment procedure on the WGS activity of Ru(III)-hexammine in zeolite NaY Activation of Ru(III)-hexammine in inert atmosphere When the Ru(III)(NH<sub>3</sub>)<sub>6</sub> complex exchanged in NaY-zeolite is heated at temperatures below 323 K in vacuum or in an inert atmosphere, the volumetric and spectroscopic results indicate that the complex is hydrolyzed into a pentammine-hydroxy

complex (Table 1), which does not catalyze the WGS-reaction. This type of hydrolysis has been repeatedly reported for the same complex on different zeolites or on similar zeolites with different complexes (7-10).

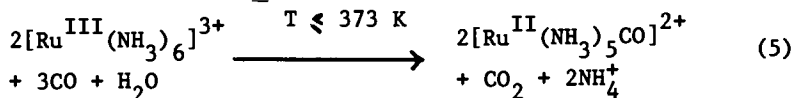
At higher temperatures, the residual hydration water causes further hydrolysis and Ru-Red becomes a dominating species (Table 2). The color of the sample (wine-red) as well as the absorption in the UV-VIS region (7, 10) are typical. The volumetric techniques indicate that almost 80 % of the Ru contributes to this species. The continuing hydrolysis of the Ru(III)pentammine-hydroxy to the final Ru-Red complex may occur in a way similar to the aqueous solution phase chemistry, as proposed earlier (7) :



The condensation of pentammine-hydroxy with trans-tetrammine dihydroxy species, explains the formation of Ru-Red.

At increasing temperatures in the presence of only zeolite hydration water, Ru-Red is transformed into a Ru(II)nitrosyl-ammine moiety, using the assignments of previous work (7, 8) (Table 3). The three remaining ligands could not be defined accurately and may consist of residual water, hydroxy groups and/or lattice oxygen atoms ( $\text{O}_\ell$ ). After activation at 523 K, the material has a very low residual WGS-activity (Figure 1) compared to a material activated in water gas (i.e. in a 1:1 molar mixture of CO and  $\text{H}_2\text{O}$ ).

Activation of Ru(III)hexammine in CO atmosphere At activation temperatures below 373 K, Ru(III)hexammine in the presence of CO is transformed into a Ru(II)pentammine complex. The identification of this complex is based on earlier work (7, 8) and the information is summarized in Table 4. This transformation is almost quantitative and the material formed shows already a low WGS-activity. Chemically, this transformation can be visualized as follows (8) :



At still higher activation temperatures, the Ru(II)pentammine carbonyl is transformed into a Ru(I)triscarbonyl, the characteristics of which are shown in Table 5a. It should be noted that the volumetric data shown, have been corrected for a simultaneously occurring WGS-activity using the method described earlier (8). This complex shows a characteristic triplet of bands in infrared

Table I

Pretreatment of 6RuNaY in helium at 323K.

|   |                                  |                       |                                  |
|---|----------------------------------|-----------------------|----------------------------------|
| $[\text{Ru}^{\text{III}}(\text{NH}_3)_6]^{3+} + \text{H}_2\text{O} \xrightarrow{T \leq 323\text{K}} [\text{Ru}^{\text{II}}(\text{NH}_3)_5\text{OH}]^{2+} + \text{NH}_4^+$ |                                  |                       |                                  |
| 265 nm  | : LMCT <sup>a</sup>              | 278 nm                | : LMCT <sup>a</sup>              |
| 325 nm  | : d-da                           |                       |                                  |
| 1360 cm <sup>-1</sup>   | : $\delta_{\text{S}}\text{NH}_3$ | 1330 cm <sup>-1</sup> | : $\delta_{\text{S}}\text{NH}_3$ |
|   |                                  | 1440 cm <sup>-1</sup> | : $\delta_{\text{NH}}^+$         |
| NH <sub>3</sub> /Ru average : 6   |                                  | 5                     |                                  |
| Ru/NH <sub>4</sub> <sup>+</sup> (IR) : -  |                                  | 4.2                   |                                  |
| WGS activity at 323K : none   |                                  |                       |                                  |
| a, ref. 7   |                                  |                       |                                  |

Table II

Pretreatment of 6RuNaY in helium at 373K.

|  |  |                        |  |
|--|--|------------------------|--|
| $[\text{Ru}^{\text{III}}(\text{NH}_3)_5\text{OH}]^{2+} \xrightarrow[T \leq 373\text{K}]{\text{H}_2\text{O}} [\text{Ru}^{\text{III}}(\text{NH}_3)_5\text{O} \text{ Ru}^{\text{IV}}(\text{NH}_3)_4\text{O} \text{ Ru}^{\text{III}}(\text{NH}_3)_5]^{6+}$ |  |                        |  |
| yellowish  |  | wine-red               |  |
| NH <sub>3</sub> /Ru : 5  |  | 3.9 (4.7) <sup>a</sup> |  |
| 278 nm   |  | 258 nm                 |  |
|  |  | 390 nm                 |  |
|  |  | 550 nm                 |  |
|  |  | 780 nm                 |  |
| WGS-activity at 373K : none  |  |                        |  |
| a : expected value   |  |                        |  |

Table III

Activation of 6RuNaY in helium at 523K.

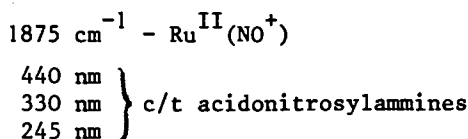
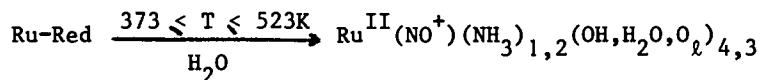
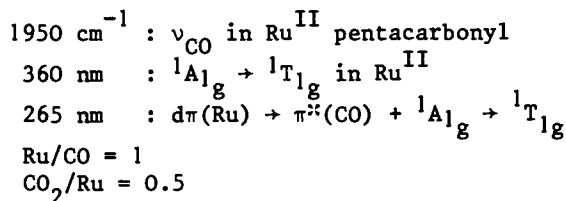
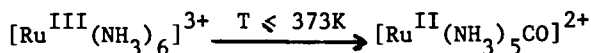


Table IV

Pretreatment of 6RuNaY in watergas atmosphere at 373 K.

WGS-activity : traces of CO<sub>2</sub>

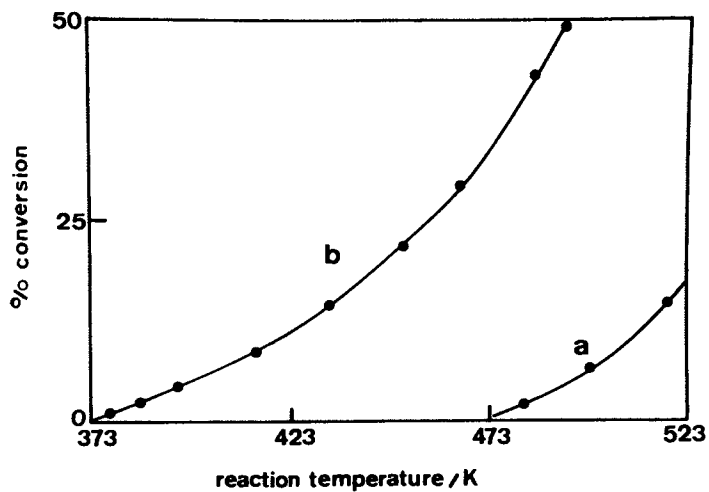


Figure 1

Activation of  $[\text{Ru}^{\text{III}}(\text{NH}_3)_6]^{3+}$  in 6RuNaY in : a, helium at 523K, and b, CO : H<sub>2</sub>O (molar ratio) at 523K.

Table V.a

Activation of 6RuNaY in watergas

---

|  |  |                                     |
|--|--|-------------------------------------|
| $\text{Ru}^{\text{II}}$ pentamminecarbonyl   | $\xrightarrow[423\text{K} < T < 523\text{K}]{\text{CO}}$ | $\text{Ru}^{\text{I}}$ triscarbonyl |
| 2055, 2005, 1960 $\text{cm}^{-1}$<br>405 nm<br>$\text{CO}/\text{Ru} = 2.8$ $\text{Ru}^{\text{I}}$<br>$\text{CO}_2/\text{Ru} = 0.4$ |  |                                     |
| WGS-activity : high  |  |                                     |

---

Table V.b

Activation of 6RuNaY in watergas

---

|  |   |                                    |
|--|---|------------------------------------|
| $\text{Ru}^{\text{I}}$ triscarbonyl  | $\xrightarrow[423\text{K} < T < 523\text{K}]{\text{H}_2\text{O}}$ | $\text{Ru}^{\text{I}}$ biscarbonyl |
| 2025 $\text{cm}^{-1}$ : $\nu_{\text{CO}}$ sym.<br>2090 $\text{cm}^{-1}$ : $\nu_{60}$ asym. |   |                                    |
| of $\text{Ru}^{\text{I}}(\text{CO})_2$   |   |                                    |
| WGS-activity : high  |   |                                    |

---

and a very high WGS-activity (Figure 1). Comparative earlier work on other zeolites and on commercially used low temperature WGS-catalysts, indicates that this material is superactive in the reaction mentioned (1, 2).

The Ru(I)triscarbonyl in an excess of water can be easily transformed into a Ru(I)triscarbonyl species. The latter entity is characterized by a doublet of IR bands in the CO stretching region. The identification of both the Ru(I)bis- and triscarbonyl species has been discussed in detail (8). Table 6 gives an assignment of Ru-CO species in IR on different supports. This table shows that the proposed assignment is consistent with the literature data.

Influence of the Al-content of the faujasite-type zeolite upon the WGS-activity It has been reported earlier that Ru(III)hexamine in zeolites upon activation in watergas can be transformed into an active catalyst when the zeolite is of the faujasite-type (1, 2). It has also been reported (1) that X-type zeolites are in this respect more active than Y-zeolites. In Figure 2, it is shown that the rate of watergas conversion at 430 K increases linearly when the Al content per unit cell of the faujasite-type zeolite is increased. The first two samples correspond to dealuminated materials using  $\text{SiCl}_4$  (13) and obey the relationship. A steamed  $\text{NH}_4\text{Y}$  sample subsequently exchanged with Ru(III)hexamine and properly activated is deviating. This relation shows that as a result of geometrical changes in the supercages, which are expected to occur upon steaming, the right geometry is no longer present to form the active complex. Mild dealumination procedures ( $\text{SiCl}_4$  treatments) do not affect the formation of this species. It is also evident that the turnover frequency of the active sites increases with the Al-content of the material and thus with its basic characteristics.

Figure 3 indicates that the increased catalytic rates are not the mere result of changes in basicity but that also the size of the counter-ions and their number present in supercages positions determine the activity. If basicity would be the only parameter determining the turnover frequency of the active Ru-complex, the following sequence would be expected :



The high activity observed for NaX and the lowest rate for BaX zeolite is an indication that the size and the number of the supercage cations are important in stabilizing the active complex. Indeed, zeolites X or Y exchanged with bivalent ions, have a decreased number of supercage cations compared to monovalent exchanged zeolites (14). Thus, it seems that the number of active Ru-species formed in faujasite-type zeolites is determined by the basicity of the zeolite as well as by number, size and location of the charge compensating cations.



Table VI

Assignment of  $\nu_{\text{CO}}$  in ruthenium-carbonyl complexes.

| $\nu/\text{cm}^{-1}$   | Treatment                                       | Support          | Assignment  | Ref. |
|------------------------|---|------------------|---|------|
| 1939                   | (I)Ru <sup>III</sup> hexamine+ NaX <sup>b</sup> |                  | Ru <sup>II</sup> (NH <sub>3</sub> ) <sub>5</sub> CO | 8    |
| 1951                   | CO at 373K                                      | NaY <sup>b</sup> | Ru <sup>II</sup> (NH <sub>3</sub> ) <sub>5</sub> CO | 8    |
| 2010,2080              | (I)+  | NaX <sup>b</sup> | Ru <sup>I</sup> (CO) <sub>2</sub> <sup>a</sup>      | 8    |
| 2025,2090              | CO at 423K                                      | NaY <sup>b</sup> | Ru <sup>I</sup> (CO) <sub>2</sub> <sup>a</sup>      | 1    |
| 1937,1988,2040         | (I)+  | NaX <sup>b</sup> | Ru <sup>I</sup> (CO) <sub>3</sub> <sup>a</sup>      | 8    |
| 1960,2005,2055         | CO at 493K                                      | NaY <sup>b</sup> | Ru <sup>I</sup> (CO) <sub>3</sub> <sup>a</sup>      | 8    |
| 2040,2080,2145         | Ru <sub>3</sub> (CO) <sub>4</sub>               | HY <sup>b</sup>  | Ru <sub>3</sub> (CO) <sub>4</sub>                   | 12   |
| 2086,2100,2156         | CO, 290K  | Ru(O)Y           | Ru <sup>II</sup> CO                                 | 1    |
| 2075                   | CO, 290K  | Ru(O)Y           | Ru(O) <sub>x</sub> CO <sup>e</sup>                  | 1    |
| (1934),2045,<br>(2134) | CO, 290K  | Ru(O)Y           | Ru(O) <sub>n</sub> CO <sup>d</sup>                  | 1    |
| 2070,2130              | CO, 290K  | Ru on silica     | Ru <sup>I</sup> (CO) <sub>2</sub> <sup>e</sup>      | 11   |
| 2002,2070              | CO, 290K  | Ru on alumina    | Ru <sup>I</sup> (CO) <sub>2</sub> <sup>e</sup>      | 11   |
| 1970,2050              | CO, 290K  | Ru on alumina    | Ru <sup>I</sup> (CO) <sub>2</sub> <sup>e</sup>      | 11   |

a, other ligands are NH<sub>3</sub>, and eventually H<sup>-</sup> and/or OH<sup>-</sup>

b, zeolites not previously degassed and containing residual water

c, Ru(O)carbonyl cluster

d, Ru(O) particle with chemisorbed CO

e, in the original work, these species are denoted as cationic-low valency mononuclearbiscarbonyl

American Chemical  
Society Library

1155 16th St. N. W.

Washington, D. C. 20036

In Intrazeolite Chemistry; Stucky, G., et al.,

ACS Symposium Series; American Chemical Society: Washington, DC, 1983.

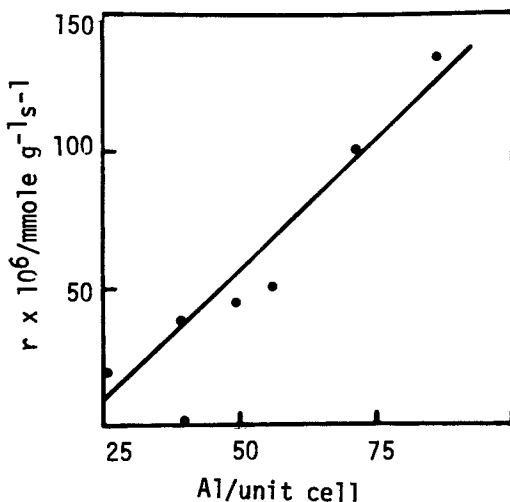


Figure 2

WGS rate at 430K of  $[\text{Ru}^{\text{III}}(\text{NH}_3)_6]^{3+}$  activated in watergas at 523K in 6RuNa faujasites with different Al contents (Al per unit cell). The 2 samples with lowest Al content are obtained via dealumination with  $\text{SiCl}_4$ . The open point correspond to a steamed zeolite support (ultrastable zeolite).

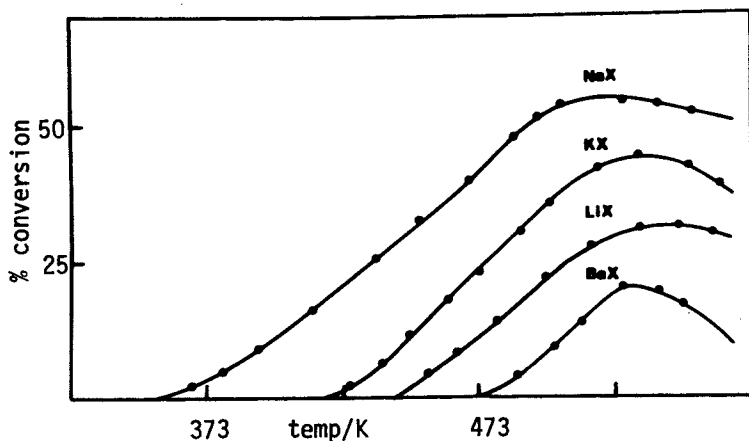


Figure 3

WGS activity of  $\text{Ru}^{\text{III}}$  hexammine in X zeolite with different counter-ions. (6RuX) after activation in watergas at 523K.

Nature of the active complex and its influence on the WGS activity The activation of Ru-complexes with a chloride ligand in its coordination sphere was then performed in order to test the basicity concept.  $[\text{Ru}(\text{I})(\text{NH}_3)_4\text{OHCl}]^+$  and  $[\text{Ru}(\text{II})(\text{NH}_3)_5\text{Cl}]^{2+}$  exchanged in NaY and activated in optimum conditions show improved catalytic properties (Figure 4). Chemical analysis of the catalyst gives a Ru/Cl ratio close to 0.65. This indicates that the major part of  $\text{Cl}^-$  after activation remains in the catalyst and most probably in the Ru-coordination sphere. The complex is therefore expected to have enhanced electron donor properties, so that the higher catalytic activity can be explained via this increased basicity. It is striking that the two  $\text{Cl}^-$ -containing complexes are transformed into materials with the same activity. It is therefore logical to assume that in both cases the same intermediate is formed.

The data of Figure 5 show that the presence of  $\text{OH}^-$  in the parent complex is of only minor importance. Indeed, when the two  $\text{Cl}^-$ -containing complexes exchanged in NaY are activated in very mild conditions (in watergas at 393 K), identical activity is obtained. It clearly indicates that the presence of  $\text{Cl}^-$  causes the activity increase and stresses the importance of the basic character of the active site.

Table 7 shows the IR characterization of RuNaY, using parent complexes of different chemical nature. Several conclusions can be drawn from these data :

- . the position of the bands of  $\text{Ru}(\text{I})(\text{CO})_2$  and  $\text{Ru}(\text{I})(\text{CO})_3$  species is definitely influenced by the presence of  $\text{Cl}^-$  : the expected shift to lower wavenumbers is observed. The increased basicity also seems to shift the equilibrium ratio of the bis to triscarbonyl complexes.

- . the active complex is of mononuclear nature. Indirect evidence for this was derived earlier from the dependence of catalytic activity on the degree of cation exchange (1). Table 7 shows that the trinuclear Ru-dodecacarbonyl requires a pre-steaming and therefore a hydrolyzing treatment before any WGS-activity can be generated. In Figure 6 it is illustrated that depending on the severity of the steaming treatment of  $\text{Ru}_3(\text{CO})_{12}$  impregnated on NaY, a catalyst with enhanced activity is obtained. It should be noted that this system is less selective than the previously described systems. Indeed, in the former system never is methane formed, while the catalysts derived from the Ru-carbonyl always form  $\text{CH}_4$ . This indicates that besides cationic Ru also Ru-metal is present in the latter case.

#### Rationalization of the data in a mechanism for WGS-activity

The major observations of the present and earlier work are :

- . the high activity and selectivity of Ru-faujasites in the WGS-reaction,

- . the presence of Ru(I)bis and triscarbonyl species, their possible interconversion under reaction conditions, and the low wavenumbers at which they absorb in IR,

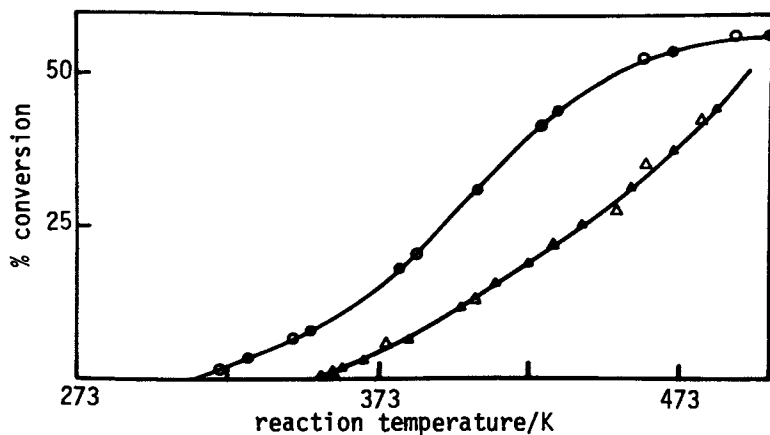


Figure 4

WGS activity of 6RuNaY prepared from :

▲,  $[\text{Ru}^{\text{III}}(\text{NH}_3)_6]^{3+}$ ; Δ, Ru-Red; ●,  $[\text{Ru}^{\text{I}}(\text{NH}_3)_4\text{OHCl}]^+$ ;

○,  $[\text{Ru}^{\text{II}}(\text{NH}_3)_5\text{Cl}]^{2+}$  after activation in watergas at 523K.

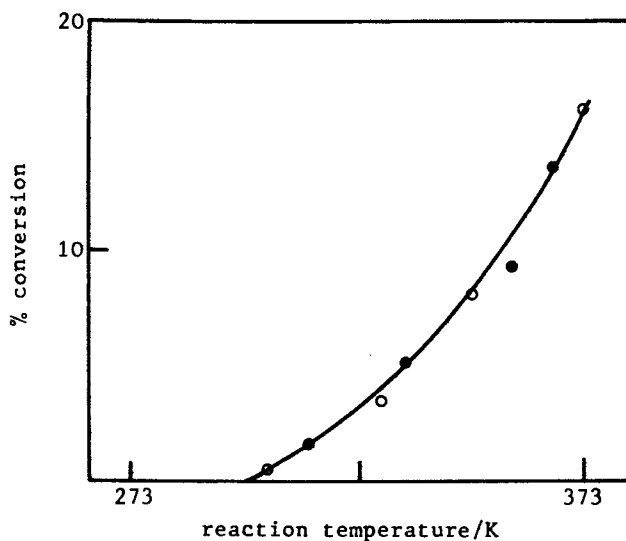


Figure 5

WGS activity of 6RuNaY prepared from ○,  $[\text{Ru}^{\text{I}}(\text{NH}_3)_4\text{OHCl}]^+$  and

●,  $[\text{Ru}^{\text{II}}(\text{NH}_3)_5\text{Cl}]^{2+}$  after activation in watergas at 393K.

Table VII IR characterization of RuNaY.

| Starting   | Activation      | in temp./K | Ru <sup>I</sup> (CO) <sub>2</sub><br>cm <sup>-1</sup> | Ru <sup>I</sup> (CO) <sub>3</sub> | $\frac{\text{bis}}{\text{tris}}$ carbonyl <sup>a</sup> |
|--|-----------------|------------|---|-----------------------------------|--|
| Ru <sub>3</sub> (CO) <sub>12</sub>                   | WG <sup>b</sup> | 523        | -   | -                                 | -  |
|  | W <sup>c</sup>  | 523        | 2020,2085   | 1955,2000,<br>2055                | 5.0  |
| Ru <sup>I</sup> (NH <sub>3</sub> ) <sub>4</sub> OHC1 | WG              | 393        | 2010,2080   | 1940,1990,<br>2035                | 2.0  |
| Ru <sup>II</sup> (NH <sub>3</sub> ) <sub>5</sub> Cl  | WG              | 393        | 2005,2080   | 1945,1990,<br>2035                | 2.1  |
| Ru-Red   | WG              | 523        | 2020,2085   | 1955,2000<br>2055                 | 3.2  |
| Ru(NH <sub>3</sub> ) <sub>6</sub>                    | WG              | 523        | 2020,2085   | 1955,2000<br>2055                 | 3.2  |

a, ratio of 2080 to 1950 bands

b, WG = watergas (1:1 molar ratio of CO and H<sub>2</sub>O)

c, 2000 kPa of steam

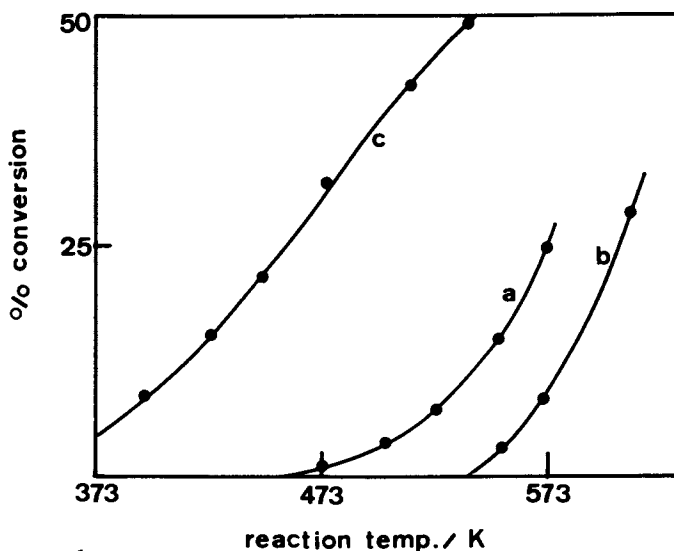


Figure 6

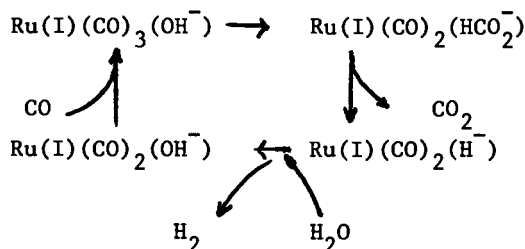
WGS activity of Ru<sub>3</sub>(CO)<sub>12</sub> impregnated NaY after activation at : a, 523K in watergas b, 473K in watergas c, 523K in 2000 kPa of steam

. the influence of basicity changes of the material on the catalytic behavior caused, either by a variation of the nature and number of the residual cations, or by a substitution of some of the ligands of the Ru-complex by  $\text{Cl}^-$ ,

. the existence of formate species on the catalyst surface (1),

. the mononuclear nature of the Ru-intermediate.

All this can be rationalized using the following catalytic cycle :



This cycle is unique in the sense that a zeolite with the structure of faujasite is required to stabilize the active intermediates. It is a typical example of the use of a zeolite as a specific solvent for the stabilization of inorganic intermediates which in the usual solvents do not seem to be formed.

### Acknowledgments

P.A.J. acknowledges a permanent research position as Senior Research Associate from N.F.W.O. (Belgium). Financial support from the same organization is appreciated.

### Literature Cited

1. Verdonck, J.J.; Schoonheydt, R.A.; Jacobs, P.A. Proc. 7th Int. Congr. Catalysis 1980, p. 911.
2. Verdonck, J.J.; Jacobs, P.A.; Uytterhoeven, J.B. J.C.S. Chem. Comm. 1979, 18.
3. Verdonck, J.J.; Jacobs, P.A.; Genet, M.; Poncelet, G. J.C.S. Faraday Trans. I 1980, 76, 403.
4. Gustafson, B.L.; Lunsford, J.H. J. Catal. 1982, 74, 393.
5. For a recent review see : Lunsford, J.H. "Studies in Surface Science and Catalysis 12", Jacobs, P.A.; Jaeger, N.I.; Jirü, P.; Schulz-Ekloff, G., eds., Elsevier : 1982, 1.
6. Pearce, J.R.; Mortier, W.J.; Uytterhoeven, J.B. J.C.S. Faraday Trans. I 1979, 75, 1395
7. Verdonck, J.J.; Schoonheydt, R.A.; Jacobs, P.A. J. Phys. Chem. 1981, 85, 2393.
8. Verdonck, J.J.; Schoonheydt, R.A.; Jacobs, P.A. J. Phys. Chem. 1983, in press.

9. Laing, K.R.; Leubner, R.L.; Lunsford, J.H. *Inorg. Chem.* 1975, 14, 1400.
10. Madhusudhan, C.P.; Patil, M.D.; Good, M.L. *Inorg. Chem.* 1979, 18, 2384.
11. Knözinger, H.; Zhao, Y.; Tesche, B.; Barth, R.; Epstein, R.; Gates, B.C.; Scott, J.P. *Faraday Disc.* 1981, 72, paper 4 and references therein.
12. Ballivet-Tkatchenko, D.; Nguyen Duc Chan; Mozzanega, H.; Roux, M.C.; Tkatchenko, I. *A.C.S. Symp. Ser.* 1981, 152, 187.
13. Beyer, H.K.; Belenykia, I. "Studies in Surface Science and Catalysis 5", Elsevier 1980, p. 203.
14. Mortier, W.J. "Compilation of extra-framework sites in Zeolites", Butterworth 1982.

RECEIVED February 25, 1983

## Zeolite Mediated Carbonylation

PATRICK GELIN, FRÉDÉRIC LEFEBVRE, BOUBAKER ELLEUCH,  
CLAUDE NACCACHE, and YOUNÈS BEN TAARIT

Institut de Recherches sur la Catalyse, C.N.R.S., 2 avenue Albert Einstein, 69626,  
Villeurbanne Cédex, France

Transition metal ions, within the zeolite framework, may undergo a reductive carbonylation to give mono-nuclear monovalent carbonyl compounds  $M(I)(CO)_n$  and ultimately to give zerovalent polynuclear carbonyl clusters. The rhodium(I) and iridium(I) carbonyls were identified using spectroscopic and volumetric methods, the zerovalent rhodium and iridium clusters  $M_4(CO)_{12}$  were also synthesized in the zeolite matrix and their structure investigated using IR, NMR and spin labelling methods.

Carbonylation of organic substrates was investigated using these well defined complexes. These carbonyl compounds exhibited catalytic properties in the carbonylation of organic substrates. In particular methanol carbonylation to methyl acetate in the gas phase was successfully attempted. Mechanistic and kinetic studies of this reaction over rhodium and iridium zeolites showed the similarities between the homogeneous and the zeolite mediated reactions. Aromatic nitro compounds were also converted to aromatic isocyanates using similar catalytic systems. The mechanistic aspect of this reaction will be also examined.

In a relatively few years zeolites were promoted from simple adsorption agents to catalysts of wide spread use in all fields of chemistry. Apart from their acidic properties generated by exchanging their  $Na^+$  or  $K^+$  starting forms by ammonium ions and subsequent decomposition of the latter, their unique properties as supports for various precious metals and their solution behaviour attracted much of the attention devoted to catalysis.

In sustained efforts to localize transition metal cations within the zeolite framework, EPR, UV, IR and X-ray diffraction studies were undertaken by several authors (1-5). This localization was thought to help clarify and possibly account for variations of catalytic properties upon various parameters including the exchange level. The overwhelming conclusions of these investigations was the high mobility of the exchanged transition metal

0097-6156/83/0218-0455\$06.00/0

© 1983 American Chemical Society



cations induced by the presence or removal of potential ligands be they organic or inorganic (1-5).

Furthermore, it was shown that these ligands when competing with lattice oxide ions may well form defined coordination complexes with the transition metal cation (1-5). In some complexes the ligands were loosely bound (almost reversibly) to the cation<sup>(3)</sup> in others the complexes may have the same structure and similar stability as those formed in solution (1, 4).

Then zeolites rapidly appeared as most convenient matrices or solid solvents capable of accomodating and solvating coordination complexes of potential catalytic use.

The valuable advantages of heterogenizing homogeneous catalysts within the zeolite porous structure was then envisioned. Some of the complexes were introduced within the zeolite using simple sublimation and adsorption techniques (6, 7). Others were directly synthesized in situ, starting usually from the appropriate transition metal cation introduced by conventional ion-exchange (1, 4, 8).

Faujasite type zeolites because of the size of their cavities and apertures were the most frequently used in this purpose. Their well known structure, acid-base and redox properties helped much in selecting those zeolites.

Many efforts were devoted to many aspects of the intrazeolitic chemistry of transition metal ions. Carbonylation reactions both of the transition metal ions themselves and organic substrates were widely investigated in view of their academic interest as well as practical use. These studies were favoured by the rapidly expanding chemistry of carbon monoxide which grew to a major research field. Carbon monoxide would appear as a potential substitute to the vanishing oil and perhaps more surely as a privileged reagent used to functionalize or to expand organic molecules (9).

Carbonylation of methanol and nitroaromatics, hydroformylation of olefins and alcohol homologation were among the principal reactions aimed at producing high added value molecules.

The various aspects of carbonylation in zeolite media usually include the carbonylation of the inorganic precursor to form the active carbonylation complex. The transfer of the activated carbon monoxide molecule to an organic one may subsequently take place. We shall restrict ourselves to the activation of carbon monoxide by the exchanged transition metal ions and the resulting formation of transition metal carbonyls.

The mechanistic aspects of the transfer of carbon monoxide to other substrates will be examined in the light of spectroscopic kinetic and other data available in the literature or provided by recent results in our laboratory.

#### Synthesis and structure of transition metal carbonyl in the zeolite medium

Early work showed the affinity of carbon monoxide for transition metal cations introduced into zeolites by conventional ion

exchange. Essentially IR, gravimetric, UV, EPR and NMR techniques were used to probe the structure of the complexes, their stability and the nature of the bonding of the CO molecule to the transition metal cation (3, 10, 11, 12). In particular, the IR spectroscopy of such complexes has been recently reviewed and it appeared that the interaction was rather weak with absorptions at high frequency usually higher than free carbon monoxide (3).

The general conclusion was that rather weak bonding was established between the cation and the carbon monoxide molecule. The scheme of the bonding was depicted as essentially a transfer of the carbon lone pair to the cation empty orbitals with a variable extent back-donation from the cation filled orbitals to the antibonding  $\pi^*$  orbitals of the CO molecule. This bonding scheme generally resulted in an electron deficient carbonyl carbon especially in view of the weak back-donation to the  $\pi^*$  molecular orbitals of CO. This makes the carbon particularly suitable for nucleophilic attacks by electrophiles.

However more stable and better defined complexes are also formed with rhodium, iridium and ruthenium exchanged zeolites. Upon reaction with CO; we shall restrict ourselves to the first two elements to give a detailed picture of their carbonyls. These may involve one or more metal nucleus at a time. Therefore we shall distinguish mononuclear and polynuclear carbonyls.

The Mononuclear Carbonyls When exchanged into the zeolite as  $[\text{Rh}(\text{NH}_3)_5\text{Cl}]^{2+}$ , the rhodium ammine complex could decompose in an oxygen stream at temperatures ranging 150-350°C into a rhodium III-hydroxy-species with a partial reduction into diamagnetic Rh(I) and paramagnetic (less than 10%) RhII species.

Equilibration with carbon monoxide at room temperature and low pressure (a few torr) yielded the rhodium(I)-dicarbonyl compound (13) in addition to the Rh(I)(CO) paramagnetic complex (11). The structure of this complex was elucidated by ESCA and UV measurements (13) which showed that the trivalent rhodium was indeed reduced to the monovalent state and by infrared spectroscopy which provided evidence for a gem dicarbonyl (14). Use of 1:1  $^{12}\text{CO} : ^{13}\text{CO}$  mixture confirmed the identification of the complex. Assuming a  $C_{2v}$  symmetry for the complex, prediction of the adsorption frequencies depending on the degree of CO substitution is possible (15) and it was confirmed that the observed frequencies agreed remarkably with the predicted ones thus confirming the assumed symmetry and therefore the number of CO ligands per rhodium (14).

Whether the rhodium dicarbonyl was attached to the zeolite lattice or to an extra-framework anion such as OH,  $\text{O}^{2-}$  or a labile ion, could be also decided upon using IR spectroscopy. Indeed lattice vibration between 1300 and 300  $\text{cm}^{-1}$  characteristic of an NaY zeolite (16) are sensitive to the interaction of lattice oxide ions with cations. In particular, it was observed that an IR absorption band at 877  $\text{cm}^{-1}$  grew simultaneously with the growth of CO absorptions at 2115-2048 characteristic of the dicarbonyl (13). This

former band was interpreted as due to the lengthening of T-O bonds as a result of the interaction of the concerned oxide ion with the monovalent rhodium. This provided evidence for the bonding of the rhodium I dicarbonyl to a lattice oxide ion.

Moreover using  $^{13}\text{C}$  NMR spectroscopy only a broad featureless absorption was observed even though the sample was highly enriched with  $^{13}\text{C}$  while more cumbersome molecules such as  $\text{Mo}(\text{CO})_6$  (17),  $\text{Cr}(\text{CO})_6$  (17),  $\text{Ni}(\text{CO})_4$  (18),  $\text{Fe}(\text{CO})_5$  and even  $\text{Fe}_3(\text{CO})_{12}$  sublimed into NaY zeolites gave rather sharp  $^{13}\text{C}$  resonances. This is a clear indication that while these latter compounds retained their degrees of freedom, the rhodium dicarbonyl motion is particularly restricted thus giving rise to an important anisotropy. Indeed fast spinning ( $\sim 3000$  Hz) at the Magic Angle (M.A.S.) gave rise to a sharp absorption at 183 ppm downfield with respect to TMS consistent with a Zeo-O-Rh(I)(CO)<sub>2</sub> complex. In table 1 values of the  $^{13}\text{C}$  chemical shift of various X-Rh(I)(CO)<sub>2</sub> are gathered. It is apparent that the zeolite lattice acted as ligand for the central ion.

Table 1 : Values of  $\delta(^{13}\text{C})$  for  $\text{XRh}(\text{CO})_2$  compounds.

| Compound  | Solvent                  | $\delta(^{13}\text{C})$ |
|---|--------------------------|-------------------------|
| $(\eta^5\text{-C}_5\text{H}_5)\text{Rh}(\text{CO})_2$ | $\text{CH}_3\text{Cl}_3$ | 190.9                   |
| $(\text{pyridine})\text{Rh}(\text{CO})_2\text{Cl}$    | $\text{CH}_2\text{Cl}_2$ | 181.1, 181.2            |
| $(\text{acac})\text{Rh}(\text{CO})_2$                 | $\text{CH}_2\text{Cl}_2$ | 183.8                   |

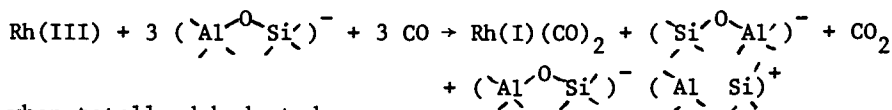
IR studies showed that each band of the  $\nu\text{CO}$  doublet characteristic of the Rh(I) gem dicarbonyl was split into two components. Recent experiments (14) showed that the presence of residual water in variable contents significantly altered the intensity ratio of the two components of each of the two bands. Only the low frequency components appeared in the case of the strictly anhydrous zeolite. As the residual water content increased (as monitored by the  $\nu\text{OH}$  absorptions at 3640 and 3550  $\text{cm}^{-1}$ ), the high frequency components grew simultaneously.

A fully hydrated zeolite was characterized by a clean doublet at 2090-2030  $\text{cm}^{-1}$ . Evacuation of excess water restored the low frequency components of the doublet. Thus the presence of one or more water molecules as ligands of the monovalent rhodium significantly altered its back-donating potential towards the  $\pi^*$  of the CO molecule and modified the bond angle as well (table 2).

Table 2 : Values of  $\nu_{\text{CO}}$  for  $\text{Rh(I)(CO)}_2$  in NaY zeolite.

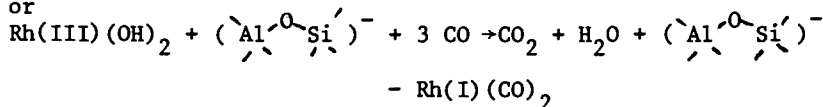
| Compound                               | $\nu_{\text{CO}}$ ( $\text{cm}^{-1}$ ) |      |
|--|--|------|
| $\text{Rh(I)(CO)}_2$ in NaY            | 2101                                   | 2022 |
| $\text{Rh(I)(CO)}_2$ with water in NaY | 2090                                   | 2030 |

Hence the rhodium III solvated by lattice oxide ions and presumably extra framework oxide ions or hydroxo ligands (depending on the dehydration state) could be carboxylated reductively to rhodium I dicarbonyl according to one of the following reaction scheme depending on the hydration state



when totally dehydrated.

or



when hydrated.

$\text{Rh(I)}$  could complete its coordination shell by binding to lattice oxide ions or to free water molecules in addition to at least one oxide ion.

The Iridium Carbonyl Iridium(III)zeolite could be obtained by conventional ion-exchange of sodium ions by  $\text{Ir(NH}_3)_5\text{Cl}^{2+}$  complex in aqueous solution and subsequent activation in flowing oxygen at temperatures not exceeding  $250^\circ\text{C}$ . Then  $\text{Ir(III)}$ -hydroxo species were obtained (8). This latter may undergo subsequent carbonylation at low or atmospheric pressure in the temperature range  $150$ – $170^\circ\text{C}$ .

The resulting complex was analyzed using different volumetric spectroscopic and spin labeling methods.

Volumetric measurements showed that, upon treatment with carbon monoxide at  $170^\circ\text{C}$  under about 5 torr, assuming all iridium has been involved, 4 CO molecules were consumed per cation. Hence assuming reduction of the trivalent cation to the monovalent state, as usual for iridium, the carbonyl compound should include three CO ligands. Indeed IR determinations showed two strong  $\nu_{\text{CO}}$  bands at  $2086$ – $2001 \text{ cm}^{-1}$  which could be due to either  $\text{Ir(CO)}_2$  ( $\text{C}_{2v}$  symmetry) or  $\text{Ir(CO)}_3$  ( $\text{C}_{3v}$  symmetry). Unambiguous assignment could be sought through analysis of the IR spectra of the  $^{12}\text{CO}$ :  $^{13}\text{CO}$  compound. Indeed it was confirmed that the compound included a  $\text{M(CO)}_3$  moiety thus equally demonstrating the reduction of the trivalent iridium to the monovalent state. Similarly the shift of the lattice

vibration upon formation of the iridium compound to about  $877\text{ cm}^{-1}$  again provided evidence for the binding of the monovalent iridium tri-carbonyl to the zeolite lattice.

Polynuclear Carbonyls Zeolite attached  $\text{Rh(I)(CO)}_2$  complexes, though fairly stable at room temperature under  $\text{CO}$  and water, slowly transform to another compound when subjected to  $\text{CO:H}_2\text{O}$  mixture. The slow transformation was perceptible at room temperature but was more important around  $50^\circ\text{C}$ . The new species was again characterized via its IR and NMR spectra.

As the  $\nu\text{CO}$  absorption bands due to the dicarbonyl decreased an IR band at  $2340\text{ cm}^{-1}$  due to  $\text{CO}_2$  developed gradually together with a set of absorptions around  $2100\text{--}2000\text{ cm}^{-1}$  due to new linear carbonyls and absorptions around  $1800\text{ cm}^{-1}$  presumably due to bridged carbonyls (14).  $\text{CO}_2$  appearance was interpreted as an indication of the further reduction of the monovalent rhodium either by  $\text{CO}$  or via the water gas shift reaction producing  $\text{H}_2$  which is reported to occur on monocuclear monovalent carbonyls (19, 20). As rhodium I was reduced to the zerovalent state, the observed  $\nu\text{CO}$  bands were ascribed to  $\text{Rh}_4(\text{CO})_{12}$  compound, in view of the excellent agreement between the observed frequencies and those reported for  $\text{Rh}_4(\text{CO})_{12}$  in  $\text{CH}_2\text{Cl}_2$  or nujol or when adsorbed on fully dehydrated zeolite.

Again  $^{13}\text{C}$  labeling gave rise to an IR spectrum in the bridged  $\nu\text{CO}$  region which confirmed the assignment to a  $\text{M}_3(\text{CO})_3$  system with a  $\text{D}_{3h}$  symmetry thus confirming the structure of the compound (14). Also  $^{13}\text{C}$  NMR measurements obtained under the (M.A.S.) conditions gave two sharp absorptions corresponding to the linear and bridged carbonyls at the same chemical shifts reported in solution (34) except that the resolution reached in solid state NMR precluded observation of Rh-C coupling usually of previous help in structure determinations. However the chemical shifts values being close to those observed in solution indicate that the interactions between the zeolite and the carbonyl compound do not exceed Van der Waals interaction similar to that prevailing between  $\text{Rh}_4(\text{CO})_{12}$  and such solvents as  $\text{CHCl}_3$ ,  $\text{CH}_2\text{Cl}_2$ , etc... a situation similar to that reported for mononuclear zerovalent carbonyls (17). Kinetics of the formation of  $\text{Rh}_4(\text{CO})_{12}$  in zeolites showed that the rate of formation decreased with increasing temperature, an indication of a reaction order  $> 2$  and of a rather complex mechanism of formation starting from zeolite bound  $\text{Rh(I)(CO)}_2$ .

The stability domain of  $\text{Rh}_4(\text{CO})_{12}$  in zeolites does not expand over a few tens of degrees ( $30\text{--}70^\circ\text{C}$ ) and at even mild temperatures yet a new carbonyl compound formed also readily obtainable using a  $\text{CO:H}_2$  mixture as reported by Mantovani et al. (21) who identified this compound characterized by an infrared spectrum showing  $\nu\text{CO}$  bands at 2095, 2080, 2060 and  $1765\text{ cm}^{-1}$  which they assigned to the linear and bridged carbonyls of  $\text{Rh}_6(\text{CO})_{16}$ . In agreement with Mantovani et al. recent synthesis of  $\text{Rh}_6(\text{CO})_{16}$  using a  $\text{CO:H}_2$  mixture at atmospheric pressure, starting from Rh I  $(\text{CO})_2$  was carried out at  $100\text{--}150^\circ\text{C}$ . Characterization of the structure was made by analogy of the IR spectra of sublimed  $\text{Rh}_6(\text{CO})_{16}$  into the

zeolite. Further use of  $^{12}\text{CO} : ^{13}\text{CO}$  in a 1:1 ratio in the synthesis mixture gave rise to CO bands due to the face bridged carbonyls which fitted a Td symmetry consistent with an  $\text{Rh}_6(\text{CO})_4$  model thus confirming the assignment of the IR spectrum to the  $\text{Rh}_6(\text{CO})_{16}$  compound.

The zeolite interaction with this compound was evidenced by the low frequency shift experienced by the CO vibration of the face bridged carbonyls. Competition between residual or added water was witnessed suggesting that the solvating properties of the zeolite and water were similar and rather weak. Therefore the stabilization of these zerovalent carbonyls within the zeolite porous structure should be attributed to a cage rather than to a chemical effect.

When treated with a  $\text{CO}:\text{H}_2\text{O}$  mixture or a  $\text{CO}:\text{H}_2$  mixture  $\text{Ir}(\text{I})(\text{CO})_3$  could be transformed into a new compound showing a different IR absorption pattern characteristic of  $\text{Ir}_4(\text{CO})_{12}$ . Again procedures identical to those described previously helped to determine the structure of the new carbonyl compound: mass spectrometry and IR spectroscopy associated with  $^{13}\text{CO}$  labeling, magic Angle Spinning  $^{13}\text{C}$  high resolution NMR and finally extraction of this commonly known as an inert compound in refluxing toluene and further spectroscopic measurements to confirm the "in situ" identification. Higher nuclearity iridium carbonyl clusters were also thought to form under more severe conditions i.e. higher  $\text{CO}:\text{H}_2$  pressures. However the interesting feature concerning the  $\text{Ir}_4(\text{CO})_{12}$  synthesis in the zeolite medium is certainly the rather mild conditions used compared to those imposed in solution chemistry where  $\text{IrCl}_3\cdot\text{H}_2\text{O}$  yielded  $\text{Ir}_4(\text{CO})_{12}$  provided a CO pressure of over 100 atmospheres is used. Also it is noteworthy that zeolites appear to be better solvating material than any other known solvent for  $\text{Ir}_4(\text{CO})_{12}$ . This is a particularly interesting example of solvating abilities of zeolites towards inert compounds.

### Carbonylation of organic substrates

Apart from the property of inorganic species to add carbon monoxide, this molecule could add to or be inserted into organic substrates.

Carbonylation of Methanol Carbonylation of methanol provides an example of a reaction catalyzed in homogeneous and heterogeneous media using monovalent rhodium or iridium carbonyl complexes. Due to the tremendous importance of this reaction from the practical point of view, numerous studies were devoted to the investigation of its mechanism and kinetics. On the other hand this reaction provides yet an interesting example of the first C-C bond formation which could be matched with that occurring during conversion of methanol to hydrocarbons. Generally this reaction proceeds under mild conditions in the presence of an iodide promoter ( $\text{HI}$  or  $\text{CH}_3\text{I}$ ). The homogeneous phase studies (22, 23) established three major steps following the formation of the monovalent carbonyl:

these could be summarized as : (i) oxidative addition of the promotor essentially the methyl halide (formed by the reaction  $\text{CH}_3\text{OH} + \text{HI}$  if not added directly) (ii) methyl migration to insert the carbonyl between the metal and the alkyl. The C-C bond is then formed (iii) the reductive elimination of the acetyl halide and subsequent esterification to methylacetate.

The relative importance of these steps from the kinetic point of view may vary depending on the nature of the catalyst.

In the case of zeolites with the declared aim of heterogenizing soluble catalysts sustained effort was devoted to understand the reaction mechanism, the role of the central metal, the importance of the promotor, the importance of the medium, etc...

The Kinetics of Methanol Carbonylation Over RhX, RhY and IrY zeolites Carbonylation of methanol proceeds readily at atmospheric pressure under mild temperature conditions 150°-180°C. This reaction  $2\text{CH}_3\text{OH} + \text{CO} \rightarrow \text{CH}_3\text{COOCH}_3 + \text{H}_2\text{O}$  produces mainly methyl acetate and water. Acetic acid was detected at high conversions and high temperatures. Traces of dimethyl ether could also form. In most cases the selectivity to methyl acetate was at least 90% in presence of the iodide promotor.

As in homogeneous media carbonylation of methanol exhibited a first order rate law with respect to methyl iodide and a zero order with respect to CO and  $\text{CH}_3\text{OH}$  when Rh-Zeolites were used. Similarly when Ir-zeolites were employed the reaction rate was first order with respect to methanol and zero order with respect to CO and  $\text{CH}_3\text{I}$ .

Thus the kinetics of the zeolite catalyzed reactions clearly paralleled closely those of the homogeneous reaction using the same transition metal as catalyst. Again zeolites acted as simple solvents for the carbonylation reaction though perhaps a specific role of the zeolite should not perhaps be entirely excluded. The kinetic similarities strongly suggested nearly identical reaction pathways in the zeolite medium and in solution with identical rate limiting step (24, 27).

Reaction pathways There is general agreement as to the nature of the catalyst precursor (26, 30). It is well admitted that even under CO low pressure Rh(III)-Y was reduced to the monovalent rhodium dicarbonyl attached to the zeolite framework via one or more oxide ions irrespective of the rhodium introduction procedure onto the zeolite.

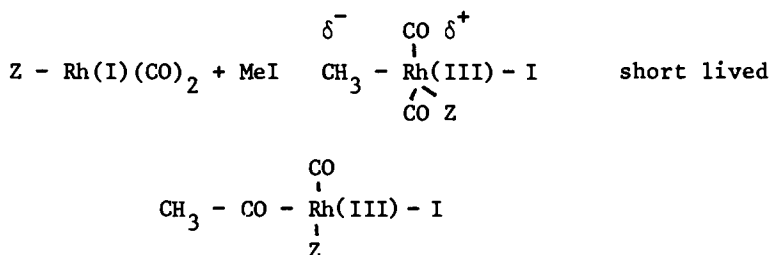
Similarly, it was shown, though few studies were reported for iridium-zeolites, that Ir(I) tricarbonyl was formed upon reaction of CO with Ir(III)-Y zeolites at 170°C which is within the methanol carbonylation temperature range.

These compounds added methyl iodide at room temperature either slowly in the case of  $\text{Rh(I)(CO)}_2\text{Z}$  (27) (Zeolite = Z) or readily in the case of the  $\text{Ir(I)(CO)}_3\text{Z}$  (27). It was suggested that this was an oxidative addition as might be concluded from the high frequency shift of the  $\nu\text{CO}$  bands of the resulting complex. UV

measurements performed in the case of the addition of MeI to  $\text{Rh}(\text{CO})_2\text{Z}$  showed that indeed rhodium(I) was reoxidized to the trivalent state (35). On the other hand the  $\text{CH}_3\text{I}$  addition to the rhodium carbonyl gave rise to a species characterized by a  $\nu\text{CO}$  at  $1725\text{ cm}^{-1}$  which was identified as an acetyl group coordinated to the trivalent rhodium.

In both cases  $^{13}\text{C}$  NMR showed the carbonyls attached to the rhodium or iridium precursor exhibited an important high field shift (31) upon  $\text{CH}_3\text{I}$  addition, indicative of CO coordinated to high oxidation state cation. Furthermore it was shown that such carbonyl carbons were highly electron deficient thus particularly suited for a nucleophilic attack by species such as alkyls etc...

Accordingly an overall reaction scheme was postulated



The low concentration of the adduct compound is probably due to a slow addition of the methyl iodide and a rapid rearrangement of the adduct to form the acetyl. This is reasonable in view of the first order rate found for methyl iodide.

The following step could be the reductive elimination of the acetyl halide to react with methanol. The growth of IR bands in the  $1710\text{--}1685\text{ cm}^{-1}$  domain might be interpreted as due to  $\text{CH}_3\text{COI}$  accumulation and possibly further reaction with substrates present in the medium. Nevertheless readdition of CO restored the monovalent rhodium dicarbonyl thus indicative that somehow  $\text{CH}_3\text{COI}$  was eliminated.

In the case of iridium zeolite the acetyl formation was not reported to occur spontaneously though the oxidative addition was a rapid step. The resulting complex was stable and did not rearrange even at  $170^\circ\text{C}$ . Only partial decarbonylation occurred. However under carbon monoxide pressure the adduct complex seemed to rearrange into the acetyl or perhaps give rise to yet another surface organic carbonyl species.

Methanol reacted also rapidly with the adduct to form what might be an alkoxy carbonyl ligand to the trivalent iridium by direct attack of the methoxy group on the electrophilic carbonyl carbon. Such an alkoxy group would account for the  $\nu\text{CO}$  band which appeared at  $1705\text{ cm}^{-1}$  following methanol addition onto the adduct. However a methanol assisted rearrangement of the adduct cannot be excluded. Subsequent introduction of CO resulted in the formation of the methyl acetate presumably by a concerted elimination of the alkyl and the alkoxy group and simultaneous carbonylation. This might be an indication of a more covalent  $\text{CH}_3 - \text{Ir}(\text{I})$  bond which



then would prevent the cis nucleophilic attack on the carbonyl carbon of the addition complex.

The differences displayed by rhodium and iridium zeolites when interacting with the reaction partners are consistent with their different kinetic behaviour. These differences seem to be independent upon the nature of the medium (solution or zeolitic) and appear to be essentially relevant to the chemistry of rhodium and iridium.

The Role of Zeolites Where zeolites seem to play a more specific role appears probably when activities and selectivities are examined. Though few comparative studies were made possible upon examination of the literature, it would appear that both rhodium and iridium exhibited lower activities than in the homogeneous reaction systems but far larger activities than exhibited when supported over traditional carriers ( $\text{Al}_2\text{O}_3$ ,  $\text{Al}_2\text{O}_3\text{-SiO}_2$ , carbon, etc...). This is probably due to the better molecular dispersion of the rhodium and iridium catalytic precursors in zeolite media than over any of these carriers and still more important diffusion limitations than in solution.

The catalytic influence seemed to be reflected by a number of features :

- Rhodium Y zeolites appear to be efficient at significantly lower temperature than rhodium X zeolites. This might be due to the higher polarization ability of the Y type zeolite which would favor the methyl addition onto the rhodium dicarbonyl which is the slow step in the case of rhodium.

- Compared to other carriers and particularly functionalized polymers the stability of the rhodium catalyst in the zeolite medium is far superior presumably due to the stronger Rh-O bond compared to P-Rh bond in phosphine bound rhodium(I)dicarbonyl. Also the cage structure of the zeolite almost precluded inner interaction of the active species and therefore their association into inactive compounds.

- In the case of ethanol and higher alcohols the zeolite matrix may well have a negative effect in that it might favor dehydration or dehydrogenation reactions to form ethers and olefins.

The Importance of the Nature of the Alcohol It was shown by Scurrrel and Coworkers (32) that alcohols were not equally carbonylated. Under identical conditions the rates follow the sequence  $\text{CH}_3 > \text{C}_2\text{H}_5 \gg \text{isoC}_3\text{H}_7$  where only propene was produced.

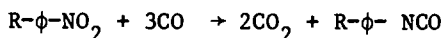
As the actually carbonylated species is the alkyl halide it is expected that the activity should depend on the polar or non polar character of the R-X bond. Therefore the size and the nucleophilic character of the  $\sigma$  alkyl attached to the transition metal should be considered.

Further the alkyl migration to effect the nucleophilic attack on the carbonyl should also depend on the M-R polarizability as  $\text{R}\delta^- - \text{M}\delta^+$  and indeed on the tendency of the radical to give rise to elimination processes.

This intricate behaviour was reflected in the competitive carbonylation of the methyl and ethyl radicals when EtI + MeOH and MeI + EtOH mixtures were reacted. Ethyl acetate but also trace methyl acetate were produced. No ethyl propionate was detected on the one hand and essentially methyl acetate and lower amounts of propionic acid, methyl propionate and ethyl acetate were formed (25) using rhodium zeolites indicating that various exchange reactions were proceeding with high enough rates so as to result in a different effective feed composition. These side reactions reveal the importance of the polarity of the medium as well as the nature of the transition metal.

The polarity of the medium and the complexing ability of the transition metal may well account for the activity differences observed between the X and Y type zeolites. On the other hand the intrinsic activity of each of these elements decreased with increasing the loading. This could be due to a progressive washing of the active metal (which has been reported to occur) or to a lesser accessibility of the reactants which may not reach the inner depth of individual zeolite crystals where the active substance could yet reside. It is not unreasonable to assume that the zeolite-M(I)(CO)<sub>n</sub> interaction could be modified by higher exchange levels and therefore effect the electron density at the active metal and therefore its catalytic properties. This would be in agreement with reports in homogeneous carbonylation of the effect of the polarity of the medium on the activity where an optimum electric constant exists (33). Indeed the ion-exchange level may modify dramatically be proton content of the zeolite thus affecting its dielectric constant.

#### Carbonylation of Nitroaromatics Carbonylation of nitroaromatics to isocyanates



was reported to proceed in a homogeneous mixture of PdCl<sub>2</sub>-pyridine in various solvents at 180-240°C under CO pressures of 50-500 atmospheres (34).

In view of the severe experimental conditions used, little is known as to the nature of the active species. Yet two possibilities could be considered. Either the palladium operates as a soluble complex or as metal particles in a heterogeneous reaction. In support of the latter claim formation of metal particles was evidenced. However it could be argued that such particles result from the deactivation of the catalyst.

Zeolites as excellent stabilizing agents for Pd(II) or well dispersed Pd(0) were then used as a carrier for this reaction (35). It was shown that the activity of the catalyst depended chiefly on the ability of the transition metal ion to undergo easily redox cycles. In this respect, transition metal with quasi-permanent cationic state such as cobalt or with quasi permanent metallic state such as platinum exhibited the lowest activity. By contrast copper, rhodium, iridium and particularly palladium showed the highest activity though with varying selectivities.

Association of oxygen transfer agents such as Fe(III), Cu(II) MoO<sub>3</sub> to palladium increased its activity. Furthermore both oxidized and reduced forms of Pd-zeolite appeared to be equally active and selective. Partial oxidation of the reduced form and reduction of the oxidized form were observed. Hence a redox cycle during catalysis seems highly probable in view of these results which is not unreasonable considering the redox nature of the reaction where nitrogroups have yet to be reduced by carbon monoxide before the isocyanate could form. Indeed IR studies showed that actually nitrogroups were reduced to nitroso before elimination of the latter on further heating adsorbed nitrobenzene adsorbed on Pd-zeolite in presence of carbon monoxide. The reduction could then lead ultimately to the nitrene group eventually coordinated to the transition metal ion. The nitrene ligand could well be part of carbonyl complex. As most carbonyls of palladium, iridium, etc... have rather electron deficient carbons even in zerovalent complexes (36), the nitrene may well effect a nucleophilic attack of these carbonyls. Such a rearrangement would be assisted by such bases as pyridine when present in the coordination sphere of the metal center. Thus the key to a high activity would be an easy redox cycle of the transition metal center so as to catalyze the reduction of the nitrogroup to a nitrene group. However the selectivity to the isocyanate would depend on the preferential nucleophilic attack of the carbonyl carbon by the nitrene by comparison to association of the nitrene condensation with other groups etc... Such a reaction path would be favoured by a pronounced positive character of the carbonyl carbon, which is solely dependent on the nature of transition metal center when the same coordinates are available, and by an increased electron density on the nitrene group. Such a mechanism is quite similar to methanol carbonylation in its essence. The ideal transition metal center would have to meet essentially two contradictory conditions : dramatically increase the electron density of the nitrene while depleting the carbonyl electrons. This is probably the reason for which very few transition metal elements exhibit both high activity and selectivity to isocyanates. The presence of the organic base would presumably help the cation meet these extreme conditions by a trans effect which would increase the electron density at the nitrene without affecting to a large extent the electron deficient character of the carbonyl. Thus clearly carbonylation proceeds via two important functions of zeolite hosted transition metal ions and/or complexes i) the ability to undergo easy redox cycle ii) the stabilization of  $\delta^+$  carbonyl carbons together with a nucleophilic substrate which would then migrate to insert CO prior to reductive elimination.

The key feature of the adequate transition element seems to be in this ability to stabilize both electrophiles and nucleophiles within the same complex. Extra ligands may or may not increase the reactivity of one of these two species and therefore make the design of a transition metal zeolite based catalyst within the same ease or difficulty as their homogeneous analogues.

Litterature Cited

1. Naccache, C.; Ben Taarit, Y.; *Acta Physica et Chemica*. 1978, 24, 23.
2. Klier, K.; Hutta, P. J.; Kellerman, R.; *ACS Symposium Series*. 1977, 40, 120.
3. Ward, J. W.; Rabo, J. A.; Ed. "Zeolite Chemistry and Catalysis", *ACS Monograph*, 1976, 171, 118.
4. Lunsford, J. H.; *ACS Symposium Series*. 1977, 40, 473.
5. Gallezot, P.; Ben Taarit, Y.; Imelik, B.; *J. Chem. Phys.* 1973, 77, 2364.
6. Gallezot, P.; Coudurier, G.; Primet, M.; Imelik, B.; *ACS Symposium Series*. 1977, 40, 144.
7. Gelin, P.; Ben Taarit, Y.; Naccache, C.; *J. Catal.* 1979, 59, 357.
8. Gelin, P.; Coudurier, G.; Ben Taarit, Y.; Naccache, C.; *J. Catal.* 1981, 70, 32.
9. Falbe, J.; Ed. "Reactivity and structure concepts in Organic Chemistry, vol. 11, Syntheses with Carbon Monoxide", Springer-Verlag Berlin Heidelberg, 1980.
10. Naccache, C.; Primet, M.; Mathieu, M. V.; *Advances in Chemistry Series*. 1973, 121, 266.
11. Naccache, C.; Ben Taarit, Y.; Boudart, M.; Katzer, J. R.; Edit. "ACS Symposium Series 40", 1977, 156.
12. Ben Taarit, Y.; *Chem. Phys. Letters*. 1979, 62, 211.
13. Primet, M.; Védérine, J.C.; Naccache, C.; *J. Mol. Catal.* 1978, 4, 411.
14. Lefebvre, F.; et al.; to be published.
15. Braterman, P. S.; "Metal Carbonyl Spectra", Academic Press, New York, 1975.
16. Flanigen, E. M.; Rabo, J. A.; Ed. "Zeolite Chemistry and Catalysis", *ACS Monograph* . 1976, 171, 80.
17. Ben Taarit, Y.; Wicker, G.; Naccache, C.; Fraissard, J. P.; Resing, H. A.; Edit., "Magnetic Resonance in Colloid and Interface Science, NATO advanced Study Institute Series, Series C", 1980, 497.
18. Nagy, J. B.; Van Eenoo, M.; Derouane, E. G.; Védérine, J. C.; Fraissard, J. P.; Resing, H. A.; Edit., "Magnetic Resonance in Colloid and Interface Science, NATO advanced Study Institute Series, Series C", 1980, 591.
19. Niwa, N.; Lunsford, J. H.; *J. Catal.* 1982, 75, 302.
20. Cheng, C. H., Hendriksen, D. E.; Eisenberg, R.; *J.A.C.S.* 1977, 99, 2791.
21. Mantovani, E.; Palladino, N.; Zanobi, A.; *J. Mol. Cat.* 1977/78, 3, 285.
22. Roth, J. F.; Craddock, J. H.; Hershman, A.; Paulik, P. E.; *Chem. Tech.* 1971, 600.
23. Forster, D.; *J.A.C.S.*; 1976, 93, 846.
24. Christensen, B.; Scurrrell, M. S.; *J.C.S. Faraday I.* 1978, 74, 2313.

25. Matsumoto, T.; Mizoroki, T.; Ozaki, A.; J. Catal. 1978, 51, 96.
26. Takahashi, N.; Orikasa, Y.; Yashima, T.; J. Catal. 1979, 59, 61.
27. Gelin, P.; Ben Taarit, Y.; Naccache, C.; 7th Intern. Congr. Catal. Tokyo, Japan 1980.
28. Anderson, L. T.; Scurrrell, M. S.; J. Catal. 1979, 59, 340.
29. Yamanis, J.; Yang, K. C.; J. Catal. 1981, 69, 498.
30. Primet, M.; Garbowski, E.; Chem. Phys. Letters. 1980, 72, 472.
31. Gelin, P.; et al. to be published.
32. Christensen, B., Scurrrell, M. S.; J.C.S. Faraday I. 1977, 73, 2036.
33. Hjortkjaer, J.; Jensen, D. R.; I & Ec. Prod. Res. & Development, 1977, 16, 281.
34. Olin Mathieson., Chem. Corp. U.S. P. 3 743664, 1973.
35. Kervennal, J.. Ben Taarit, Y.; Elleuch, B.; French Patent : 79.29123
36. Ganson, O. A.; Vernon, W. D.; Levy, G. C.; Ed. "Topics in  $^{13}\text{C}$  NMR spectroscopy Vol.II", Wiley, J.; Sons., New York 1976, 270.

RECEIVED November 16, 1982

# INDEX

- A**
- Acidity in zeolite ZSM-5, investigation of sources and nature ..... 369
- Acidity in zeolites  
 experimental method ..... 371, 372*t*  
 source ..... 370  
 techniques used to determine ..... 370  
 titrations ..... 371-81
- Acid-type catalysts, activity polymerization of olefin ..... 383
- Adsorption isotherms, nitrogen  
 in mordenite ..... 336-41
- Adsorption of organic molecules ..... 51
- Adsorption properties, aluminophosphate molecular sieves ..... 100-105
- Agitation, effect on ZK4 crystallization rate ..... 270
- Alumina octahedra ..... 80
- Aluminophosphate gel ..... 80, 88
- Aluminophosphate molecular sieves ..... 79, 105  
 adsorption properties ..... 102*t*  
 crystal structure ..... 109  
 difference-Fourier map ..... 113, 116*f*  
 diffraction data ..... 110, 112*t*  
 hydrophilicity ..... 105  
 pore volumes ..... 102  
 stereoplot ..... 112*f*  
 structure ..... 93, 97*f*-99*f*, 110  
 surface character ..... 105  
 synthesis ..... 80  
 thermal stability and adsorption properties ..... 100-105  
 various ..... 81  
 x-ray powder diffraction data ..... 81, 82*t*
- Aluminosilicate hydrogels ..... 21
- Aluminosilicate zeolites ..... 79
- Aluminosilicates, chemical shift ranges ..... 231, 232
- Alumina-silica molar ratio ..... 15
- Aluminum-27 nuclear quadrupole interaction, silicon-29 NMR ..... 246  
 MASNMR ..... 177, 178*f*
- Aluminum atoms, distribution in faujasite type zeolites ..... 424*f*
- Aluminum concentrations, variation across zeolite particles ..... 199
- Aluminum detection in silicon-29  
 Aluminum-oxygen  
 bond, zeolite-A ..... 135*t*  
 bridges ..... 146  
 dehydrated varieties of  
 zeolite A ..... 121, 123
- Aluminum-silicon distributions in square planar lattice ..... 223*f*, 224*f*
- Ammonia selectivity, ZSM-5 ..... 64, 67*f*
- Amorphous aluminum, effect on chemical profiles ..... 214
- Amygdaloidal basalt ..... 21
- Analcime ..... 81
- Angular misorientation ..... 123
- Anionic field strength, ZSM-5 ..... 77
- A1-Si distributions in square planar lattice, Loewenstein's and Dempsey's rules ..... 223*f*, 224*f*
- Atomic coordinates, thallium zeolite A ..... 135*t*
- Atomic positions and displacements, TPA(OH)-A1P04 #5 ..... 115*t*
- A-type zeolites  
 pathways for formation ..... 247*f*  
 synthesis and characterization ..... 267
- Autocatalytic crystallization reaction.. 24
- Average particle sizes, ZSM-5 ..... 200
- Axial dispersion contribution, elimination and estimation ..... 349, 350*f*
- B**
- Backscattering amplitude functions, Na,K(Fe) chabazite and H(Fe) chabazite ..... 327*f*, 329*f*
- Bare ionic radius related to selectivity ..... 75
- Benzene diffusion in type Y zeolites .... 359
- Berlinite ..... 117
- Bifunctional metal/zeolite catalysts, synthesis gas conversion ..... 397
- Boehmite ..... 80
- Bond angles, TPA(OH)-A1P04 ..... 117
- Bronsted acid sites ..... 47  
 acidity in zeolites ..... 375  
 effect on synthesis gas conversion .. 405
- n*-Butane cracking ..... 45  
 fluorinated zeolites ..... 52, 54*t*, 55
- 1-Butanol-water shake test, fluorinated zeolites ..... 51, 53*t*
- Butyl complexes, role in synthesis of ZSM-11 ..... 128



- Delta hexane loading ..... 45, 49  
 Dempsey's rules ..... 218, 220  
 Density of second nearest neighbor  
   aluminum pairs, calculation ..... 220  
 Deshielding related to Si/Ga ratio ..... 239  
 Difference profiles of thallium  
   zeolite A ..... 134f  
 Difference-Fourier maps  
   aluminophosphate molecular  
     sieves ..... 113, 116f  
   electron density ..... 126f  
 Diffuse reflectance spectra  
   silver species in faujasite zeolites  
     silver species in rare gas solids  
       419, 421f  
     417, 418f  
 Diffusion equation ..... 346  
 Diffusion of olefins, effect of ion  
   exchange ..... 359  
 Diffusion  
   type A zeolites, discussion ..... 353-58  
   type X zeolites, discussion ..... 358-63  
 Diffusional activation energy, variation  
   with van der Waals radius ..... 355f  
 Diffusivity  
   effect of crystal size ..... 354  
   effect of temperature and crystal  
     size ..... 351, 352f  
   variation with ion exchange in  
     Na/CaA zeolites ..... 354  
 Direct hydrothermal synthesis ..... 41  
 Distances and angles, framework in  
   TPA(OH)-A1P04 #5 ..... 117  
 Distribution of Al and Si, equations 218-20  
 Distribution of hydrocarbons, synthesis  
   gas conversion ..... 400, 403f, 404f  
 Divalent cations, isotherms,  
   ZSM-5 ..... 68, 72-74f  
 Double-four-ring unit, A type  
   zeolites ..... 149  
 DTA profile, offretite ..... 29, 30  
 Dynamic and energetic properties,  
   silver species, vibronic coupling  
   model ..... 425, 426f
- E**
- Electric-quadrupole field-gradient  
   energy, formula ..... 334  
 Electron density, zeolite A ..... 123, 124f  
 Electron paramagnetic resonance  
   samples, mixed metal zeolites ..... 304  
 Electron spin echo modulation  
   silver atom species in zeolite  
     lattice ..... 290, 291f  
     background ..... 284-87  
     very weak hyperfine interactions ..... 284
- Electron spin echo studies, paramag-  
   netic species in zeolites ..... 283  
 Electrostatic energy interaction,  
   calculation ..... 76  
 Electrostatic model, zeolite A ..... 121  
 Electrostatic repulsion, 4-ring ..... 219  
 Equations, chromatography study of  
   intracrystalline diffusion ..... 348  
 Erionite, framework structure ..... 81, 93, 95f  
 EXAFS spectra  
   Fourier transforms ..... 326f  
   Na,K(Fe)-chabazite and H(Fe)-  
     chabazite ..... 325f, 328f  
   various metal-containing zeolites,  
     discussion ..... 320, 322-28
- Excitation profiles  
   silver species in faujasite zeolites  
     silver species in rare gas solids  
       411, 413f  
     419, 421f
- Experimental methods, compositional  
   variations across zeolite particles ..... 200  
 Extended x-ray absorption fine  
   structure—See EXAFS
- F**
- Fast tracer desorption ..... 353  
 NMR method, diffusion study ..... 358  
 Faujasite  
   absorption peaks ..... 267  
   aluminum neighbor distribution,  
     calculation ..... 251-53  
   discussion ..... 182, 160-65  
   formation schematic ..... 247f, 254  
   framework ..... 231, 257f  
   lattice ..... 358  
   neutron diffraction patterns ..... 140f, 141  
   silicon-aluminum ordering ..... 251  
   synthesis, various Si/Ga ratios ..... 233  
 Ferrocene sublimed onto zeolite  
   ZSM-5 ..... 303  
 Ferrocene-exchanged ZSM-5 zeolite,  
   Mössbauer spectrum analysis ..... 308-15  
 Fischer-Tropsch reaction, important  
   factors ..... 315  
 Fluorescence emission and absorption  
   profiles, silver species in rare gas  
   solids ..... 411, 413f  
 Fluorescence emission and excitation  
   spectra, silver species in faujasite  
   zeolites ..... 417, 418f,  
     422f, 428, 429f  
 Fluorescence indicator absorption,  
   hydrocarbon fraction ..... 405  
 Fluorescence spectra, silver atoms and  
   clusters in rare gas solids ..... 410  
 Fluoride-silicalite ..... 120



|   |                      |   |   |
|---|----------------------|---|---|
| Fluorinated zeolites  |                      | Hindrance, ZSM-5  | 60  |
| <i>n</i> -butane cracking   | 52, 54 <i>t</i> , 55 | Hydronium ion exchange isotherm, ZSM-5                  | 69 <i>f</i>   |
| 1-butanol-water shake test  | 51, 53 <i>t</i>      | Hydrophilic surfaces                                    | 41  |
| catalytic activity  | 52                   | Hydrophilicity of aluminophosphate molecular sieves     | 105   |
| dealumination, hydrophobicity, and structure stabilization                        | 54, 55               | Hydrophobicity, fluorinated zeolites                    | 54  |
| direct gaseous phase  | 42                   | Hydroxoaluminum cation species                          | 377   |
| experimental methods  | 42-44, 47            | Hydroxyl group loss                                     | 54  |
| McBain-Bakr adsorption  | 49, 51 <i>t</i>      | Hydroxyl groups, effects of fluorination                | 49, 50 <i>f</i>   |
| water adsorption  | 49, 52 <i>t</i>      | Hydroxyl nest   | 42  |
| x-ray diffraction spectra   | 45, 46 <i>f</i>      | Hydroxysodalite   | 6, 11   |
| Fluorination effect on hydroxyl groups  | 49, 50 <i>f</i>      | formation   | 16, 17 <i>t</i>   |
| Framework oxide molecular sieves  | 79                   | conversion to zeolite A                                 | 16  |
| Framework positions, dehydrated varieties of zeolite A                            | 120                  |   |   |
| Freundlich equation and isotherm model  | 336                  | <b>I</b>  |   |
| Functional site, ZSM-5  | 64                   | Infrared analysis                                       |   |
| <b>G</b>  |                      | offretite   | 29, 34 <i>f</i> , 35 <i>f</i> , 36 <i>f</i> , 37 <i>f</i> , 38 <i>f</i> |
| Gallium faujasites and a gallium sodalite, high resolution silicon-29 NMR studies | 231                  | olefin conversion                                       | 394   |
| Gallium faujasites  |                      | band shifting and sharpening                            | 54  |
| deshielding and chemical shift and relative peak intensities                      | 239                  | fluorinated zeolites                                    | 47, 48 <i>f</i>   |
| Gallosodalite, Si/Ga ratio  | 174                  | Initial dehydration conditions, effect on diffusion     | 358   |
| Gallozeolitic structures, structural properties                                   | 174, 175 <i>f</i>    | Interatomic distances and angles, TPA(OH)-A1P04 #5      | 116 <i>t</i>  |
| Ground state molecular orbital schemes, silver species in faujasite zeolites      | 433, 434             | Intergrowth structures, ZSM-5 and ZSM-11 catalysts      | 186-97  |
| Growth aggregates   | 81, 88               | Intracrystalline diffusion                              |   |
| Guest-host interactions   |                      | experimental tests                                      | 346, 347 <i>f</i>   |
| silver species in faujasite zeolites  | 425                  | isothermal system                                       | 346   |
| silver species in rare gas solids   | 414                  | study, chromatography method                            | 348   |
|   |                      | in zeolites   | 345   |
| <b>H</b>  |                      | Intracrystalline TMA ions, breakdown                    | 29  |
| Heat of adsorption  |                      | Ion exchange  | 60  |
| constants, nitrogen on mordenite  | 339 <i>t</i>         | Ion exchange isotherms, various, ZSM-5                  | 63-68, 65 <i>f</i> -67 <i>f</i> , 69 <i>f</i> -74 <i>f</i>              |
| equation  | 337                  | Ion exchange properties, ZSM-5                          | 59, 75  |
| Heating times for crystallization of ZK4  | 270                  | Ion exchange temperature, effect on ammonia selectivity | 64, 67 <i>f</i>   |
| Henry's law equilibrium constant, theoretical expressions                         | 363                  | Iridium carbonylation                                   | 459   |
| Hexagonal symmetry  | 110                  | Iron-containing zeolites                                |   |
| High resolution electron microscopy (HREM)  | 181                  | Mössbauer studies                                       | 301   |
| High resolution solid state silicon-29 NMR, zeolites and other aluminosilicates   | 231                  | novel preparation method                                | 303   |
| High-cristobalite   | 113                  | Iron mordenites   | 302   |
| High-resolution electron microscopy, zeolites                                     | 181                  | Iron/zeolite catalysts, catalytic evaluation            | 400-407   |
| High-tridymite  | 113                  | Isomorphous substitution                                | 24  |
|   |                      | Isosteric heats of adsorption                           | 29, 32 <i>f</i> , 33 <i>f</i> , 337-41                                  |
|   |                      | Isotropic chemical shift                                | 267, 275  |
|   |                      | Isotropic coupling constant, silver atom in gas phase   | 289   |
|   |                      | Isotropic hyperfine coupling                            | 285   |

- Isotropic hyperfine splitting, silver in zeolites ..... 289
- J**
- Jahn-Teller effects, divalent cupric ion in A-zeolites ..... 293
- K**
- Kaolinite, thermogravimetric curve .... 373  
Kinetics, acidity in zeolites ..... 381  
Kolbel-Engelhardt synthesis ..... 440
- L**
- Location and coordination, silver species in faujasite zeolites ... 419, 420f  
Loewenstein's and Dempsey's models, difference ..... 225  
Loewenstein's rule ..... 141, 143, 144, 163, 182, 219, 232, 234, 244, 263, 273
- M**
- Magic-angle sample spinning, ZK4 ..... 273, 274f  
Magic-angle spinning NMR (MASNMR) ..... 159  
MASNMR chemical shifts, framework effects ..... 120  
McBain-Bakr adsorption, fluorinated zeolites ..... 49, 51f  
McBain water adsorption ..... 55  
Metal-containing zeolites, various preparations ..... 314  
Metal clusters, experimental techniques ..... 409  
Metal ion site geometry, in zeolites .... 319  
Metal-support effects, silver species in zeolites ..... 410, 427-34  
Metavariscite ..... 80  
Methanol carbonylation ..... 461  
kinetics, various zeolites ..... 462  
reaction pathways ..... 462-64  
Microporous crystalline inorganic solids ..... 79  
Mineral zeolites ..... 79  
Mixed metal zeolite  
data ..... 308, 309r, 310r  
preparation ..... 304  
Modification of zeolites, various methods ..... 42  
Modulation of two pulse electron spin echo decay envelope, illustration ..... 286f  
Molar ratio interactions ..... 6
- Molar ratio  
silica to aluminum ..... 15  
sodium oxide to silica ..... 1  
water to sodium oxide ..... 11  
Molecular sieve silicalite ..... 105  
Moment analysis of NMR spectra .... 218  
Mononuclear carbonylation ..... 457  
Monte Carlo calculations, simulated spectra ..... 218  
Mordenite ..... 42  
dealumination ..... 165  
Mössbauer spectra  
effect of dehydration ..... 322  
ferrocene on zeolite ZSM-5  
305, 306f, 307f, 308-315  
mixed metal, Scherzer-Fort type  
preparation ..... 305, 308, 309r, 310r  
Mössbauer spectrum  
H(Fe) chabazite, discussion ..... 322, 323f  
Na,K(Fe) chabazite mineral, discussion ..... 321, 323f  
reduced zinc(II)nitroprusside/  
NH<sub>4</sub>Y ..... 312f  
zinc(II)nitroprusside/NH<sub>4</sub>Y ..... 311f  
Mössbauer studies  
in area of catalysis ..... 302  
iron-containing zeolites ..... 301, 302, 304
- N**
- Na-A zeolite conversion to carnegieite ..... 171, 173f  
Neopentane adsorption ..... 100  
Neopentylamine ..... 93  
Neutron diffraction study  
experimental method ..... 132, 145  
faujasite ..... 140f, 141  
Na-A zeolite ..... 143  
scope and limitations ..... 131, 132  
synthetic faujasite ..... 131  
thallium and silver derivatives ..... 132  
zeolite A ..... 131, 149-51  
Nitroaromatics, carbonylation ..... 465  
Nitrogen-15 NMR spectra,  
mordenites ..... 341, 342f  
Nitrogen adsorption by mordenite  
experimental method ..... 334-36  
steric effects ..... 333  
NMR application to study of diffusion  
in zeolites, various methods ... 349-53  
NMR experimental method ..... 145  
NMR results, sodium faujasites and a gallium sodalite ..... 234  
NMR and sorption diffusivities,  
comparison ..... 353  
NMR spectra, moment analysis ..... 218  
NMR spectra simulation, various zeolites ..... 220-25

|  |                             |
|--|-----------------------------|
| Nonframework cations, effect on              |                             |
| chemical shifts .....                        | 232                         |
| Nucleation and growth rates .....            | 16                          |
| Nucleophilic attack of carbonyls .....       | 466                         |
| Nucleophilic attack, carbonylation .....     | 463, 464                    |
| <b>O</b>                                     |                             |
| Offretite                                    |                             |
| crystallization .....                        | 24                          |
| DTA profile .....                            | 29, 30f                     |
| gel composition .....                        | 25t                         |
| infrared analysis .....                      | 29, 34f, 35f, 36f, 37f, 38f |
| (Rb, TMA), scanning electron                 |                             |
| micrographs .....                            | 27f                         |
| thermogravimetric curve .....                | 29, 31f                     |
| x-ray diffractogram .....                    | 26f                         |
| Offretite type zeolite, characterization     |                             |
| and synthesis .....                          | 21                          |
| Olefin conversion                            |                             |
| comparison of product carbon                 |                             |
| numbers .....                                | 391t                        |
| effect of pressure .....                     | 386f                        |
| effect of space velocity .....               | 38                          |
| over synthetic zeolite ZSM-5 .....           | 383                         |
| reaction steps .....                         | 389                         |
| Olefins, diffusivity in NaX zeolite .....    | 359                         |
| Olefin isomers, isolation .....              | 389, 391t                   |
| Optical absorption and emission spectra,     |                             |
| silver species in rare                       |                             |
| gas solids .....                             | 411, 412f, 413f             |
| Optical diffractometry, zeolites .....       | 181                         |
| Optically excited Jahn-Teller active         |                             |
| state, silver species in rare                |                             |
| gas solids .....                             | 414                         |
| Ordered sodalite building unit,              |                             |
| faujasite .....                              | 258                         |
| Ordered sodalite cage model,                 |                             |
| deviations .....                             | 244, 246                    |
| Ordered sub-unit hypothesis, faujasite       |                             |
| structure .....                              | 244-46                      |
| Organic amine, templating agent .....        | 80                          |
| Organic carbonylation, effect of             |                             |
| nature of alcohol .....                      | 464                         |
| Organic templates                            |                             |
| molecular sieve synthesis .....              | 88                          |
| structure-directing agents .....             | 88-100                      |
| Organophilic surface .....                   | 41, 49                      |
| Orientational parameter, formulas .....      | 341                         |
| Oxidation state in zeolites .....            | 319                         |
| Oxide molar ratio .....                      | 6                           |
| Oxygen adsorption                            |                             |
| isotherms of selected                        |                             |
| aluminophosphate                             |                             |
| molecular sieves .....                       | 102, 103f, 105              |
| measure of total crystallinity .....         | 49, 51t                     |
| Oxygen atom displacements .....              | 113                         |
| Oxygen in tetrahedral atom .....             | 117                         |
| <b>P</b>                                     |                             |
| Paramagnetic transition metal ions ....      | 283                         |
| Particle size                                |                             |
| effect on synthesis gas conversion ..        | 400                         |
| related to extracrystalline                  |                             |
| resistance .....                             | 349                         |
| Pathways                                     |                             |
| formation of faujasite and A-type            |                             |
| zeolites .....                               | 247f                        |
| formation of faujasite and ZK4 .....         | 246                         |
| Peak shift, x-ray diffraction spectra ....   | 45                          |
| Percent conversion of H <sub>2</sub> and CO, |                             |
| iron/zeolite catalysts .....                 | 401f, 402f                  |
| Perovskite .....                             | 174                         |
| Perrotta synthesis .....                     | 22                          |
| pH measurements, acidity in zeolites ..      | 381                         |
| Phillipsite .....                            | 171                         |
| Phosphate tetrahedra .....                   | 80                          |
| Photoaggregation, silver species in rare     |                             |
| gas solids .....                             | 414                         |
| Photochemical activation, iron               |                             |
| carbonyl complexes .....                     | 303                         |
| Photochemical isomerization of olefins       |                             |
| by iron-containing zeolites .....            | 308, 313t                   |
| Photodissociative-recombination              |                             |
| process, silver species in                   |                             |
| rare gas solids .....                        | 415                         |
| Polar array, definition .....                | 113                         |
| Polar template and diffusion .....           | 117                         |
| Polynuclear carbonylation .....              | 460                         |
| Polyvalent cations, selectivity in           |                             |
| ZSM-5 .....                                  | 77                          |
| Pore size, aluminophosphate                  |                             |
| molecular sieves .....                       | 100                         |
| Pore volumes, aluminophosphate               |                             |
| molecular sieves .....                       | 102                         |
| Post-synthesis modification .....            | 41                          |
| Potential field within zeolite,              |                             |
| theoretical model .....                      | 363                         |
| Potentiometric titration curves,             |                             |
| acidity in zeolites .....                    | 377                         |
| Powder x-ray data, ZK4 .....                 | 275                         |
| Probabilities for formation of Si-O-Al       |                             |
| linkages, 6-ring sub-units .....             | 255f                        |
| Probabilities for formation of Si-O-Al       |                             |
| linkages, 4-ring sub-units .....             | 264f                        |
| Propylene conversion                         |                             |
| effect of contact time .....                 | 384, 388f                   |
| effect of pressure .....                     | 384, 386f                   |
| effect of temperature .....                  | 384, 387t                   |
| Proton dipolar decoupling, ZK4 .....         | 273, 274f                   |
| Pulsed field gradient (PFG) self             |                             |
| diffusion measurement .....                  | 351, 352f                   |

- Pyridine, chemisorbed, adsorption bands ..... 29
- Q**
- Quaternary ammonium salt, templating agent ..... 80
- Quinuclidine ..... 93
- R**
- Rb-, TMA-offretite, scanning electron micrographs ..... 27*f*
- Rb-offretite crystals ..... 29
- Rb-zeolite ..... 24
- Reaction steps, olefin conversion ..... 389
- Reaction time, effect of zeolite phase transformation ..... 12*f*, 13*f*, 14*f*
- Reactions during fluorination of zeolites ..... 55, 56
- Reactive hydrated alumina ..... 80
- Redox cycle during catalysis ..... 466
- Reduced iron species in zeolite, preparation ..... 302
- Refined lattice parameters, least squares interative procedure ..... 275
- Relative crystallization times ..... 11
- Relaxation processes, silver species in rare gas solids ..... 411
- Relaxation time measurements ..... 349
- R-factor, using model of Pluth and Smith ..... 133
- Rhodium carbonylation ..... 457
- reaction scheme ..... 459
- Rhodium dicarbonyl ..... 457
- chemical shift ..... 458
- Rhombohedral distortion ..... 144, 149, 150*f*
- Rietveld profile analysis technique ..... 131
- Rietveld refinement, neutron powder data, Na-A zeolite ..... 152-153*t*
- Ring size, aluminophosphate molecular sieves ..... 100
- Rubidium-TMA-offretite ..... 22
- Ruthenium complexes in faujasite zeolites, chemical transformation ..... 439
- Ruthenium transformation, schematic ..... 441
- Ruthenium-zeolite activation
- effect of aluminum content of zeolite ..... 446, 448*f*
- effect of CO atmosphere ..... 441
- effect of pretreatment temperature.. 440
- effect of zeolite basicity ..... 446
- S**
- Salt inclusion, variation in chemical shifts ..... 234
- Salt occlusion, ZSM-5 ..... 60
- Saturated hydrocarbons, diffusion in type X zeolites ..... 359, 360*f*, 361*f*, 362*f*
- Scanning electron micrographs
- A1PO4-5 ..... 81, 84*f*, 85*f*
- A1PO4-11 ..... 81, 87*f*
- A1PO4-17 ..... 88, 90*f*
- Scherzer-Fort preparations, x-ray powder diffraction data ..... 308
- Seeding effect on ZK4 synthesis ..... 270
- Selected area electron diffraction (SAED) ..... 181
- Selectivity correlation, ZSM-5 ..... 68
- Selectivity ranking, alkali metals and NH<sub>4</sub><sup>+</sup> ..... 68
- Self diffusivity, concentration dependence ..... 360*f*
- Separation factor, ZSM-5 ..... 75, 76*r*
- Shape-selective polymerization
- olefins over HZSM-5 ..... 384
- Silicon-aluminum
- ordering ..... 145
- aluminosilicate framework ..... 163
- zeolite X ..... 165, 166*f*
- Silicon-aluminum ratio
- aluminosilicate ..... 163
- effect on ordering in framework ..... 165, 167*f*
- formula ..... 163
- NaA zeolite ..... 203
- Sieving action, ZSM-5 ..... 68, 70*f*
- Silicalite ..... 79, 110
- Silicalite channel system ..... 125*f*
- Silicalite polymorph of SiO<sub>2</sub> ..... 123
- Silica-alumina molar ratio ..... 15
- Silica-sodium oxide molar ratio ..... 11
- Siliceous zeolites, effect of acidic solutions ..... 68
- Silicon-29 MASNMR ..... 243
- resonances, discussion ..... 160, 161*r*
- spectra ..... 164*f*
- silicalite, detection of aluminum ..... 177, 178*f*
- silicalite, detection of tetrahedral sites ..... 177, 178*f*
- six-coordinated silicon zeolites ..... 174
- Silicon-29 NMR chemical shifts, various samples ..... 146-49
- Silicon-29 NMR data
- comparison of simulated with experimental ..... 225, 229*f*, 230
- discussion, faujasite and 2K4 ..... 246-53*f*
- gallium faujasites and a gallium sodalite ..... 231
- Na-A zeolite ..... 143
- Na faujasites ..... 249*r*
- statistical interpretation of zeolites.. 217
- ZK4 ..... 273, 275, 276*r*
- Silicon-29 NMR shifts, geometrical and steric effects ..... 149

|   |                     |
|---|---------------------|
| Silicon-29 NMR spectra                      |                     |
| comparison of faujasitic and ZK4            | 280f                |
| faujasites                                  | 236f, 243, 251      |
| peak definition                             | 219                 |
| peak intensities vs. composition,           |                     |
| ZK4   | 279f                |
| various zeolites                            | 235f                |
| in ZK4, calculation                         | 243, 262-65         |
| Silicon-aluminum ratio                      |                     |
| equation                                    | 273                 |
| various                                     | 41                  |
| zeolite particles                           | 199                 |
| Silicon-oxygen bond, zeolite A              | 135f                |
| Silica polymorphs, microporous              | 79                  |
| Silver atom species                         |                     |
| X- and Y-zeolites                           | 292                 |
| A-zeolites                                  | 289                 |
| Silver atoms and clusters                   |                     |
| faujasite zeolites, results and             |                     |
| discussion                                  | 409, 416-36         |
| rare gas solids, results and                |                     |
| discussion                                  | 409, 410-16         |
| Silver clusters, in cavities of zeolites    |                     |
| A, X, and Y                                 | 416                 |
| Silver ion                                  |                     |
| in A-zeolites                               | 287                 |
| conversion to silver atom                   | 287                 |
| catalytic reactions in exchanged            |                     |
| zeolites                                    | 283                 |
| Silver isotropic hyperfine coupling,        |                     |
| X and Y zeolites                            | 292                 |
| Silver species                              |                     |
| formation schemes in rare gas               |                     |
| solids                                      | 414s, 415s          |
| position and types in faujasite             |                     |
| zeolites                                    | 417, 419            |
| relaxation processes in rare gas            |                     |
| solids                                      | 411                 |
| Silver zeolite-A                            | 132-37              |
| Simulation of NMR spectra, various          |                     |
| zeolites                                    | 220-25              |
| Single-crystal photographs,                 |                     |
| TPA(OH)-AlPO <sub>4</sub> #5                | 110                 |
| Single-crystal x-ray                        | 131                 |
| Six-coordinated silicon zeolites            | 174, 176f           |
| Sodalite                                    | 81                  |
| cage sub-units in faujasite                 |                     |
| structure                                   | 244-46              |
| framework structure                         | 88, 92f             |
| Sodalite-type phase, new                    | 24                  |
| Sodium oxide-silica molar ratio             | 11                  |
| Sodium zeolite-A                            |                     |
| lattice parameters                          | 137                 |
| Sodium zeolite-Y—See Faujasite              | 141                 |
| Sodium ZK-4                                 | 131-41              |
| Sorption diffusivities and NMR,             |                     |
| comparison                                  | 353                 |
| Sorption isotherms, normal and              |                     |
| isobutane                                   | 29                  |
| Sorption and PFG NMR                        |                     |
| measurements, comparison                    | 363                 |
| Species selectors                           | 15                  |
| Spectroscopic properties, silver            |                     |
| species in rare gas solids                  |                     |
| and faujasite zeolites,                     |                     |
| compared                                    | 428, 430, 431f, 432 |
| Spread-eagle shape, tetra- <i>n</i> -propyl |                     |
| ammonium bromide                            | 117                 |
| Square planar lattice, occupation           |                     |
| of sites by Al-Si under Loewen-             |                     |
| stein's restriction                         | 222, 223f, 224f     |
|   | 225, 226f           |
| Stability of zeolites under electron        |                     |
| bombardment                                 | 201                 |
| Statistical interpretation, silicon-29      |                     |
| NMR of zeolites                             | 217                 |
| Steroplot                                   |                     |
| aluminophosphate molecular sieve            | 112f                |
| sodalite unit and one tetrahedral           |                     |
| unit in dSrA                                | 124f                |
| Stereoview of TPAF complex                  | 127f                |
| Stishovite                                  | 174                 |
| Strained double four-membered               |                     |
| rings, zeolite A                            | 171                 |
| Structural analysis, A-type zeolites        | 151-55              |
| Structural stabilization                    | 47, 56              |
| fluorinated zeolite                         | 54                  |
| Structure defects from fluorination         | 55                  |
| Structure-template specificity,             |                     |
| synthesis of aluminophosphate               | 88                  |
| Study of structural properties, zeolites    | 131                 |
| Superlattice intensity maxima and           |                     |
| periodicity                                 | 192                 |
| Superlattice reflection, thallium           |                     |
| zeolite-A                                   | 139f                |
| Support interactions, silver species        |                     |
| in faujasite zeolites                       | 427-34              |
| Surface character, aluminophosphate         |                     |
| molecular sieves                            | 105                 |
| Surface hydrophobicity                      | 45, 49              |
| Surface morphology, zeolite particles       | 203                 |
| Surface organophilicity                     | 45                  |
| Synthesis data, ZK4                         | 271t                |
| Synthesis gas conversion                    |                     |
| effect of Bronsted acid sites               | 405                 |
| effect of particle size                     | 402                 |
| zeolite-supported metal catalysts           | 397                 |
| Synthesis of zeolite A, variables           | 18                  |
| Synthesis of zeolites A, X, and Y           | 3                   |
| Synthesis of zeolites                       |                     |
| batch composition ranges                    | 3                   |
| effect of batch composition                 | 7t, 8f, 9f          |
| experimental batch composition              | 5f                  |
| influencing factors                         | 3                   |

- Synthesis of zeolites—*Continued*  
 offretite-type ..... 21  
 patented batch compositions ..... 4*f*
- Synthesis of aluminophosphate  
 molecular sieves ..... 80
- Synthetic faujasite, neutron  
 diffraction studies ..... 131
- Synthetic routes to ZK4 ..... 269–70
- T**
- TBAF complex, occupation in  
 silicalite ..... 123
- Temperature, effect on preparation of  
 iron-containing zeolites ..... 314
- Template mechanism  
 crystallization ..... 123  
 change of shape ..... 128
- Template packing in A1PO4-5  
 structure ..... 101*f*
- Template steric component in  
 aluminophosphate molecular  
 sieve synthesis ..... 88
- Templates  
 in aluminophosphate synthesis,  
 various ..... 93  
 discussion ..... 80, 88–100  
 position in aluminophosphate  
 framework ..... 93  
 synthesis of A1PO4-5 ..... 96*f*  
 synthesis of A1PO4-17 ..... 94*f*
- Tetrahedral shape, TPAF complex ..... 117
- Tetrahedral sites  
 detection in silicon-29  
 MASNMR ..... 177, 178*f*  
 faujasitic framework ..... 182
- Tetrahedrally coordinated oxide  
 networks ..... 80
- Tetramethylammonium—See also TMA
- Tetramethylammonium-  
 KOH-NaOH ..... 21
- Tetramethylammonium (TMA)  
 template ..... 88
- Tetrapropylammonium—See also TPA
- Tetrapropylammonium cations,  
 ZSM-5 ..... 60
- Tetrapropylammonium fluoride  
 silicalite ..... 123, 124–127*f*, 128
- Thallium atoms, positions ..... 133, 136*f*
- Thallium zeolite ..... 132–37
- Thaumasite ..... 174
- Theoretical aluminum neighbor  
 distributions, ordered sodalite  
 case building units ..... 261*t*
- Theoretical and experimental  
 aluminum neighbor distributions,  
 faujasite ..... 259*t*
- Thermal activation, iron carbonyl  
 complexes ..... 303
- Thermal decay, silver atom species  
 in A-zeolite ..... 289
- Thermal stability  
 aluminophosphate molecular  
 sieves ..... 100–105  
 crystals ..... 22
- Thermogravimetric curve, offretite ..... 29, 31*f*
- Thermogravimetric system ..... 22, 23*f*
- Thermogravimetry data, acidity  
 in zeolites ..... 371–376*t*
- Three pulse electron spin echo spectra  
 cupric ion species in A-zeolite ..... 295*f*  
 silver atom in A-zeolite ..... 291
- Timetable selectors ..... 15
- TMA—See also Tetramethyl-  
 ammonium ..... 93
- TMA trapped by crystallization  
 sodalite cases ..... 93
- TMA-Rb sodalite, x-ray data ..... 25*t*
- TMA ions ..... 29
- TPA—See also Tetrapropyl-  
 ammonium
- TPA, template role ..... 123
- TPA(OH) complex, shape ..... 113
- TPA(OH)-A1PO4 #5 ..... 113  
 atomic positions and displacements ..... 115*t*  
 crystal structure ..... 109  
 interatomic distances and angles ..... 116*t*
- Transient adsorption or desorption  
 rate measurements, discussion  
 of model systems ..... 345
- Transition metal carbonyl, synthesis  
 and structure ..... 456–61
- Triangular component diagram for  
 synthesis of ZK4 ..... 272*f*
- Triangular coordinate graphics ..... 3
- Tridymite ..... 100, 110
- Tripod configuration, TPA(OH)  
 complex ..... 117
- Twinnings in faujasite  
 crystals ..... 182, 184*f*, 185*f*
- U**
- Unit cell data, sodium exchanged  
 samples of ZK4 ..... 278*t*
- V**
- Variable atomic coordinates ..... 131, 141
- Variscite ..... 80
- W**
- Water adsorption  
 fluorinated zeolites ..... 49, 52*t*

- Water adsorption—*Continued*  
 isotherms for selected aluminophosphate molecular sieves ..... 102, 104*f*, 105
- Water gas shift activity  
 effect of nature of ruthenium-zeolite complex ..... 449, 450*f*, 451*t*  
 influence of various pretreatment procedures ..... 440-46
- Water molecule modulation, detection ..... 290
- Water-sodium oxide molar ratio, control of reaction time and related to zeolite type ..... 11
- Weak superlattice reflections ..... 137
- X**
- x-Ray diffraction, changes in peak intensities and shifting in peak positions ..... 54
- x-Ray powder diffraction data  
 aluminophosphate molecular sieves ..... 81, 82*t*  
 fluorine treated zeolites ..... 45, 46*f*  
 mixed metal zeolites ..... 304  
 Scherzer-Fort preparations ..... 308
- x-Ray powder diffraction pattern  
 AlPO<sub>4</sub>-5 ..... 81, 83*f*  
 AlPO<sub>4</sub>-11 ..... 81, 86*f*  
 AlPO<sub>4</sub>-17 and erionite ..... 88, 89*f*  
 AlPO<sub>4</sub>-20 and a TMA-sodalite ..... 88, 91*f*  
 disadvantages ..... 268  
 various ..... 111*f*, 114*f*
- x-Ray scattering studies of metal-containing zeolite, problems ..... 320
- x-Ray structural refinements, zeolite A and silicalite ..... 119
- Z**
- Zeolite catalytic selectivity, related to channel size ..... 119
- Zeolite conversion ..... 11, 16
- Zeolite crystallization, function of time ..... 10*f*
- Zeolite gas absorption, discussion ..... 333
- Zeolite modification by direct fluorination ..... 41
- Zeolite-NaY, structure image ..... 182, 183*f*
- Zeolite particles, typical shapes ..... 203, 205*f*-207*f*
- Zeolite phase transformation, effect of reaction time ..... 12*f*, 13*f*, 14*f*
- Zeolite structure, A, X, and Y zeolites ..... 287, 288*f*
- Zeolite synthesis  
 A, X, and Y ..... 3  
 batch composition ranges ..... 3  
 effect of batch composition ..... 8*f*, 9*f*  
 experimental batch compositions .. 5*f*  
 influencing factors ..... 3  
 patented batch compositions ..... 4*f*  
 variables ..... 18
- Zeolite systems, effect of crystal size and sample bed configuration .... 346
- Zeolite trapping site, metal atoms  
 discussion of structure and symmetry ..... 423, 424*f*
- Zeolite type  
 related to crystallization time ..... 7*t*  
 related water to sodium oxide molar ratio ..... 11
- Zeolite X and Y framework, computational procedure ..... 225, 227*f*, 228*f*
- Zeolite-A  
 construction ..... 132  
 neutron diffraction studies ..... 131
- Zeolite-supported iron catalysts, characterization studies ..... 399
- Zeolitic gallosilicates ..... 162, 174
- Zone-axis orientations, ZSM-5 ..... 186
- ZSM-5  
 anionic field strength ..... 77  
 chemical profiles across particles ..... 203, 209*f*-213*f*  
 crystal morphologies ..... 60, 62*f*  
 divalent cations, isotherms ..... 68, 72-74*f*  
 electrostatic energy interactions ..... 76  
 functional site ..... 64  
 hindrance ..... 60  
 hydronium ion exchange isotherm .. 69*f*  
 inorganic cation exchange properties ..... 59
- ion exchange isotherms, various ..... 63-68, 65*f*-67*f*, 69*f*-74*f*
- ion exchange selectivity ..... 75
- molecular sieve ..... 123
- salt occlusions ..... 60
- selectivity correlation ..... 68
- separation factor ..... 76*t*
- sieving action ..... 68, 70*f*
- structure ..... 60, 61*f*
- synthesis ..... 60, 62*f*, 63*t*
- tetrapropylammonium cations ..... 60